UNIVERSITY OF OKLAHOMA

GRADUATE COLLEGE

EFFECTS OF FUEL UNSATURATION ON POLLUTANT EMISSIONS FROM THE LAMINAR FLAMES OF PREVAPORIZED PETROLEUM AND BIODIESEL BLENDS IN AIR

A DISSERTATION

SUBMITTED TO THE GRADUATE FACULTY

in partial fulfillment of the requirements for the

Degree of

DOCTOR OF PHILOSOPHY

By

ARUN BALAKRISHNAN
Norman, Oklahoma
2017

EFFECTS OF FUEL UNSATURATION ON POLLUTANT EMISSIONS FROM THE LAMINAR FLAMES OF PREVAPORIZED PETROLEUM AND BIODIESEL BLENDS IN AIR

A DISSERTATION APPROVED FOR THE
SCHOOL OF AEROSPACE AND MECHANICAL ENGINEERING

BY

_____
Dr. Subramanyam Gollahalli, Co-Chair

_____
Dr. Ramkumar Parthasarathy, Co-Chair

_____
Dr. Wilson Merchán-Merchán

_____
Dr. Li Song

_____
Dr. Steven Crossley

This dissertation is dedicated to

all the engineers who constantly work on making this world

a better place to live

கற்க கசடறக் கற்பவை கற்றபின்

நிற்க அதற்குத் தக.

-திருக்குறள் (எண்: 391)

Let a man learn thoroughly whatever he may learn,

and let his conduct be worthy of his learning.

-Thirukkural (Verse: 391)

(A classical Tamil literature)

ACKNOWLEDGEMENTS

I sincerely thank and express my deep sense of gratitude to my 'GURUs' Dr. Subramanyam Gollahalli and Dr. Ramkumar Parthasarathy, for their mentoring and remarkable guidance for the past five years. I am indebted to the constant motivation and thought provoking discussions during our combustion lab research meetings that evolved me into a better individual both professionally and personally. They always believed in my potential and posed challenges that have brought the best out of me in my academic and research life. I thank Dr. Gollahalli for also sharing his professional and personal life experiences with me that would enable me taking wiser decisions at various stages of my life. Over the course of my stay, he has taught me valuable lessons, particularly on logical thinking with fundamental concepts and developing independence and originality in research, which I will hold on to, throughout my career. I thank Dr. Parthasarathy who has demonstrated what it is to be dedicated and passionate about teaching and learning; his patience while correcting my writing samples and reports has always amazed me and I am always thankful for his guidance and advice throughout my degree program. I thank both my advisors for financially supporting me throughout my stay at OU, allowing me to focus solely on the completion of the degree.

I thank my dissertation committee members Dr. Wilson Merchan-Merchan, Dr. Li Song and Dr. Steven Crossley for their belief in my ability to do an independent dissertation work. I value their commitment, time and constructive comments that improved the quality of my work. I also thank my former dissertation committee member Dr. Richard

Mallinson for his valuable comments from the chemical engineering perspective. I would like to dedicate a special mention to Dr. Charles Westbrook, Scientist at Lawrence Livermore National laboratory for helping and providing with the chemical kinetic mechanisms for biodiesel combustion.

I would like to thank the financial assistance provided by the NSF-EPSCoR, U.S. Department of Energy and John Zink Company. I extend my humble regards to the school of Aerospace and Mechanical Engineering (AME) at the University of Oklahoma for providing me financial assistance in the form of teaching and research assistantships, travel support for conferences and awarded me with graduate scholarships like Thomas Milam Sr. Graduate scholarship and Chevron Centennial Scholarship. These scholarships from AME helped me to concentrate on my research work without having to think much about my financial burdens and inspired me to progress with additional momentum.

I thank Mr. Billy Mays and Mr. Greg Williams of AME Machine shop for their help in the design modifications and fabrication of my experimental setup. I thank the present and past members of the Combustion and Flame Dynamics Laboratory: Diego Romero, Victor Tran, Cory Morton, Michael Richichi, Mathew Smeltzer, Katherine Willingham, Scott Carter, Mohammad Imran, Alexander Spens and Flavio Moreno, for the several fruitful discussions we had on every possible topic. I thank Dr. Chodchanok Mink Attaphong for her valuable inputs on authoring journal articles and discussions on surfactants and micro-emulsion fuels.

I also thank OU Indian Student Association, various student associations, AME - Graduate student community (GSC), my past and present room-mates for making my

life in Norman pleasant. A special appreciation goes to my best friends, Kavitha and Sabarisha, whom I can always depend upon regardless of my easy and hard times. I feel indebted for their love and support that always helped me overcoming my challenges.

My accomplishments today root back to the unparalleled guidance and undaunted support from my undergraduate thesis advisor - Dr. Dharmahinder Singh Chand, high school physics teacher - Mr. Gajendiran and high school mathematics teacher - Ms. Latha who always has faith in my ability to succeed.

I could not find words to express my deep sense of gratitude to my Amma and Appa for their unconditional love and sacrifices to provide me the best in my life. I thank my sister Gayathri who has always been a good friend and partner of mine in all my mischievous childhood acts. She always stood with me and provided support at my tougher times. Finally, I dedicate this dissertation to the friends, family and well-wishers who always strive for a pleasant smile on my face.

Thank you!

TABLE OF CONTENTS

LIST OF TABLES

LIST OF FIGURES

ABSTRACT

Biodiesels, considered as alternative fuels to petroleum diesel, are defined as fatty acid methyl or ethyl esters derived from triglycerides of vegetable oils or animal fats. The utilization of biodiesels reduces greenhouse gas emissions, assists in sustainable energy development, and enhances energy independence due to the renewable and biodegradable nature of these fuels. Besides being close to environmentally carbon-neutral, biodiesels have properties similar to those of petroleum fuels with comparable energy content and can be blended with petroleum fuels and used in existing engines without major modifications. Furthermore, they contain fuel-bound oxygen while being free of aromatic content; therefore, blends of biodiesels and petroleum fuels present the capability of reducing soot emissions from engines. Blending of biodiesels with petroleum fuels is considered feasible in the near term due to limited current availability of the commercial biodiesels and the lack of experience on the long term effects of storage, handling, transportation and combustion of these biodiesels and blends on the engines and the environment. Several studies in engine literature have revealed that the use of biodiesels and their blends in a compression ignition engine resulted in an appreciable reduction in the emissions of particulate matter (PM), unburnt hydrocarbons (UHC) and CO, compared to the use of diesel fuel. However, in case of nitric oxides (NOx) emissions, the results are variable and case dependent. The average effect of biodiesel on NOx emission was seen to be small, but with a high variance, which resulted in difficulty in discerning a clear pattern. Nitric oxides are categorized as one of the key pollutants in engine emissions that can affect human respiratory system and vegetation. Therefore, it is crucial to understand the effect of various fuel and engine

operating parameters on biodiesel NOx emissions to develop enhanced mitigation and abatement techniques for the widespread use of biodiesels in transportation. In engine literature, fuel unsaturation has been attributed to the observed change in NOx emissions with the use of biodiesels in compression ignition engines. Several results indicated the existence of a strong relationship between NOx emissions and iodine number, used as a measure of the fuel unsaturation of vegetable oils and fatty acid methyl esters. However, relevance of iodine number as a measure of total unsaturation of petroleum fuels like diesel, Jet A and their blends with biodiesels is debatable due to the significant differences in the reactivity of iodine with petroleum fuels. Bromine number, used as a measure of aliphatic unsaturation in petrofuel samples, does not account for the aromatic unsaturation from petroleum fuels. Hence, a common parameter that is relevant for both biodiesels and petroleum fuels needs to be identified to quantify the fuel unsaturation. A parameter, termed "Degree of Unsaturation (DOU)," which accounts for the total unsaturation of the fuel from all sources such as double and triple bonds, aromatics and other ring structures irrespective of the families of the fuels (alkanes, alkenes, alkynes, aromatics, ether or ester) that has been used in organic chemistry literature is proposed in this work and identified as a potential indicator of NOx emissions from biodiesel blends. In this dissertation work, experimental correlations between DOU and the NO emission index on a mass basis (EI_{NO}) in laminar flames of neat prevaporized fuels such as methyl oleate (MO), soy methyl ester (SME), canola methyl ester (CME), rapeseed methyl ester (RME), palm methyl ester (PME), heptane, toluene, diesel, JetA and petroleum/biodiesel blends at various equivalence ratios (Φ = 0.9, 1.0, 1.2 and 1.5) are developed. The NO emission

index of flames of biodiesel/petroleum blends was found to increase with DOU, but with varying trends depending on their families of origin. The effects of DOU on EI_{NO} were significantly influenced by the equivalence ratio, with the maximum influence at an equivalence ratio of 1.2. At the equivalence ratio (Φ) of 1.2, EI_{NO} increased from 2.4 g/kg at a DOU value of 1.7 to 4.4 g/kg at a DOU of 3.0 among biodiesels and their blends with petroleum fuel; toluene flame (100% aromatic content with a DOU of 4) produced an EI_{NO} of 6.94 g/kg. It is found that both NO and CO emission indices from the tested flames are influenced by two major parameters - equivalence ratio and total fuel unsaturation. Further, the presence of fuel aromatic content and the family of fuel were observed to significantly influence NOx formation particularly near stoichiometric equivalence ratios. Based on both global and inflame emission results along with the numerical analysis of tested flames, it is concluded that fuel unsaturation, fuel aromatic content, equivalence ratio and family of the respective fuel, together influence the NOx emissions in flames. The net effects of these parameters at a given condition establish the amount of EI_{NO} produced from the corresponding flames due to the fuel chemistry effect alone. Hence, DOU provides a common platform to compare and quantify the effects of fuel unsaturation across different fuel families and can be employed as an indicator of NOx emissions. DOU can be evaluated based on the average molecular formula of the fuel alone without involving complex and expensive experimental procedures such as those involved in the measurement of iodine number. The propensity of a biofuel blend for NOx emissions during combustion can be quickly ascertained with the successful development of Degree of Unsaturation (DOU) parameter, thus, providing a valuable tool for fuel developers.

PREFACE

This dissertation work is aimed at the experimental and numerical investigation of fuel unsaturation effects on the pollutant emissions from the laminar flames of prevaporized biodiesels (from a variety of feed stocks) and their blends with petroleum diesel with air as an oxidizer. This dissertation work is based on and contains information and data from the following published articles.

1. **Balakrishnan, A**., Parthasarathy, R., and Gollahalli, S. (2016) "Effects of degree of fuel unsaturation on NOx emission from petroleum and biofuel flames," *Fuel*, **182**, 798-806. doi: 10.1016/j.fuel.2016.06.052.

2. **Balakrishnan, A**., Parthasarathy, R., and Gollahalli, S. (2016) "A review on the effects of biodiesel blends on compression ignition engine NOx emissions," *Journal of Energy and Environmental Sustainability*, **1**, 67–76.

3. **Balakrishnan, A**., Parthasarathy, R., and Gollahalli, S. (2016) "Combustion characteristics of partially premixed prevaporized palm methyl ester and Jet A fuel blends," *Journal of Energy Resources Technology*, **138**(1), 012202. DOI: 10.1115/1.4031966.

4. Gollahalli, S., Parthasarathy, R., and **Balakrishnan, A**. (2014) "Flame characteristics of vaporized renewable fuels and their blends with petroleum fuels", In Novel Combustion Concepts for Sustainable Energy Development (pp. 297-328). Springer India. DOI: 10.1007/978-81-322-2211-8_13.

CHAPTER 1 INTRODUCTION

The technological advancements and growing energy demands in the recent past have emphasized the significance of demand for energy resources across the world. Until now, non-renewable fossil fuels account for major portion of the energy generated and consumed. According to the Annual Energy review report by the Unites States Energy Information Administration (2016), between 2010 and 2015, fossil fuels accounted for approximately 82% of energy consumed in the Unites States. Sources such as renewable energy and nuclear power accounted for 9.5% and 8.5% respectively (Figure 1.1). This report surveyed the various renewable energy resources utilized for the energy production; it was found that hydroelectric power topped the table and it accounted for 25% of energy production among the renewables, while biofuels accounted for 22% and wood (biomass) accounted for 21% (Figure 1.2). These values seemed to be increasing in the last few decades. Figure 1.3 shows the sector wise energy consumption in the United States; Industrial sector accounted for 32% of energy consumption and the energy consumption by transportation sector was estimated to be 28%. Among this 28% of energy consumption by transportation sector, 85% of energy need was still satisfied by petroleum fuels while less than 10% was contributed by biofuels (9%) and natural gas (6%). Moreover, the energy consumption by energy sector is predicted to increase by 30% in 2040 which inturn increase the dependence on fossil fuels for the energy requirements. In spite of the recent technological advancements in the petroleum industry such as horizontal drilling and hydraulic fracturing, the energy industry cannot completely rely on these fossil fuels because of

their non-renewable nature. In addition, the conventional methods of electricity production and energy production for transportation involve burning of fossil fuels or coal that resulted in the increase of CO_2 emissions levels in the atmosphere.

Global warming, defined as a gradual increase in overall temperature of the earth's atmosphere, is generally attributed to greenhouse gases such as CO_2 and other volatile organic compounds. The Intergovernmental Panel on Climate Change (IPCC), in its fourth assessment review (AR4 2007), reported that scientists were more than 90% certain that most of global warming was being caused by increasing concentrations of greenhouse gases produced by human activities. (National Research Council, 2010). Affirming these findings in 2013, the IPCC stated that the largest driver of global warming is carbon dioxide (CO_2) emissions from fossil fuel combustion, cement production, and land use changes such as deforestation. In addition, the unburnt hydrocarbons and pollutants such as CO and NOx that are formed during combustion have significant impact on the environment.

Major steps have been taken to consider the renewable energy resources to reduce the dependence on fossil fuels. In the transportation sector, focus has been shifted to the consumption of alternative transportation fuels such as ethanol and biodiesel (produced by the trans-esterification of vegetable oils, to be discussed subsequently). Biodiesels are considered to be close to carbon-neutral because they do not result in a net increase in atmospheric greenhouse gases.

As shown in Figure 1.3, biofuels account for only 9% energy consumption in the transportation sector. These values indicate that commercialization of biofuels is still in

a primitive stage, however, the enegy consumption in the form of biofuels is continued to grow for the past 20 years. Figure 1.4 shows the energy consumption in the form of biofuels by transportation sector, there was a consistent increase in consumption, particulalry in the last 10 years; biofuels contributed to about 340 trillion Btu in 2005 while this value was increased by three folds to 1350 trillion Btu in 2015. These numbers indicate the biofuel consumption status in the United States only. Biodiesels are getting popular across the world, particularly soy, canola and rapeseed based biodiesels in the Canada and Europe; palm, jatropha, karanja and other vegetable feedstock based biodiesels in the south east Asia and other countries.

In the United States, the overall consumption of alternative transportation fuels increased by almost 13% in 2011. Under the implementation of Renewable Fuel Standard, consumption of biodiesel grew almost 240% between 2010 and 2011. Aviation biofuel, used for aircraft propulsion, is considered to be the primary means by which the aviation industry can reduce its carbon footprint. After a multi-year technical review from aircraft makers, engine manufacturers and oil companies, biofuels were approved for commercial use in July 2011(ASTM approval of biofuels). Since then, some airlines have experimented with using biofuels on commercial flights. A well-established knowledge base of the combustion of biodiesels and their blends with petroleum diesel and Jet A fuel is required for the widespread use of biodiesels for the energy needs.

1.1 Transesterification and Biodiesels

Fatty acid alkyl esters, commonly known as biodiesels are produced by the trans-esterification of triglycerides from wide range of feedstocks especially oils from local grown crops and recycled cooking oils. Transesterification process involves mixing of the triglyceride from the feedstock at an elevated temperature (around100^{o}C) with an alcohol (e.g. ethanol or methanol) and catalyst (e.g. sodium hydroxide) results in the formation of methyl ester biodiesels (if methanol is used) and ethyl ester biodiesels (if ethanol is used) as well as a glycerol product (Ma and Hanna, 1999) which can later be used in food, medical, pharmaceutical, or cosmetic products.

1.2 Use of biodiesels - merits and challenges

The widespread use of biodiesel is encouraged based on the following positive attributes (Tyson, 2004):

- Biodiesel is renewable and non-petroleum-based;
- Biodiesel can reduce greenhouse gas emissions;
- Biodiesel is less toxic and is biodegradable;
- Biodiesel can reduce tailpipe emissions of particulate matter (PM), CO, HC, and other air toxics;
- No or minor modifications are needed for the traditional compression ignition engine to use biodiesel;
- Biodiesel compression ignition engines are similar in operation as conventionally-fueled diesel engines.

There are few challenges to overcome in realizing the widespread market of biodiesels as follows:

- Lower volatility and higher viscosity of biodiesel and less favorable cold flow properties.
- Lower storage stability and material compatibility issue
- Sustainable production issues and high production cost because of transesterification and expensive feed stocks.
- Food vs Fuel issues.

1.3 Combustion in diesel engine - A black box approach

Industrial and automotive engine/fuel testing techniques typically involve measurement of various parameters such as gaseous pollutant emissions, particulate matter, cetane/octane number, BHP, and BMEP for various fuel inputs. Figure 1.5 shows a diagram of how fuels are typically tested in an engine, where different fuels are supplied and the outputs are measured. However, several variables other than the fuel chemistry such as fuel atomization, droplet evaporation, injection timing and ignition delay also influence the output variables. This black box approach has limitations in the development and testing of new fuels. Limitations are further evident when fuels are available in small quantities which cannot be tested in applications requiring large fuel flow rates such as that of an engine or turbine. It is necessary to better understand fuels on a chemistry basis by delineating the complex variables seen in applications such as an engine.

1.4 Nitric oxide emissions and their environmental impacts

Nitrogen oxides present in atmosphere induce photochemical smog formation. The nitrogen oxides of environmental interest are NO, N_2O and NO_2 among which the NO and NO_2 are collectively referred to as NO_x (Lissianski et al., 2000 and Fattah et al., 2013). The more stable NO always predominates over the other oxides of nitrogen in the combustion flue gas. The coupled concentrations of NO and NO_2 are decided by the fast-radical reactions: NO_2 reacts with O, H and OH to form NO and NO reacts with HO_2 to form NO_2 (Lissianski et al., 2000). In several high-temperature combustion processes, the predominant form of NO_x is produced as nitric oxide (NO), while the concentrations of NO_2 are typically less than 5% of total NO_x levels. NO_x abatement techniques require a basic understanding of the kinetics behind the NO_x-forming reactions. Although the NO_x reaction mechanisms have been detailed in the literature, the following section outlines some recent literature pertaining to the various mechanisms contributing to the formation of NO, and the general reactions involved in the formation of NO_2 and N_2O.

The atmospheric nitrogen is the prevalent source of nitrogen for NO production during the combustion of petroleum and FAME (Fatty Acid Methyl Ester)-derived fuels with air as the oxidizer. The thermal (Zeldovich), prompt (Fenimore), N_2O pathway, fuel-bound nitrogen and the NNH mechanism are the identified mechanisms for NO formation in diesel combustion which are summarized below.

1.4.1. Thermal mechanism

Thermal mechanism is the primary route by which NO formation occurs at temperatures typically above 1800K (Hoekman and Robbins, 2012). At this high temperature, nitrogen (N_2) and oxygen (O_2) react through a set of chemical reactions in which the NO formation rate increases exponentially with temperature. The fundamental kinetic equations for thermal NO formation (Dean and Bozzelli, 2000) are exemplified by the following chemical reactions:

$$O + N_2 \leftrightarrow NO + N \quad (1.1)$$

$$N + O_2 \leftrightarrow NO + O \quad (1.2)$$

$$N + OH \leftrightarrow NO + H \quad (1.3)$$

NO reaction rate is influenced by the temperature, residence time and concentrations of nitrogen and oxygen in the combustion environment (Varatharajan and Cheralathan, 2012).

1.4.2. Prompt mechanism

Fenimore identified another important pathway resulting in NO formation which is termed as prompt NO mechanism. It is significant in some combustion environments where low-temperature fuel-rich conditions prevail while the residence time is short (Fenimore, 1971). Prompt NO is produced when hydrocarbon radicals react with nitrogen to form highly reactive cyano radicals such as HCN in the combustion chamber (Fernando et al., 2006). The mechanism includes a complex set of reactions

with many plausible intermediate species. Prompt NO is also more sensitive to the fuel chemistry than thermal NO because of the dependence on hydrocarbon radicals. Miller and Bowman (1989) studied the mechanism and modeling of nitrogen chemistry in combustion and concluded that the prompt NO mechanism was important in the NO formation and could not be neglected while estimating the total NO_x production, particularly in a fuel-rich combustion environment. The prompt NO mechanism involves the following set of chemical reactions (Fernando et al., 2006):

$$CH + N_2 \leftrightarrow HCN + N \quad (1.4)$$

$$CH_2 + N_2 \leftrightarrow HCN + NH \quad (1.5)$$

$$C_2 + N_2 \leftrightarrow 2\ CN \quad (1.6)$$

$$HCN + OH \leftrightarrow CN + H_2O \quad (1.7)$$

$$CN + O_2 \leftrightarrow NO + CO \quad (1.8)$$

The exact mechanism for NO production from prompt chemistry is much more complex than for thermal type because the hydrocarbon portion of the prompt scheme can come from literally several fuel hydrocarbons and partially oxidized fragments of the fuel chemistry (Studzinski et al., 1993). Prompt NO formation increases with equivalence ratio due to the availability of CH, CH_2 and HCN radicals that are prevalent in fuel-rich hydrocarbon flames. These hydrocarbon and cyano radicals are considered to be the significant contributors of prompt NO.

1.4.3. Fuel NO mechanism

Fuel NO is formed when the fuel-bound nitrogen reacts with excess oxygen during combustion and is negligible for both diesel and biodiesel combustion because of low nitrogen levels in the fuel; biodiesel has a mean nitrogen concentration of only 0.02%. The presence of nitrogen-containing compounds such as pyridine, pyrrole etc. may also tend to form more fuel NO. This is due to the weaker C-N bond present in these chemical compounds compared to the N-N bond in molecular nitrogen. The fuel NO pathway involves the formation of nitro-radicals such as HCN, NH_3, NH, or CN, which then be oxidized to form NO (Fernando et al., 2006).

1.4.4. N_2O Intermediate mechanism

The intermediate mechanism (N_2O pathway) is another essential mechanism that becomes significant in high pressure combustion processes (Dean and Bozzelli, 2000). In this mechanism, the reaction occurs between N_2 and atomic oxygen to form intermediate N_2O by a three-body recombination reaction where the collision partner M collectively represents all the molecules present in the combustion medium:

$$O + N_2 + M \leftrightarrow N_2O + M \quad (1.9)$$

Here, the molecule M is required and plays a key role in the execution of this reaction. The N_2O formed in reaction (1.9) can then react to form NO:

$$N_2O + O \leftrightarrow NO + NO \quad (1.10)$$

1.4.5. The NNH mechanism

Under certain combustion regions like flame fronts where atomic concentrations are high, Eq. (1.11) contributes to NO production.

$$O + NNH \rightarrow NO + NH \quad (1.11)$$

This mechanism requires interaction between hydrogen atoms and molecular nitrogen to form highly reactive NNH radicals which further react with atomic oxygen to form nitric oxide (Dean and Bozzelli, 2000).

1.4.6 Nitrogen dioxide (NO_2) formation mechanism

In the previous section, several reactions that led to the formation of NO were discussed. Under certain conditions, a significant amount of NO can be converted to NO_2. The fastest flame reaction (Lissianski et al., 2000) forming NO_2 is

$$HO_2 + NO \rightarrow NO_2 + OH \quad (1.12)$$

This reaction is important whenever the concentration of HO_2 is significant, typically in the temperature range of 600 to 1000 K under fuel-lean conditions. However, at higher temperatures HO_2 dissociates quickly into H atoms and O_2, and the higher prevailing concentrations of H, O and OH lead to more rapid NO_2 loss through the following reactions:

$$O + NO_2 \rightarrow NO + O_2 \quad (1.13)$$

$$H + NO_2 \rightarrow NO + OH \quad (1.14)$$

$$OH + NO_2 \rightarrow NO + HO_2 \quad (1.15)$$

This rapid loss of NO_2 is significant and is reflected as a lower NO_2 concentration in the combustion flue gas.

1.4.7 Nitrous oxide (N_2O) formation mechanism

At low combustion temperatures and high pressures, nitrous oxide formation by the ter-molecular reaction (1.9) is significant. The N_2O formed in this reaction reacts with oxygen atoms exothermally to form NO (as discussed in section 1.4.4). Various nitrogen-containing radicals contribute to the formation of N_2O:

$$NH + NO \rightarrow N_2O + H \quad (1.16)$$

$$NCO + NO \rightarrow N_2O + CO \quad (1.17)$$

However, the N_2O formed in these reactions undergoes further reactions forming NO which is more stable than N_2O (Lissianski et al., 2000).

In this section, various NO formation mechanisms and the influence of other oxides of nitrogen like NO_2 and N_2O on the overall concentration of NO were summarized. In a compression ignition engine, the combustion reactions are characterized by high temperature, varying residence time depending on the injection timing, localized fuel rich conditions (though overall fuel lean) and high pressure. These reactions favor NO formation predominantly, in different pathways described above, out of which the thermal and prompt mechanisms are considered to be significant in the biodiesel engine combustion.

1.5 Organization of the dissertation

- An introduction and background to the significance of current research problem, production and consumption of biodiesels, their merits and a comprehensive background of nitric oxide emissions together with various reaction pathways are presented and discussed in Chapter 1.
- Chapter 2 provides a comprehensive survey of literature database categorized based on various parameters that influences engine NOx emissions.
- Chapter 3 establishes the core research objectives of this dissertation work along with the motivation, background and significance of the research problem and summarizes the outcomes of this dissertation work.
- Chapter 4 constitutes the selection of fuels for the investigation, the criteria of selection, fuel properties, test conditions and the corresponding flow rate settings.
- Chapter 5 describes the experimental setup, employed instrumentation techniques to characterize the emission properties of tested flames and their operating procedures.
- Chapter 6 presents the experimental results and discussions for global NO and CO emission indices and their correlations with DOU parameter over a range of degree of unsaturation values (between DOU: 0 to DOU: 4)
- Chapter 7 presents the experimental results and discussion regarding flame appearance, in-flame radial temperature and in-flame radial species concentration measurements of species such as O_2, CO_2, CO and NO.

- Chapter 8 contains the computation analysis part of the dissertation that includes the governing equations, grid parameters, reaction mechanisms and models and the analysis of computational results in comparison with that of experimental results.
- Chapter 9 provides a general summary and conclusion of the dissertation followed by the recommendation of future investigations.

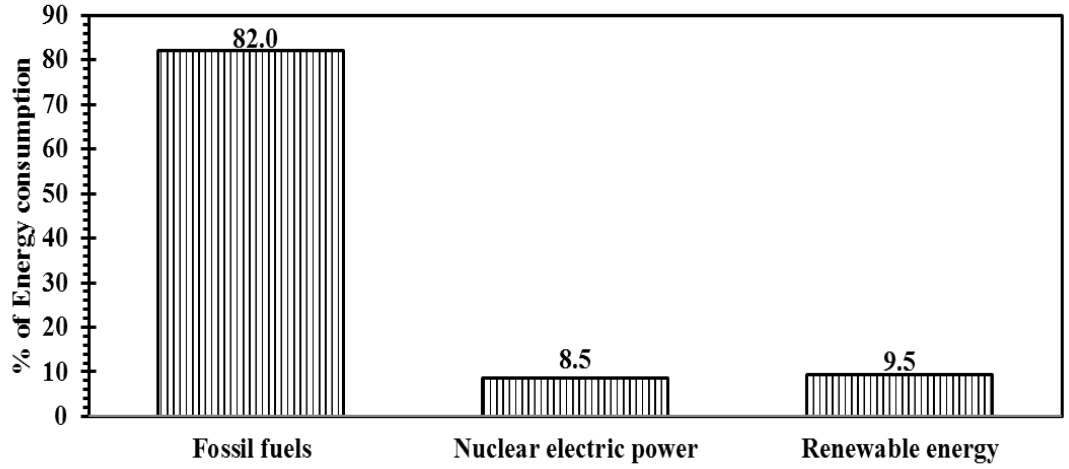

Figure 1.1 Energy consumption by resources in the United States between 2010 and 2015 (Data from US Energy information Administration, published on April 2016)

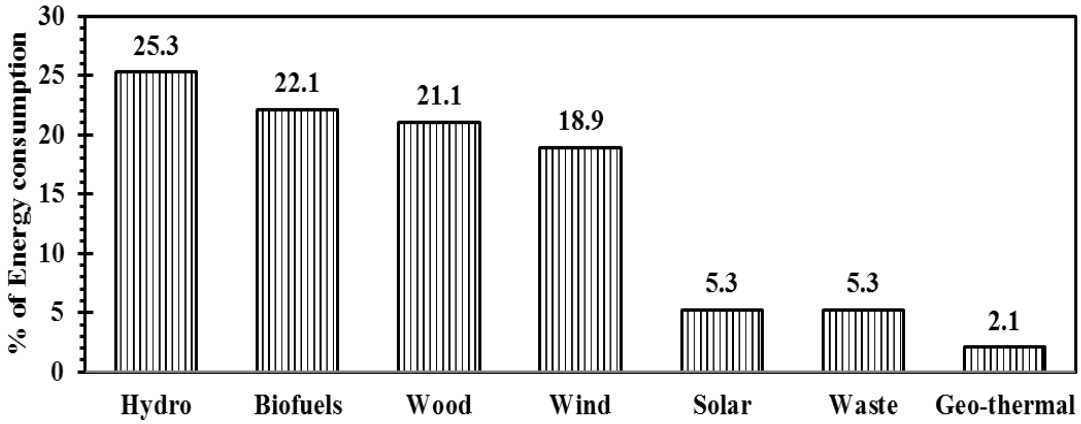

Figure 1.2 Energy consumption by renewables in the United States between 2010 and 2015 (Data from US Energy information Administration, published on April 2016)

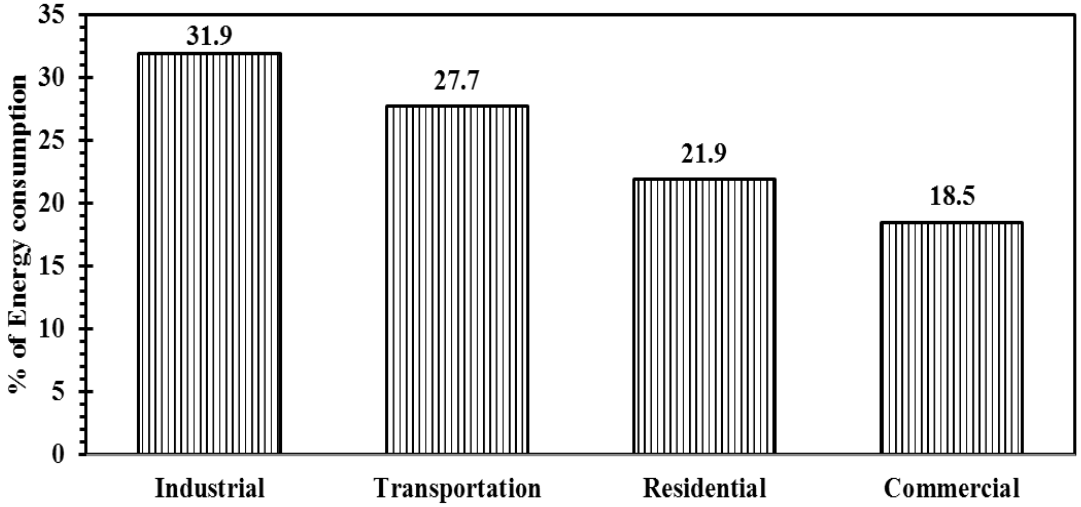

Figure 1.3 Energy consumption by sector in the United States between 2010 and 2015 (Data from US Energy information Administration, published on April 2016)

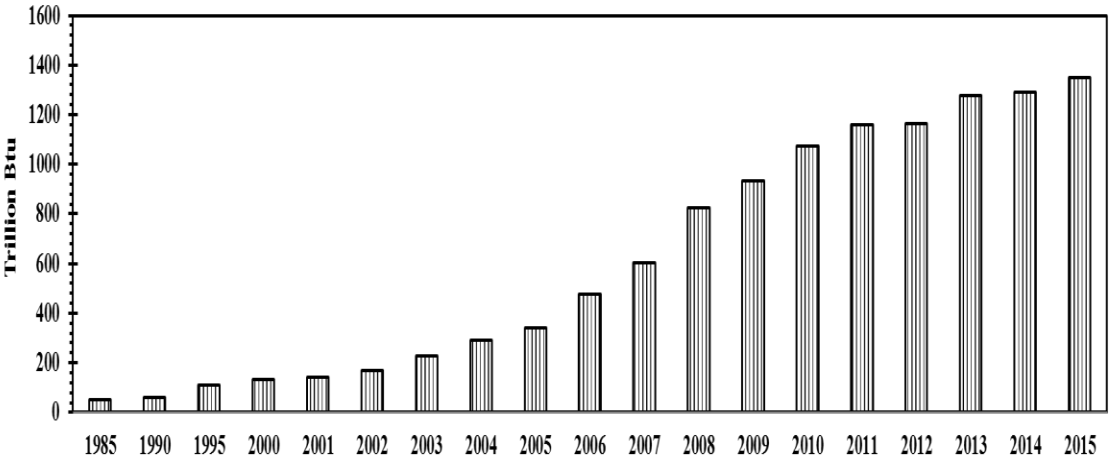

Figure 1.4 Biofuel energy consumption by transportation sector in the United States between 2010 and 2015 (Data from US Energy information Administration, published on April 2016)

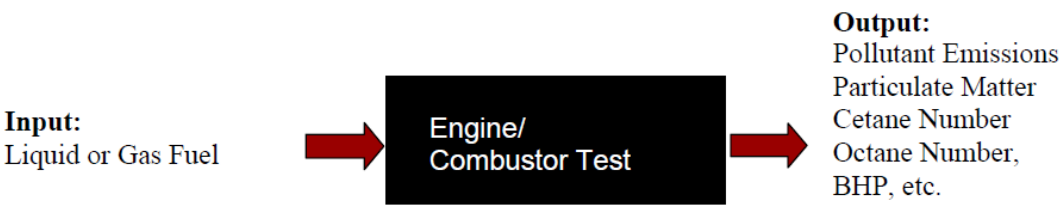

Figure 1.5 Engine testing - Black box approach

CHAPTER 2 LITERATURE REVIEW

This chapter presents a comprehensive review of the experimental and computational studies on various aspects of engine operation, fuel properties and combustion processes and their influence on the emission of NO_x measured in the engine exhaust.

2.1. Experimental studies of biodiesel impact on NOx emissions

The use of biodiesels and their blends with diesel was extensively studied in the engine environment. Although, the available results generally exhibited a reduction in the emissions of carbon monoxide (CO), hydrocarbons (HC) and particulate matter (PM) with the biodiesels, the reported NOx emissions do not exhibit definitive trends and the results are significantly influenced by many factors, including engine type and design, test cycle, start of injection, ignition delay, fuel composition, adiabatic flame temperature, radiative heat transfer, fluid dynamics and combustion phasing.

The following sections review the experimental studies on various aspects of engine operation, fuel properties and combustion processes and their influence on the emission of NOx measured in the engine exhaust. This chapter is based on and contains information from a published review article on the effects of biodiesel blends on compression ignition engine NOx emissions (Balakrishnan et al., 2016). From the available literature database, it was observed that the biodiesel effect on NOx emissions from diesel engine was influenced by different combinations of various parameters

whose coupled effects determine the amount and trend of NOx formed in a particular engine environment.

The parameters include:

- Effect of degree of fuel unsaturation
- Effect of biodiesel content
- Effect of oxygen content
- Effect of cetane and iodine numbers
- Effect of engine type and test cycle
- Effect of injection timing
- Effect of engine speed
- Effect of engine load
- Effect of fluid dynamics

The available engine literature on NOx emissions are categorized based on these parameters and discussed in the subsequent sections.

2.1.1 Biodiesel feedstock / Level of unsaturation

Several studies reported differences in NO_x emission of biodiesels from different feedstocks (Graboski et al., 2003; Hoekman and Robbins, 2012; Varatharajan and Cheralathan, 2012). Graboski et al. (2003) conducted experiments with neat methyl esters and ethyl esters in a 6- cylinder, 4- stroke, direct injection diesel engine to understand the effect of hydrocarbon chain length on the NO_x formation with saturated methyl esters based on their composition - lauric (C12), palmitic (C16) and stearic

(C18) acids and found that esters with shorter carbon chain produced higher NO_x emissions. The specific NO_x emission index of methyl stearate (C18) was about 8% lower than that of methyl laurate (C12). The authors also found a strong linear relationship between increasing NO_x with level of saturation (number of double bonds) in the fuel. For example, the specific NO_x emission index of C18 ester with three double bonds was 16% higher than that of C18 ester with one double bond. Possibly, the double bonds resulted in some pre-combustion chemistry that increased NO_x formation. Finally, the authors concluded that the NO_x emissions increased due to the decrease in average carbon chain length and increase in level of unsaturation; therefore, the most intrinsic way to revamp the emission performance was to alter the fuel chemistry, since molecular structure was the basis of fuel properties such as cetane number, density, boiling point and ignition delay. It is now widely acknowledged that increasing unsaturation and decreasing carbon chain length both lead to an increase in NO_x emission. This information has been developed from the experimental and numerical demonstration in several works (Graboski et al., 2003; Sun et al., 2010; Xue et al., 2011; Hoekman and Robbins, 2012; Varatharajan and Cheralathan, 2012; Palash et al., 2013) involving pure FAME components as well as practical biodiesel fuels employing a wide variety of engines and test cycles. Lin et al. (2009) found that palm oil methyl ester (POME) and palm kernel oil methyl ester (PKOME) resulted in a lower increase (15% and 5% respectively) in NO_x concentration (ppm) and a significant reduction (59% and 73% respectively) in smoke emissions than petroleum diesel and vegetable oil methyl ester (VOME) fuels (soy methyl ester, peanut oil methyl ester, corn oil methyl ester, sunflower oil methyl ester, rapeseed methyl ester and waste fried oil methyl

ester). The authors attributed this behavior to the more saturated carbon bonds of POME (about 50%) and PKOME (about 80%), when compared to other VOME fuels, and suggested that a fuel with more saturated carbon bonds would result in reduced NO_x emissions. The exact pathways by which the fuel composition effect influence NO_x is still ambiguous, but these parameters are recognized to critically influence the observed NO_x emissions.

2.1.2 Biodiesel content

Many publications in the literature suggest that NO_x emission increased with the biodiesel content in the blend. Lertsathapornsuk et al. (2008) noted that the NO_x emission index (g/kW-h) increased about 12% and 3% for neat palm biodiesel (B100) and B50 than diesel at 25% load condition; and an increase of about 26% and 9% in NO_x emission index for B100 and B50 while maintained the engine speed at 1500 rpm. A study by Luján et al. (2009) on high speed direct injection, 4-cylinder, diesel engine with high pressure common-rail fuel injection system during the standardized MVEG-A cycle (European Motor Vehicle Emission Group A) simulated the road load conditions. It was fueled by biodiesel (from vegetable oil) and its blends B30, B50 and B100. The authors observed that the increase in NO_x concentration (ppm) for B30, B50 and B100, compared to the base diesel fuel, was 21%, 26% and 45%, respectively. Similar trend was observed by Buyukkaya (2010) with rapeseed methyl ester/ diesel blends. Gumus and Kasifoglu (2010) tested three blends of apricot seed kernel oil methyl ester (B5, B20 and B50) with diesel fuel in a compression ignition engine and found a monotonic

increase in NO_x concentration with the biodiesel content. They attributed this behavior to the fuel-bound oxygen of the biodiesel.

On the other hand, Kalligeros et al. (2003) found a monotonic decreasing trend of NO_x concentration in the biodiesel blends containing 10%, 20%, and 50% of two types of methyl esters from sunflower oil and olive oil, in a single-cylinder diesel engine. At 3.80 kW load, B10, B20 and B50 of sunflower oil methyl ester with marine diesel produced about 3%, 5% and 6% lower NO_x concentration, while B10, B20 and B50 of olive oil methyl ester produced about 8%, 14% and 14.5% lower NO_x concentration than marine diesel. The variation in the NO_x reduction potential between the different biodiesel feedstock was attributed to the difference in cetane number of biodiesels; it was hypothesized that the higher cetane number of olive oil methyl ester (CN: 61) than that of sunflower oil methyl ester (CN: 58) resulted in increased reduction of NO_x concentration; the cetane index of marine diesel was reported as 46.

Interestingly, some other publications in the literature showed that the NO_x emissions varied non-monotonically with the biodiesel content in the blend (Labeckas and Slavinskas, 2006; Lin et al., 2007; Pereira et al., 2007; Fontaras et al., 2009; Aydin and Bayindir, 2010). The authors attributed these variations to the differences in the degree of evaporation and the combustion processes in the engine, since the calibration settings of the conventional diesel engine could have been not ideal for all proportion of biodiesel blends at all operating regimes. A non-monotonic NO_x variation was observed in a water-cooled direct injection diesel engine fueled with polanga methyl ester and its blends (20, 40, 60, and 80%) with diesel (Sahoo et al., 2007). The NO_x concentration from B20 was found to be 2% higher than diesel while neat biodiesel produced 4%

lower NO_x. The authors attributed the variations to the differences in compression ratio, residence time and temperature distribution among the tested fuels. Biodiesels derived from jatropha, karanja and polanga oil and their blends (B20, B50 and B100) were tested in a 3-cylinder compression ignition engine (Sahoo et al., 2009). It was observed that the karanja and polanga biodiesels and their blends had a monotonically increasing NO_x with the biodiesel content (with peak NO_x occurred with neat biodiesels; KB100 and PB100 produced about 15% and 21% higher NO_x (g/kW-h) than that of diesel), while a non-monotonicity was observed in NO_x with jatropha oil biodiesel. JB20 showed a 20% increase in brake specific NO_x emission index (g/kW-h) compared to baseline diesel, whereas JB50 and JB100 showed an increase of 15% and 17% respectively when compared to diesel. Several of these studies suggested that it was not appropriate to linearize the biodiesel blending effect on NO emissions due to the varied operating conditions, engine calibration and combustion phases.

2.1.3 Oxygen content

The fuel-bound oxygen content of the blend is proportional to the volumetric concentration of biodiesel in the blend. Generally, the increased NO_x emissions in biodiesel and their blends are attributed to the higher oxygen content in the biodiesel (Godiganur et al., 2010; Gumus and Kasifoglu, 2010) due to a linear increasing trend of NO_x with the increase in mass percentage of fuel oxygen. However, there are studies that do not agree with this linear increase; a linear decrease (Kalligeros et al., 2003) in NO_x emission or a non-monotonic increase or decrease with the oxygen content in the

fuel (Sahoo et al., 2007; Fontaras et al., 2009; Aydin and Bayindir, 2010) have been documented.

Canakci (2005) studied No. 2 diesel fuel (no fuel bound oxygen), No. 1 diesel fuel (no fuel-bound oxygen), SME (11% oxygen by mass / 3.6% oxygen by volume) and B20 (20% SME and 80% No.2 diesel) (2.2 % oxygen by mass / 0.7 % by volume) in a turbocharged diesel engine and observed the brake specific NO_x index (g/kWh) of the SME and B20 blend were increased by 11% and 1%, respectively compared to the No. 2 diesel. Surprisingly, the NO_x emission index of No. 1 diesel fuel was 6% lower than that of No. 2 diesel fuel, while there was no appreciable difference of oxygen concentration in the exhaust between the fuels tested. Therefore, in addition to the fuel-bound oxygen effect of biodiesel, more research is required to identify the properties that impact the combustion reactions favoring NO_x emission. Puhan et al. (2005) questioned the availability of fuel-bound oxygen for NO_x formation and argued that the esters might decarboxylate and form CO_2 early during the combustion. It is evident that additional studies are essential to understand the significance of fuel-bound oxygen effect, especially their impact in the formation of NO_x during combustion in engines.

2.1.4 Effects of cetane and iodine numbers

Auto-ignition of the injected fuel is a critical factor in the performance and operation of compression ignition engines. Cetane number is a property of the fuel that quantifies the self-ignition characteristics and ignition delay time of a fuel in an engine cycle; the higher the cetane number, the shorter the ignition delay (Pulkrabek, 2004).

Cetane numbers for various esters of the saturated fatty acids ranging from C8 to C18 have been determined according to ASTM D-613. For methyl esters, the cetane numbers were found to increase nonlinearly with the fatty acid chain length (Klopfenstein, 1985). The higher cetane number of biodiesel reduces the ignition delay and also leads to the advancement in combustion. Consequently, with the availability of oxygen, higher temperature together with longer residence time, may lead to the increase of NO_x emissions. Several researchers, e.g., Lim et al. (2014) used this reasoning to describe the increased NO_x emissions with biodiesel content. However, this reasoning is debatable. Higher cetane number results in not only an early onset of combustion, but also leads to lower amount of fuel burning in the premixed-combustion mode, which result in lower temperature and residence time in the combustion chamber, causing a lower NO_x formation. Wu et al. (2009) observed that the brake specific NO_x emission index (g/kWh) of palm methyl ester (PME) was 7% lower than that of waste oil methyl ester (WME), even though both had almost the same oxygen content of about 11.2% by mass. This was credited to the higher cetane number of PME (64 for PME compared to 56 for WME) which could reduce ignition delay and the amount of fuel consumed in the premixed phase, resulting in a reduction of in-cylinder temperature and subsequently reduced NO_x emission. Many authors (Graboski et al., 2003; Kalligeros et al., 2003; Puhan et al., 2005; Knothe et al., 2006; Karavalakis et al., 2009) concluded that NO_x emissions decreased with an increase in cetane number.

2.1.5. Influence of type of engine and test cycle

Engine type and the associated test cycles could strongly influence the NO_x emission of biodiesel. Tat (2003) demonstrated that the NO_x emission from compression ignition engines was significantly influenced by the variation in injection timing and advance due to the impact of fluid properties such as density, isentropic bulk modulus (compressibility) and viscosity. Karavalakis et al. (2009) studied the exhaust emission characteristics of ultra-low sulphur diesel and soy biodiesel blends at proportions of 10% and 30% by volume in a Euro 4 common rail injection diesel engine over various engine test cycles namely New European Driving Cycle (NEDC) and non-legislated Artemis driving cycles which simulate urban, rural and highway driving conditions in Europe. It is interesting to note that driving test cycles significantly influence the amount of NO_x emitted during the operation. Among the three Artemis driving cycle conditions, B10 and B30 produced higher NO_x (g/km) than the base line diesel. During rural driving condition, B10 and B30 produced the highest increase in NO_x as 14% and 18% respectively. However, in NEDC test cycle, NO_x emissions were slightly reduced for both B10 and B30 by 3% and 4% respectively. The authors attributed this observed reduction in NO_x to the smooth acceleration profile of NEDC, which dominated the NO_x emission mechanism than the physicochemical characteristics of biodiesel. Moreover, the Artemis driving cycles were more aggressive and transient, which would inherently favor the increase of NO_x emissions. Hence, although the physicochemical properties and fuel chemistry properties such as saturation level and cetane number play certain roles in the NO_x emissions, their relative importance when compared to the engine parameters and the nature of test cycle in

certain conditions are inconclusive. As a part of the program to quantify the effect of biodiesel fuels on engine NO_x emissions, EPA (2010) examined chassis dynamometer tests on heavy duty diesel engines to study the NO_x effects of soy-based biodiesel over light, medium and heavy duty cycles. The results indicated that brake specific NO_x index increased as a function of average cycle load, by about 5% for high loaded cycles; 2.5% increase in medium loaded cycles. However, in lightly loaded cycle, results showed inconclusive trends in NOx emissions (where a decrease and increase in NO_x emissions was observed by 1% and 2% respectively in two different trials), and hence the load-dependent nature of test cycles and their influence on NO_x emissions could not be neglected. Osborne et al. (2011) tested soy biodiesel, diesel and their blends (B2, B10, B20) in a locomotive operated in two different cycles namely line haul and switch cycle. The changes in cycle weighted average of NO_x (g/kWh) for B2, B10 and B20 were comparable between two cycles, while B100 in switch cycle increased NO_x by about 15% over the line haul cycle. Fontaras et al. (2014) studied rapeseed methyl ester and its blends B10, B20 and B50 with diesel in three different vehicles (equipped with different exhaust after treatment technologies) over test cycles namely NEDC, which is a standard test cycle in Europe and real world testing cycles such as Artemis Urban and Artemis Road. In general, among all the tested conditions, NO_x (g/km) increased up to 20% with B50 in some cases while most showed an increase in the range of 1 to 10% depending on the blend and the vehicle. Serrano et al. (2015) tested diesel and 20% biodiesel blend (from soy and palm feedstock) in three different test cycles, namely NEDC, URBAN and EXTRA URBAN test cycle. In all three cycles, B20 had lower NO_x emission index (g/km) than diesel, but the reduction percentage varied with cycles

as 10%, 20% and 5% respectively. In summary, all these studies reported different trends with different combination of engine test cycles, biodiesel feedstock and content. Hence the biodiesel and its blending effect on NO_x are inconclusive in terms of engine test cycle since several engine and combustion parameters influence the emission characteristics of a particular test cycle which can overshadow the actual emission potential of a particular fuel or fuel blend.

2.1.6. Effect of injection timing

The fuel injection is an important process in the engine operation and the timing of fuel injection into the combustion chamber is critical and affects performance and emissions to a large extent. The injection process is greatly influenced by the fluid dynamic properties of the fuel and NO_x formation appeared to be dependent on the start of injection timing in compression ignition engines. (Tat et al., 2000; Tat and Van Gerpen, 2003; Boehman et al., 2004; Agarwal et al., 2013). Carraretto et al. (2004) studied the effect of advance in injection timing (at three crank angles namely, 21^o, 24^o and 27^o) with neat biodiesel produced from vegetable oil in a 4-stroke diesel engine. They observed that NO_x concentration (ppm) increased with the injection advance by about 41% between 21^o and 24^o and by about 67% between 24^o and 27^o at both maximum torque and power speeds. Tsolakis et al. (2007) observed that the retarded injection timing by 3^o reduced NO_x concentration (ppm) while testing with rapeseed methyl ester (by about 17%) and its 50% blend (by about 23%) with diesel in a diesel engine. Szybist et al. (2007) studied the influence of methyl oleate (mono-unsaturated fatty compound) present in soy biodiesel. The experiments were conducted at three

different injection timings - early, mid and late. In early injection mode, where more premixed burn fractions occur, neat soy biodiesel and B20 produced about 11% and 3% more brake-specific NO_x (g/kWh) than ultra-low sulphur diesel. As the fuel injection timing was retarded, in mid and late injection modes, the differences in NO_x emissions between the fuels were reduced. In late injection mode, where more diffusion burn fractions occur, the NO_x emitted from all tested fuels were comparable. Hence, the authors suggested that retarding the injection timing was a potential way of reducing NO_x emissions. In agreement with this claim, a reduction in brake-specific NO_x emission index was observed with the retarded start of combustion (SOC) timing for SME/diesel blends (Moscherosch et al., 2010) and CME/diesel blends (Sequera et al., 2011).

2.1.7. Effect of engine speed

Engine speed also plays a critical role in the formation of NO_x in compression ignition engines. Several studies proposed that NO_x emissions decreased with engine speed (Lin and Li, 2009; Imtenan et al., 2014). The NO_x concentration (ppm) decreased by about 23% between engine speeds of 800 rpm and 2000 rpm for petroleum diesel and biodiesels from cooking oil and marine fish oil in a 4-stroke direct injection, naturally aspirated diesel engine (Lin and Li, 2009). The authors concluded that, although the increased engine speed caused an increase in the temperature and pressure of burning gas, the reduction of ignition delay resulted in the reduction of residence time available for NO_x formation. Interestingly, different trends of NO_x emission was reported at two different engine speeds (2000 and 4000 rpm) at the full load condition

when diesel, biodiesel from waste cooking oil and their blends of 10%, 20%, 40% and 60% (by volume) were studied in a common rail Euro 3 diesel engine (Zhang et al., 2008). At 2000 rpm, a monotonic increase of NO_x concentration (ppm) was observed with the biodiesel content in the blend, especially with blends higher than 40% of biodiesel content. B100 had about 13% higher NO_x concentration than the diesel. However, at 4000 rpm, the NO_x concentration did not show any variation with biodiesel content. The authors attributed the observed trends to the common rail injection system where the impact of advanced injection of biodiesel due to higher bulk modulus, density and mechanical pump is no longer a significant factor.

Moreover, a non-monotonic variation of NO_x was observed with engine speeds in some studies. Usta (2005) observed different effects of engine speed on NO_x concentration (ppm) at different conditions, that is, as engine speed was increased (between 1500 rpm and 3000 rpm), the NO_x concentration increased by about 74% at full load, and increased by about 33% at three fourth of rated load, but gradually decreased by 28% at half load for both diesel and its blend (D82.5/TSOME17.5, by volume) with tobacco seed oil methyl ester. Non-monotonic variation of NOx was also reported in several other studies which employed biodiesels different feedstocks ranging from waste frying oil (Utlu and Kocak, 2008), tall oil (Keskin et al., 2008), vegetable oil (Chokri et al., 2012), cooking oil (Arslan, 2011), calophyllum inophyllum lin oil which consists of mostly unsaturated fatty acids (Fattah et al., 2014). A limited source of explanation has been reported in the literature on the engine speed effect on NO_x formation. Several studies attributed various parameters such as availability of oxygen, in-cylinder combustion temperature and residence time to the variation of NO_x between fuels; but

no explanation was given to the non-monotonic effect of engine speed on NO_x emissions.

2.1.8. Effect of engine load

The biodiesel NO_x effect was significantly influenced by engine load when tested with biodiesel and its blends with diesel in diesel engines. Several studies reported a monotonic increase in NO_x with engine load due to higher temperature generated at higher engine load (Zhang and Boehman, 2007), while employing biodiesel blends from different feedstock as Neem oil (Sharma et al., 2009), Mahua and Fish oil (Godiganur et al., 2010), Jatropha oil (Tan et al., 2012; Padhee and Raheman, 2015) and Croton oil (Osawa et al., 2015). The authors attributed this monotonic increase of NO_x emissions to the increased engine temperature and pressure, availability of oxygen and increased flow rate of the biodiesel blends.

However, Murillo et al. (2007) found a surprising decrease in NO_x emissions with load in a single-cylinder, naturally aspirated direct injection diesel engine. A substantial reduction of about 60% in the specific NO_x emission (g/kWh) between 25% load and full load when tested with B100 was observed. The authors attributed this trend to the increase in turbulence inside the cylinder, which contributed to a quicker combustion and resulted in lower residence time of the species in the high temperature zones. Agarwal and Rajamanoharan (2009) tested karanja biodiesel and blends (B10, B20, B50 and B75) with diesel in a single cylinder agricultural engine. The authors observed that

the neat biodiesel and all the tested blends had comparable NO emission index (g/kWh), while they were about 45% lower than that of diesel at 20% load.

On the other hand, a non-monotonic response of NO_x for the use of biodiesels and their blends with diesel has been widely reported in the literature (Raheman and Phadatare, 2004; Sureshkumar et al., 2008; Dhar et al., 2012; Agarwal and Dhar, 2013; Chavan et al 2015). A non-monotonic variation of NO_x with the biodiesel content over a wide range of loads was observed by Raheman and Phadatare (2004) while testing karanja methyl ester and its blends (B20, B40, B60, B80, by volume) with diesel in a single cylinder, 4-stroke, water-cooled direct injection diesel engine. At full load condition, B20 and B80 produced about 23% lower NO_x concentration (ppm) than diesel; while B60 and B100 produced about 38% lower NO_x than diesel and B40 recorded about 15 % lower NO_x than diesel. Hence, it is clear that NO_x is sensitive to load where changes in the loading conditions could possibly reverse the NO_x formation trends. Sureshkumar et al. (2008) also observed a non-monotonic variation in NO_x concentration with biodiesel content for a wide range of loading conditions while testing pongamia pinnata methyl ester and its blends (B20, B40, B60, B80, by volume) in a similar engine. At 75% load condition, B20 and B100 produced 8% and 25% lower NO_x concentration (ppm) than diesel; while B40, B60 and B80 produced about 38% lower NO_x than diesel. Though the NO_x concentration was decreased with the biodiesel content in the blend, the extent of reduction in NO_x was not proportional with the biodiesel content. Agarwal and Dhar (2013) tested karanja biodiesel and blends (B10, B50) with mineral diesel in a direct injection diesel engine. It was observed that B50 and B20 consistently produced higher NO (g/kWh) on an average of about three times

than diesel, while B10 and B100 produced comparable or slightly higher NO_x than diesel. Chavan et al. (2015) studied the emission characteristics of jatropha biodiesel and its blends B10, B20 and B30 with petroleum diesel in a 4-stroke variable compression ratio engine at five different compression ratios (CRs) namely 14, 15, 16, 17 and 18 over a range of loads. It was observed that NO_x concentration (ppm) increased with increasing load and compression ratio. It may be due to the increase in temperature at high loads and lower ignition delay due to higher compression ratio that would result in increased pressure and temperature inside the cylinder. However, the NO_x emission due to biodiesel and blending effect had neither a monotonic increase nor a monotonic decrease with load and CRs. For example, at full load, diesel had lowest NO_x concentration (ppm) at CR 14 and CR 16; B100 had lowest NO_x concentration at CR 15; B30 had lowest NO_x concentration at CR 18 while diesel and B30 had lowest NO_x concentration at CR 17. Similarly, a non-monotonic trend was observed with different loads at a given compression ratio. Hence, the engine parameters and the associated phasing of combustion complicate the understanding of already entangled biodiesel and its blending effect on NO_x formation in compression ignition engines.

2.1.9. Effect of fluid dynamics

Fluid dynamics of the fuel spray is an important and highly complex phenomenon that significantly influences the phasing of combustion (Sirignano, 1993). The fuel spray characteristics such as injector penetration length, atomization and mean droplet size along with flow field and heat transfer interactions between droplets are critically influenced by various physical properties of the fuel. Especially, the differences in properties such as density, viscosity, surface tension, etc., between biodiesel and petroleum fuels influence the combustion process and can affect NO_x emission (Allen and Watts, 2000; Lee et al., 2005; Ejim et al., 2007; Suh et al., 2007; Yuan et al., 2007). The fuel viscosity and surface tension of fifteen neat biodiesels were reported in Allen and Watts (2000) using a regression model developed based on experimental results from five different biodiesels. The authors claimed that viscosity and surface tension, in turn the sauter mean diameter (SMD) of the spray, could be predicted from the fatty acid composition of biodiesels. A maximum reduction of 50% in viscosity and 8% in surface tension between rapeseed methyl ester and coconut oil methyl ester was predicted and was attributed to the differences in carbon chain lengths; major fatty acid constituents in coconut oil methyl ester have shorter carbon chain length while rapeseed methyl ester has constituents with longer carbon chain length. The SMD of coconut oil methyl ester spray was comparable to that of petroleum diesel spray, also confirmed by Ejim et al. (2007), while rapeseed methyl ester spray had 40% higher SMD than that of diesel spray; other biodiesel sprays have about 25% - 29% higher SMDs than diesel fuel spray. It is also indicated that the discrepancies in the reported data among literature sources could not be verified since most of the studies

did not report the extent of the reaction and the presence of triglycerides in the fuel after the transesterification process. The authors concluded that even a 6% by mass of triglyceride (canola oil) in the canola methyl ester could result in a 12% increase in viscosity of the biodiesel. The biodiesel blending effects on the viscosity and surface tension of the final blended fuel was studied by Lee et al. (2005) in a common-rail diesel engine with soy biodiesel and its 10%, 20% and 40% volumetric blends with petroleum diesel. It was observed that the kinematic viscosity and surface tension of the fuel linearly increased with the biodiesel content; however, the blending ratio had a minimal effect on the spray development. Lower injection velocity of biodiesel due to higher viscosity, and the associated increase in friction between biodiesel spray and nozzle surface causes shorter spray tip penetration; while higher SMD of the biodiesel spray causes a longer tip penetration. These two compensating effects resulted in a similar spray tip penetration between diesel, biodiesel and their blends. Ejim et al. (2007) reasserted the findings by Allen and Watts (2000) and reported comparable SMDs among neat palm, soybean, cotton seed, peanut and canola biodiesel and their corresponding B5 and B20 blends with No.2 diesel. In a computational study by Yuan and group (2007), for a given engine speed and load, the maximum spray cone angle of diesel and soy biodiesel was found to be 47.5^{o} and 30^{o} and soy biodiesel produced about 8% higher brake-specific NO_x than diesel. When the spray cone angle of soy biodiesel was matched with diesel (47.5^{o}), the brake-specific NO_x was reduced by 15% between cone angles of 30^{o} and 47.5^{o} of soy biodiesel spray. The authors concluded that a narrow spray angle could significantly emit higher NO_x since the narrow sprays induce strong stratification of fuel vapor which brings about local rich or stoichiometric regions

that contribute to higher NO_x. Yuan and Hansen (2009) predicted that NO_x (g/kWh) decreased up to 3.5% when the viscosity of SME was decreased to match with petroleum diesel fuel. They also suggested that smaller spray cone angles and advanced start of injection were the main reasons for increased NO_x emission of biodiesel. They concluded that the decreased spray cone angle and increased spray penetration might increase NO_x emission. Agarwal and Chaudhury (2012) investigated the spray characteristics in a constant volume spray chamber with diesel, karanja biodiesel and their blends, B5 and B20, and concluded that B100 had highest spray tip penetration, cone angle and spray area followed by B20, B5 and diesel.

In addition to density, surface tension and viscosity, the boiling point of biodiesel could also significantly alter the spray characteristics; higher boiling point of biodiesel increases the combustion duration and cylinder gas temperature both of which could favor NO formation (Ozsezen et al., 2008). In a recent study, the spray, combustion and exhaust emission characteristics of soy biodiesel in a direct injection common-rail diesel engine were investigated by Yoon et al. (2009) who observed that biodiesel produced larger droplet size (about 12%), similar spray structure, and longer spray tip penetration (about 8% higher) into the cylinder than conventional diesel, which resulted in an increased indicated specific NO_x emissions of soy biodiesel by about 19% higher than that of diesel. Ye and Boehman (2010) studied the effect of engine injection strategies on the biodiesel NO_x effect with a direct injection diesel engine fueled with ultra-low sulphur diesel and its blend with soy biodiesel (B40). For a given speed and load, a higher volume of biodiesel has to be supplied because of its lower heating value compared to petroleum diesel. The increase of fuel consumption could be accomplished

by either higher injection pressure or injection duration, which would result in increased NO_x emission. Injection characteristics such as mean injection rate, mean injection pressure, injection delay and injection duration increase with the biodiesel content, which could favor NO_x formation at certain conditions. Hence, the above discussed physical properties and their effects on the fluid dynamics of the fuel spray and atomization have critical impact on the combustion and emission characteristics of a fuel at any particular operating condition.

2.2 Computational studies of biodiesel impact on NOx emissions

Biodiesel, composed of several fatty acid methyl esters, ranges in carbon chain length from 15 to 21. Similarly, diesel is composed of various different types of paraffins and aromatic compounds. This implies that a kinetic model for a diesel/biodiesel fuel would be large and computationally expensive. To resolve this problem, in the earlier studies, authors have studied surrogate fuels which are significantly smaller in terms of chemical kinetic mechanisms and computational requirements. Fisher et al. (2000) developed detailed chemical mechanisms for the combustion of methyl butanoate ($C_5H_{10}O_2$) and methyl formate ($C_2H_4O_2$) and the computational results were compared against closed vessel experimental data obtained at low temperature, sub-atmospheric conditions. Although some qualitative agreement was observed, the experimental data consistently indicated lower overall reactivates than the model by a factor of 10 to 50 and was ascribed to the presence of wall reactions in the experiments. Dooley et al. (2008) performed auto-ignition measurements of methyl butanoate ($C_5H_{10}O_2$) in a shock tube over the temperature range of 1250 K - 1760 K and equivalence ratios of 0.25, 0.50, 1.0 and 1.5 and compared them with the auto-ignition data from a rapid compression machine. These data, together with the data reported in literature in a jet stirred reactor and opposed flow diffusion flame were used to develop a detailed chemical kinetic model. It was found that the developed model closely simulated the effect of change in equivalence ratio, fuel fraction and pressure for shock tube ignition delays. Further, the Westbrook research group from the Lawrence Livermore National Laboratory developed a series of chemical kinetic mechanisms for the oxidation of alkyl esters ranging from methyl formate, methyl acetate, ethyl formate

and ethyl acetate (Westbrook et al., 2009); methyl decanoate, a surrogate for biodiesel fuels (Herbinet et al., 2008); oxidation of two large unsaturated esters: methyl-5-decenoate and methyl-9-decenoate (Herbinet et al., 2010) and for esters with higher carbon chain length that includes methyl stearate, methyl oleate, methyl linoleate and methyl linolenate – the major constituent for commercial biodiesels like soy and canola methyl esters, termed as 'Real Biodiesel' mechanism (Westbrook et al., 2011) and methyl pentanoate and methyl hexanoate (Korobeinichev et al., 2015). In all of these above-mentioned articles, the results from the predicted model were validated with experimental results from kinetic studies, shock tube measurements and jet stirred reactor studies. Further, these studies primarily focused on the oxidation pathways of the hydrocarbon in those esters and did not include nitrogen chemistry in the reactions.

The combustion research group at the University of California, San Diego (UCSD) has developed detailed nitrogen chemistry for the formation of nitric oxide during the oxidation of fuel in air (UCSD, 2004). A few studies have incorporated this nitrogen chemistry into their primary chemical kinetic mechanisms to investigate the NO emissions in their corresponding studies. For example, Mulenga et al. (2003) studied numerical analysis of homogenous natural gas/diesel/air mixture in a diesel fuel engine with heptane as a diesel surrogate using Curran heptane mechanism (Curran et al., 1998). This heptane mechanism did not include chemical kinetic mechanisms pertinent to nitrogen chemistry. Hence the detailed NOx mechanism from UCSD was incorporated in to the numerical model to facilitate the NOx emission study. It was numerically found that an increase in heptane concentration in the methane / heptane mixture increased the NO concentration in the combustion products. For example,

between 0% and 2.5% (mole percent) of n-heptane addition to methane, the concentration of NOx increased from 16 ppm to 230 ppm. The authors attributed this increase to the increased peak temperature, residence time and the availability of oxygen during the combustion. Li et al. (2015) numerically simulated H_2/air opposed jet diffusion flames using CHEMKIN employing seven different reaction kinetic mechanisms that include UCSD NOx mechanism built into UCSD H_2/O_2 mechanism. It was observed that UCSD NOx mechanism predicted NO mole fractions comparable to the experimental results (within 15%). This UCSD NOx mechanism is employed in the computation analysis of NO formation in the present study by incorporated the NOx mechanism into the 'Real Biodiesel' mechanism developed by Westbrook et al. (2011).

CHAPTER 3 RESEARCH OBJECTIVE

The overall research objectives, motivation and background of this dissertation work are presented in this chapter.

3.1 Iodine number as an indicator of fuel unsaturation

As presented in Chapter 2, historically, iodine number (also known as iodine value) has been used to describe the oxidative stability of fats and oils, since it indicates the propensity of the oil or fat to polymerize, which may eventually lead to the formation of deposits (Bouaid et al., 2007; Knothe, 2007; McCormick et al., 2007 and Lapuerta et al., 2009). When the use of biodiesels became popular, researchers began using iodine number as a measure of the total fuel unsaturation since it indirectly provides information regarding the double bonds present in the biodiesel. The iodine number of a vegetable oil or animal fat is almost identical to that of the corresponding methyl esters (Knothe 2007). Hence, iodine number is widely used to characterize fuel unsaturation of biodiesels in terms of the presence of double bonds and has been widely reported in engine studies using biodiesels (Kyriakidis and Katsiloulis, 2000; McCormick et al., 2001; Benjumea et al., 2008; Wadumesthrige et al., 2008; Ramos et al., 2009; Puhan et al., 2010; Cecrle et al., 2012; and Giakoumis, 2013). Iodine number is defined as the number of centigrams of iodine absorbed per gram of the sample. It is commonly used as a measure of the average amount of unsaturation present in fats and oils (Knothe, 2002). The unsaturation in the oils and fatty acid methyl esters (biodiesels) derived out of these oils is in the form of double bonds present in the

carbon chain of the esters. Hence, higher the iodine number, the more C=C bonds are present in the biodiesels. The iodine numbers of various neat biodiesels are summarized in Table 3.1. In the iodometry process, different methods have been employed in the determination of iodine number, out of which, the Wijs method is widely considered as a standard method and is recommended by the American Oil Chemists' Society (Benham and Klee, 1950 and Kyriakidis and Katsiloulis, 2000). Iodine (in the form of iodine tri-chloride solution, also known as Wijs solution) is added to the sample dissolved in chloroform or carbon tetra chloride, and the iodine absorption is allowed to take place (Chamberlain, 1921). During this process, the double bonds of the fatty acids react with iodine to form iodine compounds. As long as the double bonds are available, the color of iodine does not appear in the solution as the iodine is absorbed by the double bonds (Gupta and Kanwar, 1994). Hence, more the extent of unsaturation, more iodine will be absorbed by the sample, and higher is the iodine number. However, the relevance of iodine number to petroleum fuels is questionable because the reaction of petroleum fuels with iodine differs profoundly from that of fatty acids (Brooks, 1922).

3.2 Motivation and background

With the current knowledge and understanding of combustion characteristics of biodiesels, blending biodiesels with petroleum fuels in different proportions is a feasible solution in the near future for use in existing engines without major modifications. This is also due to the limited availability of biodiesel production and the lack of experience in the long term handling, storage and combustion of these biodiesels and further, to compensate for the lower energy content of biodiesels. Early studies focused on the

combustion of neat biodiesels in engines; recent studies have included the combustion of petroleum/biodiesel blends. “Degree of unsaturation / fuel unsaturation” and “unsaturation” are the terms which have been frequently reported in literature in the context of nitric oxide emissions in biodiesel combustion. Fuel unsaturation has been attributed to the change in NOx emissions observed with the use of neat biodiesels in compression ignition engines; several results indicated the existence of a strong relationship between NOx emissions and iodine number (McCormick et al., 2002; Knothe et al., 2006; Benjumea et al., 2008; Oner and Altun, 2009 and Puhan et al., 2010), with the iodine number used to describe the biodiesel unsaturation. In the literature, parameters such as cetane number, iodine number, fuel unsaturation and their influence on combustion temperature and pressure rise inside the combustion chamber, have been widely mentioned and attributed for the increased NOx formation in IC engines with the use of neat biodiesels (Graboski et al., 2003; Bamgboye and Hansen, 2008 and Giakoumis, 2013). However, the use of iodine number to quantify fuel unsaturation is valid only for neat biodiesels and not for blends of petroleum fuel and biodiesels. As stated before, the iodine number of a biodiesel depends on the total amount of the several unsaturated fatty acid components, and represents the contribution of unsaturation due to only the presence of double bonds. Petroleum diesel contains about 25% by volume of aromatic hydrocarbons (Agency for toxic substances and disease registry, 1995). In the petroleum industry, the term “unsaturated” refers to only the presence of olefins and alkyne hydrocarbons, while the word “aromatic” generally refers to the presence of hydrocarbons of the benzene series. The reactivity of iodine with aromatic compounds, which are unsaturated with respect to molecular

structure, differs significantly from that of olefins (Dean and Hill, 1917). Thus, it would not be appropriate to employ iodine number as an indicator of fuel unsaturation, especially while dealing with petroleum fuels and their blends with biodiesels. Further, Bromine number, used as a measure of aliphatic unsaturation in petrofuel samples, also does not account for the aromatic unsaturation from petroleum fuels (Johnson and Clark, 1947). Hence, it is necessary to identify a parameter that accounts for the fuel unsaturation irrespective of the fuel origin: from fatty acids, olefins or aromatic hydrocarbons. Such a parameter is required to build a common platform for the investigation of the effects of fuel unsaturation on the emission characteristics of petroleum / biodiesel blends attributable to the chemistry of the fuel.

3.3 Identification of Degree of Unsaturation (DOU) parameter

The primary objective of this work is to explore a parameter that accounts for and quantify the unsaturation arising from various components of the fuel irrespective of their parent hydrocarbon families such as alkanes, alkenes, alkynes, cyclic hydrocarbons, aromatics, alcohols, esters etc. and which can be correlated with the engine emission characteristics with the use of that fuel. A parameter called Degree of Unsaturation (DOU) has been extensively used in the field of organic chemistry as a quick way to determine and quantify the degree of unsaturation of any molecule based on its structure (Vollhardt and Schore, 2011). It is defined as the sum of the number of rings and double / triple bonds present in the molecule and can be evaluated using the formula presented in Equation 3.1.

$$DOU = \frac{(2C + 2 + N - X - H)}{2} \quad (3.1)$$

where C, N, X and H are the number of carbon, nitrogen, halogen and hydrogen atoms respectively.

The parameter Degree of unsaturation (DOU) has several significant applications:

- DOU can be used to correlate the NOx emission parameters (indices) to the molecular hydrogen / carbon ratio of the fuel, irrespective of whether the hydrocarbon is a fossil fuel, alcohol, ester or ether.
- DOU can capture the differences in the influence of molecular chemistry of the fuel on the NOx emission characteristics, based on the parent hydrocarbon families.
- DOU can be readily evaluated for any fuel under study with acceptable uncertainty, without the use of elaborate experiments.

Based on Equation 3.1, a degree of unsaturation (DOU) value of one is equivalent to the presence of one ring or one double bond; a DOU of 2 is equivalent to having two double bonds or two rings or one ring and one double bond or one triple bond. For example, a saturated hydrocarbon, such as methane (CH_4) has a DOU of 0 and a saturated fatty acid methyl ester (FAME), say methyl laurate ($C_{13}H_{26}O_2$), has a DOU of 1. As seen in this example, a saturated FAME and a saturated alkane do not have the same degree of unsaturation due to the differences in the hydrocarbon family and DOU is able to capture this difference. Toluene (C_7H_8), an aromatic hydrocarbon has three double bonds and an aromatic ring and therefore, a DOU of 4. Here, DOU accounts for the unsaturation due to double bonds as well as a ring structure. In an alkane, the

number of hydrogen atoms is (2C+2), and the DOU value is zero. In equation 3.1, the number of halogen atoms is subtracted because halogens replace hydrogen atoms in the molecule. For instance, chloroethane (C_2H_5Cl) has a hydrogen atom replaced by chlorine atom when compared to the corresponding saturated alkane- ethane (C_2H_6), and both have DOU values of zero. Similarly, the number of nitrogen atoms is added because a nitrogen atom is accompanied by a hydrogen atom and the nitrogen is connected to the carbon atom in the molecule. Thus, both ethylmethylamine (C_3H_9N) and propane (C_3H_8) have DOU values of zero. Oxygen and sulfur do not play a role in the determination of unsaturation. For example, methane (CH_4) and methanol (CH_3OH) have the same hydrogen to carbon ratio and according to the formula, both have a DOU number of 0. Thus, DOU is capable of evaluating the degree of unsaturation of different fuels based on the molecular hydrogen and carbon content and does not require prior information about the molecular structure of the fuel, meaning, the configuration and arrangement of hydrogen and carbon atoms within the molecule. Furthermore, DOU can be easily evaluated based on the molecular formulae alone without involving complex and expensive experimental procedures. The values of degree of unsaturation, iodine number and cetane number for petroleum diesel, Jet A and various biodiesels are presented in Table 3.1.

3.4 Research objectives

The objectives of this research work are stated as follows:

- Establish experimental correlations between DOU and emission indices (EI_{NO} and EI_{CO}) from the laminar flames of different families of fuels at various combustion conditions, namely fuel-lean condition (Φ = 0.9), stoichiometric (Φ = 1.0) and moderate fuel-rich condition (Φ = 1.2 and 1.5).
- Identify the equivalence ratio at which DOU (fuel chemistry) effect is predominant on the combustion chemistry of NO and CO formation and investigate the relative significance of equivalence ratio (Φ) effects and fuel unsaturation effects on EI_{NO} and EI_{CO}.
- At that identified equivalence ratio, demonstrate the fuel chemistry effects (with similar degree of unsaturation arising from different families of origin) on the emission indices (EI_{NO} and EI_{CO}) from flames as a function of the aromatic content of the tested fuels and discern the predominant NO formation mechanism in the tested flames.

3.5 Project impact

This research project is primarily aimed at understanding the fundamental reaction pathways and dominant NO formation mechanisms particularly in a combustion environment employing biodiesel/ petrofuel blends. With the developed correlations and understanding based on the current study, the effects of fuel unsaturation and their relative degree of influence (particularly the role of aromatic content) on the formation of nitric oxide will be discerned in a laminar flame environment, in the absence of interference of coupled engine parameters, fuel atomization and droplet evaporation phenomena.

In summary, the following contributions will be made:

I. The significance of the fuel chemistry interactions between individual components within the same family and different fuel families on the EI_{NO} of flame will be presented. EI_{NO} vs. DOU will be plotted based on the emission results from flames of individual methyl esters, individual alkanes and aromatic hydrocarbons and will be compared with EI_{NO} vs. DOU plots from flames of neat petroleum fuels, biodiesels and their blends. Based on the understanding from these results, biodiesels and their blends with petroleum fuels can be engineered to match specific degree of fuel unsaturation (by blending the parent fuels at different proportions corresponding to their DOU values) in accordance with the target NO emission index.

II. The significance of the aromatic content of petroleum fuels on the EI_{NO} of neat petroleum flames and the interactions of the aromatic content with the saturated

and unsaturated compounds of biodiesels on the EI_{NO} of petroleum/biodiesel flames will be analyzed by comparing the EI_{NO} curves of commercial petroleum/biodiesel blends and methyl ester/petrofuel blends. This analysis will signify how similar or different is the effect of DOU and the aromatic content on the EI_{NO} between interaction of individual fuel components in the flames and the net combined effect of interactions of various fuel components within the flames.

III. EI_{NO} vs. DOU correlations at different equivalence ratios will be presented to display the relative dominance of fuel unsaturation and equivalence ratio effects in determining the net amount of EI_{NO} from the flames.

In the context of diesel engine combustion where the local equivalence ratio varies widely from almost a rich premixed reaction zone to thin diffusion flame sheaths (Flynn et al., 1999), various parameters significantly influence the end NO formation. Hence the NO emissions from a diesel engine exhaust can be regarded as a combined final product of NO formed during various stages of combustion associated with different equivalence ratios. The results and findings of the fuel unsaturation effect on EI_{NO} at various equivalence ratios from this research work will help in understanding the influence of total fuel unsaturation on the NO emissions from the engine exhaust and complex combustion systems like gas turbine engines, boiler burners, furnaces etc.

Table 3.1 Properties of selected fuels

Fuel	C	H	O	Iodine Number[a]	Cetane Number[a]	DOU[b]
Canola methyl ester	19.0	36.0	2.0	104.0	54.8	2.0
Coconut methyl ester	14.1	27.9	2.0	7.8	61.0	1.1
Cottonseed methyl ester	18.4	34.3	2.0	106.0	53.3	2.3
Jatropha methyl ester	18.6	35.0	2.0	99.0	55.7	2.1
Karanja methyl ester	18.9	35.8	2.0	85.0	55.4	2.0
Linseed methyl ester	18.9	33.4	2.0	185.0	51.3	3.2
Mahua methyl ester	18.9	35.9	2.0	70.8	56.9	2.0
Neem methyl ester	18.9	36.4	2.0	86.0	54.2	1.7
Olive methyl ester	18.5	35.7	2.0	80.3	58.9	1.7
Palm methyl ester	17.1	32.9	2.0	54.0	61.2	1.7
Peanut methyl ester	19.0	35.7	2.0	80.5	54.9	2.1
Rapeseed methyl ester	18.9	35.2	2.0	111.0	54.1	2.4
Safflower seed methyl ester	18.9	34.3	2.0	137.0	51.8	2.7
Soybean methyl ester	18.8	34.6	2.0	126.0	51.8	2.5
Sunflower seed methyl ester	18.9	34.5	2.0	129.0	51.9	2.6
Tallow methyl ester	18.3	35.5	2.0	55.0	60.9	1.5
Jet A	13.0	23.0	0	3.5	42.0	2.5
Petroleum Diesel	14.4	24.9	0	8.6	49.0	3.0

[a] Giakoumis (2013); [b] calculated using equation 3.1

CHAPTER 4 SELECTION OF FUELS FOR INVESTIGATION

The basis of the selection of investigated fuels, their properties and test conditions are presented in this chapter. Three families of fuels, namely fatty acid methyl esters (commonly known as biodiesels), petroleum fuels and petrofuels/methyl ester blends are selected for the investigation. These families are further classified into sub-families for delineating the fuel chemistry interaction effects on $EI_{NO.}$ A combination of 63 fuels from these families of fuels were selected for the investigation and are listed in Table 4.1.

The details of the classification of families and sub-families (Figure 4.1) are presented in the following section:

4.1 Methyl ester family

The methyl ester family of fuels comprises of an ester functional group (XCOOR; with X representing the fatty acid chain and R representing alkyl group). In this study, the methyl esters are further classified into four categories as follows:

4.1.1 Individual Esters

The biodiesels are produced by the transesterification of triglycerides of vegetable and animal feedstocks. The vegetable feedstocks such as soy, canola, rapeseed and palm oil are made up of wide range of fatty acids with various carbon chain lengths. These fatty acids undergo a transesterification process to form the

corresponding fatty acid methyl esters. Hence, biodiesels are made up of combinations of several individual fatty acid methyl esters. In this study, methyl oleate (abbreviated as MO) ($C_{19}H_{36}O_2$), an individual methyl ester is selected for the investigation. A fundamental knowledge of the emission characteristics of an ester would serve as a baseline in understanding the emissions from the biodiesel, a mixture of several individual esters.

4.1.2 Neat commercial biodiesels

Laminar flames of neat commercial biodiesels such as SME, CME, RME and PME (composition of these biodiesels is presented in Table 4.2) are selected for investigation due to the significant differences in their fuel chemistry and degree of unsaturation. Among these fuels, SME is primarily composed of unsaturated methyl esters, while PME is composed of saturated methyl esters. Although CME and RME are produced from the same rapeseed oil feedstock which has higher erucic acid content, CME does not contain methyl erucate (methyl ester of erucic acid) since the erucic acid is removed from the canola oil due to its undesirable characteristics (Allen et al., 1999; Code of Federal Regulations, 2016). Hence the DOU of CME (2.0) is lesser than that of RME (2.4).

4.1.3 Commercial biodiesel/ biodiesel blends

This classification includes blends made from aforementioned neat biodiesels namely CP blends, CR blends, CS blends and RS blends where C, P, R and S stands for

methyl esters of canola, palm, rapeseed and soy respectively. Different combinations of these blends are selected for investigation (Table 4.1) to cover a wide range of DOU values.

A careful breakdown of the three classifications of methyl ester family displays an incremental complexity in the fuel chemistry interactions. Thus, the comparison of the EI_{NO} results from the flames of individual esters, neat biodiesels and biodiesel blends of same DOU will provide a baseline to understand the differences in the molecular interactions of the corresponding fuels, the significance of the effects of number of different esters present in the fuel and their interactions that influence NO emissions. Here, it is worthy to note that the unsaturation in all these three classifications is derived from the double bonds present in the acid and alcohol chain of esters; aromatic hydrocarbons do not play any role in the nitric oxide formation from these fuels since methyl esters do not contain aromatics.

4.2 Petroleum family

The petroleum family includes commercial petroleum fuels like diesel and Jet A and their fuel components like alkanes, alkenes and aromatic hydrocarbons. The petroleum family is further classified into four categories as follows:

4.2.1 Alkanes/Alkenes/Aromatics

Alkanes, alkenes and aromatic hydrocarbons are the fundamental building blocks of commercially available petroleum fuels. Petroleum diesel and Jet A are

mixtures of components like mono and cyclo paraffins, olefins, aromatic hydrocarbons etc. In this study, two petrofuel components: n-heptane (C_7H_{16}), to represent saturated alkane (DOU: 0) and toluene (C_7H_8), to represent highly unsaturated aromatic ring structure (DOU: 4) are selected for the investigation. The EI_{NO} results from the flames of heptane and toluene will provide insight into the effect of chemistry of petrofuel components with contrasting value of degree of unsaturation.

4.2.2 Blends of saturated alkane and aromatic hydrocarbons

Blends of n-heptane and toluene are selected for investigating the fuel chemistry effect on NO emissions with an added complexity to the individual petro-fuel components. In this study, blends of n-heptane and toluene made out of completely saturated n-heptane and highly unsaturated toluene (Table 4.1) are examined. The EI_{NO} results from the flames of various proportions of heptane/toluene blends will help understand the chemistry interactions between a saturated and unsaturated petrofuel component with contrasting values of degree of unsaturation on the NO emissions.

4.2.3 Neat commercial petrofuels

Laminar flames of neat commercial petrofuels such as diesel and JetA are selected for investigation due to differences in their composition of saturated and unsaturated components and the resulting degree of unsaturation. Petrodiesel ($C_{14.4}H_{24.9}$) consists of about 75% of saturated hydrocarbons and 25% of unsaturated aromatics; while JetA ($C_{13}H_{23}$) is composed of 80% of saturated and 20% of unsaturated

components (composition of petro-diesel and Jet-A are presented in Table 4.3). Although both the fuels are made up of same fuel components, the difference in the quantity of those components results in different degree of unsaturation (diesel: 3.0 and JetA: 2.5).

4.2.4 Commercial petrofuel blends

This classification includes blends made out of petrodiesel and Jet A at various proportions to cover the DOU range from 2.5 to 3.0 and to correlate the DOU with the EI_{NO} of the flames of fuels containing varying amount of aromatic content.

Similar to the classification of ester family, the four classifications of petrofuel family display an increased complexity in the fuel chemistry interactions among the fuels of petrofuel family. Thus, the comparison of the EI_{NO} results from the flames of individual alkanes/alkenes/aromatic hydrocarbons, their blends, neat commercial petrofuels and commercial petrofuel blends having same DOU will provide a fundamental understanding of differences in the molecular interactions of the corresponding fuels and how significant is the effects of number of different fuel components present in the fuel, their interactions and the net aromatic content that influence NO emissions.

4.3 Petro-Methyl ester blends family

The significance of petro-methyl ester blends is the presence of a wide range of individual fuel components from the methyl ester and petroleum family. Essentially, this is a derived family of fuels from the primary fuel families - ester and petroleum fuels. These are further classified into two categories as follows:

4.3.1 Methyl ester/petrofuel blends

This classification includes blends of individual ester - methyl oleate (MO) and petrofuel components such as n-heptane and toluene. The EI_{NO} results from the flames of MO/heptane blends will provide insight about the effect of DOU primarily derived from the double bonds of ester and their interaction with the saturated alkane with no aromatics. Similarly, flames of MO/toluene blends reveal the effect of DOU on EI_{NO} with an added complexity of the presence of aromatic content. In summary, the EI_{NO} results from the flames of aforementioned blends at the same DOU would assist in delineating the effect of aromatic content.

4.3.2 Commercial petro/biodiesel blends

Laminar flames of blends of commercial biodiesels and petroleum fuels such as SD, CD, RD, PD and PJ blends are selected for the study under this category; where S, C, R, P, D and J stands for methyl esters of soy, canola, rapeseed and palm, petrodiesel and Jet A respectively.

4.4 Test conditions

The average molecular formula, degree of unsaturation, hydrogen to carbon ratio, carbon content and oxygen content of the selected fuels from methyl ester family, petroleum family and petro-fuel / methyl ester blends family are presented in Table 4.4, Table 4.5 and Table 4.6 respectively. The biodiesels have about 11 - 12% (by weight) of fuel bound oxygen content while petro-fuels like heptane, toluene, Jet A and diesel do not have fuel bound oxygen present in the fuel. Among the tested fuels, heptane (C_7H_{16}) has the highest H/C ratio of 2.29 and toluene (C_7H_8) has the lowest H/C ratio of 1.14. Among methyl esters family, the H/C ratio is in the range of 1.8 to 1.9 while among the blends, the H/C ratio has a wide range of 1.5 to 2.1. Toluene has the highest carbon content of about 91% while PME has the lowest carbon content of 76% among the tested fuels. In general, biodiesels have lower carbon content in the range of 76% to 77% while petroleum fuels have relatively higher carbon content of about 84% to 90% (Table 4.4 - 4.6). The degree of fuel unsaturation, which encompasses the effects of carbon and oxygen content and H/C ratio, plays a significant role in the formation of end pollutants.

As already mentioned, this research study involves the investigation of the emission characteristics of laminar flames of pre-vaporized fuels at a fuel-lean condition (Φ = 0.9), near stoichiometric (Φ = 1.0), and moderate fuel-rich condition (Φ = 1.2 and 1.5). The test conditions and the corresponding flow rates of the selected fuels from methyl ester family, petroleum family and petro-fuel / methyl ester blends family are presented in Table 4.7, Table 4.8 and Table 4.9 respectively. The fuel flow rate was held constant at a given equivalence ratio and the air flow rate was adjusted accordingly; thus, the

carbon input rate was approximately constant for a given equivalence ratio. The fuel flow rates at equivalence ratios of 0.9 and 1.0 were 28% lower than those corresponding to the equivalence ratios of 1.2 and 1.5.

Table 4.1 List of fuels considered for the investigation

DOU	Methyl ester Family							Petroleum family				Petroleum / Methyl ester blends					
	Individual Ester	Neat commercial biodiesels	Commercial biodiesel/biodiesel blends					Alkanes and aromatics	Blends of alkanes and aromatics	Neat commercial petrofuels	Commerical petro/petro fuel blends	Ester/petrofuel blends	Commercial petro/biodiesel blends				
			CP blends	CR blends	CS blends	PR blends	PS blends						SD blends	CD blends	RD blends	PD blends	PJ blends
0.0								Heptane									
0.2																	
0.4									H92T08			H65MO35					
0.6																	
0.8																	
1.0									H80T20			H30MO70					
1.3																	
1.5																	
1.7		PME							H65T35			H08MO92					
1.8			C43P57			P80R20	P82S18										
1.9			C71P29			P67R33	P71S29										P75J25
2.0	MO	CME				P53R47	P59S41		H58T42							P75D25	
2.1				C75R25	C80S20	P40R60	P47S53										P50J50
2.2				C50R50	C60S40	P27R73	P35S65										
2.3				C25R75	C40S60	P14R86	P24S76							C75D25			P25J75
2.4		RME			C20S80		P12S88									P50D50	
2.5		SME							H45T55	Jet A		T10MO90					
2.6											J80D20		S75D25	C50D50	R25D75		
2.7											J60D40				R50D50	P25D75	
2.8											J34D66		S50D50	C25D75	R25D75		
2.9											J20D80		S25D75				
3.0									H32T68	Diesel		T23MO77					
3.2																	
3.4																	
3.6									H12T88			T55MO45					
3.8																	
4.0								Toluene									

All the blends are in volumetric proportions; Refer to “Nomenclature” section for the abbreviations

Table 4.2 Composition of commercial biodiesels investigated in this work

Individual methyl esters			PME[a]	CME[b]	RME[b]	SME[a]
Name	Molecular formula	No. of double bonds				
Methyl caprylate	$C_9H_{18}O_2$	1	0.0	0.0	0.0	0.0
Methyl caprate	$C_{11}H_{22}O_2$	1	0.0	0.0	0.0	0.0
Methyl laurate	$C_{13}H_{26}O_2$	1	0.0	0.0	0.0	0.0
Methyl myristate	$C_{15}H_{30}O_2$	1	1.5	0.0	0.0	0.0
Methyl palmitate	$C_{17}H_{34}O_2$	1	43.0	3.7	2.7	10.2
Methyl margarate	$C_{18}H_{36}O_2$	1	0.0	0.0	0.0	0.0
Methyl stearate	$C_{19}H_{38}O_2$	1	4.4	1.8	2.8	4.1
Methyl arachidate	$C_{21}H_{42}O_2$	1	0.0	0.6	0.0	0.0
Methyl behenate	$C_{23}H_{46}O_2$	1	0.0	0.4	0.0	0.0
Methyl lignocerate	$C_{25}H_{50}O_2$	1	0.0	0.0	0.0	0.0
Methyl palmitoleate	$C_{17}H_{32}O_2$	2	0.3	0.4	0.0	0.3
Methyl oleate	$C_{19}H_{36}O_2$	2	40.6	60.0	21.9	23.1
Methyl eicosanoate	$C_{21}H_{42}O_2$	2	0.0	0.5	0.0	0.0
Methyl linoleate	$C_{19}H_{34}O_2$	3	10.1	21.2	13.1	54.2
Methyl linolenate	$C_{19}H_{32}O_2$	4	0.1	11.3	8.6	8.1
Methyl erucate	$C_{23}H_{44}O_2$	2	0.0	0.3	50.9	0.0

[a] Conglio et al. (2013); [b] Allen et al. (1999)

Table 4.3 Composition of No:2 Diesel and Jet-A fuel

Hydrocarbon composition (wt. %)	Petro-diesel [a]	Jet A[b]
Paraffins (n and iso)	41.3	46.7
Monocycloparaffins	22.1	26.2
Bicycloparaffins	9.6	5.9
Tricycloparaffins	2.3	0.8
Alkyl benzenes	5.9	13.0
Teralins	4.1	4.1
Dinaphthenobenzenes	1.8	1.0
Naphthalenes	8.2	1.9
Acenaphthenes ($C_{12}H_{10}$)	2.6	0.3
Acenapthylenes ($C_{12}H_8$)	1.4	0.2
Phenanthrenes ($C_{14}H_{10}$)	0.7	0.0
Total saturated hydrocarbons	75.3	79.5
Total aromatic hydrocarbons	24.7	20.5

[a] Agency for Toxic substance and Disease Registry (1995);

[b] American Petroleum Institute (2010)

Table 4.4 Properties of selected fuels from the methyl ester family

Type	Fuel	Equivalent molecular formula	DOU	H/C	Carbon content (% wt.)	Oxygen content (% wt.)
Individual methyl ester	MO	$C_{19}H_{36}O_2$	2.0	1.89	77.0	10.8
Neat biodiesels	PME	$C_{17.1}H_{32.9}O_2$	1.7	1.92	76.0	11.8
	CME	$C_{19}H_{36}O_2$	2.0	1.89	77.0	10.8
	RME	$C_{19}H_{35.2}O_2$	2.4	1.85	77.2	10.8
	SME	$C_{18.8}H_{34.6}O_2$	2.5	1.84	77.2	11.0
Canola/Palm methyl ester blends	C43P57	$C_{17.9}H_{34.2}O_2$	1.8	1.91	76.4	11.4
	C71P29	$C_{18.4}H_{35.1}O_2$	1.9	1.91	76.7	11.1
Canola/rapeseed methyl ester blends	C75R25	$C_{19}H_{35.8}O_2$	2.1	1.88	77.1	10.8
	C50R50	$C_{19}H_{35.6}O_2$	2.2	1.87	77.1	10.8
	C25R75	$C_{19}H_{35.4}O_2$	2.3	1.86	77.2	10.8
Canola/soy methyl ester blends	C80S20	$C_{19}H_{35.7}O_2$	2.1	1.88	77.1	10.8
	C60S40	$C_{18.9}H_{35.4}O_2$	2.2	1.87	77.1	10.9
	C40S60	$C_{18.9}H_{35.2}O_2$	2.3	1.86	77.1	10.9
	C20S80	$C_{18.8}H_{34.9}O_2$	2.4	1.86	77.1	10.9
Palm/rapeseed methyl ester blends	P80R20	$C_{17.5}H_{33.3}O_2$	1.8	1.90	76.3	11.6
	P67R33	$C_{17.7}H_{33.6}O_2$	1.9	1.90	76.4	11.5
	P53R47	$C_{18}H_{33.9}O_2$	2.0	1.88	76.6	11.4
	P40R60	$C_{18.2}H_{34.2}O_2$	2.1	1.88	76.7	11.2
	P27R73	$C_{18.5}H_{34.5}O_2$	2.2	1.86	76.9	11.1
	P14R86	$C_{18.7}H_{34.9}O_2$	2.3	1.87	77.0	11.0
Palm/soy methyl ester blends	P82S18	$C_{17.4}H_{33.2}O_2$	1.8	1.91	76.2	11.7
	P71S29	$C_{17.6}H_{33.4}O_2$	1.9	1.90	76.4	11.6
	P59S41	$C_{17.8}H_{33.6}O_2$	2.0	1.89	76.5	11.5
	P47S53	$C_{18}H_{33.8}O_2$	2.1	1.88	76.7	11.4
	P35S65	$C_{18.2}H_{34}O_2$	2.2	1.87	76.8	11.3
	P24S76	$C_{18.4}H_{34.2}O_2$	2.3	1.86	76.9	11.1
	P12S88	$C_{18.6}H_{34.4}O_2$	2.4	1.85	77.1	11.0

Table 4.5 Properties of selected fuels from the petro-fuel family

Type	Fuel	Equivalent molecular formula	DOU	H/C	Carbon content (% wt.)	Oxygen content (% wt.)
Saturated hydrocarbon	n-heptane	C_7H_{16}	0.0	2.29	84.0	0.0
Aromatic hydrocarbon	toluene	C_7H_8	4.0	1.14	91.3	0.0
Heptane / toluene blends	H92T08	$C_7H_{15.1}$	0.4	2.16	84.8	0.0
	H80T20	$C_7H_{13.9}$	1.0	1.99	85.8	0.0
	H65T35	$C_7H_{12.6}$	1.7	1.80	87.0	0.0
	H58T42	$C_7H_{12.6}$	2.0	1.71	87.5	0.0
	H45T55	C_7H_{11}	2.5	1.57	88.4	0.0
	H32T68	C_7H_{10}	3.0	1.43	89.4	0.0
	H12T88	$C_7H_{8.7}$	3.6	1.24	90.6	0.0
Neat petroleum fuels	Jet A	$C_{13}H_{23}$	2.5	1.77	87.2	0.0
	Diesel	$C_{14.4}H_{24.9}$	3.0	1.73	87.4	0.0
JetA / Petrodiesel blends	J80D20	$C_{13.3}H_{23.4}$	2.6	1.76	87.2	0.0
	J60D40	$C_{13.5}H_{23.7}$	2.7	1.76	87.2	0.0
	J34D66	$C_{13.9}H_{24.2}$	2.8	1.74	87.3	0.0
	J20D80	$C_{14.4}H_{24.5}$	2.9	1.74	87.4	0.0

Table 4.6 Properties of selected fuels from the petro-fuel/methyl ester blends family

Type	Fuel	Equivalent molecular formula	DOU	H/C	Carbon content (% wt.)	Oxygen content (% wt.)
Heptane / methyl oleate blends	H65MO35	$C_{9.3}H_{19.8}O_{0.4}$	0.4	2.13	81.0	4.6
	H30MO70	$C_{13}H_{26.1}O_{1}$	1.0	2.01	78.7	8.1
	H08MO92	$C_{17}H_{32.7}O_{1.7}$	1.7	1.92	77.3	10.3
Toluene / methyl oleate blends	T10MO90	$C_{15.9}H_{28.7}O_{1.5}$	2.5	1.81	78.4	9.9
	T23MO77	$C_{13.1}H_{22.3}O_{1}$	3.0	1.70	80.4	8.2
	T55MO45	$C_{9.4}H_{13.7}O_{0.4}$	3.6	1.46	84.9	4.8
SME / Petro-diesel blends	S75D25	$C_{17.4}H_{31.5}O_{1.4}$	2.6	1.81	79.5	8.5
	S50D50	$C_{16.2}H_{28.9}O_{0.8}$	2.8	1.78	82.3	5.4
	S25D75	$C_{15.2}H_{26.8}O_{0.4}$	2.9	1.76	84.6	3.0
CME / Petro-diesel blends	C75D25	$C_{17.5}H_{32.4}O_{1.4}$	2.6	1.85	79.3	8.5
	C50D50	$C_{16.3}H_{29.5}O_{0.8}$	2.6	1.81	82.2	5.4
	C25D75	$C_{15.3}H_{27}O_{0.4}$	2.8	1.76	84.6	2.9
RME / Petro-diesel blends	R75D25	$C_{17.5}H_{31.9}O_{1.4}$	2.6	1.82	79.5	8.5
	R50D50	$C_{16.3}H_{29.1}O_{0.8}$	2.7	1.79	82.4	5.4
	R25D75	$C_{15.3}H_{26.9}O_{0.4}$	2.8	1.76	84.6	3.0
PME / Petro-diesel blends	P75D25	$C_{16.3}H_{30.4}O_{1.4}$	2.0	1.87	78.7	9.0
	P50D50	$C_{15.6}H_{28.3}O_{0.9}$	2.4	1.81	81.4	6.3
	P25D75	$C_{14.9}H_{26.5}O_{0.4}$	2.7	1.78	84.5	3.0
PME / Jet A blends	P75J25	$C_{15.8}H_{29.8}O_{1.4}$	1.9	1.89	78.4	9.3
	P50J50	$C_{14.7}H_{27.1}O_{0.8}$	2.1	1.84	81.6	5.9
	P25J75	$C_{13.8}H_{24.9}O_{0.4}$	2.3	1.80	84.1	3.3

Table 4.7 Test conditions of selected fuels from the methyl ester family

Fuel	Φ = 0.9			Φ = 1.0			Φ = 1.2			Φ = 1.5		
	Fuel flow rate (cm^3/s)	Air flow rate (cm^3/s)	Carbon input rate (mg/s)	Fuel flow rate (cm^3/s)	Air flow rate (cm^3/s)	Carbon input rate (mg/s)	Fuel flow rate (cm^3/s)	Air flow rate (cm^3/s)	Carbon input rate (mg/s)	Fuel flow rate (cm^3/s)	Air flow rate (cm^3/s)	Carbon input rate (mg/s)
MO		100	7.7		91	7.7		104	10.8		84	10.8
PME		97	7.6		88	7.6		102	10.6		82	10.6
CME		100	7.7		91	7.7		104	10.8		84	10.8
RME		100	7.7		91	7.7		104	10.8		84	10.8
SME		100	7.7		91	7.7		104	10.8		84	10.8
C43P57		100	7.6		88	7.6		104	10.7		82	10.7
C71P29		100	7.7		91	7.7		104	10.7		84	10.7
C75R25		100	7.7		91	7.7		104	10.8		84	10.8
C50R50		100	7.7		91	7.7		104	10.8		84	10.8
C25R75		100	7.7		91	7.7		104	10.8		84	10.8
C80S20		100	7.7		91	7.7		104	10.8		84	10.8
C60S40		100	7.7		91	7.7		104	10.8		84	10.8
C40S60		100	7.7		91	7.7		104	10.8		84	10.8
C20S80	0.010	100	7.7	0.010	91	7.7	0.014	104	10.8	0.014	84	10.8
P80R20		97	7.6		88	7.6		102	10.7		82	10.7
P67R33		100	7.6		88	7.6		102	10.7		82	10.7
P53R47		100	7.7		88	7.7		104	10.7		82	10.7
P40R60		100	7.7		88	7.7		104	10.7		84	10.7
P27R73		100	7.7		91	7.7		104	10.8		84	10.8
P14R86		100	7.7		91	7.7		104	10.8		84	10.8
P82S18		97	7.6		88	7.6		102	10.7		82	10.7
P71S29		100	7.6		88	7.6		102	10.7		82	10.7
P59S41		100	7.7		88	7.7		104	10.7		82	10.7
P47S53		100	7.7		88	7.7		104	10.7		84	10.7
P35S65		100	7.7		91	7.7		104	10.8		84	10.8
P24S76		100	7.7		91	7.7		104	10.8		84	10.8
P12S88		100	7.7		91	7.7		104	10.8		84	10.8

Table 4.8 Test conditions of selected fuels from the petro-fuel family

Fuel	Φ = 0.9			Φ = 1.0			Φ = 1.2			Φ = 1.5		
	Fuel flow rate (cm^3/s)	Air flow rate (cm^3/s)	Carbon input rate (mg/s)	Fuel flow rate (cm^3/s)	Air flow rate (cm^3/s)	Carbon input rate (mg/s)	Fuel flow rate (cm^3/s)	Air flow rate (cm^3/s)	Carbon input rate (mg/s)	Fuel flow rate (cm^3/s)	Air flow rate (cm^3/s)	Carbon input rate (mg/s)
n-heptane		93	8.4		84	8.4		97	11.8		77	11.8
toluene		106	9.1		95	9.1		111	12.8		88	12.8
H92T08		95	8.5		86	8.5		100	11.9		79	11.9
H80T20		97	8.6		88	8.6		102	12.0		82	12.0
H65T35		100	8.7		91	8.7		104	12.2		84	12.2
H58T42		102	8.8		91	8.8		104	12.3		84	12.3
H45T55		102	8.8		93	8.8		106	12.4		86	12.4
H32T68	0.010	104	8.9	0.010	93	8.9	0.014	109	12.5	0.014	86	12.5
H12T88		106	9.1		95	9.1		111	12.7		88	12.7
Jet A		104	8.7		93	8.7		109	`		86	12.2
diesel		111	8.7		100	8.7		116	12.2		93	12.2
J80D20		106	8.7		95	8.7		111	12.2		88	12.2
J60D40		106	8.7		95	8.7		111	12.2		88	12.2
J34D66		109	8.7		97	8.7		113	12.2		91	12.2
J20D80		109	8.7		97	8.7		113	12.2		91	12.2

Table 4.9 Test conditions of selected fuels from the petro-fuel/methyl ester blends family

Fuel	Φ = 0.9			Φ = 1.0			Φ = 1.2			Φ = 1.5		
	Fuel flow rate (cm^3/s)	Air flow rate (cm^3/s)	Carbon input rate (mg/s)	Fuel flow rate (cm^3/s)	Air flow rate (cm^3/s)	Carbon input rate (mg/s)	Fuel flow rate (cm^3/s)	Air flow rate (cm^3/s)	Carbon input rate (mg/s)	Fuel flow rate (cm^3/s)	Air flow rate (cm^3/s)	Carbon input rate (mg/s)
H65MO35		93	8.1		82	8.1		95	11.3		77	11.3
H30MO70		93	7.9		84	7.9		97	11.0		77	11.0
H08MO92		97	7.7		88	7.7		102	10.8		82	10.8
T10MO90		100	7.8		91	7.8		104	11.0		84	11.0
T23MO77		102	8.0		91	8.0		104	11.3		84	11.3
T55MO45		102	8.5		93	8.5		106	11.9		86	11.9
S75D25		102	8.0		93	8.0		106	11.1		86	11.1
S50D50		104	8.2		95	8.2		109	11.5		88	11.5
S25D75		109	8.5		97	8.5		113	11.8		91	11.8
C75D25		102	7.9		93	7.9		106	11.1		86	11.1
C50D50	0.010	104	8.2	0.010	95	8.2	0.014	109	11.5	0.014	88	11.5
C25D75		109	8.5		97	8.5		113	11.8		91	11.8
R75D25		102	8.0		93	8.0		106	11.1		86	11.1
R50D50		104	8.2		95	8.2		109	11.5		88	11.5
R25D75		109	8.5		97	8.5		113	11.8		91	11.8
P75D25		102	7.9		91	7.9		88	11.0		84	11.0
P50D50		104	8.1		93	8.1		109	11.4		86	11.4
P25D75		106	8.5		97	8.5		111	11.8		91	11.8
P75J25		100	7.8		88	7.8		102	11.0		82	11.0
P50J50		100	8.2		91	8.2		104	11.4		84	11.4
P25J75		102	8.4		93	8.4		106	11.8		86	11.8

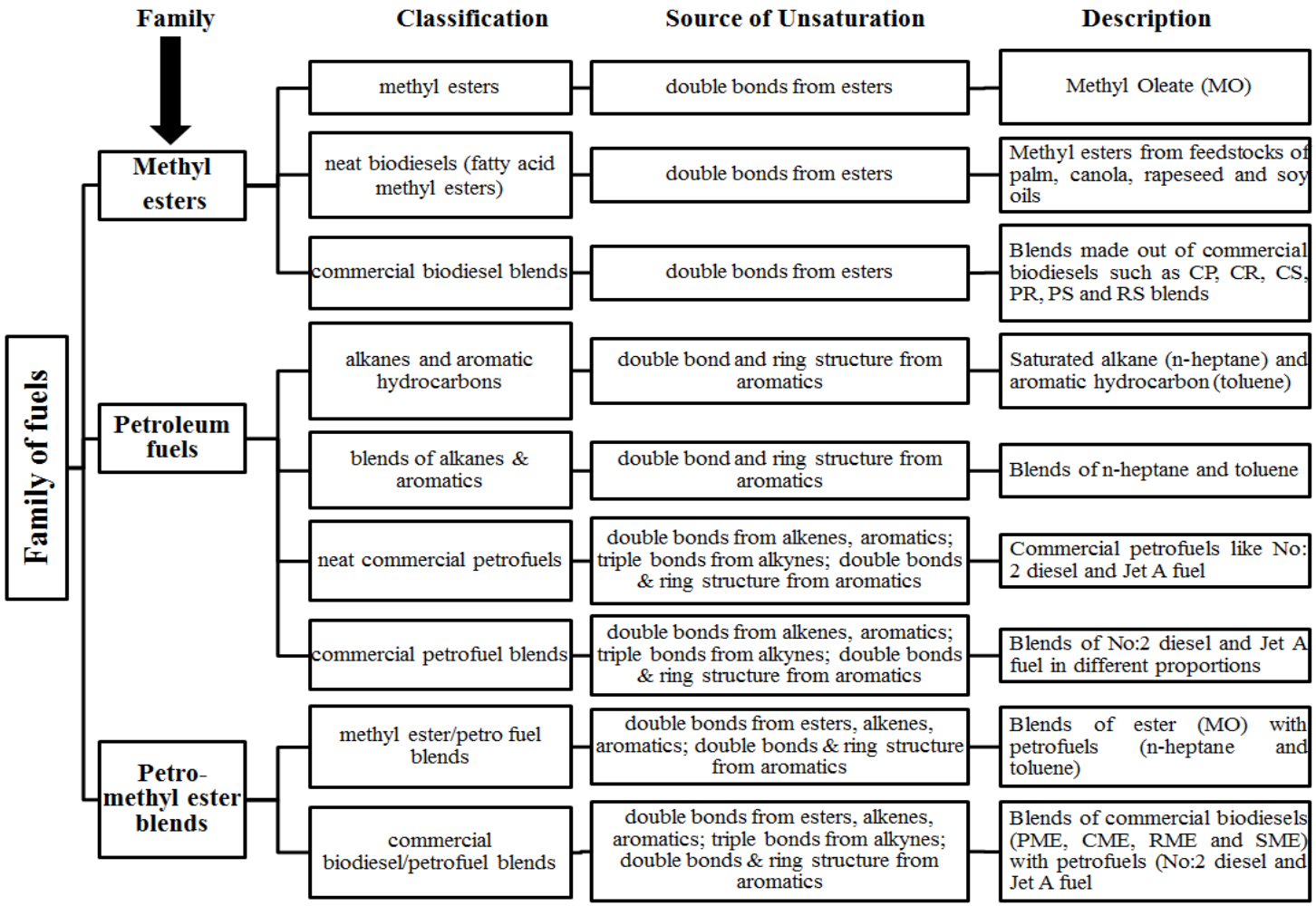

Figure 4.1Classification of the family of fuels investigated in this study

CHAPTER 5 EXPERIMNETAL SETUP AND PROCEDURE

In this chapter, the components of experimental setup and the appropriate selection of instruments for the experiments performed are described along with the measurement techniques.

5.1 Experimental setup

A schematic diagram of the setup is presented in Figure 5.1. The experiments were conducted in a large steel combustion chamber (76 cm by 76 cm and 150 cm in height). The burner used for the experiments was housed within the chamber at its bottom center. The walls of the chamber contained high-temperature glass windows provided with removable slotted metal sheet covers measuring 96 cm x 25 cm to allow optical access. The top of the combustion chamber was open to atmosphere through an exhaust duct. The ambient pressure of the laboratory was maintained at slightly above the atmospheric pressure (~20 Pa) to provide a positive draft inside the test chamber to prevent leakage of the combustion products into the laboratory.

5.1.1 Laminar flame tubular burner

A rapid characterization technique was employed to ascertain the influence of fuel chemistry on the combustion and emission characteristics of flames tested at different equivalence ratios. This technique consisted of a laminar flame arrangement in which pre-vaporized fuels were tested at a wide range of equivalence ratios to simulate

various reaction regions that exist during combustion in a compression ignition engine. The advantage of this experimental arrangement is that it requires a small quantity of fuel (less than 100 ml) to characterize the emission characteristics of the tested fuels and the trends of measured emission results agreed with those observed in engine studies. The experimental arrangement included a stainless-steel tubular burner of circular cross section (ID of 9.5 mm and OD of 12.7 mm, Figure 5.2) with a beveled rim served as the burner. Because of its robust design, and feasibility for simple fabrication and heating, the tubular burner was selected for this study. This burner provided repeatable flame measurements and supported stable flames in a variety of flame configurations such as lean premixed and partially premixed flames of petroleum and biodiesel fuels and their blends, as presented in previous studies by Love et al. (2009, 2009a, 2011), Singh et al. (2013), Romero et al. (2014) and Balakrishnan et al. (2016a).

5.1.2 Fuel and air delivery system

The liquid fuel was injected into a high-temperature air stream to vaporize the fuel completely without liquid-phase pyrolysis that could lead to coking of the fuel. The air flow was provided from a compressed air tank through a 12.7 mm (OD) steel tube with a temperature-controlled heating tape wrapped around it. The temperature of the air stream was monitored and controlled by a temperature controller connected to a relay-controlled power supply. The air flow temperature at the fuel injection location was maintained at 390^{o}C, which was sufficiently high above the final boiling point of the fuels so as to completely vaporize the injected fuel and low enough to prevent coking in the feed lines. The heated line was long enough (230 cm) to ascertain that the

liquid fuel was completely vaporized in the air stream before exiting the burner. The liquid fuel was delivered to the heated air through a high temperature silica-based septum with a 50 cm^3 capacity syringe attached to a syringe pump. The volume flow rate of air was monitored using a calibrated rotameter (calibration information is provided in Appendix B). A periodic examination of the walls of air-fuel mixture carrier tube indicated the absence of any coking. Also, measurements with an air/fuel ratio analyzer indicated that the entire mass flow of liquid fuel injected into the heated air stream exited the burner in vapor state (based on the carbon balance calculations presented in the following section). The fuel-air mixture was ignited at the exit of the burner with an external pilot flame which was removed after ignition.

5.2 Verification that all the injected liquid fuel was evaporated

Experiments were conducted to confirm that all the liquid fuel that was injected through the septum was completely evaporated and came out of the burner without any pyrolysis or deposits within the carrier tube.

5.2.1 Validation using gas composition analyzer

Two analyzers, namely an Air-Fuel Ratio (AFR) analyzer and a gas sample composition analyzer were used in the experiment. Jet - A flame at a test condition of equivalence ratio, $\Phi = 2$ was studied. The test condition was achieved by operating at a constant fuel flow rate of 2.2 lpm using a 50-cc syringe and an air flow rate of about 10.46 lpm. A copper tube (63 mm internal diameter and 470 mm in length) was used to enclose the tubular burner and the flame. Aluminum tape was used to seal the bottom

end of the copper tube enclosure to control the air entrainment in to the flame. An AFR analyzer (Horiba Instruments, Model: MEXA - 101λ) was used to measure the air-fuel ratio at the flame tip. This analyzer had the provision to measure the air-fuel ratio and percentage content of oxygen based on the product stream coming out of the flame.

In addition, a gas sample analyzer (Nova Analytical Instruments, Model: 7466K) was used to measure the concentration of species such as CO_2, CO, NO and O_2 in the product stream of combustion. The product gas sample from the flame was drawn continuously through a 1 mm internal diameter tip quartz probe and was expanded through a 6 mm tube and passed through a condenser ice bath to condense and remove moisture and a pre-filer element made of Cole Parmer fiber glass wool to remove particulate and other impurities along the sample line before the gas sample was fed into the gas analyzer.

The results obtained from the measurements using AFR analyzer and gas analyzer are presented in Tables 5.1 and 5.2 for three conditions: bottom of the copper tube completely sealed to eliminate any external air entrainment from the bottom, bottom of the copper tube partially sealed, and the bottom completely open. For Jet A, the stoichiometric air-fuel ratio (by volume) is 89.25; for an injector exit equivalence ratio of 2, the air-fuel ratio is 44.63. Without the copper tube, the measured air fuel ratio was 78 - 83, which is comparable to the value obtained with the bottom of the copper enclosure open. This indicates that the primary entrainment of air was from the bottom of the enclosure, and that sufficient air had been entrained to increase the value from 44.63 to almost double the value.

When the bottom end of copper tube was blocked by aluminum tape, the air fuel ratio dropped down to the range of 24 - 27. This value corresponded to an equivalence ratio of around $\Phi = 3.3$ instead of $\Phi = 2$, suggesting that there was some fuel vapor left inside the enclosure without being burnt, even though there was left over oxygen (with a concentration of 13%). This may be due to the fuel not having sufficient time to completely burn before leaving the copper enclosure. Nevertheless, the small value of air-fuel ratio (24 - 27) indicates that all the injected fuel came out of the tube. When the bottom of the copper tube was partially open, the measured air-fuel ratio was 32 - 33 (again lower than 44.63), indicating that all the fuel had not been burnt at this condition also. Only when the bottom was completely open, sufficient air was entrained to burn the fuel completely, with left-over air in the products, resulting in an air-fuel ratio of 78 - 82.

5.2.2 Validation using carbon balance

Carbon balance is another technique employed to confirm the complete evaporation of liquid fuel that was injected into the septum and the evaporated fuel vapor came out of the burner without any pyrolysis or deposits. Since mass is conserved, the mass flow rate of carbon (from the fuel) injected into the septum should be equal to the mass flow rate of carbon (in the form of carbon dioxide) leaving the flame after combustion. The concentration of CO measured at this condition was at parts per million levels (13 ppm, refer Table 5.3) and soot measured at 75% of flame height was 1.5 ppm (Balakrishnan et al., 2014), hence the contributions from CO and soot are neglected in the mass conservation analysis.

A test condition of Φ = 2 - Jet A flame was considered for the study and the configuration of global emission measurement (presented in section 5.3.2) was incorporated for the experiment. The temperature, dynamic pressure and concentration of species such as CO_2, CO, NOx and O_2 were measured and presented in Table 5.3.

The mass flow rate of carbon as fuel was measured to be 2.55×10^{-5}kg/s and the mass flow rate of carbon in the form of carbon dioxide after combustion was found to be 2.86×10^{-5} kg/s. (The detailed calculations are presented in Appendix C). Hence, the mass flow rate of carbon injected into the septum as fuel is comparable to the mass flow rate of carbon liberated as carbon dioxide from the flame, with the variation attributed to the involved uncertainties in the experiment (refer Table 5.4 for the estimate of uncertainties in the measurements).

In summary, based on the validation using gas composition analyzer and carbon balance calculations, it has been confirmed that all the liquid fuel that was injected through the septum was completely evaporated and came out of the burner without any pyrolysis or deposits within the carrier tube.

5.3 Instrumentation Techniques

In this section, the instrumentation techniques and operational procedures involved in the measurement of global emission indices, inflame temperature measurements, inflame concentration measurements, PLIF measurements and capture of flame images are presented. A detailed list of equipments and instruments employed in this work along with their manufacturer information are presented in Table 5.5.

5.3.1 Flame visualization

The visible flame images were captured through an 8-mega pixel digital AF SLR camera. The images were obtained at similar lighting and exposure conditions with a dark background at different shutter speeds such as $1/10^{th}$, $1/50^{th}$, $1/100^{th}$ and $1/200^{th}$ of a second. Images were taken 50 cm away from the flame point. Images captured at $1/50^{th}$ of a second exposure were considered for flame length measurement, since in that condition, the exposed image rendered enough time required to trace the entire visible flame field and clearly distinguish the inner and outer cone reaction zones of the flames. Microsoft Paint software was used to count the pixels and convert them into the length scale using the burner width (12.7 mm) as the calibration reference. The flame length was calculated by measuring the number of pixels between the burner exit and the farthest visible point of the visible flame and the number of pixels was then converted into equivalent length scale using burner width pixels as the reference. Three images per condition were captured at arbitrary time intervals and the flame lengths were calculated and the resultant flame lengths were averaged.

5.3.2 Global emission index measurement

A Pyrex funnel with a height of 27 cm, bottom diameter of 16 cm and top diameter of 4 cm was mounted above the flame, where all the flue gases were collected and guided to an uncooled quartz probe with a 1 mm inner diameter orifice that rapidly expanded to 6 mm (inner diameter). These gas samples were passed through a water condenser immersed in an ice bath, in order to report all the emissions results on a dry basis and to remove any moisture, and subsequently were directed through a fiber filter to trap particulate matter. Measurements of the volumetric concentration of CO, CO_2 and NOx in the exhaust were carried out using a portable gas analyzer. The analyzer consisted of a built-in infrared detector for CO and CO_2 concentration measurements and electrochemical sensors for the measurement of O_2 and NOx concentrations. The schematic diagram of the global emission set up is shown in Figure 5.3.

The measurements were converted into emission indices on a mass basis (g of species/kg of fuel) (Turns, 2011). The emission index is the mass of pollutant produced per unit mass of fuel burned independent of any dilution of the product stream. The emission index is expressed as:

$$EI_i = \left(\frac{\chi_i}{\chi_{co}+\chi_{co_2}}\right)\left(\frac{N*MW_i}{MW_{fuel}}\right) * 1000 \qquad (5.1)$$

where χ_i, χ_{co} and χ_{co_2} are the mole fraction of the species, CO and CO_2 respectively, N is the number of atoms of carbon in a mole of fuel, and MW_i and MW_{fuel} are the molecular weights of the species, i and fuel respectively. It is assumed that all the

carbon in the fuel is converted into CO and CO_2 with negligible amounts of soot. This assumption was found to be valid since all the tested flames appeared blue without yellow luminous regions in the present work.

5.3.3 In-flame temperature measurement

The schematic diagram of the in-flame temperature measurement is shown in Figure 5.4. The in-flame temperature profiles were measured using an in-house built R-Type (Pt-Pt/13% Rh) thermocouple with a bead diameter of 0.2 mm. Catalytic action was reduced by coating the tip of the thermocouple with a fine layer of silica. The thermocouple was positioned along the length of the flame using a manually guided two-dimensional traverse mechanism. Measurements were taken at 2 mm radial distance intervals at three different heights: 10 mm, 20 mm and 40 mm above the burner. Data acquisition was accomplished using LabView software. The temperature readings were averaged over a period of 30 s with 1Hz of sampling rate and corrected for radiation and conduction losses (as shown in appendix D.7).

5.3.4 In-flame gas species concentration measurement

The schematic diagram of the in-flame gas species concentration measurement is shown in Figure 5.5. The in-flame gas concentration measurements were performed using an uncooled quartz probe that was similar to that used in the emission index measurements. The gas samples were treated to remove the moisture and particulates and then passed to a portable flue gas analyzer that was used for the global emission measurement. The sampling probe was mounted on a two-dimensional linear traverse

mechanism which facilitated the axial and radial movement of the probe across the flame field. The size of the probe (with a 1.5 mm outer diameter orifice) was small compared to the size of the flame; no visual disturbance of the flame due to the probe was observed. In-flame concertation measurements were performed at the same locations as those of in-flame temperature measurements. The concentrations are reported on a dry basis since the water vapor formed during combustion was removed to protect the sensors.

5.3.5 Planar Laser Induced Fluorescence (PLIF) measurement

Planar Laser Induced Fluorescence (PLIF) is an optical technique used to measure the local flow field parameters such as temperature, velocity and concentration of species. This technique has been extensively used to determine the relative population densities of intermediate radicals within a combustion test medium. In a PLIF measurement, a laser source, usually pulsed and tunable in wavelength, is used to form a thin sheet of light which traverses the flow field of interest. If the laser wavelength is resonant with an optical transition of a species present in the flow, a fraction of the incident light will be absorbed at each point within the illumination plane. A fraction of the absorbed photons may subsequently be re-emitted with a modified spectral distribution, which changes for different molecules and varies with local flow field conditions. The emitted light, known as fluorescence, is collected and typically imaged onto a solid-state array camera, usually image-intensified or cooled to provide time-gating and improved sensitivity. The amount of light detected by a pixel of the camera depends on the concentration of the interrogated species within the

corresponding measurement volume and the local flow field conditions, i.e., temperature, pressure and mixture composition. The results provide information about combustion kinetics, flame front, reaction zone, formation of pollutants and soot. PLIF is a highly selective, sensitive and non-intrusive method for the measurement of various flow field properties such as species concentration, which is of interest to combustion researchers.

A detailed knowledge about the formation and the destruction of the intermediate radicals such as OH and CH is necessary to understand the fundamental combustion chemistry of a fuel. The laser system used for the measurements in current study included Quanta-Ray GCR 200 pulsed Nd: YAG laser and Quanta- Ray MOPO-730 Optical Parametric Oscillator (OPO) with Frequency Doubler Option (FDO). The GCR 200 generated a laser beam at a wavelength of 355 nm, which pumped the OPO. The OPO was a coupled dual oscillator system including the power oscillator, which was seeded by the narrow output master oscillator. The gain in the OPO system was accomplished from the nonlinear interaction between the intense optical wave (laser) and crystal having a large nonlinear polarizability coefficient. Tuning of wavelengths of the passing laser was obtained by altering the angle of the OPO crystals made from Type I Beta Barium Borate (BBO) crystal. The tuning wavelengths range from 190 - 2000 nm (ultraviolet to infrared) when using the FDO.

PLIF images were acquired with Nd-Yag laser and a Princeton Instruments Model PI-MAX3: 1024i ICCD camera with an optical filter of narrow bandwidth, which reduced effects of background noise or stray light. The output beam of the OPO/FDO was directed with a highly reflective optical turning mirror onto a cylindrical lens creating a

2-D laser sheet. The 2-D sheet of excitation signal, about 20 mm in height and 4 mm in width, was directed into the combustion testing section. Fluorescence images were then acquired at 90^{o} to the incident laser sheet with the ICCD camera, which was interfaced with laser diagnostic system for synchronized triggering. The employed laser pulse width was over duration of 10 ns with a repetition rate of about 50Hz. A schematic diagram of this setup can be seen in Figure 5.6. The laser was tuned to the corresponding excitation wavelength of OH (283.5 nm) and the resulting fluorescence signal was collected at the fluorescence wave length of OH (315 nm). Similarly, for CH measurements, laser was tuned to the corresponding excitation wavelength of CH (431 nm) and the resulting fluorescence signal was also collected at the same wave length (431 nm). Since the transition was highly diagonal, the excitation and detection were done in the same band for CH radicals.

Table 5.1 Measurements using AFR analyzer in a Φ = 2 - Jet A flame for three conditions

Condition	Air Fuel Ratio range*	% Oxygen by volume*
Bottom of copper enclosure- completely closed	24 - 27	10.0
Bottom of copper enclosure- 10% closed	31 - 33	12.0
Bottom of copper enclosure- completely open	78 - 82	17.2

*Measured from the product stream

Table 5.2 Measurements using gas sample analyzer in a Φ = 2 - Jet A flame for three conditions

Condition	% O_2 by volume*	% CO_2 by volume*
Bottom of copper enclosure- completely closed	13.2	5.2
Bottom of copper enclosure- 10% closed	17.6	2.1
Bottom of copper enclosure- completely open	18.1	2.0

*Measured from the product stream

Table 5.3 Measured data for Φ = 2 - Jet A flame condition

Measured Parameters		
Species Concentration	O_2 (%)	17.1
	CO_2 (%)	2.1
	CO (ppm)	13
	NO_x (ppm)	18
Temperature (°C)		395
Dynamic pressure head (inches of water)		0.007

Table 5.4 Estimated experimental uncertainties

Flame Temperature (K)	5.0 %
Global emission index of NO (gNO/kg fuel)	12.0 %
Global emission index of CO (gCO/kg fuel)	11.0 %
Concentration of NO (ppmv)	12.0 %
Concentration of CO (Vol. %)	10.0 %
Concentration of O_2 (Vol. %)	5.0 %
Concentration of CO_2 (Vol. %)	8.0 %
Radiative Fraction	6.0 %

*Values obtained at 95% confidence level assuming Student - t distribution

Table 5.5 Equipment and Instrumentation

Key Parts and Instrumentation	**Manufacturer/ Model Number**
Syringe Pump	Harvard Apparatus 975
50 cc Interchangeable Syringe	B-D Multifit 512135
High Temperature 11 mm Inlet Septa	Agilent 5183-4757
High Temperature Heavy Insulated Heat Tape	Omega Engineering Inc. STH051-080
Rotameter with Tantalum Ball	Lo-Flo with Tube Type SK ¼''-15-G-5
Omega Temperature Control	Omega Engineering Inc. CN79022
Digital AF SLR 8 MP Camera	EOS Digital Rebel XT/EOS 350D
NO_x, CO, CO_2, O_2 Emission Analyzer	NOVA 7466K
Type R and Type K Thermocouple	Omega Engineering Inc.
Radiometer	96PY-20142
Precision Laser Power Meter	Coherent Field Mate 1028297
5 mW He-Ne Laser	Spectra Physics 105-1
Pulsed Nd: YAG Laser	Spectra Physics GCR 250-10
Optical Parametric Oscillator (OPO)	Spectra Physics MOPO-730
Frequency Doubler (FDO)	Spectra Physics FDO 970
Pulsed Laser Power Meter	Ophir Optronics Ltd. NOVA 30
ICCD Camera	Princeton Instrument PI-MAX3: 1024i
ICCD Camera Image Acquisition Computer	HP Workstation Z210
Data Acquisition Hardware	National Instruments LabView Board SCB-100
Data Acquisition Software	National Instruments LabView 2010
Data Acquisition Computer	HP Workstation Z210
ICCD Image Acquisition Software	Light Field 4.7
Traversing Mechanism	Unislide / Velmex Inc.

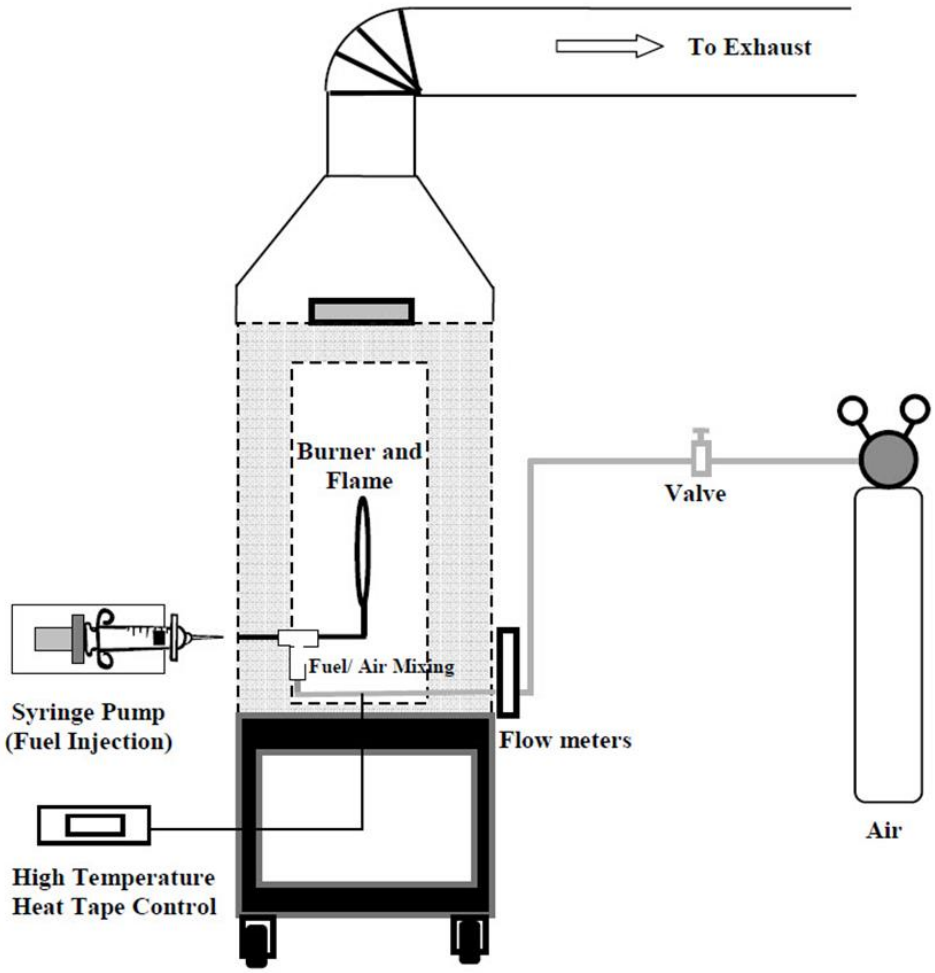

Figure 5.1 Schematic diagram of the experimental setup

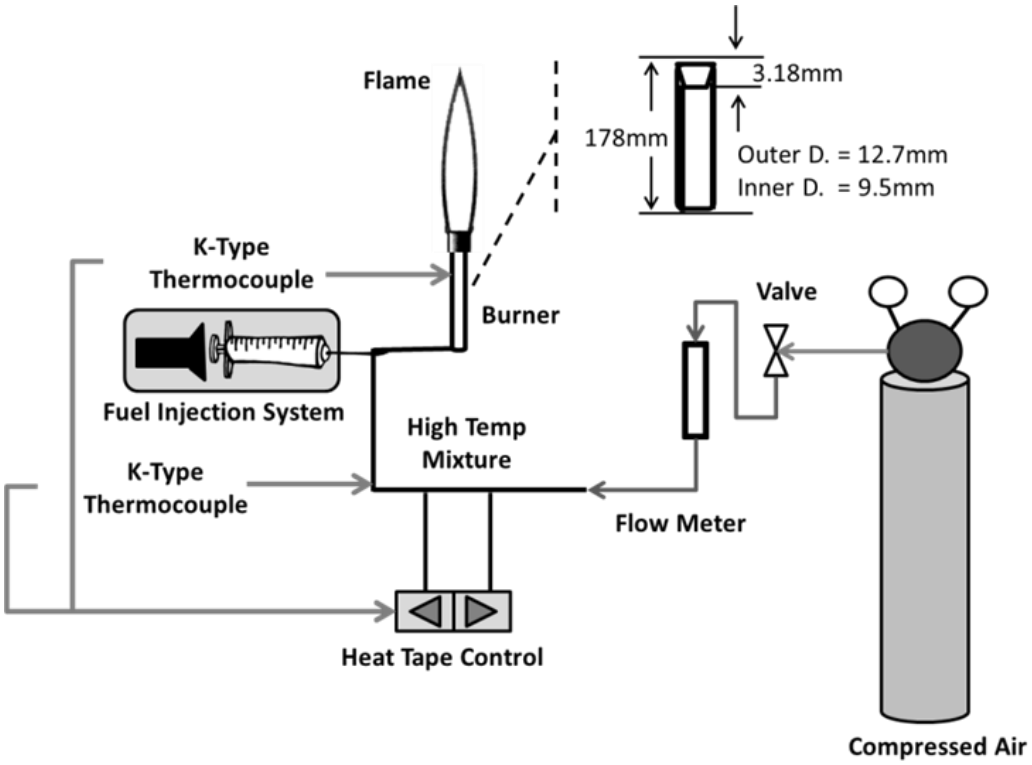

Figure 5.2 Schematic diagram of the fuel vapor / air delivery system

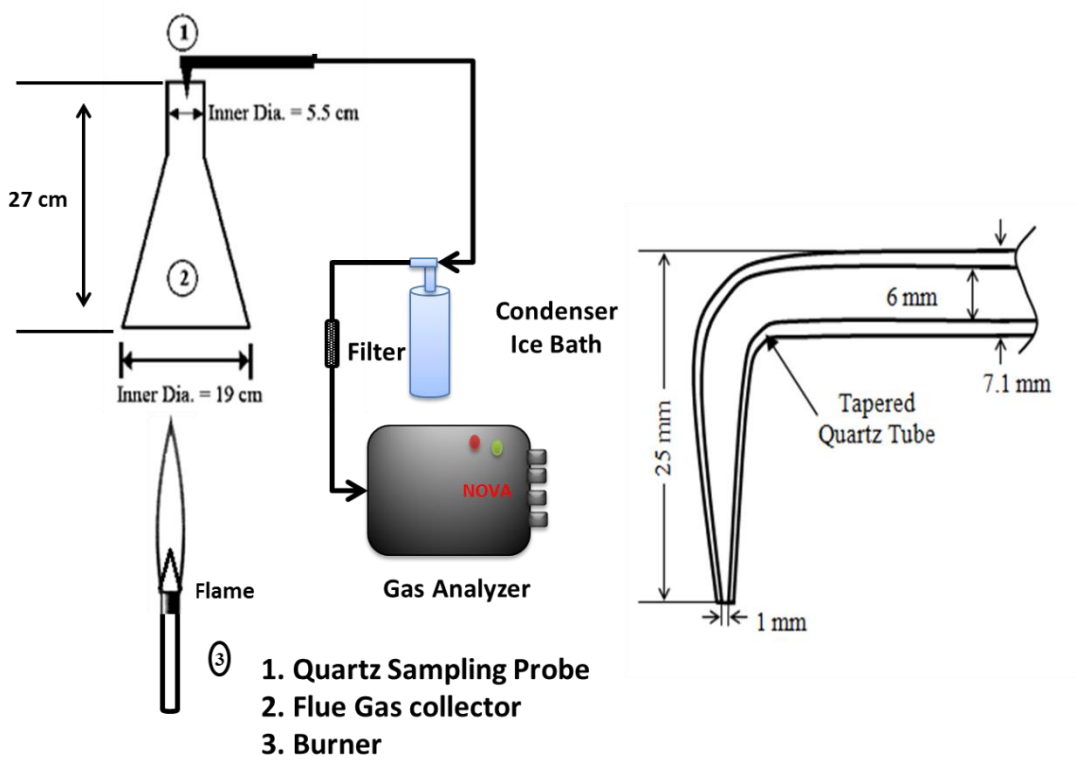

Figure 5.3 Schematic diagram of the global emission index measurement technique

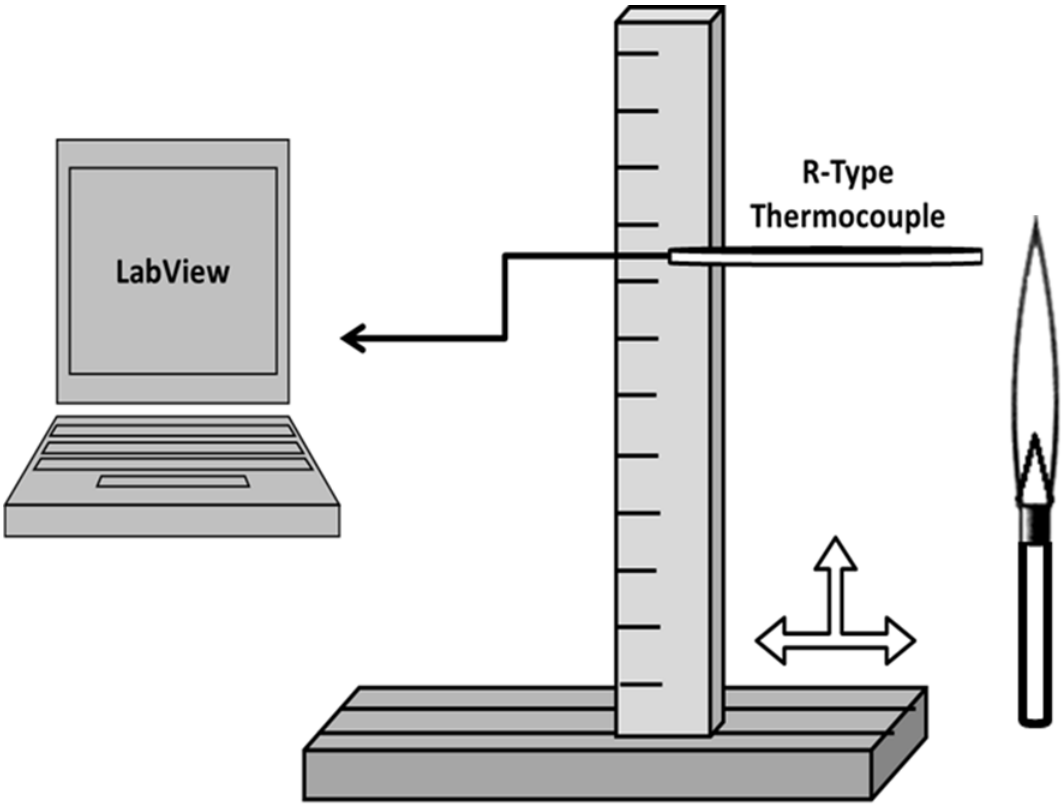

Figure 5.4 Schematic diagram of the in-flame temperature measurement technique

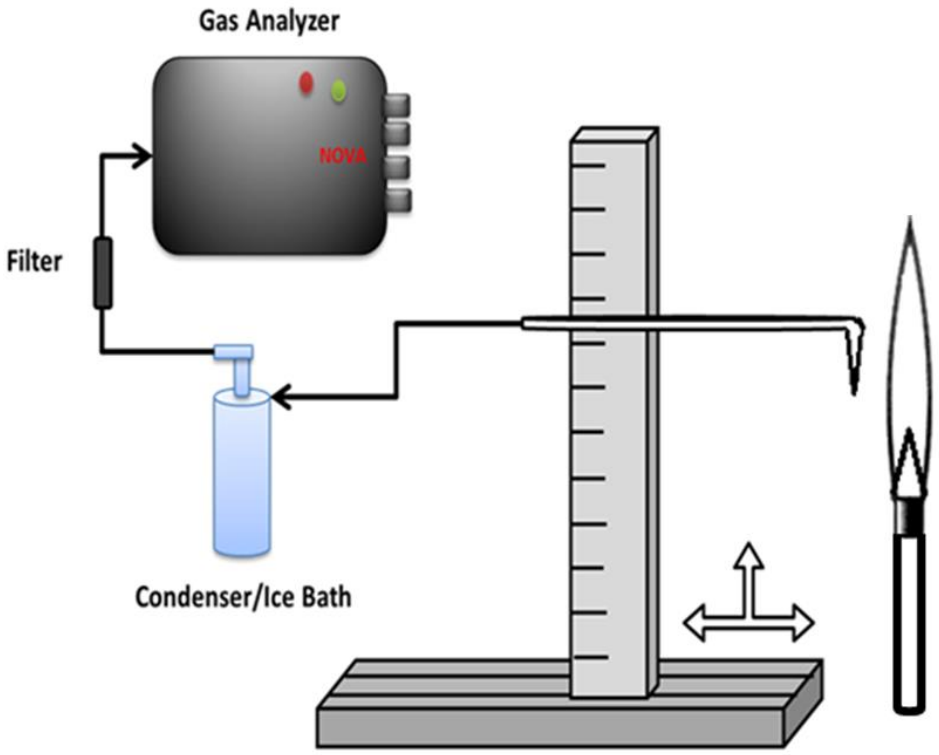

Figure 5.5 Schematic diagram of the in-flame species concentration measurement technique

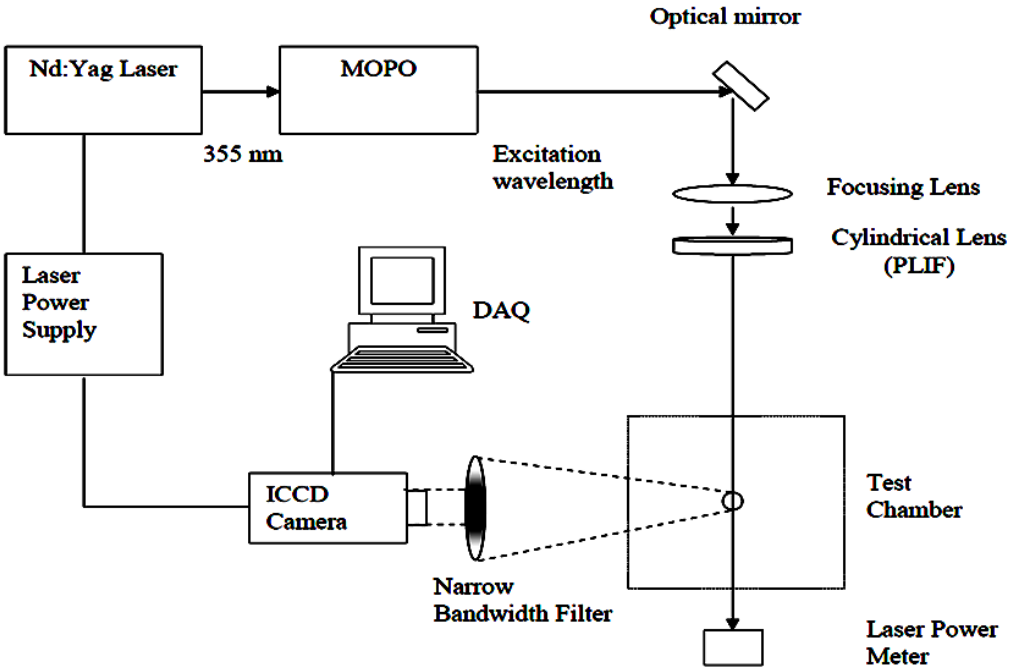

Figure 5.6 Schematic diagram of the PLIF measurement technique

CHAPTER 6 EXPERIMENTAL RESULTS - GLOBAL EMISSION INDICES

In this chapter, the global emission indices of CO and NO from the experimental investigation of laminar premixed flames of prevaporized MO (individual methyl ester), heptane and toluene (components of petroleum diesel), commercial petroleum fuels (petro-diesel and Jet A), commercial biodiesels (SME, CME, RME and PME), MO/heptane blends, MO/toluene blends and commercial petroleum/biodiesel blends are presented.

As mentioned earlier in Chapter 3, the primary objective of this research work was to investigate the effect of degree of fuel unsaturation on nitric oxide emissions from laminar flames of petro-fuels, biodiesels and their blends. The following experimental methodology was employed to accomplish the research objectives:

- Global EI_{NO} and EI_{CO} measurements were performed in the laminar flames of selected 63 fuels (Table 4.1) at equivalence ratios of 0.9, 1.0, 1.2 and 1.5 to develop experimental correlations between DOU and EI at different equivalence ratios.
- Then, to understand the influence of fuel (family) origin, fuels from different families but with same degree of unsaturation (DOU: 2) were selected as follows (refer Table 4.1): MO (individual methyl ester), CME (neat commercial biodiesel), P53R47 (palm/rapeseed methyl ester blend), P59S41 (palm/soy methyl ester blend), H58T42 (heptane/toluene blend; No fuel bound oxygen), P75D25 (palm methyl ester /petro-diesel blend).

- Detailed inflame measurements such as inflame radial temperature and radial species concentration measurements were performed in the laminar flames of aforementioned six fuels at Φ = 1.2, where the measured EI_{NO} was found to be maximum among the tested flames (based on the preliminary results; presented in the following sections).

The results derived out of these measurement techniques would furnish the necessary information to delineate and understand the fuel chemistry interactions, and to relate those findings with the observation of complex interactions between extensive spectrum of individual components present in commercial petroleum and biodiesel flames.

6.1 Global NO emission indices

6.1.1 Laminar flames of neat petroleum and biodiesel fuels

The previously published NO emission index (EI_{NO}) results from laminar flame studies that involved various neat fuels like diesel, JetA, soy methyl ester (SME), canola methyl ester (CME) and palm methyl ester (PME) and their blends at equivalence ratios (Φ) of 2, 3 and 7 have been compiled in Figure 6.1 (Love et al., 2009, 2009a, 2011; Singh et al., 2013; Romero et al., 2014; Gollahalli et al., 2014 and Balakrishnan et al., 2016a). Besides these results, EI_{NO} of prevaporized laminar flames of aforementioned fuels in addition to rapeseed methyl ester (RME) and diesel/RME blends were measured at equivalence ratios of 0.9, 1.0, 1.2 and 1.5. These results are also included in Figure 6.1 to cover a wide range of equivalence ratios and DOU values. As noted earlier, NO formation depends on various complex and coupled physio-chemical parameters

(Hoekman and Robbins, 2012). Therefore, the extent of influence of fuel unsaturation on EI_{NO} is not the same at all equivalence ratios. At equivalence ratios of 0.9 and 1, EI_{NO} increases with increasing DOU; the magnitude of rise increases from Φ = 0.9, reaches a maximum at Φ = 1.2 and decreases to a lower value at Φ = 1.5. At higher equivalence ratios, particularly at Φ = 3 and 7, fuel chemistry and unsaturation effects have a minimal influence on the EI_{NO} due to the significant soot formation under these conditions. In summary, fuel unsaturation has its maximum influence on EI_{NO} at Φ = 1.2.

6.1.2 Influence of hydrocarbon family on EI_{NO} of fuels with same DOU

The degree of unsaturation is calculated based on the molecular hydrogen and carbon atoms, regardless of the hydrocarbon family. However, the sources of fuel unsaturation, such as double bonds and aromatics, engender differences in the combustion chemistry that result in varying amounts of EI_{NO} though the fuels have the same degree of unsaturation. Consider the fuels, Jet A and SME with the average molecular formula reported as $C_{13}H_{23}$ and $C_{18.8}H_{34.6}O_2$ (Conglio et al., 2013). Interestingly, according to the formula for the degree of unsaturation, both Jet A and SME have the same DOU of 2.5. However, Jet A is composed of primarily alkanes (50-65% by weight), cyclo-alkanes (10-20 % by weight) and poly-aromatics (20-30 % by weight) (Dagut and Sandro, 2007), while SME is primarily composed of poly-unsaturated components like methyl linoleate and methyl linolenate (about 60% by weight), mono - unsaturates like methyl oleate (about 25% by weight) and saturates like methyl palmitate and methyl stearate (about 15 % by weight) (Conglio et al., 2013).

Although both Jet A and SME have the same DOU value, the source of unsaturation for Jet A is primarily due to the presence of aromatics in addition to the double and triple bonds from alkenes and alkynes, whereas the total fuel unsaturation of SME is from the double bonds present in the acid and the alcohol chain of the esters. This distinction results in a difference in the reaction chemistry of the fuels among various equivalence ratios tested.

The differences in the influence of hydrocarbon family on EI_{NO} of Jet A and SME flames are presented in Figure 6.2. While the variation of EI_{NO} with equivalence ratio is similar in laminar flames of both the fuels, the SME flame consistently produced lower EI_{NO} when compared to the JetA flame at all corresponding equivalence ratios.

Hence, in summary, in addition to the fuel unsaturation effect, the fuel origin also significantly influences EI_{NO}. It is worth noting that the unsaturation effect from FAMEs (Fatty Acid Methyl Esters) has been widely discussed in engine literature whereas the unsaturation of petroleum fuels that primarily includes the poly aromatic hydrocarbons has been under-represented in the context of fuel chemistry effect on the pollutant formation.

6.1.3 Influence of DOU on EI_{NO} of petroleum and biodiesel blends

Neat petroleum fuels like petrodiesel and JetA are by themselves a mixture of various components that include aliphatic and aromatic compounds; similarly, neat biodiesels like SME, CME, RME and PME are composed of a range of saturated and unsaturated methyl esters. Consequently, complex interactions of individual components of parent (neat) fuels from different families are expected during the

combustion reactions in the flames of petroleum/biodiesel blends. In addition, fuels from different families, though with same DOU, had different extent of influence on EI_{NO} (as shown in Figure 6.2). As a result, EI_{NO} of flames of petroleum/biodiesel blends depends on various coupled parameters that may either reinforce or cancel the molecular chemistry effects of the two parent fuels. In this section, the influence of two major parameters: a) equivalence ratio and b) total fuel unsaturation, on the NO emission index in tested flames are discussed.

With respect to equivalence ratio, similar to flames of neat fuels, flames of blends also exhibited an increase in EI_{NO} with DOU (Figures 6.3 - 6.9). At Φ = 7, the fuel unsaturation had almost no effect on the EI_{NO} and the flames of all the tested fuels recorded the lowest EI_{NO} at this equivalence ratio. The influence of DOU on EI_{NO} of biodiesel/diesel blends at Φ = 0.9 is shown in Figure 6.3. EI_{NO} increased with DOU in the flames of all the blends, namely SME, CME, RME and PME with petroleum diesel, but with differing trends. The biodiesel content in the blend, the corresponding unsaturation components and their interaction with petroleum diesel components resulted in the difference in the increasing trends of EI_{NO} with DOU. For example, in flames of diesel/PME blends, EI_{NO} gradually increases with DOU between PME (DOU: 1.7) and diesel (DOU: 3.0). Here, PME is primarily composed of saturated methyl esters; while diesel consisted of significant number of double bonds from aliphatic compounds and ring structure from aromatics. Hence diesel/PME blends are made up of components from two contrasting parent fuels. The interactions of saturated and unsaturated components from PME and diesel could leverage a balance between the influences of their corresponding fuel chemistry on the NO formation mechanism that

resulted in a gradual increase of EI_{NO} with DOU. Likewise, in diesel/SME blends, both SME (DOU: 2.5) and diesel (DOU: 3.0) have higher degree of unsaturated components. Hence, the overall unsaturation components from both the parent fuels would favor the NO formation in the reaction zone, resulting in a steeper increase of EI_{NO} with DOU. The same explanation is valid for the flames of other blends, like CME (DOU: 2.0) and RME (2.4) with diesel which exhibited increasing trends in EI_{NO} with DOU.

The influence of DOU on EI_{NO} of biodiesel/diesel blends at $\Phi = 1.0$ is shown in Figure 6.4. The trends look similar to those observed for $\Phi = 0.9$, but with a slight increase in the magnitude of EI_{NO}. The influence of aromatic content in the biodiesel blend (derived from the parent petroleum diesel) on the EI_{NO} is readily seen in this figure. Consider the data points from diesel/PME, and diesel/RME flames around DOU of 2.5; P50D50 (DOU: 2.4) and RME (DOU: 2.4). Although P50D50 and RME have the same DOU values, the differences in the source of unsaturation significantly influenced the NO formation in the flames; the P50D50 flame produced about 14% higher EI_{NO} than the RME flame. The DOU of RME is totally from the unsaturation of esters, whereas the DOU of P50D50 originates from a mixture of aromatics from diesel (primary contributor of unsaturation) and unsaturated methyl esters (minor contribution since neat PME contains about only 20% of unsaturated methyl esters).

The influence of DOU on EI_{NO} of flames of biodiesel/diesel blends at $\Phi = 1.2$ is shown in Figure 6.5. Among all tested flames of blends, the EI_{NO} increased with DOU. The variation of EI_{NO} of diesel/PME flames was almost linear while that of other blends increased steeply with DOU. However, at higher equivalence ratios like $\Phi = 2$, 3 and 7, EI_{NO} decreased with equivalence ratio and in addition, the effect of fuel unsaturation on

EI_{NO} slowly faded away. In Figures 6.7 - 6.9, considering experimental uncertainties, the EI_{NO} had almost become independent of DOU. As a corollary from the presented results, besides correlating EI_{NO} with DOU, Figures 6.3 - 6.9 captured the influence of differences due to the various sources of unsaturation and their interactions on the EI_{NO}. If there were no significant differences in the nature and interaction of unsaturation, all the curves would have collapsed to a single curve; the choice of DOU helps in capturing these trends since DOU accounted for unsaturation based on the molecular carbon and hydrogen atoms regardless of the family of the fuel.

In general, the exhaust NO emission index (EI_{NO}) from the flames was influenced by degree of fuel unsaturation, equivalence ratio and family of the parent fuels in the fuel blend. The relative significance of each of these parameters on EI_{NO} depended on the respective combustion conditions. As seen before, EI_{NO} was found to be maximum at Φ = 1.2 for all tested DOUs irrespective of fuel origin, however, the effect of fuel unsaturation on EI_{NO} slowly faded away at equivalence ratios greater than $\Phi = 2$.

6.1.4 Laminar flames of commercial biodiesel/biodiesel blends

In the previous section, it was found that EI_{NO} increased with DOU among petroleum fuels, neat biodiesels and petroleum/biodiesel blends. However, the increasing trends among the fuel families were not the same between all the tested flames and were also significantly influenced by the equivalence ratios. The EI_{NO} results suggested differences between fuel families, for instance, although the EI_{NO} of flames of diesel/PME blends and diesel/SME blends increased with DOU; the increasing trend was not the same between two classifications where diesel/PME blends

exhibited an almost linear increase of EI_{NO} with DOU while diesel/SME exhibited a much steeper increase of EI_{NO} with DOU. To understand these differences better, a further simpler breakdown of current research problem is warranted.

As mentioned earlier, in a petroleum diesel/biodiesel blend the fuel unsaturation comes from double bonds of biodiesels and double bonds, triple bonds and aromatics from petroleum diesel. The interaction of fuel chemistry from these varied sources of unsaturation in a flame is less understood. In order to better perceive the observed EI_{NO} trends in the flames of diesel/biodiesel blends (Figures 6.3 - 6.9), a fundamental understanding on the fuel unsaturation effects on EI_{NO} from only the biodiesels (double bonds from methyl esters) is required.

Hence, four popular neat biodiesels, soy methyl ester (SME), rapeseed methyl ester (RME), canola methyl ester (CME) and palm methyl ester (PME) were selected as parent biodiesels (the methyl ester compositions of these biodiesels are presented in Table 4.2). Blends of various combinations of these neat biodiesels were also considered; canola/palm methyl ester blends (CP), canola/rapeseed methyl ester blends (CR), canola/soy methyl ester blends (CS), palm/rapeseed methyl ester blends and palm/soy methyl ester blends (PS). The naming convention of these blends is given by "AXXBYY" where A and B stands for the parent biodiesels; XX and YY stands for the volumetric percentage of A and B biodiesels respectively present in the fuel blend. For example, C43P57 stands for 43% by volume of CME and 57% by volume of PME present in the fuel blend. The selected fuels for the investigation in this work are presented in Table 4.1 and their properties are presented in Table 4.4. These fuels are considered to cover the possible range of DOU values which is limited by the DOU of

the parent biodiesels. In addition to these blends, methyl oleate (MO) was considered to compare the results of mixture of various esters (neat biodiesels and biodiesel blends) with an individual methyl ester and to check whether DOU is capable of capturing the differences in their fuel chemistry.

The NO emission index of all the tested biodiesel/biodiesel flames at Φ = 0.9, 1.0, 1.2 and 1.5 are presented in Figures 6.10 - 6.13. A brief table comprised of selected fuels and their corresponding DOU is provided within each figure for the readers' convenience. The DOU values of all these tested fuels range between 1.7 (PME) and 2.5 (SME) and the developed correlations presented in Figures 6.10 - 6.13 are valid only for methyl esters whose DOU values fall within the range of 1.7 and 2.5.

At Φ = 0.9, the EI_{NO} values of all the fuel blends namely PR, PS, CR, CS and CP blends collapse into a single curve within experimental uncertainties. On the other hand, neat biodiesels like PME, CME, RME, SME and individual methyl ester - methyl oleate produced slightly lower EI_{NO} than the corresponding fuel blends with similar DOU values. This observation was found to be consistent with all other tested equivalence ratios namely Φ = 1.0, 1.2 and 1.5. The EI_{NO} of CME flame and MO flame (both having same DOU value of 2) were found to be 1.28 and 1.31 g/kg respectively at Φ = 0.9. At Φ = 1.0, the EI_{NO} values of flames of all fuel blends and neat biodiesels were found to follow closely with a marginal increasing trend of EI_{NO} with DOU. However, unlike Φ = 0.9 and 1.0, which had a wide scatter in data points, Φ = 1.2 and 1.5 revealed a harmonious increasing trend of EI_{NO} values with DOU from fuel blends as well as neat biodiesels with less scatter in experimental data. For instance, at Φ = 1.2, for a DOU value of 2.1 (Figure 6.12), the EI_{NO} produced by flames of P40R60, P47S53, C75R25,

C80S20 are 3.11, 2.88, 2.66 and 2.81 respectively. These EI_{NO} values were comparable within experimental uncertainties; however, it has to be noted that DOU treats the double bonds from all sources of unsaturation as same irrespective of whether the esters are mono, di or poly unsaturated. But, studies indicated that the reactivity and decomposition of carbon main chain in the esters also depended on the number and position of the double bond in the carbon chain (Knothe, 2002). For example, methyl linolenate (four double bonds), methyl linoleate (three double bonds) and methyl oleate (two double bonds) would not react or undergo the decomposition of carbon main chain in the same way. Hence the equal treatment of double bonds from mono, di or poly unsaturated esters by DOU would add further to the experimental uncertainty. Although DOU values of P40R60, P47S53, C75R25, and C80S20 are same, the differences in the composition (and the location of double bonds) of their constituent methyl esters and the complexity in the blending of multiple methyl esters also contribute to the scatter in the experimental data. However, a closer observation of fuel composition along with the usage of DOU tool still enable us to understand the fuel chemistry interaction and develop correlations of EI_{NO} versus DOU with acceptable uncertainties. Despite the above said limitation, DOU was proved to be an effective and efficient tool in characterizing the fuel unsaturation effect on NOx emissions, particularly as a common platform for petroleum/biodiesel blends.

The EI_{NO} trends from the Figures 6.11 - 6.13 were captured and presented in Figure 6.14 to understand the influence of two major parameters: (a) equivalence ratio and (b) total fuel unsaturation, on the NO emission index. From Figure 6.14, it can be clearly seen that EI_{NO} increased between $\Phi = 0.9$ and 1.0 and then peaked at $\Phi = 1.2$ followed

by a reduction in EI_{NO} at $\Phi = 1.5$. This trend shows the significance of equivalence ratio on the NO formation regardless of the fuel and with reference to the fuel unsaturation effect, the EI_{NO} increases with DOU at all tested equivalence ratios. At $\Phi = 0.9$, a 16% increase of EI_{NO} between DOU of 1.7 (EI_{NO} = 1.61g/kg) and 2.5 (EI_{NO} = 1.86g/kg) was observed based on the developed correlation. Similarly, at $\Phi = 1.0$, EI_{NO} of 1.97 and 2.28 g/kg was recorded at DOUs of 1.7 and 2.5 respectively which was again a 16% increase. Further, at $\Phi = 1.2$, the increasing trend was conspicuous with EI_{NO} of 2.57 and 3.23 g/kg between DOU of 1.7 and 2.5 with a 26% increase. Similarly, EI_{NO} of 1.76 and 2.39 were recorded between DOU of 1.7 and 2.5 at $\Phi = 1.5$. In summary, the EI_{NO} results from all the tested flames of various combinations of methyl esters, whose unsaturation arises from only double bonds, followed an increasing trend with DOU (within the range of 1.7 and 2.5) at all tested equivalence ratios, however with varying magnitude of increase depending on the tested equivalence ratio.

Further, it has to be noted that DOU formula (Equation 3.1) does not account for the effect of fuel bound oxygen present in the fuel, hence questions may arise as how the fuel bound oxygen effect of methyl esters on the EI_{NO} is accounted for. Interestingly, all the tested flames (presented in this section) are either individual methyl ester (MO) or neat biodiesels (composed of individual esters) or biodiesel blends, and their percentage oxygen content were about the same (between 10.8% - 11.8%). Having said that, at a particular equivalence ratio, the EI_{NO} results showcased only the effect of fuel unsaturation (based on hydrogen to carbon ratio) on the global NO emission indices at almost similar availability of fuel bound oxygen content between the tested flames. This is an explicit evidence to prove that fuel unsaturation definitely plays a significant role

in the NO formation and this effect is quantified in this study as experimental correlations presented (Figure 6.14) as follows:

$$\Phi = 0.9 \rightarrow EI_{NO} = [-0.25*(DOU)^2] + [1.37*(DOU)] \pm [0.29] \quad (6.1)$$

$$\Phi = 1.0 \rightarrow EI_{NO} = \left[-0.31*(DOU)^2\right] + [1.69*(DOU)] - 0.01 \pm [0.37] \quad (6.2)$$

$$\Phi = 1.2 \rightarrow EI_{NO} = [-0.28*(DOU)^2] + [1.99*(DOU)] \pm [0.44] \quad (6.3)$$

$$\Phi = 1.5 \rightarrow EI_{NO} = \left[-0.10*(DOU)^2\right] + [1.20*(DOU)] + 0.01 \pm [0.39] \quad (6.4)$$

Equations 6.1 to 6.4 are valid for the range, $1.0 \leq DOU \geq 2.5$.

6.1.5 Laminar flames of methyl oleate, heptane, toluene and their blends

In this section, the influence of DOU on the EI_{NO} from the laminar flames of prevaporized heptane/toluene blends, JetA/diesel blends, heptane/methyl oleate (MO) blends, toluene/methyl oleate (MO) blends are discussed. A brief table comprised of selected fuels and their corresponding DOU is provided within the figure for each family of fuels for the readers' convenience. These families of fuels are grouped together for the discussion due to the following reasons:

- Heptane/toluene blends do not have ester components (no fuel bound oxygen). The effect of unsaturation due to aromatics alone can be delineated from the EI_{NO} results.
- JetA/ diesel blends also do not have ester components (no fuel bound oxygen). However, the fuel unsaturation is due to both olefins and aromatics due to the presence of a wide range of components in commercial Jet A and diesel fuels.
- The fuel unsaturation of heptane/MO blends is due to the double bonds of ester present in methyl oleate since heptane is an alkane. However, the fuel unsaturation of toluene/MO blends is due to both the double bond of MO and aromatic ring of toluene.

Hence, the EI_{NO} results from the laminar flames of each of these families of fuels provide an insight to any particular combination of sources of fuel unsaturation that would help in the better understanding of the contribution of different sources of unsaturation to the NO emissions from these flames. Heptane/toluene blends cover the range of DOU of 0 and 4; heptane/MO blends cover the range of 0 to 2 while toluene/MO blends cover the range of 2 to 4. Hence the results from these three set of

fuels will help in understanding the effect of DOU over the range of 0 to 4, with unsaturation arising from various sources.

The EI_{NO} from the laminar flames of prevaporized aforementioned fuels at $\Phi = 0.9$ are presented in Figure 6.15. Among heptane/toluene blends, the EI_{NO} increases with DOU between heptane (1.57 g/kg) and toluene (2.96 g/kg). JetA/diesel blends which cover a narrow range of DOU between 2.5 and 3 closely followed the results of heptane/toluene blends. In addition, the laminar flames of heptane/MO and toluene/MO blends produced consistently lower EI_{NO} than the heptane/toluene blends at the corresponding DOUs. At the equivalence ratio of 0.9, the presence of MO in the fuel blend reduced the EI_{NO} at all DOUs when compared to the corresponding heptane/toluene blends. Moreover, unsaturated ester - methyl oleate (DOU: 2) produced an EI_{NO} of about 1.31 g/kg while the saturated alkane – heptane (DOU: 0) produced an EI_{NO} of 1.57 g/kg. Hence DOU effect on EI_{NO} is different for different families of fuels. These observations reiterate the significance of differences in the chemistry based on the fuel family and the efficacy of the established DOU parameter in identifying and quantifying the effect of degree of fuel unsaturation from different sources.

The EI_{NO} from the laminar flames of prevaporized aforementioned fuels at $\Phi = 1.0$ are presented in Figure 6.16. The EI_{NO} increased with equivalence ratio as well as DOU; EI_{NO} of toluene flame increased from 2.96g/kg to 4.93g/kg between $\Phi = 0.9$ and 1 while EI_{NO} results from heptane/toluene blends at $\Phi = 1.0$ revealed a clearly increasing trend of EI_{NO} with DOU. Although MO (1.80 g/kg) produced slightly higher EI_{NO} than heptane flame (1.66 g/kg), MO still produced consistently lower EI_{NO} than the corresponding heptane/toluene blend - H58T42 (DOU: 2) that produced an EI_{NO} of 2.86

g/kg. However, all the blends were found to produce similar EI_{NO} for the corresponding DOUs within experimental uncertainties.

The EI_{NO} from the laminar flames of prevaporized aforementioned fuels at $\Phi = 1.2$ are presented in Figure 6.17. At this equivalence ratio of 1.2, the difference in the fuel chemistry is prominent and all tested flames produced their maximum EI_{NO}. The EI_{NO} of heptane/toluene blends clearly indicated the significance of equivalence ratio and degree of fuel unsaturation at this condition. While heptane produced about twice as much EI_{NO} as at $\Phi = 1.0$, toluene produced about 40% more EI_{NO} at $\Phi = 1.2$ than at $\Phi = 1.0$. A perspicuous trend of increasing EI_{NO} with DOU was observed among heptane/toluene blends; toluene (DOU: 4) produced 6.94g/kg of EI_{NO} while heptane (DOU: 0) produced 3.23 g/kg. However, JetA/diesel blends produced significantly lower EI_{NO} than corresponding heptane/toluene blends (similarities between heptane/toluene blends and JetA/diesel blends are due to absence of fuel bound oxygen). The reason for this behavior could be due to the available sources of fuel unsaturation (only aromatic rings for heptane/toluene blends whereas both olefins and aromatics in case of JetA/diesel). The observed trend suggested that the aromatic content influences the NO formation more than olefins or double bonds from esters. Adding to that argument, heptane/MO blends and toluene/MO blends produced consistently lower EI_{NO} than the corresponding heptane/toluene blends. Again, the presence of methyl oleate in the fuel blend reduced the corresponding EI_{NO} value; at $\Phi = 1.2$, EI_{NO} of heptane (DOU: 0) was 3.23g/kg while the EI_{NO} of MO (DOU: 2) was 2.69 g/kg.

The EI_{NO} from the laminar flames of prevaporized aforementioned fuels at $\Phi = 1.5$ are presented in Figure 6.18. At this equivalence ratio, all fuel blends produced similar EI_{NO} trends as that of $\Phi = 1.2$ but with reduced magnitude of EI_{NO} values. Heptane produced about 50% lower EI_{NO} at $\Phi = 1.5$ than at $\Phi = 1.2$. Similarly, toluene and MO produced about 13% and 35% lower EI_{NO} respectively.

The EI_{NO} trends from the Figures 6.15 - 6.18 were captured and presented in Figure 6.19 to understand the influence of two major parameters: (a) equivalence ratio and (b) total fuel unsaturation, on the NO emission index. From Figure 6.19, it can be clearly seen that EI_{NO} increased between $\Phi = 0.9$ and 1.0 and then peaked at $\Phi = 1.2$ followed by a reduction in EI_{NO} at $\Phi = 1.5$. This trend shows the significance of equivalence ratio on the NO formation regardless of the fuel.

With reference to the fuel unsaturation effect, although EI_{NO} increases with DOU at all tested equivalence ratios, the increase was steeper particularly with degree of unsaturation values higher than 2. At $\Phi = 0.9$, the EI_{NO} was found to be almost doubled between DOU of 0 (EI_{NO} = 1.54g/kg) and 4 (EI_{NO} = 3.18g/kg) based on the developed correlation. Similarly, at $\Phi = 1.0$, EI_{NO} of 1.85 and 4.33 g/kg was recorded at DOUs of 0 and 4 respectively. Further, at $\Phi = 1.2$, the increasing trend was conspicuous with EI_{NO} of 3.53 and 6.53 g/kg between DOU of 0 and 4 with an 85% increase. EI_{NO} of 1.95 and 5.39 were recorded between DOU of 0 and 4 at $\Phi = 1.5$.

In summary, the EI_{NO} results from all the tested flames of various combinations of unsaturation sources followed an increasing trend with DOU (within the range of 0 and 4) at all tested equivalence ratios, however with varying magnitude of increase depending on the tested equivalence ratio.

The developed correlations on the EI_{NO} from the laminar flames of prevaporized heptane/toluene blends, JetA/diesel blends, heptane/methyl oleate (MO) blends, toluene/methyl oleate (MO) blends are given below:

$$\Phi = 0.9 \rightarrow EI_{NO} = [0.05*(DOU)^2] + [0.21*(DOU)] + 1.54 \pm [0.29] \quad (6.5)$$

$$\Phi = 1.0 \rightarrow EI_{NO} = [0.18*(DOU)^2] - [0.10*(DOU)] + 1.85 \pm [0.37] \quad (6.6)$$

$$\Phi = 1.2 \rightarrow EI_{NO} = [0.31*(DOU)^2] - [0.49*(DOU)] + 3.53 \pm [0.44] \quad (6.7)$$

$$\Phi = 1.5 \rightarrow EI_{NO} = [0.29*(DOU)^2] - [0.30*(DOU)] + 1.95 \pm [0.39] \quad (6.8)$$

Equations 6.5 to 6.8 are valid for the range, $0 \leq DOU \geq 4$.

By analyzing the above developed correlations, it can be discerned that two major parameters influence the EI_{NO} values - degree of fuel unsaturation and equivalence ratio. The constants in the above presented equations reveal the dependence of EI_{NO} on equivalence ratio regardless of the degree of unsaturation, while the first two terms represent the significance of DOU values on the end EI_{NO} formation.

6.2 Global CO emission indices

6.2.1 Laminar flames of neat commercial petro-fuels, biodiesels and their blends

The variation of CO emission index with DOU at the tested equivalence ratios for neat petroleum diesel and biodiesel (SME, CME, RME and PME) fuels are presented in Figure 6.20; for petro-biodiesel blends are presented in Figures 6.21 - 6.24 and for biodiesel/biodiesel blends in Figures 6.25 - 6.28. In all of these tested flames, the EI_{CO} produced was about less than 1g/kg and it was found that, within experimental uncertainties, the EI_{CO} did not exhibit a significant variation with the degree of unsaturation.

Among, Figures 6.21 - 6.24, the EI_{CO} values from the flames of commercial petro-biodiesel blends were found to be independent of degree of fuel unsaturation between the tested values of DOU: 1.7 and DOU: 3.0. The unsaturation from aromatic rings, double bonds of alkenes from petro-diesel and double bonds of methyl esters did not significantly influence the amount of EI_{CO} formed in these flames. Similarly, among the flames of commercial biodiesel/biodiesel blends, EI_{CO} was found to be independent of degree of fuel unsaturation between the tested values of DOU: 1.7 and DOU: 2.5. Both at $\Phi = 0.9$ and 1.0 (Figures 6.25 - 6.26), the scatter in the EI_{CO} values from flames of different fuel blends at the same DOU was found to be large and the values seemed to collapse to a single curve with increase in equivalence ratio ($\Phi = 1.2$ and 1.5), presented in Figures 6.27 and 6.28. The representative trend lines from these experimental data were plotted in Figure 6.29 and the corresponding correlations are presented in equations 6.9 - 6.12, which showed the effect of fuel unsaturation on the CO emission index at various equivalence ratios.

$$\Phi = 0.9 \rightarrow EI_{CO} = \left[-0.17*(DOU)^2\right] + [0.72*(DOU)] - 0.01 \pm [0.17] \quad (6.9)$$

$$\Phi = 1.0 \rightarrow EI_{CO} = \left[-0.23*(DOU)^2\right] + [0.89*(DOU)] - 0.01 \pm [0.21] \quad (6.10)$$

$$\Phi = 1.2 \rightarrow EI_{CO} = \left[-0.23*(DOU)^2\right] + [0.94*(DOU)] - 0.01 \pm [0.23] \quad (6.11)$$

$$\Phi = 1.5 \rightarrow EI_{CO} = \left[-0.20*(DOU)^2\right] + [0.91*(DOU)] - 0.01 \pm [0.19] \quad (6.12)$$

Equations 6.9 to 6.12 are valid for the range, $1.0 \leq DOU \geq 2.5$.

In Figure 6.29 and from the presented correlations, the average EI_{CO} value was almost independent of DOU at all the tested conditions (Φ = 0.9, 1.0, 1.2 and 1.5) from all the tested flames of biodiesel blends. This observation is in agreement with our previous findings on the fuel chemistry and equivalence ratio effects on EI_{CO} from neat Jet A, CME and SME flames over a wide range of equivalence ratios (Φ = 0.9 to 7.0) (Balakrishnan et al., 2016b) where EI_{CO} was found to be less sensitive to fuel chemistry effects at lower equivalence ratios (Φ = 0.9 to 1.5) but EI_{CO} increased rapidly with equivalence ratios beyond 2. Hence, similar trends of EI_{CO} with DOU and equivalence ratio are observed among biodiesel fuel blends as well as neat fuels.

6.2.2 Laminar flames of methyl oleate, heptane, toluene and their blends

In this section, the influence of DOU on the EI_{CO} from the laminar flames of prevaporized heptane/toluene blends, JetA/diesel blends, heptane/methyl oleate (MO) blends, toluene/methyl oleate (MO) blends are discussed. At an equivalence ratio of 0.9 (Figure 6.30), the EI_{CO} from heptane/toluene blends were found to slightly increase with DOU. This was expected since with the increase in aromatic content, the combustion reactions would yield increased partially oxidized products of carbon such as CO, soot and smoke depending on the equivalence ratio (availability of oxygen for the oxidation). Since the tested equivalence ratios are either fuel lean (Φ = 0.9), near stoichiometric (Φ = 1.0) or moderate fuel rich conditions (Φ = 1.2 and 1.5), no observable soot or smoke was produced in the tested flames. However, the partial oxidation of aromatic ring (toluene) at these conditions resulted in an increase of EI_{CO} from heptane/toluene flames. Among, heptane/ MO flames, the fuel unsaturation is from the double bonds of MO and in the absence of aromatic content, the EI_{CO} was found to be almost constant between DOU of 0 and DOU of 1.7. Nevertheless, among toluene/MO flames, EI_{CO} increased with DOU, yet not to the extent of heptane/toluene blends. This could be due to the fuel bound oxygen present in MO that facilitated pyrolysis of toluene and subsequent oxidation, which is not favored in heptane/toluene flames due to the absence of fuel-bound oxygen. Further, the EI_{CO} from JetA/diesel flames were found to be lower than that of heptane/toluene flames and toluene/MO flames; this is due to the aromatic content of diesel (24.7%) and Jet-A (20.5%) being lower than the aromatic content of toluene (100%) which reiterated the observation that aromatic content in the fuel significantly influences the EI_{CO} from the corresponding

flames. The effect of fuel aromatic content on the emission indices from the tested flames is discussed in detail in the subsequent sections. Similar trends were observed from the EI_{CO} values measured at Φ = 1.0, 1.2 and 1.5 (presented in Figures 6.31 - 6.33). Among tested flames at Φ = 1.2 and 1.5, in addition to fuel unsaturation effect, the equivalence ratio effect also contributed to the increase in EI_{CO} which reflected in the increased magnitude of the values observed at higher values of equivalence ratios and degree of fuel unsaturation, as shown in the representative trend lines in Figure 6.34 and the correlations (equation 6.13 - 6.16).

$$\Phi = 0.9 \rightarrow EI_{CO} = [0.09*(DOU)^2] - [0.20*(DOU)] + 0.91 \pm [0.17] \quad (6.13)$$

$$\Phi = 1.0 \rightarrow EI_{CO} = [0.02*(DOU)^2] + [0.22*(DOU)] + 0.87 \pm [0.21] \quad (6.14)$$

$$\Phi = 1.2 \rightarrow EI_{CO} = [0.14*(DOU)^2] - [0.32*(DOU)] + 1.48 \pm [0.23] \quad (6.15)$$

$$\Phi = 1.5 \rightarrow EI_{CO} = [0.12*(DOU)^2] - [0.22*(DOU)] + 1.52 \pm [0.19] \quad (6.16)$$

Equations 6.13 to 6.16 are valid for the range, $0 \leq DOU \geq 4$.

6.3 Effect of aromatic content and fuel bound oxygen on emission indices

In this section, the influence of aromatic content and fuel bound oxygen on the emission indices of CO and NO are discussed.

Consider heptane (C_7H_{16}), toluene (C_7H_8) and their blends investigted in this study: H92T08 ($C_7H_{15.1}$), H80T20 ($C_7H_{13.9}$), H65T35 ($C_7H_{12.6}$), H58T42 (C_7H_{12}), H45T55 (C_7H_{11}), H32T68 (C_7H_{10}) and H12T88 ($C_7H_{8.7}$). All these 9 fuels have no fuel bound oxygen, posses same number of carbon atoms (n: 7) with the H/C ratio decreasing with toluene content in the fuel blend, between heptane (H/C ratio : 2.29) and toluene (H/C ratio : 1.14). At all tested equivalene ratios of 0.9, 1.0, 1.2 and 1.5 (Figures 6.35 - 6.38), the EI_{NO} of heptane /toluene flames were found to increase with the aromatic content of the fuel. From this observation, it is evident that, even without the availability of fuel bound oxygen, EI_{NO} was significantly influenced by the H/C ratio, an indirect representation of hydrogen deficiency and degree of unsaturation. Furthermore, among toluene/MO flames, in addition to aromatic content, fuel bound oxygen was available from the methyl oleate. Hence the EI_{NO} results from these flames signify the combined effect of aromatic content and fuel bound oxygen on the EI_{NO}. At all tested equivalence ratios of 0.9, 1.0, 1.2 and 1.5 (Figures 6.35 - 6.38), the EI_{NO} of toluene/ MO flames were also found to increase with the aromatic content of the fuel. At Φ = 1.2, EI_{NO} of toluene/MO blends were slightly lower than that of heptane/toluene blends with corresponding aromatic content. However, at other tested equivalence ratios of 0.9, 1.0 and 1.5, the EI_{NO} curves between heptane/toluene blends (no fuel bound oxygen) and toluene/MO blends (fuel bound oxygen of about 5% - 10%) exhibited similar increasing trends with respect to the aromatic content of the fuel blend. This is a crucial

observation, since, in biodiesel-engine combustion literature, biodiesel-fuel bound oxygen and local flame temperature were primarily attributed to the NOx formed during engine combustion. But, based on the observed results from this study, the contribution of oxygen for EI_{NO} would not be as significant as it was primarily attributed and at the same time the contribution of aromatic content to the EI_{NO} would be more signficant than it thought to be. The availabilty of oxygen was claimed to be unclear in a study (Puhan et al., 2005) where the esters may undergo decarboxylation reaction and produce CO_2 early in the combustion process. More detailed information on the local temperature and species concentration profiles would help in discerning the dominant contributor of NO formation thereby identifying the primary NO formation mechanisms under each of these combustion conditions.

The developed correlations beween EI_{NO} of flames as a function of aromatic content in the fuel blends (plotted in Figure 6.39) are given by:

$$\Phi = 0.9 \rightarrow EI_{NO} = [0.01*(\text{fuel aromatic content\_Vol. \%})] + 1.87 \pm [0.29] \quad (6.17)$$

$$\Phi = 1.0 \rightarrow EI_{NO} = [0.02*(\text{fuel aromatic content\_Vol. \%})] + 1.95 \pm [0.37] \quad (6.18)$$

$$\Phi = 1.2 \rightarrow EI_{NO} = [0.03*(\text{fuel aromatic content\_Vol. \%})] + 3.18 \pm [0.44] \quad (6.19)$$

$$\Phi = 1.5 \rightarrow EI_{NO} = [0.03*(\text{fuel aromatic content\_Vol. \%})] + 1.91 \pm [0.39] \quad (6.20)$$

Similarly, the EI_{CO} values as a function of aromatic content of the fuel were presented in Figures 6.40 - 6.43. The EI_{CO} was found to increase with (1) equivalence ratio, due to the reduced availability of oxygen for combustion and increase with the (2) aromatic content in the fuel blend, due to the higher carbon content associated with aromatics and the combined effect of reduced availability of oxygen resulted in partial oxidation of carbon leading to the emissions of more CO.

The developed correlations beween EI_{CO} of flames as a function of aromatic content in the fuel blends (plotted in Figure 6.44) are given by:

$$\Phi = 0.9 \rightarrow EI_{CO} = [0.01*(\text{fuel aromatic content\_Vol. \%})] + 0.73 \pm [0.17] \quad (6.21)$$

$$\Phi = 1.0 \rightarrow EI_{CO} = [0.01*(\text{fuel aromatic content\_Vol. \%})] + 1.11 \pm [0.21] \quad (6.22)$$

$$\Phi = 1.2 \rightarrow EI_{CO} = [0.01*(\text{fuel aromatic content\_Vol. \%})] + 1.29 \pm [0.23] \quad (6.23)$$

$$\Phi = 1.5 \rightarrow EI_{CO} = [0.01*(\text{fuel aromatic content\_Vol. \%})] + 1.29 \pm [0.19] \quad (6.24)$$

In summary, the experiemental results from this study primarily attribute to the chemistry of the fuel with other thermo-fluid properties such as droplet vaporization, fuel atomization and engine parameters such as injection timing being eliminated. Hence the developed EI_{NO} and EI_{CO} correlations with respect to the aromatic content of

the fuel account only for the chemistry inteaction of the fuel and not on the dependence of various physio-thermo parameters and their interactions with coupled engine parameters found in diesel engine combustion.

6.4 Effect of equivalence ratio and fuel family on emission indices

In this section, the effect of equivalence ratio and origin of fuel on the NO and CO emission indices are discussed at a given degree of fuel unsaturation. The NO emission indices of flames of fuels (CME, MO, P53R47, H58T42 and P75D25) with same degree of unsaturation (DOU : 2) are plotted as a function of equivalence ratio in Figure 6.45. A general trend of increasing EI_{NO} between Φ = 0.9 and Φ = 1.2 was observed and a drop in EI_{NO} was observed between Φ = 1.2 and Φ = 1.5. Among the tested flames, except H58T42, all other flames produced similar EI_{NO} at the corresponding equivalence ratios. H58T42 flame produced about 45% higher EI_{NO} (at Φ = 1.2) than the other flames. This observation reiterates the influence of fuel aromatic content on the NO emission index. The fuels like CME, MO and P53R47 do not contain aromatic hydrocarbons and their fuel unsaturation derives from only double bonds present in the fuel. P75D25 and H58T42 comprise of about 7.9% and 42.0% by volume of aromatics present in the fuel. It is worth to note that all the five fuels considered in this discussion has an equivalent degree of unsaturation of 2. However, as mentioned earlier, H58T42 flame produced higher EI_{NO} than other flames of considered fuels that have considerably lower aromatic content in the fuel. Hence, it is apparent that aromatic content has signifacntly influenced EI_{NO} from the flames at tested equivalence ratios.

The CO emission indices of flames of fuels (CME, MO, P53R47, H58T42 and P75D25) with same degree of unsaturation (DOU : 2) are plotted as a function of equivalence ratio in Figure 6.46. It was observed that EI_{CO} did not vary significantly with equivalence ratio within the tested range of $\Phi = 0.9$ and $\Phi = 1.5$. Within this tested range, all tested flames except H58T42 almost produced identical EI_{CO} (between 0.5 to 1.0 gCO/kg-fuel burnt). Among H58T42 flames, EI_{CO} increased slightly with equivalence ratio within the tested range of $\Phi = 0.9$ and $\Phi = 1.5$. At an equivalence ratio of 1.5, H58T42 flame (EICO : 2.1 g/kg) produced more EI_{CO} than that of other flames (EI_{CO} : 0.91g/kg). The presence of aromatic content in the fuel favored more CO formation that that of other fuels having same degree of unsaturation. Further, from the previously published results, EI_{CO} of CME flame increased substantially with higher equivalence ratios ($\Phi > 2$) (Singh et al., 2013). These observations revealed that higher equivalence ratios significantly influences CO emission index while the influence of fuel aromatic content is signficant at all tested equivalence ratios whose effects are conspicuous at higher equivalence ratios.

6.5 Chapter conclusions

The following conclusions were drawn based on the global emission index results from the laminar flames of prevaporized neat petroleum fuels, biodiesels, methyl oleate, heptane, toluene and their blends investigated in this study :

- The NO and CO emission indices from the tested flames are influenced by two major parameters - equivalence ratio and total fuel unsaturation.
- Among all the tested flames, EI_{NO} increases with increasing DOU; the magnitude of rise increases from $\Phi = 0.9$, reaches a maximum at $\Phi = 1.2$ and decreases to a lower value at $\Phi = 1.5$. At higher equivalence ratios, particularly at $\Phi = 3$ and 7, fuel chemistry and unsaturation effects have a minimal influence on the EI_{NO} due to the significant soot formation under these conditions. In general, fuel unsaturation has its maximum influence on EI_{NO} at $\Phi = 1.2$.
- The influence of degree of fuel unsaturation on EI_{NO} become signficant at higher values of DOU particularly greater than 2. This observation was evident in the flames of heptane/toluene blends, heptane/MO and toluene/MO blends whose DOU values range bewtween 0 and 4. Toluene (DOU : 4) produced the highest EI_{NO} at all tested equivalence ratios ($\Phi = 0.9$, 1.0, 1.2 and 1.5)
- Origin of fuel (fuel family) plays an important role in determining the DOU effect on EI_{NO} from the corresponding flames. Fuels containing methyl esters produced lower EI_{NO} than petroleum based fuels having similar value of degree of unsaturation.

- EI_{NO} was found to increase with DOU, even in the absence of fuel bound oxygen (heptane/toluene blends) in the fuel blend, thereby delineated the DOU effect on NOx formation from the fuel bound oxygen effect.
- Similarly, EI_{NO} was found to increase with DOU, among biodiesel/biodiesel blends (fuel bound oxygen content of about 11% -12%) where DOU influenced EI_{NO} between flames of fuels having similar fuel bound oxygen content. These observations provided evidence to the claim that fuel unsaturation contributes to the NOx emissions observed in diesel engine combustion studies reported in the literature.
- EI_{CO} did not vary significantly with DOU among neat biodiesels, petroleum diesel, biodiesel/petrodiesel blends and the emitted EI_{CO} was less than 1g/kg at all tested equivalence ratios. EI_{CO}, however, was found to increase with higher toluene (aromatic) content, patricularly in the flames of heptane/toluene and toluene/MO blends.
- Both EI_{NO} and EI_{CO} were found to increase with aromatic content in the fuel blend and the increase become substantial at higher volume content of aromatics present in the fuel.

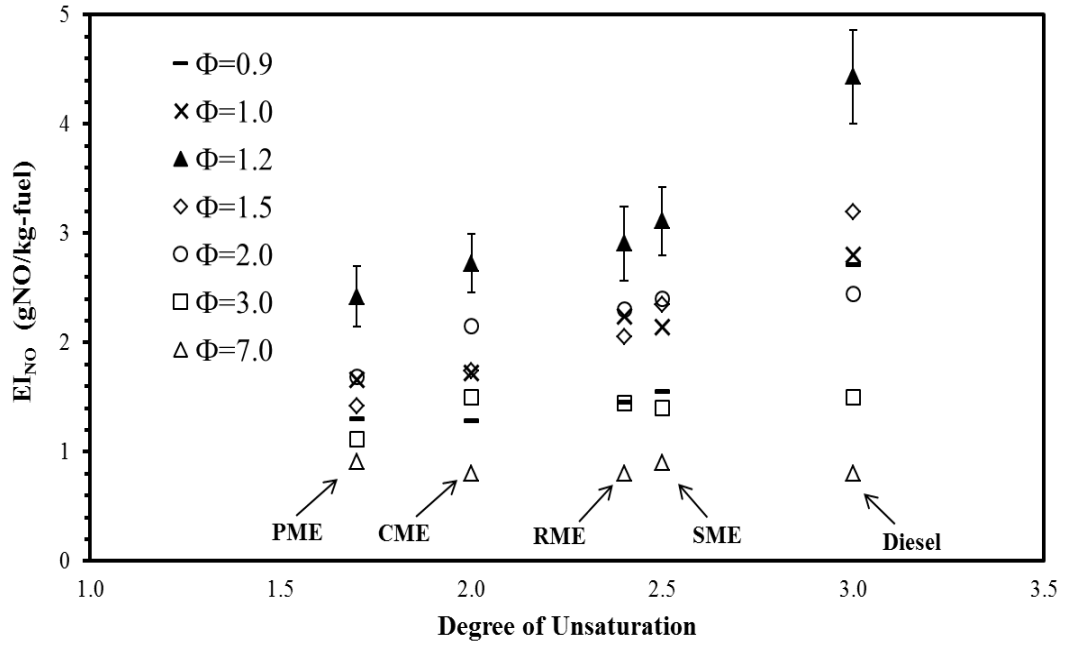

Figure 6.1 Correlation of DOU with EI_{NO} of flames of neat petroleum and biodiesel fuels at different equivalence ratios

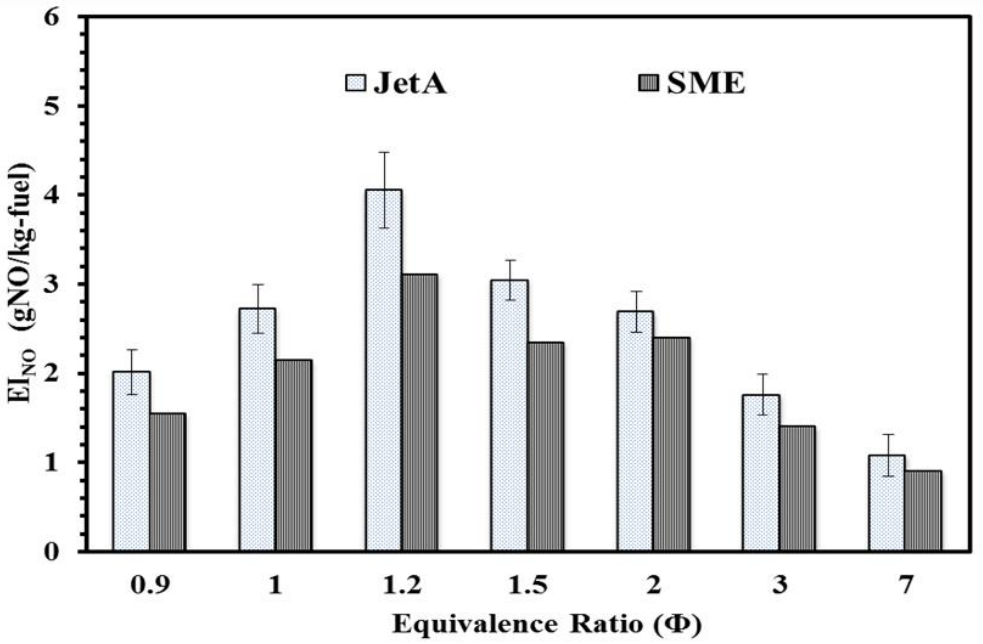

Figure 6.2 Influence of hydrocarbon family on EI_{NO} of fuels with same DOU at different equivalence ratios

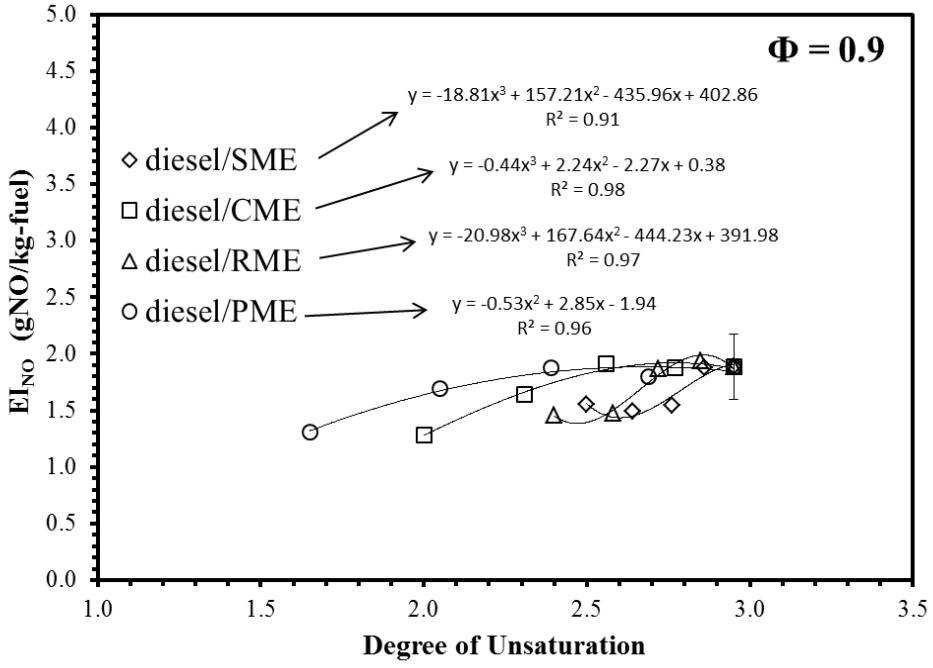

Figure 6.3 Correlation of DOU with EI_{NO} of flames of petrodiesel / biodiesel blends at Φ = 0.9

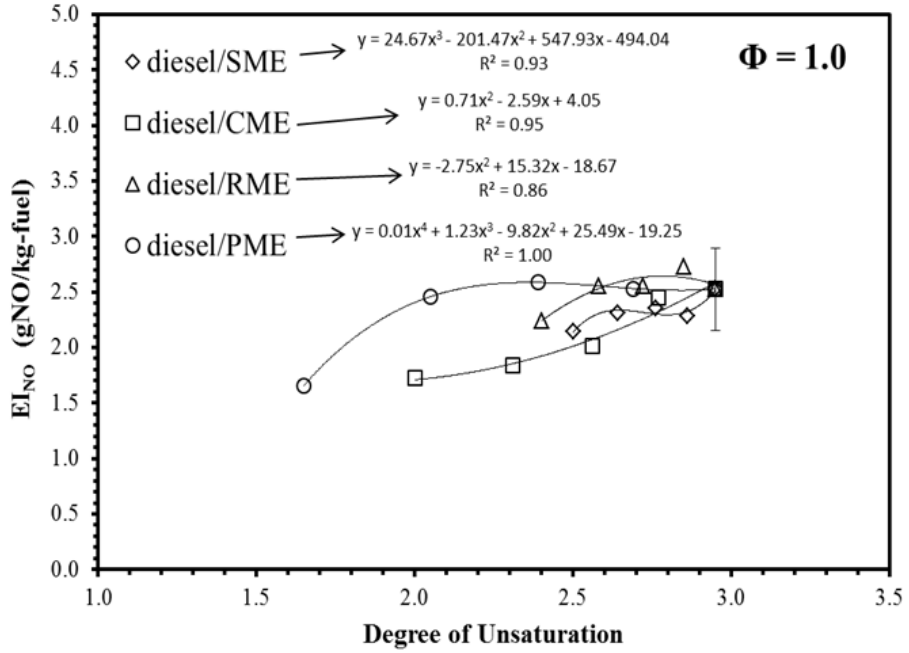

Figure 6.4 Correlation of DOU with EI_{NO} of flames of petrodiesel / biodiesel blends at $\Phi = 1.0$

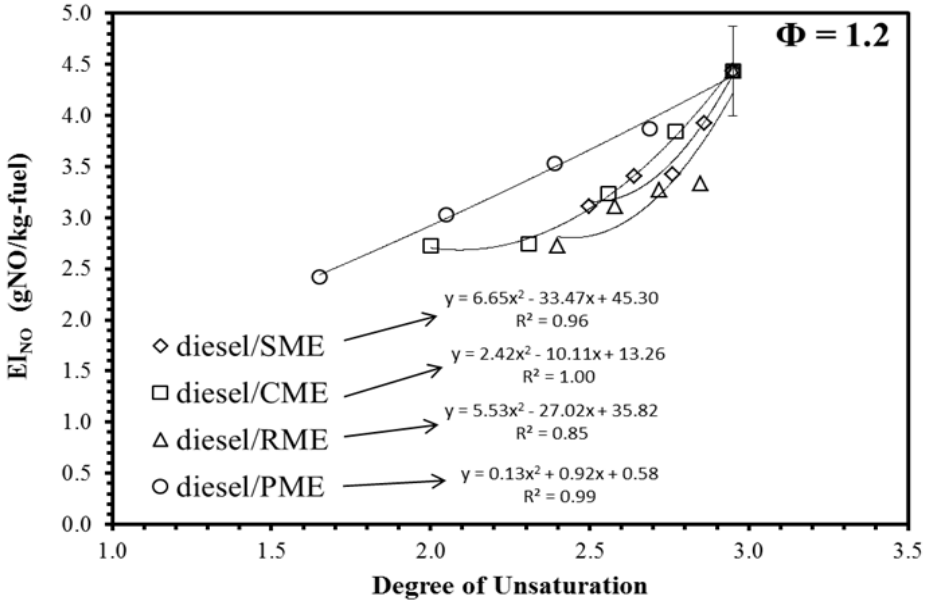

Figure 6.5 Correlation of DOU with EI_{NO} of flames of petrodiesel / biodiesel blends at $\Phi = 1.2$

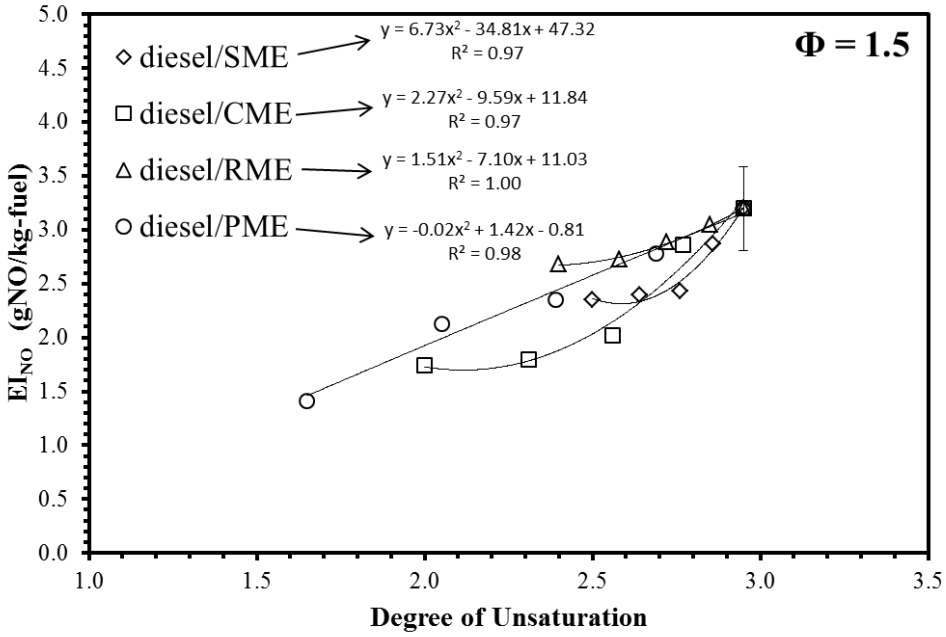

Figure 6.6 Correlation of DOU with EI_{NO} of flames of petrodiesel / biodiesel blends at $\Phi = 1.5$

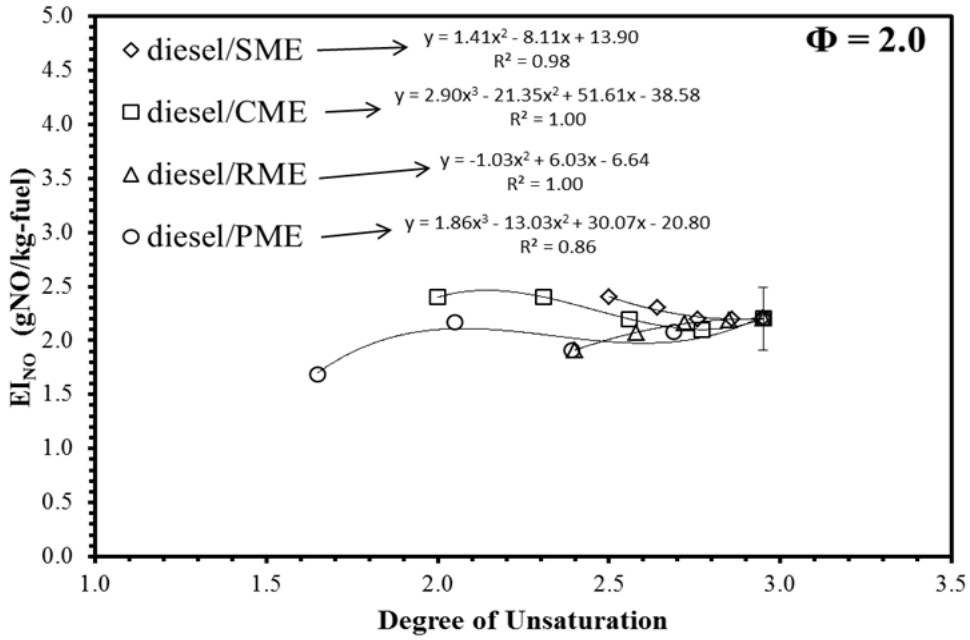

Figure 6.7 Correlation of DOU with EI_{NO} of flames of petrodiesel / biodiesel blends at $\Phi = 2.0$

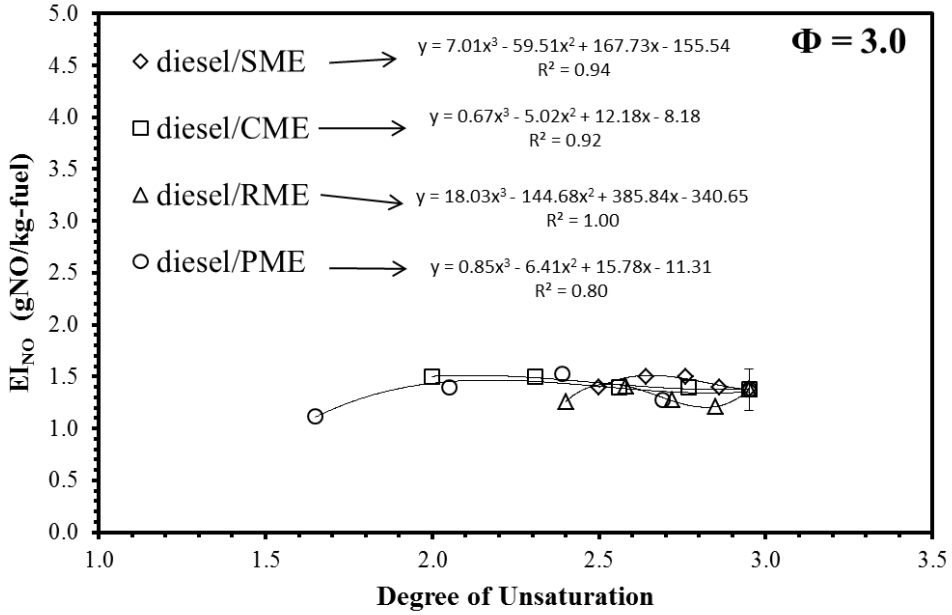

Figure 6.8 Correlation of DOU with EI_{NO} of flames of petrodiesel / biodiesel blends at $\Phi = 3.0$

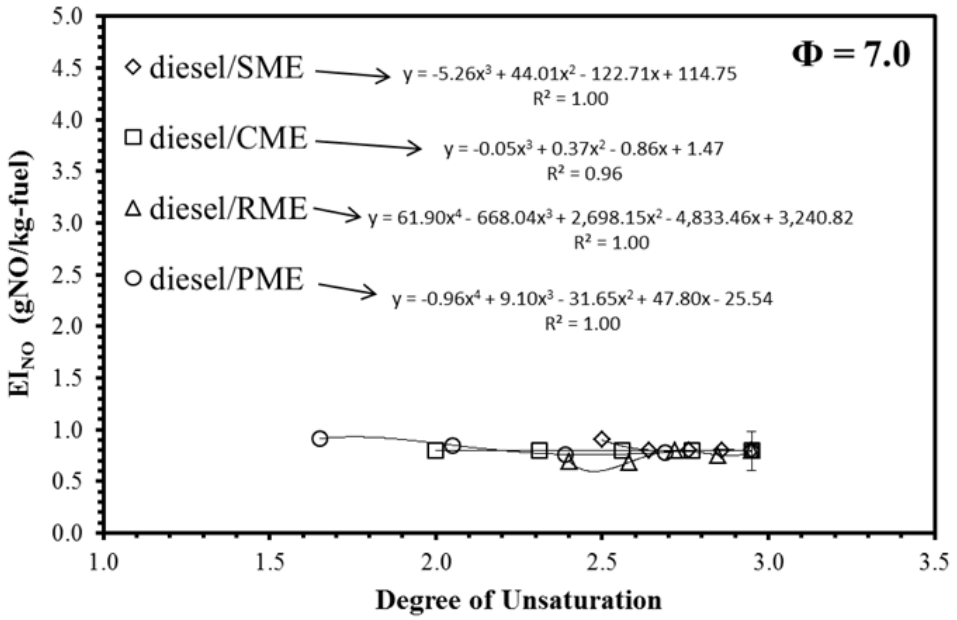

Figure 6.9 Correlation of DOU with EI_{NO} of flames of petrodiesel / biodiesel blends at $\Phi = 7.0$

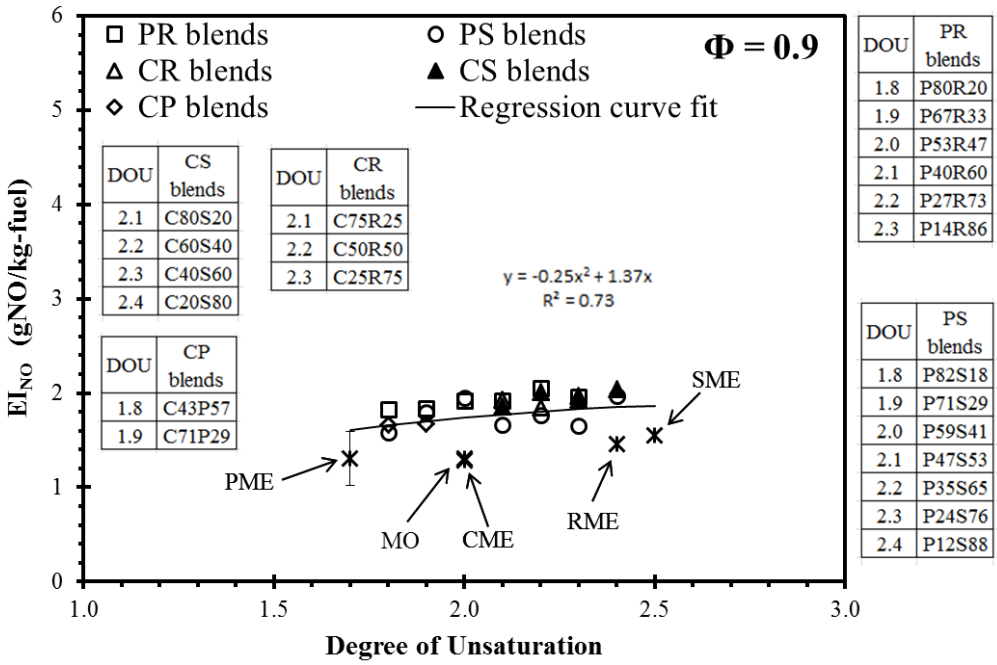

DOU	CS blends
2.1	C80S20
2.2	C60S40
2.3	C40S60
2.4	C20S80

DOU	CR blends
2.1	C75R25
2.2	C50R50
2.3	C25R75

DOU	CP blends
1.8	C43P57
1.9	C71P29

DOU	PR blends
1.8	P80R20
1.9	P67R33
2.0	P53R47
2.1	P40R60
2.2	P27R73
2.3	P14R86

DOU	PS blends
1.8	P82S18
1.9	P71S29
2.0	P59S41
2.1	P47S53
2.2	P35S65
2.3	P24S76
2.4	P12S88

Figure 6.10 Correlation of DOU with EI_{NO} of flames of commercial biodiesel blends at $\Phi = 0.9$

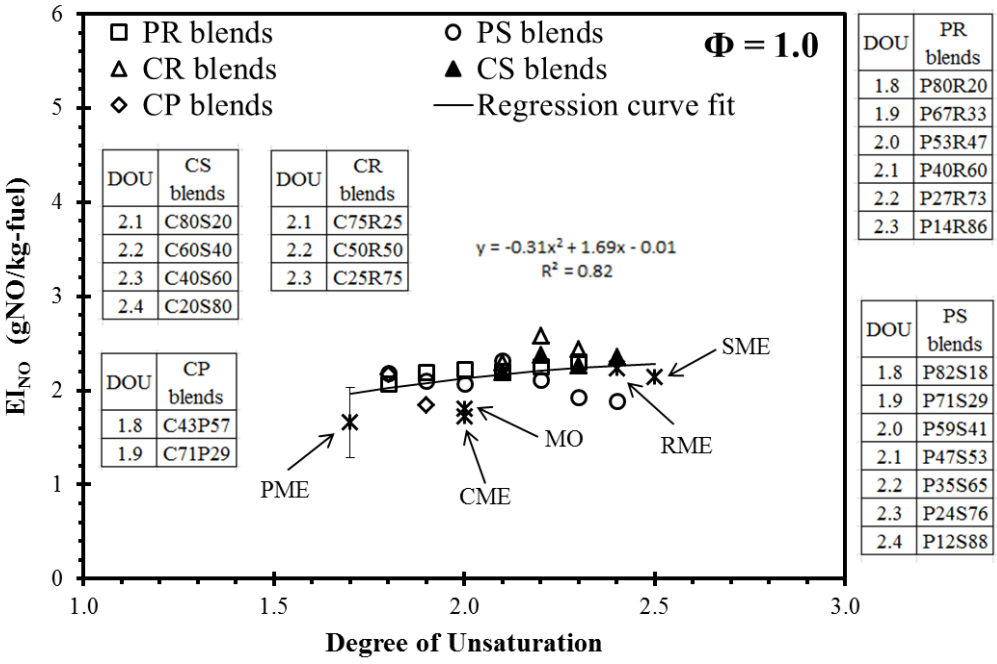

DOU	CS blends
2.1	C80S20
2.2	C60S40
2.3	C40S60
2.4	C20S80

DOU	CR blends
2.1	C75R25
2.2	C50R50
2.3	C25R75

DOU	CP blends
1.8	C43P57
1.9	C71P29

DOU	PR blends
1.8	P80R20
1.9	P67R33
2.0	P53R47
2.1	P40R60
2.2	P27R73
2.3	P14R86

DOU	PS blends
1.8	P82S18
1.9	P71S29
2.0	P59S41
2.1	P47S53
2.2	P35S65
2.3	P24S76
2.4	P12S88

Figure 6.11 Correlation of DOU with EI_{NO} of flames of commercial biodiesel blends at $\Phi = 1.0$

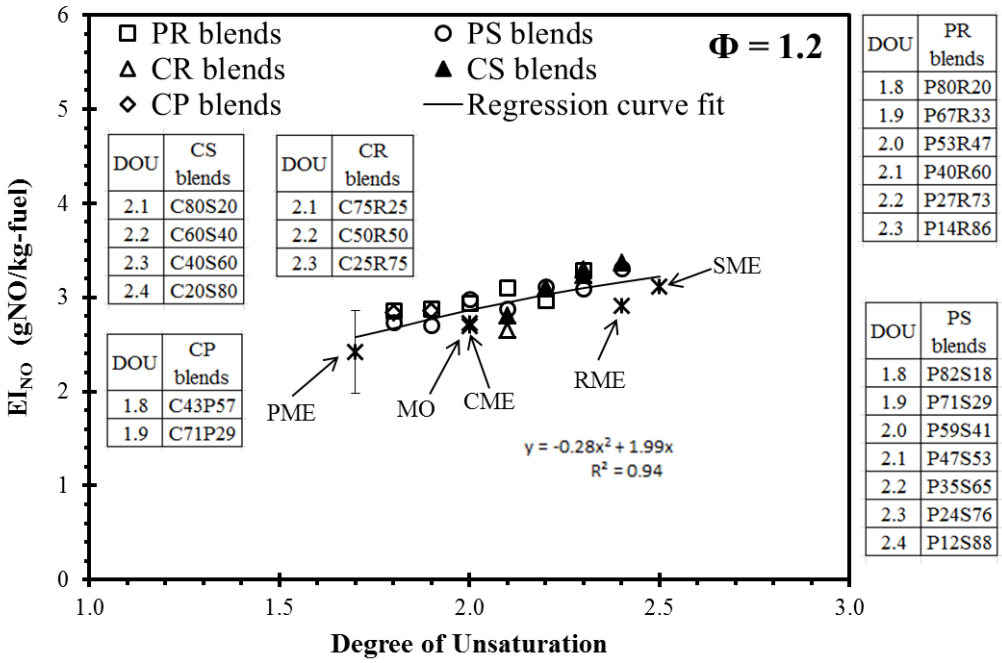

Figure 6.12 Correlation of DOU with EI_{NO} of flames of commercial biodiesel blends at Φ = 1.2

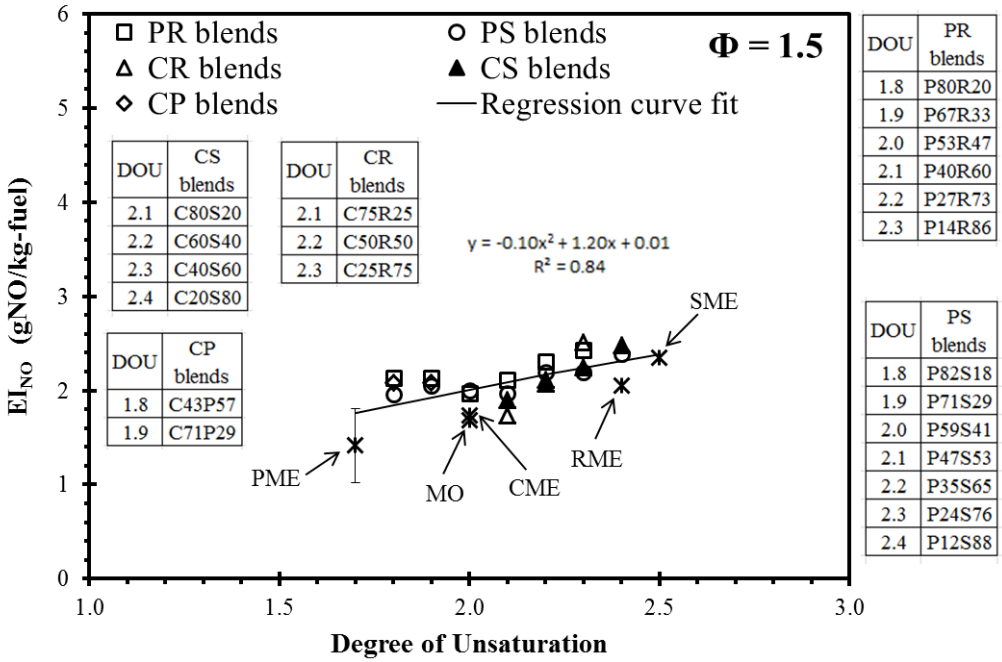

Figure 6.13 Correlation of DOU with EI_{NO} of flames of commercial biodiesel blends at Φ = 1.5

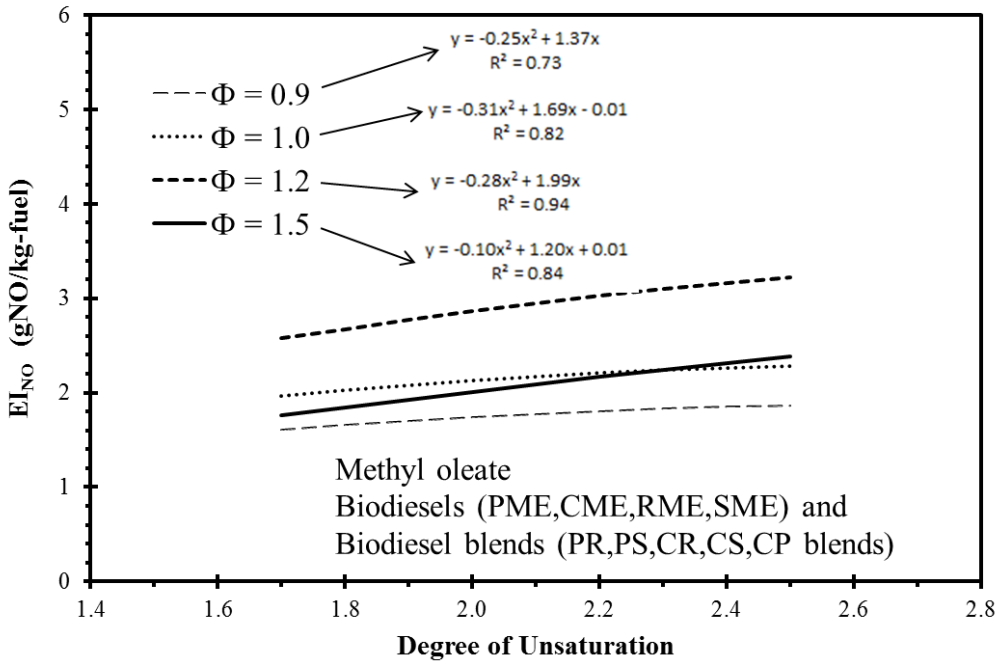

Figure 6.14 Influence of DOU on EI_{NO} from flames of biodiesels at various equivalence ratios

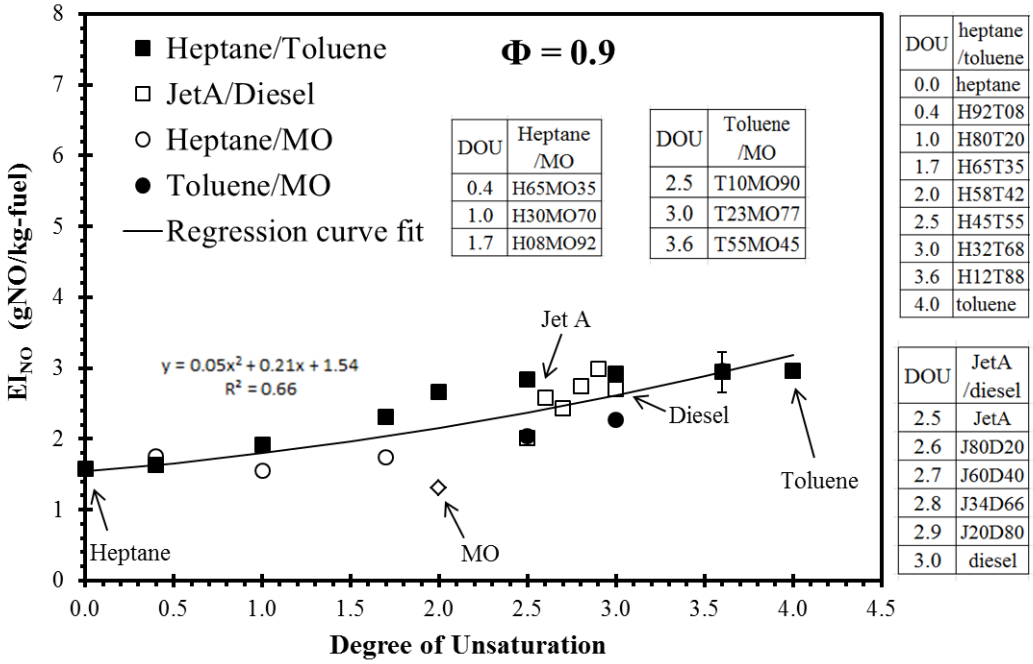

DOU	Heptane /MO
0.4	H65MO35
1.0	H30MO70
1.7	H08MO92

DOU	Toluene /MO
2.5	T10MO90
3.0	T23MO77
3.6	T55MO45

DOU	heptane /toluene
0.0	heptane
0.4	H92T08
1.0	H80T20
1.7	H65T35
2.0	H58T42
2.5	H45T55
3.0	H32T68
3.6	H12T88
4.0	toluene

DOU	JetA /diesel
2.5	JetA
2.6	J80D20
2.7	J60D40
2.8	J34D66
2.9	J20D80
3.0	diesel

Figure 6.15 Correlation of DOU with EI_{NO} of flames of petrofuel /MO blends at Φ = 0.9

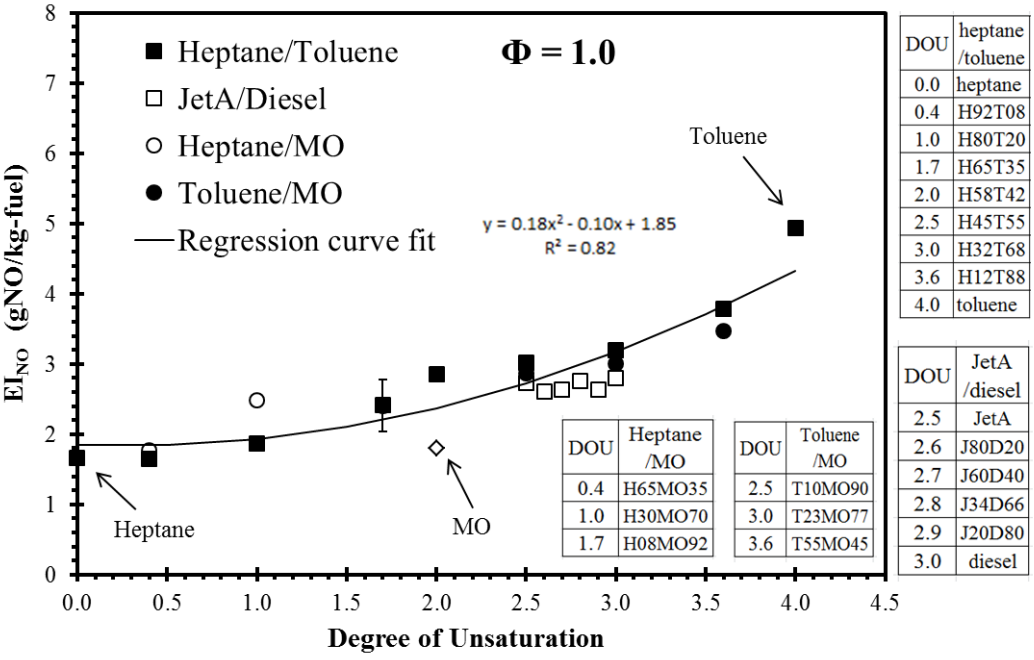

DOU	Heptane /MO
0.4	H65MO35
1.0	H30MO70
1.7	H08MO92

DOU	Toluene /MO
2.5	T10MO90
3.0	T23MO77
3.6	T55MO45

DOU	heptane /toluene
0.0	heptane
0.4	H92T08
1.0	H80T20
1.7	H65T35
2.0	H58T42
2.5	H45T55
3.0	H32T68
3.6	H12T88
4.0	toluene

DOU	JetA /diesel
2.5	JetA
2.6	J80D20
2.7	J60D40
2.8	J34D66
2.9	J20D80
3.0	diesel

Figure 6.16 Correlation of DOU with EI_{NO} of flames of petrofuel /MO blends at Φ = 1.0

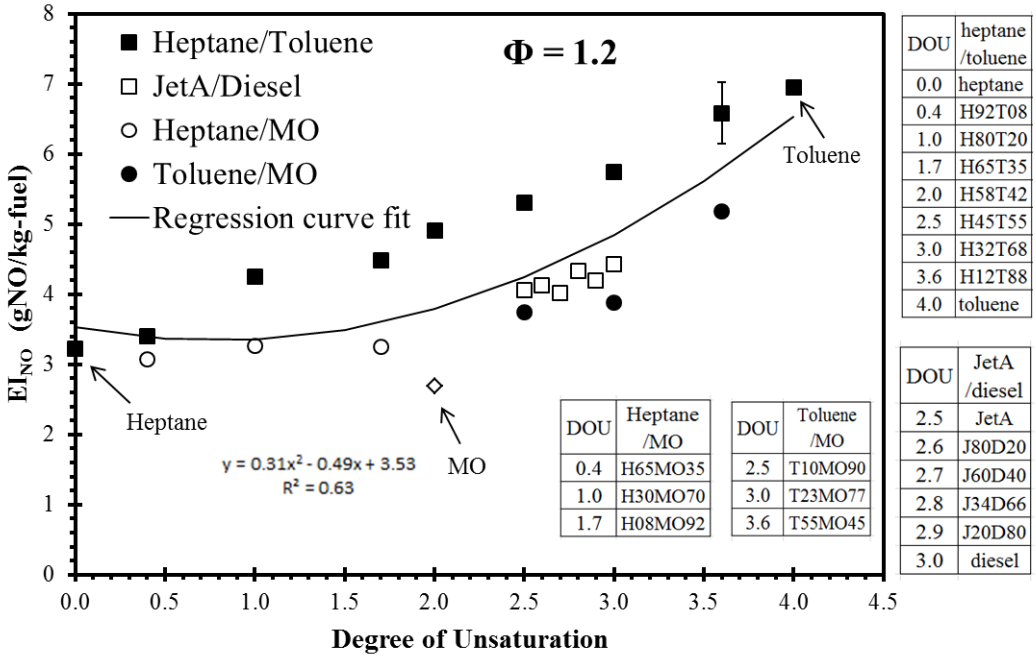

DOU	Heptane /MO
0.4	H65MO35
1.0	H30MO70
1.7	H08MO92

DOU	Toluene /MO
2.5	T10MO90
3.0	T23MO77
3.6	T55MO45

DOU	heptane /toluene
0.0	heptane
0.4	H92T08
1.0	H80T20
1.7	H65T35
2.0	H58T42
2.5	H45T55
3.0	H32T68
3.6	H12T88
4.0	toluene

DOU	JetA /diesel
2.5	JetA
2.6	J80D20
2.7	J60D40
2.8	J34D66
2.9	J20D80
3.0	diesel

Figure 6.17 Correlation of DOU with EI_{NO} of flames of petrofuel /MO blends at Φ = 1.2

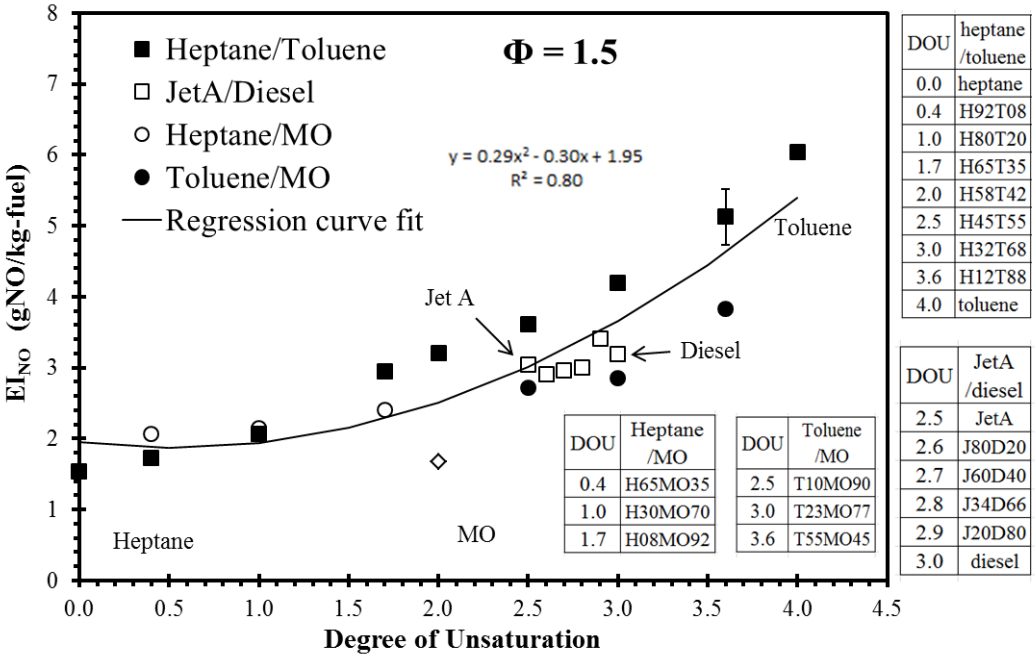

DOU	Heptane /MO
0.4	H65MO35
1.0	H30MO70
1.7	H08MO92

DOU	Toluene /MO
2.5	T10MO90
3.0	T23MO77
3.6	T55MO45

DOU	heptane /toluene
0.0	heptane
0.4	H92T08
1.0	H80T20
1.7	H65T35
2.0	H58T42
2.5	H45T55
3.0	H32T68
3.6	H12T88
4.0	toluene

DOU	JetA /diesel
2.5	JetA
2.6	J80D20
2.7	J60D40
2.8	J34D66
2.9	J20D80
3.0	diesel

Figure 6.18 Correlation of DOU with EI_{NO} of flames of petrofuel /MO blends at Φ = 1.5

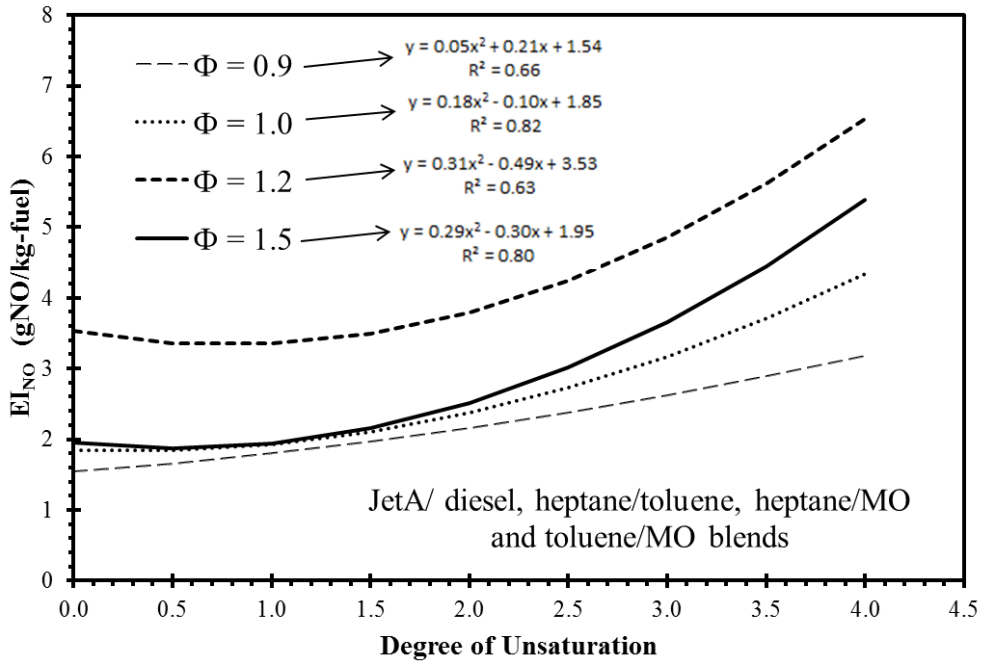

Figure 6.19 Influence of DOU on EI_{NO} of petrofuel / MO biodiesels at various equivalence ratios

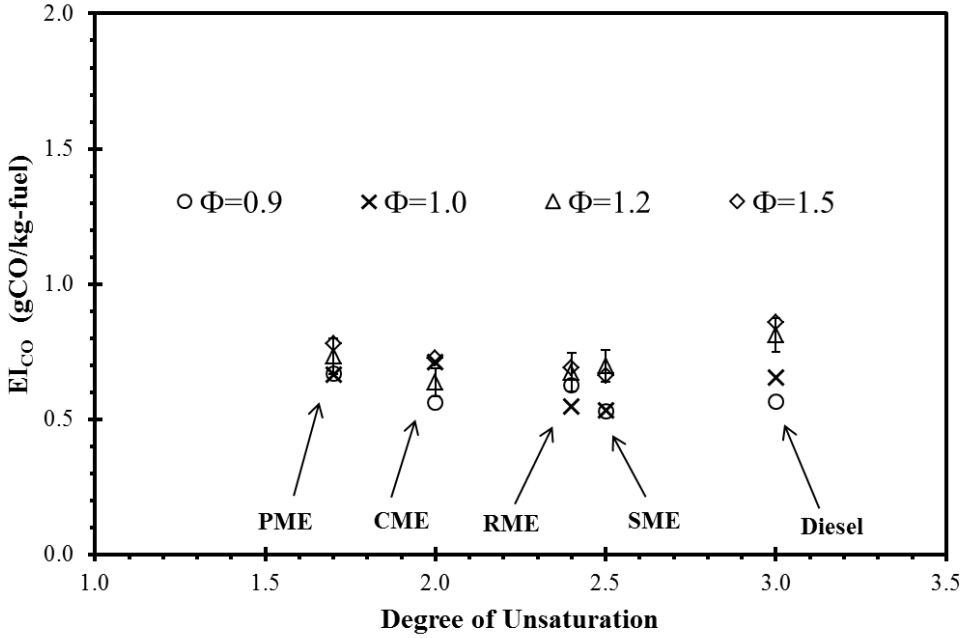

Figure 6.20 Correlation of DOU with EI_{CO} of flames of neat petroleum and biodiesel fuels at different equivalence ratios

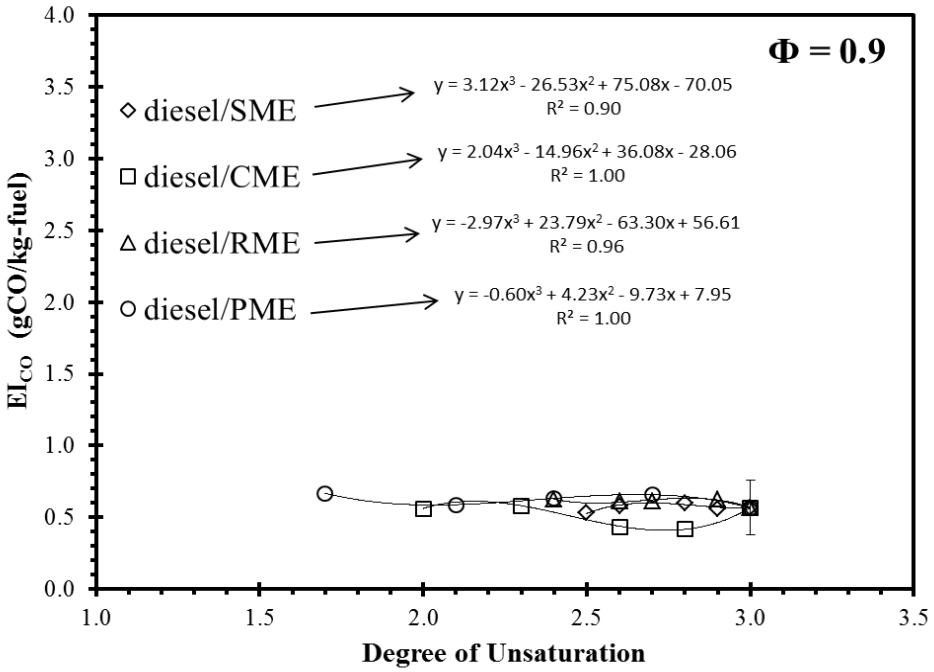

Figure 6.21 Correlation of DOU with EI_{CO} of flames of petrodiesel / biodiesel blends at $\Phi = 0.9$

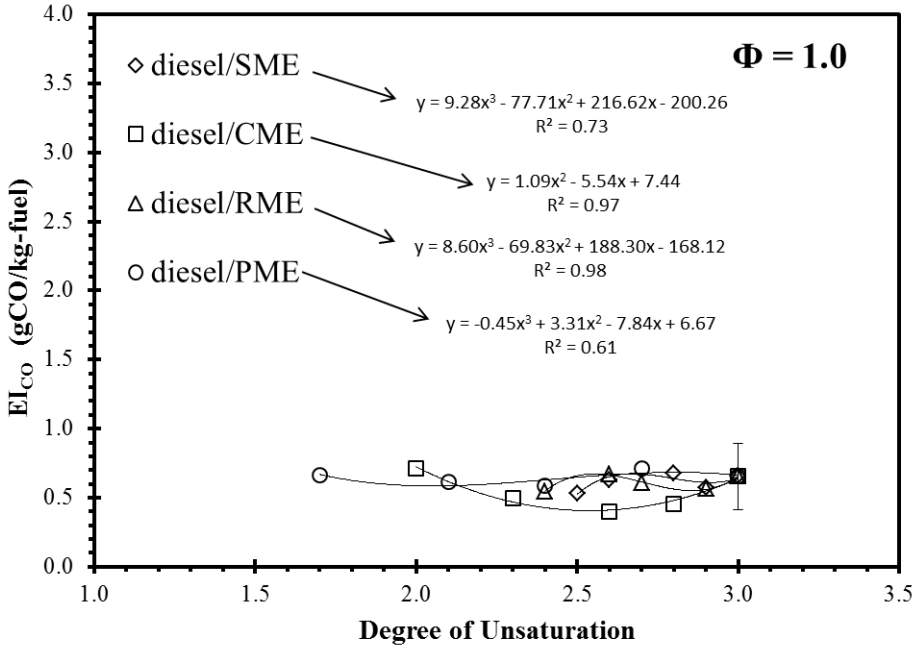

Figure 6.22 Correlation of DOU with EI_{CO} of flames of petrodiesel / biodiesel blends at $\Phi = 1.0$

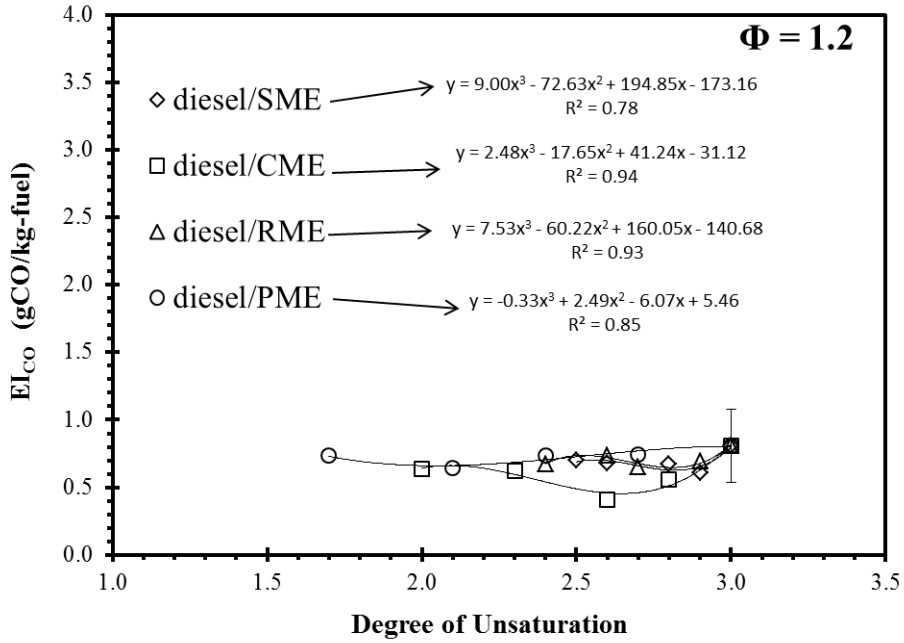

Figure 6.23 Correlation of DOU with EI_{CO} of flames of petrodiesel / biodiesel blends at $\Phi = 1.2$

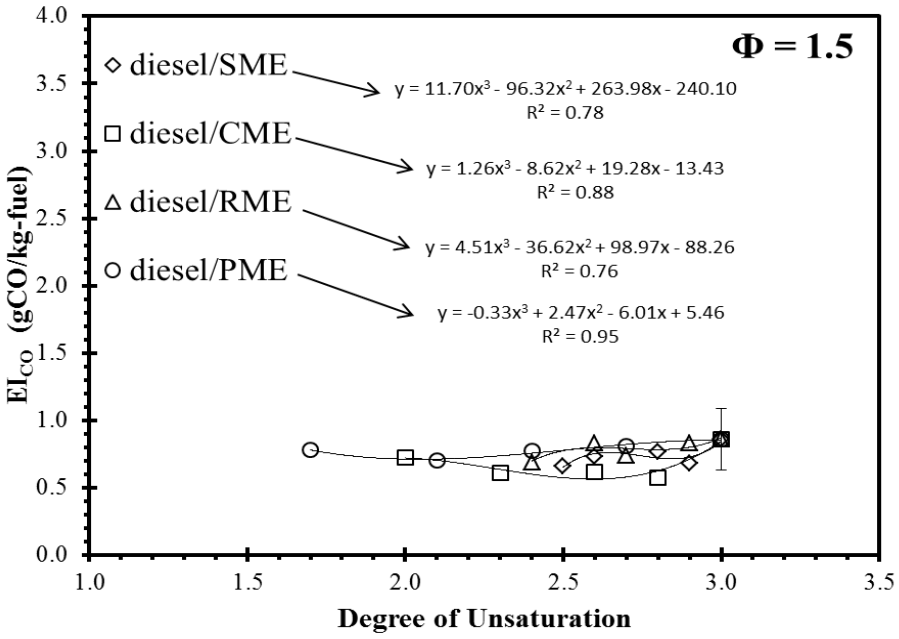

Figure 6.24 Correlation of DOU with EI_{CO} of flames of petrodiesel / biodiesel blends at $\Phi = 1.5$

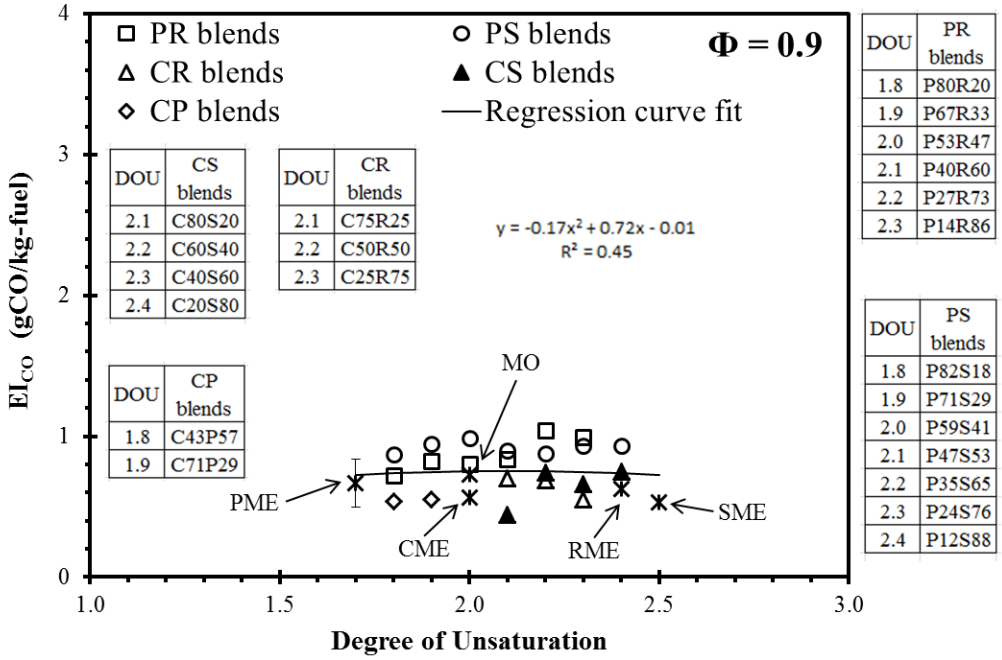

Figure 6.25 Correlation of DOU with EI_{CO} of flames of petrofuel /MO blends at Φ = 0.9

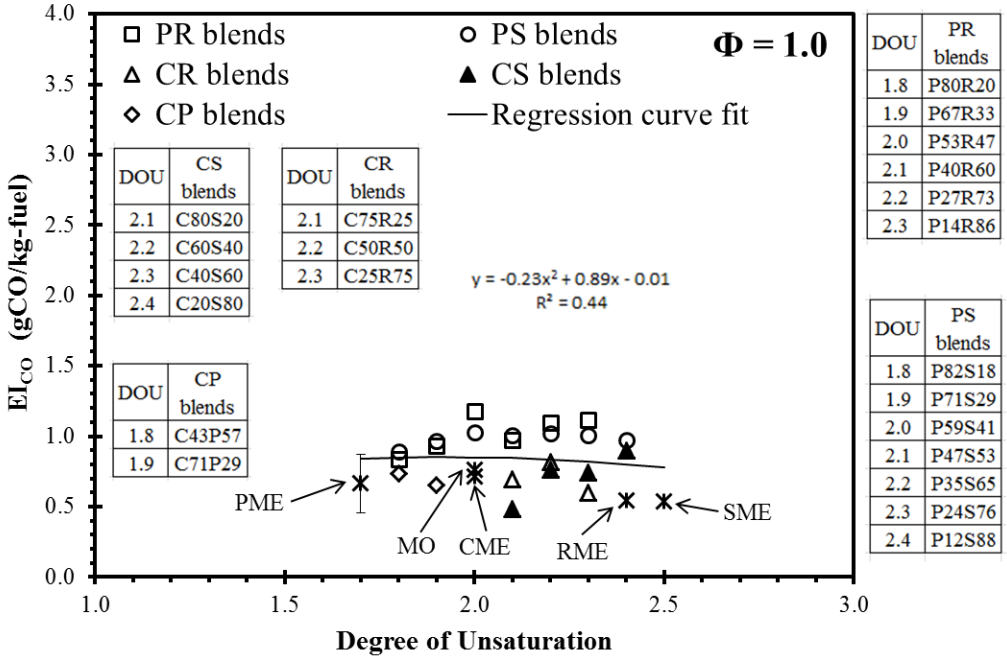

Figure 6.26 Correlation of DOU with EI_{CO} of flames of petrofuel /MO blends at Φ = 1.0

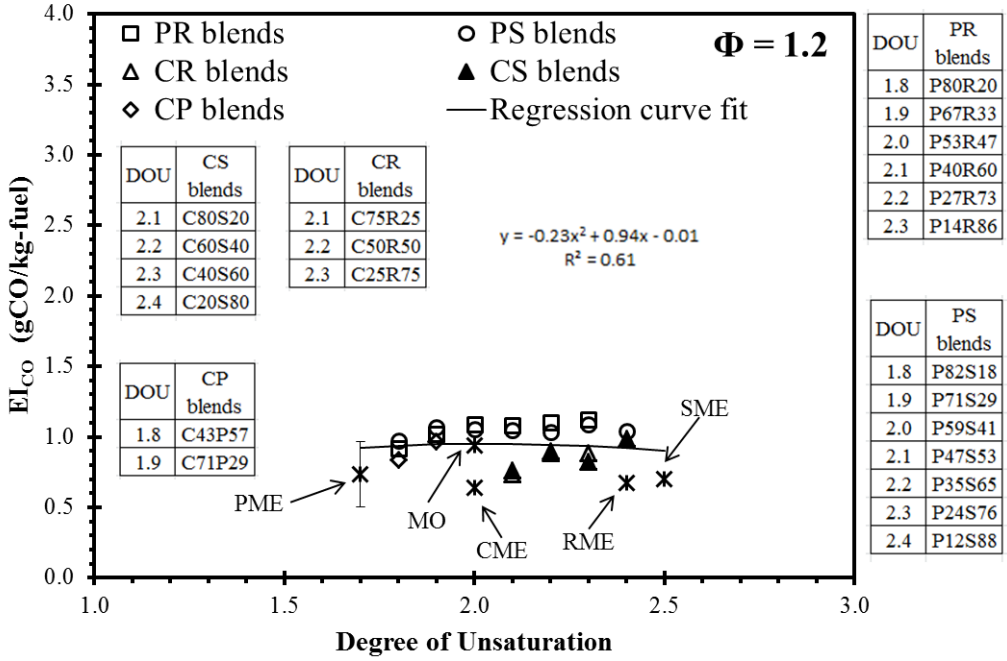

Figure 6.27 Correlation of DOU with EI_{CO} of flames of petrofuel /MO blends at Φ = 1.2

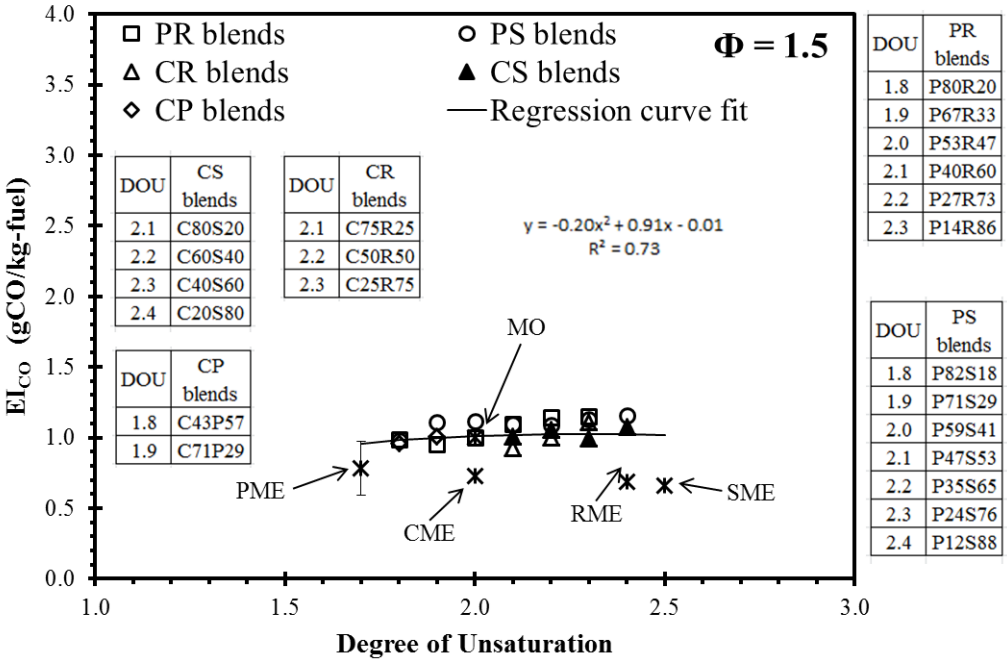

Figure 6.28 Correlation of DOU with EI_{CO} of flames of petrofuel /MO blends at Φ = 1.5

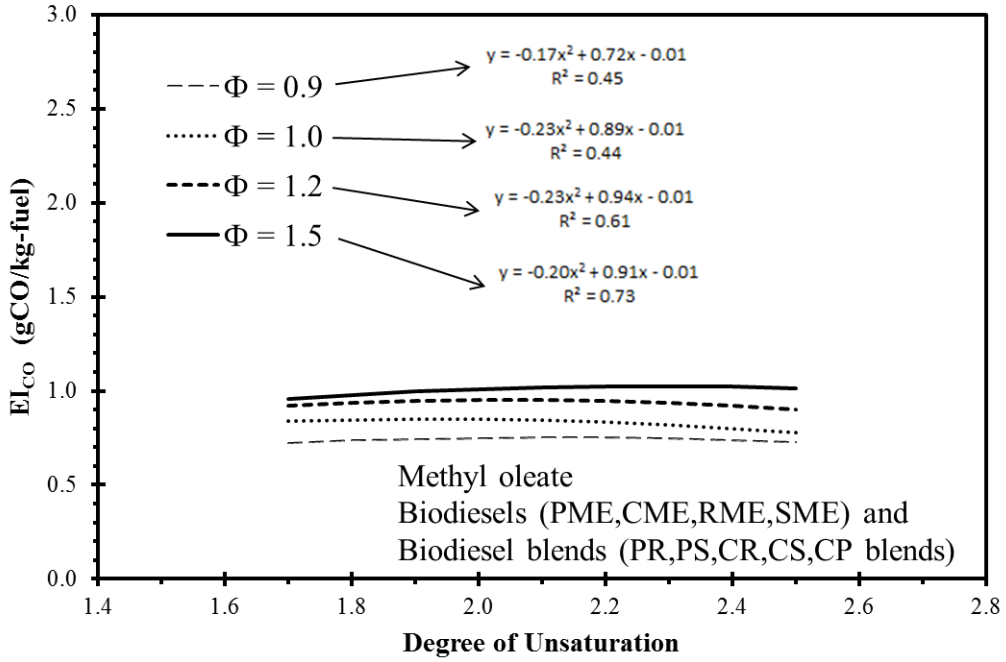

Figure 6.29 Influence of DOU on EI_{CO} from flames of petrofuel /MO blends at various equivalence ratios

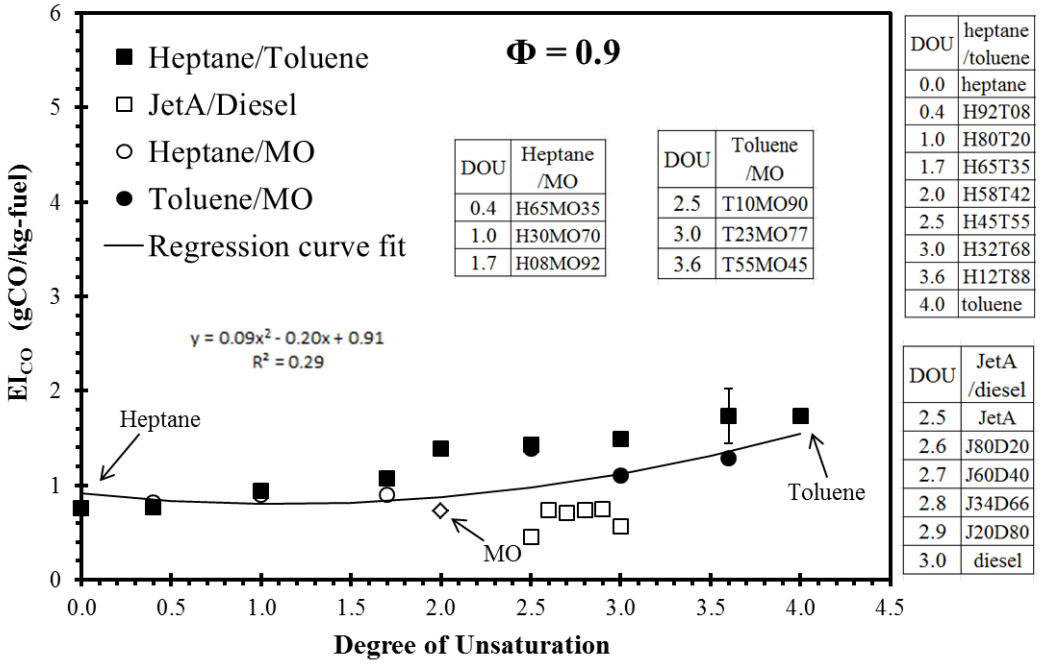

DOU	Heptane /MO
0.4	H65MO35
1.0	H30MO70
1.7	H08MO92

DOU	Toluene /MO
2.5	T10MO90
3.0	T23MO77
3.6	T55MO45

DOU	heptane /toluene
0.0	heptane
0.4	H92T08
1.0	H80T20
1.7	H65T35
2.0	H58T42
2.5	H45T55
3.0	H32T68
3.6	H12T88
4.0	toluene

DOU	JetA /diesel
2.5	JetA
2.6	J80D20
2.7	J60D40
2.8	J34D66
2.9	J20D80
3.0	diesel

Figure 6.30 Correlation of DOU with EI_{CO} of flames of petrofuel /MO blends at Φ = 0.9

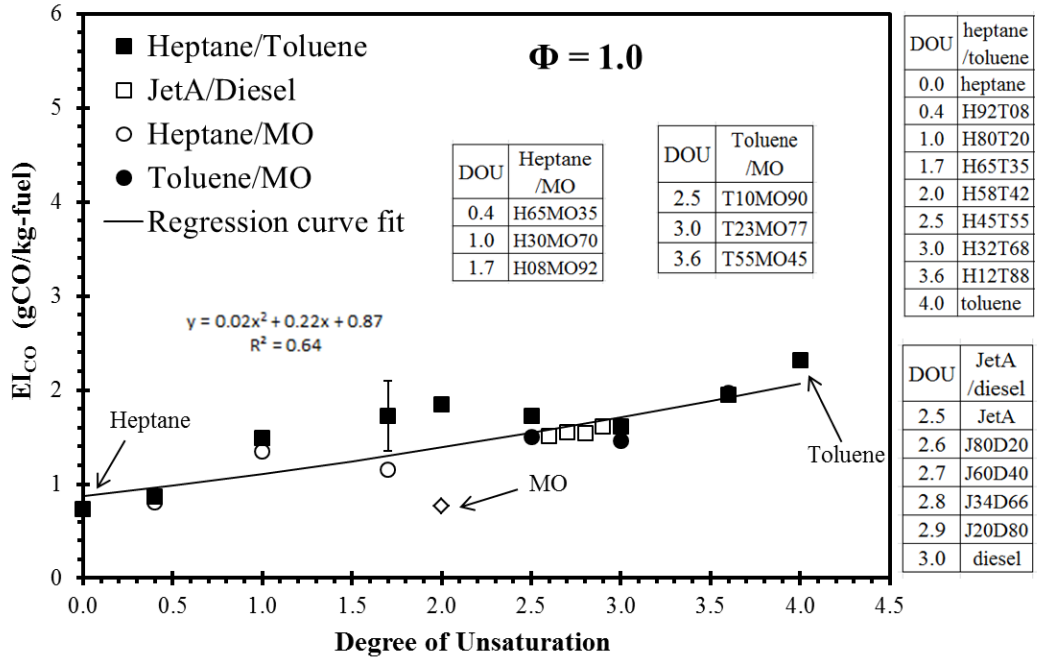

DOU	Heptane /MO
0.4	H65MO35
1.0	H30MO70
1.7	H08MO92

DOU	Toluene /MO
2.5	T10MO90
3.0	T23MO77
3.6	T55MO45

DOU	heptane /toluene
0.0	heptane
0.4	H92T08
1.0	H80T20
1.7	H65T35
2.0	H58T42
2.5	H45T55
3.0	H32T68
3.6	H12T88
4.0	toluene

DOU	JetA /diesel
2.5	JetA
2.6	J80D20
2.7	J60D40
2.8	J34D66
2.9	J20D80
3.0	diesel

Figure 6.31 Correlation of DOU with EI_{CO} of flames of petrofuel /MO blends at Φ = 1.0

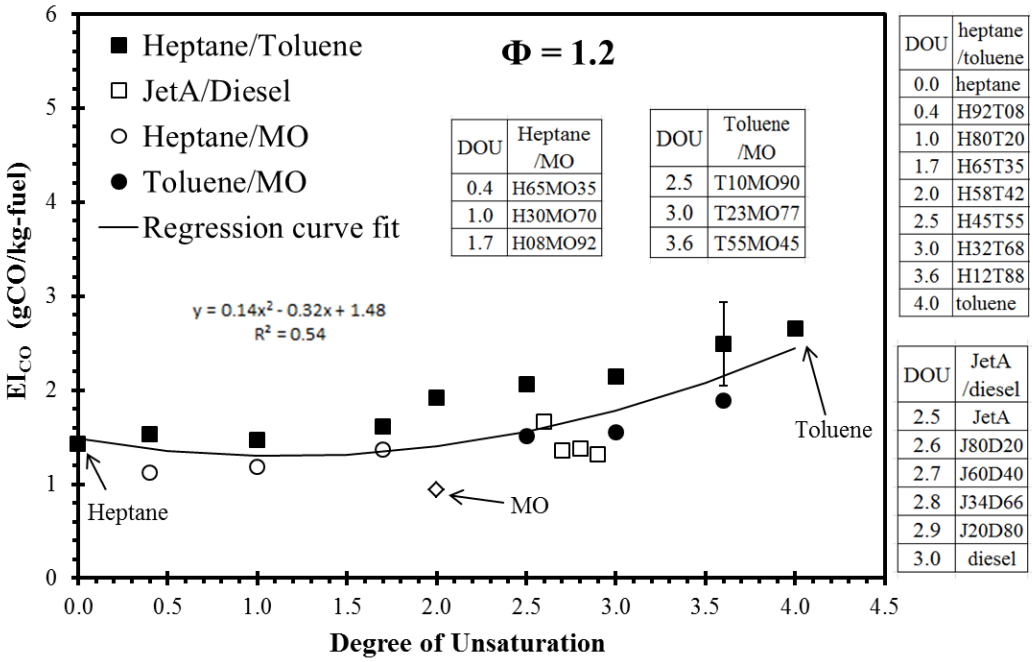

DOU	Heptane /MO
0.4	H65MO35
1.0	H30MO70
1.7	H08MO92

DOU	Toluene /MO
2.5	T10MO90
3.0	T23MO77
3.6	T55MO45

DOU	heptane /toluene
0.0	heptane
0.4	H92T08
1.0	H80T20
1.7	H65T35
2.0	H58T42
2.5	H45T55
3.0	H32T68
3.6	H12T88
4.0	toluene

DOU	JetA /diesel
2.5	JetA
2.6	J80D20
2.7	J60D40
2.8	J34D66
2.9	J20D80
3.0	diesel

Figure 6.32 Correlation of DOU with EI_{CO} of flames of petrofuel /MO blends at Φ = 1.2

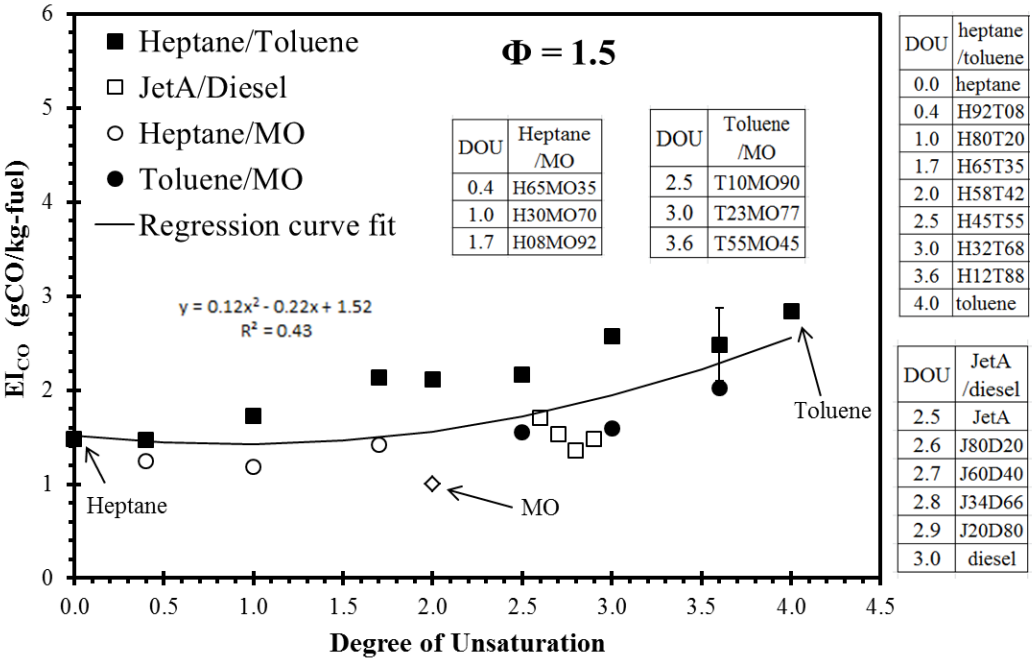

DOU	Heptane /MO
0.4	H65MO35
1.0	H30MO70
1.7	H08MO92

DOU	Toluene /MO
2.5	T10MO90
3.0	T23MO77
3.6	T55MO45

DOU	heptane /toluene
0.0	heptane
0.4	H92T08
1.0	H80T20
1.7	H65T35
2.0	H58T42
2.5	H45T55
3.0	H32T68
3.6	H12T88
4.0	toluene

DOU	JetA /diesel
2.5	JetA
2.6	J80D20
2.7	J60D40
2.8	J34D66
2.9	J20D80
3.0	diesel

Figure 6.33 Correlation of DOU with EI_{CO} of flames of petrofuel /MO blends at Φ = 1.5

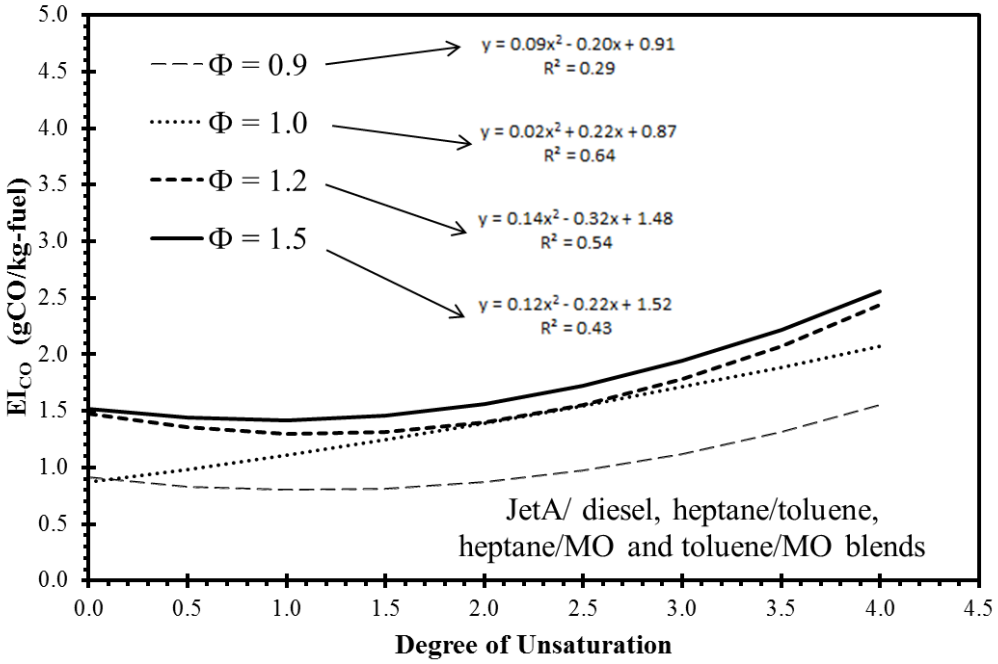

Figure 6.34 Influence of DOU on EI_{CO} from flames of petrofuel /MO blends at various equivalence ratios

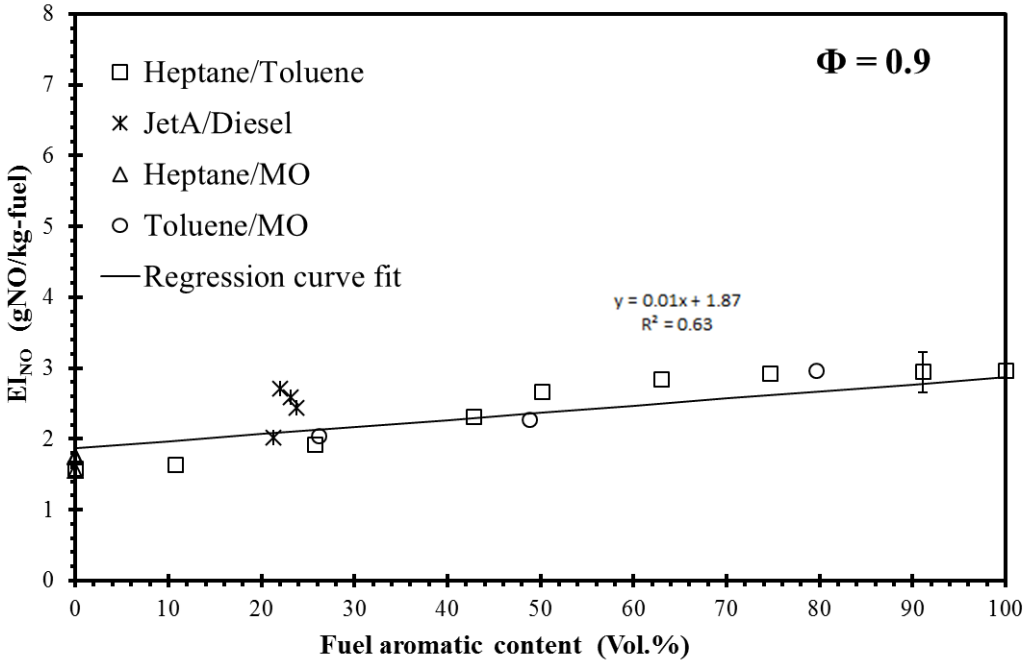

Figure 6.35 Influence of aromatic content on EI_{NO} of tested flames at $\Phi = 0.9$

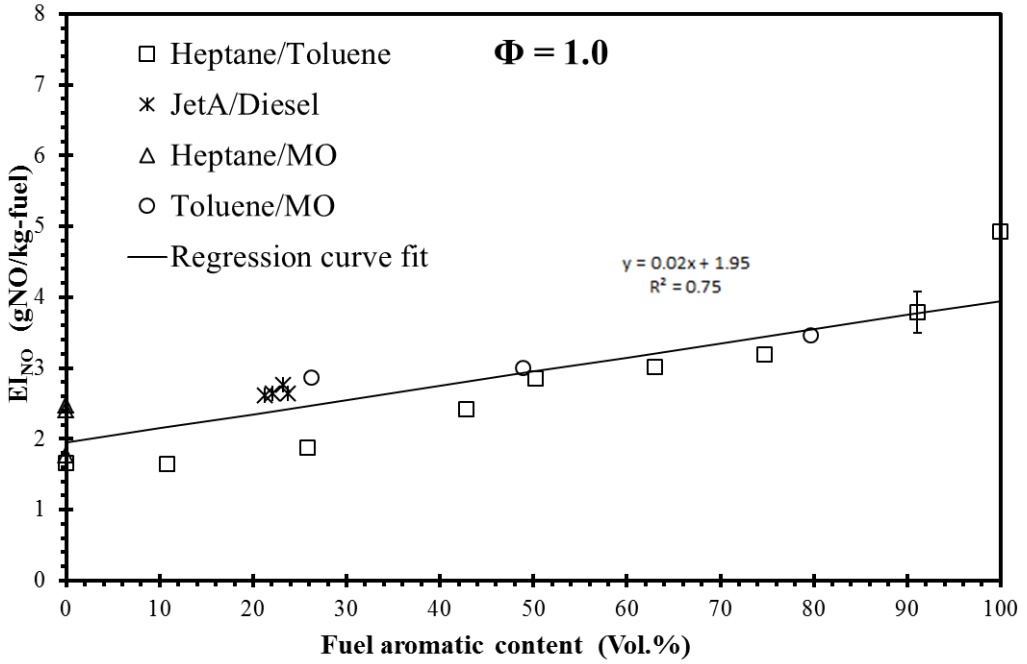

Figure 6.36 Influence of aromatic content on EI_{NO} of tested flames at $\Phi = 1.0$

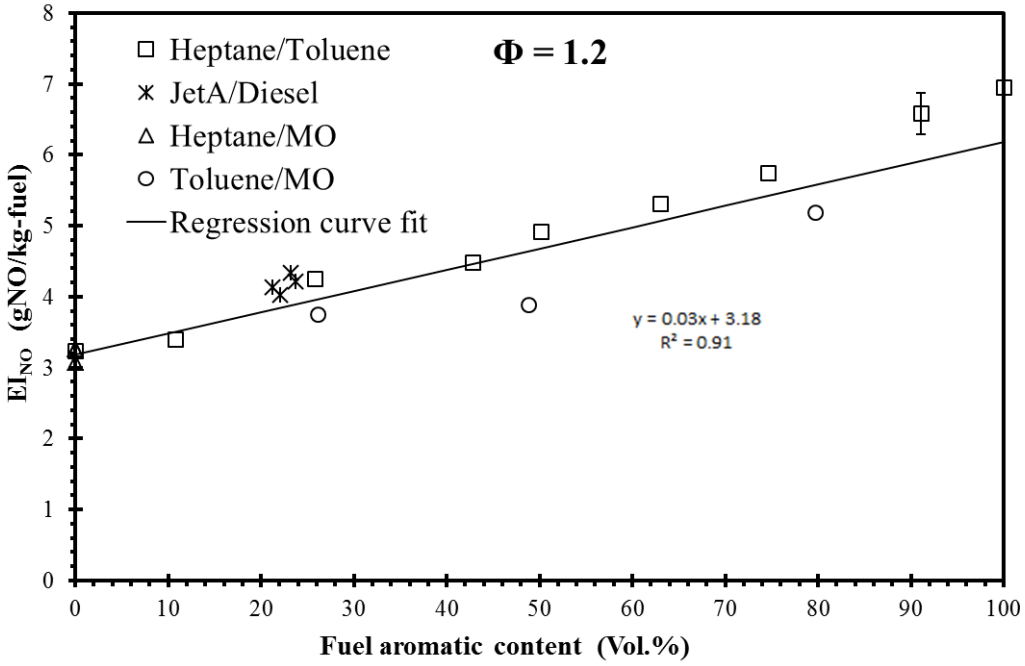

Figure 6.37 Influence of aromatic content on EI_{NO} of tested flames at $\Phi = 1.2$

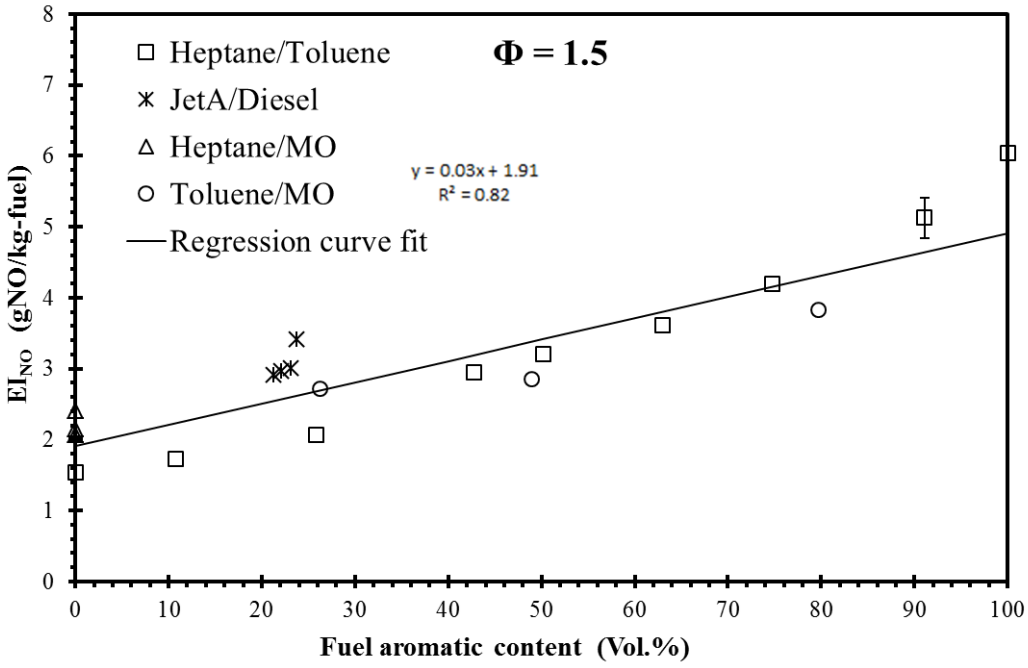

Figure 6.38 Influence of aromatic content on EI_{NO} of tested flames at $\Phi = 1.5$

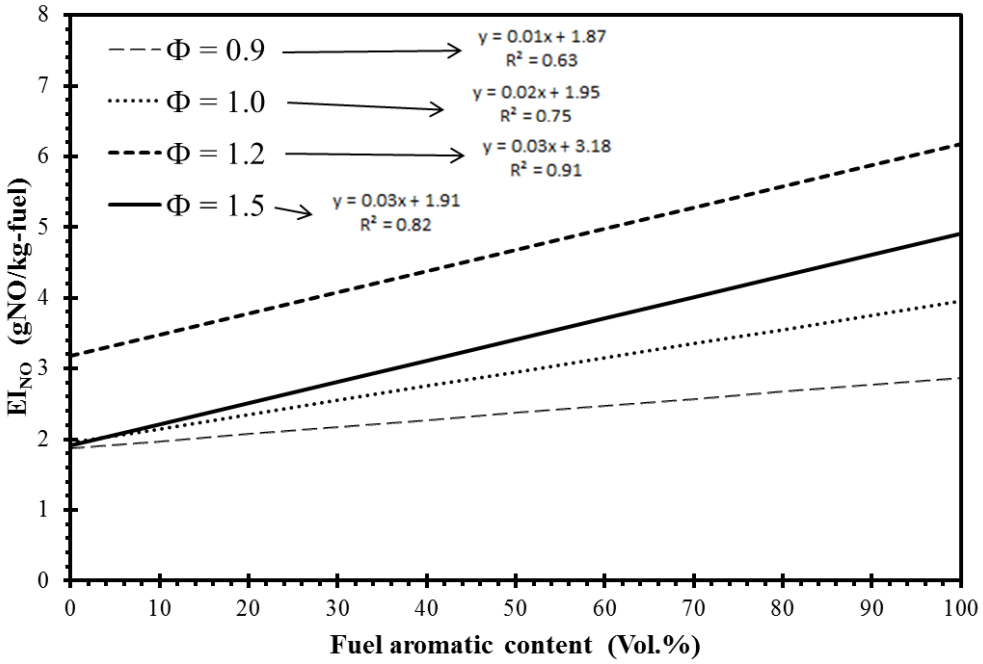

Figure 6.39 Influence of aromatic content on EI_{NO} of tested flames at various equivalence ratios

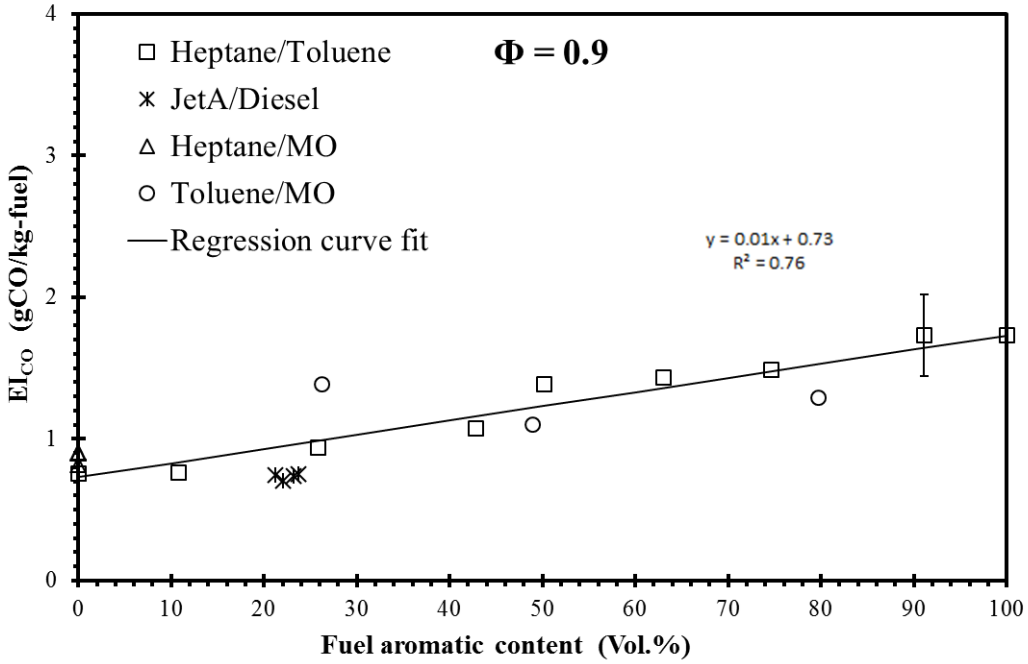

Figure 6.40 Influence of aromatic content on EI_{CO} of tested flames at $\Phi = 0.9$

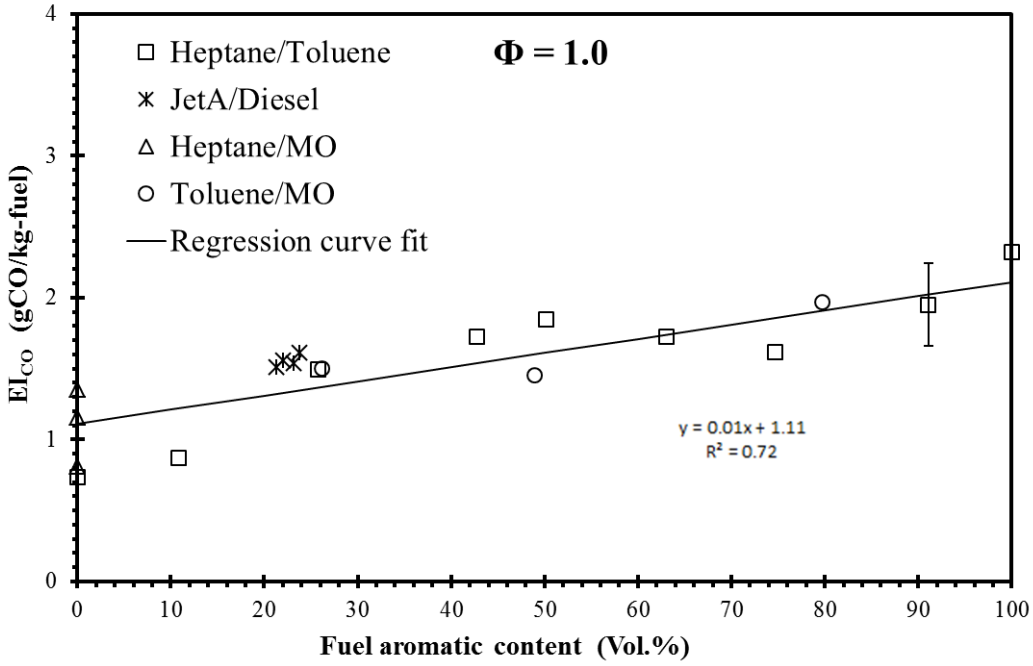

Figure 6.41 Influence of aromatic content on EI_{CO} of tested flames at $\Phi = 1.0$

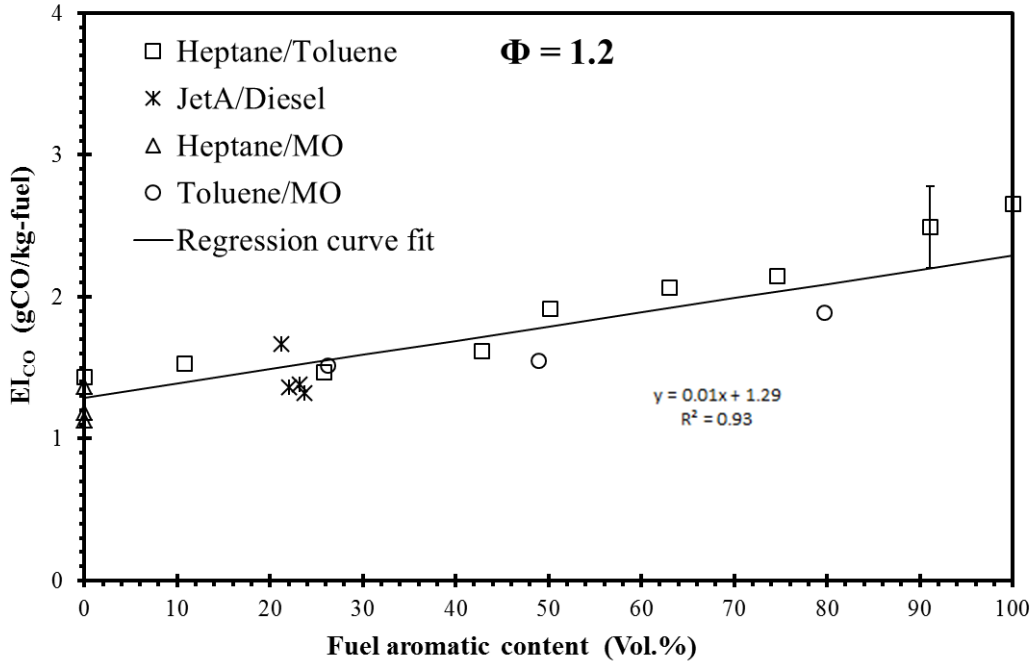

Figure 6.42 Influence of aromatic content on EI_{CO} of tested flames at $\Phi = 1.2$

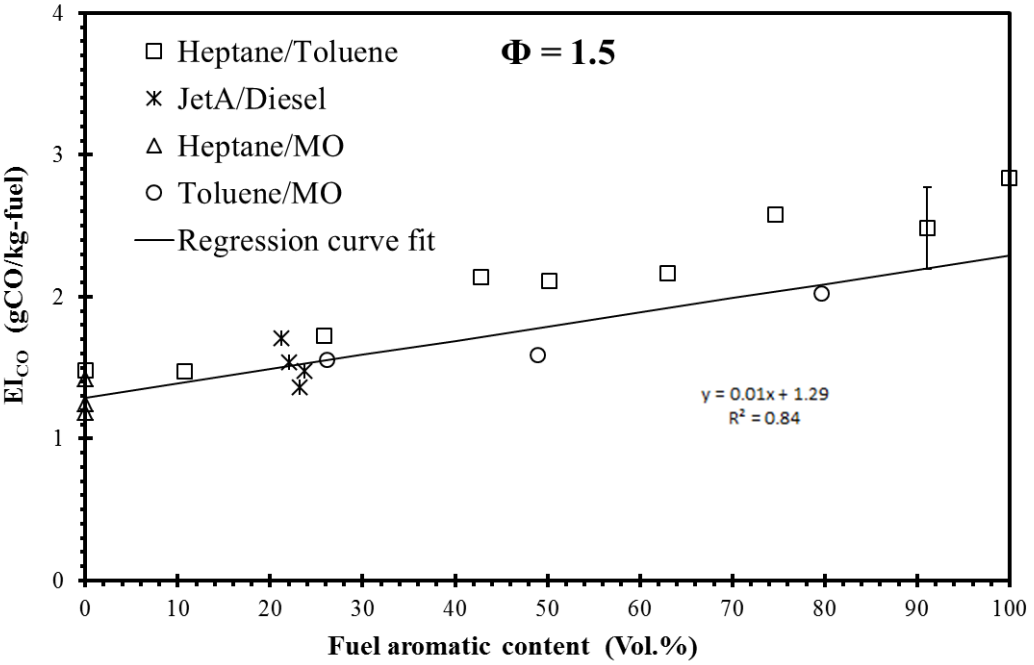

Figure 6.43 Influence of aromatic content on EI_{CO} of tested flames at $\Phi = 1.5$

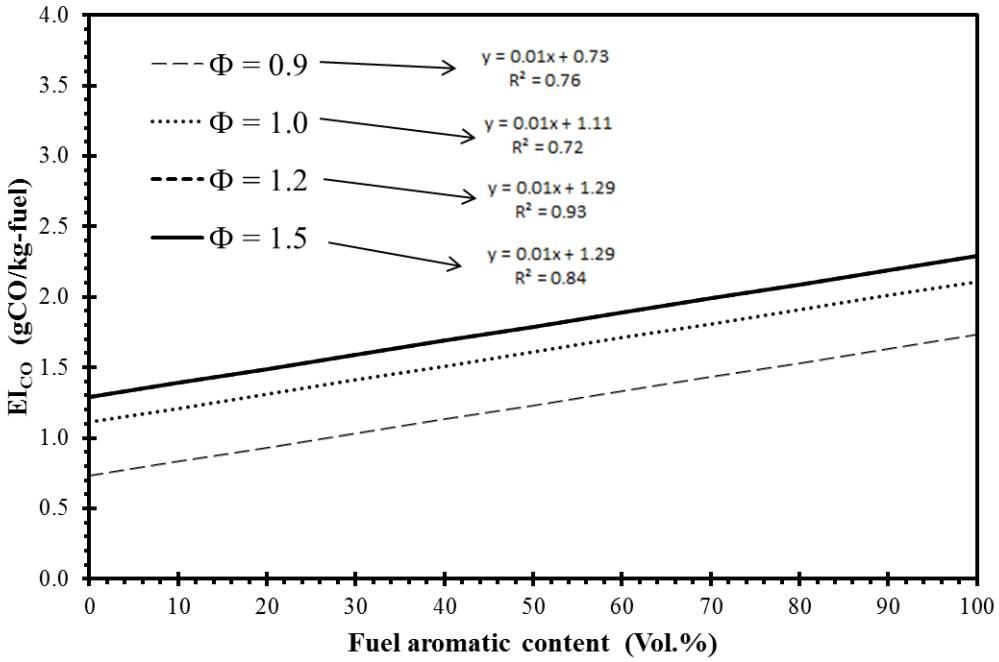

Figure 6.44 Influence of aromatic content on EI_{CO} of tested flames at various equivalence ratios

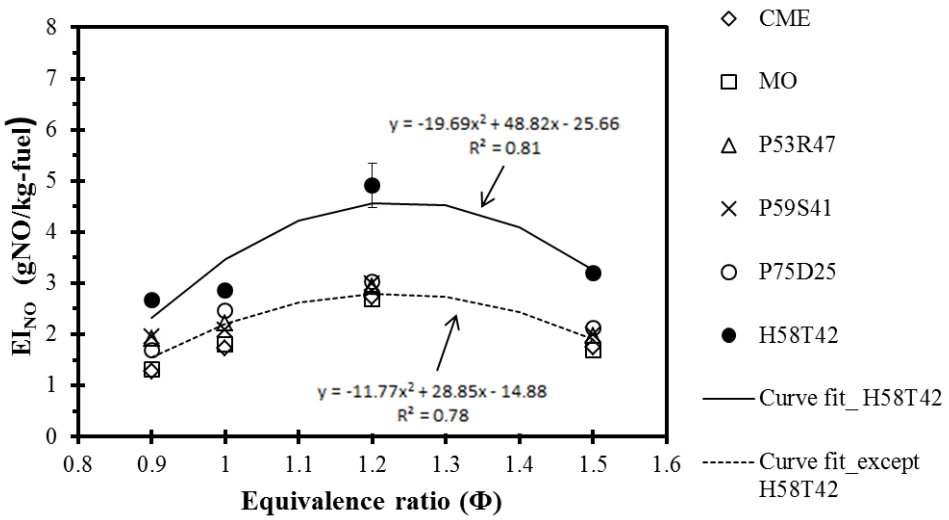

Figure 6.45Influence of equivalence ratio on EI_{NO} of tested flames at DOU = 2

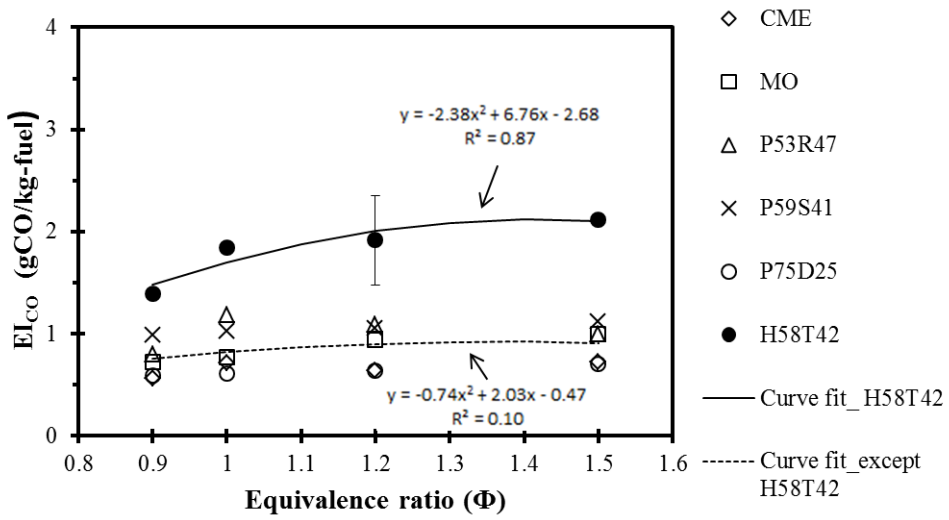

Figure 6.46 Influence of equivalence ratio on EI_{CO} of tested flames at DOU = 2

CHAPTER 7 EXPERIMENTAL RESULTS - FLAME STRUCTURE

The global flame characteristics such as NO and CO emission indices of flames of all the selected fuel blends over a DOU range of 0 to 4 (presented in chapter 6) provided a broad picture of fuel unsaturation and equivalence ratio effects on end emissions. To further augment the understanding of the observed results and trends, a detailed analysis of flame structure, local temperature and species concentration of flames was required. In this chapter, the flame images and in-flame measurements such as in-flame radial temperature profiles and in-flame species concentration profiles of O_2, CO_2, CO and NO from the laminar premixed flames of prevaporized fuels at Φ = 1.2 are presented. The results are discussed in this section on two aspects as:

- ***Effect 1: Degree of fuel unsaturation***

  Fuels with different DOU values - heptane (DOU: 0), PME (DOU: 1.7), CME (DOU: 2.0), SME (DOU: 2.5), petro-diesel (DOU: 3.0) and toluene (DOU: 4.0)

- ***Effect 2: Fuel origin (at same DOU)***

  Fuels with same values of degree of unsaturation (DOU: 2) belongs to different families of fuel origin - MO (individual methyl ester), CME (commercial biodiesel-combination of different methyl esters), P53R47 (palm/rapeseed biodiesel blend), P59S41 (palm/soy biodiesel blend), H58T42 (heptane/toluene blend) and P75D25 (palm/petrodiesel blend)

Hence, in brief, the inflame results from the aforementioned 11 flames at $\Phi = 1.2$ (the equivalence ratio where EI_{NO} was found to be maximum as seen in chapter 6) will be presented and discussed in this chapter.

For studying the effect of DOU, fuels with increasing DOU were considered and the results from the tested flames will be discussed in terms of increasing DOU values. While, for studying the effect of fuel origin, the results from the tested flames will be discussed in terms of fuel characteristics that differentiate the selected fuels though having similar degree of unsaturation. Methyl esters such as MO, CME, P53R47 and P59S41, in addition to same effective degree of unsaturation (DOU: 2), also possess similar oxygen content (10.8% - 11.4%) and similar source of fuel unsaturation (double bonds). Any observed differences from these results could be due to the fact that each fuel blend is made up of different combination of individual methyl esters whose number and position of double bonds in the carbon main chain may differ. In addition, H58T42 flame does not have fuel bound oxygen and the unsaturation in the fuel is only due to aromatic content (toluene). The P75D25 flame has fuel bound oxygen; unsaturation arises from both alkene and aromatic content in addition to double bonds from methyl esters.

The following sections are presented with comprehensive discussions on results from each of the aforementioned flame measurement techniques.

7.1 Flame Appearance

The flame images of fuels selected to investigate the effect 1 (heptane, PME, CME, SME, petrodiesel and toluene) and the effect 2 (MO, CME, P53R47, P59S41, H58T42 and P75D25) at Φ = 0.9, 1.0, 1.2 and 1.5 are presented in Figures 7.1 - 7.8 (the flame images of all the tested 63 fuels are presented in appendix E).

In all these tested flames, three primary regions were observed: 1) a dark space between the burner exit and the inner bright cone, 2) a bright blue inner cone surrounded by 3) an outer less luminous blue cone. The dark space revealed a pre-flame reaction (pre-heating zone) with markedly changing gas composition. The brighter blue inner cone represented the primary gas phase oxidation reaction zone. The reaction product from this inner cone comprised of reactants capable of further oxidation in the outer cone. The outer cone represented the burning of unburned reactants in the surrounding flame zone with oxygen diffusing from the ambient air. Since the test conditions considered here (Φ = 0.9, 1.0, 1.2 and 1.5) are either fuel lean or near stoichiometric, all the flames appeared blue without any continuum radiation from burning soot.

7.1.1 Effect of DOU on flame appearance

At Φ = 0.9, the tested flames had comparable inner cone flame lengths of about 20 mm (Figure 7.1). The appearance of the flames did not vary with the DOU values within the tested range. The flames of petrodiesel and biodiesels such as PME, CME, RME and SME looked similar in flame color (whitish blue) with a bright blue inner cone surrounded by an outer less luminous outer cone. However, the heptane and toluene flames had an inner cone of greenish-blue (cyan) in color. This distinguishable

differences in the flame appearance were also observed at other tested equivalence ratios (Φ = 1.0, 1.2 and 1.5). The reason for these observed differences in flame color will be discussed in section 7.1.2. At Φ = 1.0, the outer cone was longer than that of corresponding flames at Φ = 0.9 (Figure 7.2) due to the less amount of air supplied and this effect is even more conspicuous at higher equivalence ratios (Φ = 1.2 and 1.5). At Φ = 1.5, the inner cone flame lengths of tested flames were measured about 20 mm while the outer cone flame lengths were measured about 80 mm. By comparing Figures 7.1 - 7.4, it is observed that the flame length and flame appearance were primarily influenced by the reactant input rate and equivalence ratio among the flames tested in the equivalence ratio range of Φ = 0.9 and Φ = 1.5.

7.1.2 Effect of fuel origin on flame appearance

As seen in the previous section, the appearance of flames did not vary within the tested range of DOU values. However, the heptane and toluene flames looked prominently different from other tested flames at all tested equivalence ratios. Apparently, even diesel flame (that belongs to petroleum family) looked similar to biodiesel flames (ester family). In 1857, Swan experimentally investigated the spectra produced by various flames. Based on the observations, it was concluded that the spectra produced by the flames, either of the form (C_xH_y) or of the form ($C_xH_yO_z$), have been identical. The observation of similarities in flame appearance between petrodiesel and biodiesel flames is in agreement with the observations reported by Swan (1857) from the flames of oxygenated fuels. Now, with regards to heptane and toluene flame, heptane is a saturated hydrocarbon (alkane) while toluene is an aromatic hydrocarbon

(ring structure); however, the similarities between the observed flame appearances could be due to the excited diatomic carbon (C_2) radicals emitted during the fuel pyrolysis and oxidation. The excited C_2 radicals have peak band emissions in the wavelength range of 430 nm - 530 nm (also known as swan band) which corresponds to the greenish blue region of the visible spectrum and secondary peak of C_2 radicals around 550 nm that corresponds to the yellowish green region of the spectrum (Vandergriff, 2008). The observed greenish blue color flame with reddish yellow tint in the heptane and toluene flames at $\Phi = 1.5$ could be due to the excited C_2 radicals from the swan band of spectral emission. In Swan (1857) study, it was also observed that the brightness of the spectral lines varies with the proportion of hydrogen to carbon ratio, with higher carbon content being brightest. This provides the reason for the brighter appearance of toluene flame than that of heptane flame particularly at $\Phi = 1.5$. In Figures 7.5 - 7.8, the tested flames of fuels with DOU of 2, indicated that the flame appearance varies between the fuels even with same degree of unsaturation and the difference in flame appearance was due to the hydrogen / carbon ratio and origin of the fuel. The flame length was primarily influenced by the reactant input rate and equivalence ratio rather than degree of unsaturation at the tested equivalence ratios.

7.2 In-flame radial temperature profiles

The in-flame radial temperature profiles were recorded at three axial flame heights namely 10 mm, 20 mm and 40 mm above the burner as shown in Figure 7.9. Similar to flame appearance, the inflame temperature results are discussed on two aspects as effect of degree of unsaturation and effect of fuel origin at a particular DOU.

7.2.1 Effect of DOU on flame temperature

The temperature profiles of flames of fuels with increasing degree of unsaturation at $\Phi = 1.2$ are presented in Figures 7.10 - 7.16. The measured temperature profiles of all the flames were symmetric about the flame axis and the peak temperatures were observed at the flame axis at all the three measured axial locations. The peak flame temperatures of heptane, PME, CME, RME, SME, diesel and toluene flames at 10 mm height above the burner (HAB) were 1810K, 1950K, 1958K, 1958K, 1918K, 1848K and 1844K respectively. The peak temperatures of these tested flames occurred in the near burner region and were comparable within experimental uncertainties (5%) regardless of the corresponding degree of fuel unsaturation. Similar comparable temperature trend was observed in an engine study by Hellier et al. (2013) with fuel blends of heptane and toluene, having contrasting DOU values (n-heptane: 0 and toluene: 4). In that study, the combustion and emission characteristics of n-heptane/toluene blends in a direct injection compression ignition engine was investigated at four different modes namely, with constant injection timing, constant ignition timing, constant ignition delay (with fixed start of injection and fixed start of combustion). Petrodiesel was tested as a baseline fuel in addition to heptane/ toluene

blends (up to 40% toluene in n-heptane). At all these test conditions, the maximum average in-cylinder temperature was comparable with no apparent effect of increasing level of toluene in the fuel blend was observed and these values were close to the temperature (1400K) when tested with petrodiesel.

The adiabatic flame temperatures were calculated in the present study using the computer code developed by Olikara and Borman (1975). Adiabatic flame temperatures and the corresponding enthalpies of reactants for selected fuels are presented in Table 7.1. The adiabatic flame temperature of MO, CME, heptane, toluene and diesel were found to be similar within 100K. This is confirmed by the similarities in the appearance and structure of the flames, demonstrated by comparable flame heights and appearance of the flames.

7.2.2 Effect of fuel origin on flame temperature

The temperature profiles of flames of fuels with a DOU value of 2 at $\Phi = 1.2$ are presented in Figures 7.17 - 7.21. The measured temperature profiles of all the flames were symmetric about the flame axis and the peak temperatures were observed at the flame axis at all the three measured axial locations. The peak flame temperatures of MO, CME, P53R47, P59S41, H58T42 and P75D25 at 10mm height above the burner (HAB) were 1808K, 1939K, 1824K, 1836K, 1809K and 1784K respectively. All peak temperatures occurred in the near burner region and did not vary significantly between the tested fuels from different origin (esters, petroleum fuels, blends). Although the recorded temperatures were comparable within experimental uncertainties, MO flame recorded a slightly lower temperature than P53R47 and P59S41 while CME recorded

the highest among the tested flames. H58T42 flame that has highest aromatic content and P75D25 flame recorded similar temperature as that of biodiesel flames. Among all these flames, a gradual decrease in peak temperature with flame height was observed; a decrement of about 150-200K was observed between 10 mm and 40 mm heights above the burner. This reduction in temperature with flame height was due to the diffusion and mixing of ambient air within the flames.

In summary, the measured flame temperatures were almost comparable within experimental uncertainties and did not vary appreciably with the degree of unsaturation or the family of fuel origin.

7.3 In-flame radial O_2 concentration profiles

In this section, the in-flame radial oxygen concentration profiles of tested flames are discussed on two aspects, namely, effect of degree of unsaturation and effect of fuel origin at a DOU value of 2.

7.3.1 Effect of DOU on O_2 concentration profiles

The in-flame radial O_2 concentration profiles of flames of fuels with increasing degree of unsaturation at Φ = 1.2 are presented in Figures 7.22 - 7.28. The O_2 concentration was small near the flame axis and increased towards the edge due to the consumption of oxygen in the combustion reactions within the flame. At 10 mm flame height, the recorded O_2 concentration of heptane, PME, CME, RME, SME, diesel and toluene were 0.8%, 0.1%, 0.1%, 0.1%, 0.9%, 1% and 0.9% respectively. The

experimental uncertainties in these measurements were estimated to be ± 1%. The difference in the amount of fuel bound oxygen between biodiesels and petroleum fuels did not reflect in the measured O_2 concentration profiles. This is expected because the total availability of oxygen (fuel bound and pre-supplied) at the injector exit was same for all the flames. Further downstream of the flames, at 40 mm height above the burner, the measured O_2 concentration was increased to about 1% - 3%. This increase in local oxygen concentration downstream of the flame was due to the entrainment and mixing of ambient air which is confirmed by the reduction of temperature by about 150K - 200K at the corresponding flame heights. The observed results indicated that the measured local oxygen concentration did not correlate statistically with the increase in the degree of fuel unsaturation. In other words, local O_2 concentration in the flame was independent of the increase in the degree of fuel unsaturation.

7.3.2 Effect of fuel origin on O_2 concentration profiles

The in-flame radial O_2 concentration profiles of flames of fuels with a DOU value of 2 at $\Phi = 1.2$ are presented in Figures 7.29 - 7.33. As previously discussed, the O_2 concentration was small near the flame axis and increased towards the edge due to the consumption of oxygen in the combustion reactions within the flame. At 10 mm flame height, the recorded O_2 concentration of MO, CME, P53R47, P59S41, H58T42 and P75D25 flames at the axis were 0.7%, 0.1%, 0.2%, 0.3%, 0.8% and 0.3% respectively. This indicated the occurrence of ongoing oxidation reactions consuming the local available oxygen. The fuel bound oxygen content of biodiesels was in the range of 10.8% - 11.5%, while P75D25 has about 9% of fuel bound oxygen and

H58T42 does not have fuel bound oxygen. As seen before, in spite of the differences in the fuel bound oxygen between the flames, the availability of total oxygen (fuel bound and pre-supplied) at the injector exit was same for all the flames, which was reflected in the near burner measured values of O_2 concentration. Further downstream of the flame, at 40 mm height above the burner, the O_2 concentration was increased to about 1% - 3%. The observed results indicated that the flames of fuels from different family of origin had similar local oxygen concentration profiles at the corresponding flame heights. Hence, in summary, the local O_2 concentration in the flame did not vary significantly with the fuel unsaturation as well as the origin of fuel rather primarily influenced by the equivalence ratio and the composition of the reactant flow.

7.4 In-flame radial CO_2 concentration profiles

In this section, the in-flame radial CO_2 concentration profiles of tested flames are discussed on two aspects, namely, effect of degree of unsaturation and effect of fuel origin at a DOU value of 2.

7.4.1 Effect of DOU on CO_2 concentration profiles

The in-flame radial CO_2 concentration profiles of flames of fuels with increasing degree of unsaturation at $\Phi = 1.2$ are presented in Figures 7.34 - 7.40. The peak CO_2 concentrations were observed closer to the flame axis at all measured (10 mm, 20 mm and 40 mm) heights. The CO_2 concentration increased with flame height indicating the presence of ongoing oxidation reactions. At 10 mm flame height, the measured peak CO_2 concentration of heptane, PME, CME, RME, SME, diesel and toluene were 8.1%,

12.5%, 13.4%, 13.1%, 12.8%, 12.0% and 12.7% respectively. This observation is reasonable, since the hydrogen/carbon (H/C) ratio of PME, CME, RME, SME and diesel were in the range of 1.7 - 1.9 with comparable carbon content (76% - 77%), and heptane with a higher hydrogen to carbon ratio (H/C ratio of 2.3) produced lower CO_2 value of about 8.1%. However, toluene with lower hydrogen to carbon ratio (H/C: 1.1) also produced similar amount of CO_2 (12.7%) as that of biodiesels and petrodiesel at the corresponding locations. Further, at 40 mm flame height, the measured CO_2 concentration of heptane, PME, CME, RME, SME, diesel and toluene were almost constant in the range of 12.2% - 14.1%. The experimental uncertainties in these measurements were estimated to be 1%.

In summary, although the local CO_2 concentration seemed to increase slightly with DOU between 0 (heptane) and 1.7 (PME), no discernable dependence of CO_2 concentration on DOU was observed at DOU values greater than 1.7 at 10 mm height, and the measured CO_2 concentration was almost constant in the range of 12.2% - 14.1% at 40 mm height. Hence, it is concluded that no statistically significant dependence of local CO_2 concentration on the degree of unsaturation was observed from the available experimental results.

7.4.2 Effect of fuel origin on CO_2 concentration profiles

The in-flame radial CO_2 concentration profiles of flames of fuels with a DOU value of 2 at $\Phi = 1.2$ are presented in Figures 7.41 - 7.45. At 10 mm flame height, the measured CO_2 concentration of MO, CME, P53R47, P59S41, H58T42 and P75D25 flames were 9.9%, 14.1%, 14.3%, 13.9%, 13.6%, and 13.6% respectively. Similarly, at

40 mm flame height, the measured CO_2 concentration of MO, CME, P53R47, P59S41, H58T42 and P75D25 flames were 9.9%, 14.1%, 14.3%, 13.9%, 13.6% and 13.6%. Between the tested flames, the CO_2 concentration did not significantly vary with the family of the fuel. For instance, at 40 mm flame height, CME (biodiesel), H58T42 (heptane/toluene blend) and P75D25 (Palm biodiesel/petrodiesel blend) produced similar amount of CO_2, except for MO flame that produced about 27% lower CO_2 compared to the average value of other flames.

Hence, in summary, the local CO_2 concentration did vary significantly with neither the degree of fuel unsaturation nor the fuel family origin, but was primarily influenced by the equivalence ratio and composition of the reactant flow, similar to that of O_2 concentration profiles.

7.5 In-flame radial CO concentration profiles

In this section, the in-flame radial CO concentration profiles of tested flames are discussed on two aspects namely, effect of degree of unsaturation and effect of fuel origin at a DOU value of 2.

7.5.1 Effect of DOU on CO concentration profiles

The in-flame radial CO concentration profiles of flames of fuels with increasing degree of unsaturation at $\Phi = 1.2$ are presented in Figures 7.46 - 7.52. The peak CO concentrations were observed within 2 mm from the flame axis at all measured (10mm, 20 mm and 40 mm) heights. The peak CO concentration progressively decreased with flame height; from about 5% at 10 mm HAB (height above the burner) to about 2% at

40 mm HAB. This observation is found to be in agreement with the CO_2 concentration profile indicating the oxidation of fuel fragments into CO at lower flame heights and into CO_2 further downstream.

At 10 mm flame height, the measured peak CO concentration of heptane, PME, CME, RME, SME, diesel and toluene flames were 3.5%, 4.9%, 3.8%, 3.8%, 5%, 5.3% and 4.3% respectively while at 40 mm flame height, the measured peak CO concentration of heptane, PME, CME, RME, SME, diesel and toluene flames were 2.5%, 1.2%, 1.3%, 1.6%, 1%, 1.8% and 2.4% respectively. Similar to the dependence of CO emission index (EI_{CO}) on the degree of fuel unsaturation, the local CO concentration also remains reasonably insensitive (with values between 1.0% and 2.5% at 40 mm HAB) to the changes in the degree of unsaturation within tested range of DOU values. As already discussed in chapter 6, at $\Phi = 1.2$, the EI_{CO} from all the tested flames produced less than 1g of CO/ kg of fuel burnt and the fuel chemistry effect (in turn, the fuel unsaturation effect) on CO emission was not dominant at these conditions. This observation is in agreement with the previous studies, where it was observed that both fuel chemistry and equivalence ratio affected CO emission index at equivalence ratios greater than $\Phi = 2$, particularly at $\Phi = 7$ (Balakrishnan et al., 2016b).

7.5.2 Effect of fuel origin on CO concentration profiles

The in-flame radial CO concentration profiles of flames of fuels with a DOU value of 2 at $\Phi = 1.2$ are presented in Figures 7.53 - 7.57. Again, in all these flames, peak CO concentration occurred within 2 mm from the flame axis at 10 mm flame height and the peak CO concentrations progressively decreased from about 5% at 10

mm HAB to about 1% at 40 mm HAB. At 10 mm flame height, the peak CO concentrations of MO, CME, P53R47 and P59S41 flames were 4.1%, 3.8%, 4.5% and 4.8% respectively; at 40 mm flame height the peak CO concentration values reduced to 2.2%, 1.3%, 1.3% and 2.3%. These marginal variations of inflame CO concentrations among the flames of fuels of different origin, at corresponding flame locations, are in agreement with the global CO emission index which did not vary significantly between fuels that belong to different families.

Hence, in summary, the local measured peak CO concentrations did not vary significantly with the degree of fuel unsaturation and fuel origin at the tested equivalence ratio of $\Phi = 1.2$. However, based on the previously published results (Balakrishnan et al., 2016b), the CO concentration and in turn the CO emission index was significantly influenced by the fuel chemistry at equivalence ratios greater than 2, particularly the trend was conspicuous at $\Phi = 7$.

7.6 In-flame radial NO concentration profiles

In this section, the in-flame radial NO concentration profiles of tested flames are discussed on two aspects namely, effect of degree of unsaturation and effect of fuel origin at a DOU value of 2.

7.6.1 Effect of DOU on NO concentration profiles

The in-flame radial NO concentration profiles of flames of fuels with increasing degree of unsaturation at $\Phi = 1.2$ are presented in Figures 7.58 - 7.64. At 10 mm height, the peak NO concentrations occurred at a radial location of 4-6 mm and shifted closer to

flame axis at 40 mm height. At 10 mm flame height, the measured peak NO concentration of heptane, PME, CME, RME, SME, diesel and toluene flames were 89 ppm, 55 ppm, 65 ppm, 67 ppm, 70 ppm, 110 ppm and 160 ppm. From the PLIF measurements of flames of CME and SME and their blends with petroleum diesel at Φ = 1.2 (Love, 2009 and Singh, 2013), it was observed that both OH and CH local concentrations were maximum within the flame reaction zone (within 20 mm above the burner exit) indicating the occurrence of primary gas phase oxidation region. This concentrated pool of OH and CH radicals within the primary gas oxidation region was expected due to the occurrence of ongoing fuel unimolecular decomposition and H atom abstraction from the fuel molecules. These primary radicals further determine the dominant reaction pathways and local concentration of combustion products such as CO_2 and pollutant such as CO and NO within the flames. With reference to NO formation at 10 mm flame heights, peak NO concentrations occurred at a radial location of 4-6 mm from the flame axis. This observation signifies the fact that peak NO was observed at the regions of higher CH concentration and temperature. Although all the known NO formation reactions (thermal / prompt / N_2O) are temperature dependent, the thermal reaction pathways were relatively more temperature sensitive than other modes. Hence, for instance, if the thermal NO mechanism alone is dominant in these reaction zones, a comparable amount of NO concentrations would have expected between the tested flames (due to comparable local temperature profiles), which is NOT the case between the tested flames, particularly in the flames of PME, CME, RME, SME and diesel flames, whose local temperature profiles were comparable within experimental uncertainty (5%). A clearly discernable variation of local NO concentration was

observed between the tested flames, particularly at a flame height of 40 mm where the measured peak NO concentration of PME, CME, RME, SME, diesel and toluene flames were 155 ppm, 163 ppm, 173 ppm, 180 ppm, 327 ppm and 601 ppm This observation indicated that in addition to thermal reaction mechanism, there are some other reactions that contributed to the variations in the local NO concentrations. These "other" reactions could possibly be the prompt (Fenimore) reaction pathways whose key reactions involve CH radicals. Among the reported PLIF measurement results (Love, 2009; Singh, 2013 and Balakrishnan et al., 2015), the tested flames with a lower degree of unsaturation produced relatively lesser CH concentration distribution than with that of higher DOU values. For example, although similar extent of CH concentration distribution was observed between the diesel, SME and CME flames, diesel (DOU: 3.0) flame produced up to 30% higher CH concentration (Love et al., 2009) than both SME (DOU 2.5) and CME (DOU: 2.0) flames at $\Phi = 1.2$. Further, this observation was reconfirmed by other studies (Singh, 2009 and Balakrishnan et al., 2015) and found that the increase of CH concentration in diesel flame when compared to SME, CME or PME flames were conspicuous at higher equivalence ratios, particularly at $\Phi = 7$.

Furthermore, at 40 mm flame height, it can be observed that the NO concentrations were progressively increased with flame height, in contrast to the trend observed with CO concentrations. Also, among the biodiesel flames, the NO concentrations were found to be in correlation with the degree of unsaturation. For example, at 40 mm height, the reported NO values were in the increasing order of degree of fuel unsaturation: PME (DOU: 1.7), CME (DOU: 2.0), RME (DOU: 2.4) and SME (DOU: 2.5). Similarly between heptane (DOU: 0) and toluene (DOU: 4.0) flames, the NO

concentration increased with the DOU values. However, between heptane (DOU: 0) and PME (DOU: 1.7) flames, the NO concentration decreased with DOU. This is where the effect of fuel family comes into picture in addition to the effect of DOU (subsequently explained in section 7.6.2).

In summary, within a particular family of fuel, the NO concentration increased with the degree of fuel unsaturation. This is in agreement with several reported engine studies that claimed degree of unsaturation as an important parameter that influences NOx emissions (McCormick et al., 2002; Kalligeros e t al., 2003; Knothe et al., 2006; Benjumea et al., 2008; Puhan et al., 2010; Cecrle et al., 2012 and Altun, 2014). In particular, Hellier et al. (2013) investigated the combustion characteristics of heptane/toluene blends and petrodiesel in a compression ignition engine in four different modes namely, with constant injection timing, constant ignition timing, and constant ignition delay (with fixed start of injection and fixed start of combustion). These four modes were employed to delineate the fuel chemistry effect on the observed results. It was observed that, in all these modes, the NOx emissions increased with the level of toluene in the blend (up to 40%); however, there was no concurrent increase in the maximum cylinder temperature (similar to the observation in the present study). Hence, it is evident that, the current experimental technique employed in this study is proved to capture the fuel unsaturation effect on the combustion characteristics in a diesel engine without employing complex equipment and techniques, particularly with the consumption of significantly lesser quantity of fuel as compared to that consumed in an engine study.

7.6.2 Effect of fuel origin on NO concentration profiles

In addition to the effect of fuel unsaturation on the local NO concentration, the effect of family of fuel was also found to significantly influence the local NO formation in the flames. The in-flame radial NO concentration profiles of flames of fuels with a DOU value of 2 at $\Phi = 1.2$ are presented in Figures 7.65 - 7.69. At 10 mm flame height, the peak NO concentrations of MO, CME, P53R47, P59S41, H58T42 and P75D25 flames (similar DOU of 2) were 52 ppm, 65 ppm, 71 ppm, 72 ppm, 153 ppm and 76 ppm respectively. Similarly, at 40 mm flame height, the peak NO concentrations of MO, CME, P53R47, P59S41, H58T42 and P75D25 flames were 162 ppm, 163 ppm, 168 ppm, 213 ppm, 483 ppm. If there were no influence of fuel origin on the dependence of NO emission on degree of unsaturation, all of the aforementioned values would ideally be the same, which is not true in the present case.

Among the biodiesel flames, the measured peak NO concentrations at 40 mm flame height were in agreement with the observed trend of EI_{NO} among these flames; the EI_{NO} of MO, CME, P53R47 and P59S41 flames were 2.69, 2.72, 2.94 and 2.99 g/kg respectively. As mentioned earlier, among these selected fuels (MO, CME, P53R47 and P59S41), the effective degree of unsaturation was same in addition to similar oxygen content and source of fuel unsaturation (double bonds). The observed differences from these NO results (EI_{NO} and peak NO concentration) could be due to the fact that CME, P53R47 and P59S41 is made up of different combination of individual methyl esters in addition to experimental uncertainty. For example, both MO and CME have the same DOU of 2. While methyl oleate is an individual methyl ester (whose unsaturation comes from only the double bonds of methyl oleate), the primary source of unsaturation for

CME is partly from the two double bonds of methyl oleate (60%), three double bonds of methyl linoleate (20%) and four double bonds of methyl linolenate (10%). Hence, although the average degree of unsaturation number was 2 for both MO and CME, the composition of individual methyl ester content that makes up the fuel is different.

Similarly, between fuels of different family origin, say between MO flame and H58T42 (both have DOU: 2), the unsaturation arises from different sources; in double bond of ester in methyl oleate while aromatic ring structure of toluene in H58T42. It was observed that H58T42 flame produced about three times higher NO concentration at 40 mm flame height, this is in agreement with the corresponding EI_{NO} values (MO flame: 2.69 g/kg and H58T42 flame: 4.91 g/kg).

Hence, in summary, the measured peak NO concentration was found to increase with the degree of unsaturation and the effect of fuel origin also played an important role in determining the quantity of end NO emission. Here, the identified parameter, DOU is found to capture the increasing NO trend with DOU for a particular family of fuel, and corrections to the developed correlations are required if fuels belong to different family of origin are used together. In general, this experimental investigation provided a better understanding of the complex dependence of NO formation on the complex coupled parameters, although considering only the fuel chemistry parameters such as degree of fuel unsaturation and family of fuel, at a given equivalence ratio, in this study. This explains the dispersed observation of biodiesel (and their blends with petroleum diesel) effect on NOx emissions found in engine literature, which involved interactions of even more complex parameters such as fuel atomization, droplet evaporation, injection timing, ignition delay and other coupled engine parameters in addition to the fuel

chemistry parameters. This intercoupled complex dependence of parameters could mask the actual propensity of biodiesels' molecular chemistry to form NO regardless of the associated thermo-fluid parameters. The developed DOU correlations from this study with necessary corrections will help in engineering newer developed fuels for specific end NOx emissions by delineating the fuel chemistry effect from other coupled influential non-fuel chemistry parameters exist in the diesel engine combustion.

7.7 Chapter conclusions

The following conclusions were drawn based on the in-flame temperature and species concentration measurement results from the laminar flames of prevaporized heptane, PME, CME, RME, SME, diesel, MO, P53R47, P59S41, H58T42 and P75D25 flames investigated in this study :

- The flame appearance of all the tested flames revealed three primary regions: 1) a dark space between the burner exit and the inner bright cone, 2) a bright blue inner cone surrounded by 3) an outer less luminous blue cone.
- At $\Phi = 1.5$, the inner cone flame length of tested flames were measured about 20 mm while the outer cone flame length was measured about 80 mm.
- Among the tested flames of fuels with DOU of 2, the flame appearance varied between the fuels even with same degree of unsaturation and the difference in flame appearance was due to the hydrogen/ carbon ratio and origin of the fuel.
- The measured flame temperatures were almost comparable within experimental uncertainties and did not vary appreciably with the degree of unsaturation or the family of fuel origin at the tested equivalence ratio of 1.2.
- The local O_2 and CO_2 concentrations in the flame did not vary significantly with the fuel unsaturation as well as the origin of fuel rather primarily influenced by the equivalence ratio and the composition of the reactants.
- the local measured peak CO concentrations did not vary significantly with the degree of fuel unsaturation and fuel origin at the tested equivalence ratio of $\Phi = 1.2$; however, the CO concentration was significantly influenced by the fuel

chemistry at equivalence ratios greater than 2, particularly the trend was conspicuous at $\Phi = 7$.

- The measured peak NO concentration was found to increase with the degree of unsaturation and the effect of fuel origin also played an important role in determining the quantity of end NO emission at $\Phi = 1.2$.
- The measured in-flame NO concentration at 40 mm flame height, was found to increase with the degree of unsaturation, which is in agreement with the global NO emission indices (EI_{NO}) of the corresponding flames.

Table 7.1 Adiabatic flame temperature of selected fuels

Fuel	Heating value[a] MJ/kg)	Enthalpy of formation[a] (KJ/kmol)	Adiabatic stoichiometric flame temperature[b,c] (K)	Measured peak temperature at Φ =1.2 (K)
Jet A	42.8	-349300	2264	1865
Diesel	42.6	-256037	2282	1848
SME	37.0	-771217	2265	1919
CME	37.4	-760220	2267	1958
Methyl oleate	40.1	-789270	2265	1808
Heptane	44.6	-225900	2264	1810
Toluene	40.2	-12000	2308	1844

[a] NIST WebBook (2016); [b] calculated using Olikara and Borman (1975)

[c]Initial temperature = 700K and Initial Pressure = 1 atm

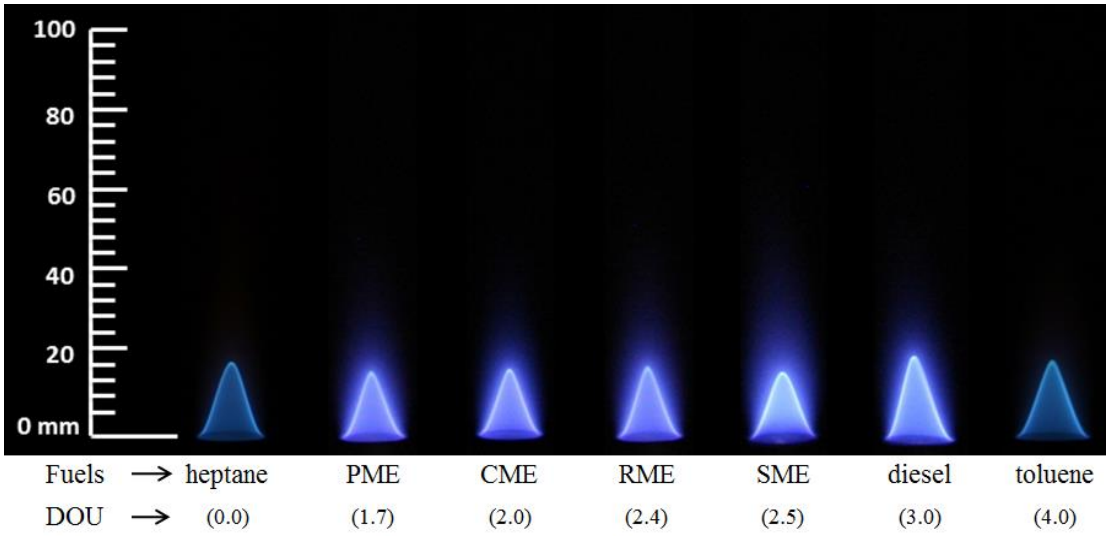

Figure 7.1 Flame images of fuels with increasing DOU at Φ = 0.9 (Exposure time of 1/50th of a second)

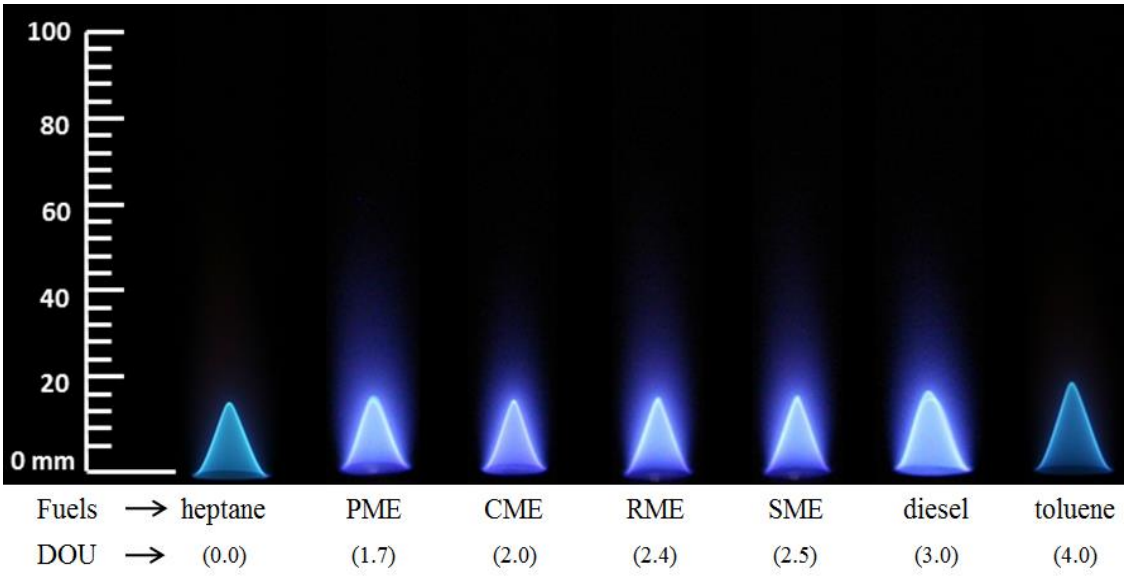

Figure 7.2 Flame images of fuels with increasing DOU at Φ = 1.0 (Exposure time of 1/50th of a second)

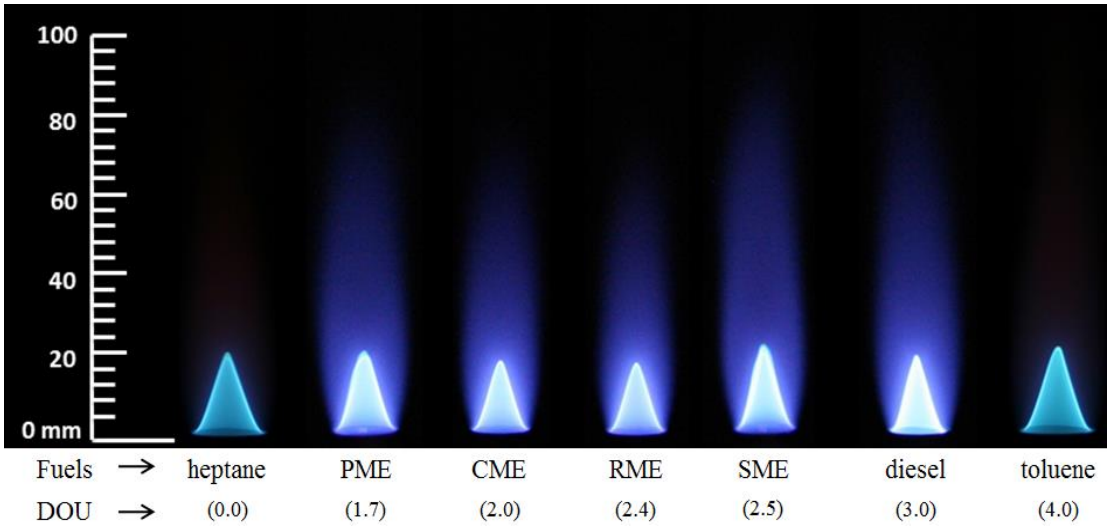

Figure 7.3 Flame images of fuels with increasing DOU at Φ = 1.2 (Exposure time of 1/50th of a second)

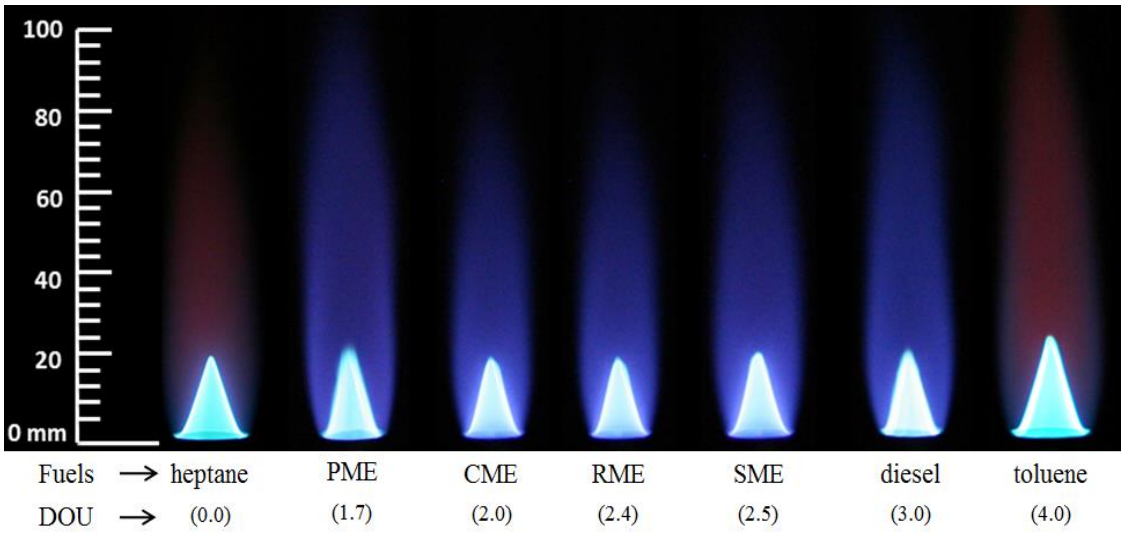

Figure 7.4 Flame images of fuels with increasing DOU at Φ = 1.5 (Exposure time of 1/50th of a second)

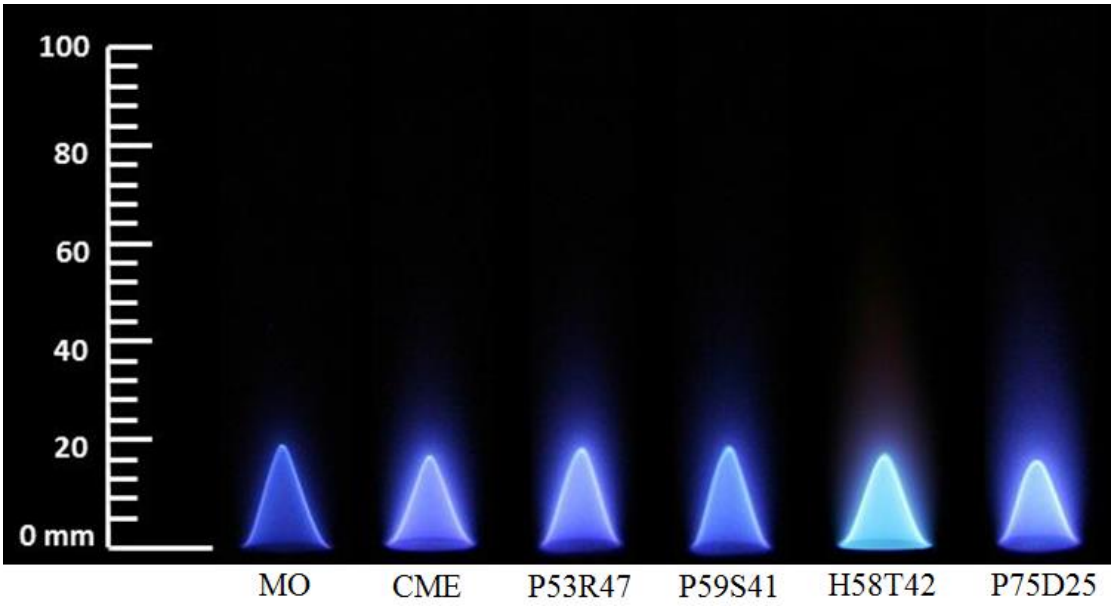

Figure 7.5 Flame images of fuels with DOU value of 2 at Φ = 0.9 (Exposure time of 1/50th of a second)

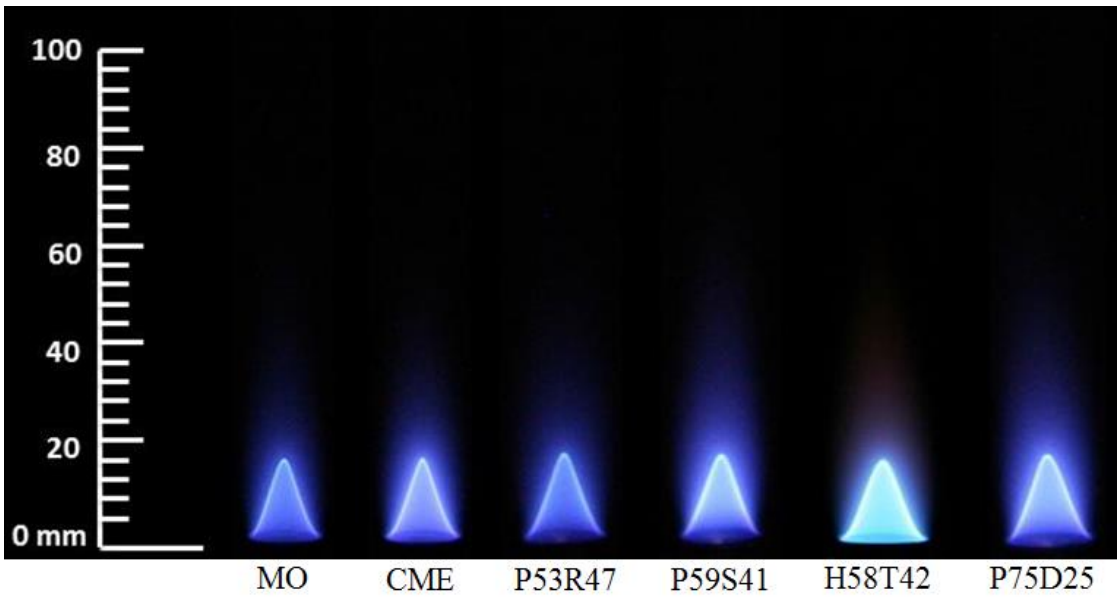

Figure 7.6 Flame images of fuels with DOU value of 2 at Φ = 1.0 (Exposure time of 1/50th of a second)

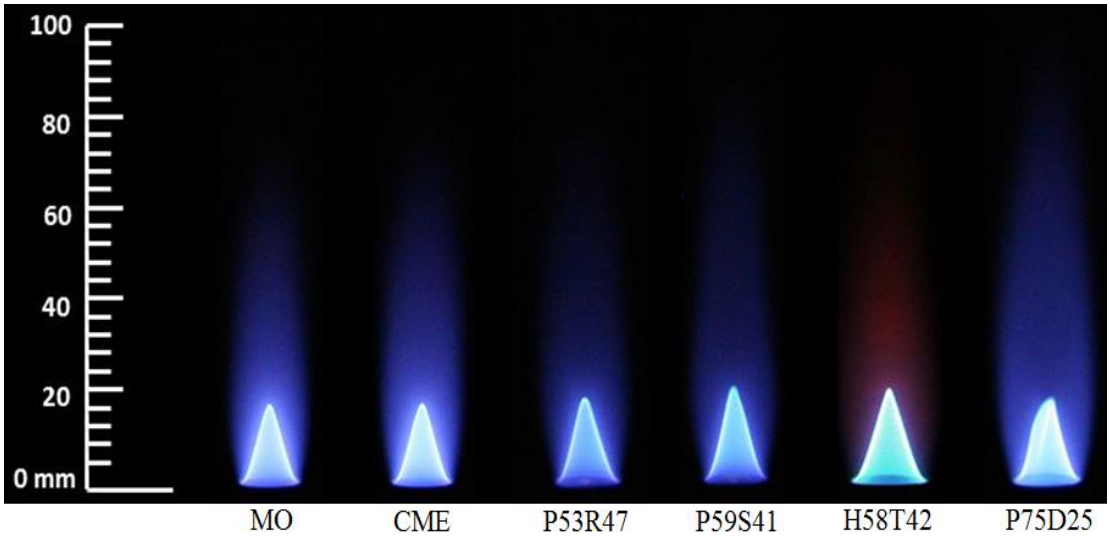

Figure 7.7 Flame images of fuels with DOU value of 2 at Φ = 1.2 (Exposure time of 1/50th of a second)

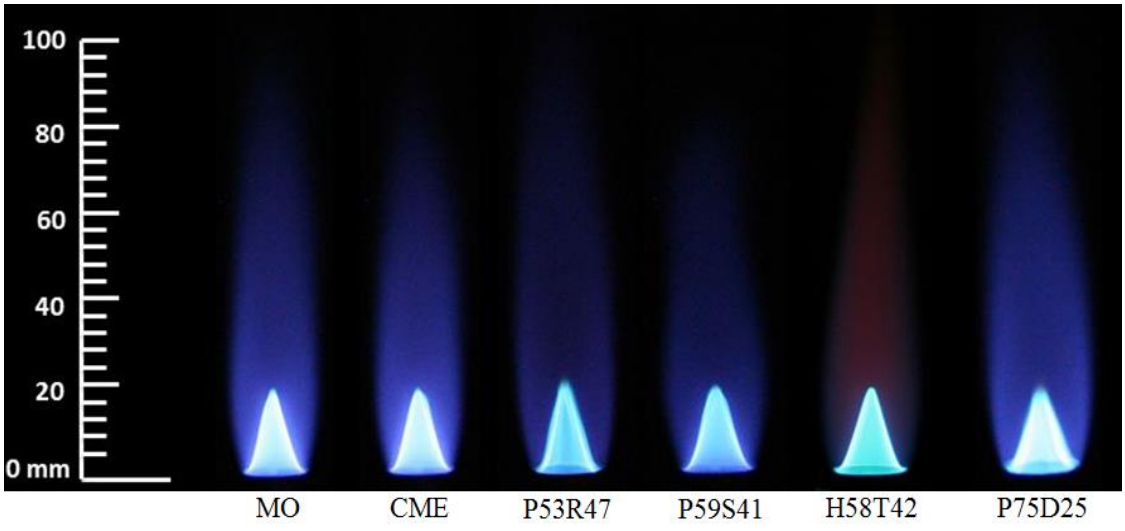

Figure 7.8 Flame images of fuels with DOU value of 2 at Φ = 1.5 (Exposure time of 1/50th of a second)

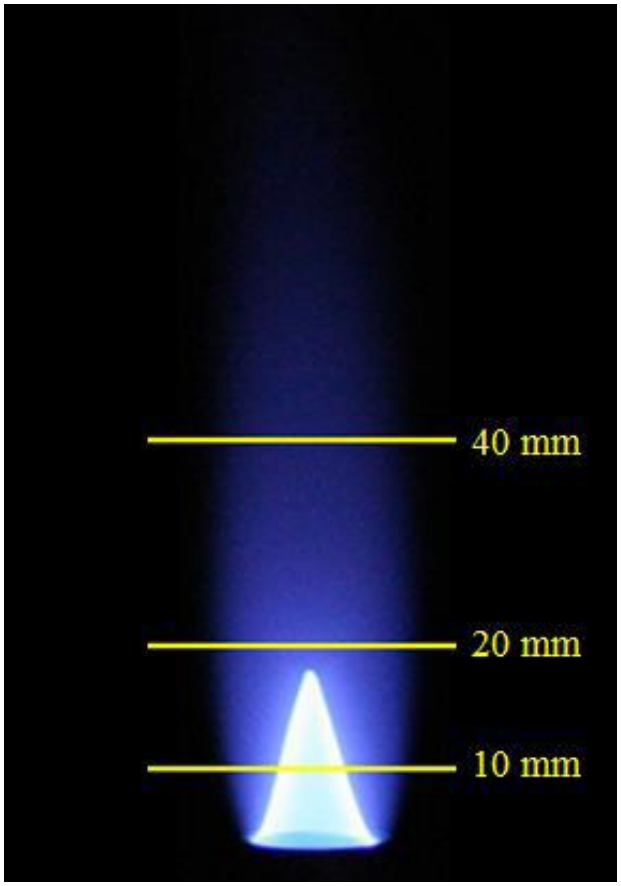

Figure 7.9 Axial locations of measured radial inflame temperature and species concentrations

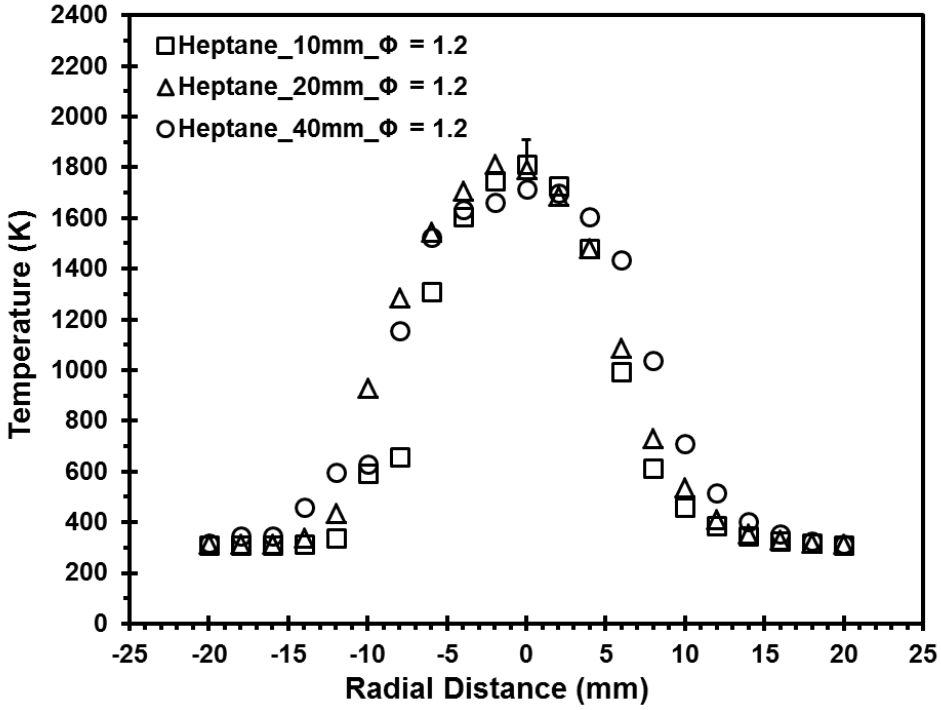

Figure 7.10 Radial in-flame temperature profile of heptane flame at Φ = 1.2

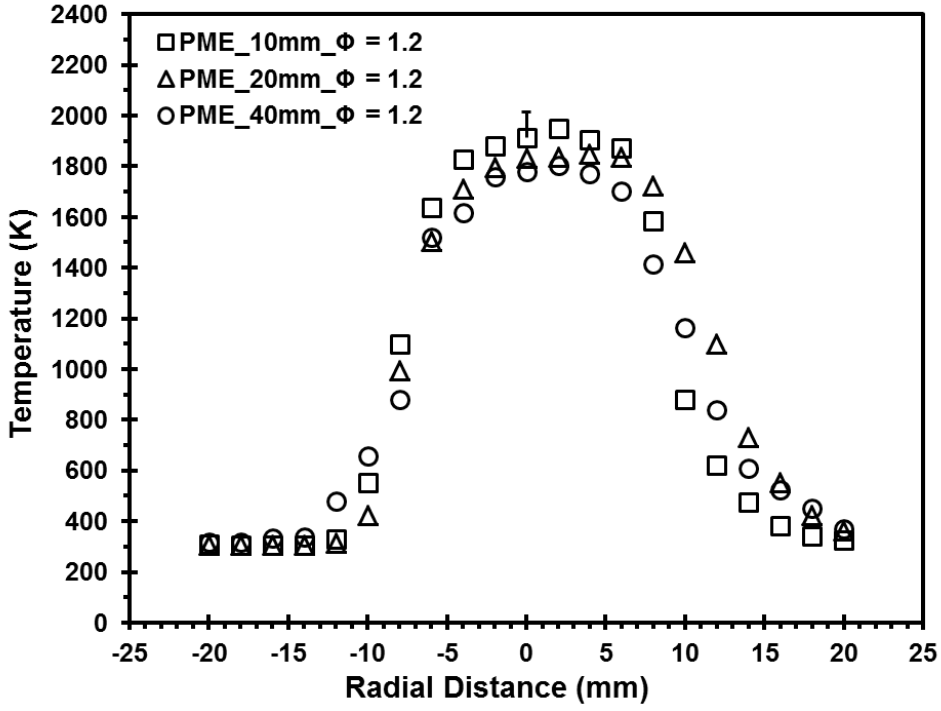

Figure 7.11 Radial in-flame temperature profile of PME flame at Φ = 1.2

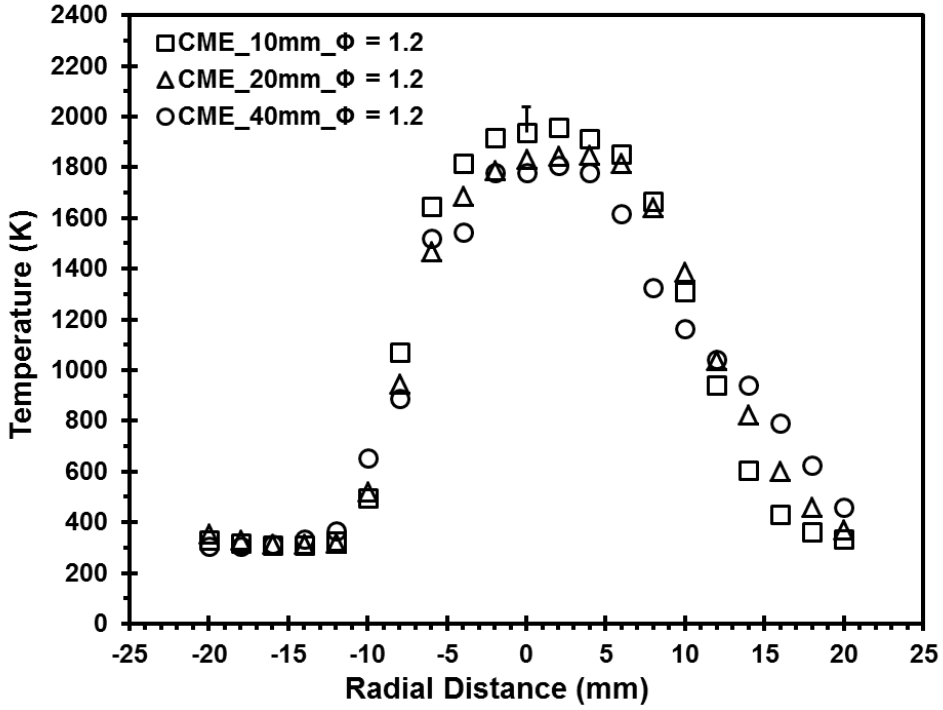

Figure 7.12 Radial in-flame temperature profile of CME flame at Φ = 1.2

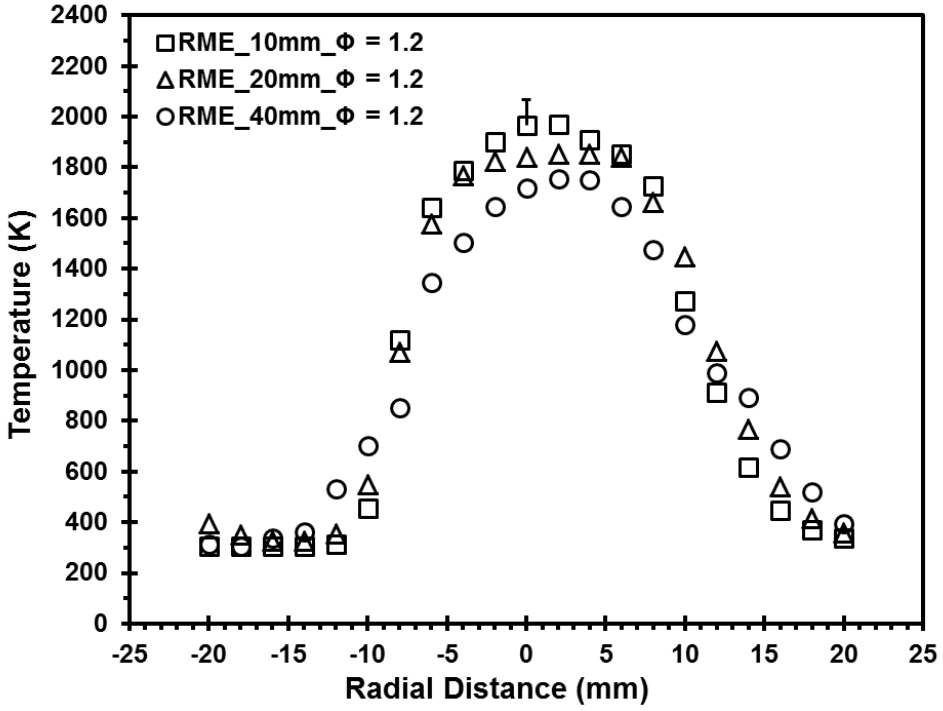

Figure 7.13 Radial in-flame temperature profile of RME flame at Φ = 1.2

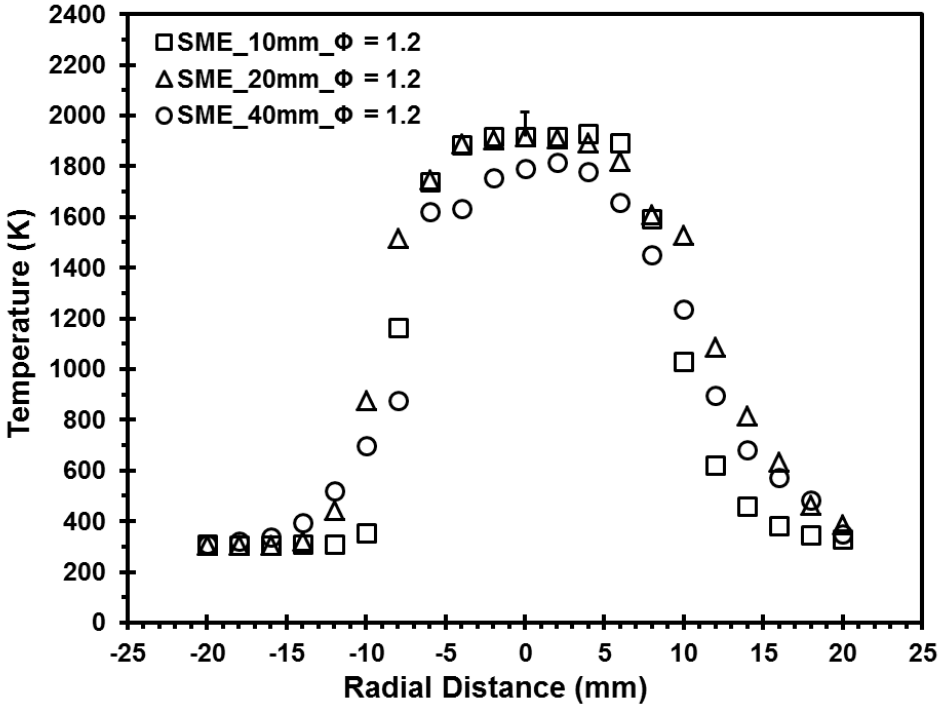

Figure 7.14 Radial in-flame temperature profile of SME flame at Φ = 1.2

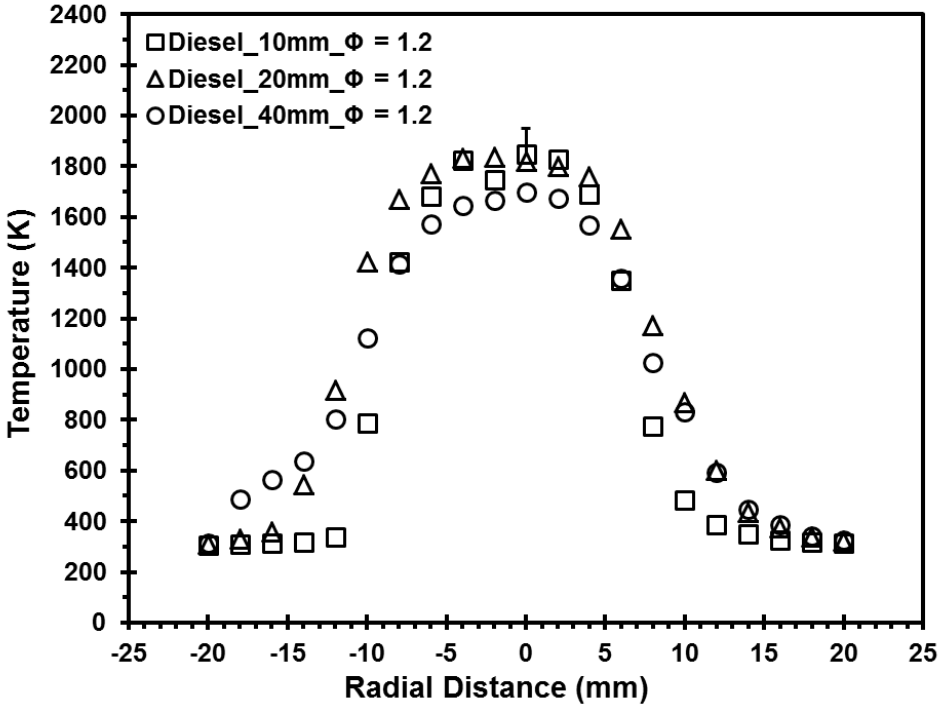

Figure 7.15 Radial in-flame temperature profile of diesel flame at Φ = 1.2

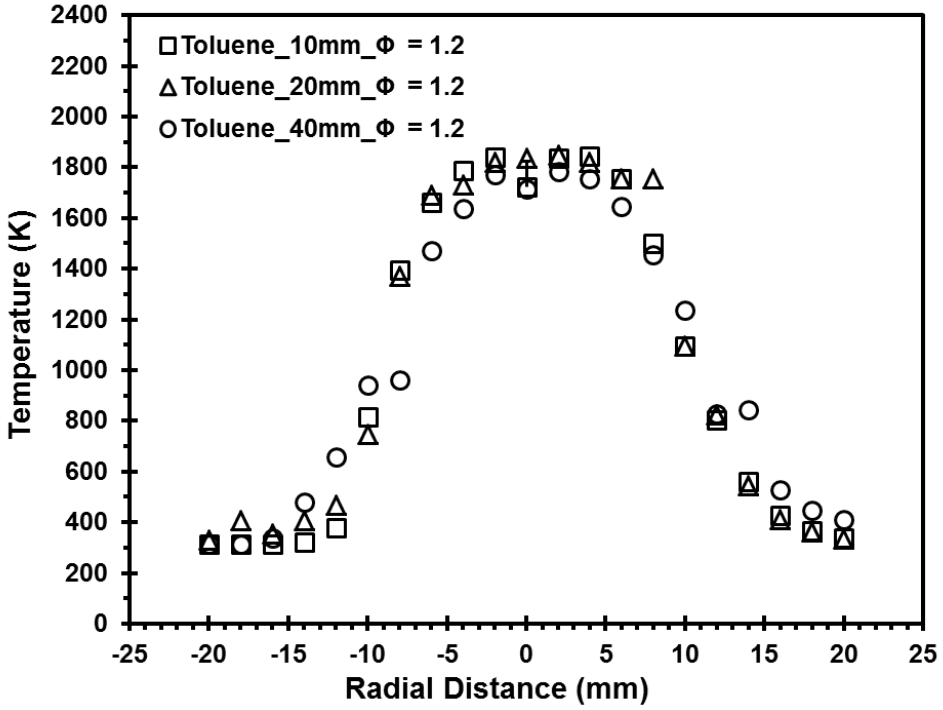

Figure 7.16 Radial in-flame temperature profile of toluene flame at Φ = 1.2

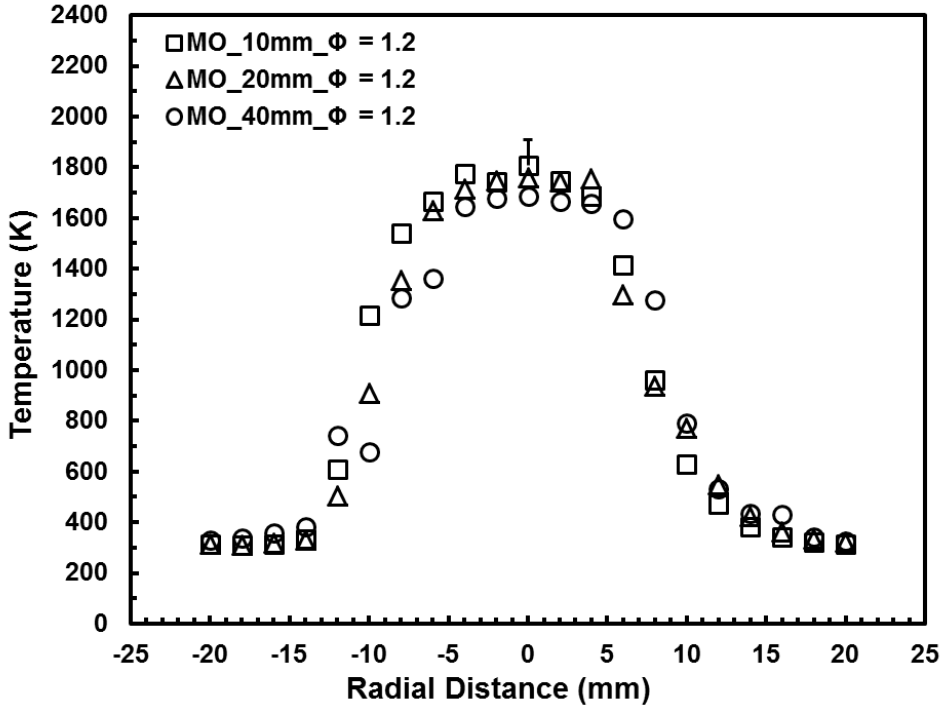

Figure 7.17 Radial in-flame temperature profile of MO flame at Φ = 1.2

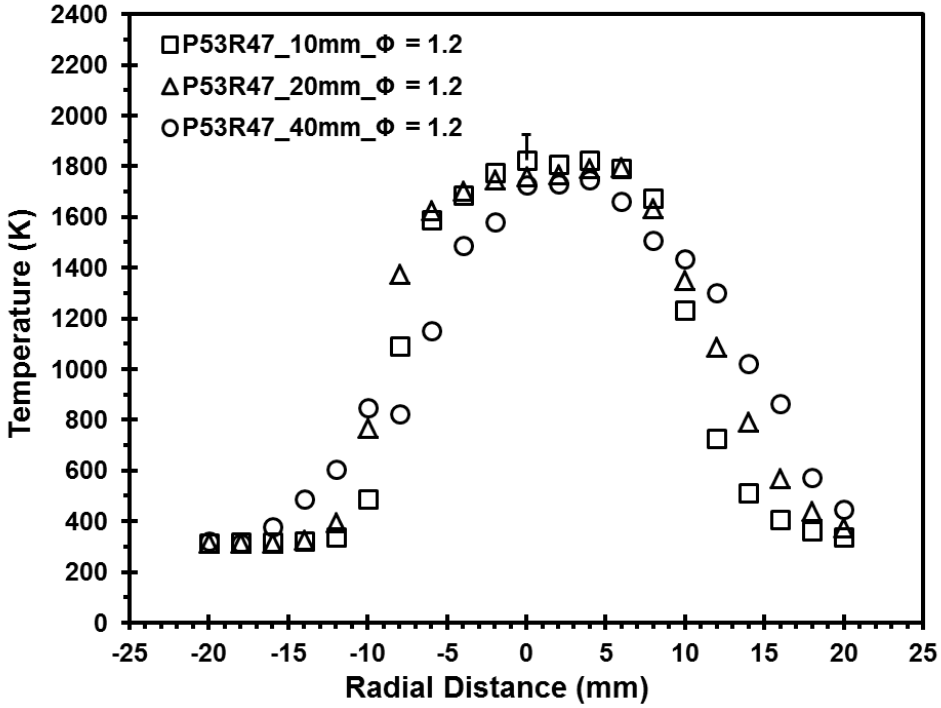

Figure 7.18 Radial in-flame temperature profile of P53R47 flame at Φ = 1.2

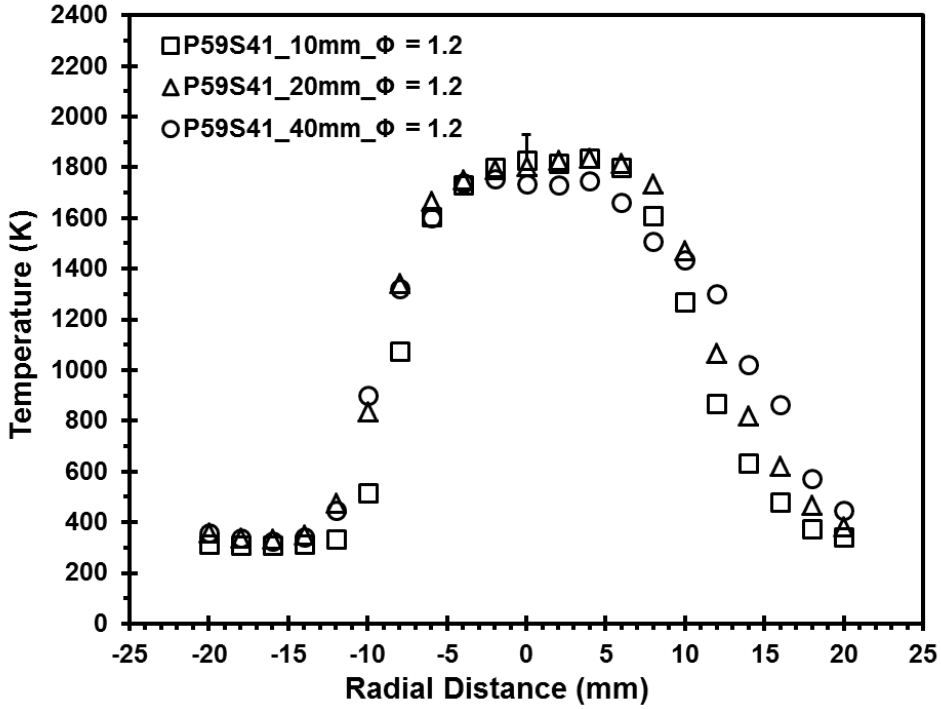

Figure 7.19 Radial in-flame temperature profile of P59S41 flame at Φ = 1.2

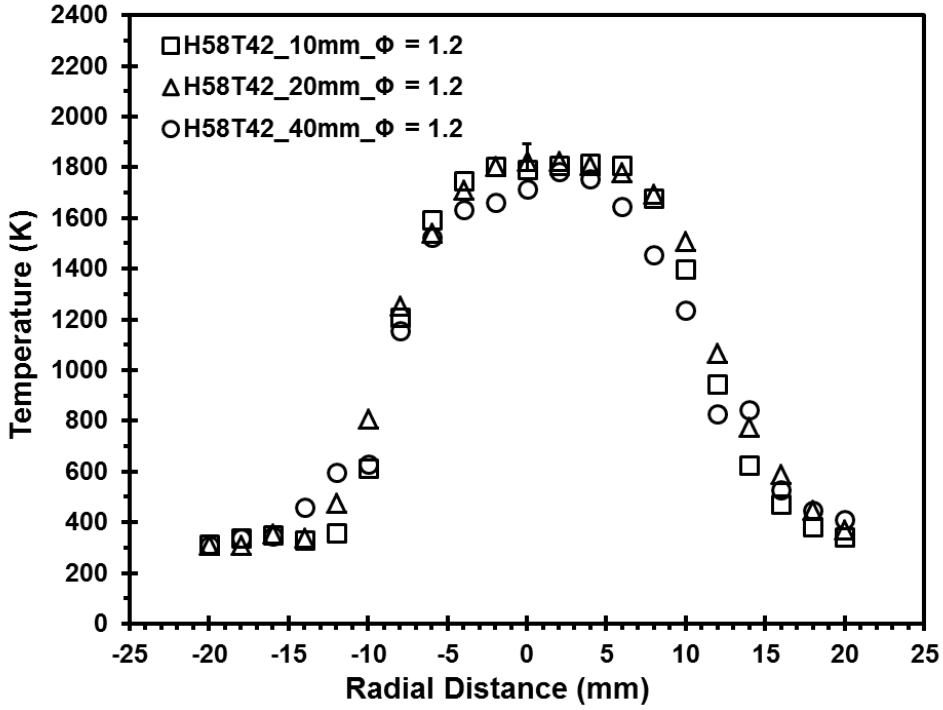

Figure 7.20 Radial in-flame temperature profile of H58T42 flame at Φ = 1.2

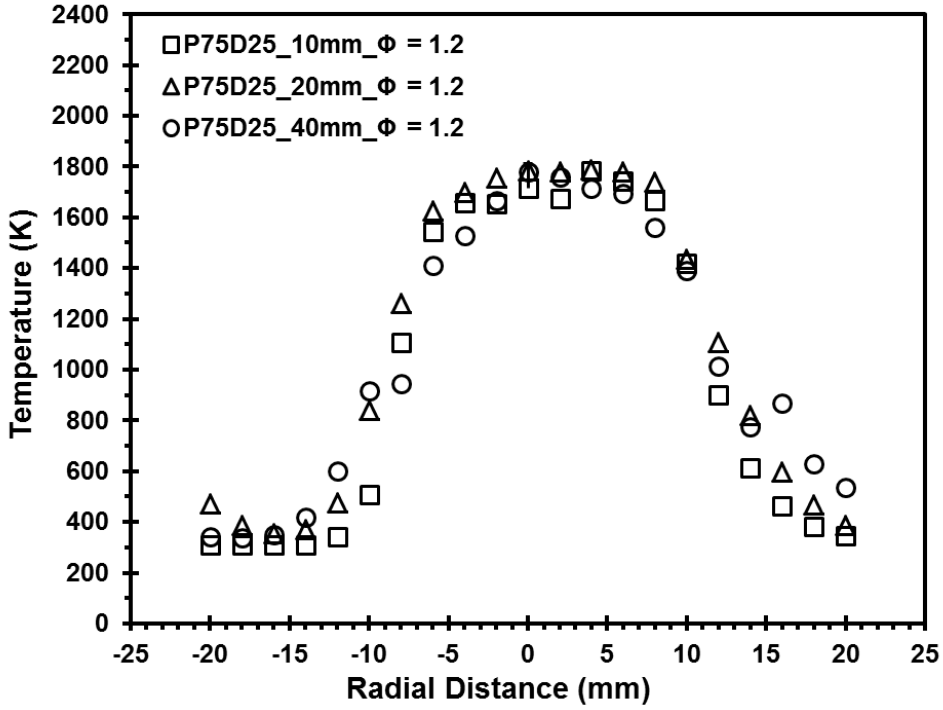

Figure 7.21 Radial in-flame temperature profile of P75D25 flame at Φ = 1.2

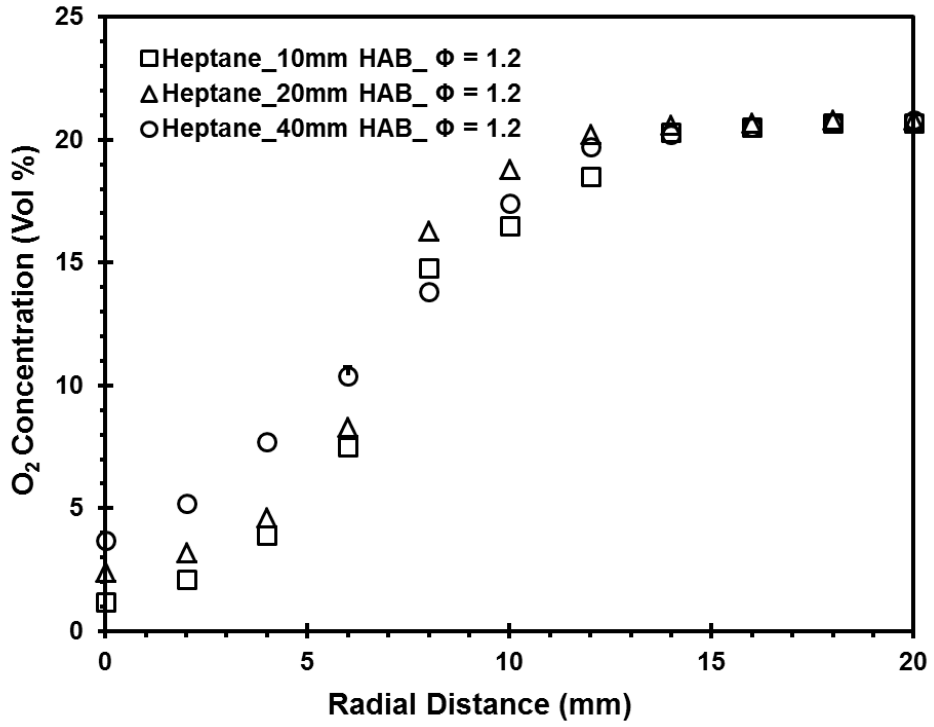

Figure 7.22 Radial in-flame O_2 concentration profile of heptane flame at $\Phi = 1.2$

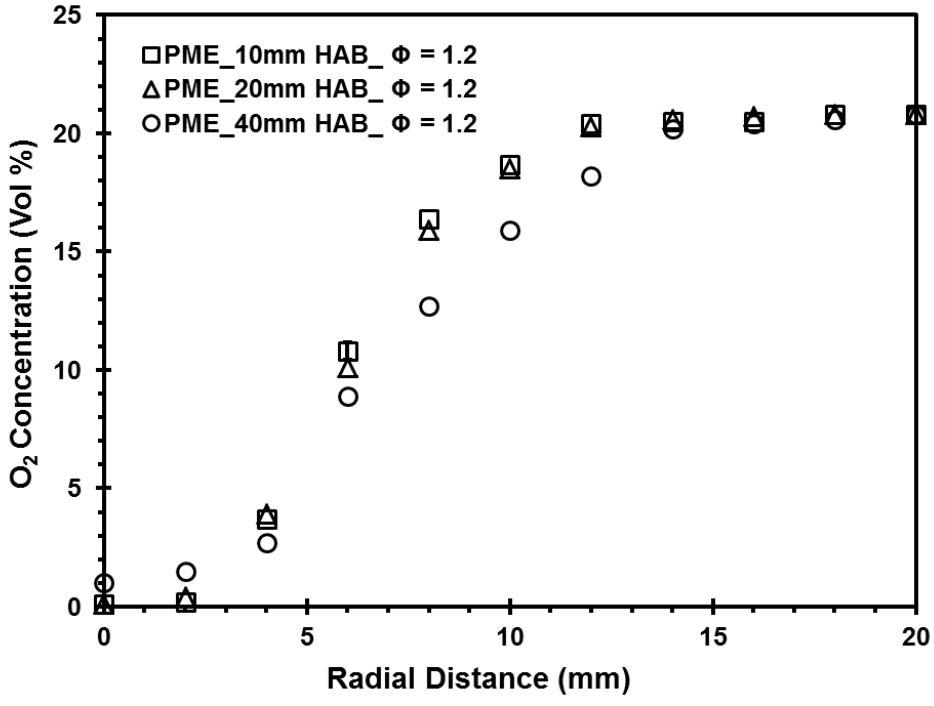

Figure 7.23 Radial in-flame O_2 concentration profile of PME flame at $\Phi = 1.2$

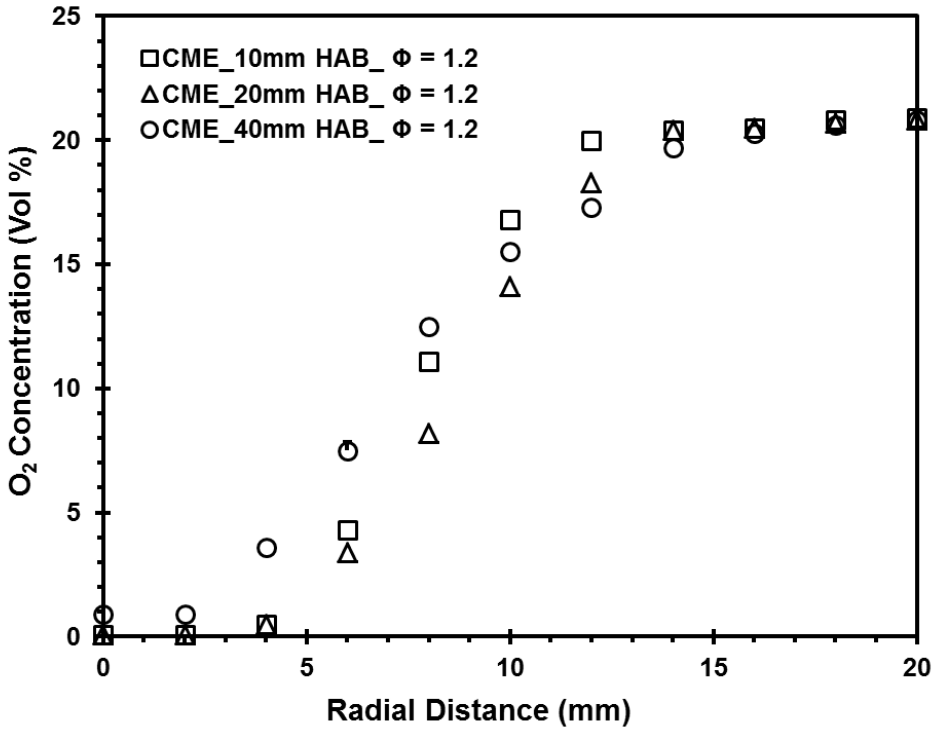

Figure 7.24 Radial in-flame O_2 concentration profile of CME flame at $\Phi = 1.2$

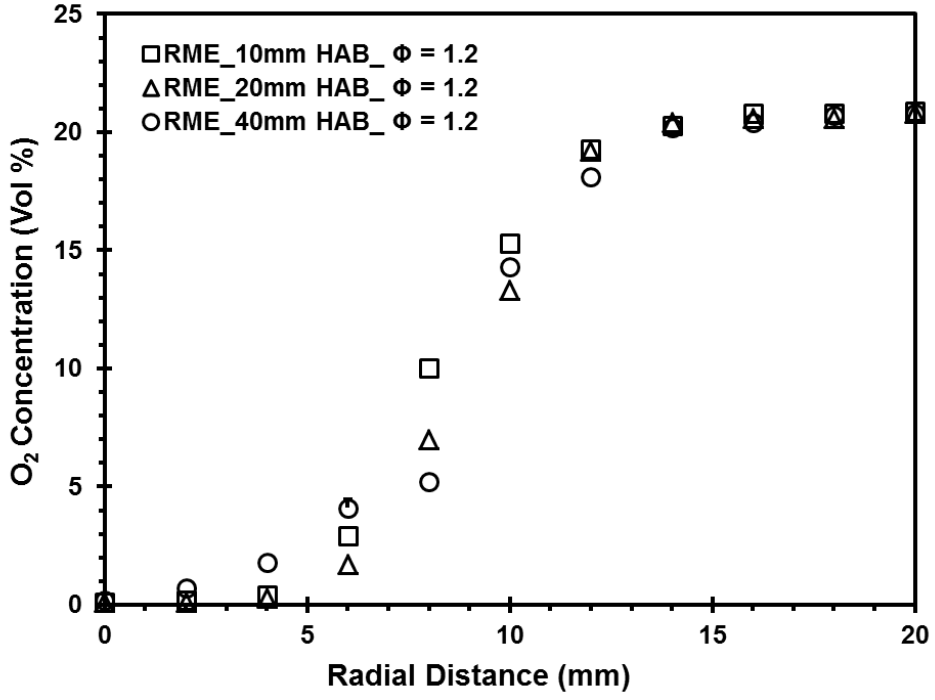

Figure 7.25 Radial in-flame O_2 concentration profile of RME flame at $\Phi = 1.2$

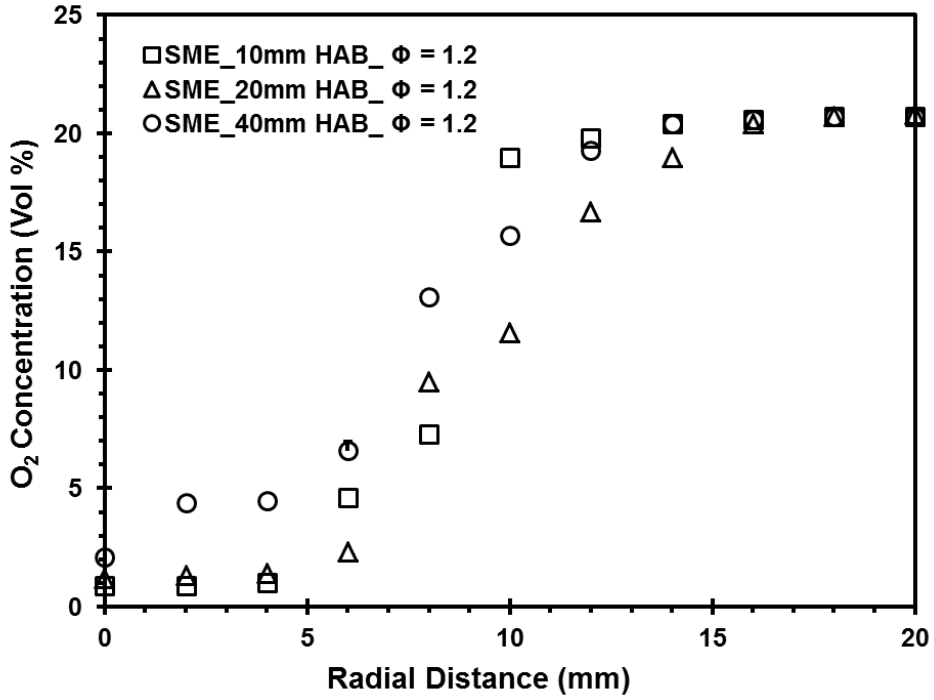

Figure 7.26 Radial in-flame O_2 concentration profile of SME flame at $\Phi = 1.2$

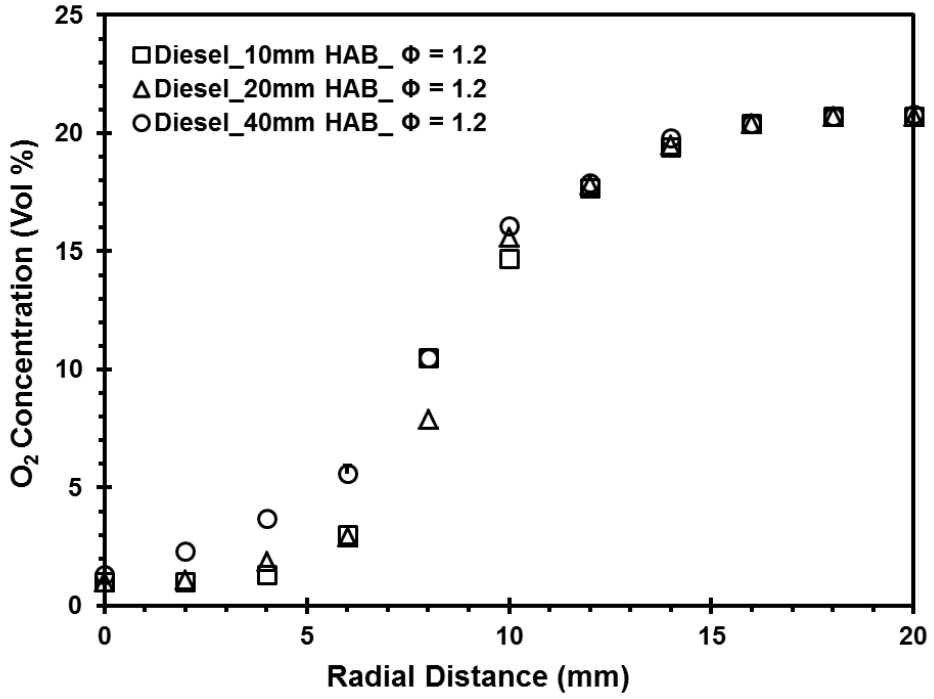

Figure 7.27 Radial in-flame O_2 concentration profile of diesel flame at $\Phi = 1.2$

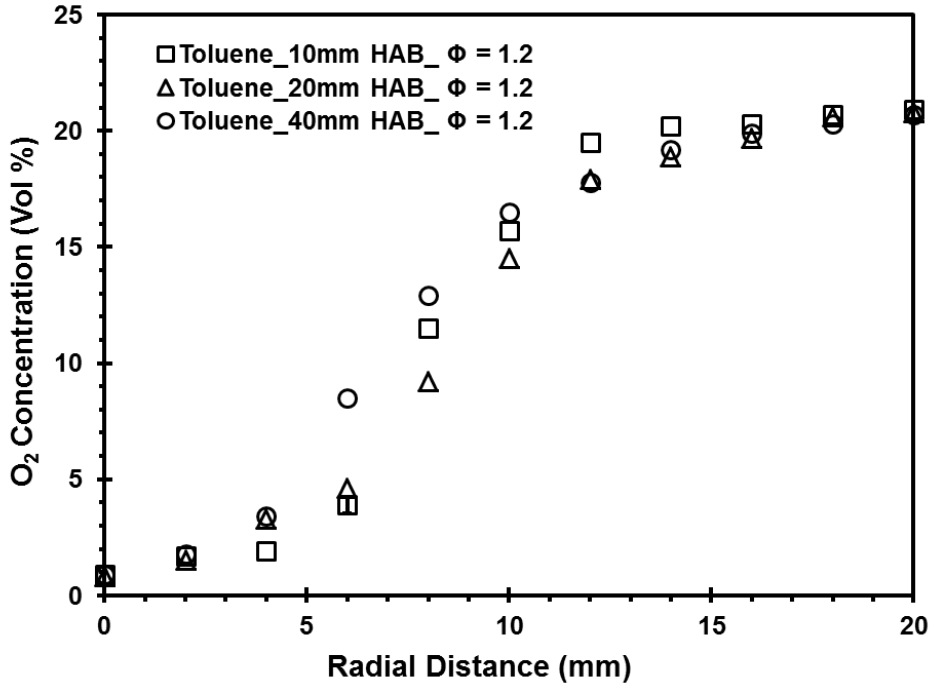

Figure 7.28 Radial in-flame O_2 concentration profile of toluene flame at $\Phi = 1.2$

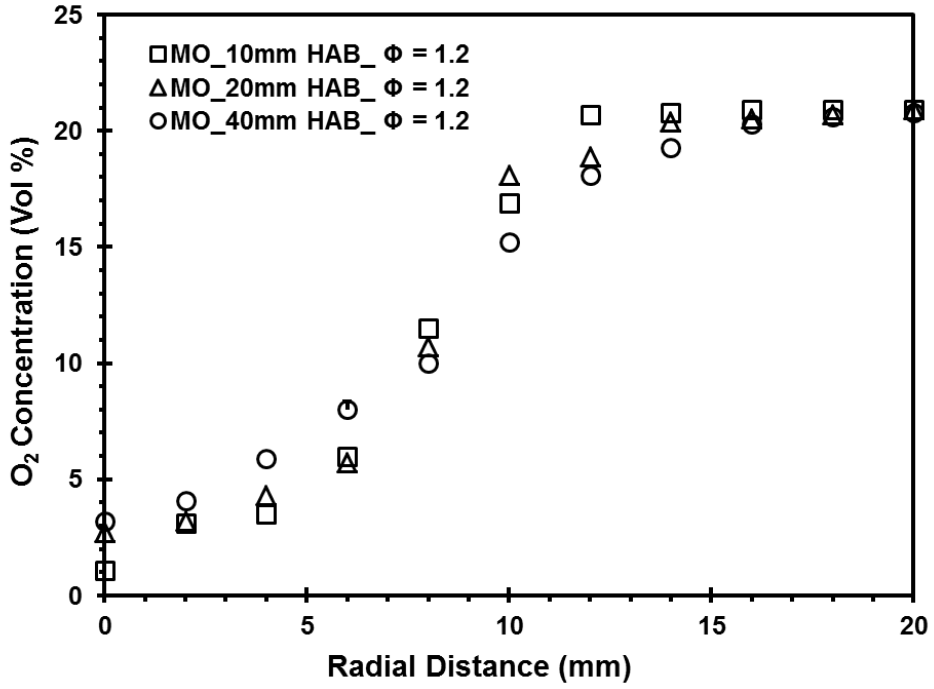

Figure 7.29 Radial in-flame O_2 concentration profile of MO flame at $\Phi = 1.2$

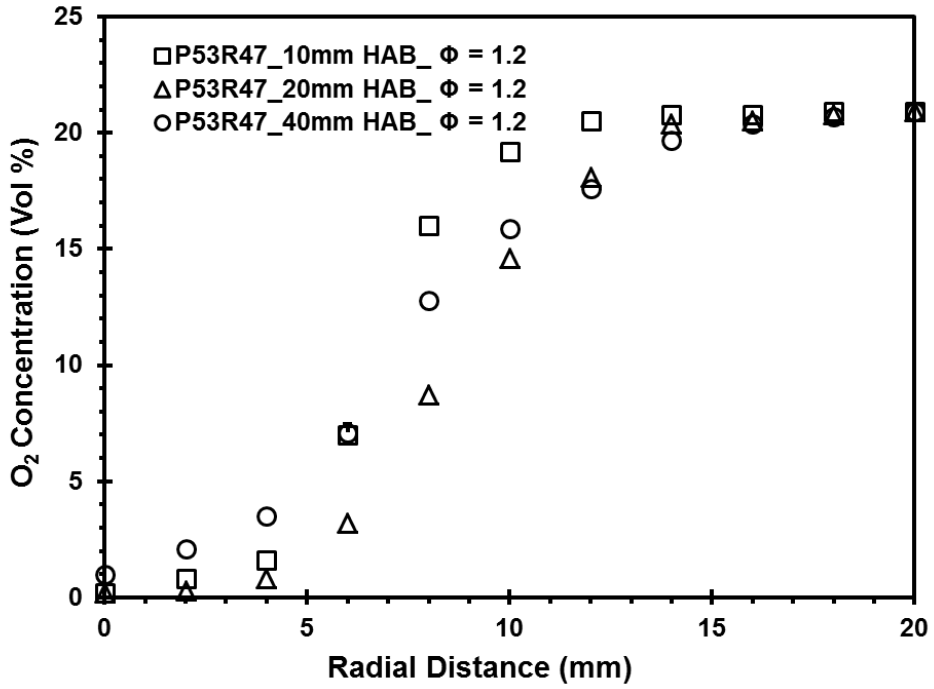

Figure 7.30 Radial in-flame O_2 concentration profile of P53R47 flame at $\Phi = 1.2$

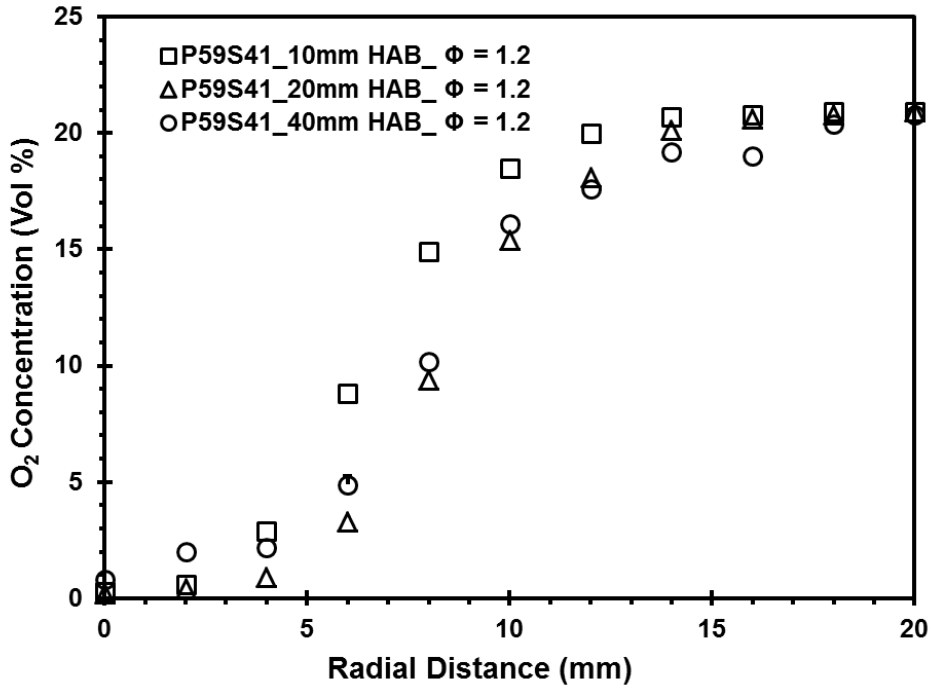

Figure 7.31 Radial in-flame O_2 concentration profile of P59S41 flame at $\Phi = 1.2$

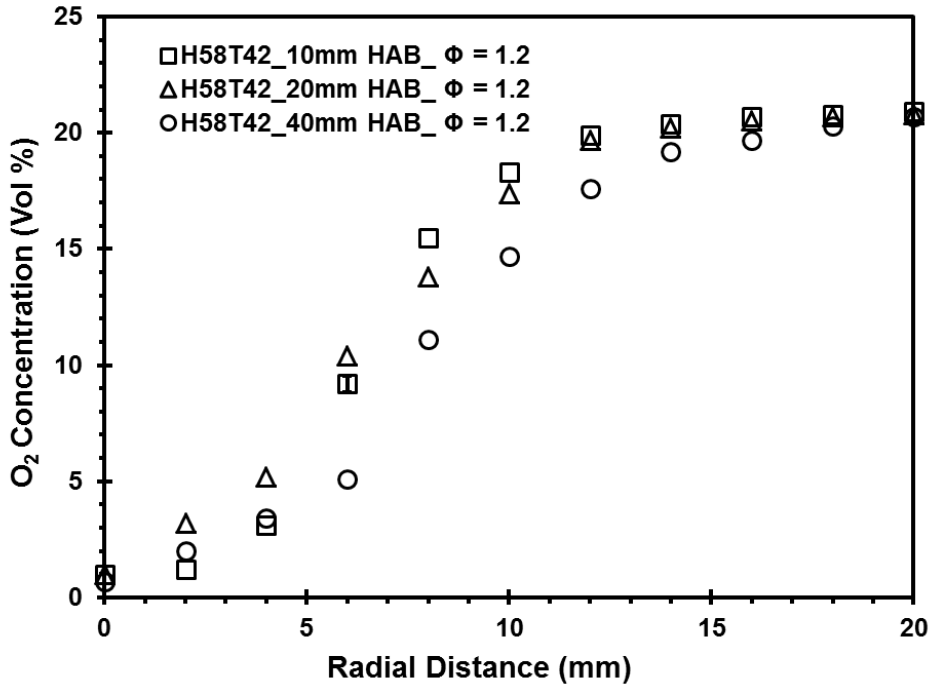

Figure 7.32 Radial in-flame O_2 concentration profile of H58T42 flame at Φ = 1.2

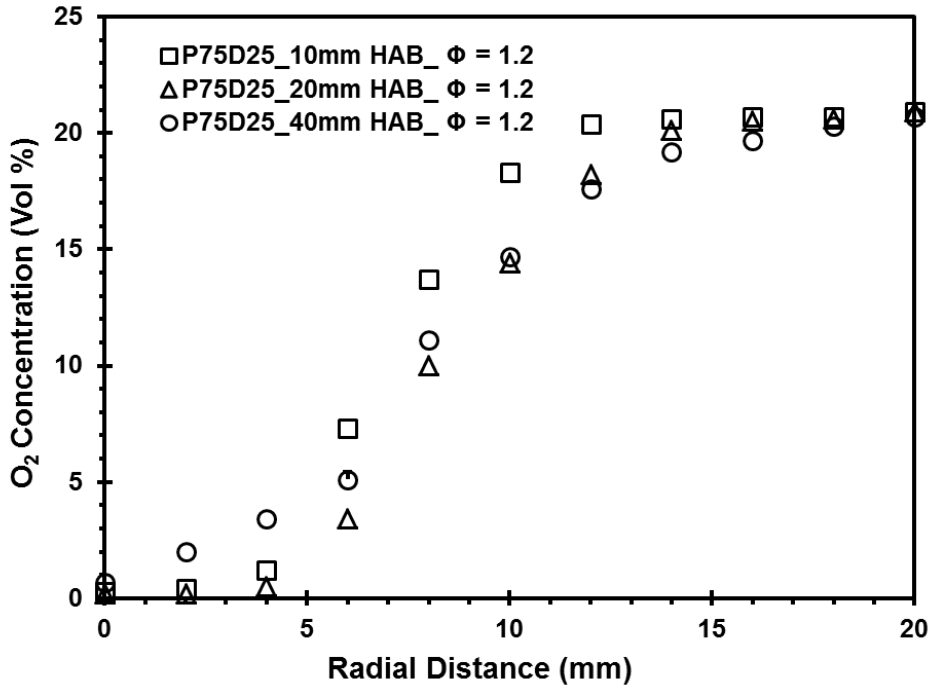

Figure 7.33 Radial in-flame O_2 concentration profile of P75D25 flame at Φ = 1.2

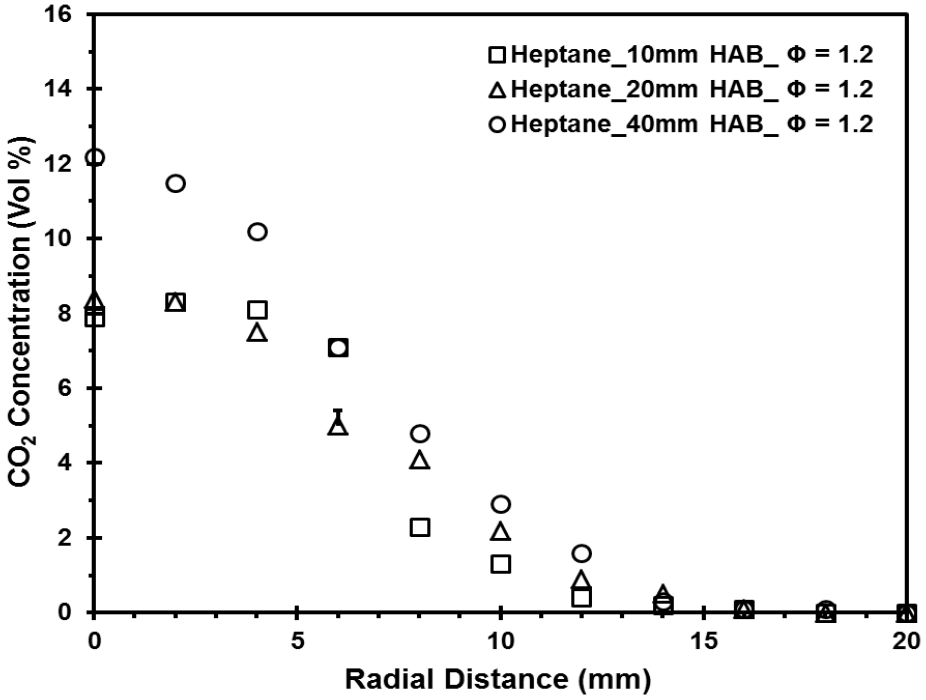

Figure 7.34 Radial in-flame CO_2 concentration profile of heptane flame at $\Phi = 1.2$

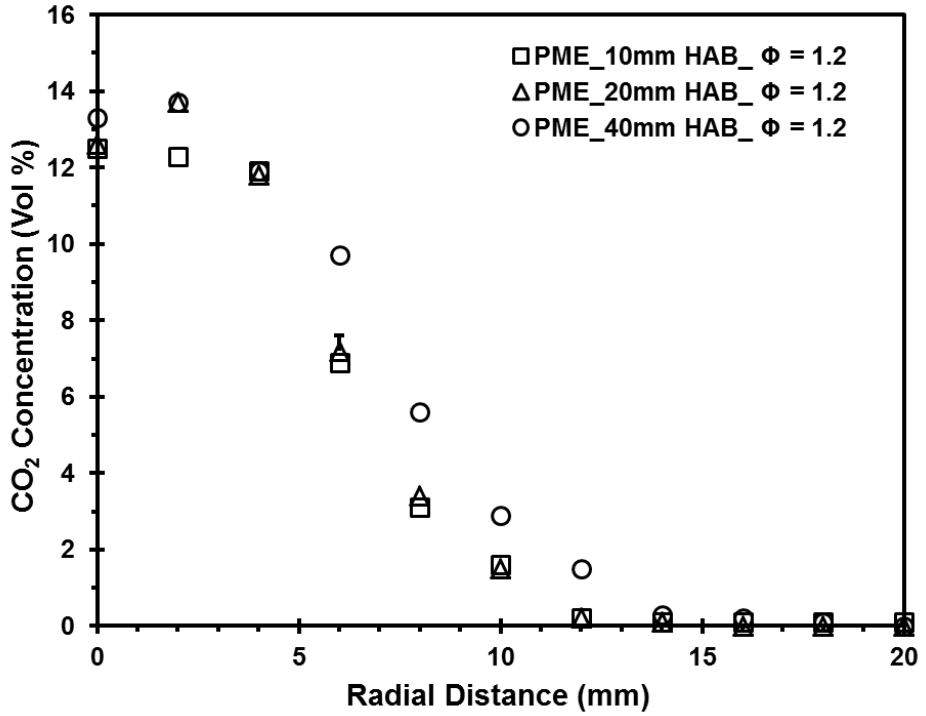

Figure 7.35 Radial in-flame CO_2 concentration profile of PME flame at $\Phi = 1.2$

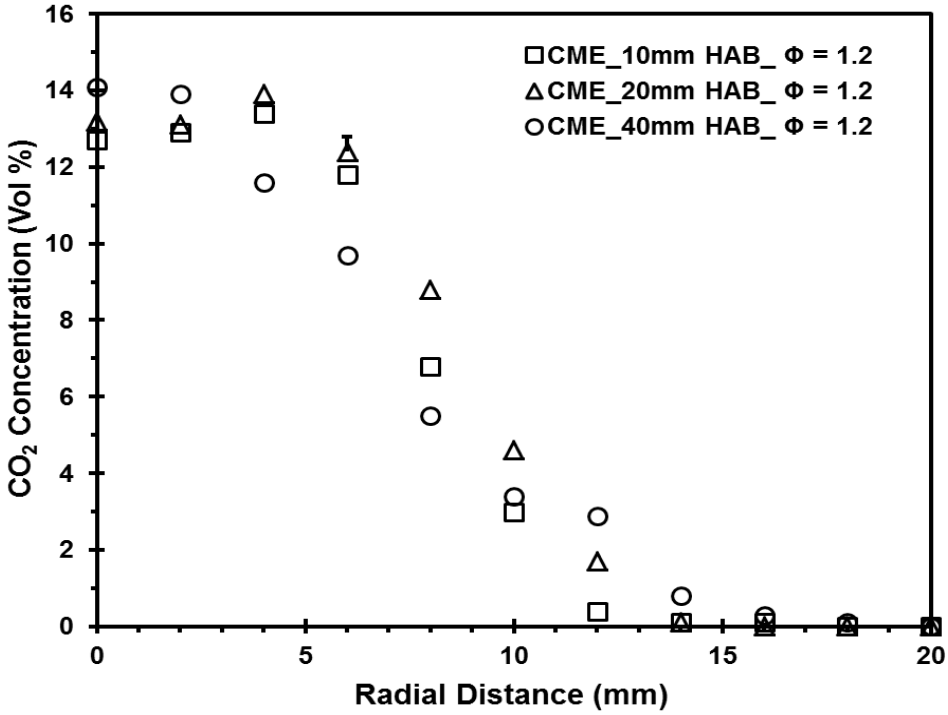

Figure 7.36 Radial in-flame CO_2 concentration profile of CME flame at Φ = 1.2

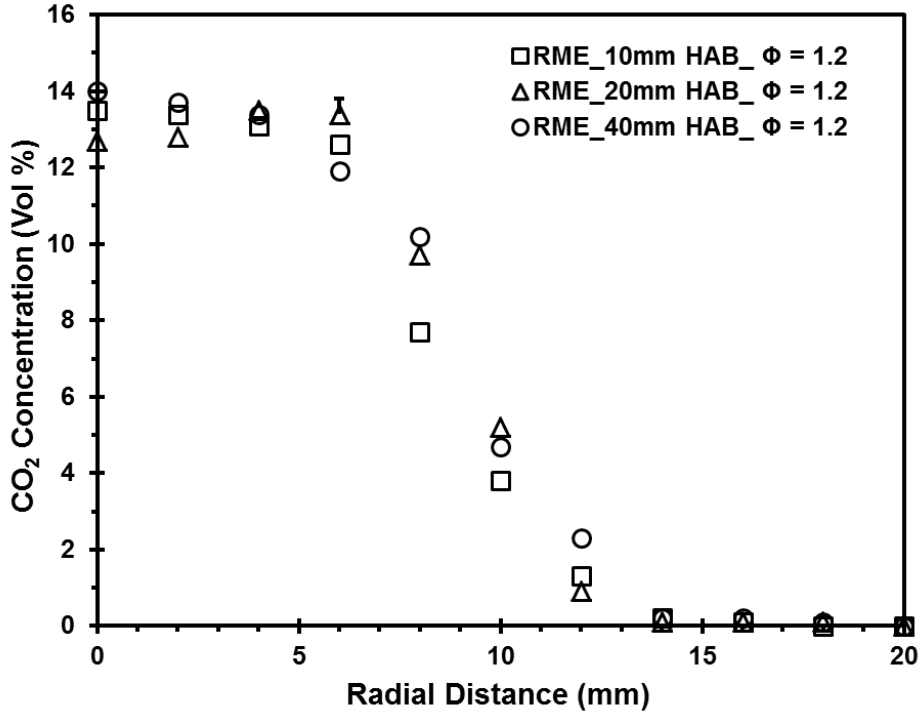

Figure 7.37 Radial in-flame CO_2 concentration profile of RME flame at Φ = 1.2

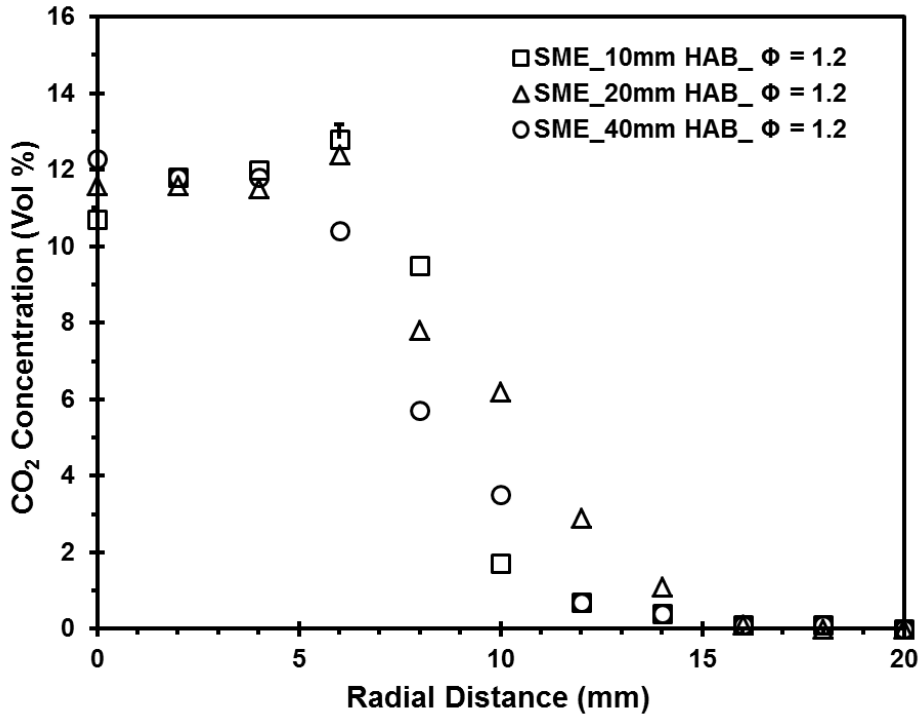

Figure 7.38 Radial in-flame CO_2 concentration profile of SME flame at $\Phi = 1.2$

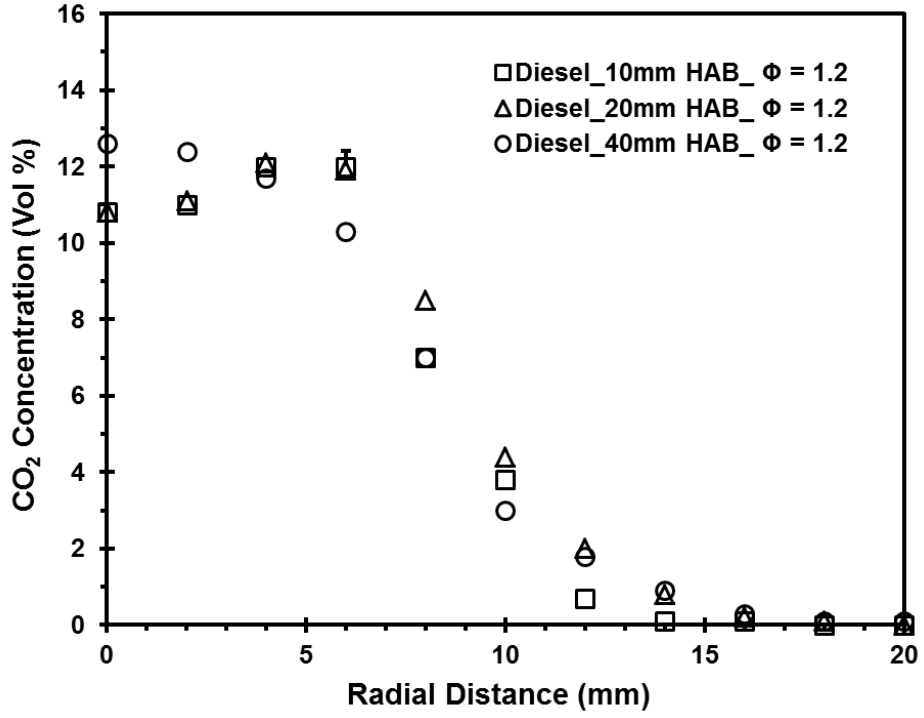

Figure 7.39 Radial in-flame CO_2 concentration profile of diesel flame at $\Phi = 1.2$

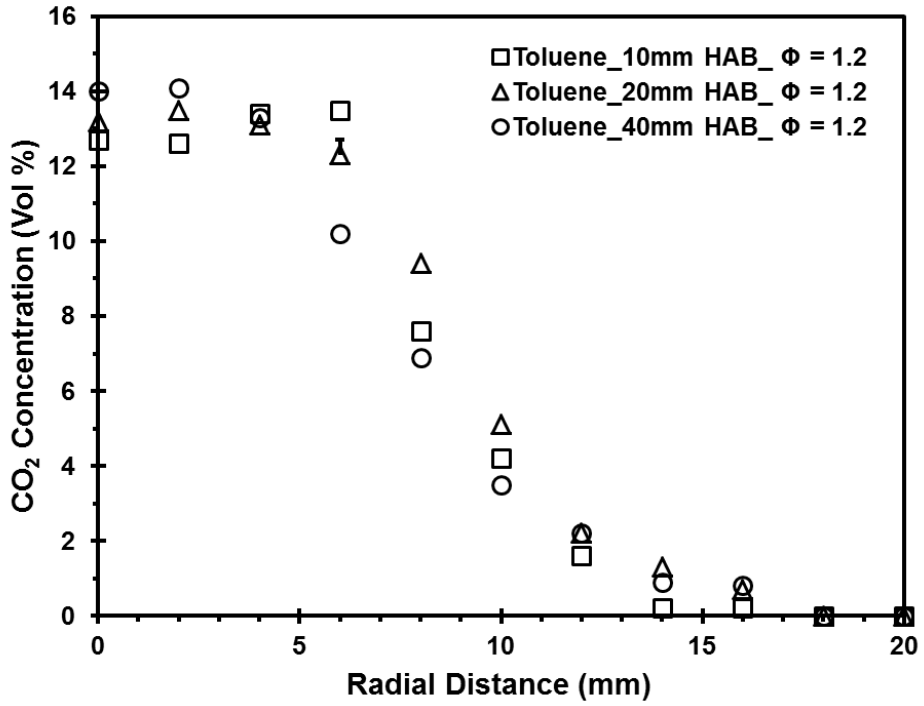

Figure 7.40 Radial in-flame CO_2 concentration profile of toluene flame at $\Phi = 1.2$

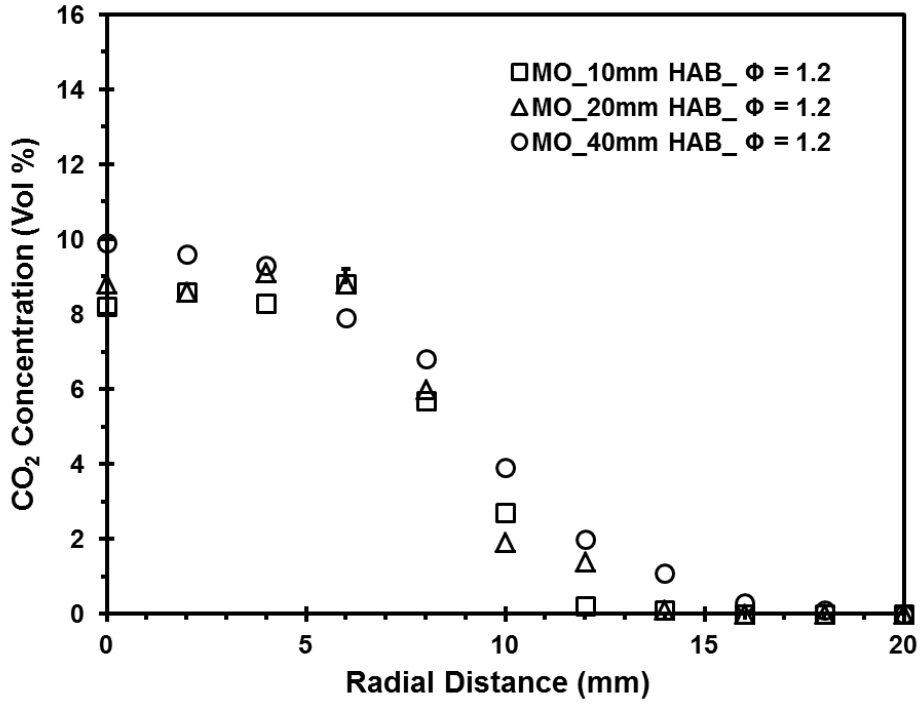

Figure 7.41 Radial in-flame CO_2 concentration profile of MO flame at $\Phi = 1.2$

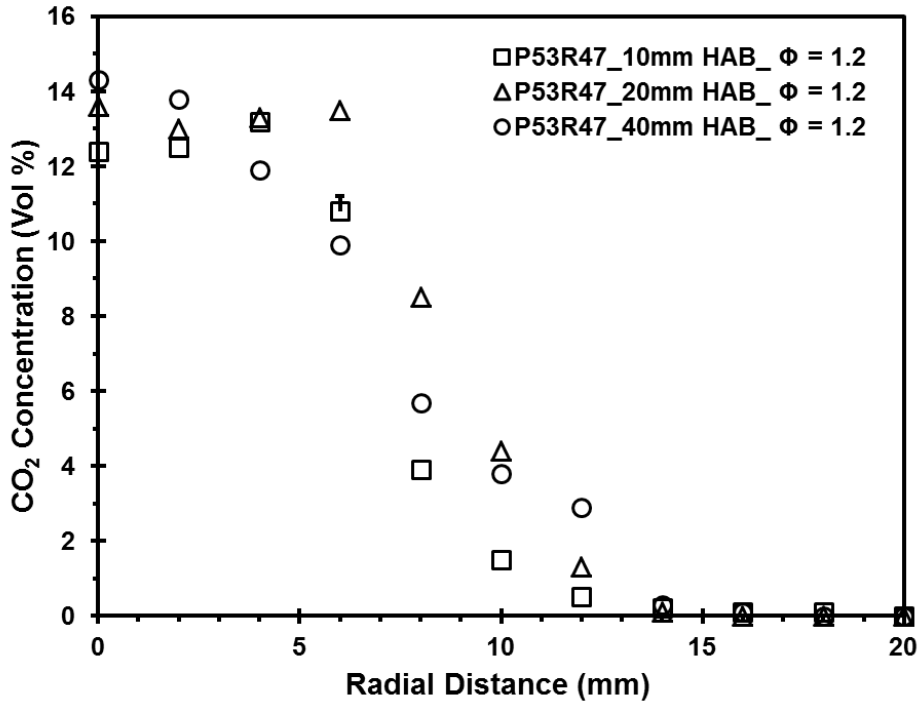

Figure 7.42 Radial in-flame CO_2 concentration profile of P53R47 flame at $\Phi = 1.2$

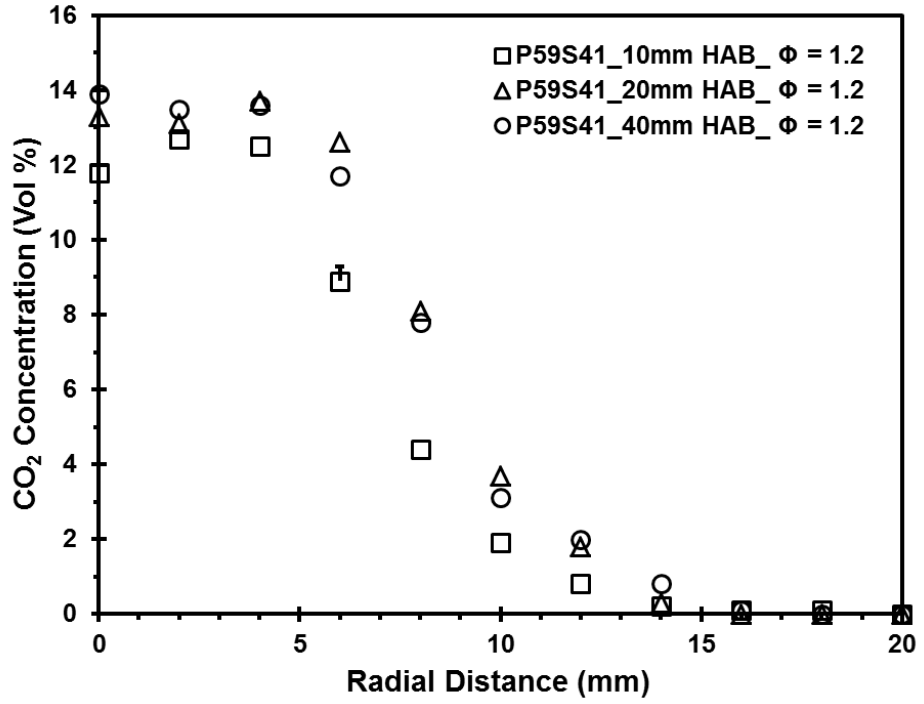

Figure 7.43 Radial in-flame CO_2 concentration profile of P59S41 flame at $\Phi = 1.2$

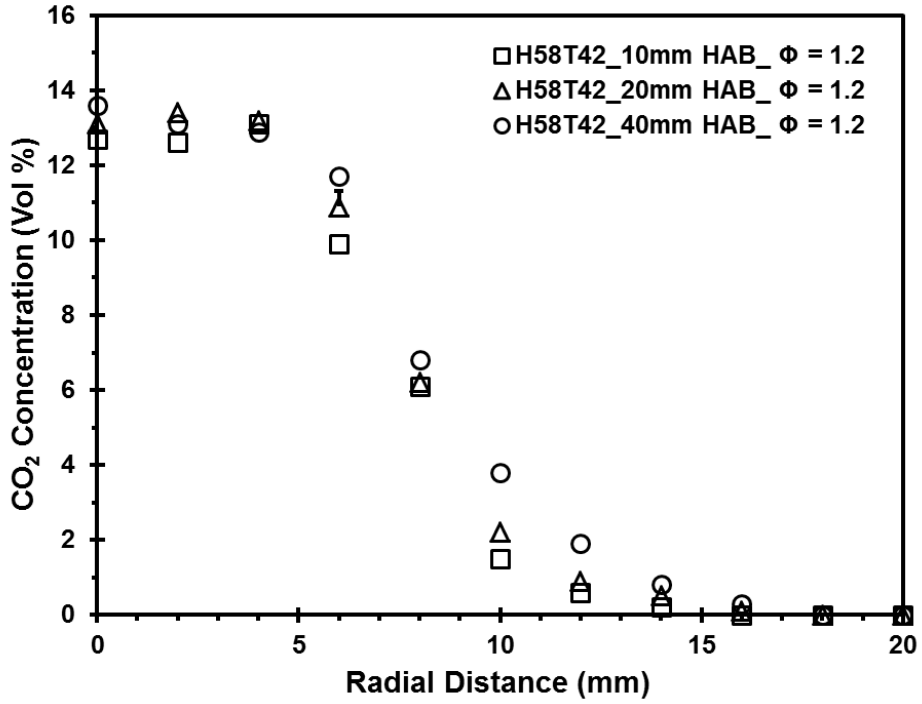

Figure 7.44 Radial in-flame CO_2 concentration profile of H58T42 flame at $\Phi = 1.2$

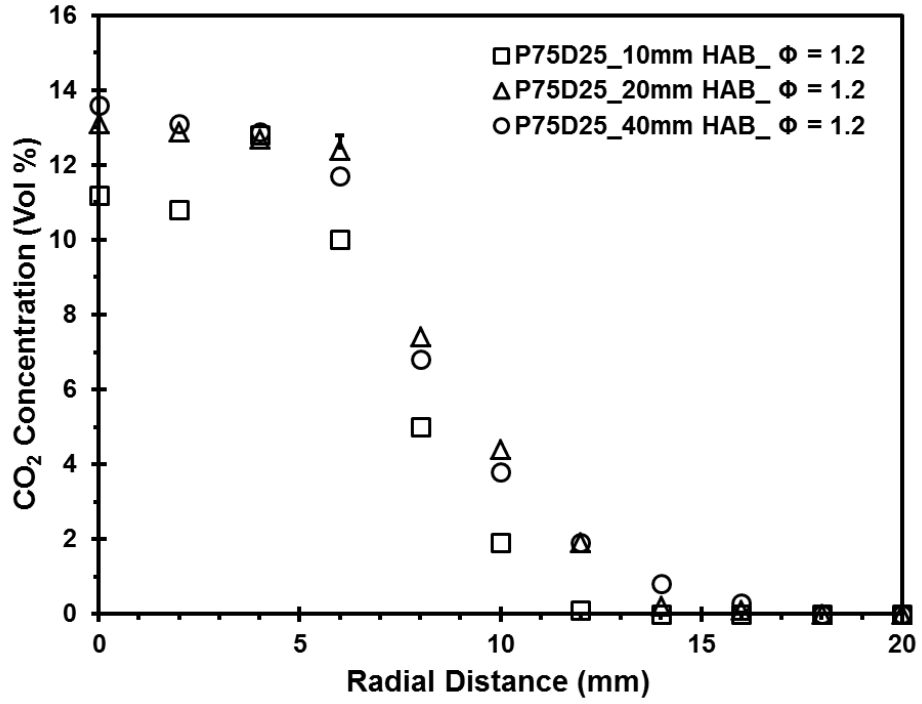

Figure 7.45 Radial in-flame CO_2 concentration profile of P75D25 flame at $\Phi = 1.2$

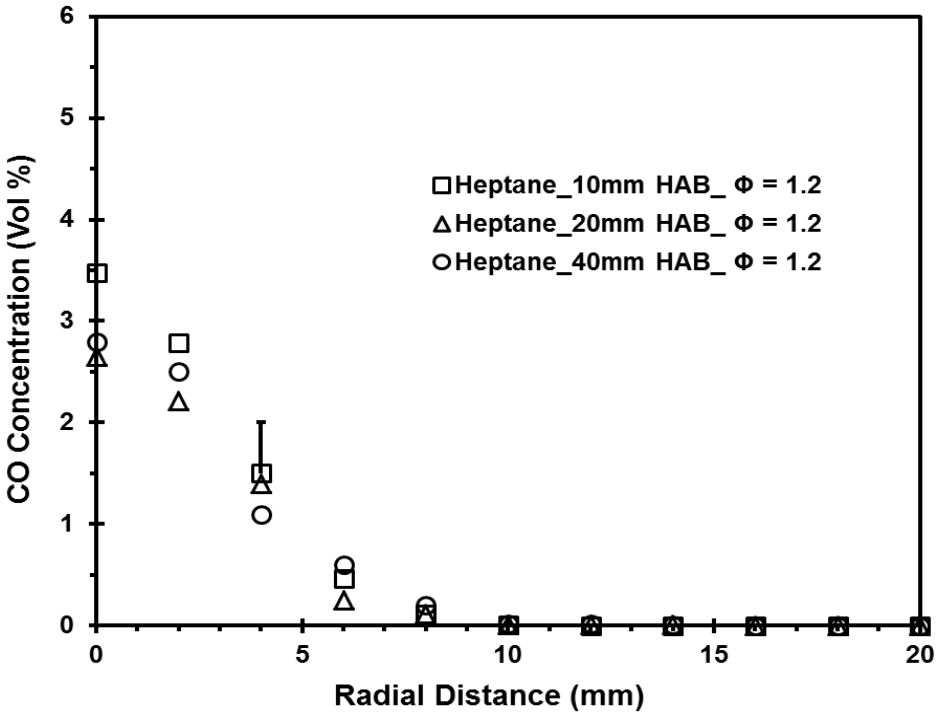

Figure 7.46 Radial in-flame CO concentration profile of heptane flame at Φ = 1.2

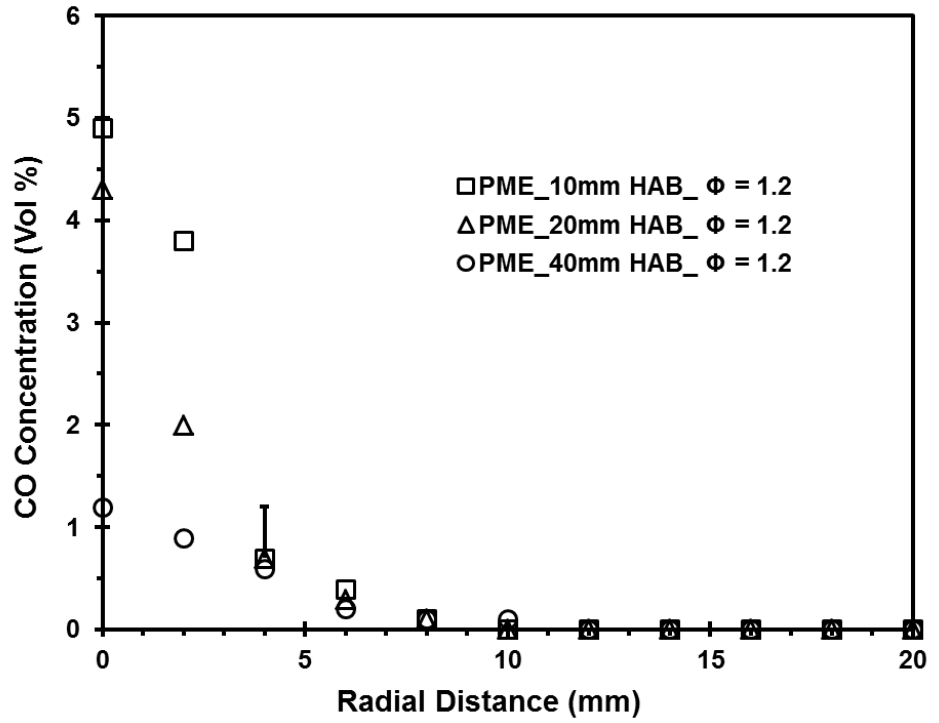

Figure 7.47 Radial in-flame CO concentration profile of PME flame at Φ = 1.2

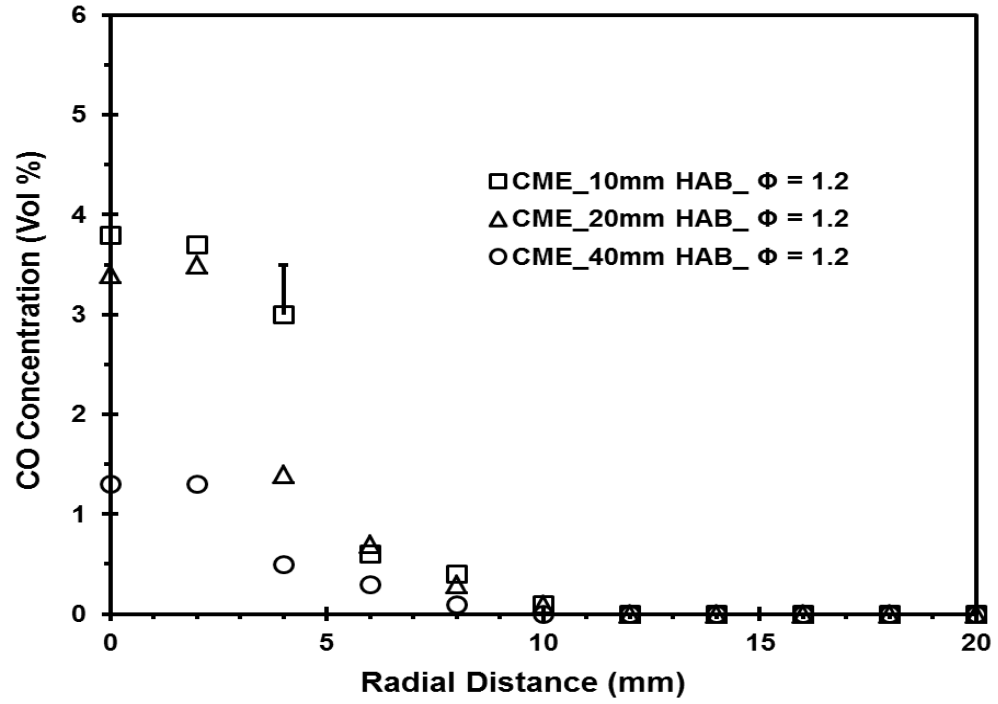

Figure 7.48 Radial in-flame CO concentration profile of CME flame at Φ = 1.2

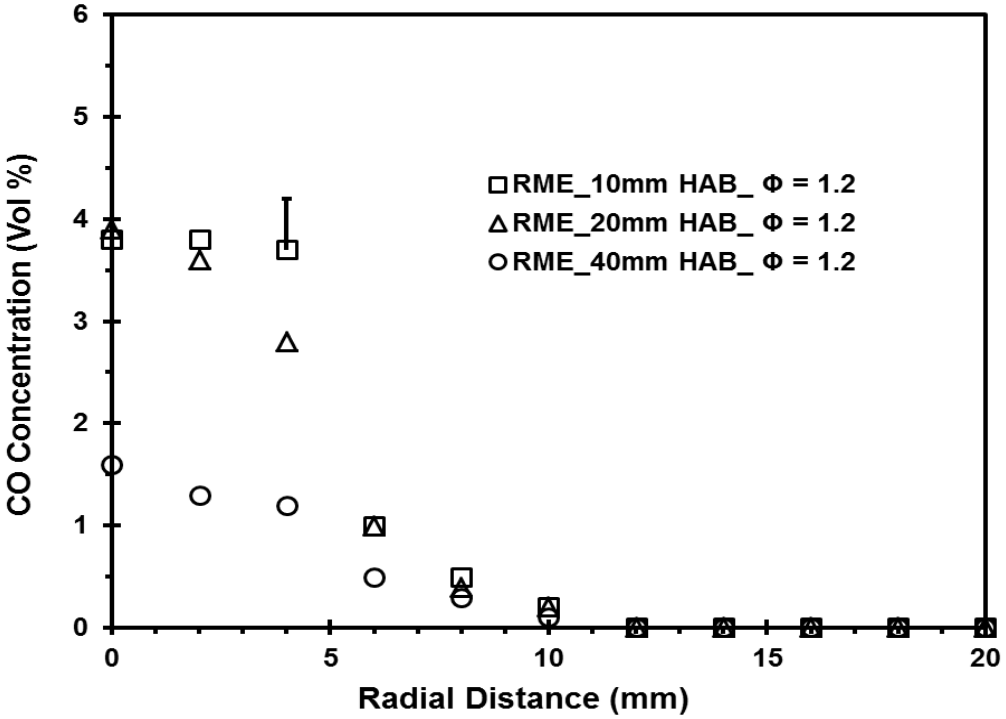

Figure 7.49 Radial in-flame CO concentration profile of RME flame at Φ = 1.2

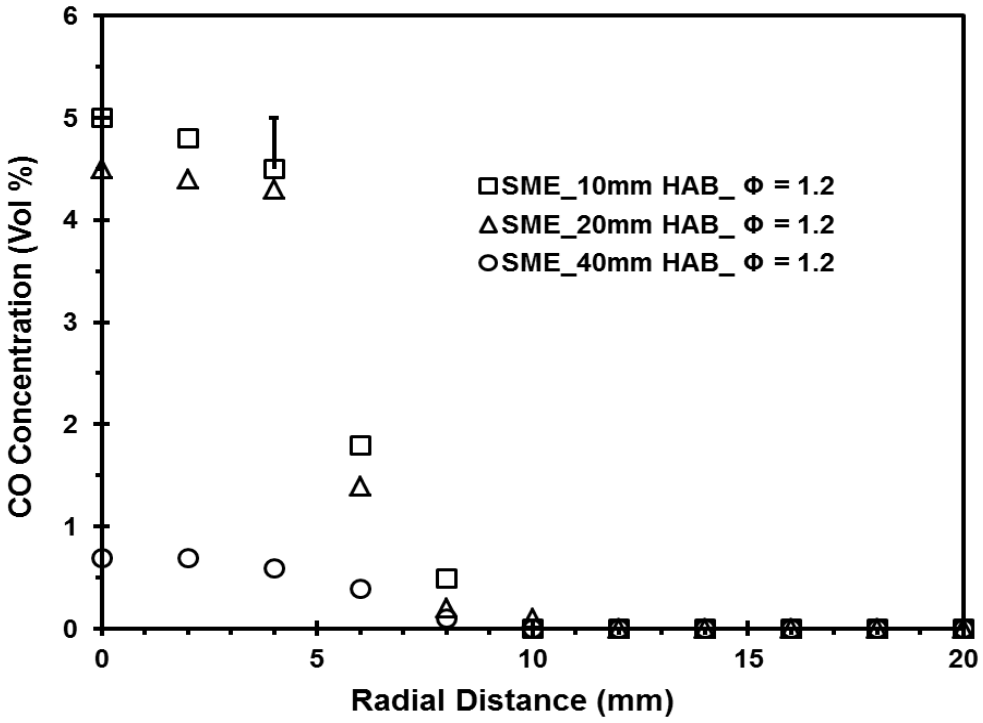

Figure 7.50 Radial in-flame CO concentration profile of SME flame at Φ = 1.2

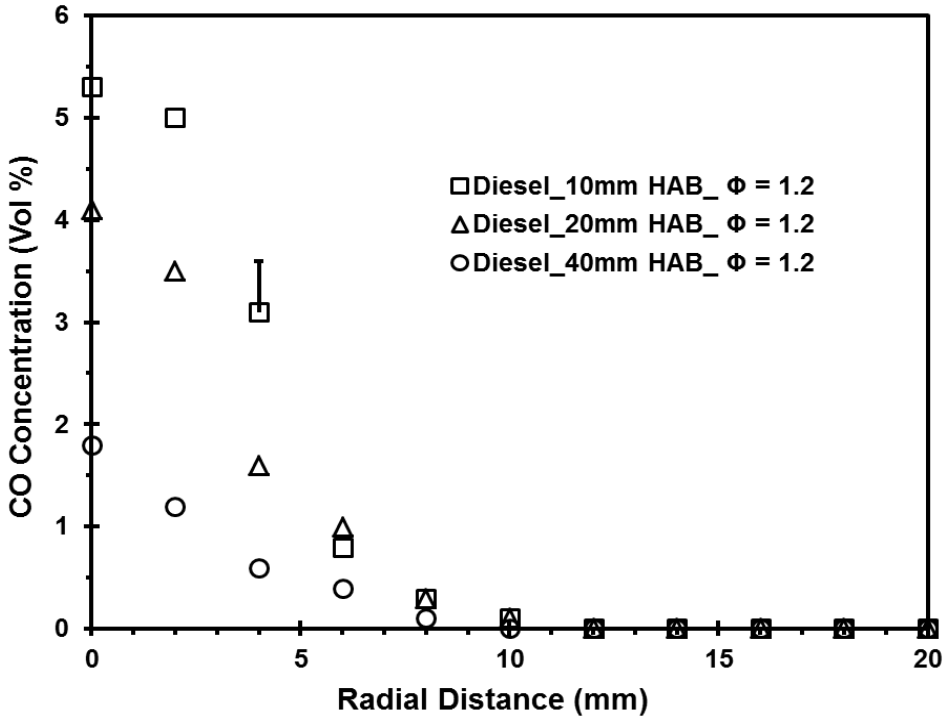

Figure 7.51 Radial in-flame CO concentration profile of diesel flame at Φ = 1.2

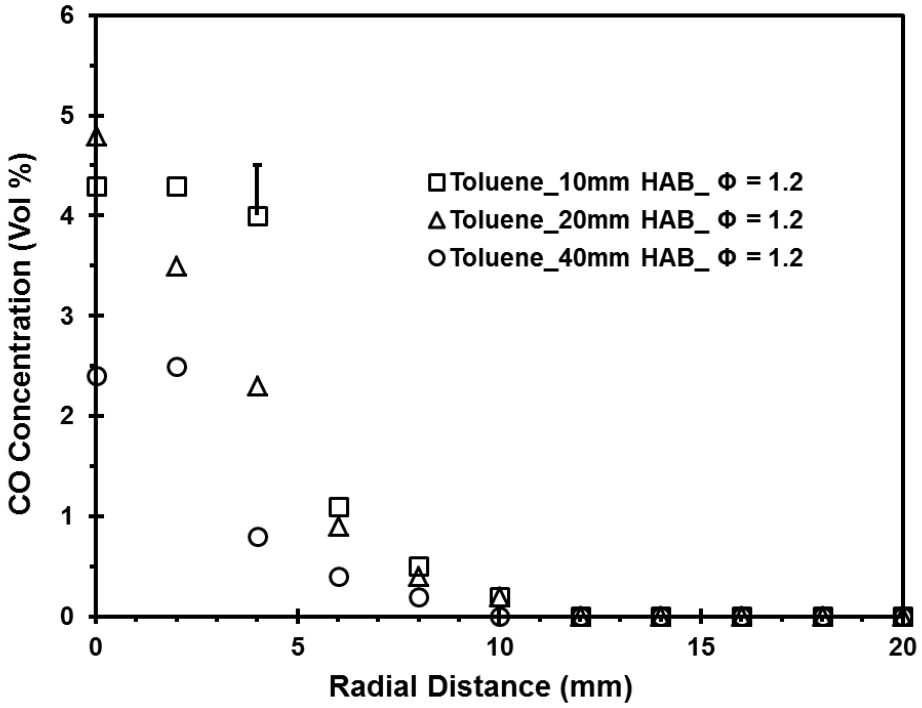

Figure 7.52 Radial in-flame CO concentration profile of toluene flame at Φ = 1.2

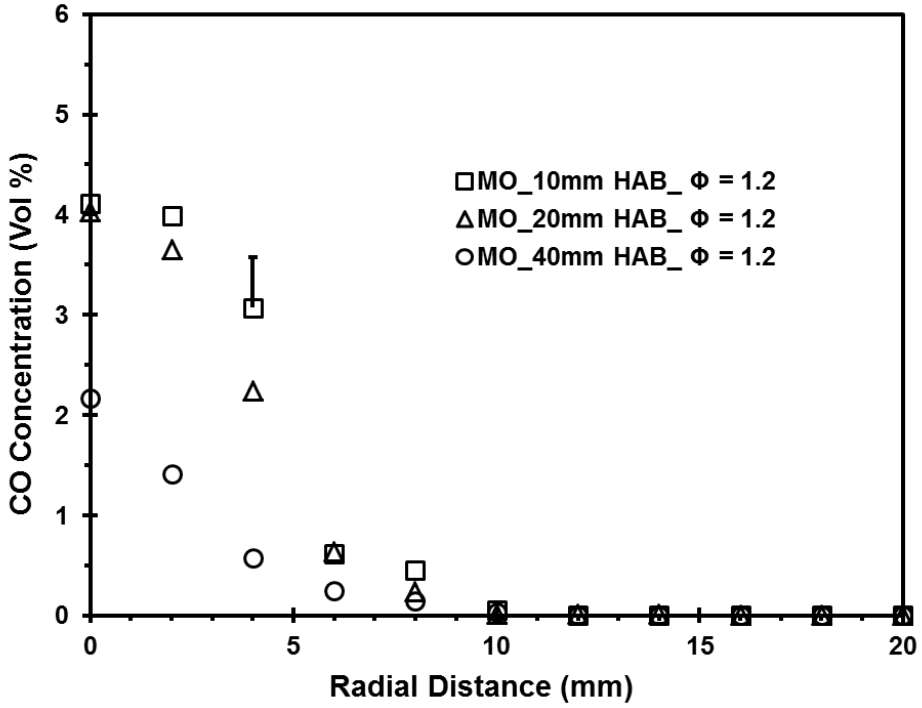

Figure 7.53 Radial in-flame CO concentration profile of MO flame at Φ = 1.2

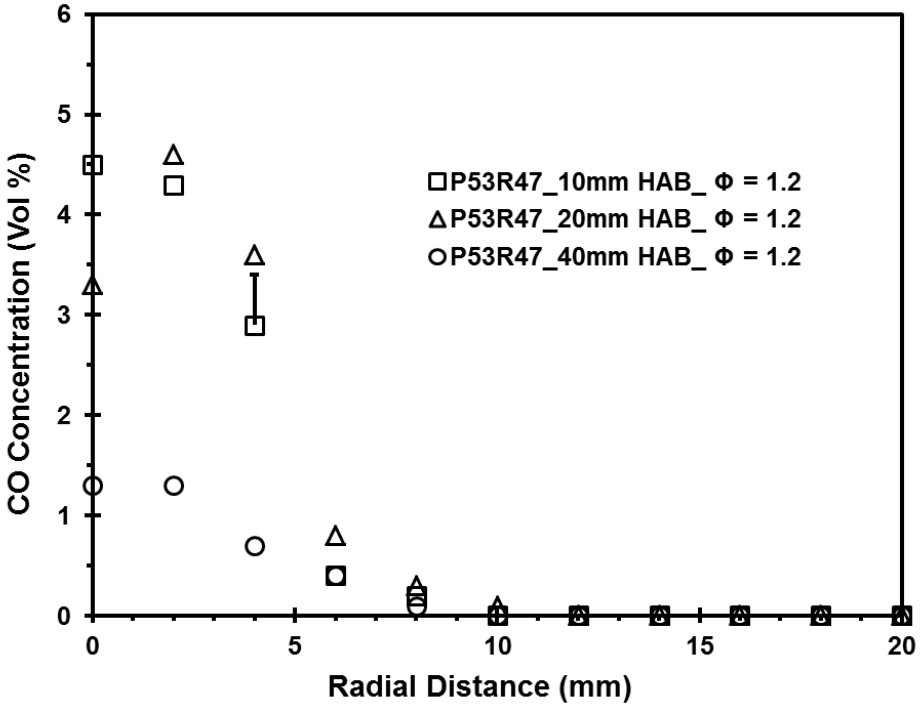

Figure 7.54 Radial in-flame CO concentration profile of P53R47 flame at Φ = 1.2

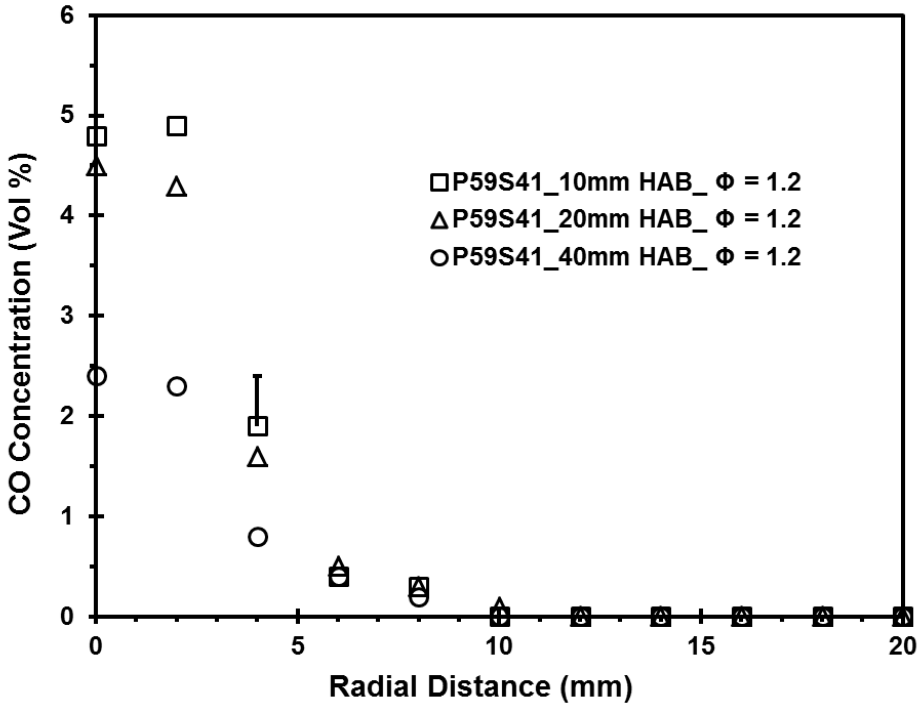

Figure 7.55 Radial in-flame CO concentration profile of P59S41flame at Φ = 1.2

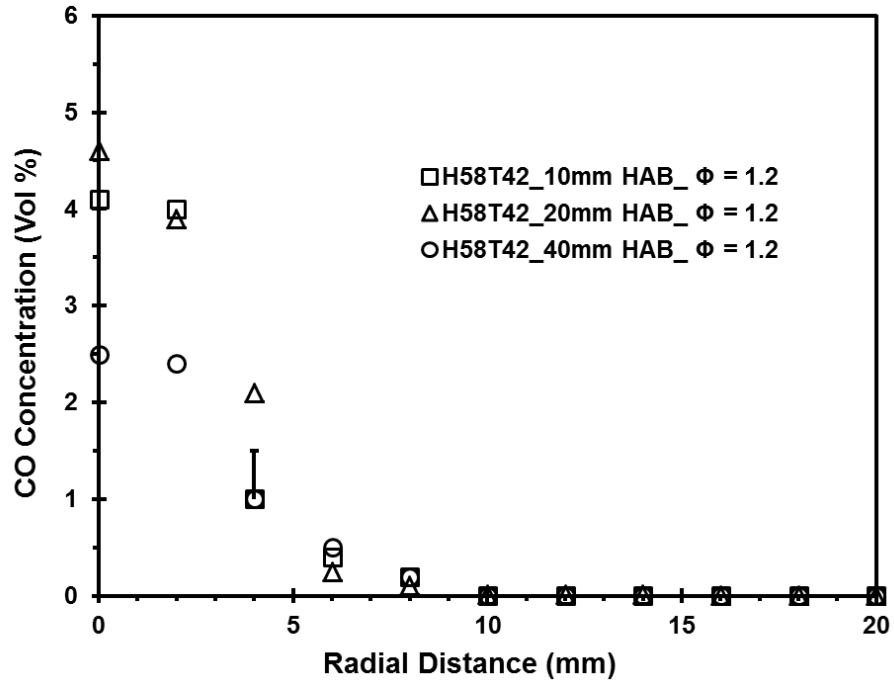

Figure 7.56 Radial in-flame CO concentration profile of H58T42 flame at Φ = 1.2

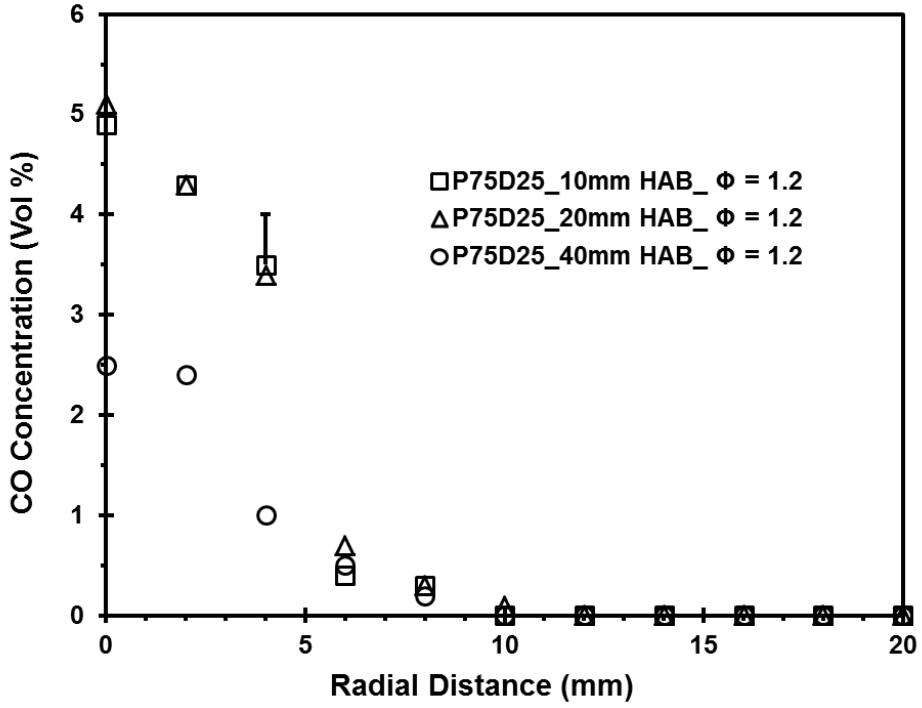

Figure 7.57 Radial in-flame CO concentration profile of P75D25 flame at Φ = 1.2

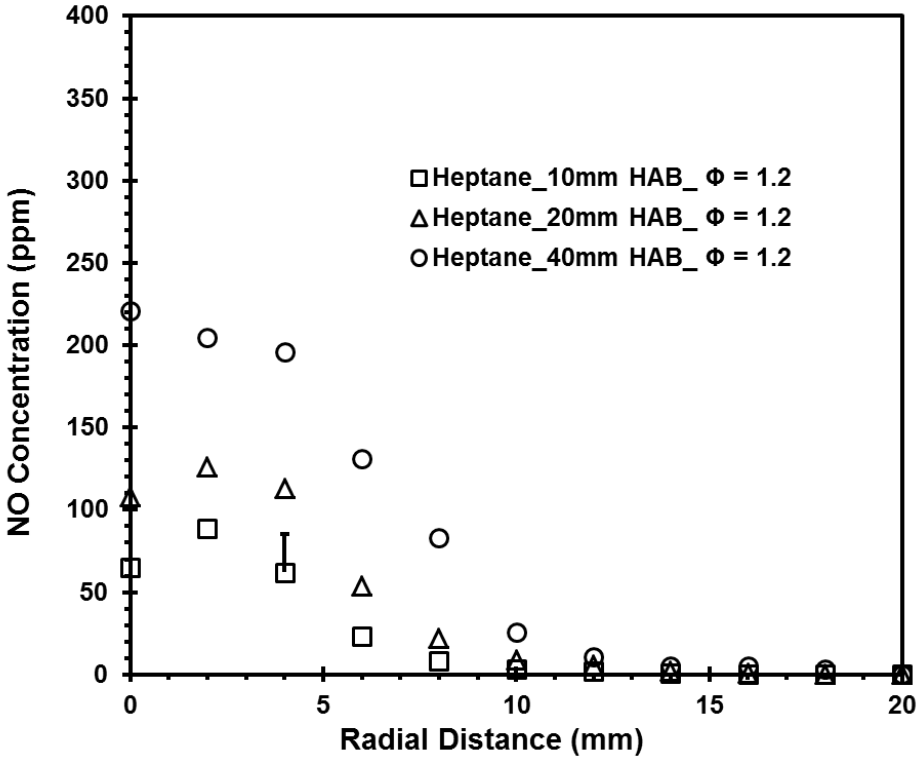

Figure 7.58 Radial in-flame NO concentration profile of heptane flame at Φ = 1.2

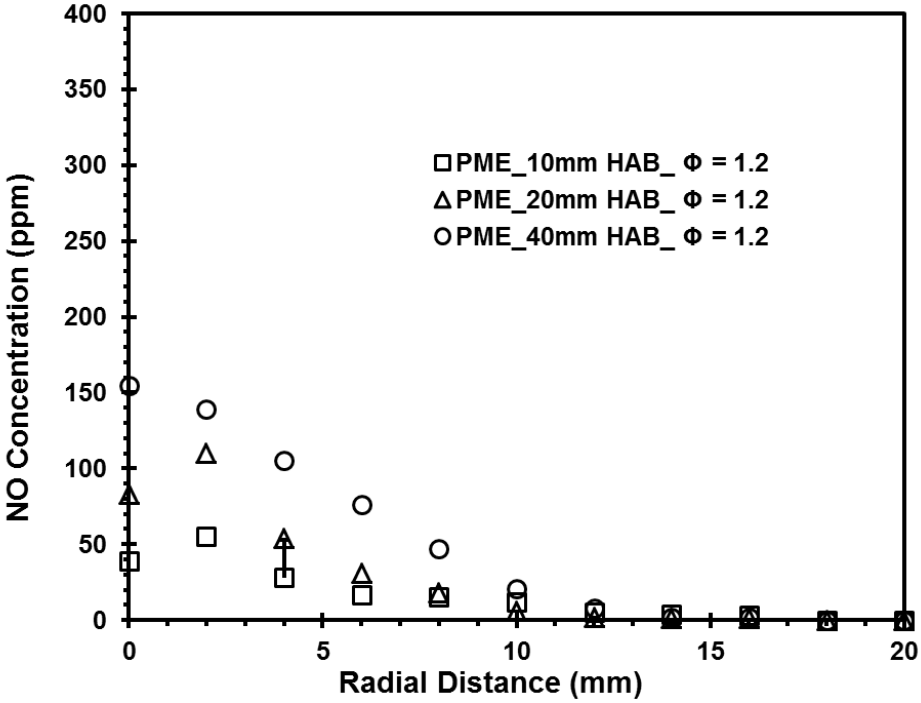

Figure 7.59 Radial in-flame NO concentration profile of PME flame at Φ = 1.2

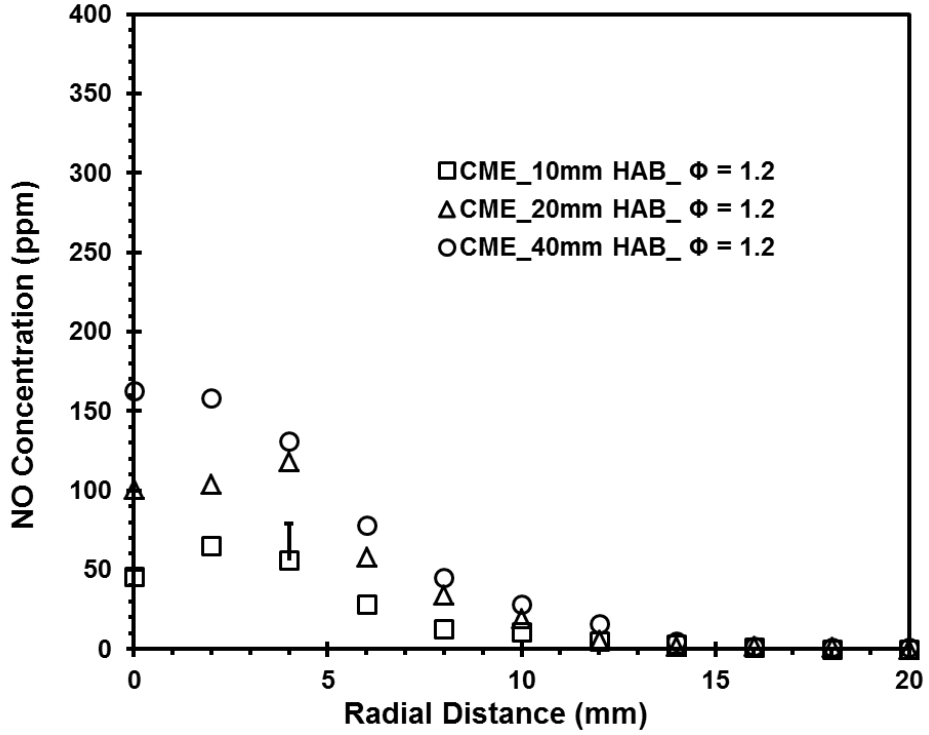

Figure 7.60 Radial in-flame NO concentration profile of CME flame at Φ = 1.2

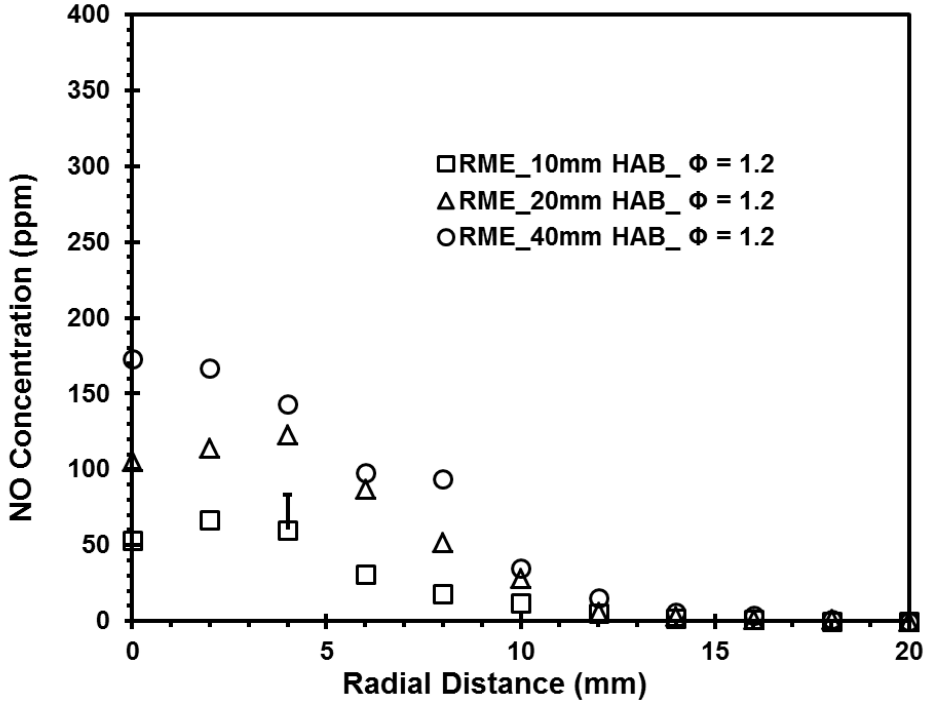

Figure 7.61 Radial in-flame NO concentration profile of RME flame at Φ = 1.2

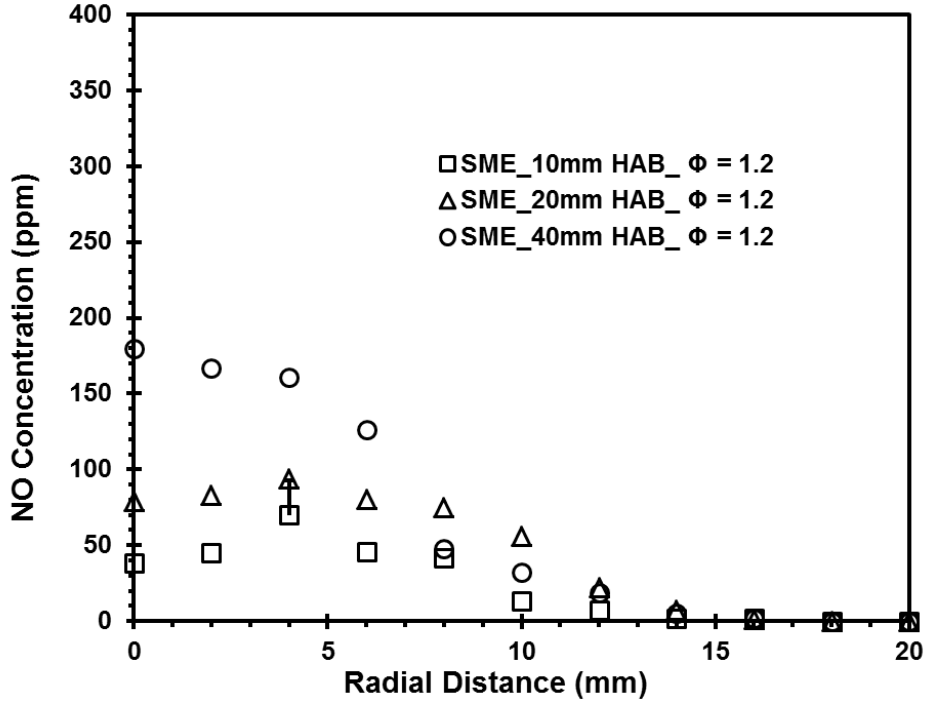

Figure 7.62 Radial in-flame NO concentration profile of SME flame at Φ = 1.2

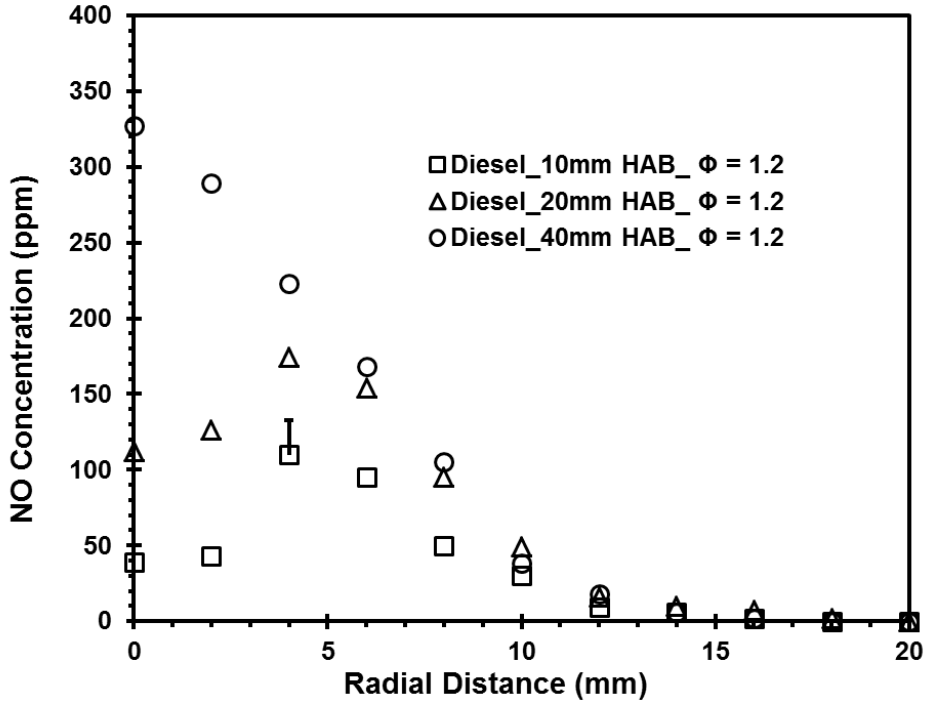

Figure 7.63 Radial in-flame NO concentration profile of diesel flame at Φ = 1.2

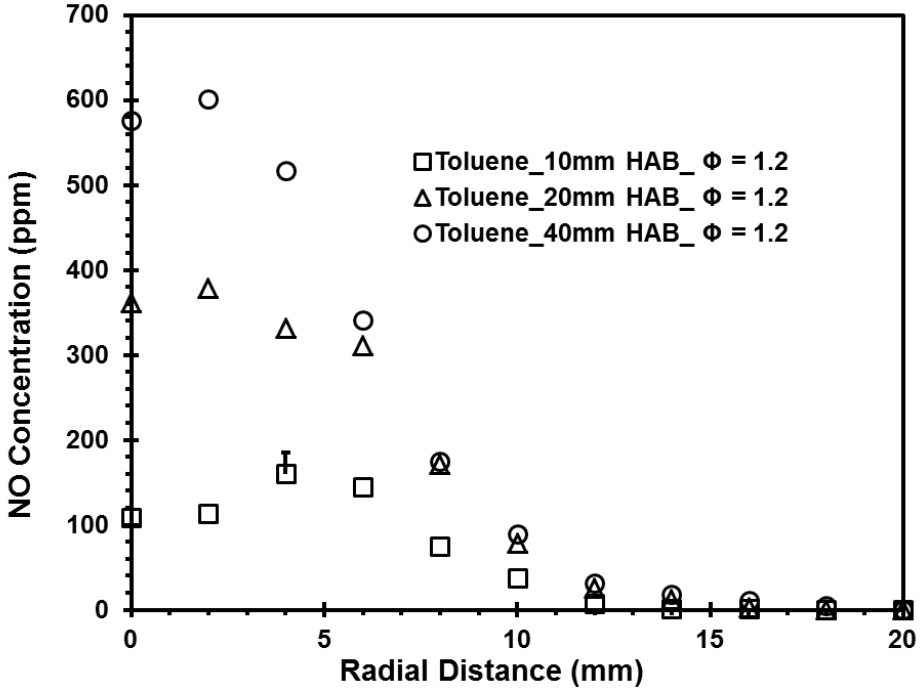

Figure 7.64 Radial in-flame NO concentration profile of toluene flame at Φ = 1.2

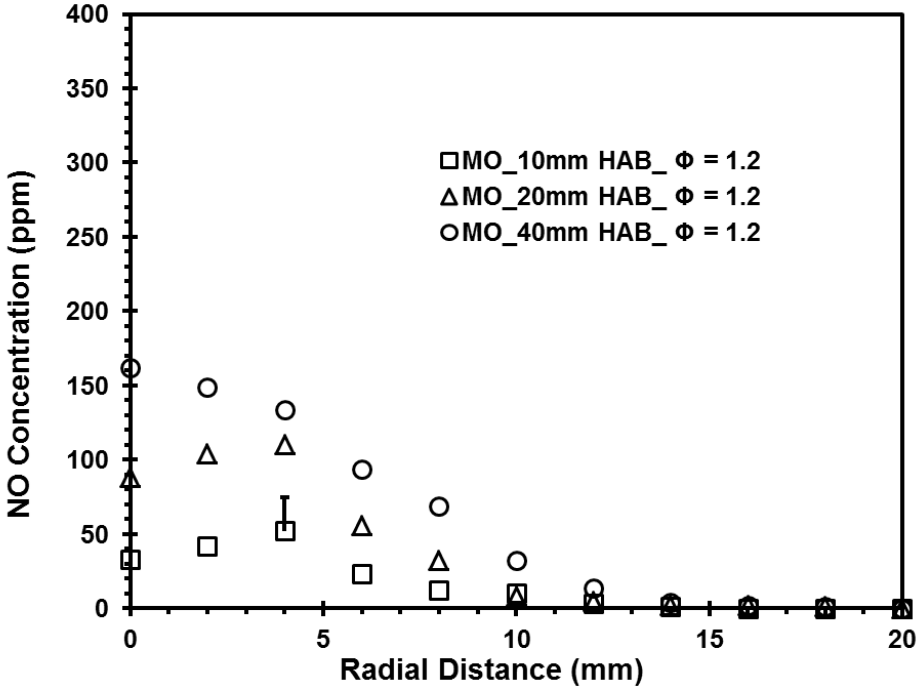

Figure 7.65 Radial in-flame NO concentration profile of MO flame at Φ = 1.2

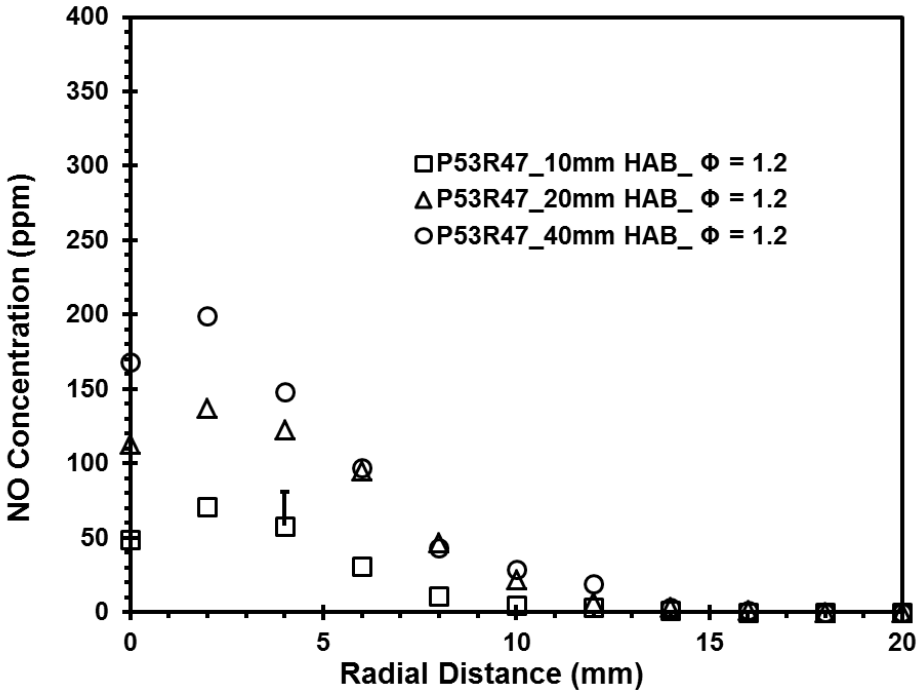

Figure 7.66 Radial in-flame NO concentration profile of P53R47 flame at Φ = 1.2

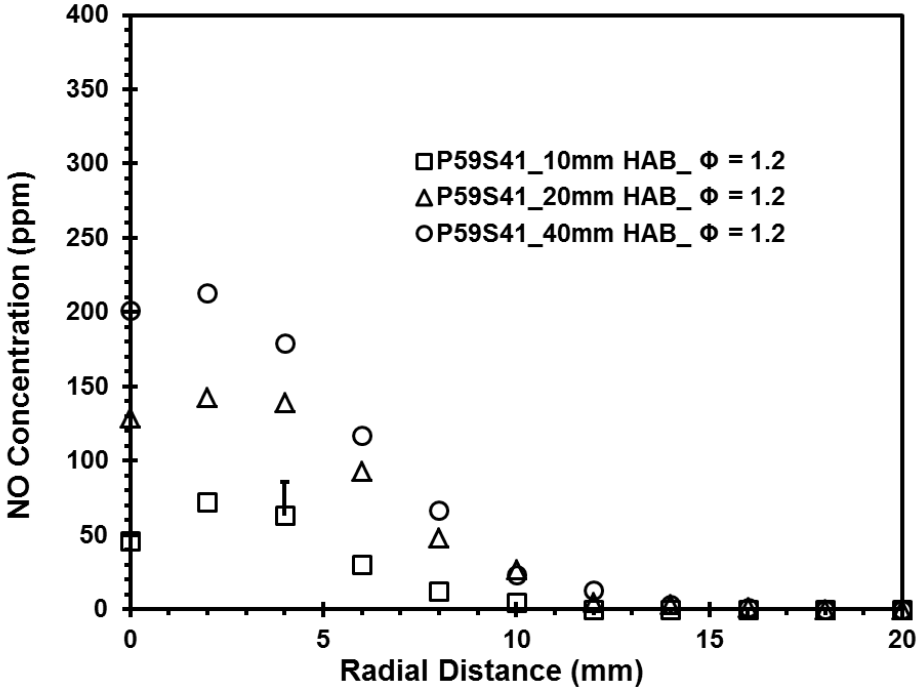

Figure 7.67 Radial in-flame NO concentration profile of P59S41 flame at Φ = 1.2

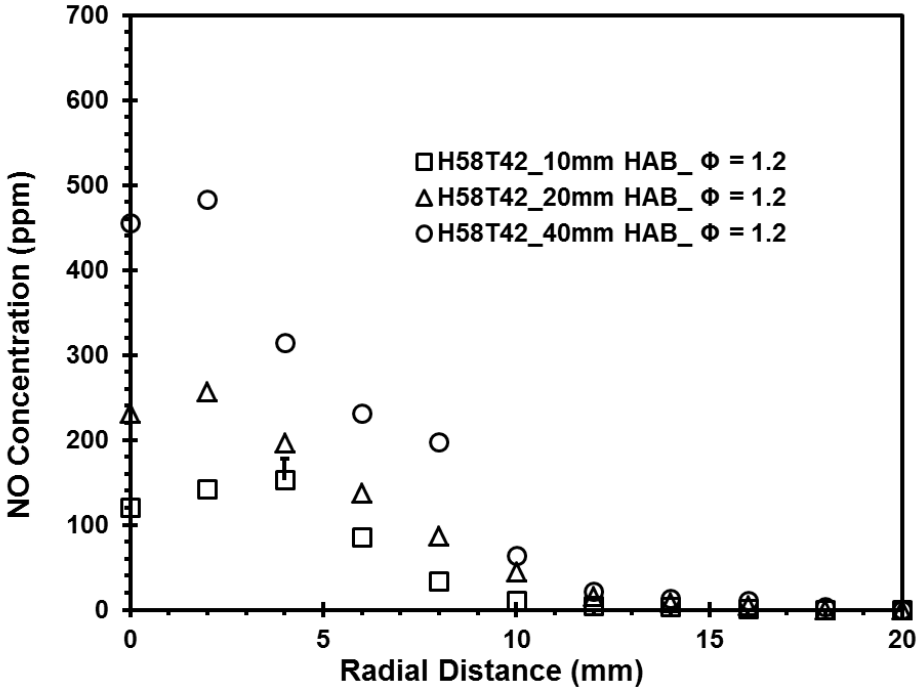

Figure 7.68 Radial in-flame NO concentration profile of H58T42 flame at Φ = 1.2

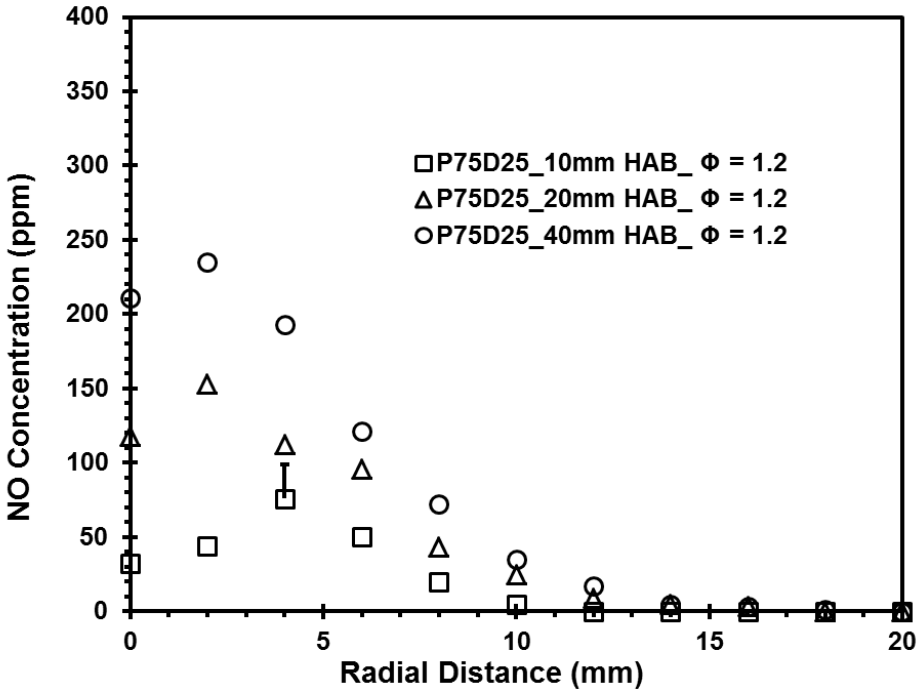

Figure 7.69 Radial in-flame NO concentration profile of P75D25 flame at Φ = 1.2

CHAPTER 8 COMPUTATIONAL ANALYSIS

In this chapter, the numerical investigation of laminar premixed flames of prevaporized methyl oleate (individual methyl ester), heptane and toluene (components of petroleum diesel), petroleum diesel surrogate and biodiesel surrogates for PME, CME and SME at $\Phi = 1.2$ is presented. The initial equivalence ratio of 1.2 was chosen for the investigation since the largest global NO emission index was measured at that equivalence ratio in the experiments, as discussed earlier.

The primary objective of this computational analysis was to develop a computational model to predict the local temperature and CO, CO_2, O_2 and NO concentrations in petroleum and biodiesel flames and to identify the dominant reaction pathway in the formation of pollutants from these flames. The flow field of heated fuel vapor-air mixture issued from a circular burner in quiescent atmosphere was numerically computed using FLUENT computational fluid dynamics software. The Jet flame reactor network model of CHEMKIN software package was employed to solve the combustion chemistry using prebuilt chemical kinetic mechanisms. The dimensions of the modeled burner were the same as the dimensions of the burner used for the experiments (9.5mm ID and 12.7 mm OD). The local residence time calculated from the non-reacting jet results was then used to determine the temperature and concentrations of CO, CO_2, O_2 and NO at each point using the Jet Flame Reactor Network (JFR) model in CHEMKIN software package.

The development of the computational model involved the following systematic investigation techniques:

1. Model definition
2. Grid development and sensitivity analysis
3. Identification of available chemical kinetic mechanisms for selected fuels
4. Inclusion of pertinent reactions for nitric oxide chemistry (The San Diego Mechanism)
5. Development of Jet flame reactor network model (CHEMKIN) with inclusion of ambient air entrainment into the flame
6. Result Analysis

8.1 Model definition

Modeling the injection of heated fuel vapor and air jet require the energy, momentum and mass conservation equations to be solved. Further, modeling the combustion reactions of these mixtures requires information on the specific chemical kinetic mechanisms, reaction parameters and thermodynamic properties of the species involved in the reactions. Since combustion chemistry reactions involve complex non-linear dependence of thermo-physio-chemical parameters, solving fluid mechanics and chemical reactions simultaneously is computationally expensive. In literature, frequently, chemical kinetics is greatly reduced to make computational simulations possible for chemically reactive flows (CHEMKIN, 2011). When pollutant emissions (especially pollutants like nitric oxides) are to be predicted, the assumption of local

chemical equilibrium is not appropriate and employment of detailed reaction mechanism is warranted. Building a jet flame reactor network from non-reacting flow simulations is a plausible approach as this method utilizes the detailed reaction mechanisms, while preserving some key fluid dynamic features that are important to emission predictions such as residence time. Hence, the results from this model were obtained with the use of a perfectly stirred reactor network based on a predefined jet flame network model in CHEMKIN database. The model did not consider the transport processes and hence results are based on the chemical kinetics, residence time and composition of the reactant mixtures. Residence time and velocity information for this reactor model were based on the results from the non-reacting heated fuel vapor/air jet numerical simulations from FLUENT.

8.1.1 Model Assumptions

To simplify the complexities involved in solving the equations, the following assumptions were made:

1. The computational domain is assumed to be symmetric about the injector axis.
2. Heat transfer between the heated fuel vapor/air jet and burner tip was neglected and the radiative heat losses from the flame in the combustion model were also neglected.
3. The fuel vapor was injected above the boiling point of fuels and assumed to be completely in vapor form.

8.1.2 Continuity and momentum equations

FLUENT software package was used for solving of the laminar flow field, the 2-D axisymmetric conservation and momentum equations. The continuity equation is expressed in Eq. (8.1). Equation (8.2) presents the momentum equation where $\rho\vec{g}$ is the gravitational body force in the x direction, $\vec{v}$ the velocity, $\bar{\bar{\tau}}$ is the stress tensor given in Eq. (8.2a), μ the dynamic viscosity, and P the static pressure.

$$\vec{\nabla}.(\rho\vec{v}) = 0 \tag{8.1}$$

$$\vec{\nabla}(\rho\vec{v}\vec{v}) = -\vec{\nabla}P + \vec{\nabla}.(\bar{\bar{\tau}}) + \rho\vec{g} \tag{8.2}$$

$$\bar{\bar{\tau}} = \mu\left(\vec{\nabla}.\vec{v} + \vec{\nabla}.\vec{v}^{T}\right) \tag{8.2a}$$

8.1.3 Energy equation

Flows in this study also involved heat transfer thus required additional equations for energy conservation. Equation (8.3) shows the energy equation used for this purpose where the dissipation due to viscosity was assumed small.

$$\frac{\partial}{\partial x_i}\left[u_i(\rho E + P)\right] = \frac{\partial}{\partial x_j}\left(k\frac{\partial T}{\partial x_j}\right) \tag{8.3}$$

Here k is the thermal conductivity, T is the temperature, and E is defined in Eq. (8.3a) as:

$$E = h - \frac{P}{\rho} + \frac{\upsilon^2}{2} \tag{8.3a}$$

where h, P, ρ and v are the enthalpy, pressure, density and velocity of the flow respectively at the inlet. The values used in the numerical model for the tested fuels are presented in Table 8.1

8.1.4 Species transport equation

Further, since flows in this study involved species mixing, the species conservation equation was also solved, Eq. (8.4) and Eq. (8.4a).

$$\nabla . (\rho \vec{v} Y_i) = -\nabla . \vec{J_i} \tag{8.4}$$

where $\vec{J_i}$ is defined as,

$$\vec{J_i} = -\sum_{j=1}^{N_o-1} \rho D_{ij} \nabla Y_i \tag{8.4a}$$

where D_{ij} is the binary mass diffusion coefficient in the mixture, N_o is the number of chemical species, and Y_i is the mass fraction of species i. The fluid material properties such as thermal conductivity, viscosity and binary mass diffusion coefficients for all the tested fuel/air mixtures are presented in Table 8.1. The density of the mixtures was solved using the ideal gas assumption and the composition dependent specific heat capacity for the mixture was defined by the mixing law option in the FLUENT where the mixture's specific heat capacity was computed as a mass fraction average of pure species heat capacities by the solver. The mass fractions of the individual methyl esters that constitute the commercial biodiesels present in the fuel/air mixture are presented in Table 8.2. The FLUENT solver setting parameters such as under relaxation parameters and employed discretization methods are presented in Tables 8.3 and 8.4. The inlet and boundary conditions of the computation domain are presented in Tables 8.4 and 8.5.

8.2 Grid development and sensitivity analysis

A schematic diagram of the computational domain with boundary conditions and the coordinate system used is presented in Figure 8.1. The grid extended to 2000 mm and 50 mm in the axial and radial directions respectively. The computational domain was axisymmetric about the burner axis. The grid was initially assigned a fine mesh of 0.0016 m to find the initial computational time. This grid has 38975 cells, 79231 faces and 40257 nodes (Figure 8.2). After the solution was obtained, a mapped face meshing was applied to the grid. In this process, the grid size was adapted primarily along the axis of the jet where gradients were large. The first adapted grid had 5200 cells, 10626 faces and 5427 nodes. This adaptation technique was found efficient since the computational domain is discretized coarsely away from the influence of jet thereby reducing the number of cells. This process was repeated again and the second adapted grid had 12400 cells, 25238 faces and 12839 nodes. The velocity profiles computed using the three different grids at three axial locations are shown in Figure 8.3. The location and magnitude of peak velocity remained the same between the three grid variations and the velocity profiles computed by the three grids coincide on top of each other, indicating that the solution was grid independent.

8.3 Non-reacting heated fuel vapor/air laminar jet results

The laminar jet results from the non-reacting heated fuel vapor/air simulations using FLUENT are presented in this section. The axial velocity and temperature contour plots of heated non- reacting jets of fuel/air mixture for the six test fuels namely MO, CME, SME, PME, toluene, heptane and diesel surrogate are presented in Figures 8.4 - 8.10. Although, the jet was simulated for the entire grid (2000 mm), only the region extends to 150 mm above the injector exit are presented in these plots. In all these figures, the axial velocity of the jet decreased downstream and the fuel vapor/air jet grown wider due to the entrainment of ambient air. This observation was also reflected in the temperature contour plots where the centerline temperature decreased downstream of the jet due to the mixing and entrainment of ambient air into the jet.

As mentioned earlier, FLUENT solved the 2D laminar field considering the simpler case of a non-reacting laminar jet (fuel/air mixture) flowing into an infinite reservoir of quiescent fluid (air). This simplification provided a fundamental understanding of the basic flow and diffusional processes that occur in laminar jets without involving the effects of chemical reaction. Further, throughout the entire flow field, the initial jet momentum is conserved. As the fuel/air mixture jet issued into the surrounding air, some of its momentum is transferred to the ambient air. Thus, the velocity of the jet decreases while greater amount of air is entrained into the jet as it proceeds downstream. Based on this understanding, with constant density approximation, the dimensionless centerline velocity decay relationship was developed (Turns, 2011), as shown in equation 8.5.

$$\frac{V_x}{V_e} = 0.375 * \left(\frac{\rho_e V_e R}{\mu}\right) * \left(\frac{x}{R}\right)^{-1} \quad (8.5)$$

where V_x is the axial velocity at x distance from the injector exit; V_e is the injector exit velocity; ρ_e is the injector exit density; μ is the dynamic viscosity and R is the radius of the injector. This equation shows that the velocity decays inversely with the axial distance and is directly proportional to the jet Reynolds number. However, this solution is not valid near the nozzle, since $\frac{V_x}{V_e}$ should not exceed unity.

In this study, the centerline velocity decay predicted by the FLUENT simulations was compared against the theoretical relationship presented in equation 8.5. The centerline velocity decay of heated non- reacting laminar jets of fuel/air mixture for the six test fuels namely MO, CME, SME, PME, toluene, heptane and diesel surrogate are presented in Figures 8.11 - 8.17. The theoretical centerline velocity decay corresponding to values greater than x/R = 100 was plotted in addition to the computationally predicted values. It can be noted that, among all the simulated laminar jet results, the computational prediction and theoretical calculation of the centerline velocity decay closely followed each other. The FLUENT model predicted slightly faster decay of centerline velocity (about 10% lower centerline velocity at x/R = 400) than the theoretical calculation (using equation 8.5) among MO (Figure 8.11), CME (Figure 8.12), SME (Figure 8.13), PME (Figure 8.14) and diesel (Figure 8.17) jets. Among the heptane (Figure 8.16) and toluene (Figure 8.15) vapor jets, the fluent model predicted slightly slower decay of centerline velocity (about 8% higher centerline velocity at x/R = 400) than the theoretical equation. These plots revealed the

conformity of the numerically predicted laminar jet results from this study with the well-established theoretical results.

The observed differences in these plots could be due to the differences in the molecular weight and the viscosity of the fuel vapors at an elevated temperature of 700K. Although the definite viscosity values of biodiesel vapors were not known, the current discussion utilizes the already developed interrelationship between viscosity of hydrocarbon vapors as a function of molecular weight and temperature (Maxwell, 1950). The viscosity of hydrocarbon vapors is inversely proportional to molecular weight and directly proportional to temperature (Maxwell, 1950). Hence at a higher temperature (about 700K), fuels with low molecular weight like toluene and heptane (Table 8.1) would have higher viscosity than fuels with higher molecular weight like diesel, MO, CME, PME and SME (Table 8.1). The higher viscosity of fuel vapor leads to slower decay of centerline velocity in case of heptane and toluene jets. This is in agreement with the observation in the FLUENT temperature contour plot of heptane and toluene vapor jets (Figures 8.8 and 8.9). In these plots, the centerline temperature of the vapor jet was still closer to 640K (in both toluene and heptane vapor jets) at an axial height of 150 mm from the injector exit, while in higher molecular weight fuels like diesel, MO, CME, PME and SME the centerline temperature at an axial distance of 150 mm was about 543K, 560K, 562K, 558K and 561K respectively. Hence these observations suggested that at a given inlet temperature, fuels with low molecular weights have higher viscosity than fuels with high molecular weights, which in turn would influence the diffusion rate of momentum, temperature and species. Further, the agreement of FLUENT numerical simulations with the established laminar jet results

suggested the effectiveness of the adopted approach in understanding the fundamental flow characteristics of heated non-reacting laminar jets.

8.4 Identification of available chemical kinetic mechanisms

As discussed in Chapter 2, the most recent development in the chemical kinetic mechanisms and reaction parameters were analyzed from the available literature. The chemical kinetic reaction mechanisms developed by Lawrence Livermore National Laboratory (LLNL) for the oxidation of n-heptane, toluene, methyl oleate and commercial biodiesels were utilized for the numerical investigation in this study.

The following section presents comprehensive information about the selected mechanisms and their salient features:

8.4.1 The "real" biodiesel surrogate mechanism

The "real" biodiesel surrogate mechanism includes the detailed chemical kinetic reaction mechanism for the five-major component of biodiesels namely methyl palmitate, methyl stearate, methyl oleate, methyl linoleate and methyl linolenate which have carbon number greater than 17. This mechanism was built on the already developed C10 methyl ester surrogates for biodiesels which include the chemical kinetic mechanisms for esters having less than 10 carbon atoms (like methyl butanoate and methyl decanoate) and used as a single component biodiesel surrogates for biodiesels.

The selected mechanism includes more than 4800 chemical species and nearly 20,000 elementary chemical reactions (Westbrook et al. 2011).

The advantage of “real” biodiesel surrogate mechanism is that the chemical kinetic mechanisms for various esters ranging from C2 to C19 are included in the current mechanism. Hence the reaction mechanism of various commercial biodiesels like SME, CME and PME can be investigated with this mechanism since these biodiesels primarily consists of aforementioned five methyl esters that are already included in this mechanism.

Broadly, the selected mechanism includes the reaction classes as follows:

- Fuel unimolecular decomposition
- H atom abstraction from the fuel
- Alkyl and ester alkyl radical decomposition
- Alkyl and ester alkyl radical + O_2 to produce alkene and HO_2 directly
- Alkyl and ester alkyl radical isomerization
- Abstraction reactions from alkenes by OH, H, O, and CH_3
- Addition of radical species to alkenes
- Alkenyl radical decomposition
- Alkene decomposition

More detailed information specific to this mechanism is presented in Westbrook et al. (2011).

8.4.2 Petroleum diesel surrogate mechanism

A petroleum diesel surrogate kinetic mechanism describing the oxidation of n-dodecane/m-xylene mixture was developed by the Lawrence Livermore National Laboratory. This diesel surrogate mechanism includes 163 species and 887 reactions (Pei et al., 2015).

8.4.3 Toluene mechanism

The toluene mechanism developed by Nakamura et al. (2014) was selected for the numerical investigation of toluene flame in this study and compared with the results from the experimental portion of this dissertation. The toluene mechanism includes 960 species and 4330 reactions.

8.4.4 n-heptane mechanism

The n-heptane mechanism developed by Seiser et al. (2000) was selected for the numerical investigation of n-heptane flame in this study and compared with the results from the experimental portion of this dissertation. This mechanism includes 159 species and 770 elementary reactions.

8.4.5 Nitrogen chemistry - San Diego mechanism

The chemical kinetic mechanisms presented in sections 8.4.1 to 8.4.4 include the chemical reactions pertinent to only hydrocarbon oxidation and did not include the nitrogen chemistry. Hence the nitrogen chemistry responsible for the formation of

various oxides of nitrogen during combustion was included from the "Nitrogen chemistry kinetic mechanism" developed by the combustion research group at the University of California, San Diego. Each of the above presented mechanisms was incorporated with nitrogen chemistry to predict the amount of NO produced in flames and compared with the experimental results. The included nitrogen chemistry comprised of reaction sets pertinent to the thermal (Zeldovich), Prompt (Fenimore), Intermediate (N2O) mechanisms. This nitrogen chemistry mechanism includes 24 species and 52 reactions (the reactions along with kinetic parameters are presented in Appendix F). Several studies have incorporated this mechanism in their computational investigation to predict the NOx formation successfully, for example, in homogenous natural gas/diesel/air mixture in a diesel fuel engine with heptane as a diesel surrogate (Mulenga et al., 2003) and H_2/air opposed jet diffusion flames (Li et al., 2015).

8.5 Jet flame reactor network model

A schematic diagram of the jet flame reactor network is presented in Figure 8.18. It consists of five perfectly stirred reactors connected with an inlet stream and an exhaust product stream. The input parameters such as inlet mass flow, inlet temperature and initial gas composition are specified at the inlet. The inlet reactant stream is fed through the reactor (R1) and the product stream leaving reactor (R1) enters reactor (R2) and so on. Hence the species composition at any reactor is the cumulative effect of reactions that have occurred until that point, analogous to the chemical reactions that occur in a jet flame. The first reactor acts as a mixing zone while the next three reactors correspond to the axial locations namely 10 mm, 20 mm and 40 mm heights above the

burner. These reactors are fed with air entrainment streams to incorporate the effect of entrainment of ambient air in to the flame at these locations. The procedure for calculating the air entrainment is presented in Appendix H.

The residence time for these reactors is obtained from the velocity solutions of the FLUENT simulations. The residence time is calculated based on the computed local velocity and the axial distance from the burner at the corresponding locations. This method of calculating residence time is valid since the centerline velocity decay for all the simulated non-reacting fuel/air jet mixtures (Figures 8.11 - 8.17) was found to be negligible well beyond an axial distance of 47.5 mm (10 x/R and R = 4.75 mm), whereas, the region of interest of this study extends up to an axial distance of 40 mm. The computed residence time along with the inlet composition of fuel-air mixture were fed into the inlet stream of jet flame reactor network and the corresponding in-flame temperature and species concentration profiles were predicted at 10 mm, 20 mm and 40 mm heights above the burner.

8.6 Results and Discussion

The numerically predicted in-flame temperature profiles and in-flame species concentration profiles of MO, CME, SME, PME, toluene, heptane and diesel flames at $\Phi = 1.2$ are presented in the following section. The numerically predicted values are compared with the corresponding experimental results and are found to be in reasonable agreement.

8.6.1 In-flame temperature profiles

The radial in-flame temperature profiles of the MO flame are presented in Figure 8.19. The measured peak temperature at 10 mm flame height was 1808K and the predicted peak temperature was 1971 K. Similarly, at 20 mm and 40 mm flame heights, the measured peak temperatures were 1760 K and 1685 K respectively while the predicted temperatures were 1994K and 1882 K. The jet flame reactor model over predicted peak temperatures by about 9%, 13% and 12% at 10 mm, 20 mm and 40 mm flame heights respectively.

The temperature profiles of the CME, PME and SME flames are presented in Figures 8.20 - 8.22. The predicted temperature values were about 9% to 16% higher than the corresponding measured temperature values. It is to be noted that the same detailed chemical kinetic mechanism was used for both MO (an individual methyl ester) and commercial biodiesels like CME, SME and PME (mixture of five major components of biodiesels) and it is observed that the biodiesel model successfully predicted the locations of peak temperature, variations of radial temperature profiles at three axial locations (10 mm, 20mm and 40 mm) and the reduction in the temperature with flame

height due to the diffusion and mixing of ambient air. However, the predicted temperature values were about 10% higher than the measured temperature values (experimental uncertainty in temperature measurement was about 5%).

The temperature profiles of toluene, heptane and diesel flames are presented in Figures 8.23 - 8.25. The individual detailed chemical reaction mechanisms pertinent for toluene, heptane and diesel surrogate were included in the corresponding jet flame network models. In general, the predicted temperature values were higher than the corresponding measured temperature values. The toluene model predicted about 9% to 11% higher temperature values than measured temperature values (Figure 8.23). The predictions from heptane and diesel models were about 16% to 18% higher than that of corresponding measured values (Figures 8.24 - 8.25).

These over predictions of temperature were expected since the heat loss from the flames by gas radiation was not accounted for in the model. As discussed in chapter 6, the appearance of tested flames was completely blue without any yellow luminous region; hence the radiation heat loss due to continuum radiation from soot in these flames is negligible. However, the gas band radiation due to water vapor, CO and CO_2 has significant contribution towards the radiation heat loss at this condition (Singh et al., 2016). In order to illustrate this point, the radiation heat loss from the flames was estimated and the temperature profiles were corrected for gas band radiation losses with the emissivity factor of combustion products taken into consideration. A sample calculation of temperature correction is presented in Appendix H. The corrected temperature profiles of MO, CME, SME and PME flames are presented in Figures 8.26 - 8.29. The corrected temperature profiles were found in good agreement with the

measured temperature profiles with the difference being less than 5% of the values. Further, the jet flame reactor network model did not consider radial diffusion of momentum, temperature and species. Thus, the predicted flame widths were about half of those observed experimentally. The detailed chemical kinetic reactions considered in this model along with the required corrections for radiation loss predicted reasonably accurate temperature results. Similarly, the corrected temperature values from the toluene model (Figure 8.30) were in good agreement with the measured values with difference being less than 5%. The over predictions of temperature in heptane (Figure 8.31) and diesel (Figure 8.32) models were reduced from 18% to 8% after corrected for heat loss from gas band radiation.

8.6.2 In-flame species concentration profiles

The predicted in-flame oxygen concentration profiles of the simulated flames are presented in Figures 8.33 - 8.39. The measured oxygen concentration was small near the flame axis and increased towards the edge due to the consumption of oxygen in the combustion reactions within the flame. The jet flame network models successfully predicted this trend in all the simulated flames. The O_2 concentration near the flame axis at 10 mm height was slightly over predicted in the biodiesel flames (MO, CME, SME and PME flames). For instance, in the CME flame (Figure 8.34) the measured oxygen concentration in the flame was close to zero while the model predicted about 4% O_2 concentration near the flame axis. The differences in the predicted values could be due to the assumption of negligible diffusion of species in the radial direction made

in this model. However, the model provided reasonably accurate predictions in determining the extent of reaction zone and the trends of oxygen concentration profiles.

The predicted inflame CO_2 concentration profiles of the simulated flames are presented in Figures 8.40 - 8.46. The CO_2 concentration increased with flame height, indicating the presence of ongoing oxidation reactions. This experimental observation was captured by all the employed models in this study. In the MO flame (Figure 8.40), the location and value of peak CO_2 concentration was accurately predicted by the model. In other biodiesel flames such as CME, SME and PME (Figure 8.41 - 8.43), the model predicted slightly lower values than the experimental results, particularly evident in PME flame (of about 13% lower value), however the computed CO_2 concentration profiles followed the trend of experimentally measured CO_2 concentration profiles. Similar observations were noted in the CO_2 concentration results from the toluene (Figure 8.44) and diesel (Figure 8.46) models. However, the heptane model (Figure 8.45) over predicted CO_2 concentration (by 13%) at 20 mm height, but under predicted the CO_2 values (by 12%) at 40 mm height. This observation signifies that the heptane model assumes a faster CO_2 formation rate at 20 mm flame height, hence over predicted the CO_2 concentration, whereas the oxidation process forming CO_2 continued even at 40 mm height revealed by higher measured peak CO_2 concentration than the model predicted value especially along the flame axis. It is to be noted that the uncertainty in CO_2 concentration measurement was estimated to be ± 8%.

The predicted inflame CO concentration profiles of the simulated flames are presented in Figures 8.47 - 8.53. The experimental results suggested that CO concentration progressively decreased with flame height. The model captured the experimental trend

of CO concentration observed in the tested flames. For instance, in the MO flame (Figure 8.47), the experimental peak CO concentration decreased from 4.1% to 2.2% between 10 mm and 20 mm heights, whereas the predicted CO concentration decreased from 5.2% to 3.0% between 10 mm and 20 mm heights above the burner. In CME (Figure 8.48) and SME (Figure 8.49) flames, the CO prediction at 10 mm flame height exactly matches with the measured CO concentration indicating that the employed biodiesel mechanism was accurate in predicting the CO production from commercial biodiesels by specifying the composition of five principal methyl esters. Similar to the biodiesel model, the original heptane, toluene and diesel surrogate models without nitrogen chemistry primarily focused on the fuel decomposition and subsequent oxidation reactions forming end CO and CO_2 as products. Thus, these models predicted the local CO concentration in the corresponding flames with reasonably good agreement (Figure 8.51 - 8.53). Typically, the CO values predicted at 40 mm height were slightly higher than the measured values, which hinted the reason for the observation of under predicted CO_2 concentration values at the corresponding locations.

The predicted inflame NO concentration profiles of the simulated flames are presented in Figures 8.54 - 8.60. As already mentioned in section 8.4.5, the nitrogen chemistry pertinent to the formation of NO was added to the original chemical reaction mechanisms for biodiesels, heptane, toluene and diesel surrogates. As mentioned earlier, the included nitrogen chemistry comprised of reaction sets pertinent to the thermal (Zeldovich), Prompt (Fenimore), Intermediate (N_2O) mechanisms. Hence, the employed models in this study extensively considered the reactions responsible for the formation of NO through all known reaction pathways. The experimental results

(discussed in chapter 7) suggested that NO concentration progressively increased with flame height, in contrast to CO concentration. The model captured this experimental trend of increasing NO concentration with height observed in the tested flames. In the MO flame (Figure 8.54), the measured peak NO concentration increased from 52 ppm to 162 ppm between 10 mm and 40 mm heights, while the computed peak concentration increased from 101 ppm to 157 ppm. The difference between the measured and predicted NO concentration values decreased with flame height. At 10 mm flame height, the predicted NO concentration was about twice that of measured NO concentration while at 40 mm height, the predicted and measured NO values were about the same. Similar trends were observed in biodiesel flames: CME, SME and PME (Figures 8.55 - 8.57) flames in which the measured peak values at 40 mm flame height were 163 ppm, 180 ppm and 155 ppm respectively while the predicted peak NO values were 168 ppm, 176 ppm and 162 ppm respectively. The minimal observed difference between the predicted and measured NO value in the far burner region is due to the residence time effect, that is, the characteristic chemical time scale of NO is large since NO formation chemistry is much slower than the combustion chemistry (Turns, 2011). Hence the local NO concentration level depends on the chemical state, age and history of the gas mixture. Therefore, the deviations between the measured and predicted values decreased with increased residence time, in other words, increased flame height. Further, the predicted peak NO concertation values at the 40 mm height were found to correlate with the DOU of the corresponding fuel, in agreement with the experimental results. Among the methyl esters, the predicted peak NO concentrations were 162 ppm, 168 ppm, and 176 ppm for PME (DOU:1.7), CME (DOU:2.0) and SME (DOU:2.5)

flames respectively. Similarly, the among the petroleum fuels, the predicted peak NO concentration at 40 mm height for heptane, diesel and toluene flames were 293 ppm, 412 ppm and 665 ppm respectively, in accordance with their corresponding DOU values (0 for heptane, 3 for diesel and 4 for toluene).

8.7 Chapter conclusions

The following conclusions were derived from the computational analysis of MO, CME, SME, PME, toluene, heptane and diesel surrogate flames performed in this study:

- Numerical models for the combustion of laminar flames of aforementioned fuels were successfully developed using FLUENT and CHEMKIN software packages (Jet flow reactor network model).
- The model predicted slightly higher temperature (9% to 16%) values since heat loss due to gas band radiation was not considered and the predicted temperature results were found to closely agree with measured temperature results when corrected for heat loss due to gas band radiation.
- Models were able to capture the location of peak values and the general behavior of the O_2, CO_2, CO and NO concentration profiles in the flames of both methyl ester and petroleum family of fuels.
- Computational results reaffirmed the experimental observation of increasing NO concentration with the degree of fuel unsaturation. In general, the discrepancies found in the numerical predictions could be due to the computational limitations as discussed previously and the reaction parameters considered in the chemical kinetic mechanisms.

Table 8.1 Properties of fuel/air mixture

Fuel	[a,b]Thermal conductivity (W/m-K)	[c]Viscosity (kg/m-s)	[d]Mass diffusivity (m^2/s)	[b]Density (kg/m^3)	[b]Cp (J/kg-K)
MO	0.0831	3.05E-06	6.16E-06	Ideal gas	Mixing-law
CME	0.0831	3.05E-06	6.16E-06	Ideal gas	Mixing-law
SME	0.0831	3.05E-06	6.08E-06	Ideal gas	Mixing-law
PME	0.0831	6.12E-06	2.51E-05	Ideal gas	Mixing-law
Toluene	0.0454	1.29E-05	2.88E-05	Ideal gas	Mixing-law
Heptane	0.0454	1.17E-05	2.88E-05	Ideal gas	Mixing-law
Diesel	0.0454	7.28E-06	2.88E-05	Ideal gas	Mixing-law

[a]Kanury (1975); [b]FLUENT (2011); [c]Maxwell (1950); [d]Gilliland (1934);

Table 8.2 Mass fraction of biodiesel component in the fuel/air mixture

Components	Formula	PME	CME	SME
Methyl myristate	$C_{15}H_{30}O_2$	0.0013	0.000	0.000
Methyl palmitate	$C_{17}H_{34}O_2$	0.0381	0.004	0.009
Methyl stearate	$C_{19}H_{38}O_2$	0.0042	0.002	0.004
Methyl oleate	$C_{19}H_{36}O_2$	0.0360	0.053	0.020
Methyl linoleate	$C_{19}H_{34}O_2$	0.0090	0.019	0.048
Methyl linolenate	$C_{19}H_{32}O_2$	0.0001	0.010	0.007
	ΣY_{fuel}	0.0886	0.0874	0.0881

Table 8.3 Under - relaxation parameters

Pressure	0.3
Density	1.0
Body forces	1.0
Momentum	0.7
Fuel	0.8
O_2	0.8
Energy	0.9

Table 8.4 Discretization methods

Pressure	Standard
Momentum	First order upwind
Fuel	First order upwind
O_2	First order upwind
Energy	First order upwind

Table 8.5 Inlet conditions

Fuel	[a]Inlet velocity	Inlet temperature (K)	[a]Y_{fuel}	[a]Y_{O2}	[a]Y_{N2}
MO	3.26	700	0.0874	0.2191	0.6935
CME	3.29	700	0.0874	0.2191	0.6935
SME	3.28	700	0.0881	0.2188	0.6931
PME	3.20	700	0.0886	0.2176	0.6938
Toluene	3.55	700	0.082	0.1956	0.7224
Heptane	3.10	700	0.0736	0.2015	0.7249
Diesel	3.60	700	0.0773	0.2151	0.7076

[a]calculated

Table 8.6 Boundary conditions

Outlet		
Boundary type	Pressure outlet	
Gauge Pressure (Pa)	0	
Back flow total temperature (K)	300	
Backflow direction specification method	Normal to boundary	
Species mass fraction	YO_2	0.2331
	YN_2	0.7669
Velocity inlet		
Boundary type	Inlet	
Velocity specification method	Magnitude, Normal to boundary	
Reference frame	Absolute	
Velocity magnitude (m/s)	Ref Table 8.1	
Inlet temperature (K)	700	
Species mass fraction	Y_{fuel}	Given in Table 8.1 and 8.2
	YO_2	Given in Table 8.1 and 8.2
	YN_2	Given in Table 8.1 and 8.2
Burner		
Boundary type	Wall	
Wall motion	Stationary	
Shear condition	No slip	
Heat flux (W/m^2)	0	
Heat generation (W/m_3)	0	
Species	Zero diffusivity flux	
Symmetry		
Boundary type	Axi-symmetry	

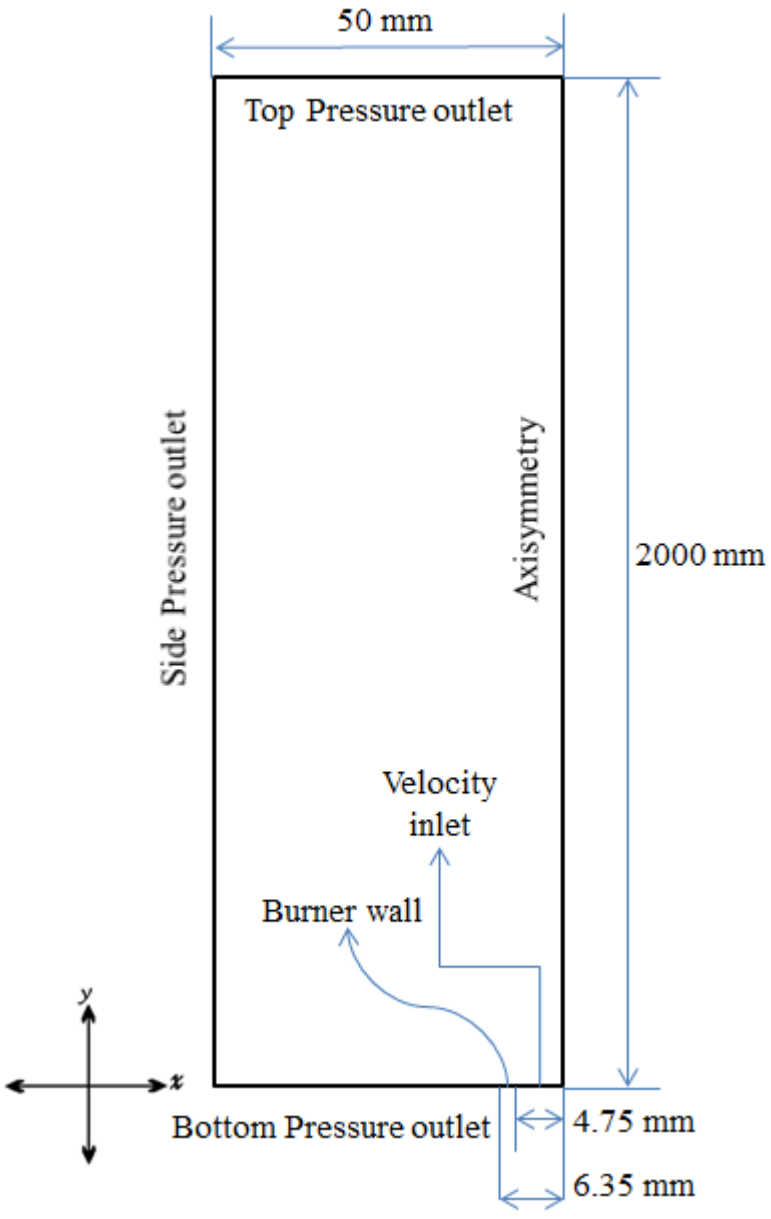

Figure 8.1 Schematic diagram of the computational domain

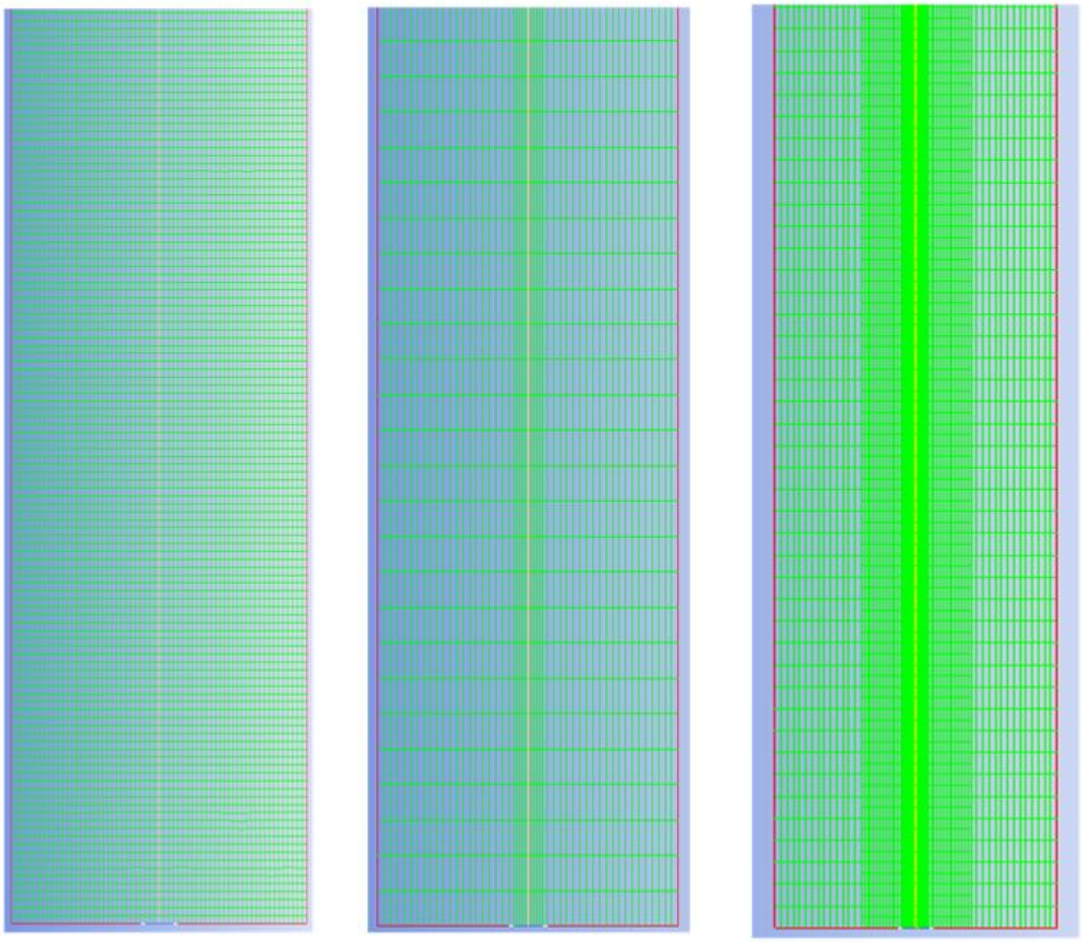

(a) (b) (c)

Figure 8.2 Variation of grid type (a) No adaptation (b) Adaptation 1 (c) Adaptation 2

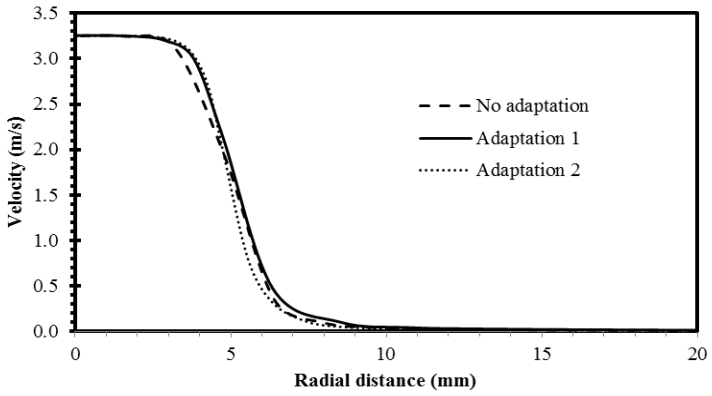

(a)

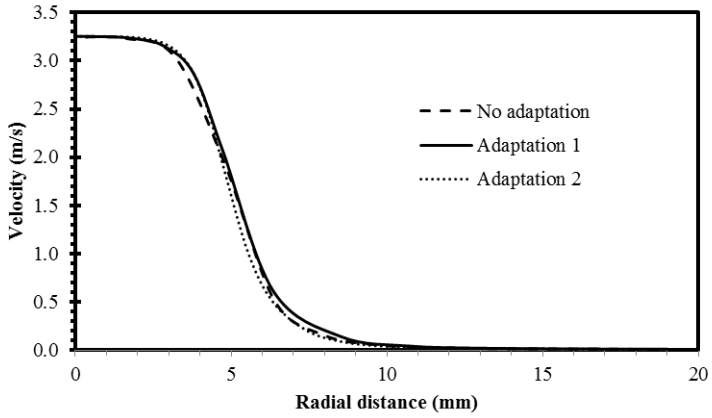

(b)

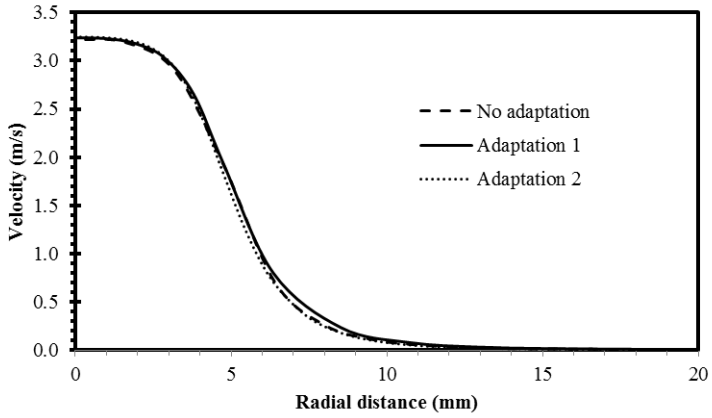

(c)

Figure 8.3 Velocity variations with grid size for (a) 10 mm (b) 20 mm (c) 40 mm height above the burner for non-reacting methyl oleate/ air mixture

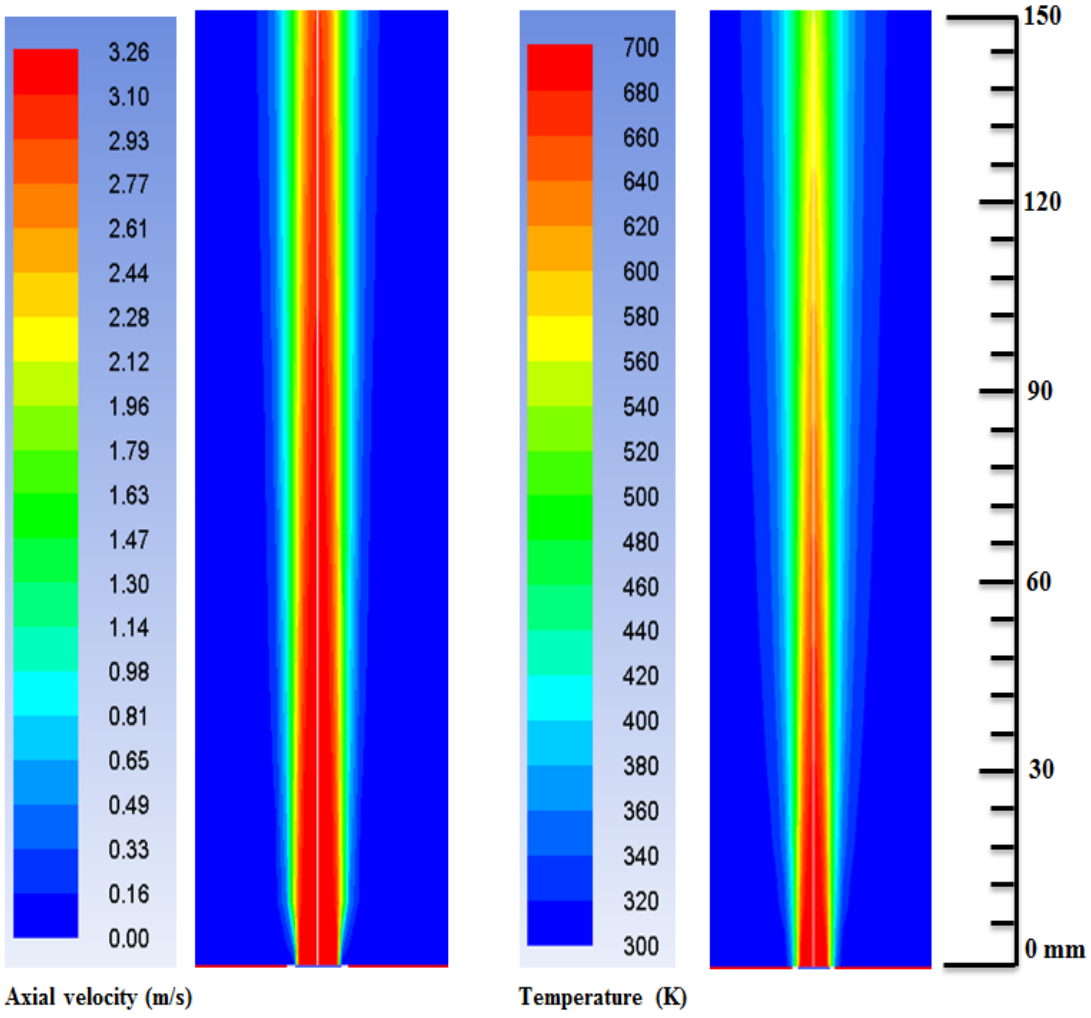

(a) (b)

Figure 8.4 Contour plots of (a) axial velocity and (b) temperature in a non-reacting methyl oleate/air jet

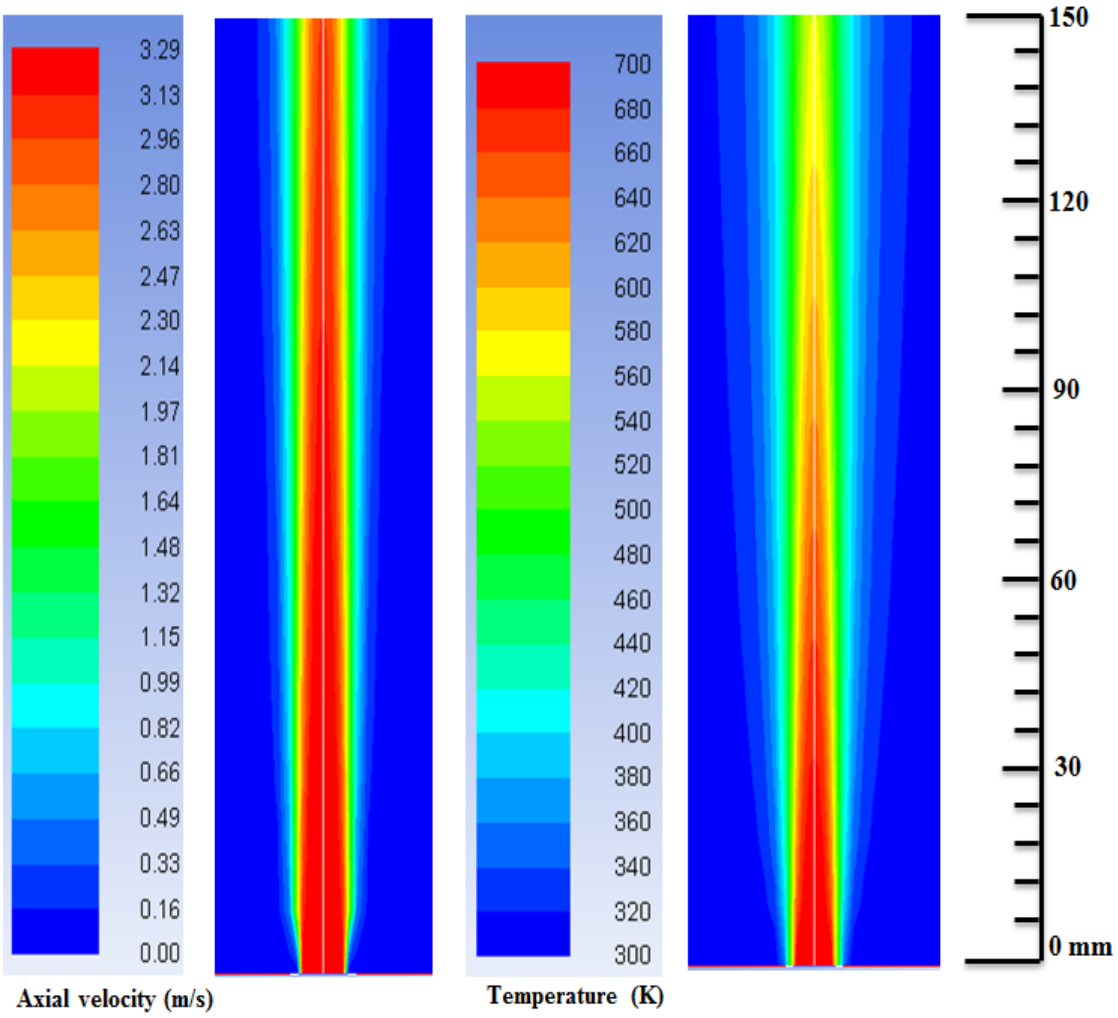

(a) (b)

Figure 8.5 Contour plots of (a) axial velocity and (b) temperature in a non-reacting CME/air jet

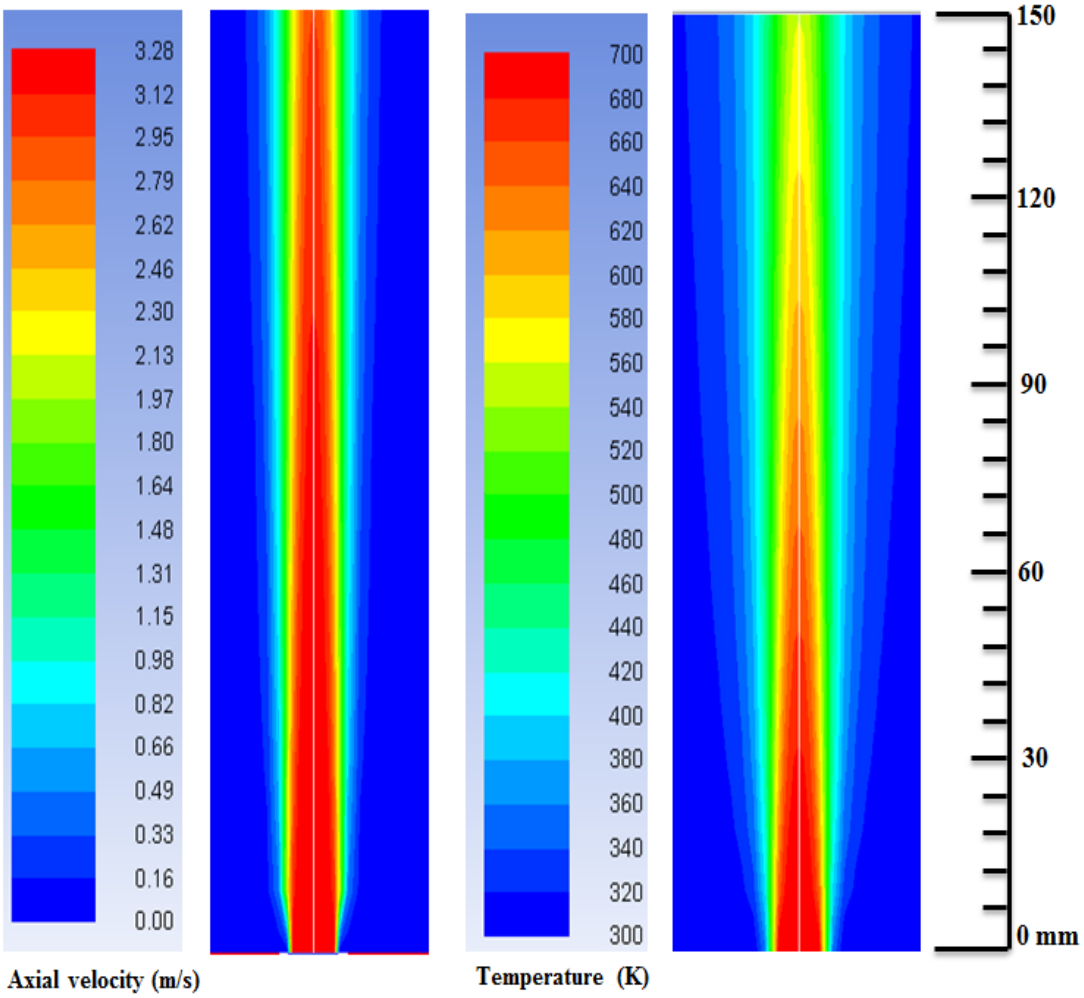

(a) (b)

Figure 8.6 Contour plots of (a) axial velocity and (b) temperature in a non-reacting SME/air jet

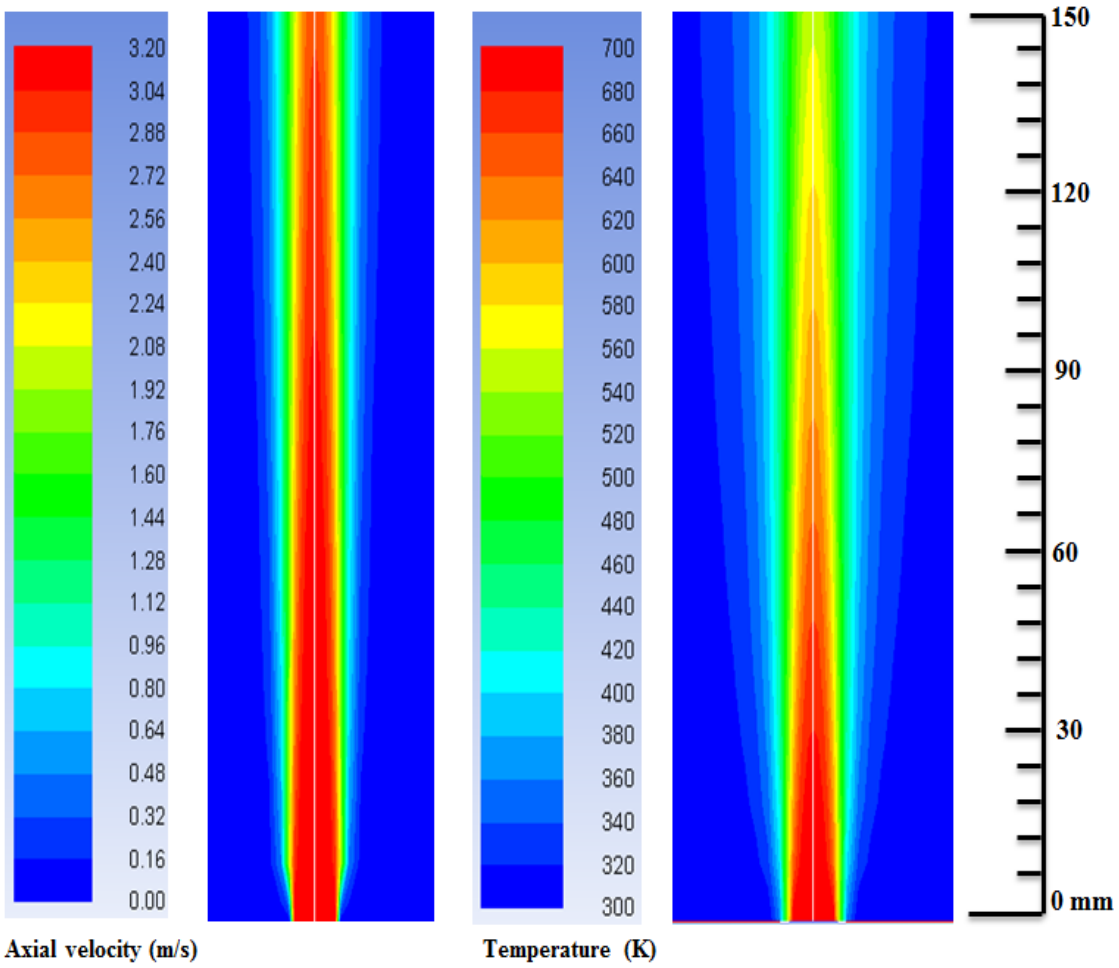

(a) (b)

Figure 8.7 Contour plots of (a) axial velocity and (b) temperature in a non-reacting PME/air jet

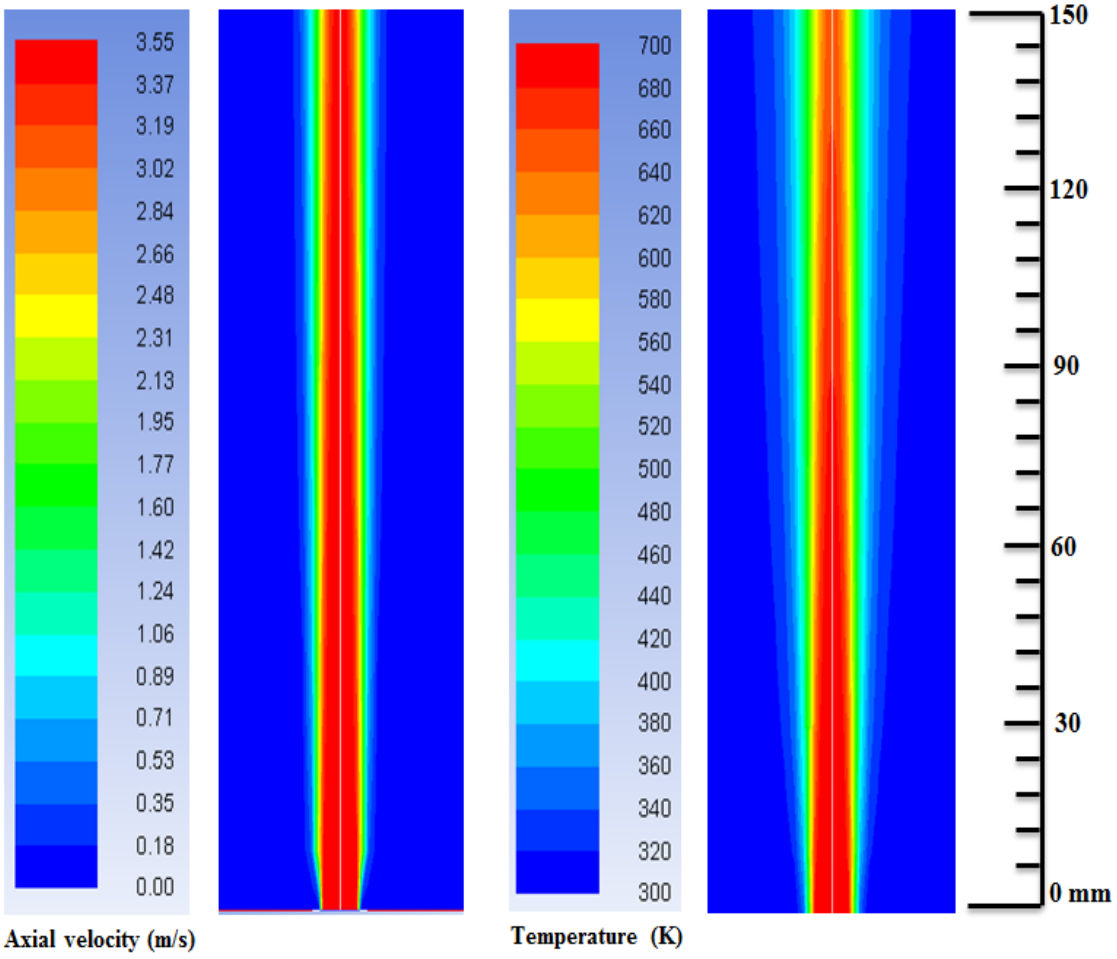

(a) (b)

Figure 8.8 Contour plots of (a) axial velocity and (b) temperature in a non-reacting toluene/air jet

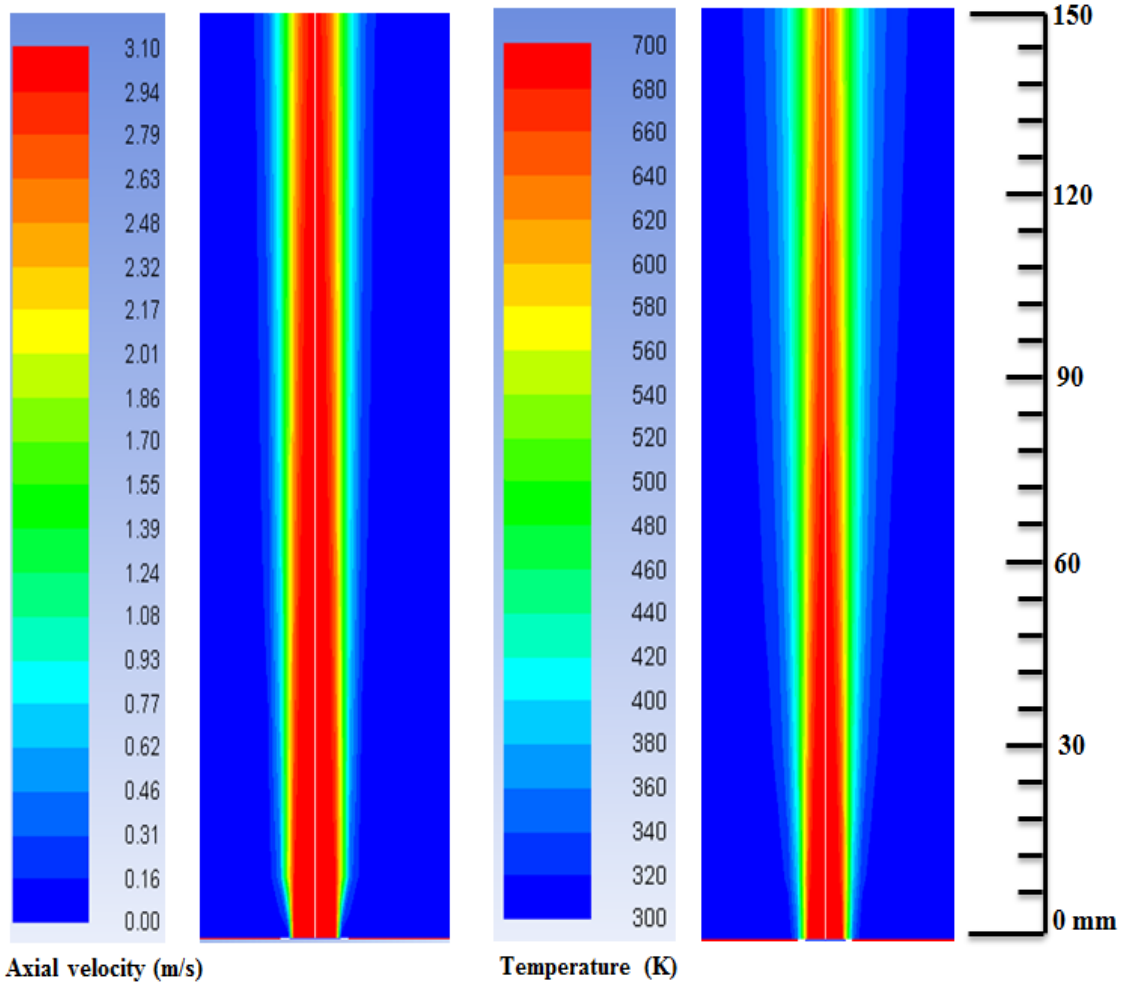

(a) (b)

Figure 8.9 Contour plots of (a) axial velocity and (b) temperature in a non-reacting heptane/air jet

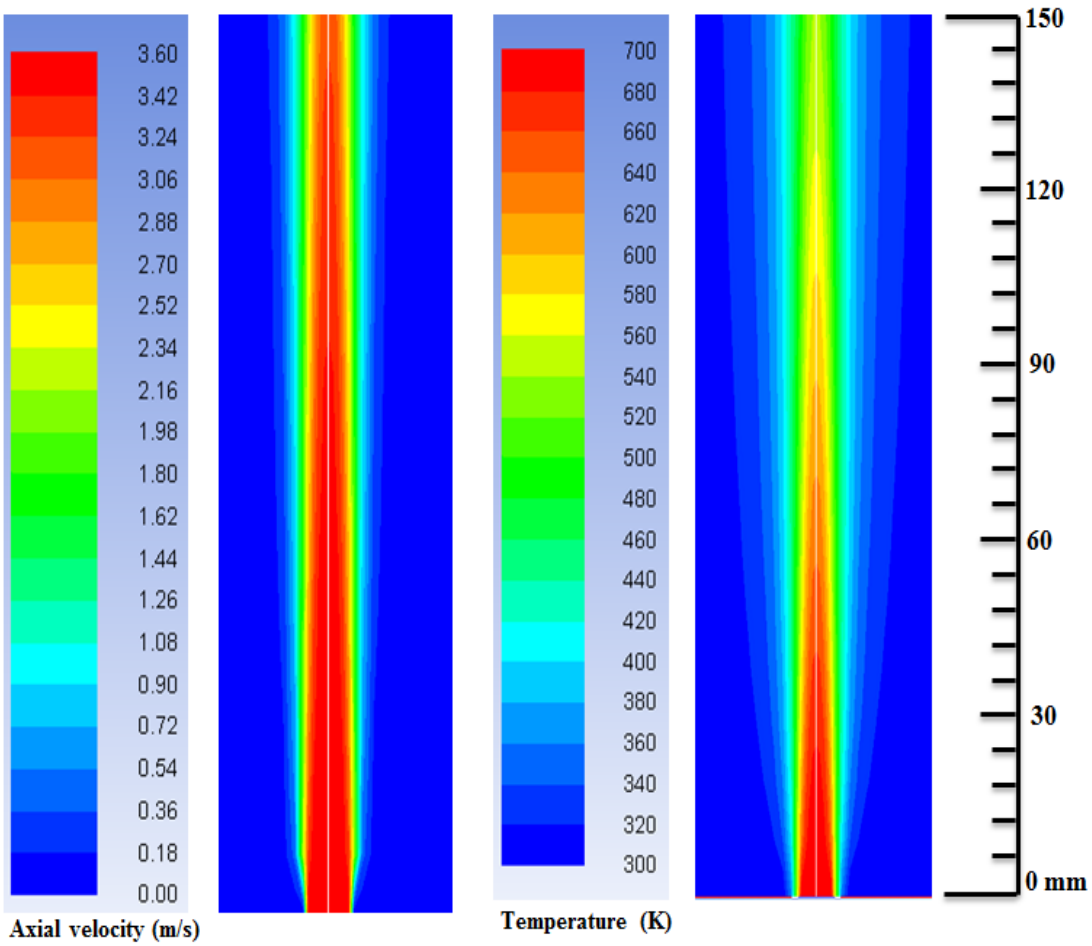

(a) (b)

Figure 8.10 Contour plots of (a) axial velocity and (b) temperature in a non-reacting diesel /air jet

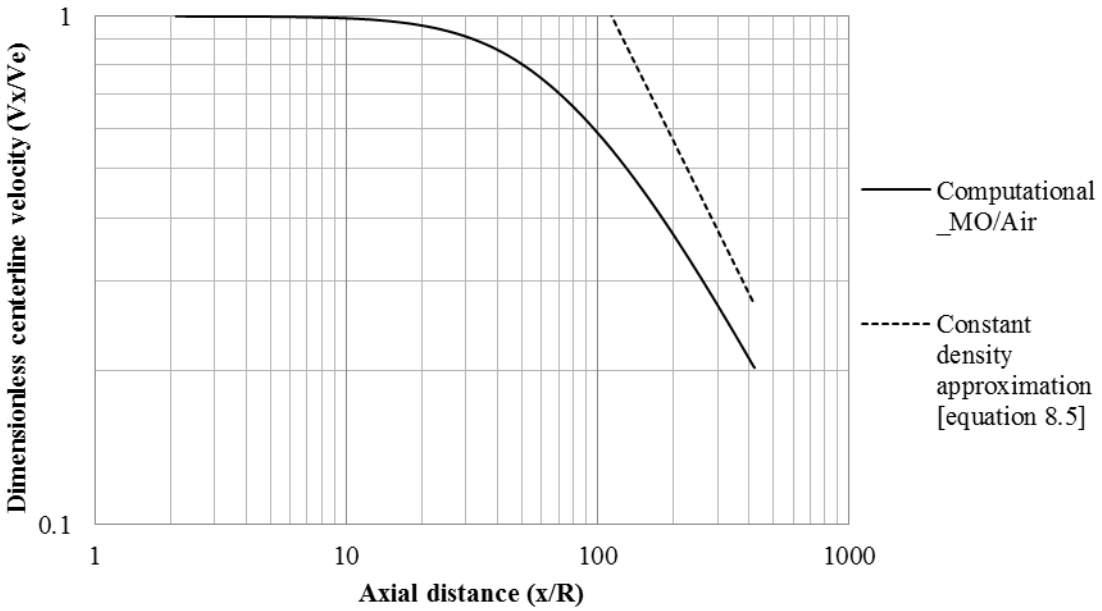

Figure 8.11 Centerline velocity decay for laminar jet of non-reacting MO/air mixture

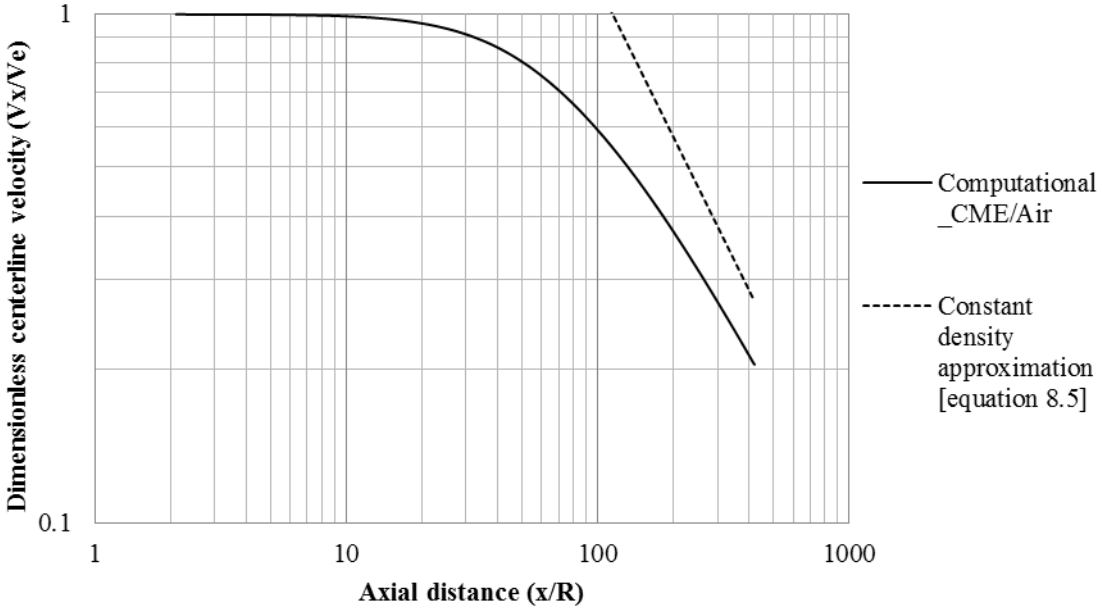

Figure 8.12 Centerline velocity decay for laminar jet of non-reacting CME/air mixture

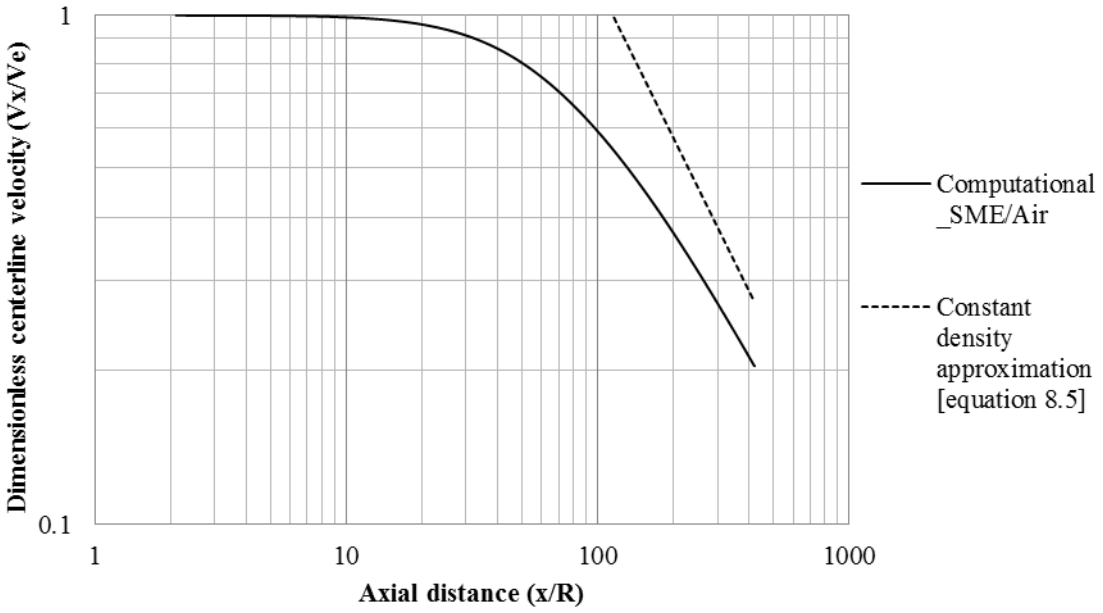

Figure 8.13 Centerline velocity decay for laminar jet of non-reacting SME/air mixture

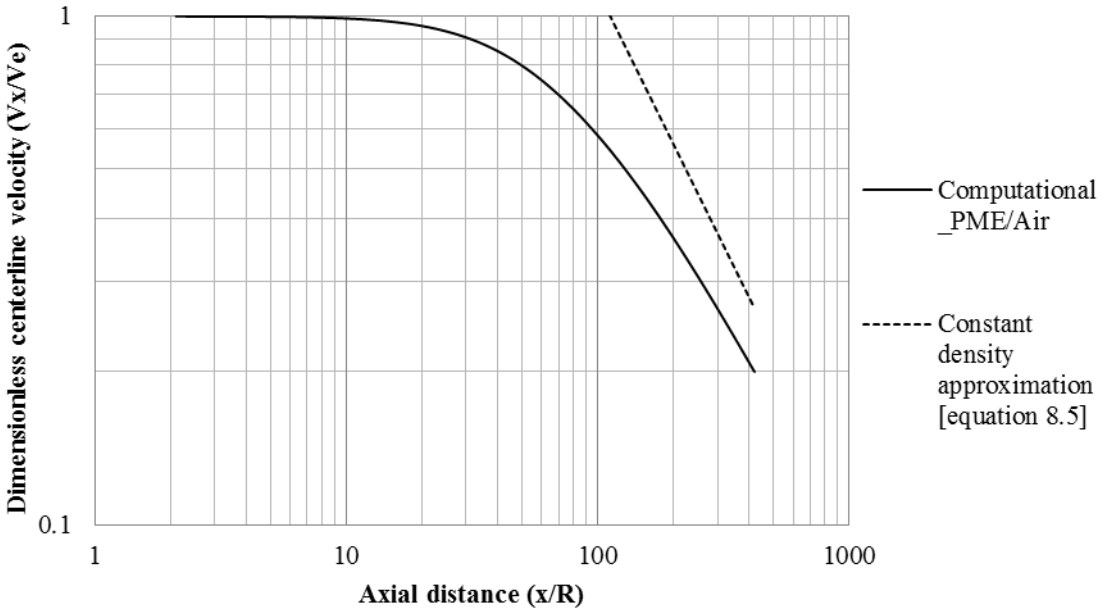

Figure 8.14 Centerline velocity decay for laminar jet of non-reacting PME/air mixture

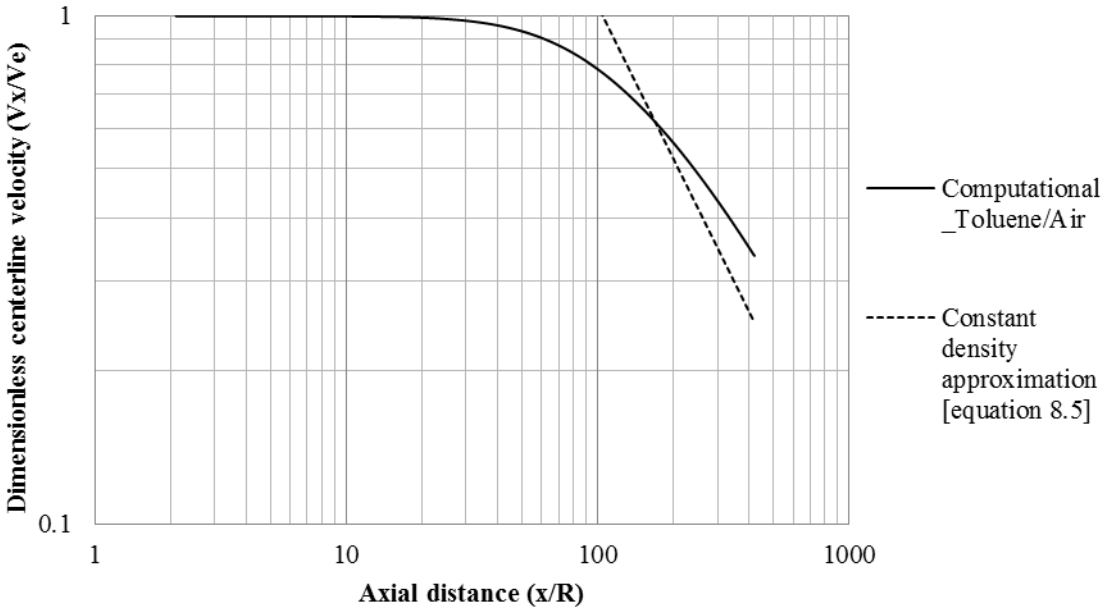

Figure 8.15 Centerline velocity decay for laminar jet of non-reacting Toluene/air mixture

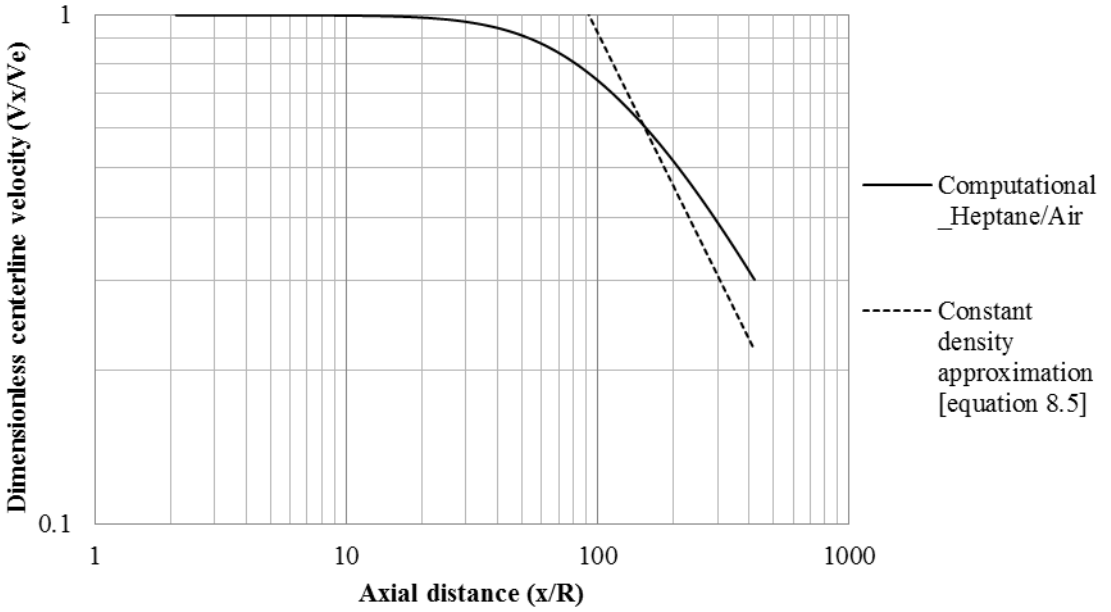

Figure 8.16 Centerline velocity decay for laminar jet of non-reacting Heptane/air mixture

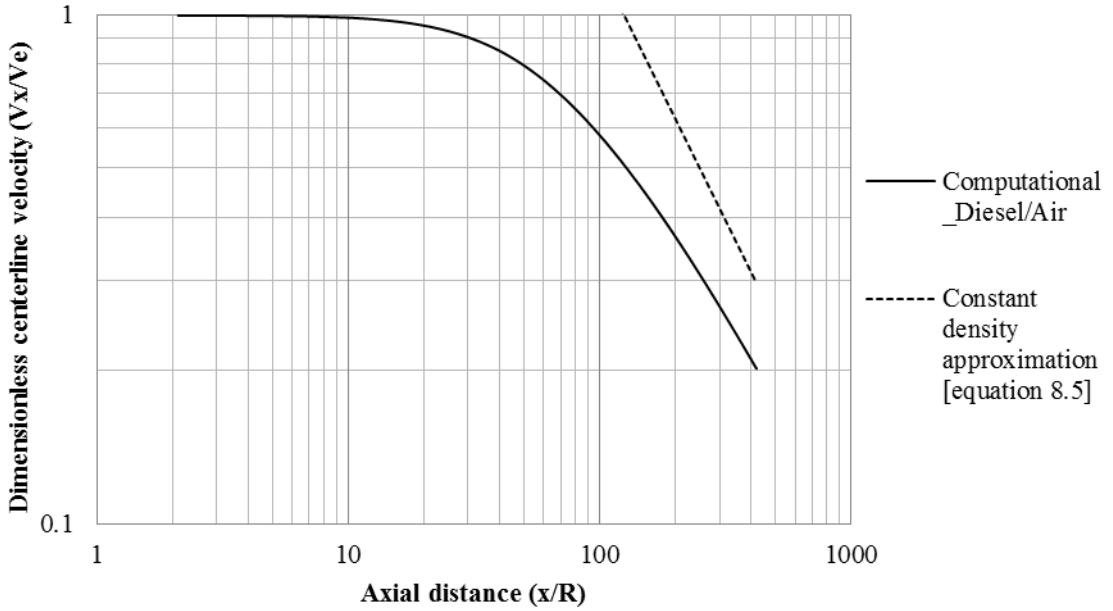

Figure 8.17 Centerline velocity decay for laminar jet of non-reacting Diesel/air mixture

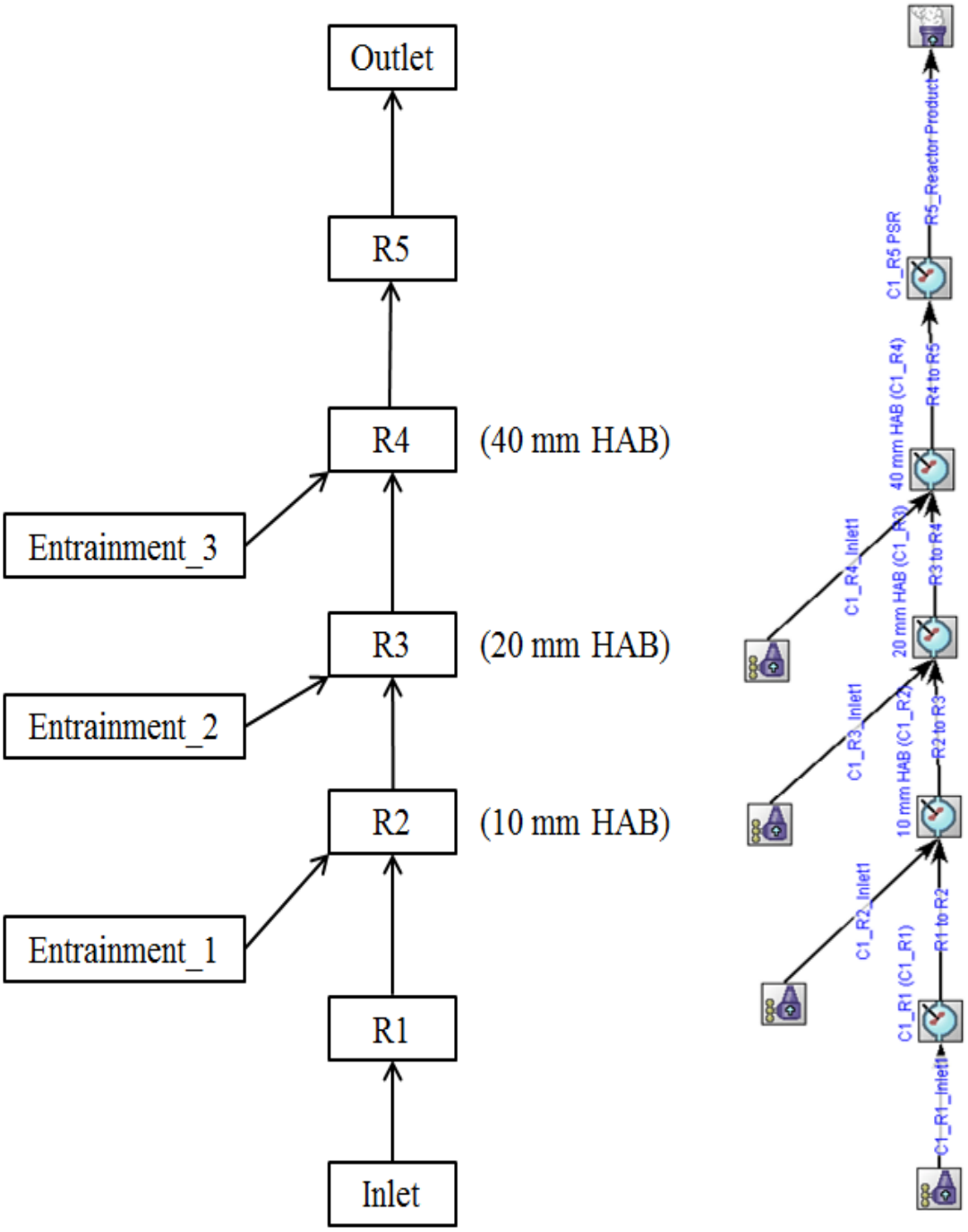

Figure 8.18 Jet flame reactor network schematic diagram and actual model in CHEMKIN interface

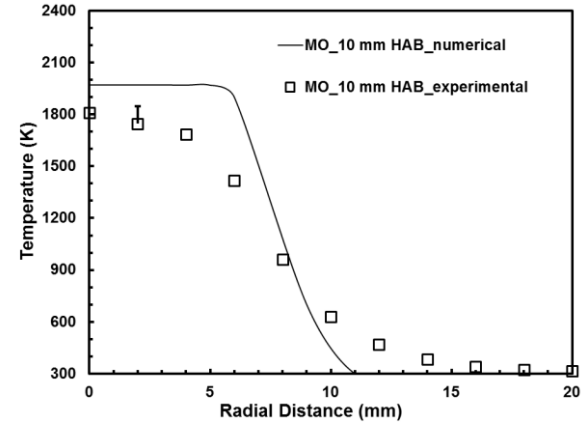

(a)

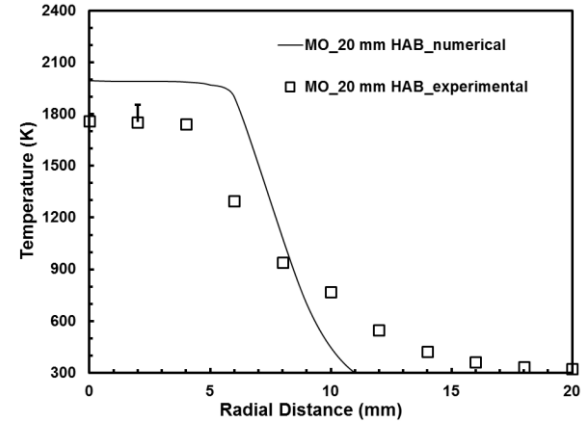

(b)

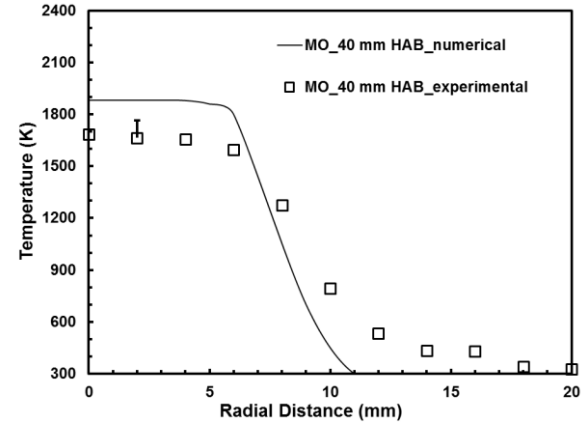

(c)

Figure 8.19 Temperature profiles for methyl oleate flame at (a) 10 mm (b) 20 mm (c) 40 mm height above the burner

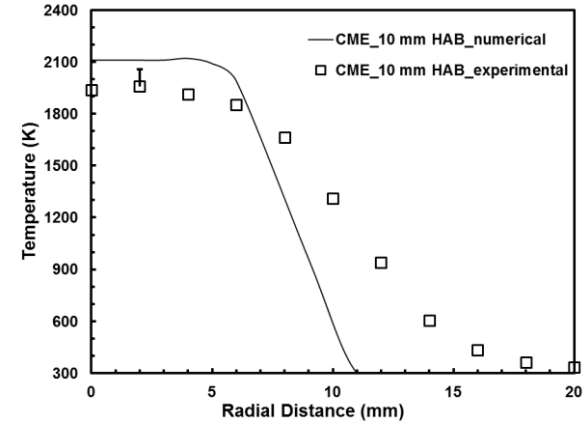

(a)

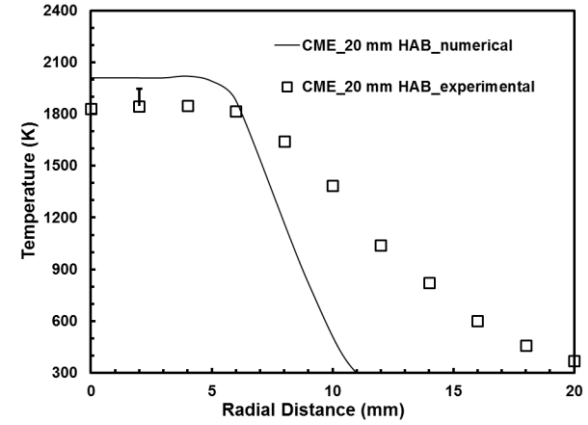

(b)

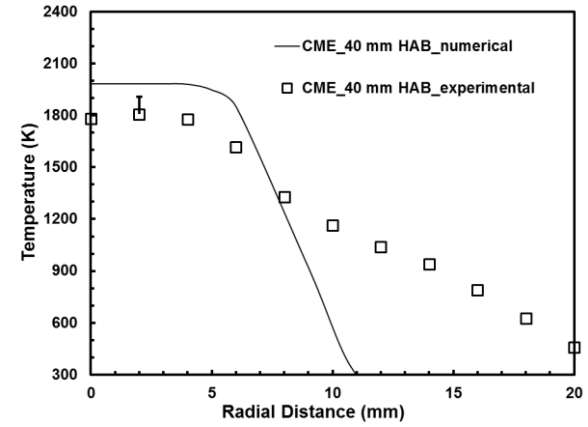

(c)

Figure 8.20 Temperature profiles for CME flame at (a) 10 mm (b) 20 mm (c) 40 mm height above the burner

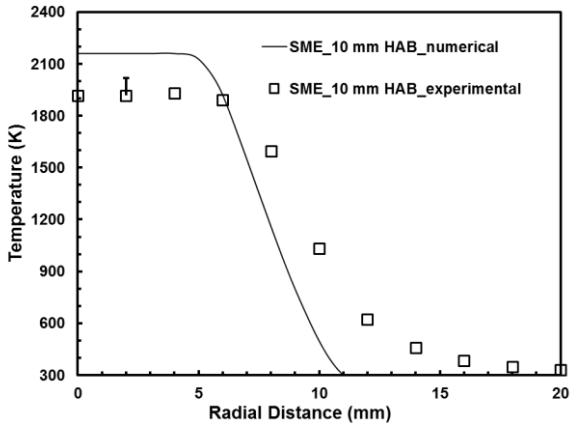

(a)

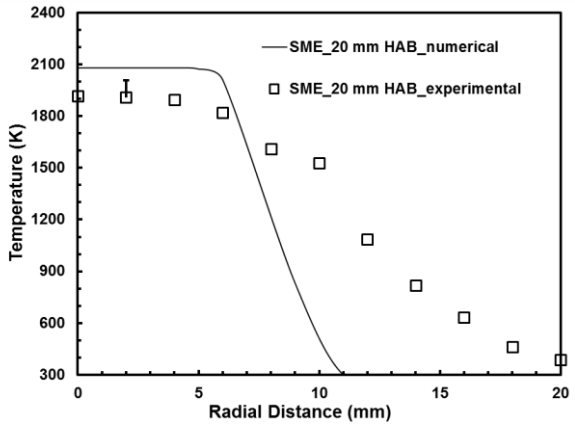

(b)

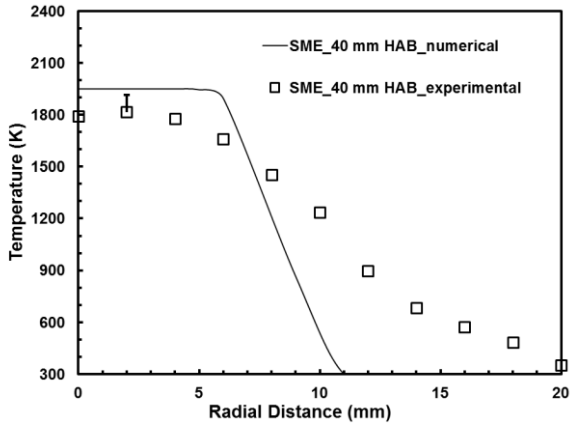

(c)

Figure 8.21 Temperature profiles for SME flame at (a) 10 mm (b) 20 mm (c) 40 mm height above the burner

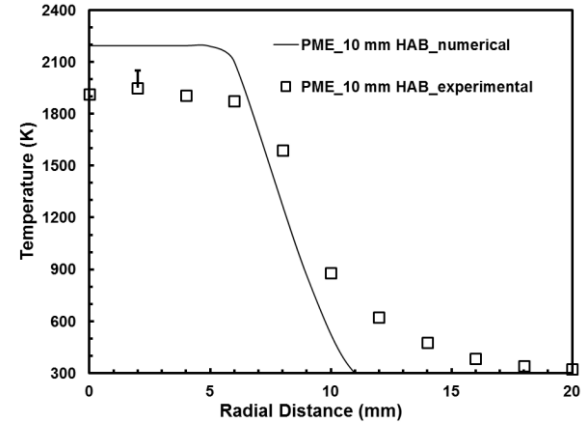

(a)

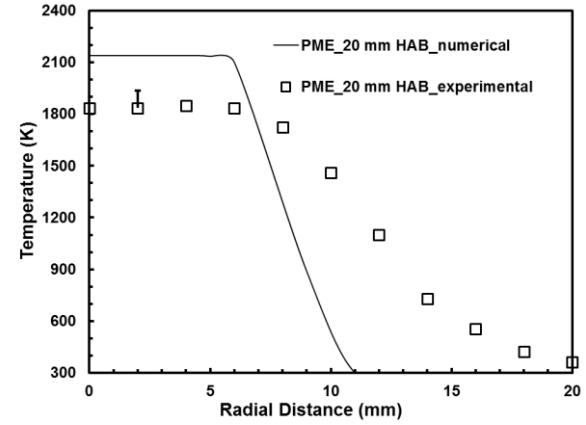

(b)

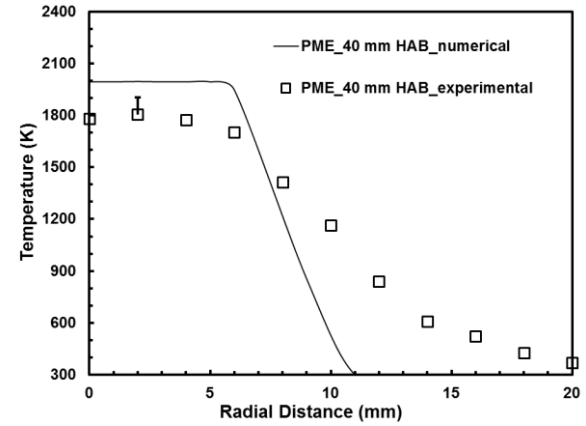

(c)

Figure 8.22 Temperature profiles for PME flame at (a) 10 mm (b) 20 mm (c) 40 mm height above the burner

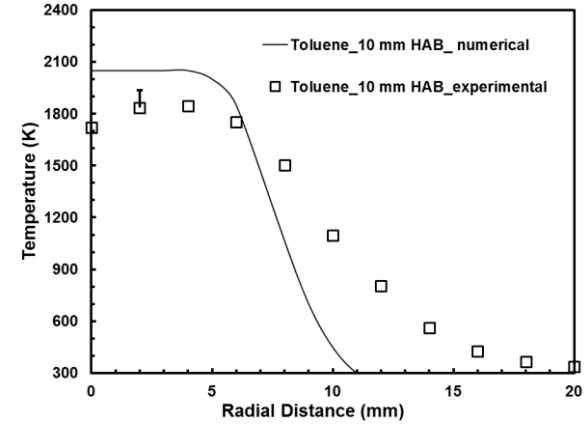

(a)

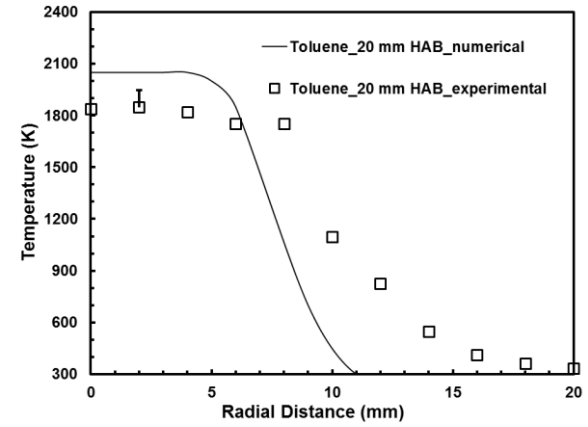

(b)

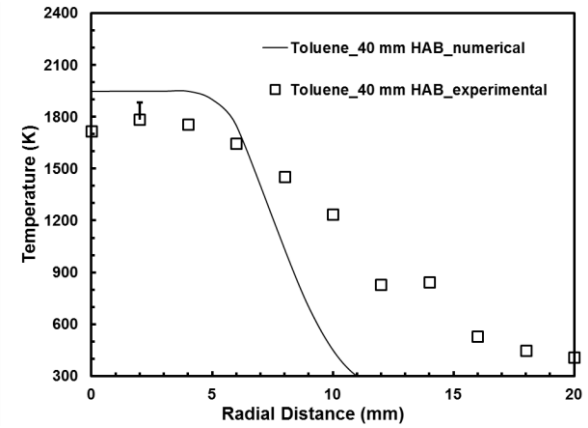

(c)

Figure 8.23 Temperature profiles for toluene flame at (a) 10 mm (b) 20 mm (c) 40 mm height above the burner

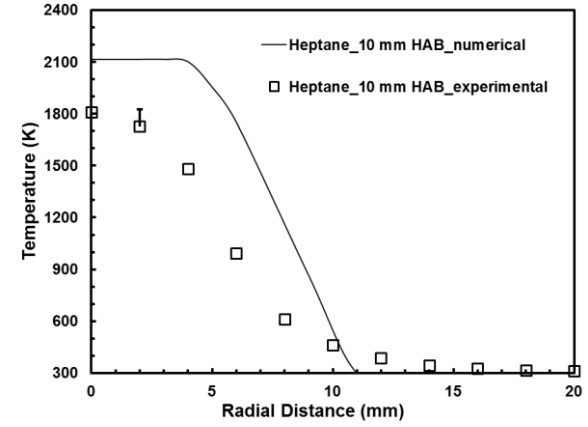

(a)

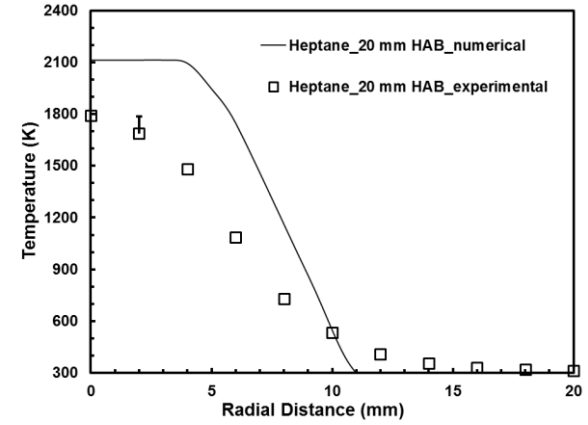

(b)

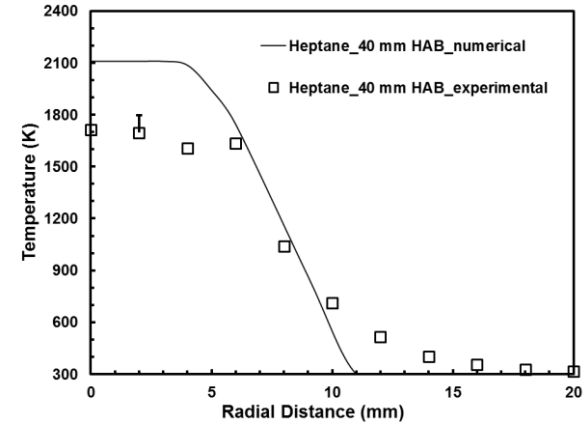

(c)

Figure 8.24 Temperature profiles for heptane flame at (a) 10 mm (b) 20 mm (c) 40 mm height above the burner

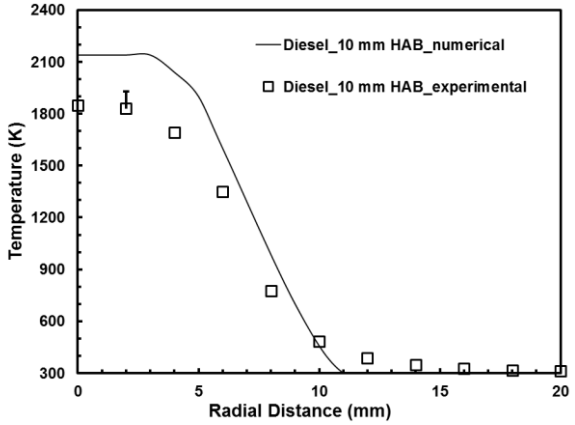

(a)

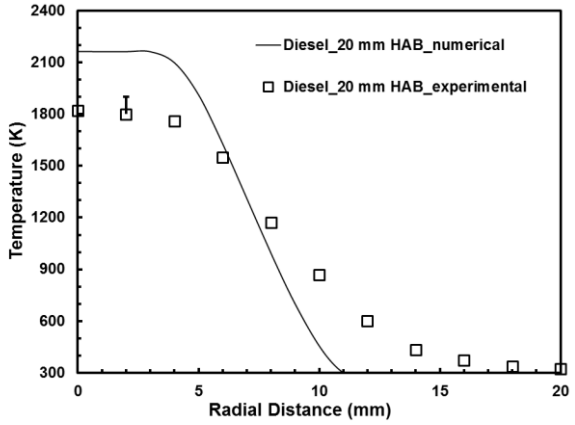

(b)

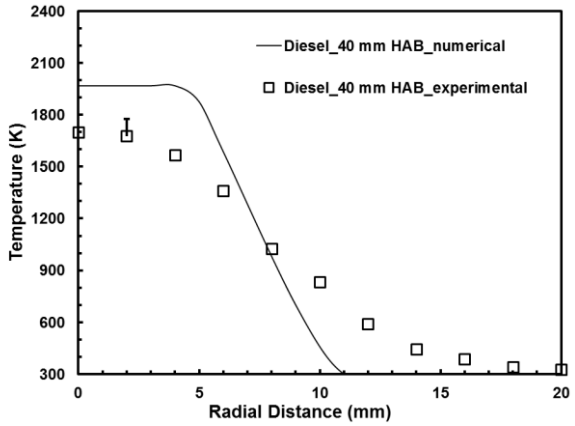

(c)

Figure 8.25 Temperature profiles for diesel flame at (a) 10 mm (b) 20 mm (c) 40 mm height above the burner

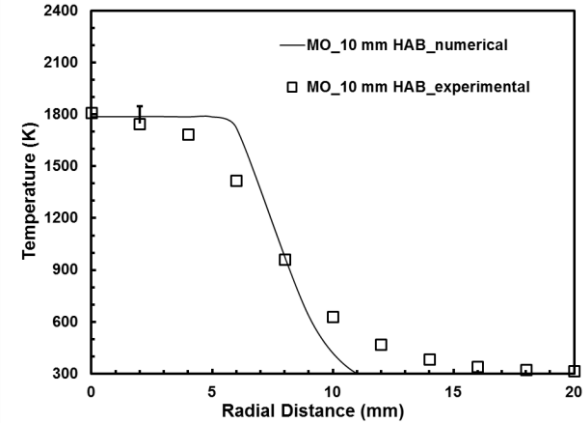

(a)

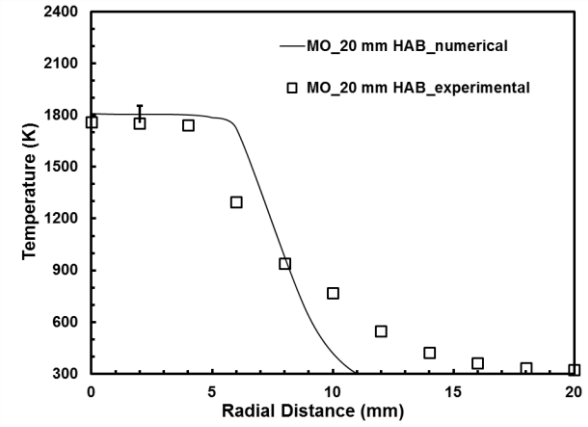

(b)

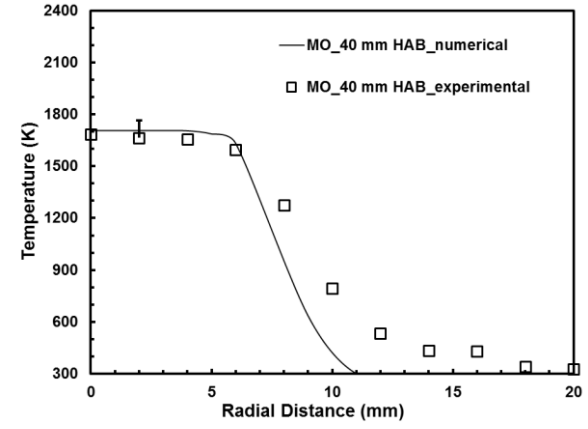

(c)

Figure 8.26 Radiation corrected temperature profiles for methyl oleate flame at (a) 10 mm (b) 20 mm (c) 40 mm height above the burner

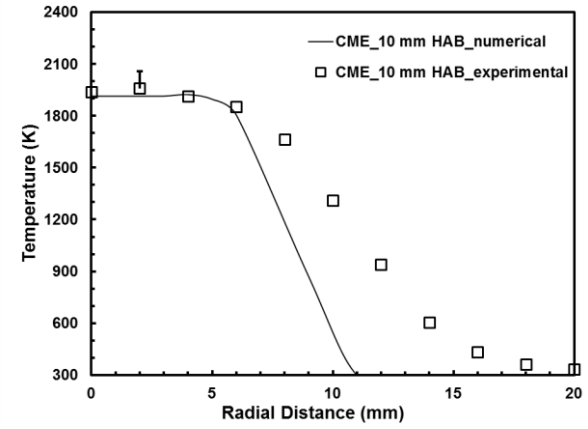

(a)

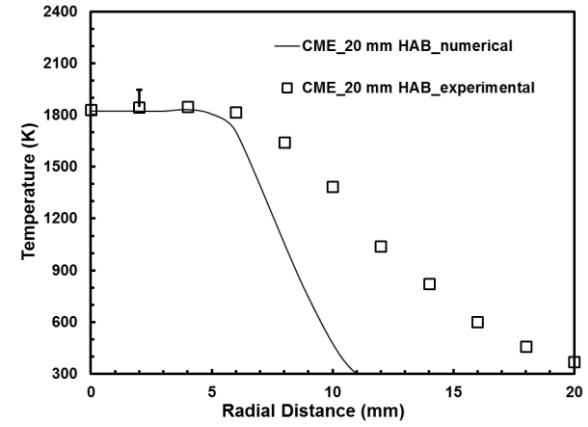

(b)

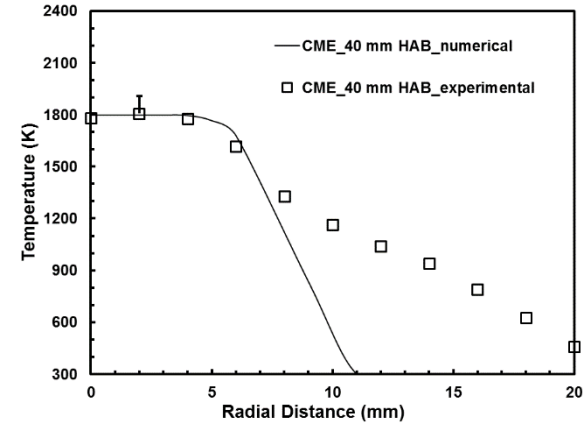

(c)

Figure 8.27 Radiation corrected temperature profiles for CME flame at (a) 10 mm (b) 20 mm (c) 40 mm height above the burner

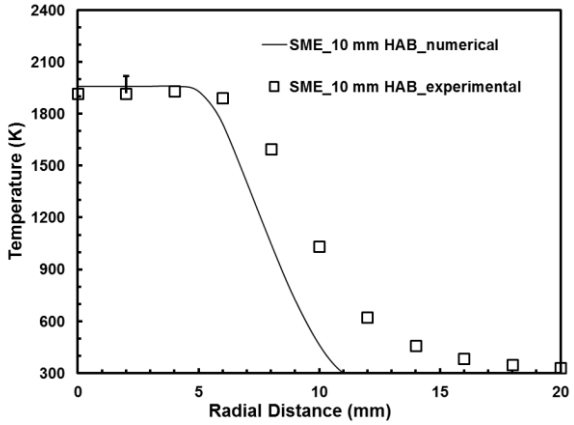

(a)

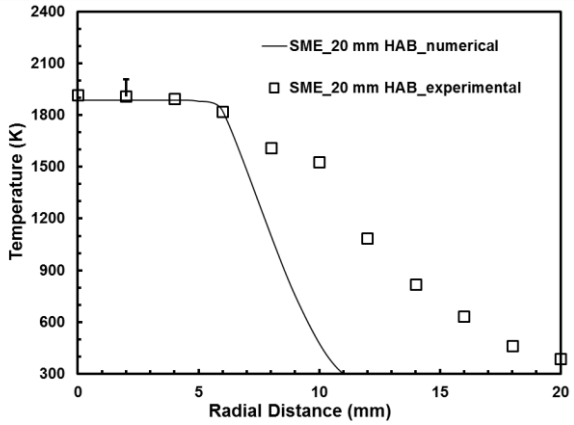

(b)

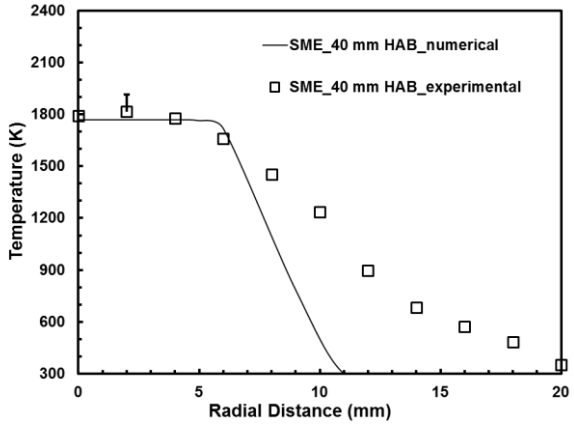

(c)

Figure 8.28 Radiation corrected temperature profiles for SME flame at (a) 10 mm (b) 20 mm (c) 40 mm height above the burner

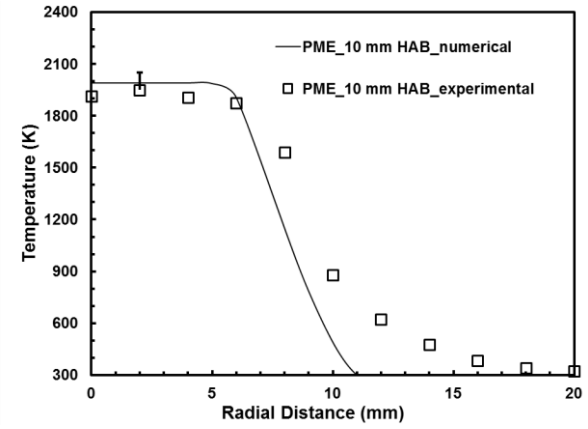

(a)

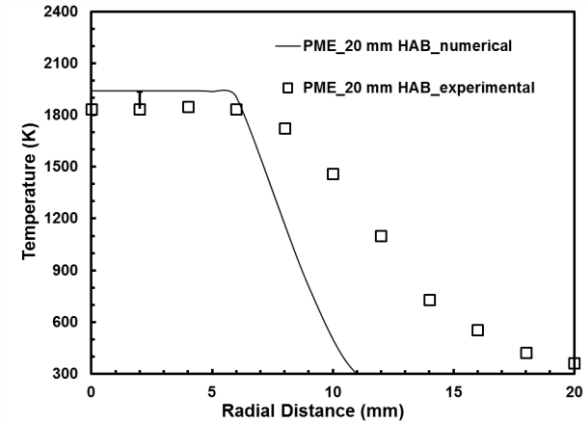

(b)

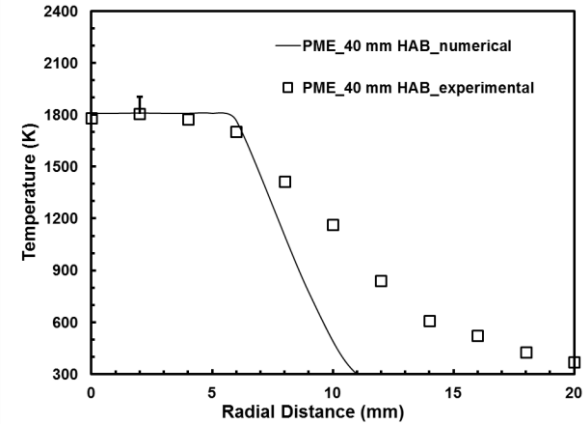

(c)

Figure 8.29 Radiation corrected temperature profiles for PME flame at (a) 10 mm (b) 20 mm (c) 40 mm height above the burner

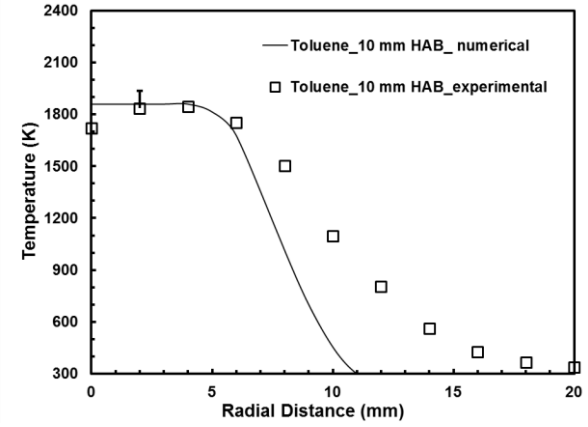

(a)

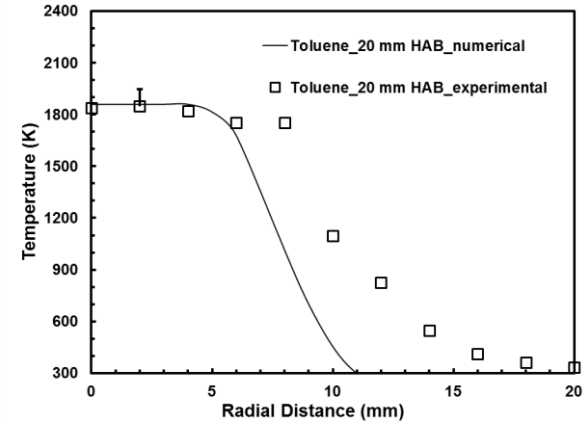

(b)

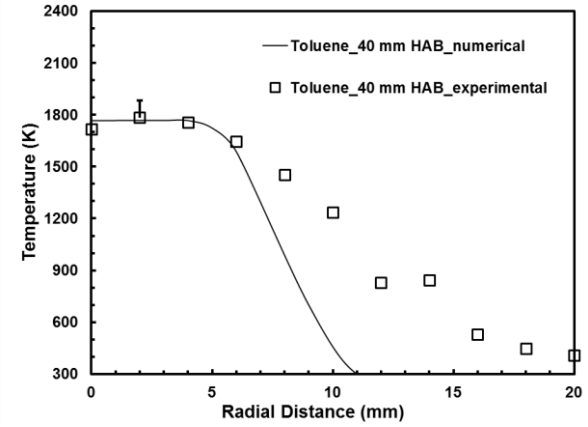

(c)

Figure 8.30 Radiation corrected temperature profiles for toluene flame at (a) 10 mm (b) 20 mm (c) 40 mm height above the burner

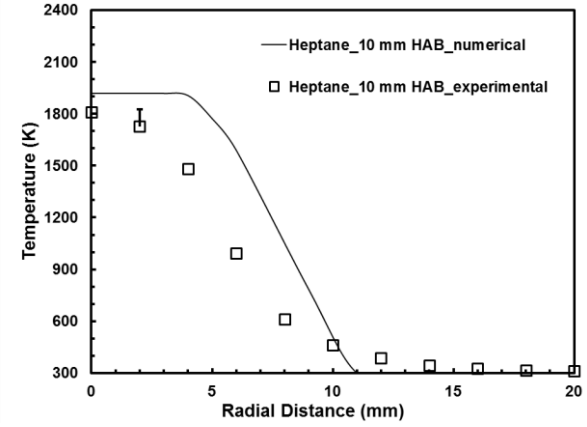

(a)

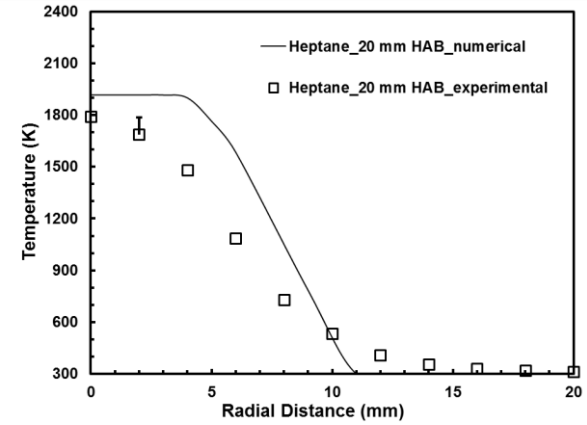

(b)

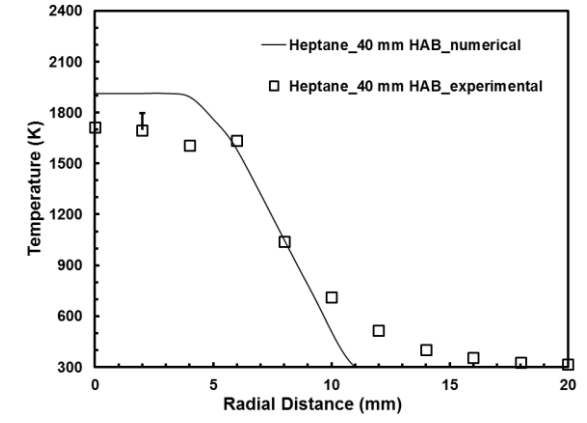

(c)

Figure 8.31 Radiation corrected temperature profiles for heptane flame at (a) 10 mm (b) 20 mm (c) 40 mm height above the burner

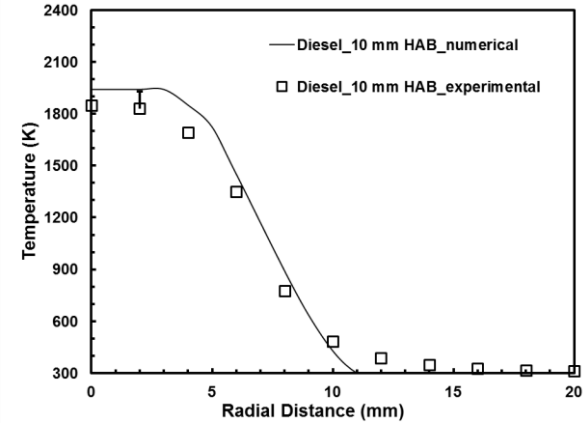

(a)

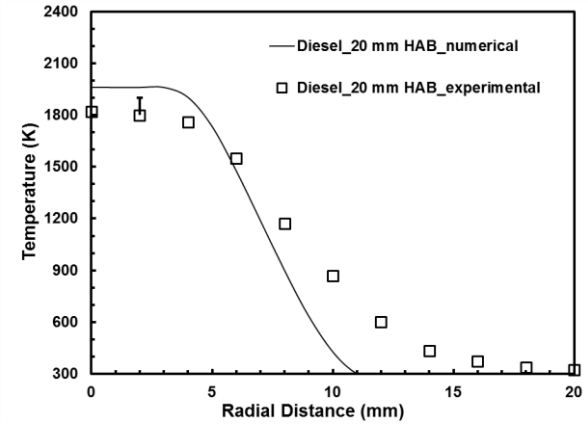

(b)

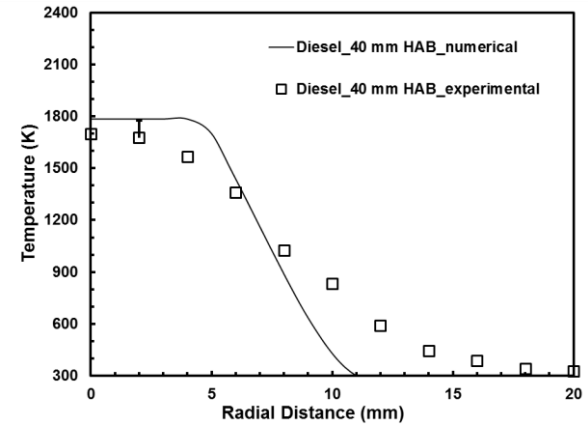

(c)

Figure 8.32 Radiation corrected temperature profiles for diesel flame at (a) 10 mm (b) 20 mm (c) 40 mm height above the burner

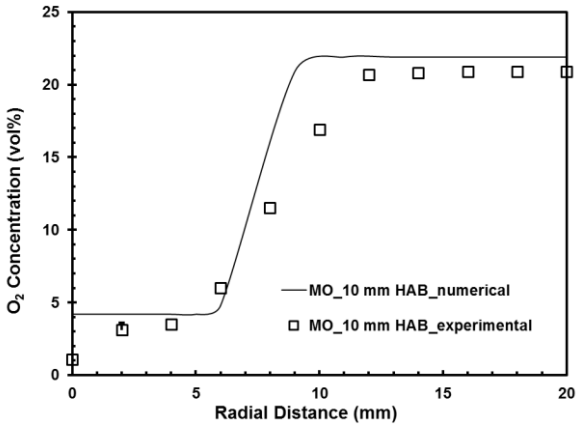

(a)

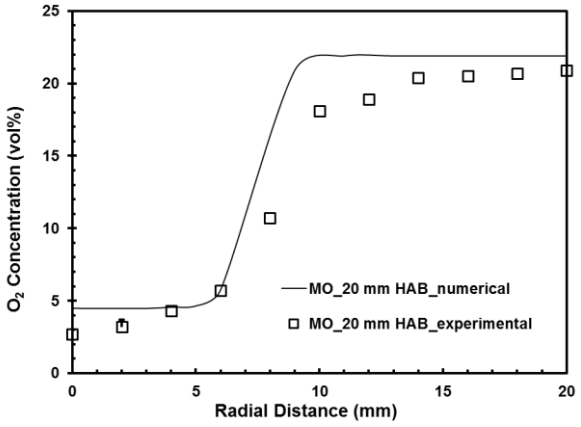

(b)

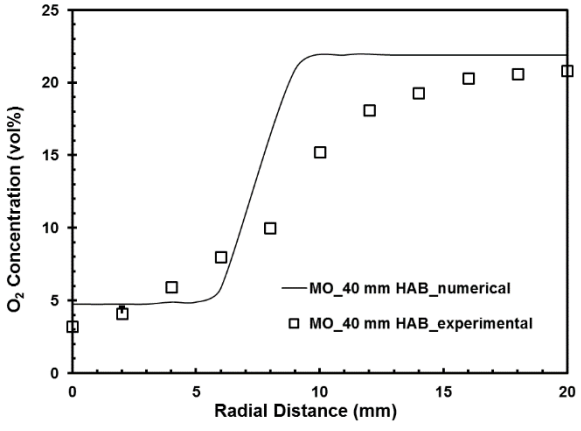

(c)

Figure 8.33 O_2 concentration profiles for methyl oleate flame at (a) 10 mm (b) 20 mm (c) 40 mm height above the burner

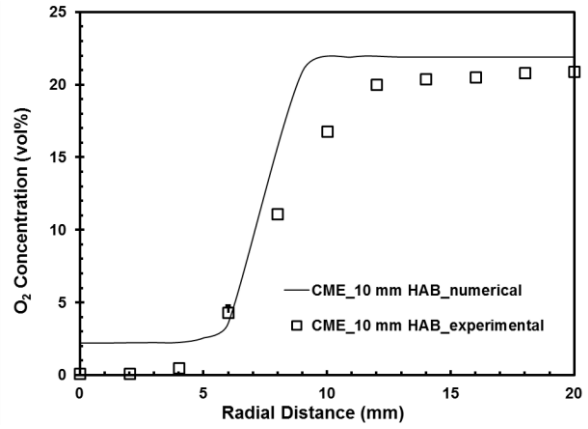

(a)

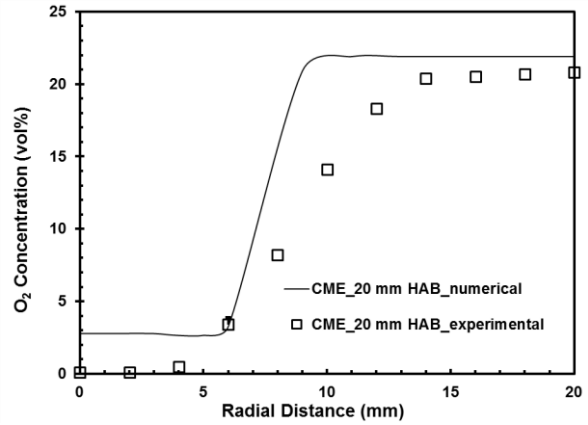

(b)

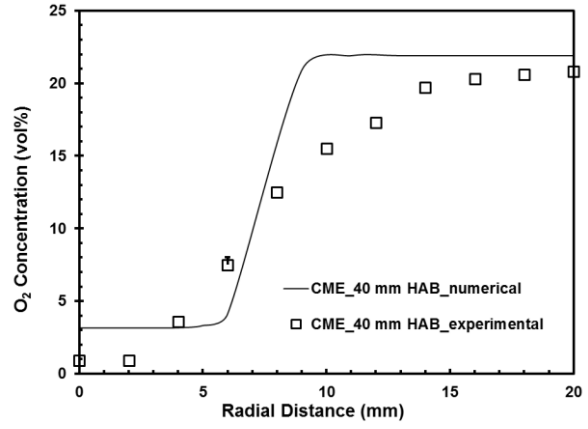

(c)

Figure 8.34 O_2 concentration profiles for CME flame at (a) 10 mm (b) 20 mm (c) 40 mm height above the burner

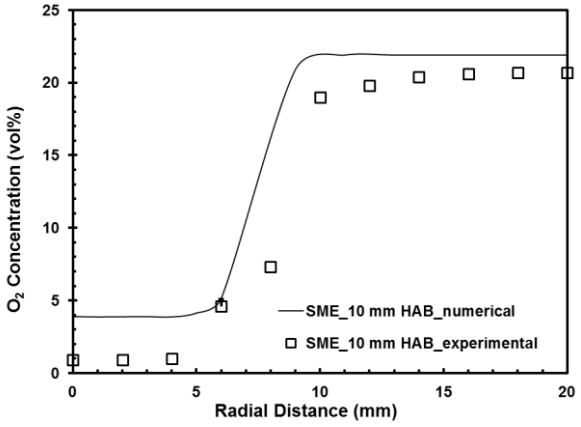

(a)

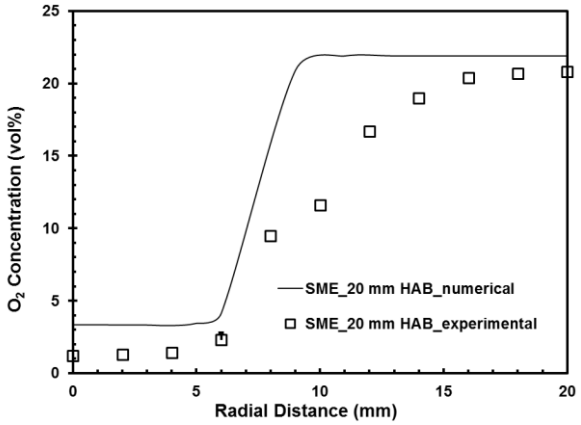

(b)

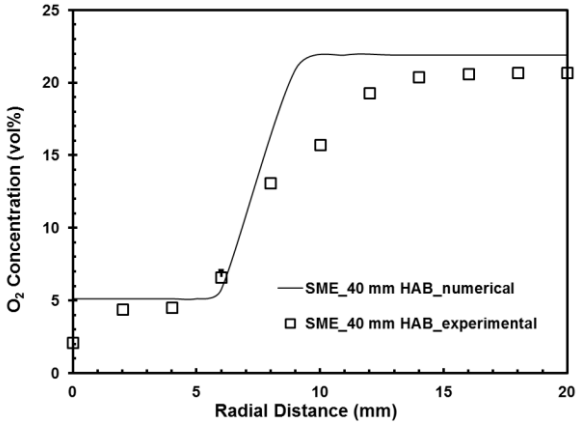

(c)

Figure 8.35 O_2 concentration profiles for SME flame at (a) 10 mm (b) 20 mm (c) 40 mm height above the burner

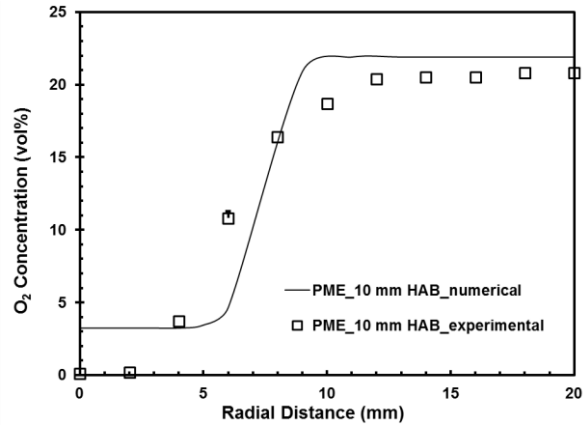

(a)

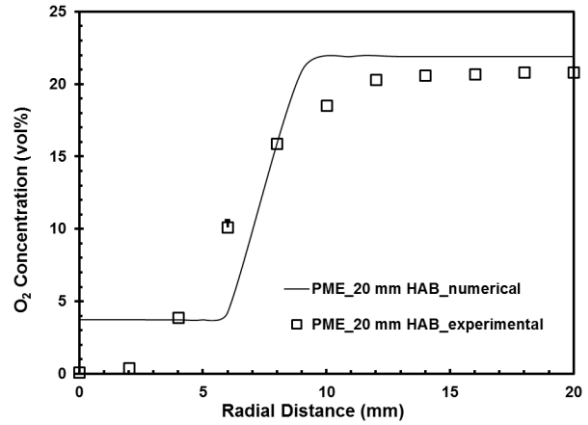

(b)

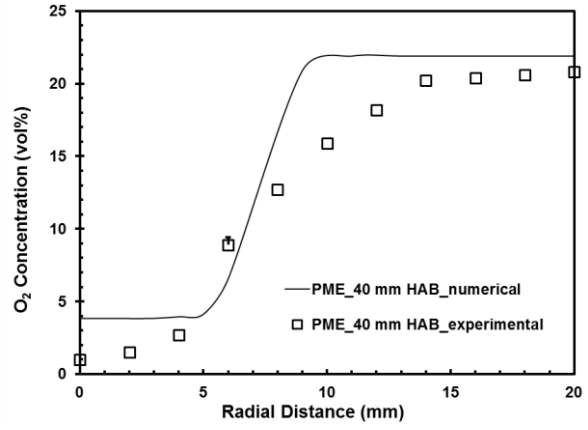

(c)

Figure 8.36 O_2 concentration profiles for PME flame at (a) 10 mm (b) 20 mm (c) 40 mm height above the burner

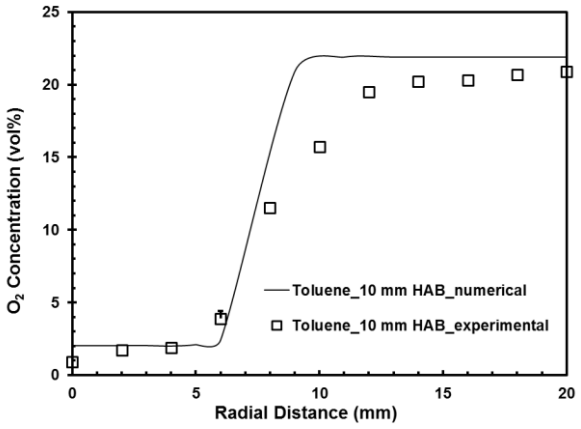

(a)

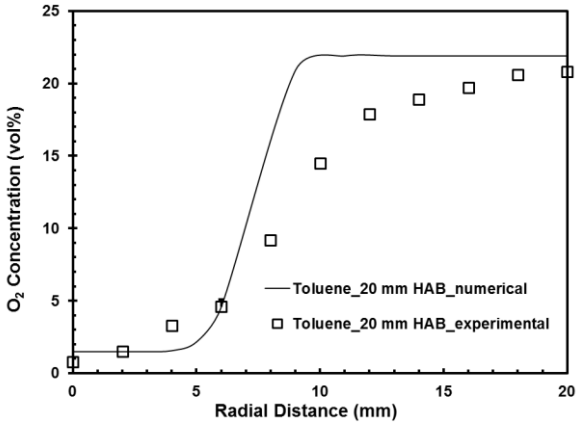

(b)

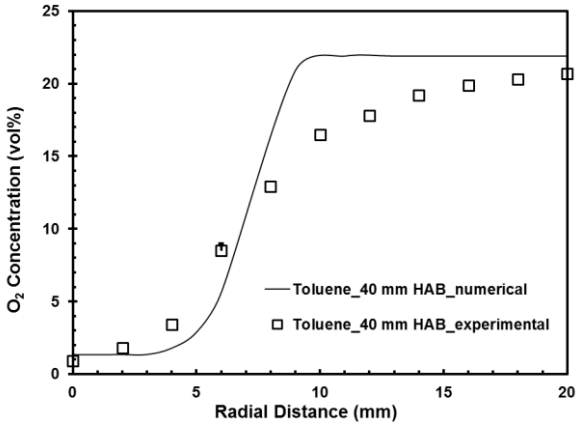

(c)

Figure 8.37 O_2 concentration profiles for toluene flame at (a) 10 mm (b) 20 mm (c) 40 mm height above the burner

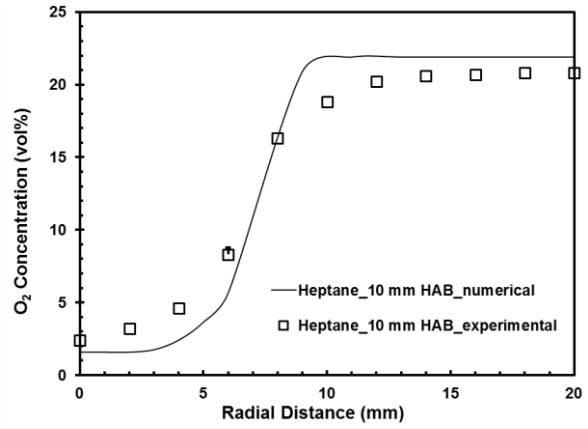

(a)

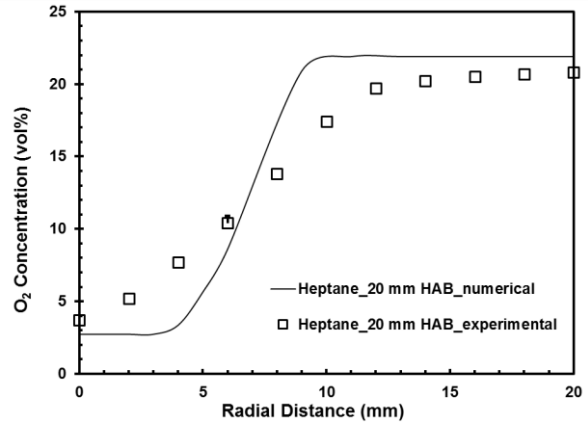

(b)

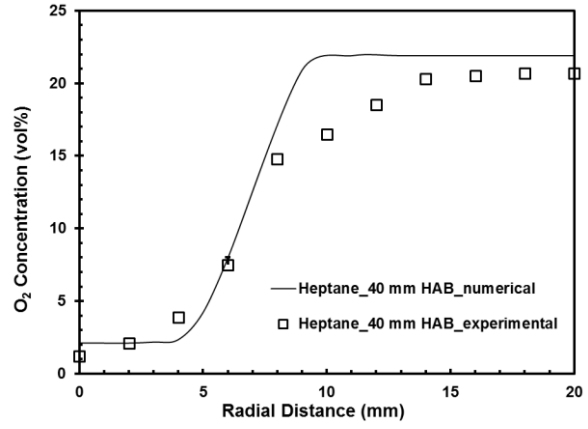

(c)

Figure 8.38 O_2 concentration profiles for heptane flame at (a) 10 mm (b) 20 mm (c) 40 mm height above the burner

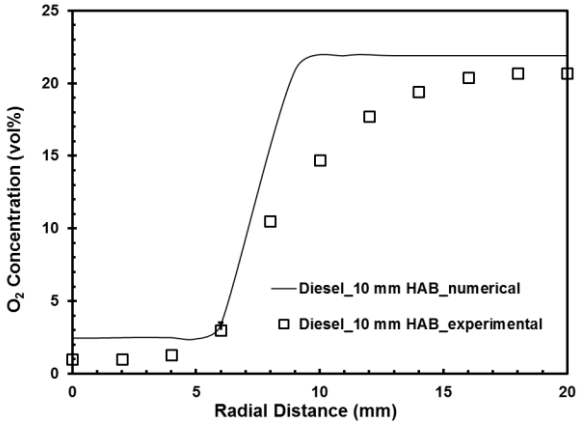

(a)

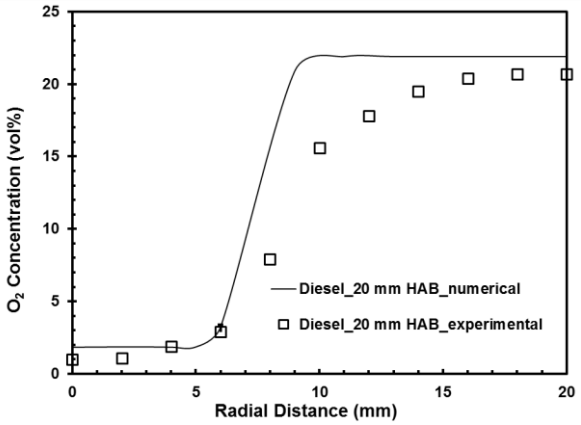

(b)

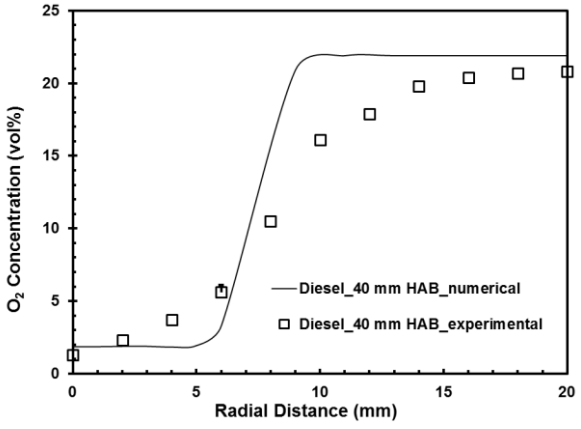

(c)

Figure 8.39 O_2 concentration profiles for diesel flame at (a) 10 mm (b) 20 mm (c) 40 mm height above the burner

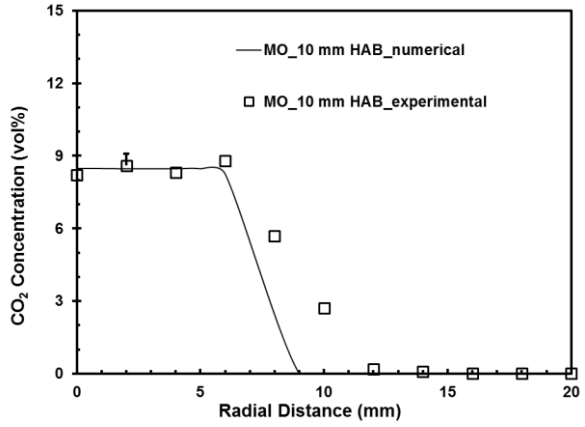

(a)

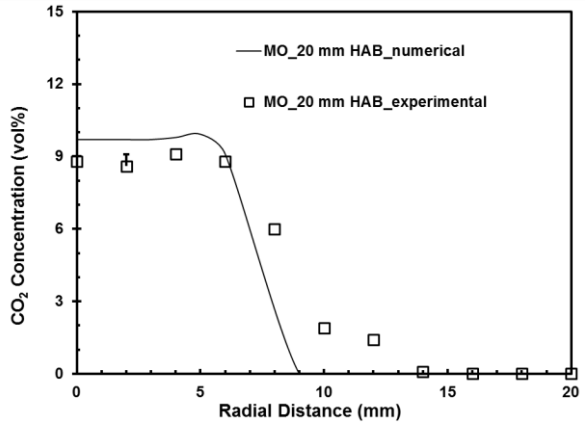

(b)

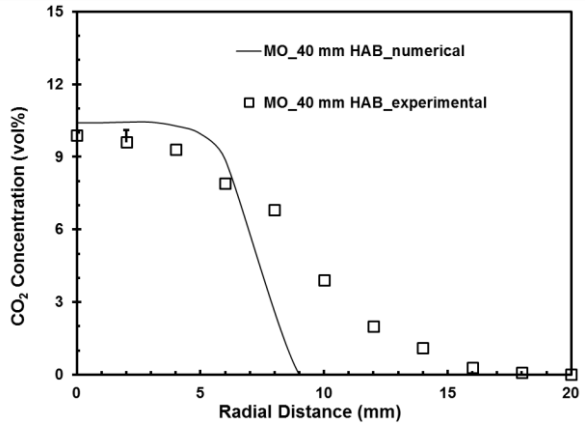

(c)

Figure 8.40 CO_2 concentration profiles for methyl oleate flame at (a) 10 mm (b) 20 mm (c) 40 mm height above the burner

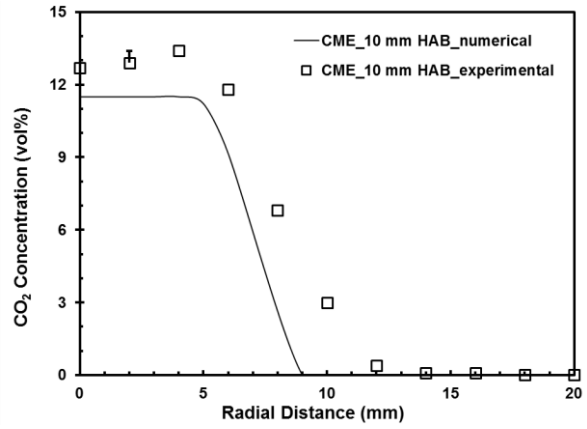

(a)

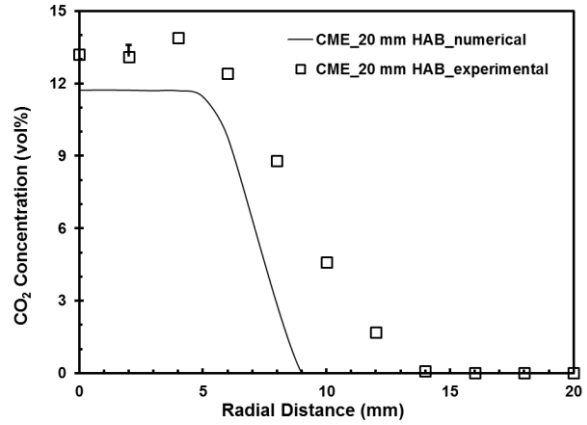

(b)

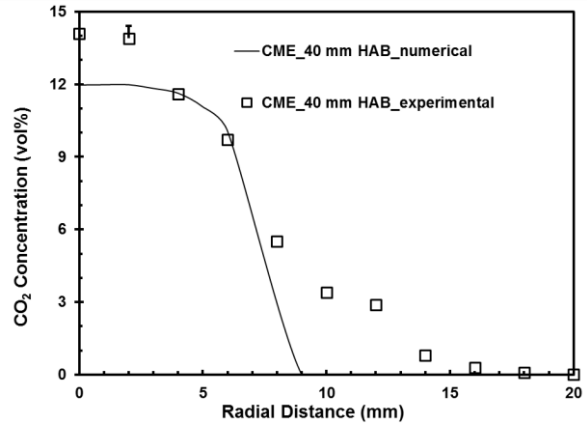

(c)

Figure 8.41 CO_2 concentration profiles for CME flame at (a) 10 mm (b) 20 mm (c) 40 mm height above the burner

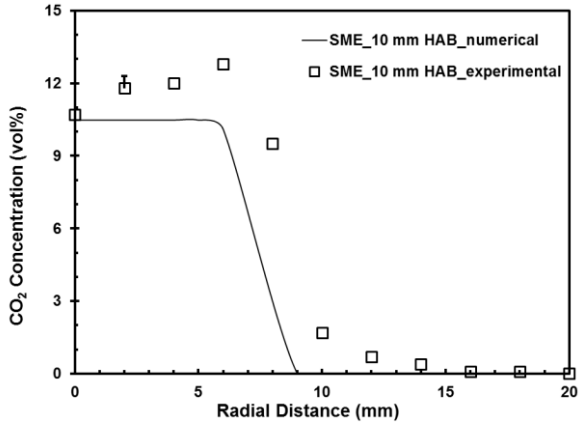

(a)

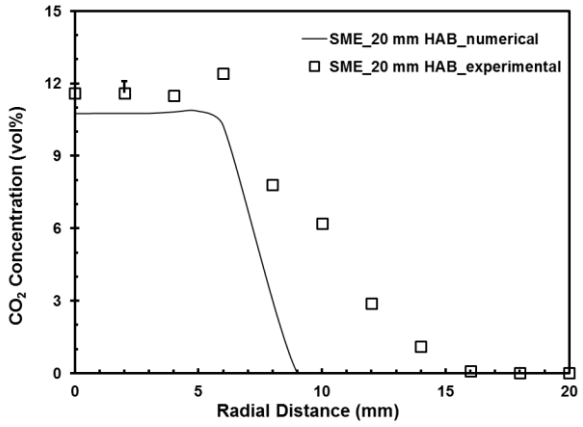

(b)

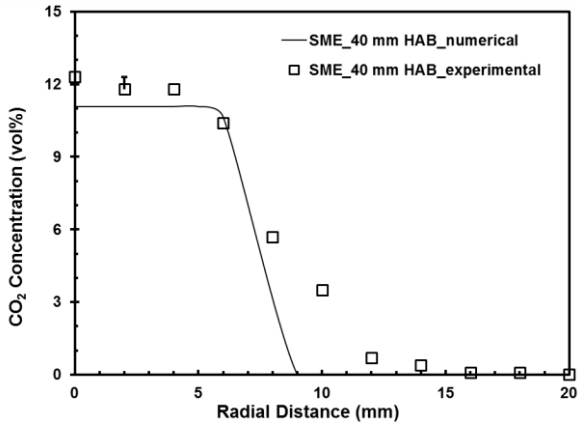

(c)

Figure 8.42 CO_2 concentration profiles for SME flame at (a) 10 mm (b) 20 mm (c) 40 mm height above the burner

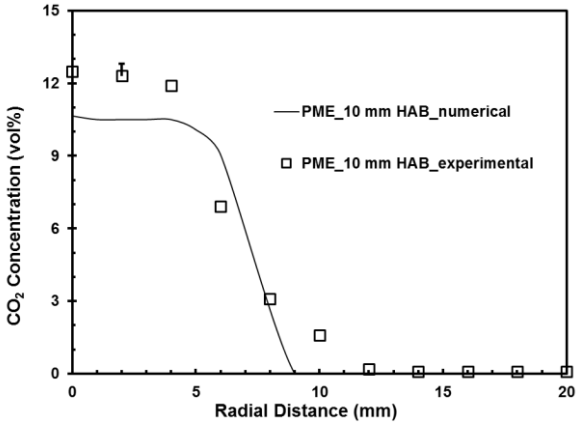

(a)

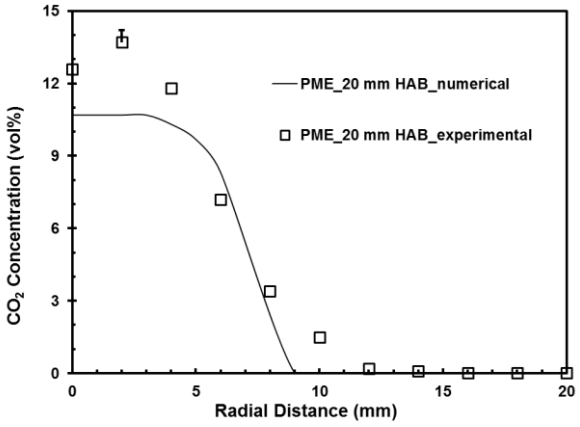

(b)

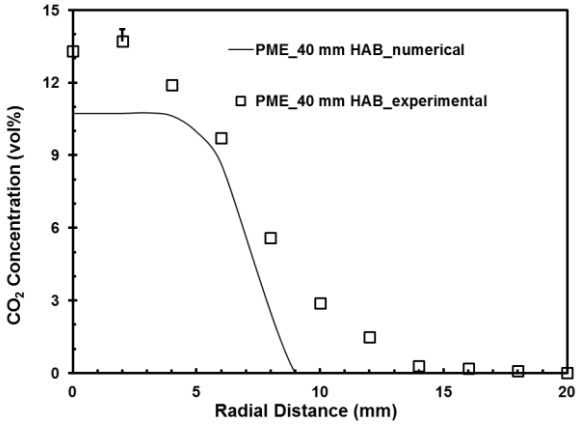

(c)

Figure 8.43 CO_2 concentration profiles for PME flame at (a) 10 mm (b) 20 mm (c) 40 mm height above the burner

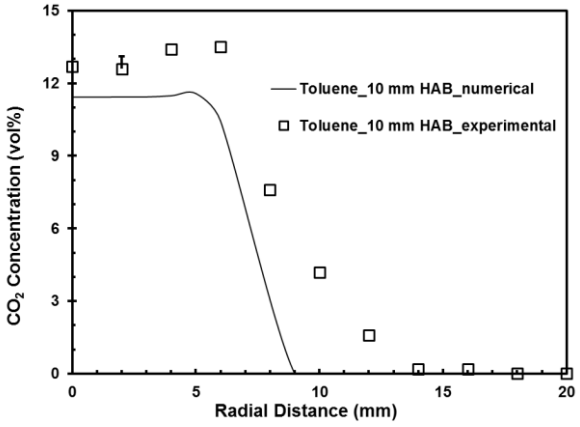

(a)

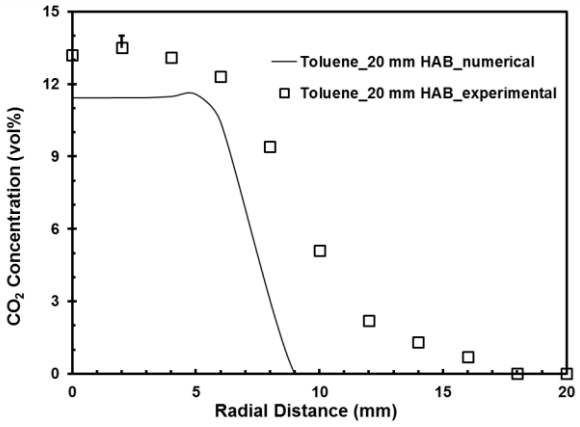

(b)

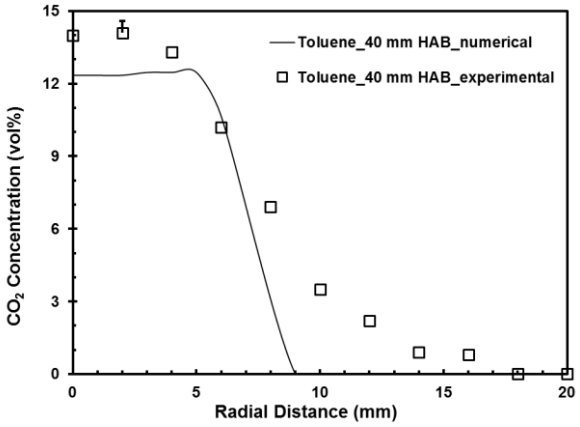

(c)

Figure 8.44 CO_2 concentration profiles for toluene flame at (a) 10 mm (b) 20 mm (c) 40 mm height above the burner

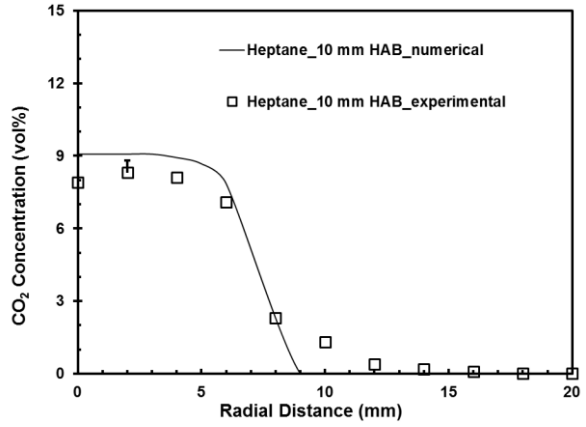

(a)

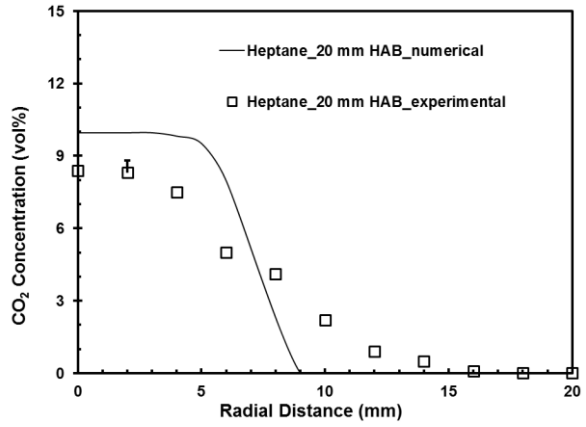

(b)

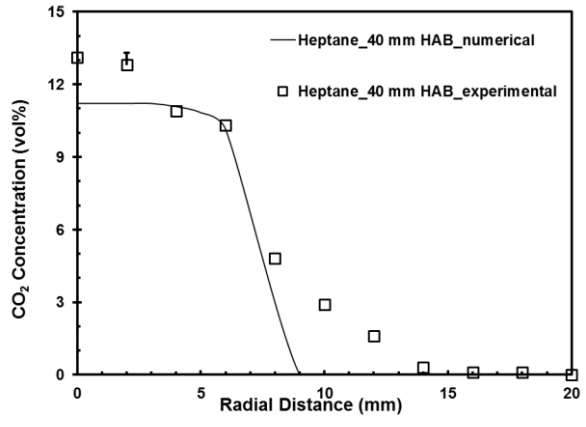

(c)

Figure 8.45 CO_2 concentration profiles for heptane flame at (a) 10 mm (b) 20 mm (c) 40 mm height above the burner

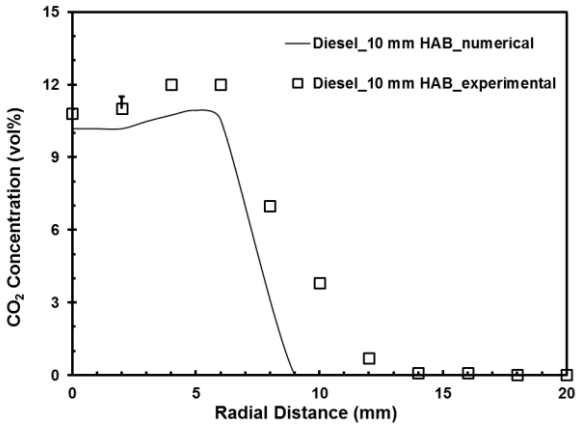

(a)

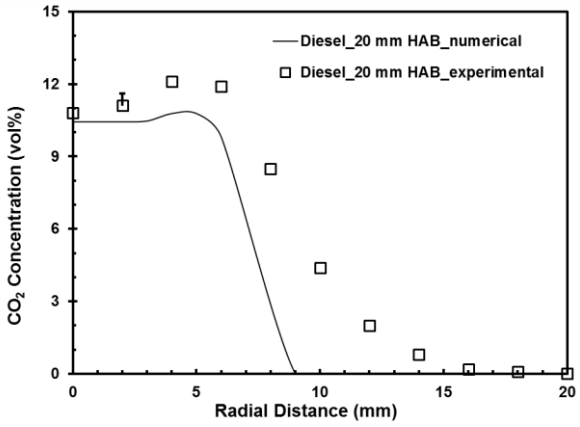

(b)

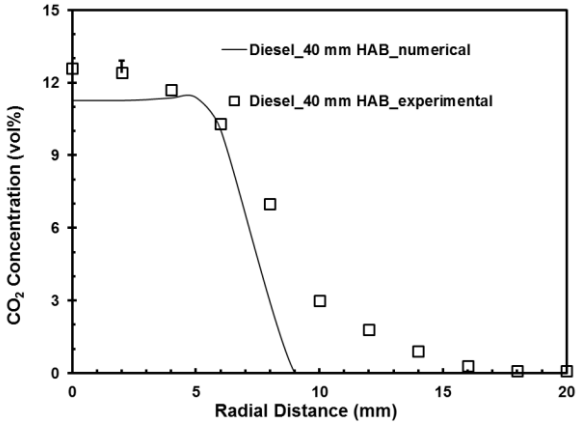

(c)

Figure 8.46 CO_2 concentration profiles for diesel flame at (a) 10 mm (b) 20 mm (c) 40 mm height above the burner

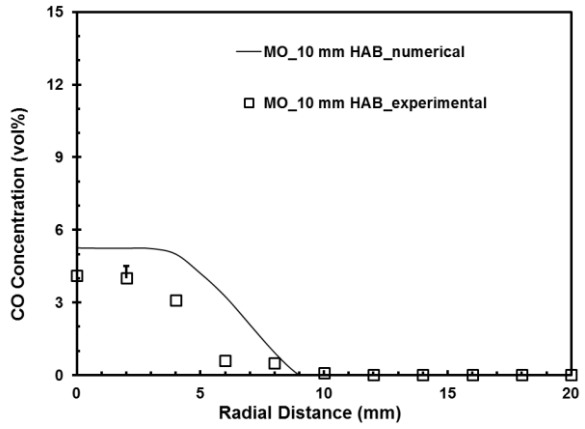

(a)

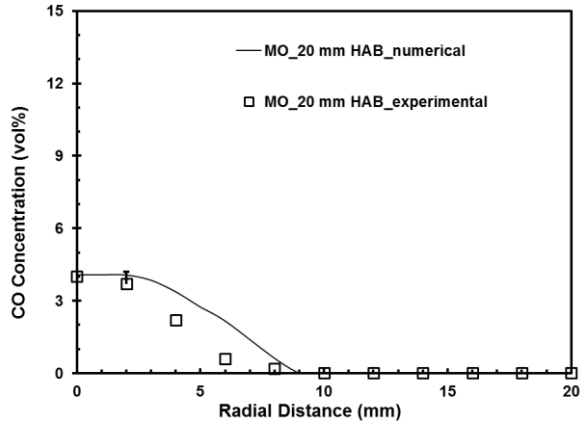

(b)

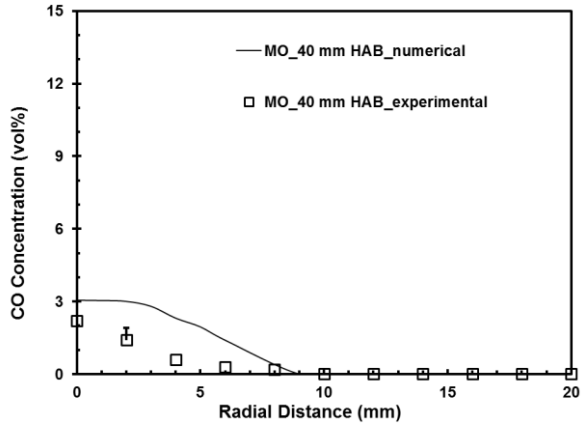

(c)

Figure 8.47 CO concentration profiles for methyl oleate flame at (a) 10 mm (b) 20 mm (c) 40 mm height above the burner

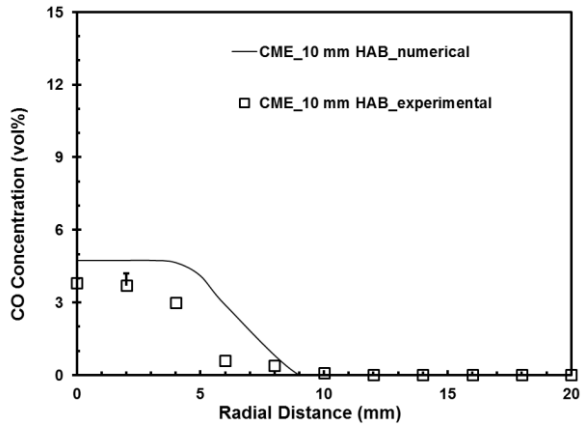

(a)

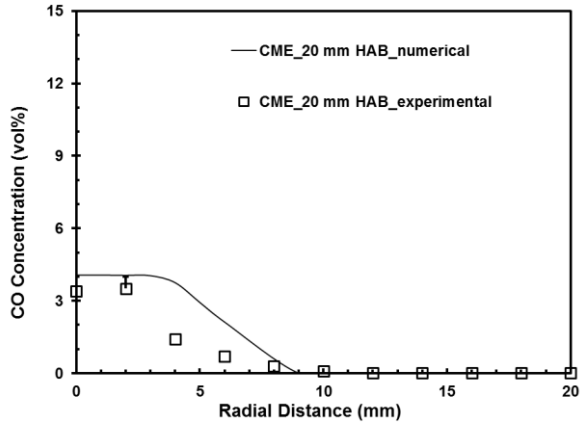

(b)

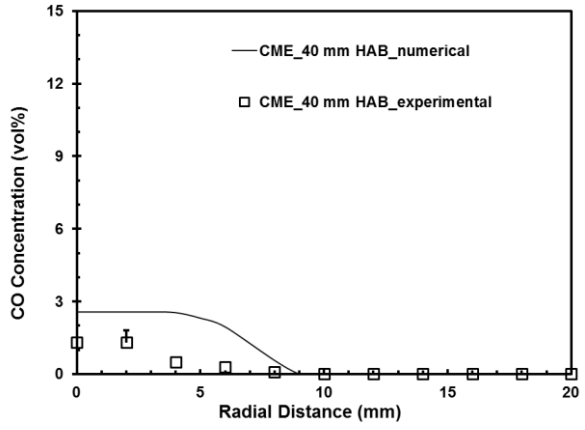

(c)

Figure 8.48 CO concentration profiles for CME flame at (a) 10 mm (b) 20 mm (c) 40 mm height above the burner

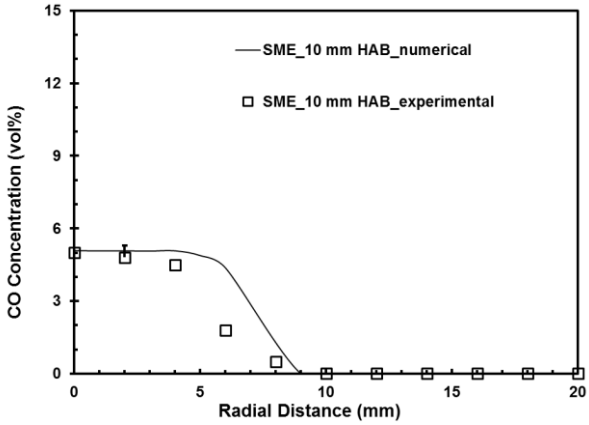

(a)

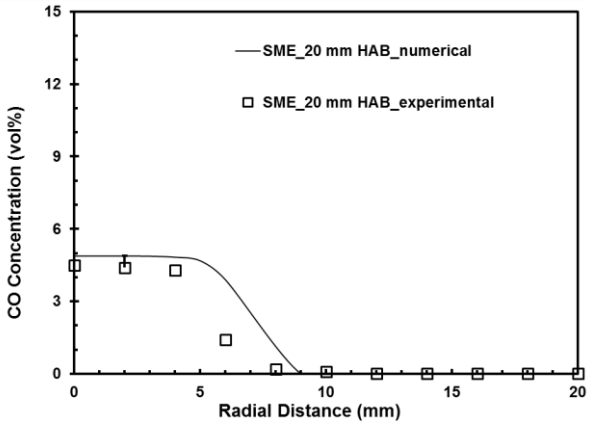

(b)

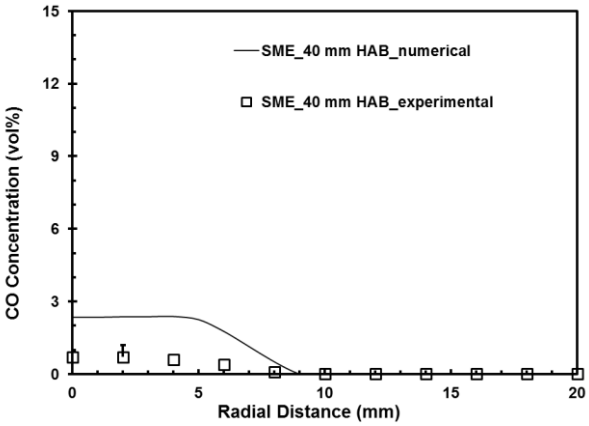

(c)

Figure 8.49 CO concentration profiles for SME flame at (a) 10 mm (b) 20 mm (c) 40 mm height above the burner

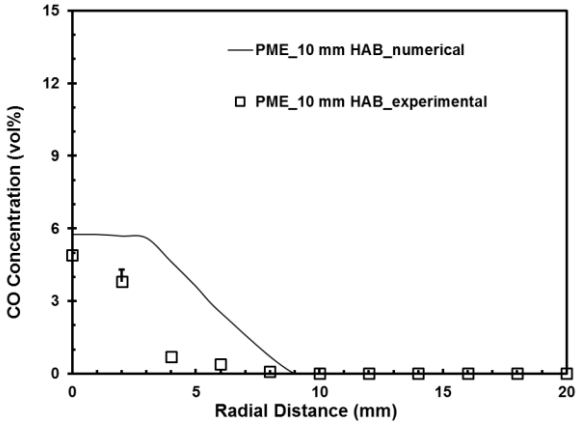

(a)

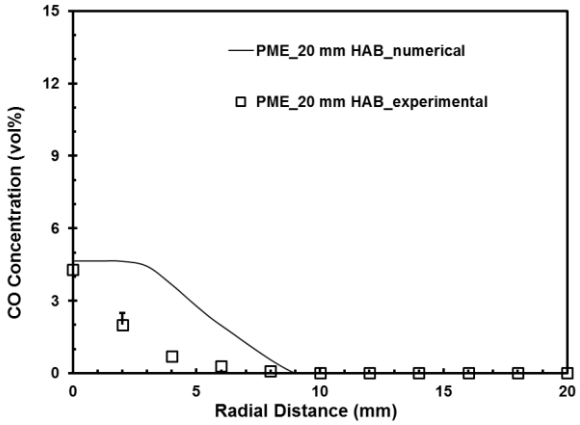

(b)

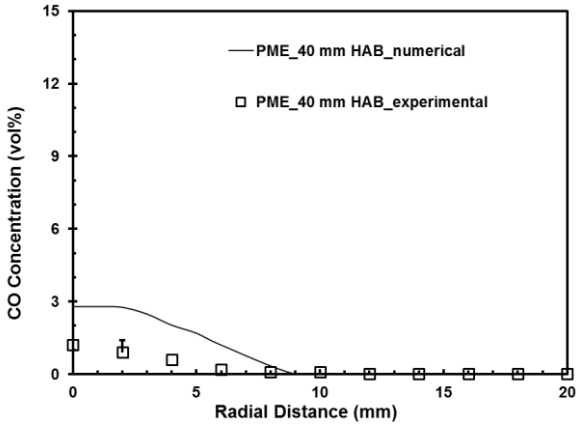

(c)

Figure 8.50 CO concentration profiles for PME flame at (a) 10 mm (b) 20 mm (c) 40 mm height above the burner

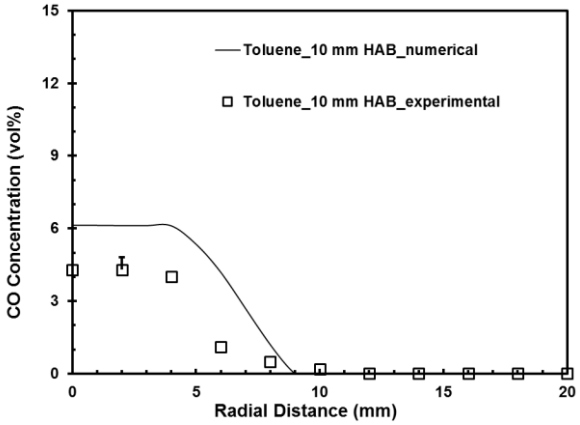

(a)

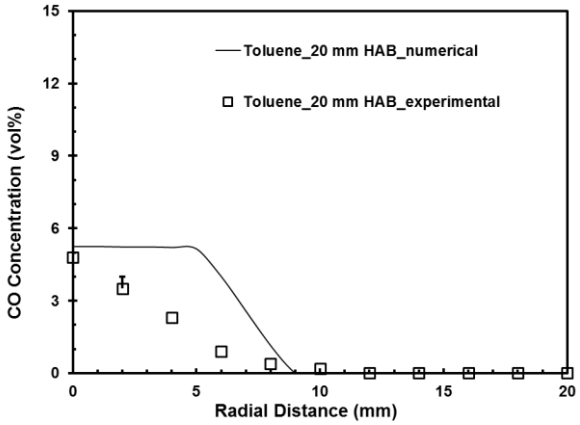

(b)

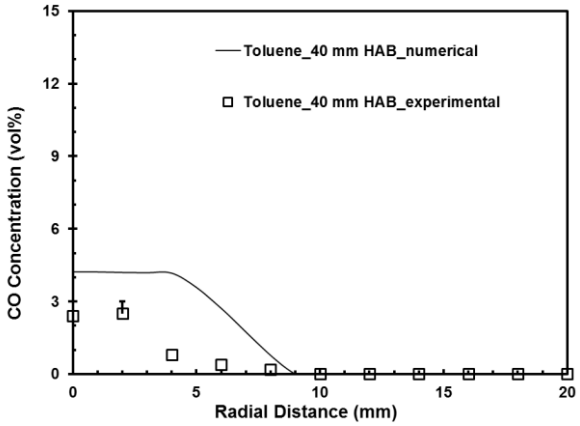

(c)

Figure 8.51 CO concentration profiles for toluene flame at (a) 10 mm (b) 20 mm (c) 40 mm height above the burner

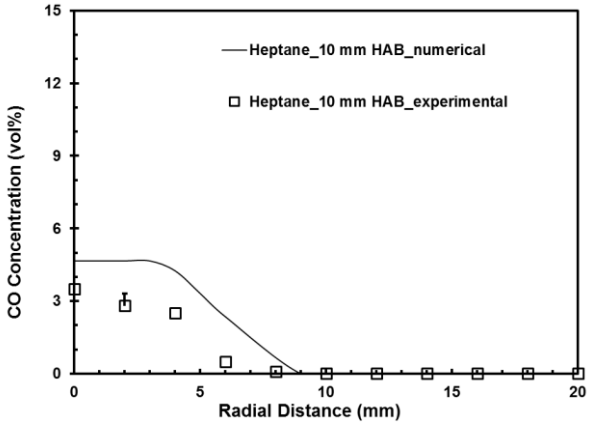

(a)

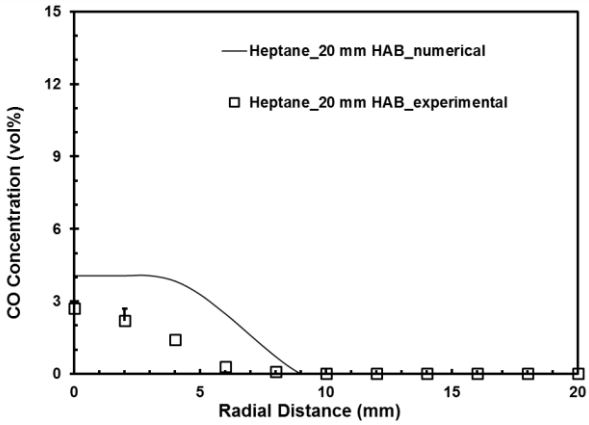

(b)

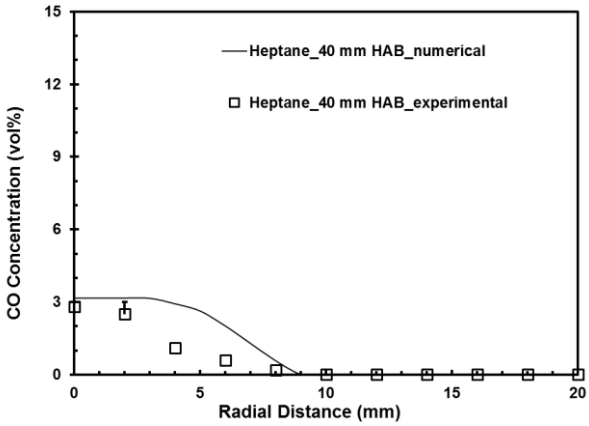

(c)

Figure 8.52 CO concentration profiles for heptane flame at (a) 10 mm (b) 20 mm (c) 40 mm height above the burner

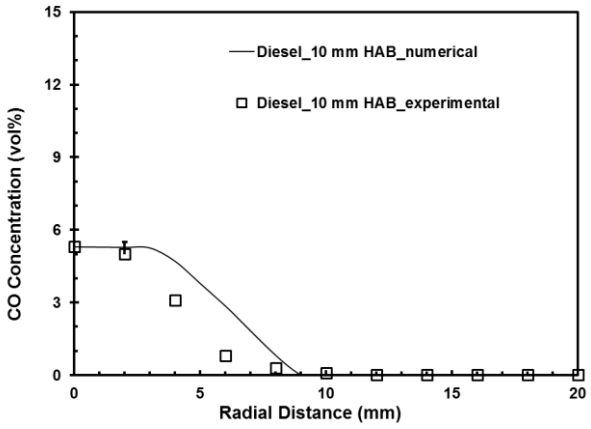

(a)

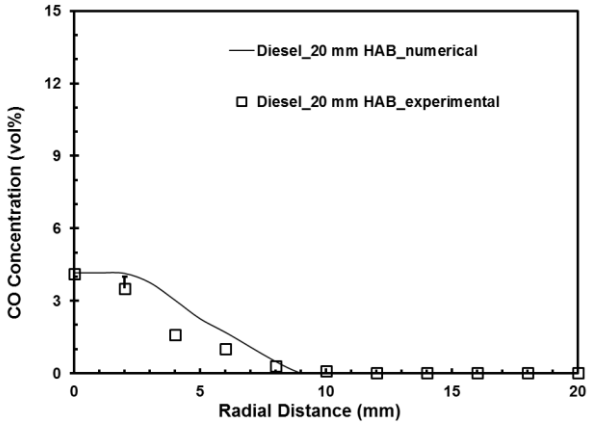

(b)

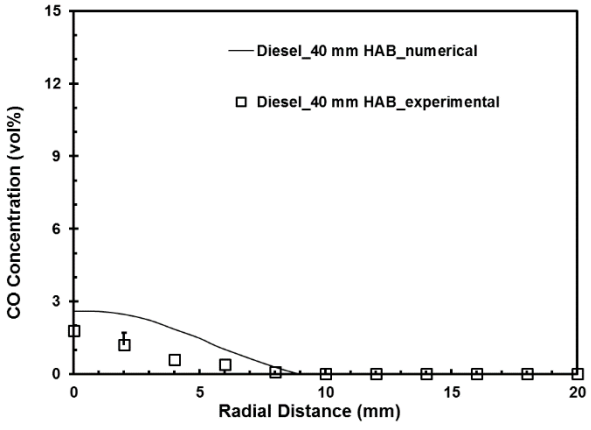

(c)

Figure 8.53 CO concentration profiles for diesel flame at (a) 10 mm (b) 20 mm (c) 40 mm height above the burner

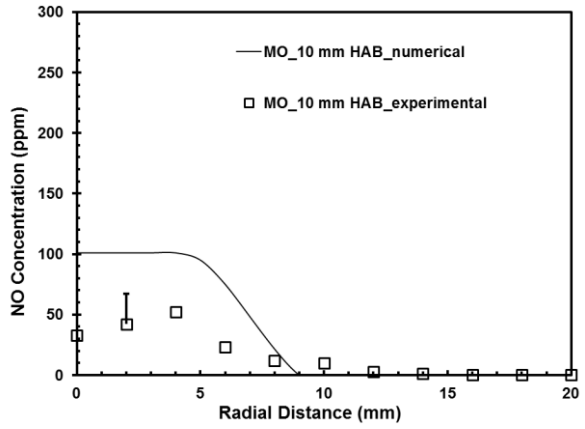

(a)

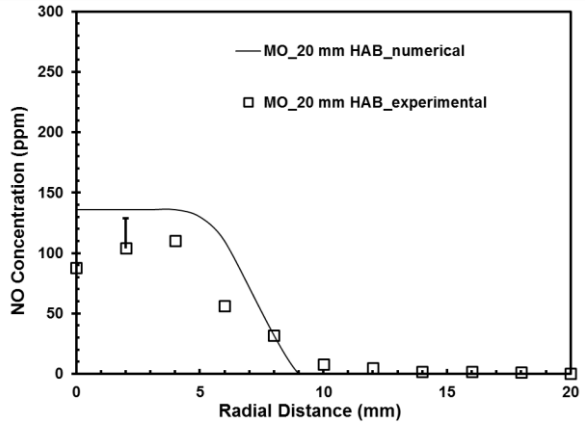

(b)

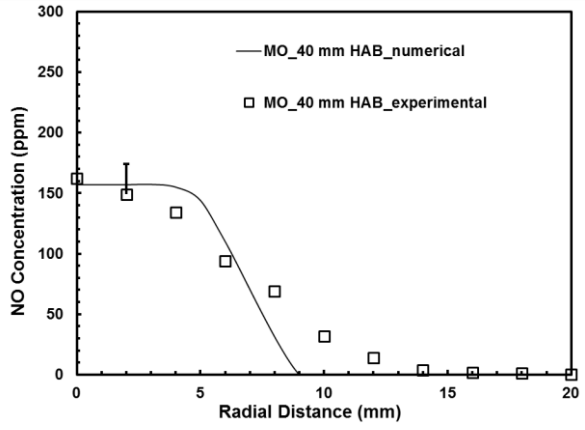

(c)

Figure 8.54 NO concentration profiles for methyl oleate flame at (a) 10 mm (b) 20 mm (c) 40 mm height above the burner

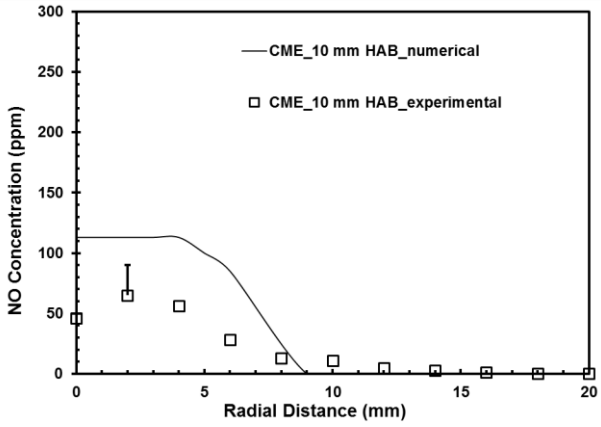

(a)

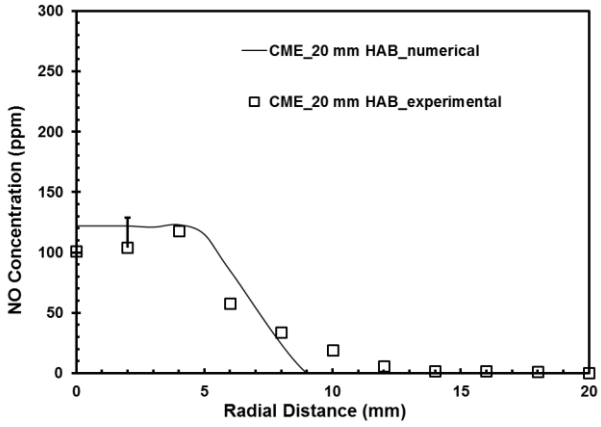

(b)

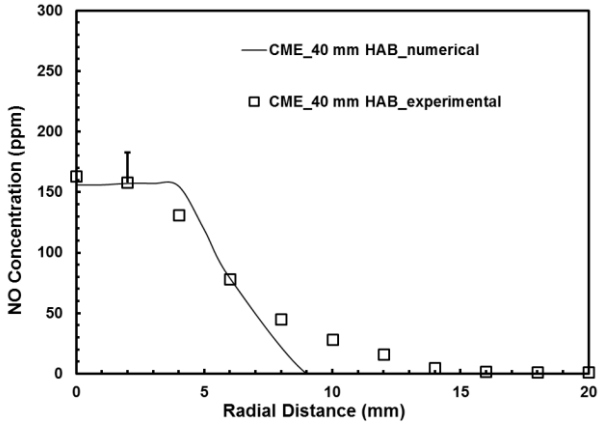

(c)

Figure 8.55 NO concentration profiles for CME flame at (a) 10 mm (b) 20 mm (c) 40 mm height above the burner

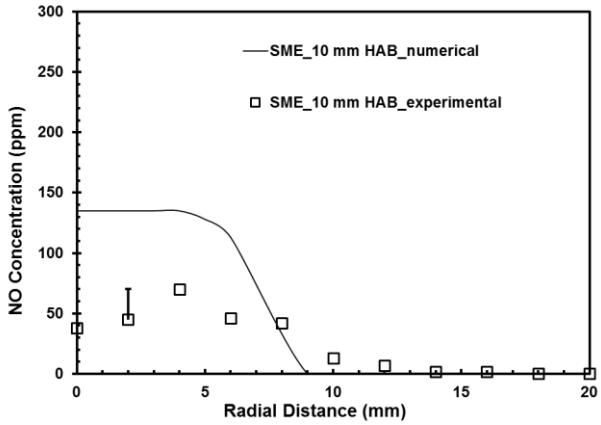

(a)

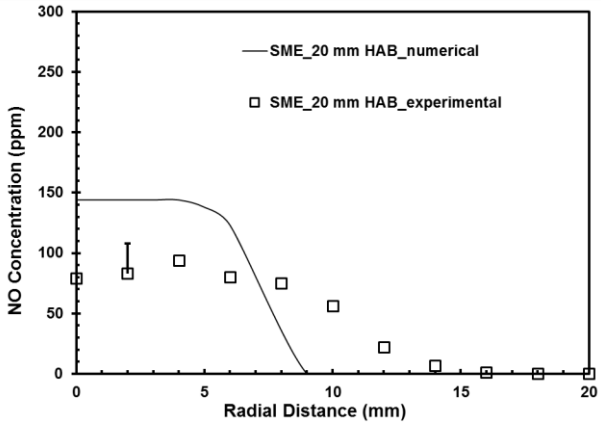

(b)

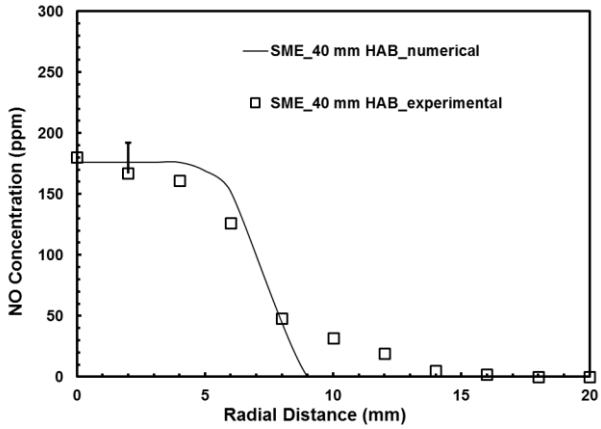

(c)

Figure 8.56 NO concentration profiles for SME flame at (a) 10 mm (b) 20 mm (c) 40 mm height above the burner

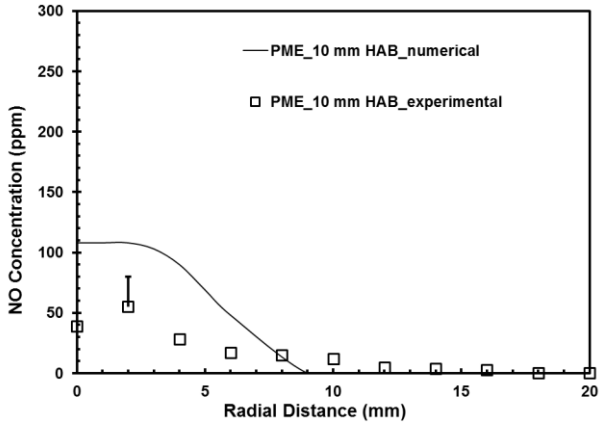

(a)

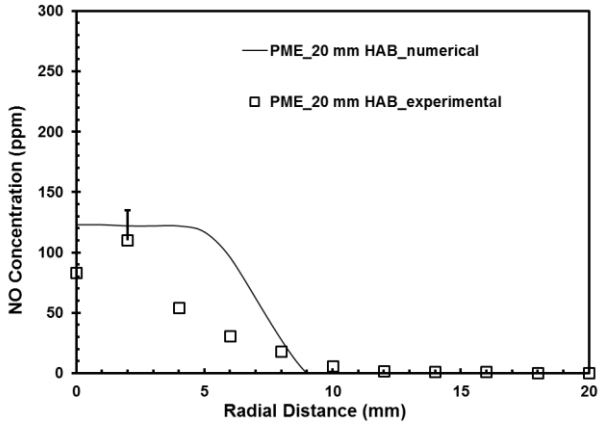

(b)

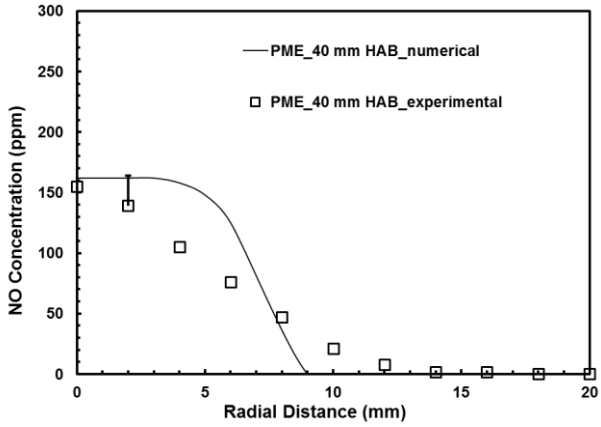

(c)

Figure 8.57 NO concentration profiles for PME flame at (a) 10 mm (b) 20 mm (c) 40 mm height above the burner

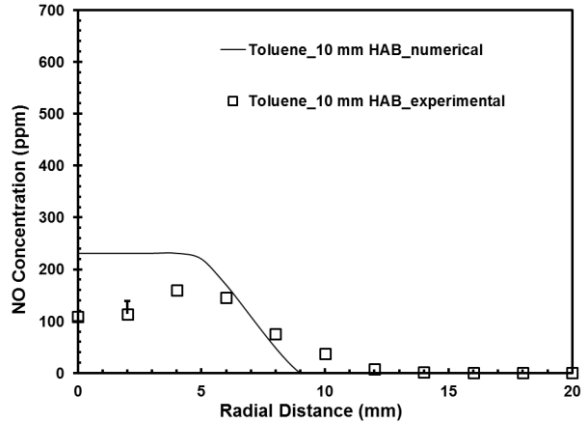

(a)

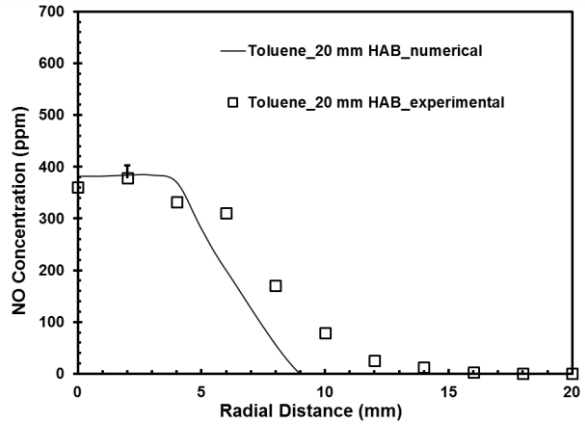

(b)

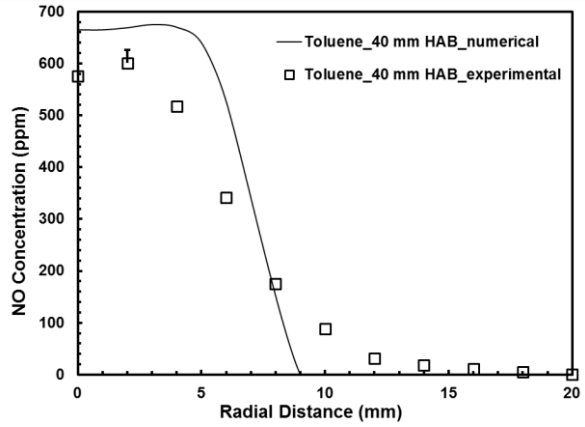

(c)

Figure 8.58 NO concentration profiles for toluene flame at (a) 10 mm (b) 20 mm (c) 40 mm height above the burner

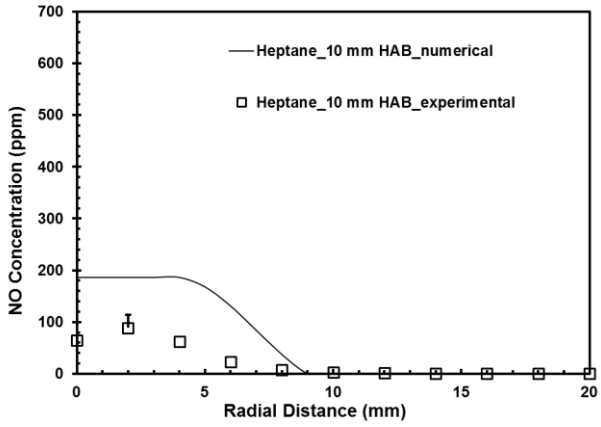

(a)

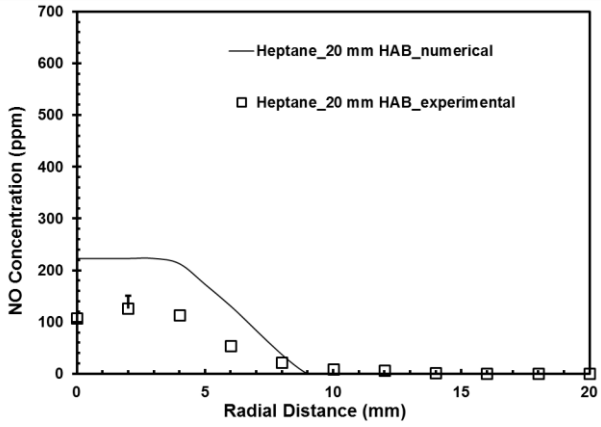

(b)

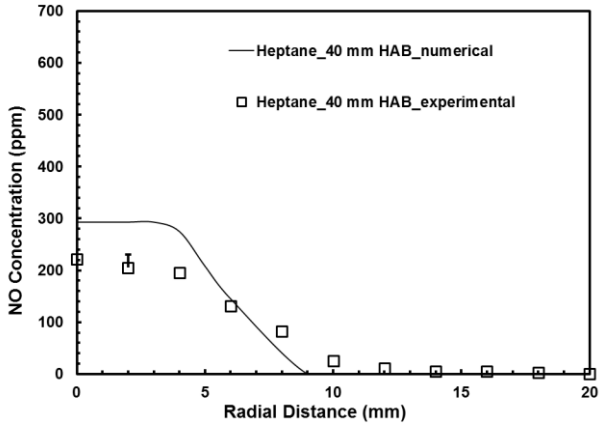

(c)

Figure 8.59 NO concentration profiles for heptane flame at (a) 10 mm (b) 20 mm (c) 40 mm height above the burner

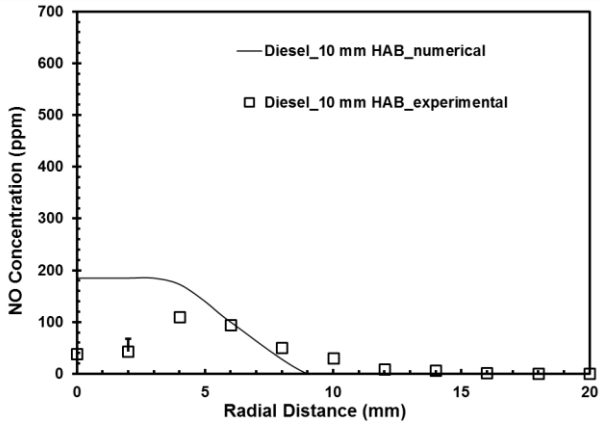

(a)

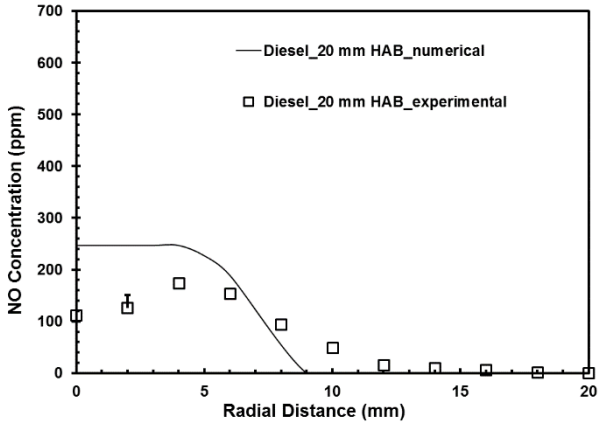

(b)

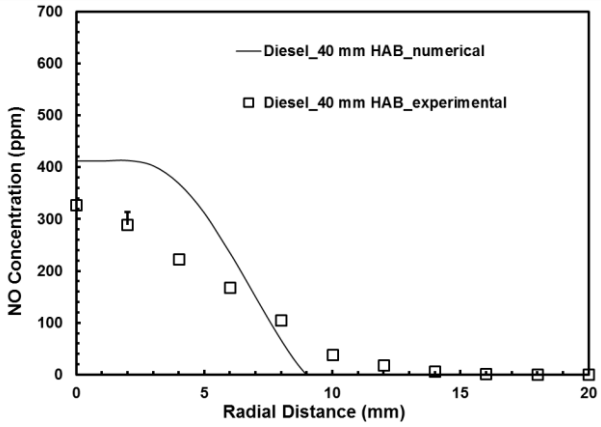

(c)

Figure 8.60 NO concentration profiles for diesel flame at (a) 10 mm (b) 20 mm (c) 40 mm height above the burner

CHAPTER 9 SUMMARY AND CONCLUSIONS

With the current knowledge and understanding of combustion characteristics of biodiesels, blending biodiesels with petroleum fuels in different proportions is a feasible solution in the near future for use in existing engines without major modifications. Several engine studies revealed that the use of biodiesels and their blends in a compression ignition engine resulted in an appreciable reduction in the emissions of particulate matter, HC and CO emissions. However, a definitive trend of biodiesel and its blending effect on NOx emissions is not yet achieved, since, although majority of studies shown marginal increase of NOx with biodiesels, few studies observed a decrease of NOx with the use of biodiesels. The average effect of biodiesel on NOx emissions was seen to be small, but with a high variance which resulted in difficulty in discerning a clear pattern. Due to the complex and intermittent nature of combustion in an engine environment, the emission behavior of biodiesels and blends attributable to the fuel chemistry cannot be clearly ascertained. Further nitric oxide emissions are found to be influenced by several combinations of complexly coupled thermo-fluid-chemistry interactions in addition to engine parameters depending on the characteristics of the combustion environment.

Hence, a holistic approach was required to investigate the biodiesel blending effect on NOx emission by discerning the influential factors and then integrating the appropriate individual findings along with the corresponding coupled effects of thermo-fluid-chemical interactions for the particular combustion environment.

A rapid characterization technique was employed to ascertain the influence of fuel chemistry on the combustion and emission characteristics of flames tested at different equivalence ratios. This technique consisted of a laminar flame arrangement in which pre-vaporized fuels were tested at a wide range of equivalence ratios to generate various reaction regions existed in diesel combustion. The advantage of this experimental arrangement is that it requires a smaller quantity of fuel (less than 100 ml) to characterize the emission characteristics of the tested fuel. Further this experimental configuration eliminates the complexities of atomization, droplet vaporization and high pressure that occur in an engine.

9.1 Degree of Unsaturation as a fuel parameter

Fuel unsaturation has been attributed to the change in NOx emissions observed with the use of neat biodiesels in compression ignition engines; several results indicated the existence of a strong relationship between NOx emissions and iodine number. However, the relevance of iodine number as a measure of total unsaturation of petroleum fuels like diesel, Jet A and their blends with biodiesels is debatable due to the significant differences in the reactivity of iodine with petroleum fuels. Bromine number, used as a measure of aliphatic unsaturation in petrofuel samples, does not account for the aromatic unsaturation from petroleum fuels. Hence, a common parameter that is relevant for both biodiesels and petroleum fuels needs to be identified to quantify the fuel unsaturation.

The primary objective of this work was to explore a parameter that accounts for and quantify the unsaturation arising from various components of the fuel irrespective of their parent hydrocarbon families such as alkanes, alkenes, alkynes, cyclic hydrocarbons, aromatics, alcohols, esters etc. and which can be correlated with the engine emission characteristics with the use of that fuel.

DOU was observed to have several significant implications:

- DOU provides a common platform to compare and contrast different families of fuels and their unsaturation from various components; this provides necessary information in engineering newer fuel blends based on their effective degree of fuel unsaturation.
- DOU is more suitable to describe fuel unsaturation of petroleum fuels and petroleum fuel/biodiesel blends than iodine number because the unsaturation due to sources other than double bonds such as aromatics are not accounted for by the iodine number due to the low reactivity of iodine with aromatics.
- DOU can be used to correlate the NOx emission parameters (indices) to the molecular hydrogen to carbon ratio of the fuel regardless of whether the hydrocarbon is a fossil fuel, alcohol, ester or ether.
- DOU can capture the differences in the influence of molecular chemistry of the fuel on the NOx emission characteristics based on the parent hydrocarbon families.
- DOU can be readily evaluated for any fuel under study with acceptable uncertainty without the use of elaborate experiments.

Fuels from different families such as commercial petroleum fuels (diesel and Jet A fuel), commercial biodiesels (PME, CME, RME and SME), alkane (n-heptane), aromatics (toluene), individual biodiesel component (methyl oleate) and different combinations of their blends were investigated at four conditions, namely fuel-lean condition ($\Phi = 0.9$), stoichiometric ($\Phi = 1.0$) and moderate fuel-rich condition ($\Phi = 1.2$ and 1.5) to understand the fuel unsaturation effect on NOx emission by adding incremental complexity to the fuel chemistry interactions.

9.2 Conclusions

Based on the results from the global NO and CO emission indices, flame appearance, in-flame radial temperature and species concentration (O_2, CO_2, CO and NO) profiles the following conclusions were drawn:

- The NO and CO emission indices from the tested laminar flames were influenced by two major parameters - equivalence ratio and total fuel unsaturation.
- Among all the tested flames, EI_{NO} increased with increasing DOU; the magnitude of rise increased from $\Phi = 0.9$, reaches a maximum at $\Phi = 1.2$ and decreases to a lower value at $\Phi = 1.5$. At higher equivalence ratios, particularly at $\Phi = 3$ and 7, fuel chemistry and unsaturation effects had a minimal influence on the EI_{NO} due to the significant soot formation under these conditions. In general, fuel unsaturation had its maximum influence on EI_{NO} at $\Phi = 1.2$.
- The influence of degree of fuel unsaturation on EI_{NO} became significant at higher values of DOU particularly greater than 2. This observation was evident in the flames of heptane/toluene blends, heptane/MO and toluene/MO blends whose DOU values range between 0 and 4. Toluene (DOU : 4) produced the highest EI_{NO} at all tested equivalence ratios ($\Phi = 0.9$, 1.0, 1.2 and 1.5)
- Origin of fuel (fuel family) played an important role in determining the DOU effect on EI_{NO} from the corresponding flames. Fuels containing methyl esters produced lower EI_{NO} than petroleum based fuels having similar value of degree of unsaturation.

- EI_{NO} was found to increase with DOU, even in the absence of fuel bound oxygen (heptane/toluene blends) in the fuel blend, thereby delineated the DOU effect on NOx formation from the fuel bound oxygen effect.
- Similarly, EI_{NO} was found to increase with DOU, among biodiesel/biodiesel blends (fuel bound oxygen content of about 11% -12%) where DOU influenced EI_{NO} between flames of fuels having similar fuel bound oxygen content. These observations provided evidence to the claim that fuel unsaturation contributes to the NOx emissions observed in diesel engine combustion studies reported in the literature.
- EI_{NO} was found to increase with aromatic content in the fuel blend and the increase become substantial at higher volume content of aromatics present in the fuel (EI_{NO} increased from 1.91 g/kg to 4.91 g/kg between 0% and 100% aromatic content in the fuel blend).
- EI_{CO} did not vary significantly with DOU among neat biodiesels, petroleum diesel, biodiesel/petrodiesel blends and the emitted EI_{CO} was less than 1g/kg at all tested equivalence ratios. EI_{CO}, however, was found to increase with higher toluene (aromatic) content, particularly in the flames of heptane/toluene and toluene/MO blends.
- The flame appearance of all the tested flames revealed three primary regions: 1) a dark space between the burner exit and the inner bright cone, 2) a bright blue inner cone surrounded by 3) an outer less luminous blue cone.
- The variation in the measured peak flame temperatures were almost comparable within experimental uncertainties (measured peak temperatures were about

1850K) and did not vary appreciably with the degree of unsaturation or the family of fuel origin at the tested equivalence ratio of 1.2.

- The local O_2 and CO_2 concentrations in the flame did not vary significantly with the fuel unsaturation as well as the origin of fuel and were primarily influenced by the burner exit equivalence ratio and the composition of the reactants.
- The local measured peak CO concentrations did not vary significantly with the degree of fuel unsaturation and fuel origin at the tested equivalence ratio of Φ = 1.2; however, the CO concentration was significantly influenced by the fuel chemistry at equivalence ratios greater than 2, particularly conspicuous at Φ = 7.
- The measured peak NO concentration was found to increase with the degree of unsaturation, in agreement with the corresponding global NO emission indices and the effect of fuel origin also played an important role in determining the quantity of end NO emission at the tested equivalence ratios.
- In the computational analysis, numerical models for the combustion of laminar flames of selected fuels were successfully developed using FLUENT and CHEMKIN software packages (Jet flow reactor network model).
- Numerical models were able to capture the location of peak values and the general behavior of O_2, CO_2, CO and NO concentration profiles in the flames of both methyl ester and petroleum fuels.
- Computational analysis reaffirmed the experimental observations of increasing NO concentration with the degree of fuel unsaturation.

9.3 Recommendations for further study

This dissertation work could be extended to investigate the following:

- In addition to the fuel chemistry, the effect of injected momentum from the burner can be studied at the same equivalence ratios investigated in this study. This provides a better understanding of the relative dominance of fuel chemistry and fluid mechanics at a particular equivalence ratio that can be utilized to develop fuels and design combustion parameters for a particular combustion environment.
- Furthermore, the effect of other parameters such as fuel atomization, droplet evaporation and other engine parameters can be studied individually with respect to DOU and the individual contribution of these parameters can be quantified. The results from these studies can be applied as corrections to the already developed EI_{NO} correlations with DOU in this work, to compare with results from engine studies.
- Fuels from other families such as alcohols and dimethyl ether (which are considered to be promising fuel blends for petroleum gasoline and diesel) can be studied with respect to DOU and to develop a database with experimental correlations of EI_{NO} with DOU for a wider range of DOU values and families of fuels.
- In the current numerical analysis, the corrections for the radiative heat loss from the flames were applied to the flame temperatures post numerical simulation. The present numerical models can be incorporated with radiative heat loss

corrections simultaneously and their implication on pollutants formation can be investigated.

REFERENCES

Agarwal, A., and Rajamanoharan, K. (2009) "Experimental investigations of performance and emissions of Karanja oil and its blends in a single cylinder agricultural diesel engine," *Applied Energy*, 86, 106-112. doi: 10.1016/j.apenergy.2008.04.008.

Agarwal, A., and Chaudhury, V. (2012) "Spray characteristics of biodiesel/blends in a high pressure constant volume spray chamber," Experimental Thermal and Fluid Science, 42, 212-218. doi: 10.1016/j.expthermflusci.2012.05.006.

Agarwal, A., and Dhar, A. (2013) "Experimental investigations of performance, emission and combustion characteristics of Karanja oil blends fueled DICI engine," *Renewable Energy*, 52, 283-291. doi: 10.1016/j.renene.2012.10.015.

Agarwal, A., Srivastava, D., Dhar, A., Maurya, R., Shukla, P., and Singh, A. (2013) "Effect of fuel injection timing and pressure on combustion, emissions and performance characteristics of a single cylinder diesel engine," *Fuel*, 111, 374-383. doi: 10.1016/j.fuel.2013.03.016.

Agency for Toxic Substances and Disease Registry (1995) "Toxological profile for fuel oils," US Department of Health and Human Services, Public Health Service. http://www.atsdr.cdc.gov/

Allen, C., Watts, K., Ackman, R., and Pegg, M. (1999) "Predicting the viscosity of biodiesel fuels from their fatty acid ester composition,". *Fuel*, 78, 1319-1326.

Allen, C., and Watts, K. (2000) "Comparative analysis of the atomization characteristics of fifteen biodiesel fuel types," Transactions of the ASAE, 43, 207-212.

Altun, Ş. (2014) "Effect of the degree of unsaturation of biodiesel fuels on the exhaust emissions of a diesel power generator," *Fuel*, 117, 450-457. doi: 10.1016/j.fuel.2013.09.028.

American Petroleum Institute (2010) "Kerosene/Jet Fuel category assessment document," submitted to the US EPA, Consortium Registration #1100997. (Accessed on November 14, 2016) http://www.petroleumhpv.org/petroleum-substances-and-categories/~/media/37A083A569294403AD230CB504AB17A6.ashx

Arslan, R. (2011) "Emission characteristics of a diesel engine using waste cooking oil as biodiesel fuel," *African Journal of Biotechnology*, 10, 3790-3794. doi:10.5897/AJB10.2202.

Aydin, H., and Bayindir, H. (2010) "Performance and emission analysis of cottonseed oil methyl ester in a diesel engine," *Renewable Energy*, 35, 588-592. doi: 10.1016/j.renene.2009.08.009.

Balakrishnan, A., Parthasarathy, R., and Gollahalli, S. (2014) "Laminar Partially Premixed Flames of Blends of Pre-Vaporized Jet-A Fuel and Palm Methyl Ester," *In ASME 2014 International Mechanical Engineering Congress and Exposition*, V06AT07A068, Montreal, Canada.

Balakrishnan, A., Parthasarathy, R., and Gollahalli, S. (2015) "Concentration Measurements of OH and CH Radicals in Laminar Partially Premixed and Prevaporized Jet A/Palm Methyl Ester Blend Flames," *In ASME 2015 International Mechanical Engineering Congress and Exposition*, V06AT07A002, Houston, Texas, USA.

Balakrishnan, A., Parthasarathy, R., and Gollahalli, S. (2016) "A Review on the effects of Biodiesel Blends on Compression Ignition Engine NOx Emissions," *Journal of Energy and Environmental Sustainability*, 1, 67-76.

Balakrishnan, A., Parthasarathy, R., and Gollahalli, S. (2016a) "Combustion Characteristics of Partially Premixed Prevaporized Palm Methyl Ester and Jet A Fuel Blends," Journal of Energy Resources Technology, 138, 12202. doi:0.1115/1.4031966.

Balakrishnan, A., Parthasarathy, R., and Gollahalli, S. (2016b) "Emission Characteristics of Laminar Prevaporized Petroleum and Biodiesel Flames at near Stoichiometric Conditions," *In 14th International Energy Conversion Engineering Conference*, 4955, Salt Lake City, Utah, USA.

Bamgboye, A., and Hansen, A. (2008) "Prediction of cetane number of biodiesel fuel from the fatty acid methyl ester (FAME) composition," *International Agrophysics*, 22, 21-29.

Benham, G., and Klee, L. (1950) "An improved method for the determination of iodine numbers," *Journal of American Oil Chemists Society*, 27, 127-129. doi:10.1007/BF02634381.

Benjumea, P., Agudelo, J., and Agudelo, A. (2008) "Basic properties of palm oil biodiesel–diesel blends," *Fuel*, 87, 2069-2075. doi: 10.1016/j.fuel.2007.11.004.

Boehman, A., Morris, D., Szybist, J., and Esen, E. (2004) "The impact of the bulk modulus of diesel fuels on fuel injection timing," *Energy & Fuels*, 18, 1877-1882. doi:10.1021/ef049880j.

Bouaid, A., Martinez, M., Aracil, J. (2007) "Long storage stability of biodiesel from vegetable and used frying oils," *Fuel*, 86, 2596-2602. doi: 10.1016/j.fuel.2007.02.014.

Bradley, D., and Entwistle, A. (1966) "The total hemispherical emittance of coated wires," *British Journal of Applied Physics*, 17, 9, 1155.
Brooks, B. (1922) *The Chemistry of the Non-benzenoid Hydrocarbons and Their Simple Derivatives,* Chemical catalog Company, Incorporated.

Buyukkaya, E. (2010) "Effects of biodiesel on a DI diesel engine performance, emission and combustion characteristics," *Fuel*, 89, 3099-3105. doi: 10.1016/j.fuel.2010.05.034.

Canakci, M. (2005) "Performance and emissions characteristics of biodiesel from soybean oil," *Proceedings of the Institution of Mechanical Engineers, Part D: Journal of Automobile Engineering*, 219, 915-922. doi: 10.1243/095440705X28736.

Carraretto, C., Macor, A., Mirandola, A., Stoppato, A., and Tonon, S. (2004) "Biodiesel as alternative fuel: experimental analysis and energetic evaluations," *Energy*, 29, 2195-2211. doi: 10.1016/j.energy.2004.03.042.

Cecrle, E., Depcik, C., Duncan, A., Guo, J., Mangus, M., Peltier, E., Stagg-Williams, S., and Zhong, Y. (2012) "Investigation of the effects of biodiesel feedstock on the performance and emissions of a single-cylinder diesel engine," *Energy & Fuels*, 26, 2331-2341. doi: dx.doi.org/10.1021/ef2017557.

Chamberlain, J. (1921) *A textbook of organic chemistry*. The Maple Press, York, PA.

Chavan, S., Kumbhar, R., Kumar, A., and Sharma, Y. (2015) "Study of biodiesel blends on emission and performance characterization of VCR engine," *Energy & Fuels*, 29, 4393-4398. doi: 10.1021/acs.energyfuels.5b00742.

CHEMKIN (2011) *Reaction Design Inc*., San Diego, California, USA.

Chokri, B., Ridha, E., Rachid, S., and Jamel, B. (2012) "Experimental Study of a Diesel Engine Performance Running on Waste Vegetable Oil Biodiesel Blend," *Journal of Energy Resource Technology*, 134, 32202. doi:10.1115/1.4006655.

Code of Federal Regulations. (2016) *U.S. Food and Drug administration*, Title 21, Volume 3, 21CFR184.1555. (Accessed on November 14, 2016)
http://www.accessdata.fda.gov/scripts/cdrh/cfdocs/cfcfr/CFRSearch.cfm?fr=184.1555

Coniglio, L., Bennadji, H., Glaude, P., Herbinet, O., and Billaud, F. (2013) "Combustion chemical kinetics of biodiesel and related compounds (methyl and ethyl esters): Experiments and modeling–Advances and future refinements," *Progress in Energy and Combustion Science*, 2013, 39, 340-382. doi: 10.1016/j.pecs.2013.03.002.

Curran, H., Gaffuri, P., Pitz, W., and Westbrook, C. (1998) "A comprehensive modeling study of n-heptane oxidation," *Combustion and flame*, 114, 1, 149-177.

Dagaut, P., and Sandro, G. (2007) "Chemical kinetic study of the effect of a biofuel additive on Jet-A1 combustion," *The Journal of Physical Chemistry,* 111, 3992-4000.

Dean, E., and Hill, H. (1917) *Determination of unsaturated hydrocarbons in gasoline*, Bureau of Mines, Washington, DC (USA).

Dean, A., and Bozzelli, J. (2000) "Combustion chemistry of nitrogen. In: Gas-phase Combustion Chemistry," *Springer New York*, 125-341. doi: 10.1007/978-1-4612-1310-9_2.

Dhar, A., Kevin, R., and Agarwal, A. (2012) "Production of biodiesel from high-FFA neem oil and its performance, emission and combustion characterization in a single cylinder DICI engine," Fuel Processing Technology, 97, 118-129. doi: 10.1016/j.fuproc.2012.01.012.

Dooley, S., Curran, H., and Simmie, J. (2008) "Autoignition measurements and a validated kinetic model for the biodiesel surrogate, methyl butanoate," *Combustion and Flame*, 153, 1, 2-32.

Ejim, C., Fleck, B., and Amirfazli, A. (2007) "Analytical study for atomization of biodiesels and their blends in a typical injector: surface tension and viscosity effects," *Fuel*, 86, 1534-1544. doi: 10.1016/j.fuel.2006.11.006.

EPA-Environmental Protection Agency US. (2010) "Renewable Fuel Standard Program (RFS2) Regulatory Impact Analysis," *Assessment and Standards Division, Office of Transportation and Air Quality*, EPA-420-R-10-006.

Fattah, I., Masjuki, H., Liaquat, A., Ramli, R., Kalam, M., and Riazuddin, V. (2013) "Impact of various biodiesel fuels obtained from edible and non-edible oils on engine exhaust gas and noise emissions," *Renewable and Sustainable Energy Reviews*, 18,552-567. doi: 10.1016/j.rser.2012.10.036.

Fattah, I., Masjuki, H., Kalam, M., Wakil, M., Ashraful, A., and Shahir, S. (2014) "Experimental investigation of performance and regulated emissions of a diesel engine with Calophyllum inophyllum biodiesel blends accompanied by oxidation inhibitors," *Energy Conversion Management*, 83, 232-240.
doi: 10.1016/j.enconman.2014.03.069.

Fenimore, C. (1971) "Formation of nitric oxide in premixed hydrocarbon flames," *Symposium (international) on combustion*, 13, 373-380. doi:10.1016/S0082-0784(71)80040-1.

Fernando, S., Hall, C., and Jha, S. (2006) "NOx reduction from biodiesel fuels," *Energy & Fuels*, 20, 376-382. doi: 10.1021/ef050202m.

Fisher, E., Pitz, W., Curran, H., and Westbrook, C. (2000) "Detailed chemical kinetic mechanisms for combustion of oxygenated fuels," *Proceedings of the combustion institute,* 28, 2, 1579-1586. doi: 10.1016/S0082-0784(00)80555-X

Flynn, P., Durrett, R., Hunter, G., Loye, A., Akinyemi, O., Dec, J., and Westbrook, C. (1999) "Diesel Combustion: An Integrated View Combining Laser Diagnostics, Chemical Kinetics, and Empirical Validation," *SAE Paper*, 1999-01-0509, 1-14.

FLUENT (2011) ANSYS FLUENT Theory Guide, Release 14.0, Pennsylvania, USA. http://www.ansys.com

Fontaras, G., Karavalakis, G., Kousoulidou, M., Tzamkiozis, T., Ntziachristos, L., Bakeas, E., Stournas, S., and Samaras, Z. (2009) "Effects of biodiesel on passenger car fuel consumption, regulated and non-regulated pollutant emissions over legislated and real-world driving cycles," *Fuel*, 88, 1608-1617. doi: 10.1016/j.fuel.2009.02.011.

Fontaras, G., Kalogirou, M., Grigoratos, T., Pistikopoulos, P., Samaras, Z., and Rose, K. (2014) "Effect of rapeseed methyl ester blending on diesel passenger car emissions-Part 1: Regulated pollutants, NO/NOx ratio and particulate emissions," *Fuel*, 121, 260-270. doi: 10.1016/j.fuel.2013.12.025.

Giakoumis, E. (2013) "A statistical investigation of biodiesel physical and chemical properties, and their correlation with the degree of unsaturation," *Renewable Energy*, 50, 858-878. doi: 10.1016/j.renene.2012.07.040.

Gilliland, E. (1934) "Diffusion coefficients in gaseous systems," *Industrial & Engineering Chemistry*, 26, 6, 681-685.

Godiganur, S., Murthy, C., and Reddy, R. (2010) "Performance and emission characteristics of a Kirloskar HA394 diesel engine operated on fish oil methyl esters," Renewable Energy, 35, 355-359. doi: 10.1016/j.renene.2009.07.007.

Gollahalli, S., Parthasarathy, R., and Balakrishnan A. (2014) "Flame Characteristics of Vaporized Renewable Fuels and Their Blends with Petroleum Fuels," *Novel Combustion Concepts in Sustainable Energy Development*, Springer, 297–328.

Graboski, M., McCormick, R., Alleman, T., and Herring, A. (2003) "The effect of biodiesel composition on engine emissions from a DDC series 60 diesel engine," *National Renewable Energy Laboratory* (Report No: NREL/SR-510-31461).

Grisanti, M., Parthasarathy, R., and Gollahalli, S. (2011) "Physical and Combustion Properties of Biofuels and Biofuel Blends with Petroleum Fuels," *9th Annual International Energy Conversion Engineering Conference*.

Gumus, M., and Kasifoglu, S. (2010) "Performance and emission evaluation of a compression ignition engine using a biodiesel (apricot seed kernel oil methyl ester) and its blends with diesel fuel," *Biomass and Bioenergy,* 34, 134-139. doi: 10.1016/j.biombioe.2009.10.010.

Gupta, R., and Kanwar, G. (1994) "Determination of iodine numbers of edible oils," Biochem Education, 22, 47.

Hasper, A., Schmitz, J., Holleman, F., and Verwey, F. (1992) "Heat Transport in Cold-wall single-wafer low pressure chemical vapor deposition reactors," *Journal of Vacuum Science Technology,* 10, 3193-3202.

Hellier, P., Ladommatos, N., Allan, R., and Rogerson, J. (2013) "Combustion and emissions characteristics of toluene/n-heptane and 1-octene/n-octane binary mixtures in a direct injection compression ignition engine," *Combustion and Flame*, 160, 2141-2158.

Herbinet, O., Pitz, W., and Westbrook, C. (2008) "Detailed chemical kinetic oxidation mechanism for a biodiesel surrogate," *Combustion and Flame,* 154, 3, 507-528. doi: 10.1016/j.combustflame.2008.03.003

Herbinet, O., Pitz, W., and Westbrook, C. (2010) "Detailed chemical kinetic mechanism for the oxidation of biodiesel fuels blend surrogate," *Combustion and Flame*, 157, 5, 893-908. doi: 10.1016/j.combustflame.2009.10.013

Hoekman, S., and Robbins, C. (2012) "Review of the effects of biodiesel on NOx emissions," *Fuel Processing Technology,* 96, 237-249. doi: 10.1016/j. fuproc.2011.12.036.

Hottel, H. (1927) "Heat Transmission by Radiation from Non–Luminous Gases," *Industrial & Engineering Chemistry*, 19, 8, 888-894.

Imtenan, S., Masjuki, H., Varman, M., Kalam, M., Arbab, M., Sajjad, H., and Ashrafur Rahman, S. (2014) "Impact of oxygenated additives to palm and jatropha biodiesel blends in the context of performance and emissions characteristics of a light-duty diesel engine," *Energy Conversation and Management,* 83, 149-158. doi: 10.1016/j.enconman.2014.03.052.

Jha, S., Fernando, S., and To, S. (2008) "Flame Temperature Analysis of Biodiesel Blends and Components," *Fuel,* 87, 1982-1988.

Johnson, H., and Clark, R. (1947) "Determination of Bromine Number of Olefinic Hydrocarbons," *Analytical Chemistry*, 19, 869-872.

Kalligeros, S., Zannikos, F., Stournas, S., Lois, E., Anastopoulos, G., Teas, C., and Sakellaropoulos, F. (2003) "An investigation of using biodiesel/marine diesel blends on

the performance of a stationary diesel engine," *Biomass and Bioenergy*, 24, 141-149. doi:10.1016/S0961-9534(02)00092-2.

Kanury , A. (1975), *Introduction to Combustion Phenomena: Combustion Science and Technology Book Series* (Vol. 2). Langhorne, PA: Gordon and Breach Science Publishers.

Karavalakis, G., Alvanou, F., Stournas, S., and Bakeas, E. (2009) "Regulated and unregulated emissions of a light duty vehicle operated on diesel/palm-based methyl ester blends over NEDC and a non-legislated driving cycle," *Fuel*, 88, 1078-1085.

Keskin, A., Gürü, M., and Altıparmak, D. (2008) "Influence of tall oil biodiesel with Mg and Mo based fuel additives on diesel engine performance and emission," *Bioresource Technology*, 99, 6434-6438. doi: 10.1016/j.biortech.2007.11.051.

Klopfenstein, W. (1985) "Effect of molecular weights of fatty acid esters on cetane numbers as diesel fuels," *Journal of American Oil Chemists' Society*, 62, 1029-1031. doi:10.1007/BF02935708.

Korobeinichev, O., Gerasimov, I., Knyazkov, D., Shmakov, A., Bolshova, T., Hansen, N., Westbrook, C., Dayma, G., and Yang, B. (2015) "An experimental and kinetic modeling study of premixed laminar flames of methyl pentanoate and methyl hexanoate," *Zeitschrift für Physikalische Chemie*, 229, 5, 759-780.

Knothe, G. (2002) "Structure indices in FA chemistry. How relevant is the iodine value?" *Journal of American Oil Chemists Society*, 2002, 79, 847-854. doi:10.1007/s11746-002-0569-4.

Knothe, G., Sharp, C., and Ryan, T. (2006) "Exhaust emissions of biodiesel, petrodiesel, neat methyl esters, and alkanes in a new technology engine," *Energy & Fuels*, 20, 403-408. doi:10.1021/ef0502711.

Knothe, G. (2007) "Some aspects of biodiesel oxidative stability," *Fuel Processing Technology*, 88, 669-677. doi: 10.1016/j.fuproc.2007.01.005.

Kyriakidis, N., and Katsiloulis, T. (2000) "Calculation of iodine value from measurements of fatty acid methyl esters of some oils: comparison with the relevant American oil chemists' society method," *Journal of American Oil Chemists Society*, 77, 1235-1238. doi:10.1007/s11746-000-0193-3.

Labeckas, G., and Slavinskas, S. (2006) "The effect of rapeseed oil methyl ester on direct injection diesel engine performance and exhaust emissions," *Energy Conversion Management*, 47, 1954-1967. doi: 10.1016/j.enconman.2005.09.003.

Lapuerta, M., Rodríguez-Fernández, J., De Mora, E. (2009) "Correlation for the estimation of the cetane number of biodiesel fuels and implications on the iodine number," *Energy Policy*, 37, 4337-4344. doi: 10.1016/j.enpol.2009.05.049.

Lee, C., Park, S., and Kwon, S. (2005) "An experimental study on the atomization and combustion characteristics of biodiesel-blended fuels," *Energy & Fuels*, 19, 2201-2208. doi:10.1021/ef050026h.

Lertsathapornsuk, V., Pairintra, R., Aryusuk, K., and Krisnangkura, K. (2008) "Microwave assisted in continuous biodiesel production from waste frying palm oil and its performance in a 100-kW diesel generator," Fuel Processing Technology, 89, 1330-1336. doi: 10.1016/j.fuproc.2008.05.024.

Li, Q., Fernandez, L., Zhang, P., and Wang, P. (2015) "Stretch and Curvature Effects on NO Emission of H2/Air Diffusion Flames," *Combustion Science and Technology*, 187, 10, 1520-1541.

Lim, C., Lee, J., Hong, J., Song, C., Han, J., and Cha, J. (2014) "Evaluation of regulated and unregulated emissions from a diesel-powered vehicle fueled with diesel/biodiesel blends in Korea," *Energy*, 77, 533-541.
doi: 10.1016/j.energy.2014.09.040.

Lin, Y., Wu, Y., and Chang, C. (2007) "Combustion characteristics of waste-oil produced biodiesel / diesel fuel blends," *Fuel*, 86, 1772–1780.
doi: 10.1016/j.fuel.2007.01.012.

Lin, B., Huang, J., and Huang, D. (2009) "Experimental study of the effects of vegetable oil methyl ester on DI diesel engine performance characteristics and pollutant emissions," *Fuel*, 88, 1779-1785. doi: 10.1016/j.fuel.2009.04.006.

Lin, C., and Li, R. (2009) "Engine performance and emission characteristics of marine fish-oil biodiesel produced from the discarded parts of marine fish," *Fuel Processing Technology*, 90, 883-888. doi: 10.1016/j.fuproc.2009.04.009.

Lissianski, V., Zamansky, V., and Gardiner, W. (2000) "Combustion Chemistry Modeling. In: Gas-Phase Combustion Chemistry, *Springer New York*, 1-123. doi: 10.1007/978-1-4612-1310-9_1.

Love, N. (2009) "Effects of equivalence ratio and Iodine number on NOx emissions from the flames of biofuels and hydrocarbons," Ph.D. Dissertation, School of Aerospace and Mechanical Engineering, University of Oklahoma, Norman, Oklahoma, USA.

Love, N., Parthasarathy, R., and Gollahalli, S. (2009) "Rapid Characterization of Radiation and Pollutant Emissions of Biodiesel and Hydrocarbon Liquid Diesel Fuels," *Journal of Energy Resources Technology*, 131, 012202-1 - 012202-8.

Love, N., Parthasarathy, R., and Gollahalli, S. (2009a) “Effect of Iodine Number on NOx Formation in Laminar Flames of Oxygenated Biofuels,” *International Journal of Green Energy*, 6, 323-332.

Love, N., Parthasarathy, R, and Gollahalli, S. (2011) “Concentration Measurements of CH and OH Radicals in Laminar Biofuel Flames,” *International Journal of Green Energy*, 8, 113-120.

Luján, J., Bermúdez, V., Tormos, B., and Pla, B. (2009) “Comparative analysis of a DI diesel engine fueled with biodiesel blends during the European MVEG-A cycle: Performance and emissions (II),” *Biomass and Bioenergy*, 33, 948-956. doi: 10.1016/j.biombioe.2009.02.003.

Ma, M., and Hanna, A. (1999) “Biodiesel production: a review,” *Bioresource Technology*, 70, 1-15.

Maxwell, J. (1950) “Data Book on Hydrocarbons Application to Process Engineering,” 9th Printing, Robert E. Krieger Publishing Company, Malabar, FL, 175.

McCormick, R., Graboski, M., Alleman, T., Herring, A., and Tyson, K. (2001) “Impact of Biodiesel Source Material and Chemical Structure on Emissions of Criteria Pollutants from a Heavy-Duty Engine,” *Environmental Science and Technology*, 35, 1742-1747. doi:10.1021/es001636t.

McCormick, R., Alvarez, J., Graboski, M., Tyson, K., and Vertin, K. (2002) “Fuel additive and blending approaches to reducing NOx emissions from biodiesel,” *SAE Technical Paper*, 2002-01-1658. doi:10.4271/2002-01-1658.

McCormick, R., Ratcliff, M., Moens, L., and Lawrence, R. (2007) “Several factors affecting the stability of biodiesel in standard accelerated tests,” Fuel Processing Technology, 88, 651-657. doi: 10.1016/j.fuproc.2007.01.006.

Miller J., and Bowman C. (1989) “Mechanism and modeling of nitrogen chemistry in combustion,” *Progress in energy and combustion science*, 15, 287-338. doi: 10.1016/0360-1285(89)90017-8.

Moscherosch, B., Polonowski, C., Miers, S., and Naber, J. (2010) “Combustion and emissions characterization of soy methyl ester biodiesel blends in an automotive turbocharged diesel engine,” *Journal of Engineering for Gas Turbines and Power*, 132, 92806. doi:10.1115/1.4000607.

Murillo, S., Miguez, J., Porteiro, J., Granada, E., and Moran, J. (2007) “Performance and exhaust emissions in the use of biodiesel in outboard diesel engines,” *Fuel*, 86, 1765-1771. doi: 10.1016/j.fuel.2006.11.031.

Mulenga, M., Reader, G., Ting, D., and Zheng, M. (2003) "Prospect of Reduced CO and NOx Emissions in Diesel Dual Fuel Engines," *In ASME 2003 Internal Combustion Engine and Rail Transportation Divisions Fall Technical Conference* 303-311, Pennsylvania, USA.

Nakamura, H., Darcy, D., Mehl, M., Tobin, C., Metcalfe, W., Pitz, W., Westbrook, C., and Curran, H. (2014) "An experimental and modeling study of shock tube and rapid compression machine ignition of n-butylbenzene/air mixtures," *Combustion and Flame*, 161(1), 49-64. doi: 10.1016/j.combustflame.2013.08.002

National Research Council (2010) "Advancing the Science of Climate Change. Washington, DC", *the National Academies Press*, ISBN 0-309-14588-0.

NIST Web Book (2016), http://webbook.nist.gov/chemistry/

Olikara, C., and Borman, G. (1975) "A Computer Program for Calculating Properties of Equilibrium Combustion Products with Some Applications to I.C. Engines,", SAE *Paper*,750468.

Öner, C., and Altun, Ş. (2009) "Biodiesel production from inedible animal tallow and an experimental investigation of its use as alternative fuel in a direct injection diesel engine," *Applied Energy*, 2009, 86, 2114-2120.
doi: 10.1016/j.apenergy.2009.01.005.

Osawa, W., Sahoo, P., Onyari, J., and Mulaa, F. (2015) "Experimental investigation on performance, emission and combustion characteristics of croton megalocarpus biodiesel blends in a direct injection diesel engine," *International Journal of Science and Technology*, 4, 26-33.

Osborne, D., Fritz, S., and Glenn, D. (2011) "The effects of biodiesel fuel blends on exhaust emissions from a general electric tier 2 line-haul locomotive," *Journal of Engineering for Gas Turbines and Power*, 133, 102803. doi:10.1115/1.4002916.

Ozsezen, A., Canakci, M., and Sayin, C. (2008) "Effects of biodiesel from used frying palm oil on the exhaust emissions of an indirect injection (IDI) diesel engine," *Energy & Fuels*, 22, 2796-2804. doi:10.1021/ef800174p.

Padhee, D., and Raheman, H. (2015) "Performance, Emissions and Combustion Characteristics of a Single Cylinder Diesel Engine Fueled with Blends of Jatropha Methyl Ester and Diesel," *International Journal of Renewable Energy Development*, 3, 125-131. doi:10.14710/ijred.3.2.125-131.

Palash, S., Kalam, M., Masjuki, H., Masum, B., Fattah, I., and Mofijur, M. (2013) "Impacts of biodiesel combustion on NOx emissions and their reduction approaches," *Renewable and Sustainable Energy Reviews*, 473-490. doi: 10.1016/j.rser.2013.03.003.

Pei, Y., Mehl, M., Liu, W., Lu, T., Pitz, W., and Som, S. (2015) "A Multicomponent Blend as a Diesel Fuel Surrogate for Compression Ignition Engine Applications," *Journal of Engineering for Gas Turbines and Power*, 137, 11, 111502. doi: 10.1115/1.4030416

Pereira, R., Oliveira, C., Oliveira, J., Oliveira, P., Fellows, C., and Piamba, O. (2007) "Exhaust emissions and electric energy generation in a stationary engine using blends of diesel and soybean biodiesel," *Renewable Energy*, 32, 2453-2460. doi: 10.1016/j.renene.2006.05.007.

Puhan, S., Vedaraman, N., Ram, B., Sankarnarayanan, G., and Jeychandran, K. (2005) "Mahua oil (Madhuca Indica seed oil) methyl ester as biodiesel-preparation and emission characteristics," *Biomass and Bioenergy*, 28, 87-93. doi: 10.1016/j.biombioe.2004.06.002.

Puhan, S., Saravanan, N., Nagarajan, G., and Vedaraman, N. (2010) "Effect of biodiesel unsaturated fatty acid on combustion characteristics of a DI compression ignition engine," *Biomass and Bioenergy*, 34, 1079-1088. doi: 10.1016/j.biombioe.2010.02.017.

Pulkrabek W. (2004) *Engineering fundamentals of the internal combustion engine*, Pearson Prentice Hall, 2004.

Raheman, H., and Phadatare, A. (2004) "Diesel engine emissions and performance from blends of karanja methyl ester and diesel," *Biomass and Bioenergy*, 27, 393-397. doi: 10.1016/j.biombioe.2004.03.002.

Ramos, M., Fernández, C., Casas, A., Rodríguez, L., and Pérez, Á. (2009) "Influence of fatty acid composition of raw materials on biodiesel properties," *Bioresource Technology*, 100, 261-268. doi: 10.1016/j.biortech.2008.06.039.

Romero, D., Parthasarathy, R., and Gollahalli, S. (2014) "Laminar Flame Characteristics of Partially Premixed Prevaporized Palm Methyl Ester and Diesel Flames," *Journal of Energy Resources Technology*, 136, 032204.

Sahoo, P., Das, L., Babu, M., and Naik, S. (2007) "Biodiesel development from high acid value polanga seed oil and performance evaluation in a CI engine," *Fuel*, 86, 448-454. doi: 10.1016/j.fuel.2006.07.025.

Sahoo, P., Das, L., Babu, M., Arora, P., Singh, V., Kumar, N., and Varyani, T. (2009) "Comparative evaluation of performance and emission characteristics of jatropha, karanja and polanga based biodiesel as fuel in a tractor engine," *Fuel*, 88, 1698-1707. doi: 10.1016/j.fuel.2009.02.015.

Seiser, R., Pitsch, H., Seshadri, K., Pitz, W., and Gurran, H. (2000) "Extinction and autoignition of n-heptane in counterflow configuration," *Proceedings of the Combustion Institute*, 28, 2, 2029-2037. doi:10.1016/S0082-0784(00)80610-4

Sequera, A., Parthasarathy, R., and Gollahalli, S. (2011) "Effects of fuel injection timing in the combustion of biofuels in a diesel engine at partial loads," *Journal of Energy Resources Technology*, 133, 22203. doi:10.1115/1.4003808.

Serrano, L., Lopes, M., Pires, N., Ribeiro, I., Cascão, P., Tarelho, L., Monteiro, A., Nielsen, O., Gameiro da Silva, M., and Borrego, C. (2015) "Evaluation on effects of using low biodiesel blends in a EURO 5 passenger vehicles equipped with a common-rail diesel engine," *Applied Energy*, 146, 230-238. doi: 10.1016/j.apenergy.2015.01.063.

Sharma, D., Soni, S., and Mathur, J. (2009) "Emission reduction in a direct injection diesel engine fueled by neem-diesel blend," *Energy Sources, Part A*, 31, 500-508. doi:10.1080/15567030701715542.

Singh, V. (2013) "Effects of equivalence ratio on combustion characteristics of laminar partially premixed flames of petroleum-biofuel flames," Ph.D. Dissertation, School of Aerospace and Mechanical Engineering, University of Oklahoma, Norman, Oklahoma, USA.

Singh, V., Parthasarathy, R., Gollahalli, S., and Aldana, C. (2013) "Radiation and Emission Characteristics of Laminar Partially Premixed Flames of Petroleum Diesel and Canola Methyl Ester Blends," *Journal of Petroleum Science Research*, 2, 97-103.

Singh, V., Parthasarathy, R., and Gollahalli, S. (2016) "Radiative Heat Transfer and Fluorescence Measurements in Laminar Prevaporized Canola Methyl Ester/Diesel Blend Flames," *Journal of Thermal Science and Engineering Applications*, 8, 1, 011006. doi: 10.1115/1.4030701.

Sirignano, W. (1993) "Fluid dynamics of sprays - 1992 Freeman scholar lecture," *Journal of fluids Engineering*, 115, 345-378. doi:10.1115/1.2910148.

Studzinski, W., Liiva, P., Choate, P., Acker, W., Litzinger, T., Bower, S., Smooke, M., and Brezinsky, K. (1993) "A computational and experimental study of combustion chamber deposit effects on NOx emissions", *SAE Technical Paper*, 932815.

Suh, H., Rho, H., and Lee, C. (2007) "Spray and combustion characteristics of biodiesel fuel in a direct injection common-rail diesel engine," ASME/IEEE 2007 Joint Rail Conference and Internal Combustion Engine Division Spring Technical Conference, *American Society of Mechanical Engineers*, 487-496. doi:10.1115/JRC/ICE2007-40082.

Sun, J., Caton, J., and Jacobs, T. (2010) "Oxides of nitrogen emissions from biodiesel-fueled diesel engines," *Progress in Energy and Combustion Science*, 36, 677-695. doi: 10.1016/j.pecs.2010.02.004.

Sureshkumar, K., Velraj, R., Ganesan, R. (2008) “Performance and exhaust emission characteristics of a CI engine fueled with Pongamia pinnata methyl ester (PPME) and its blends with diesel,” *Renewable Energy*, 33, 2294-2302. doi: 10.1016/j.renene.2008.01.011.

Swan, W. (1857) “On the Prismatic Spectra of the Flames of Compounds of Carbon and Hydrogen,” *Proceedings of the Royal Society of Edinburgh*, 3, 376-377.

Szybist, J., Song, J., Alam, M., Boehman, A. (2007) Biodiesel combustion, emissions and emission control, *Fuel Processing Technology*, 88, 679-691. doi: 10.1016/j.fuproc.2006.12.008.

Tan, P., Hu, Z., Lou, D., and Li, Z. (2012) “Exhaust emissions from a light-duty diesel engine with Jatropha biodiesel fuel,” *Energy*, 39, 356-362. doi: 10.1016/j.energy.2012.01.002.

Tat, M., Van Gerpen, J., Soylu, S., Canakci, M., Monyem, A., and Wormley, S. (2000) “The speed of sound and isentropic bulk modulus of biodiesel at 21 C from atmospheric pressure to 35 MPa,” *Journal of American Oil Chemists’ Society*, 77, 285-289. doi:10.1007/s11746-000-0047-z.

Tat, M. (2003) “Investigation of oxides of nitrogen emissions from biodiesel-fueled engines,” *Ph.D. Dissertation*, Digital Repository at Iowa State University. http://lib. dr. iastate. edu, 2003.

Tat, M., and Van Gerpen, J. (2003) “Measurement of biodiesel speed of sound and its impact on injection timing,” *National Renewable Energy Laboratory*, NREL/SR-510-31462. 2003.

Tsolakis, A., Megaritis, A., Wyszynski, M., and Theinnoi, K. (2007) “Engine performance and emissions of a diesel engine operating on diesel-RME (rapeseed methyl ester) blends with EGR (exhaust gas recirculation),” *Energy*, 32, 2072-2080. doi: 10.1016/j.energy.2007.05.016.

Turns, S. (2011) *An Introduction to Combustion*. Third Edition, McGraw Hill, New York.

Tyson, K. (2004) “Biodiesel Handling and Use Guidelines,” US Department of Energy National Renewable Energy Laboratory, http://www.nrel.gov/docs/fy06osti/40555.pdf

UCSD, (2004) "Chemical-Kinetic Mechanisms for Combustion Applications", San Diego Mechanism web page, Mechanical and Aerospace Engineering (Combustion Research), University of California at San Diego (http://combustion.ucsd.edu).

United States Energy Information Administration. (2016) *Department of Energy*, published on April 2016.

Usta, N. (2005) “An experimental study on performance and exhaust emissions of a diesel engine fueled with tobacco seed oil methyl ester,” Energy Conversion and Management, 46, 2373-2386. doi: 10.1016/j.enconman.2004.12.002.

Utlu, Z., and Koçak, M. (2008) “The effect of biodiesel fuel obtained from waste frying oil on direct injection diesel engine performance and exhaust emissions,” *Renewable Energy*, 33, 1936-1941. doi: 10.1016/j.renene.2007.10.006.

Vandergriff, L. (2008). *Nature and properties of light-Fundamentals of Photonics*, SPIE Press, Bellingham.

Varatharajan, K., and Cheralathan, M. (2012) “Influence of fuel properties and composition on NOx emissions from biodiesel powered diesel engines: a review,” *Renewable and Sustainable Energy Reviews*, 16, 3702–3710. doi: 10.1016/j.rser.2012.03.056.

Vollhardt, K., and Schore, N. (2011) *Organic chemistry: structure and function*, Sixth edition, New York.

Wadumesthrige, K., Smith, J., Wilson, J., Salley, S., and Ng, K. (2008) “Investigation of the parameters affecting the cetane number of biodiesel,” *Journal of American Oil Chemists Society*, 85, 1073-1081. doi:10.1007/s11746-008-1290-2.

Westbrook, C., Pitz, W., Westmoreland, P., Dryer, F., Chaos, M., Oswald, P., Kohse, k., Cool, T., Wang, J., Yang, B., Hansen, N., and Kasper, T. (2009) “A detailed chemical kinetic reaction mechanism for oxidation of four small alkyl esters in laminar premixed flames,” *Proceedings of the combustion institute*, 32, 1, 221-228. doi: 10.1016/j.proci.2008.06.106

Westbrook, C., Naik, C., Herbinet, O., Pitz, W., Mehl, M., Sarathy, S., and Curran, H. (2011) “Detailed chemical kinetic reaction mechanisms for soy and rapeseed biodiesel fuels,” *Combustion and Flame*, 158, 4, 742-755. doi: 10.1016/j.combustflame.2010.10.020

Wu, F., Wang, J., Chen, W., and Shuai, S. (2009) “A study on emission performance of a diesel engine fueled with five typical methyl ester biodiesels,” *Atmospheric Environment*, 43, 1481-1485. doi: 10.1016/j.atmosenv.2008.12.007.

Xue, J., Grift, T., and Hansen, A. (2011) “Effect of biodiesel on engine performances and emissions,” Renewable *and Sustainable Energy Reviews*, 15, 1098-1116. doi: 10.1016/j.rser.2010.11.016.

Ye, P., and Boehman, A. (2010) “Investigation of the impact of engine injection strategy on the biodiesel NOx effect with a common-rail turbocharged direct injection diesel engine,” *Energy & Fuels*, 24, 4215-4225. doi:10.1021/ef1005176.

Yoon, S., Suh, H., and Lee, S. (2009) “Effect of spray and EGR rate on the combustion and emission characteristics of biodiesel fuel in a compression ignition engine,” *Energy & Fuels*, 23, 1486-1493. doi:10.1021/ef800949a.

Yuan, W., Hansen, A., and Zhang, Q. (2005), “Vapor pressure and normal boiling point predictions for pure methyl esters and biodiesel fuels,” *Fuel*, 84, 943–50. doi: 10.1016/j.fuel.2005.01.007.

Yuan, W., Hansen, A., and Zhang, Q. (2007) “Computational modelling of NOx emissions from biodiesel combustion,” *International Journal of Vehicle Design*, 45, 12-32. doi:10.1504/IJVD.2007.013668.

Yuan, W., and Hansen, A. (2009) “Computational investigation of the effect of biodiesel fuel properties on diesel engine NOx emissions,” *International Journal of Agricultural and Biological Engineering*, 2, 41-48. doi: 10.3965/j.

Zhang, Y., and Boehman, A. (2007) “Impact of biodiesel on NO x emissions in a common rail direct injection diesel engine,” *Energy & Fuels*, 21, 2003-2012. doi:10.1021/ef0700073.

Zhang, X., Wang, H., Li, L., Wu, Z., Hu, Z., and Zhao, H. (2008) “Characteristics of Output Performances and Emissions of Diesel Engine Employed Common Rail Fueled with Biodiesel Blends from Wasted Cooking Oil,” *SAE Technical Paper*, 10. doi:10.4271/2008-01-1833.

APPENDIX A ESTIMATED UNCERTAINTIES

Precision (random) and bias (fixed) errors were calculated and presented in the figures of this dissertation as error bars. The precision error was statistically determined based on the sample size and standard deviation of the data points. Bias error was found based on the calibration error or least count of the instrument used, typically 0.1 - 1% of the full-scale value. The overall uncertainty (ω) can be expressed mathematically as:

$$\omega = \sqrt{P^2 + B^2}$$

where P is the precision and B the bias error of the measurements. The precision error was calculated based on the following:

$$P = t_{\alpha/2} \frac{S_x}{\sqrt{n}}$$

where S_x represents the standard deviation of the data points, n is the number of data points, and $t_{\alpha/2}$ the student's t-distribution value for a 95% confidence interval. Typical $t_{\alpha/2}$ values are presented below.

Table A.1 Student t-distribution values

n =	υ =	$t_{\alpha/2}$ for a 95% confidence interval
3	2	4.303
4	3	3.182
5	4	2.776
6	5	2.571
7	6	2.447
8	7	2.365
9	8	2.306

Precision errors were much larger than corresponding bias errors and accounted for most of the uncertainty in the present study. For this reason, the measurements were repeated 5 times and instruments were calibrated before use each day. For some cases where multiple uncertainties were present, as in the calculation of the Emission Index, the errors were propagated. Below is a sample of how the error was propagated for the Emission Index of NO.

$$\delta EI_{NO} = \sqrt{\left(\frac{\partial EI_{NO}}{\partial \chi_{NO}}\delta\chi_{NO}\right)^2 + \left(\frac{\partial EI_{NO}}{\partial \chi_{CO}}\delta\chi_{CO}\right)^2 + \left(\frac{\partial EI_{NO}}{\partial \chi_{CO_2}}\delta\chi_{CO_2}\right)^2}$$

where

$$EI_{NO} = \left(\frac{\chi_{NO}}{\chi_{CO} + \chi_{CO_2}}\right)\left(\frac{N \cdot MW_{NO}}{MW_f}\right)$$

$$\frac{\partial EI_{NO}}{\partial \chi_{NO}} = \left(\frac{1}{\chi_{CO} + \chi_{CO_2}}\right)\left(\frac{N \cdot MW_{NO}}{MW_f}\right)$$

$$\frac{\partial EI_{NO}}{\partial \chi_{CO}} = -\left(\frac{\chi_{NO}}{\left(\chi_{CO} + \chi_{CO_2}\right)^2}\right)\left(\frac{N \cdot MW_{NO}}{MW_f}\right)$$

$$\frac{\partial EI_{NO}}{\partial \chi_{CO_2}} = -\left(\frac{\chi_{NO}}{\left(\chi_{CO} + \chi_{CO_2}\right)^2}\right)\left(\frac{N \cdot MW_{NO}}{MW_f}\right)$$

$\delta\chi_{NO}$ = Overall uncertainty (ω) associated with the NO measurements

$\delta\chi_{CO}$ = Overall uncertainty (ω) associated with the CO measurements

$\delta\chi_{CO_2}$ = Overall uncertainty (ω) associated with the CO_2 measurements

The uncertainty associated with the Emission Index of NO is then expressed as:

$EI_{NO} \pm \delta EI_{NO}$

A sample calculation is provided below:

At equivalence ratio Φ = 1.2 condition of diesel flame, the measured quantities are,

Mean concentration of NO = 46 ppm

Mean concentration of CO = 9 ppm

Mean concentration of CO_2 = 2.3 %

The emission index of NO is calculated as EI_{NO} = 4.43 g $_{NO}$ / kg of fuel burnt (See Appendix D.6)

$\delta\chi_{NO}$ = 2.68 ppm

$\delta\chi_{CO}$ = 1.00 ppm

$\delta\chi_{CO_2}$ = 0.17 %

$$\frac{\partial EI_{NO}}{\partial \chi_{NO}} = 96.36$$

$$\frac{\partial EI_{NO}}{\partial \chi_{CO}} = -0.20$$

$$\frac{\partial EI_{NO}}{\partial \chi_{CO_2}} = -0.20$$

$$\delta EI_{NO} = \sqrt{\left(96.36 * (2.68 * 10^{-6})\right)^2 + \left(-0.20 * (1.00 * 10^{-6})\right)^2 + \left(-0.20 * (0.17 * 10^{-2})\right)^2}$$

δEI_{NO} = 0.43 g_{NO} / kg of fuel burnt

The uncertainty associated with the Emission Index of NO measured from a diesel flame at Φ = 1.2 is 4.43 ± 0.43 g_{NO} / kg of fuel burnt

APPENDIX B AIR AND FUEL FLOW RATE CALIBRATION

B.1 Air flow rate calibration

The detailed information regarding the rotameter employed for delivering the air flow in this study is given below:

Table B.1 Specification of airflow rotameter

Make	Lo Flo
Model	SK ¼”-15-G-5
Float	Tantalum ball

Table B.2 Air flow rate with corresponding rotameter scale calibration

Rotameter	Flow rate (Litres per minute)
0	0.00
1	1.23
2	2.59
3	3.94
4	5.30
5	6.66
6	8.02
7	9.38
8	10.74
9	12.09
10	13.45

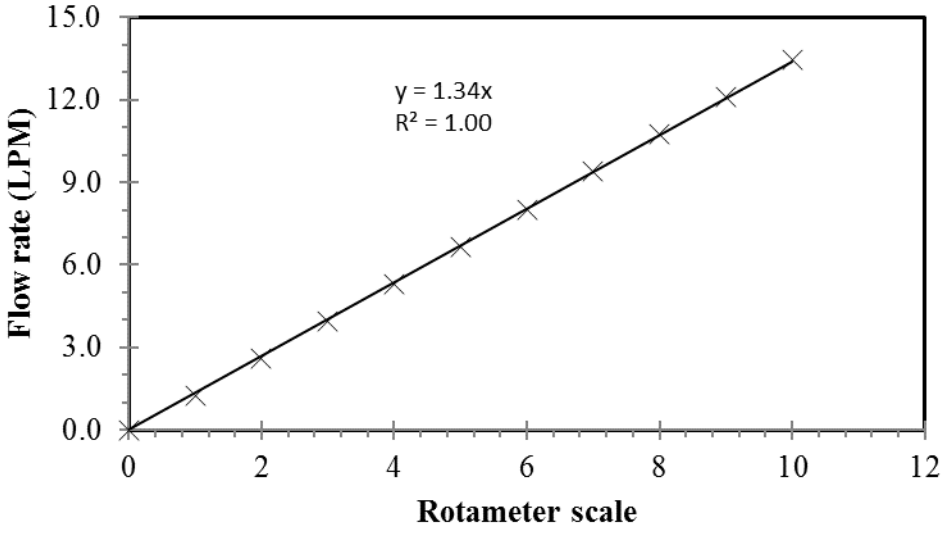

Figure B.1 Calibration curve for air flow rotameter

The calibration equation of air flow rotameter is given by:

$$\text{Flow rate } \left(\frac{\text{litres}}{\text{minute}}\right) = 1.34 * \text{Rotameter scale} \qquad \text{(B.1)}$$

B.2 Fuel flow rate calibrtion

The detailed information regarding the fuel delivery system employed in this study is given below:

Table B.3 Specification of fuel syringe pump

Syringe pump supplier	Harvard
Type	Compact infusion pump
Model	975
Syringe type	50 cc glass type syringe

Table B.4 Fuel flow rate with corresponding gear selection

Gear	Flow rate (ml/min)	Gear	Flow rate (ml/min)
1	46.00	9	3.10
2	33.00	10	2.20
3	24.00	11	1.60
4	17.00	12	1.10
5	12.00	13	0.82
6	8.60	14	0.59
7	6.20	15	0.42
8	4.40	16	0.30

Gear 14 was selected for the equivalence ratio of 0.9 and 1.0 while Gear 13 was selected for the equivalence ratio of 1.2 and 1.5 to maintain the injector exit momentum as similar as possible between the tested flames.

APPENDIX C CARBON BALANCE VALIDATION

Carbon balance is one of the techniques employed to confirm the complete evaporation of liquid fuel that was injected into the septum and the evaporated fuel vapor came out of the burner without any pyrolysis or deposits. By the law of conservation of mass, the mass flow rate of carbon (fuel) that was injected in to the septum should be equal to the mass flow rate of carbon (in the form of carbon dioxide) leaving the flame after combustion.

A test condition of $\Phi = 2$ - Jet A flame was considered for the study and the configuration of global emission measurement was incorporated for the experiment. The temperature, dynamic pressure head and concentration of species such as CO_2, CO, NOx and O_2 were measured and presented in table 4.5.

Since the concentration of CO measured at this condition was at parts per million levels, CO contribution is ignored in the mass balance and the carbon mass balance equation is presented as:

$$Y_{c\,(fuel)}\left(\frac{\text{kg of C in fuel}}{\text{kg of fuel}}\right) * \dot{m}_f \left(\frac{\text{kg of fuel}}{\text{sec}}\right) = Y_{C\,(CO_2)}\left(\frac{\text{Kg of C in } CO_2}{\text{kg of product}}\right) * \dot{m}_{product}\left(\frac{\text{kg of product}}{\text{sec}}\right)$$

The fuel (Jet A) flow rate was measured to be 2.2 cc/min and the assumed formula for Jet A is $C_{13}H_{23}$ (Grisanti et al, 2011)

Mass flow rate of carbon as fuel (Jet A)

$$\rho_{C_{13}H_{23}} = 796 \frac{kg}{m^3}$$

$$\dot{m}_f = \frac{2.2 * 10^{-6} * 796}{60} = 2.93 * 10^{-5} \frac{kg}{s}$$

$$\dot{m}_{C_{(C_{13}H_{33})}} = Y_{C_{(C_{13}H_{33})}} * \dot{m}_f = \frac{(13 * 12)}{(13 * 12) + (23 * 1)} * 2.93 * 10^{-5} = 2.55 * 10^{-5} \frac{kg}{s}$$

$$\dot{m}_{C_{(C_{13}H_{33})}} = 2.55 * 10^{-5} \frac{kg}{s}$$

Mass flow rate of carbon as carbon dioxide

$$\chi_{CO_2} = \frac{n_{CO_2}}{\left(n_{CO_2} + n_{N_2} + n_{O_2}\right)} = 0.021 \overset{\text{Implies}}{\Longrightarrow} \left(n_{CO_2} + n_{N_2} + n_{O_2}\right) = \frac{n_{CO_2}}{0.021}$$

$$\chi_{O_2} = \frac{n_{O_2}}{\left(n_{CO_2} + n_{N_2} + n_{O_2}\right)} = 0.171$$

Note:

Mole fraction of water vapor was not measured since the water vapor present in the gas sample was condensed and removed before supplying into the gas analyzer. But the amount of water vapor formed could be estimated using H/C ratio.

$$\frac{H}{C} = \frac{23}{13} \overset{\text{Yields}}{\Longrightarrow} \frac{n_{H_2O}}{n_{CO_2}} = \frac{23}{26}$$

The actual concentration of species formed in the flame could be calculated as:

$$\chi_{CO_2} = \frac{n_{CO_2}}{\left(n_{CO_2} + n_{N_2} + n_{O_2} + n_{H_2O}\right)} = \frac{n_{CO_2}}{\left(\frac{1}{0.021}\right)n_{CO_2} + \left(\frac{23}{26}\right)n_{CO_2}} = 0.0206$$

$$\chi_{H_2O} = \frac{n_{H_2O}}{\left(n_{CO_2} + n_{N_2} + n_{O_2} + n_{H_2O}\right)} = \frac{\left(\frac{23}{26}\right)n_{CO_2}}{\left(\frac{1}{0.021}\right)n_{CO_2} + \left(\frac{23}{26}\right)n_{CO_2}} = 0.0182$$

$$\chi_{O_2} = \frac{n_{O_2}}{\left(n_{CO_2}+n_{N_2}+n_{O_2}+n_{H_2O}\right)} = \frac{0.171\left(\frac{1}{0.021}\right)n_{CO_2}}{\left(\frac{1}{0.021}\right)n_{CO_2}+\left(\frac{23}{26}\right)n_{CO_2}} = 0.1679$$

$$\chi_{N_2} = 1 - \left(n_{CO_2} + n_{O_2} + n_{H_2O}\right) = 0.7933$$

Hence the mass fraction of CO_2 could be calculated as:

$$Y_{CO_2} = \frac{\left(\chi_{CO_2}\right) MW_{CO_2}}{\left(\chi_{CO_2}\right) MW_{CO_2} + \left(\chi_{H_2O}\right) MW_{H_2O} + \left(\chi_{O_2}\right) MW_{O_2} + \left(\chi_{N_2}\right) MW_{N_2}}$$

$$= \frac{(0.0206)\ 44}{(0.0206)\ 44 + (0.0182)\ 18 + (0.1679)\ 32 + (0.7933)\ 28}$$

$$Y_{CO_2} = 0.03145$$

$$MW_{product} = \left(\chi_{CO_2}\right) MW_{CO_2} + \left(\chi_{H_2O}\right) MW_{H_2O} + \left(\chi_{O_2}\right) MW_{O_2} + \left(\chi_{N_2}\right) MW_{N_2}$$

$$= 28.819 \left(\frac{\text{kg of product}}{\text{kmol of product}}\right)$$

Velocity measurement:

Conditions at the sampling point:

P = 101390 Pa

T = 668 K

$$\rho = \frac{P}{\left(\frac{R_u}{MW}\right) T} = \frac{101390}{\left(\frac{8314}{28.819}\right) 668} = 0.526 \frac{kg}{m^3}$$

$$V = \sqrt{\frac{2 * \rho_{manometer} * g * \Delta h}{\rho_{product}}} = \sqrt{\frac{2*1000*9.81*0.007*0.0254}{0.526}} = 2.574 \text{ m/s}$$

$$\dot{m}_{product} = \rho * \frac{\pi d^2}{4} * V = 0.529 * \frac{\pi (0.056)^2}{4} * 2.574 = 3.335*10^{-3} \frac{kg}{s}$$

Where d = diameter of the Pyrex funnel = 0.056m

$$\dot{m}_{CO_2} = Y_{CO_2} * \dot{m}_{product} = 0.03145 * 3.335 * 10^{-3} = 1.0489 * 10^{-4} \frac{kg}{s}$$

$$\dot{m}_C = \dot{m}_{CO_2} * \left(\frac{MW_C}{MW_{CO_2}}\right) = 1.0489 * 10^{-4} * \left(\frac{12}{44}\right) = 2.86*10^{-5} \frac{kg}{s}$$

$$\dot{m}_{C_{(CO_2)}} = 2.86 * 10^{-5} \frac{kg}{s}$$

The mass flow rate of carbon as fuel was measured to be $2.55 * 10^{-5}$ kg/s and the mass flow rate of carbon in the form of carbon dioxide after combustion was measured to be $2.86 * 10^{-5}$ kg/s. Hence the mass flow rate of carbon injected into the septum as fuel was comparable to the mass flow rate of carbon liberated as carbon dioxide from the flame, with the variation attributed to the involved uncertainties in the experiment.

APPENDIX D SAMPLE CALCULATION

D.1 Estimation of molecular formula of a fuel blend

The fuels used in the present study were assumed to have a general molecular formula based on the average composition of the hydrocarbons or fatty acid methyl ester components that comprised the fuel. The following section describes the estimation of the molecular formula of a fuel blend whose molecular composition depends on the molecular formula of the parent fuels and their composition in the fuel blend.

Sample molecular formula calculation pertinent to P50D50 fuel blend is presented in this section.

Molecular formula for palm methyl ester is $C_{17.1}H_{32.9}O_2$ (refer table 4.4)

Molecular formula for petrodiesel is $C_{14.4}H_{24.9}$ (refer table 4.5)

In a P50D50 blend that consists of 50% by volume of PME and 50% by volume of diesel,

Number of moles of diesel per unit volume of P50D50 = $0.50* \left(\frac{\rho_{diesel}}{MW_{diesel}}\right)$

$N_{diesel} = 0.50* \left(\frac{843}{197.7}\right) = \quad 2.13 \left(\frac{kmol}{m^3}\right)$

Number of moles of PME per unit volume of P50D50 = $0.50* \left(\frac{\rho_{PME}}{MW_{PME}}\right)$

$N_{PME} = 0.50* \left(\frac{869}{270.1}\right) = 1.61 \left(\frac{kmol}{m^3}\right)$

Mole fraction of diesel in P50D50,

$$\chi_{diesel} = \frac{(N_{diesel})+(N_{PME})}{(N_{diesel})} = 0.570 \left(\frac{\text{moles of diesel}}{\text{moles of P50D50}}\right)$$

Mole fraction of PME in P50D50,

$$\chi_{PME} = \frac{(N_{diesel})+(N_{PME})}{(N_{PME})} = 0.430 \left(\frac{\text{moles of PME}}{\text{moles of P50D50}}\right)$$

Molecular weight of P50D50,

$$MW_{P50D50} = \{(MW_{diesel} * \chi_{diesel}) + (MW_{PME} * \chi_{PME})\}$$

$$MW_{P50D50} = \{(197.7*0.570) + (270.1* 0.430)\}$$

$$MW_{P50D50} = 228.8 \left(\frac{\text{kg of P50D50}}{\text{kmol of P50D50}}\right)$$

Hence, the estimation of the molecular formula of P50D50 is given by,

Number of C atoms in P50D50 = $(\chi_{diesel} * C_{diesel}) + (\chi_{PME} * C_{PME}) = 15.6$

Number of H atoms in P50D50 = $(\chi_{diesel} * H_{diesel}) + (\chi_{PME} * H_{PME}) = 28.3$

Number of O atoms in P50D50 = $(\chi_{diesel} * O_{diesel}) + (\chi_{PME} * O_{PME}) = 0.9$

Hence the estimated molecular formula for P50D50 is $\mathbf{C_{15.6}H_{28.3}O_{0.9}}$

D.2 Stoichiometric calculation

Sample stoichiometric calculations for petrodiesel and palm methyl ester fuel are presented in this section.

The general stoichiometric equation is given by,

$C_xH_{2y}O_{2z} + a\,(O_2 + 3.76N_2) \rightarrow x\,CO_2 + y\,H_2O + (3.76a)\,N_2$

$$a = x + \frac{y}{2} - z$$

$$(A/F)_{stoic} = \frac{a*\left(32 + 3.76*(28)\right)}{12x + 2y + 16z}$$

For diesel fuel ($C_{14.4}H_{24.9}$):

$$a = 14.4 + \frac{12.45}{2} - 0 = 20.625$$

$$(A/F)_{stoic} = \frac{20.625*\left(32 + 3.76*(28)\right)}{12*(14.4) + 2*(12.45) + 32*(0)} = 14.322$$

For PME ($C_{17.1}H_{32.9}O_2$):

$$a = 17.1 + \frac{16.45}{2} - 1 = 24.325$$

$$(A/F)_{stoic} = \frac{24.325*\left(32 + 3.76*(28)\right)}{12*(17.1) + 2*(16.45) + 32*(1)} = 12.363$$

D.3 Flow rate calculation

According to the definition of equivalence ratio,

$$\Phi = \frac{\left(\frac{A}{F}\right)_{stoic}}{\left(\frac{A}{F}\right)_{actual}}$$

Hence, at $\Phi = 1.2$,

$$\left(\frac{A}{F}\right)actual = \frac{\left(\frac{A}{F}\right)_{stoic}}{\Phi}$$

For diesel fuel ($C_{14.4}H_{24.9}$):

$$\left(\frac{A}{F}\right)actual = \frac{14.32}{1.2} = 11.93$$

The fuel flow rate was maintained constant for a particular equivalence ratio between the tested flames in this study. At $\Phi = 1.2$, the fuel flow rate was $1.37 * 10^{-8}$ m^3/s (0.82 ml/min).

Hence,

$$\dot{Q}_{air} = \left(\frac{A}{F}\right)actual * \frac{\rho_{fuel} * \dot{Q}_{fuel}}{\rho_{air}} = \frac{11.93 * 850 * 1.37 * 10^{-8}}{1.2}$$

$\dot{Q}_{air} = 1.16 * 10^{-4} \frac{m^3}{s}$ and $\dot{Q}_{fuel} = 1.37 * 10^{-8} \frac{m^3}{s}$

D.4 Jet exit velocity from the burner

A sample calculation of estimating the burner exit jet velocity of diesel / air mixture at an equivalence ratio of 1.2 is presented below:

$$u_{exit} = \frac{\dot{m}_{mix}}{\rho_{mix} * A_{exit}} = \frac{\dot{m}_{air} + \dot{m}_{fuel}}{\rho_{mix} * A_{exit}}$$

At Φ = 1.2 diesel flame, the known parameters are:

$\dot{m}_{air} = 1.4*10^{-4}$ kg/s

$\dot{m}_{fuel} = 1.2*10^{-5}$ kg/s

$\rho_{mix} = 0.591$ kg/m^3

$$A_{exit} = \frac{(\pi * 0.0095^2)}{4} = 7.09 * 10^{-5} \text{ m}^2$$

$$u_{exit} = \frac{(1.4*10^{-4}) + (1.2* 10^{-5})}{0.591* (7.09 *10^{-5})} = 3.60 \text{ m/s}$$

D.5 Reynolds number calculation

The mixture flow rates were selected in such a way that laminar flow was maintained throughout the range of experimental test conditions. Hence to achieve a laminar flow, a low Reynolds number (Re) has to be maintained at the injector exit. To estimate the Reynolds number, densities and viscosities for the vaporized fuel and air mixture were calculated with data from Maxwell (1950) and the equations shown below from Kanury (1975).

$$\mu_{mixture} = \sum_{i=1}^{n} \frac{\chi_i \mu_i}{\sum_{j=1}^{n} \chi_j \Omega_{ij}}$$

$$\Omega_{ij} = \frac{1}{\sqrt{8}} \left(1 + \frac{MW_i}{MW_j} \right)^{-1/2} \left[1 + \left(\frac{\mu_i}{\mu_j} \right)^{1/2} \left(\frac{MW_j}{MW_i} \right)^{1/4} \right]^2$$

where;

χ	=	mole fraction
$\mu_{mixture}$	=	dynamic viscosity
MW	=	molecular weight

The above-mentioned equations can be rewritten (for n = 2; diesel and air) as:

$$\mu_{mixture} = \frac{(\chi_{diesel} * \mu_{diesel})}{(\chi_{diesel} * \Omega_{11}) + (\chi_{air} * \Omega_{12})} + \frac{(\chi_{air} * \mu_{air})}{(\chi_{diesel} * \Omega_{21}) + (\chi_{air} * \Omega_{22})}$$

For diesel/air mixture at the preheat temperature of 645K at $\Phi = 1.2$

	diesel	Air
Molecular weight	226.5	28.9
Density (kg/m^3)	4.284	0.546
μ ($N\text{-}s/m^2$)	$7.28 * 10^{-6}$	$3.24 * 10^{-5}$

Ω_{ij}		i =1	i =2
		Jet A	Air
j = 1	Jet A	1	6.8288
j = 2	Air	0.1957	1

From the stoichiometric balance for the diesel/air mixture:

$C_{14.4}H_{24.9} + 20.625\ (3.76\ N_2 + O_2) \rightarrow 14.4\ CO_2 + 12.5H_2O + 77.55\ N_2$

Thus, for an equivalence ratio of 1.2:

$C_{14.4}H_{24.9} + 17.19\ (3.76\ N_2 + O_2) \rightarrow$ combustion products

The mole fractions of the species are:

$$\chi_{diesel} = \frac{1}{1+[17.19 * (4.76)]} = 0.0121$$

$$\chi_{air} = 1 - \chi_{diesel} = 0.9879$$

The viscosity of the mixture is then:

$$\mu_{mixture} = \frac{0.0121 * \left(7.28*10^{-6}\right)}{0.0121 * (1)+0.9879 * (0.1957)} + \frac{0.9879 * \left(3.24*10^{-6}\right)}{0.0121 * (6.8288)+0.9879 * (1)}$$

$$\mu_{diesel\text{-}air\ mixture} = 3.0 * 10^{-5}\ \frac{N\text{-}s}{m^2}$$

Density of the mixture ($\rho_{mixture}$) is expressed in the equation below.

$$\rho_{mixture} = \sum_{i=0}^{n} (\chi_i * \rho_i) = (\chi_{diesel} * \rho_{diesel}) + (\chi_{air} * \rho_{air})$$

$$\rho_{mixture} = (0.0121 * 4.284) + (0.9879 * 0.546) = 0.591\ \frac{kg}{m^3}$$

Kinematic viscosity was then calculated as:

$$\vartheta_{mixture} = \frac{\mu_{mixture}}{\rho_{mixture}}$$

$$\vartheta_{mixture} = \frac{3.0 * 10^{-5}}{0.591} = 5.1 * 10^{-5} \frac{m^2}{s}$$

Given that the exit velocity of the diesel - air mixture at $\Phi = 1.2$ is 3.60 m/s (already calculated in section D.4), the Reynolds number for this mixture is approximated as:

$$Re = \frac{u_{exit} * d_{exit}}{\vartheta_{mixture}}$$

$$Re = \frac{3.60 * 0.0095}{5.1 * 10^{-5}} = 670$$

D.6 Emission index calculation

Sample NO emission index calculation for petrodiesel flame at an equivalence ratio of 1.2 is presented in this section. The measured concentrations at the end of pyrex funnel mounted above the flame (refer section 5.3.2 for detailed information) are given by:

Mean concentration of NO = 46 ppm

Mean concentration of CO_2 = 2.27 %

Mean concentration of CO = 9 ppm

The emission index is calculated using the equation,

$$EI_{NO} = \left(\frac{\chi_{NO}}{\chi_{CO} + \chi_{CO_2}}\right)\left(\frac{N^* MW_{NO}}{MW_f}\right) * 1000$$

Here,

χ_{NO} = 0.000046

χ_{CO} = 0.000009

χ_{CO_2} = 0.0227

N = 14.4

MW_{NO} = 28

MW_f = 197.7

$$EI_{NO} = \left(\frac{46 * 10^{-6}}{(9* 10^{-6})+ (0.0227)}\right)\left(\frac{14.4 * 28}{197.7}\right) *1000$$

Hence the EI_{NO} of diesel flame at $\Phi = 1.2$ is given by,

$$EI_{NO} = 4.43 \ \frac{\text{g of NO formed}}{\text{kg of fuel burnt}}$$

D.7 Corrections for measured flame temperature data

The recorded flame temperature read from the thermocouple bead would be less than the true flame temperatures due to radiative and convective heat losses. Thus, a representative correction is required to account for these losses. In this work, the flame temperature correction technique adopted by Jha et al (2008) in the flame temperature measurements of biodiesel blends with diesel was employed. The procedure involved three calculation steps, Reynolds number, approximation of the Nusselt number, and finally the radiation calculation, which yielded the corrected thermocouple values.

$$Re = (ud_{bead})/\upsilon_{air}$$

$$Nu = \left(\frac{hd_{bead}}{k_{air}}\right) = 2 + (0.4Re^{0.5} + 0.06Re^{0.667})Pr^{0.4}$$

$$T_{Corrected} = \left(\frac{\sigma\varepsilon}{h}\right)\left(T^4_{Recorded} - T^4_{\infty}\right) + T_{Recorded}$$

where u is the burner exit velocity, d_{bead} is the bead diameter, υ_{air} is the kinematic viscosity of air at measured flame temperature, k_{air} is the thermal conductivity of air also at measured flame temperature (Turns, 2011), ε is the emissivity of the thermocouple bead wire and σ is the Stefan-Boltzmann constant. The Prandtl number is fairly constant over a wide range of temperatures and the value is around Pr = 0.68 (Jha et al., 2008).

Here,

d_{Bead} = 0.2 mm (measured)

$$\sigma = 5.67 \times 10^{-8} \frac{W}{m^2 K^4}$$

For the temperature ranges of 300K-1200K and 1200K-2500K respectively (Turns, 2011):

$$k_{air} = \left(-2 \times 10^{-8}\right) T^2_{Recorded} + \left(8 \times 10^{-5}\right) T_{Recorded} + 0.0042$$

$$k_{air} = \left(1 \times 10^{-10}\right) T^3_{Recorded} - \left(5 \times 10^{-7}\right) T^2_{Recorded} + 0.0009 T_{Recorded} - 0.4868$$

For the temperature range of 300K - 2500K (Turns, 2011):

$$\upsilon_{air} = (1 \times 10^{-9}) T^{1.6836}_{Recorded}$$

The emissivity of the thermocouple bead wire, ε varied with temperature (Bradley and Entwistle, 1966 and Hasper et al., 1992), given by:

$$\varepsilon = \left(1 \times 10^{-7}\right) T^2_{Recorded} - 0.0004T + 0.5605$$

D.8 Radiative heat fraction calculation

The radiative fraction of heat release is the fraction of the heat content of the fuel that is lost as radiation from the flame due to gas band radiation and gray-body radiation from soot particles. However, in this study, all the tested flames are at fuel lean conditions or near stoichiometric (Φ = 0.9, 1.0, 1.2 and 1.5). Hence the radiative heat fraction of heat loss from the tested flames was primarily due to the gas band radiation from CO, CO_2 and water vapor. This dimensionless parameter facilitates the comparison of different fuels since the radiative heat flux measured from the flame is normalized by the lower heating value of the liquid fuel.

In this work, a wide view-angle (150^o) high sensitivity pyrheliometer, which consists of Schmidt-Boelter sensor with quartz window, was used to measure the total radiation from the flame. The pyrheliometer had a linear output with a responsivity of 44.56 mV per kW/m^2 and was located far enough (20 cm) from the burner so that its view-angle covered the entire flame length and the flame could be assumed as a point source. The measured radiative heat flux was sampled at 1 Hz for time duration of 2 minutes using LabView software. The background radiation was subtracted from the total radiation to obtain the flame radiation, and was expressed as the radiative fraction of heat release, F:

$$F = \frac{4\pi L^2 Q_{corrected}}{\dot{m}\, LHV} \tag{5.2}$$

Here, L is the distance from the flame centerline to the pyrheliometer, Q is the corrected radiative heat flux measured, $\dot{m}$ is the mass flow rate of the fuel and LHV is the lower heating value of the fuel tested.

A sample radiative heat fraction calculation of diesel flame at an equivalence ratio of 1.2 is presented in this section.

$$F = \frac{4\pi L^2 Q_{corrected}}{\dot{m} LHV}$$

$$Q_{corrected} = Q_{total} - Q_{background}$$

$Q_{total} = 43.40\ W/m^2$

$Q_{background} = 6.83\ W/m^2$

$Q_{corrected} = 36.57\ W/m^2$

$L = 20\ cm$

$\dot{m} = 1.15 * 10^{-5}\ kg/s$

$LHV = 42.6\ MJ/kg$

$$F = \frac{4\pi (0.2)^2 * (36.57)}{(1.15 * 10^{-5}) * (42.6 * 10^6)}$$

$F = 0.038$

In other words, 3.8% of the total heat released from the flame was lost to the surroundings in the form of gas band radiation. This calculated value for all the tested flames was comparable at about 0.04 and was utilized in the temperature correction calculation for Jet flame network model in the computational analysis (Appendix H).

APPENDIX E IMAGES OF ALL THE TESTED FLAMES

As discussed in section 5.3.1, the visible flame images were captured with an 8-mega pixel digital AF SLR camera. The images were obtained at similar lighting and exposure conditions with a dark background at different shutter speeds such as 1/10th, 1/50th, 1/100th and 1/200th of a second. Images were taken 50 cm away from the flame point. Images captured at 1/50th of a second exposure were considered for flame length measurement, since in that condition, the exposed image rendered enough time required to trace the entire visible flame field and clearly distinguish the inner and outer cone reaction zones of the flames. Microsoft paint software was used to count the pixels and convert them into the length scale using the burner width (12.7 mm) as the calibration reference.

In this section, the captured flame images at four tested equivalence ratios (Φ = 0.9, 1.0, 1.2 and 1.5) are presented for all the tested 63 fuels (refer table 4.1 for the list of fuels selected for the investigation). The presented flame images were captured at an exposure time of $1/50^{th}$ of a second with a constant focal ratio (f/5.6) and focal length of 55 mm.

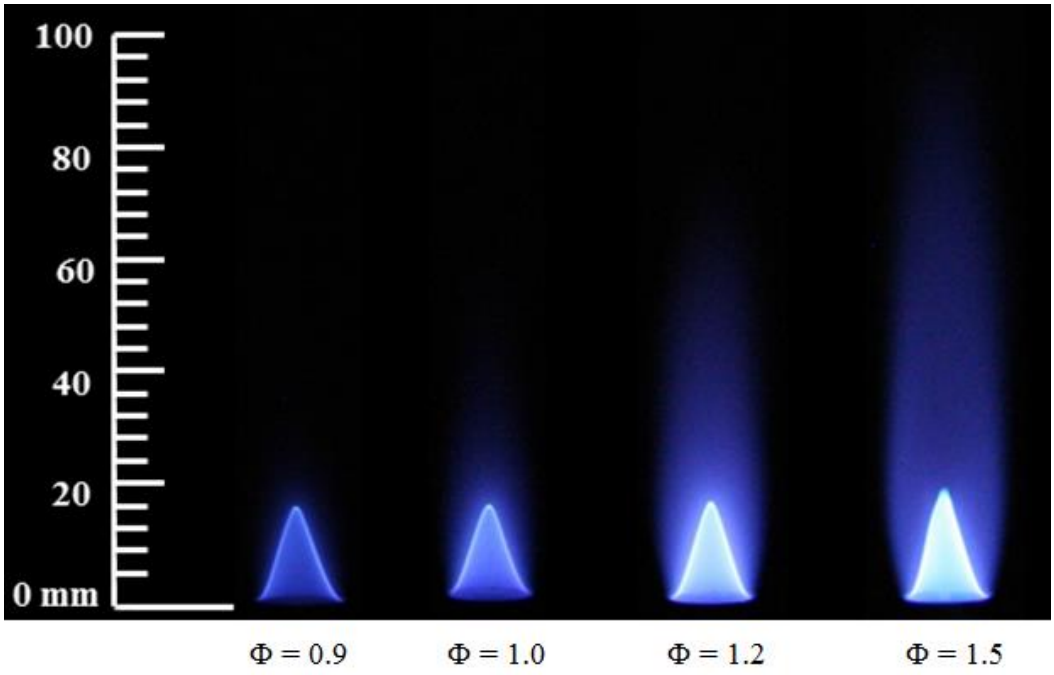

Figure E.1 Flame images of MO at the tested equivalence ratios

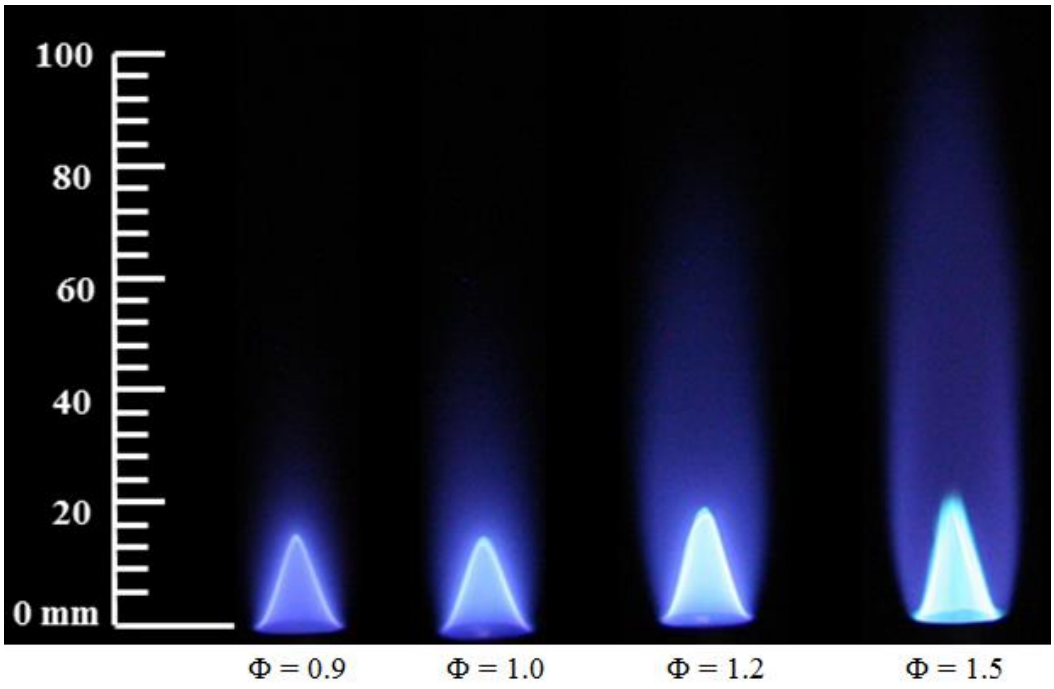

Figure E.2 Flame images of PME at the tested equivalence ratios

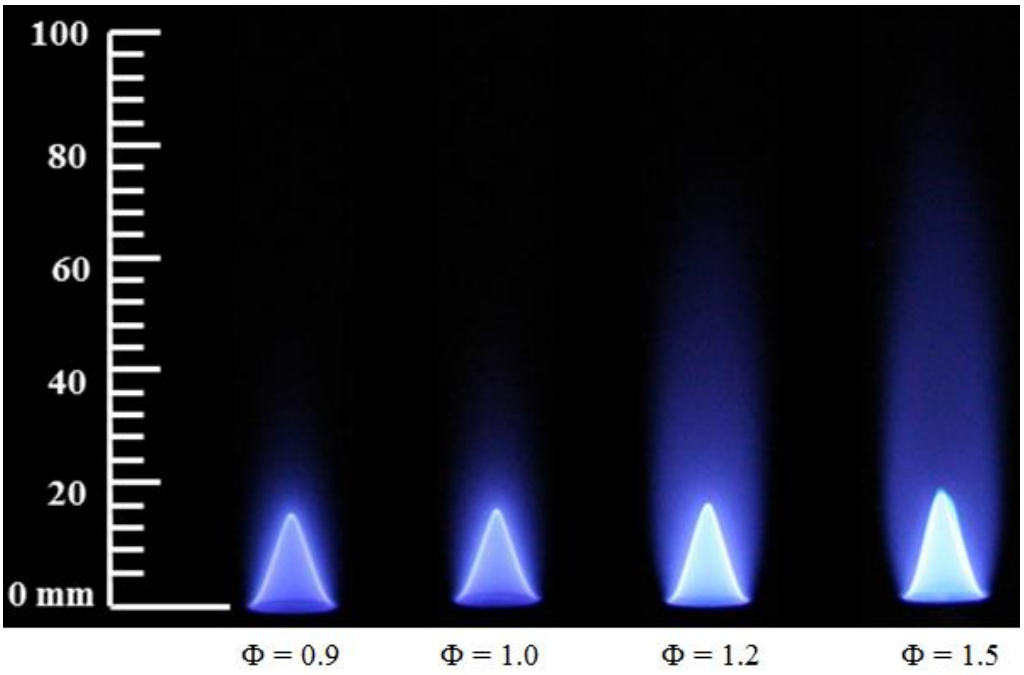

Figure E.3 Flame images of CME at the tested equivalence ratios

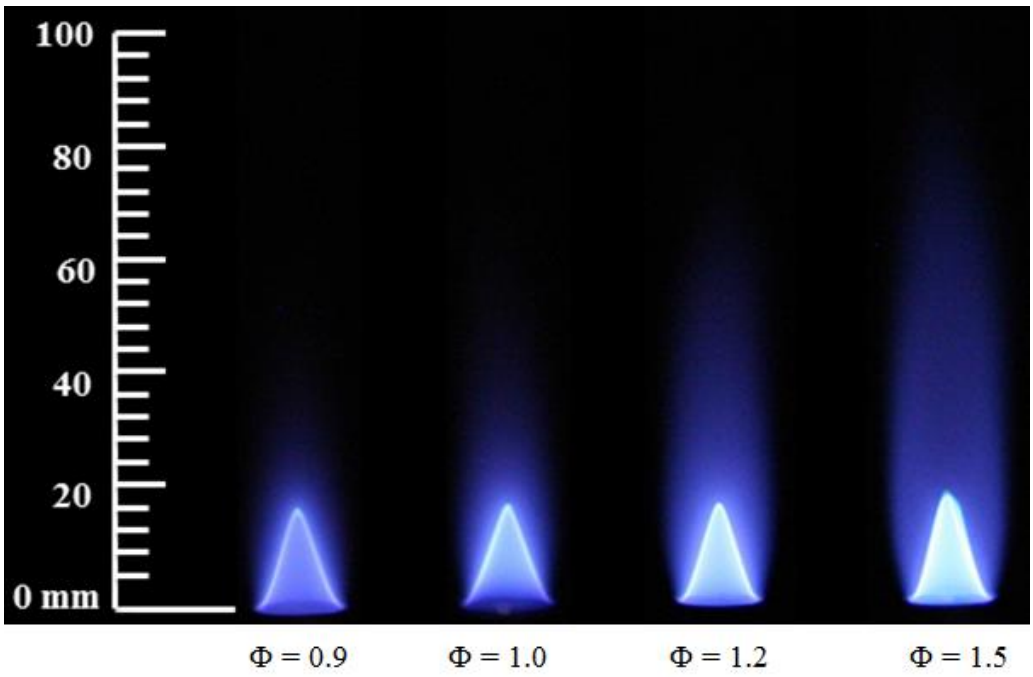

Figure E.4 Flame images of RME at the tested equivalence ratios

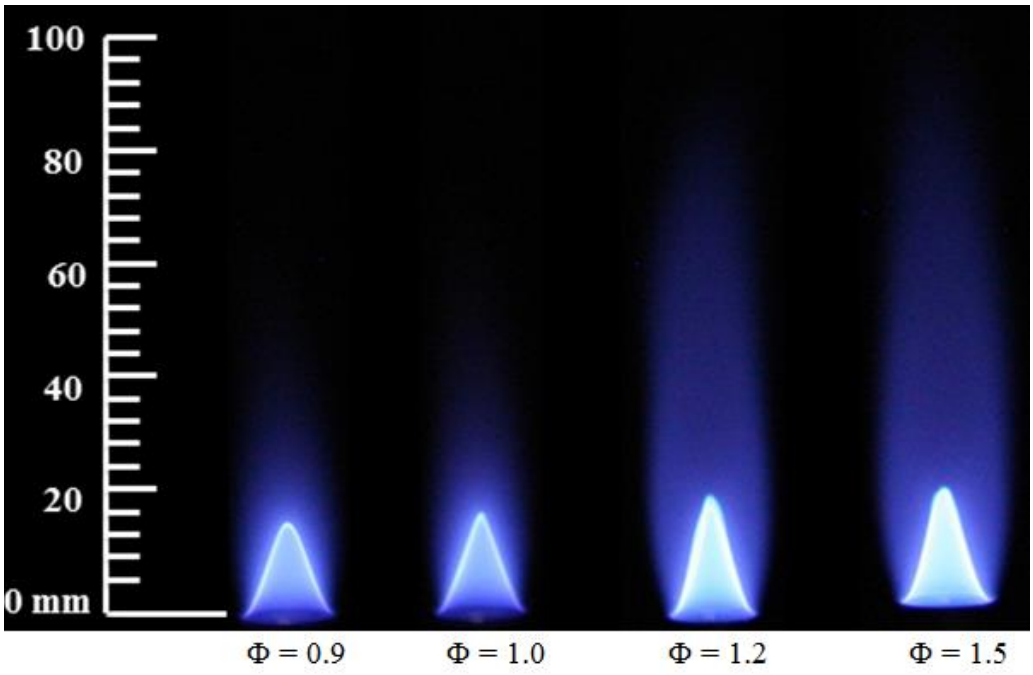

Figure E.5 Flame images of SME at the tested equivalence ratios

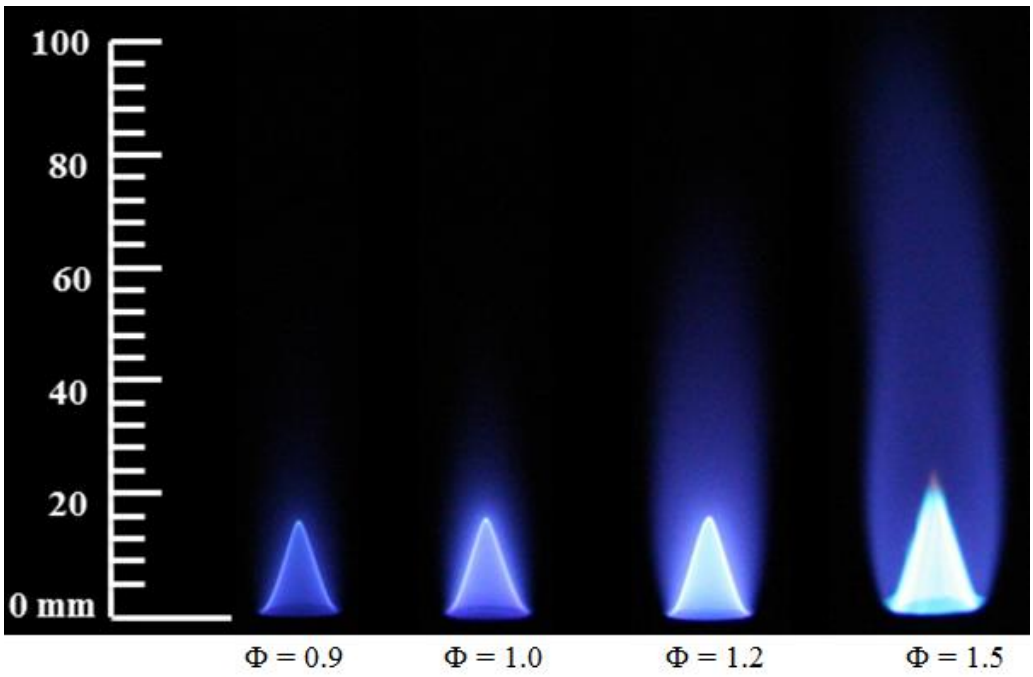

Figure E.6 Flame images of C43P57 at the tested equivalence ratios

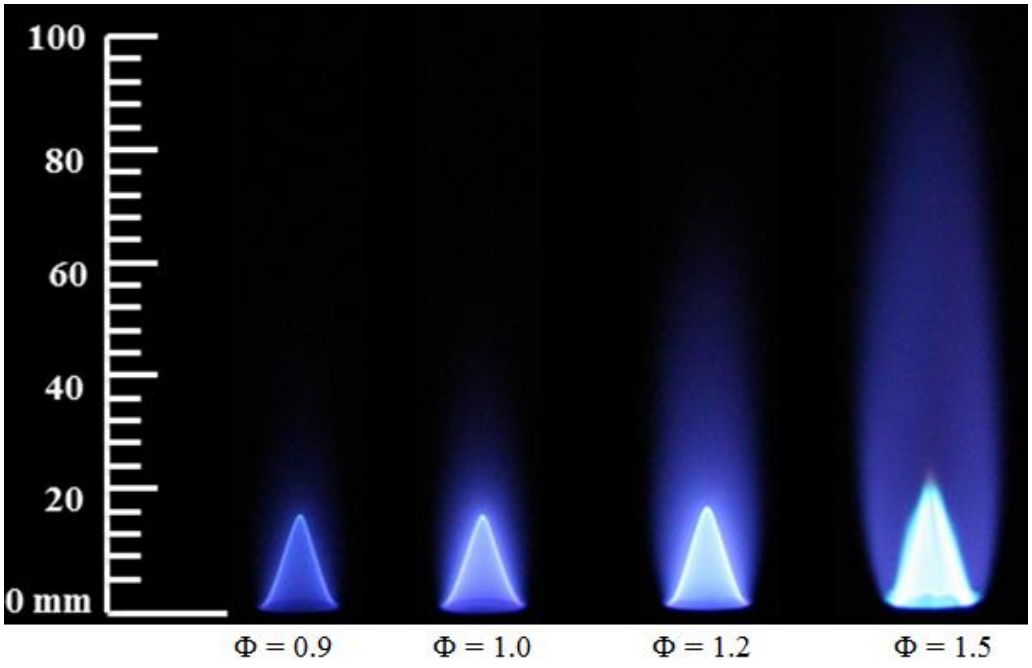

Figure E.7 Flame images of C71P29 at the tested equivalence ratios

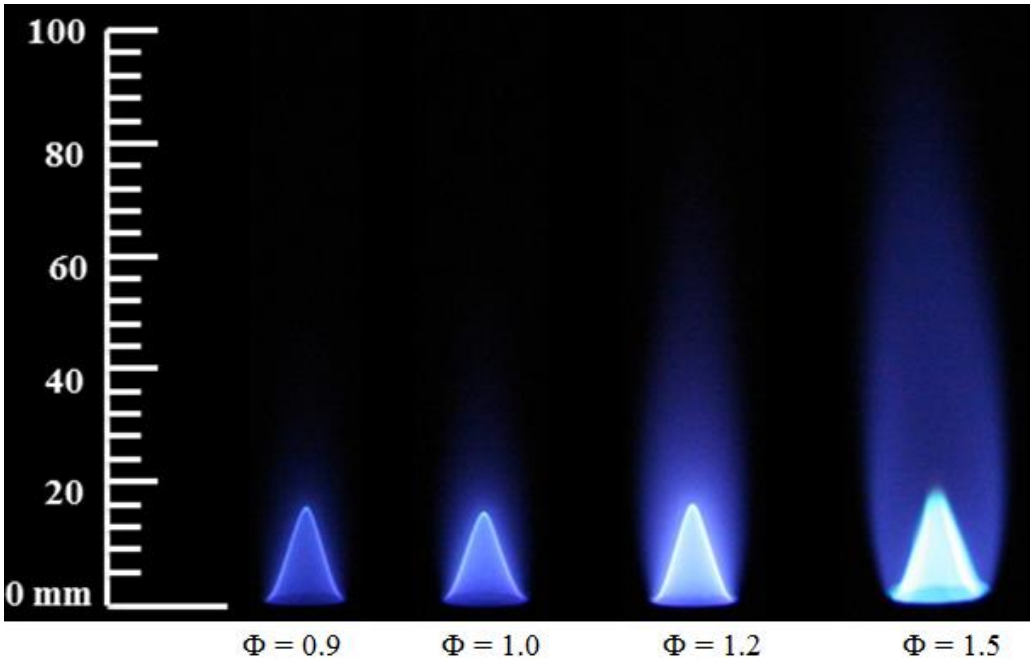

Figure E.8 Flame images of C75R25 at the tested equivalence ratios

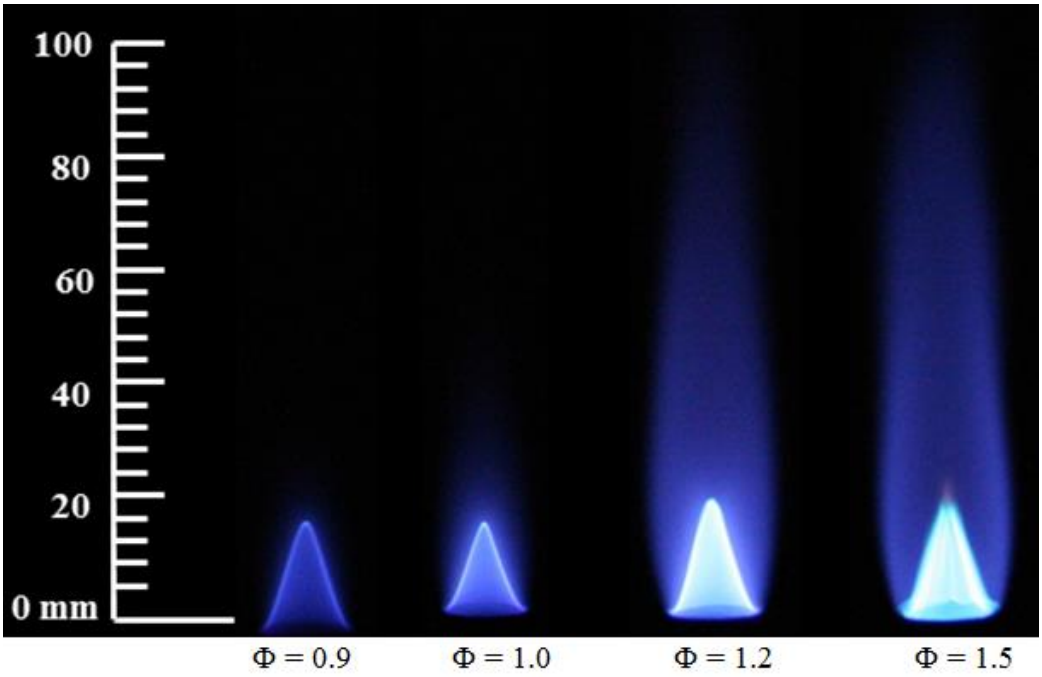

Figure E.9 Flame images of C50R50 at the tested equivalence ratios

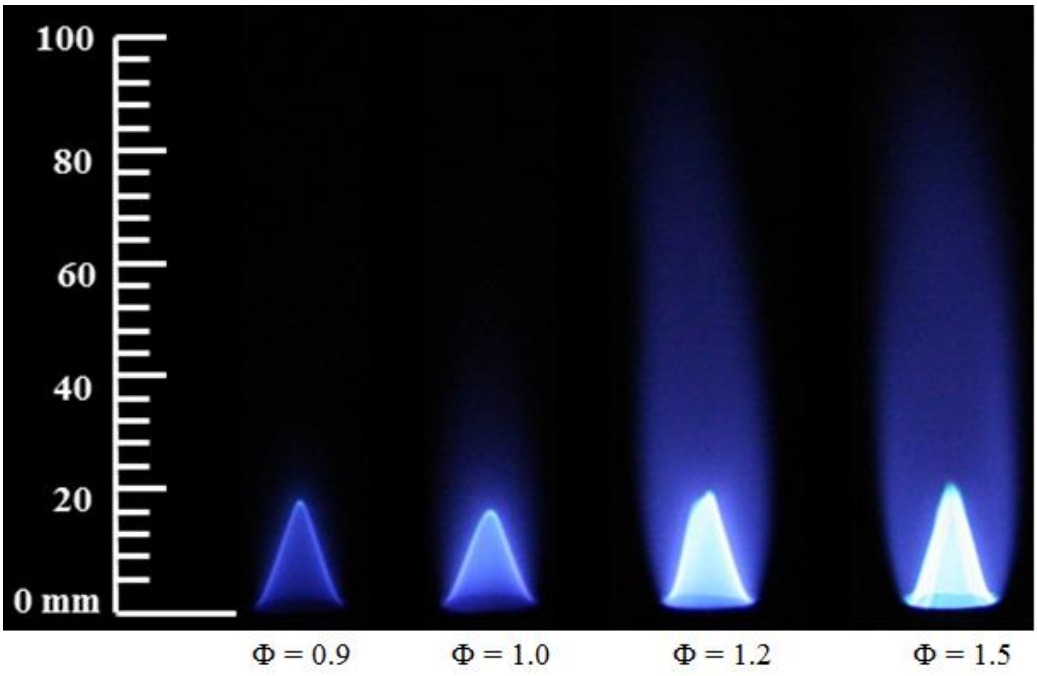

Figure E.10 Flame images of C25R75 at the tested equivalence ratios

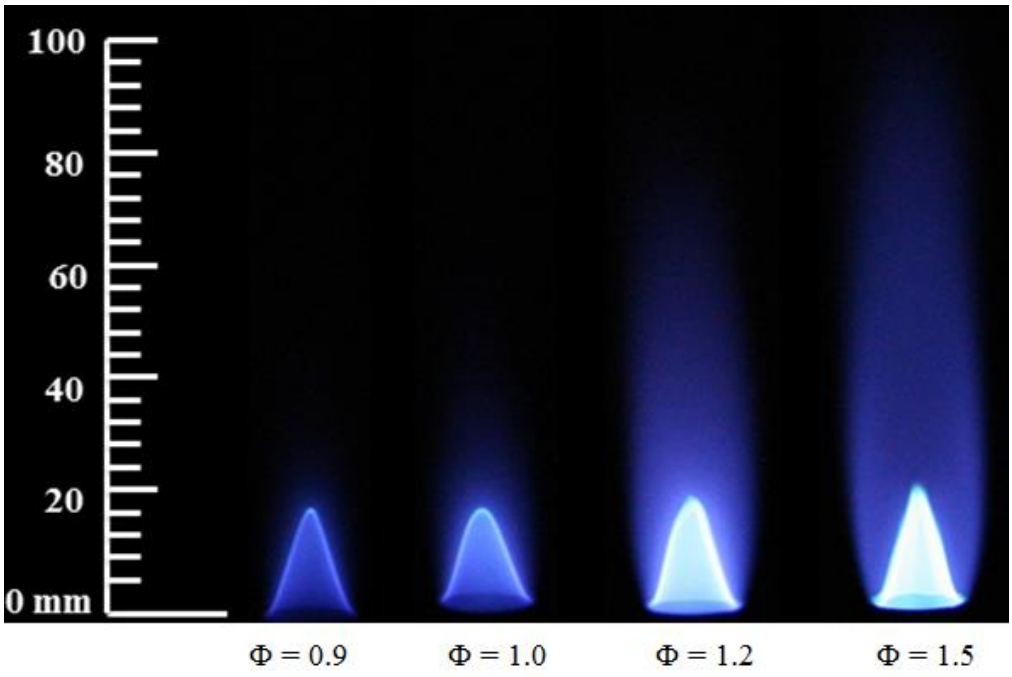

Figure E.11 Flame images of C80S20 at the tested equivalence ratios

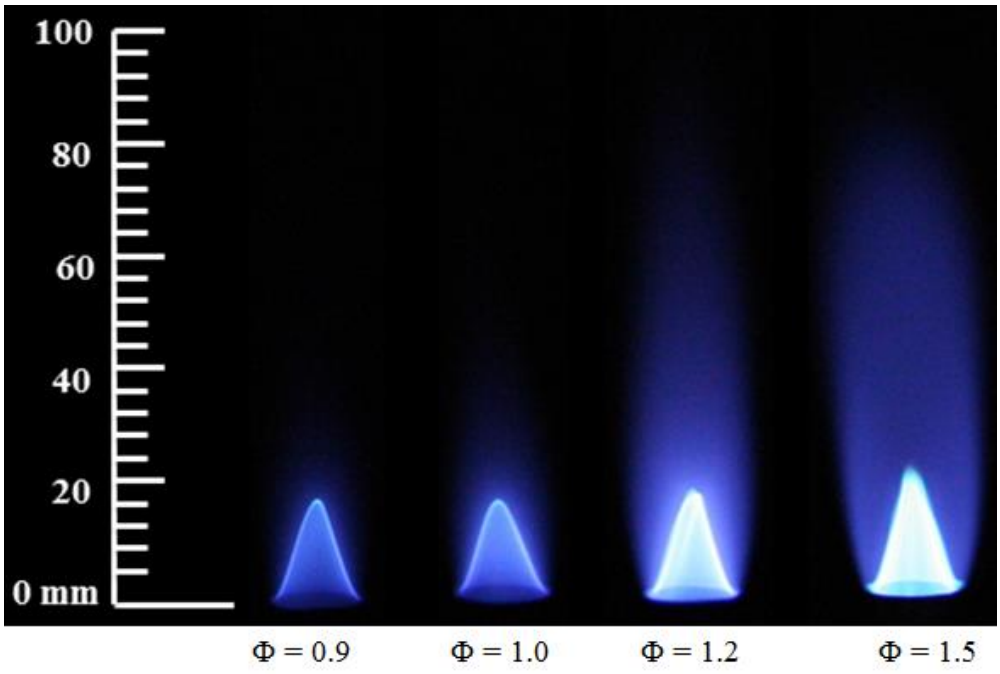

Figure E.12 Flame images of C60S40 at the tested equivalence ratios

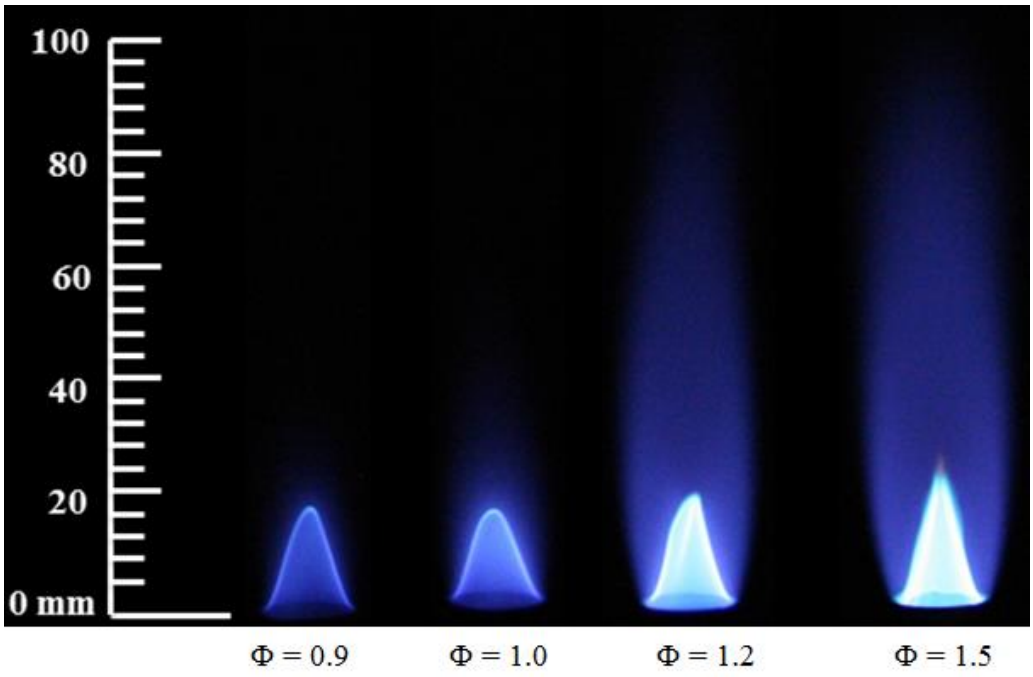

Figure E.13 Flame images of C40S60 at the tested equivalence ratios

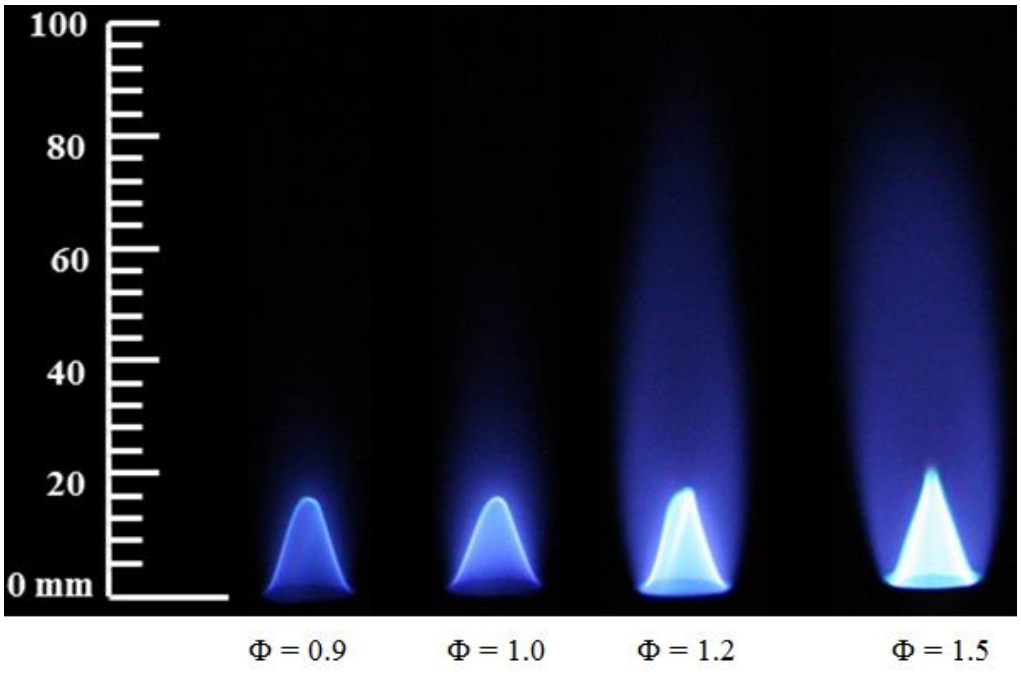

Figure E.14 Flame images of C20S80 at the tested equivalence ratios

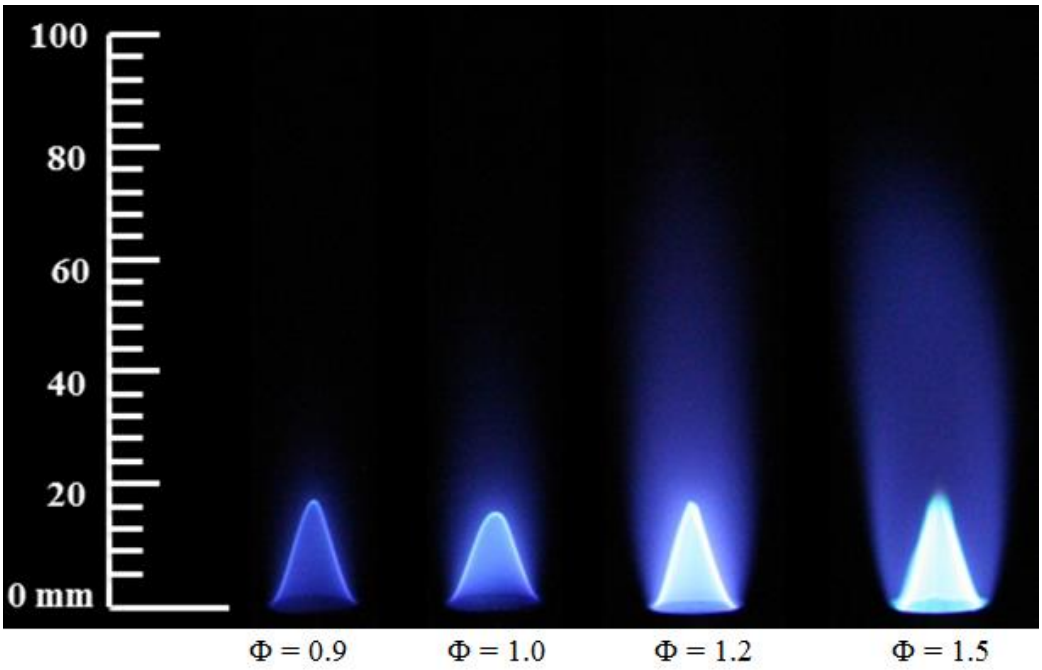

Figure E.15 Flame images of P80R20 at the tested equivalence ratios

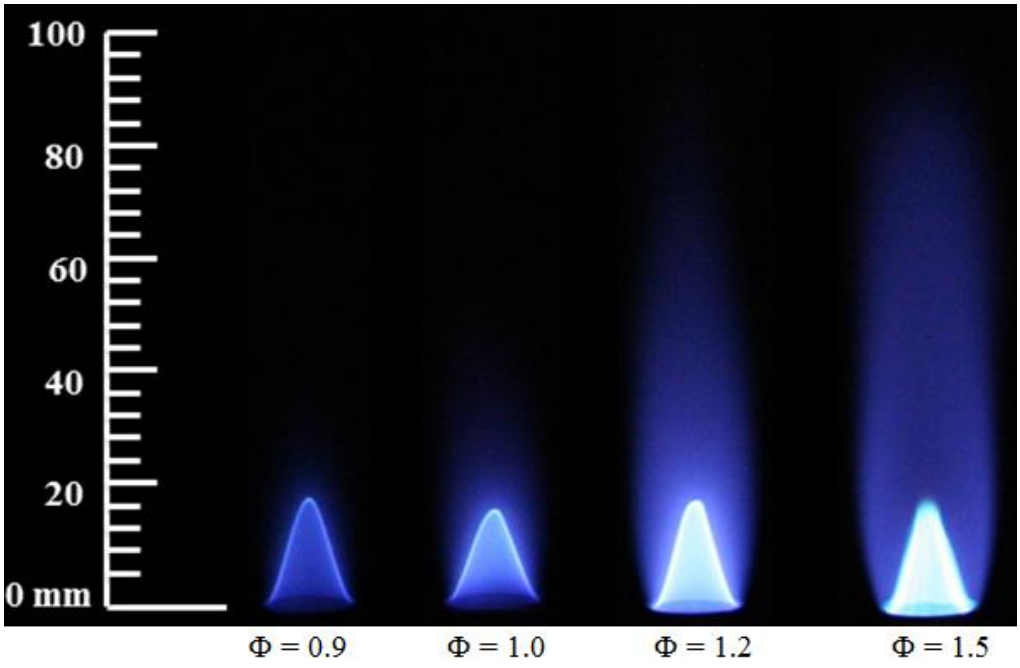

Figure E.16 Flame images of P67R33 at the tested equivalence ratios

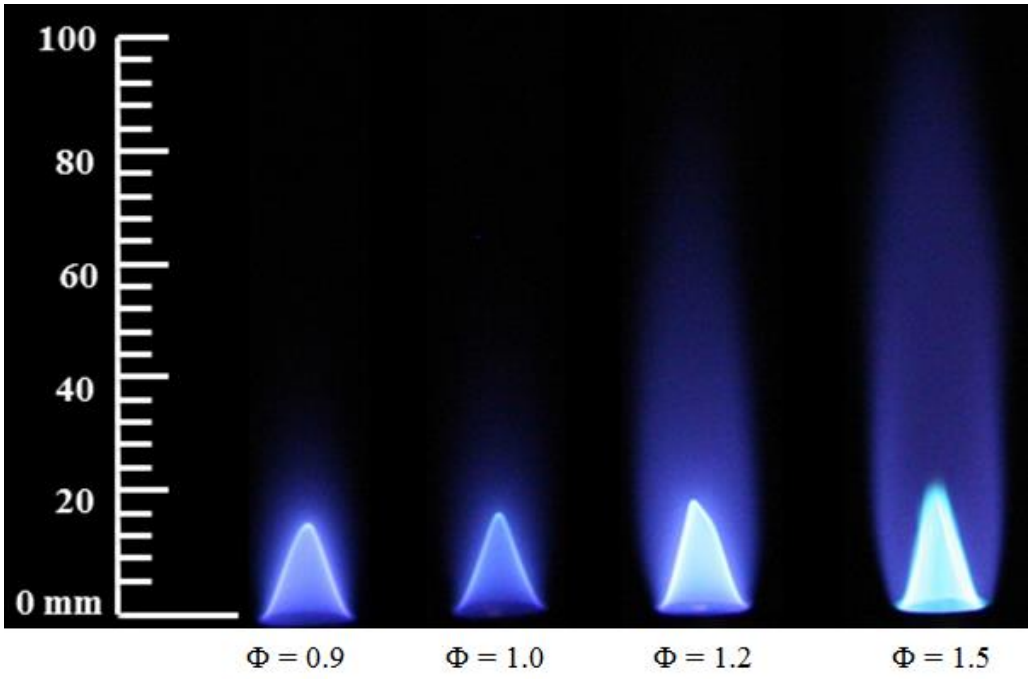

Figure E.17 Flame images of P53R47 at the tested equivalence ratios

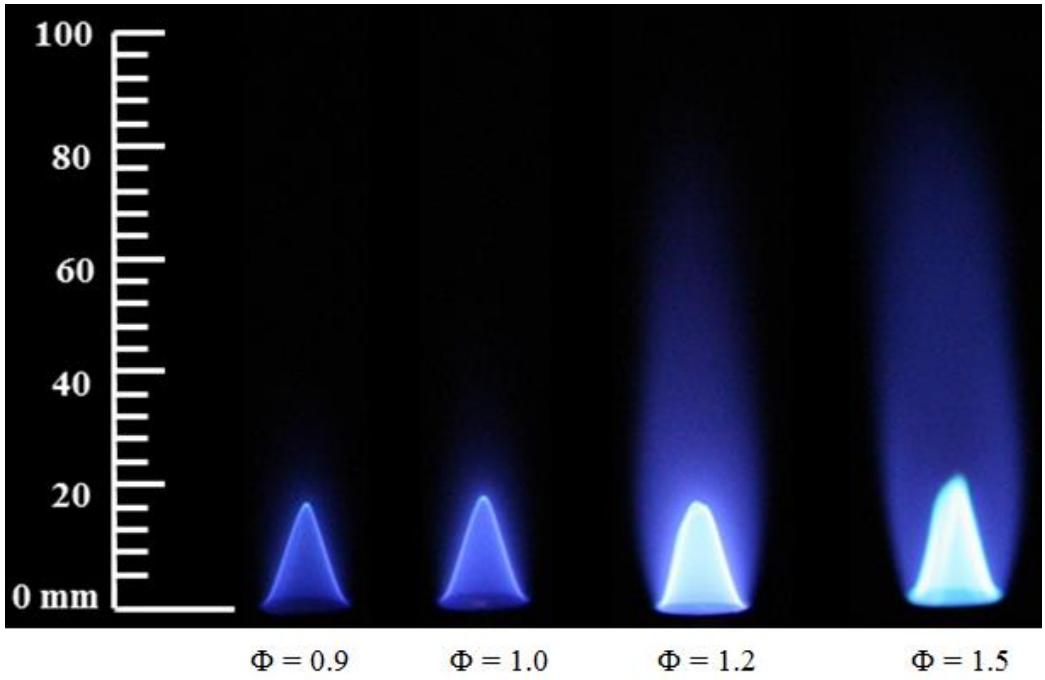

Figure E.18 Flame images of P40R60 at the tested equivalence ratios

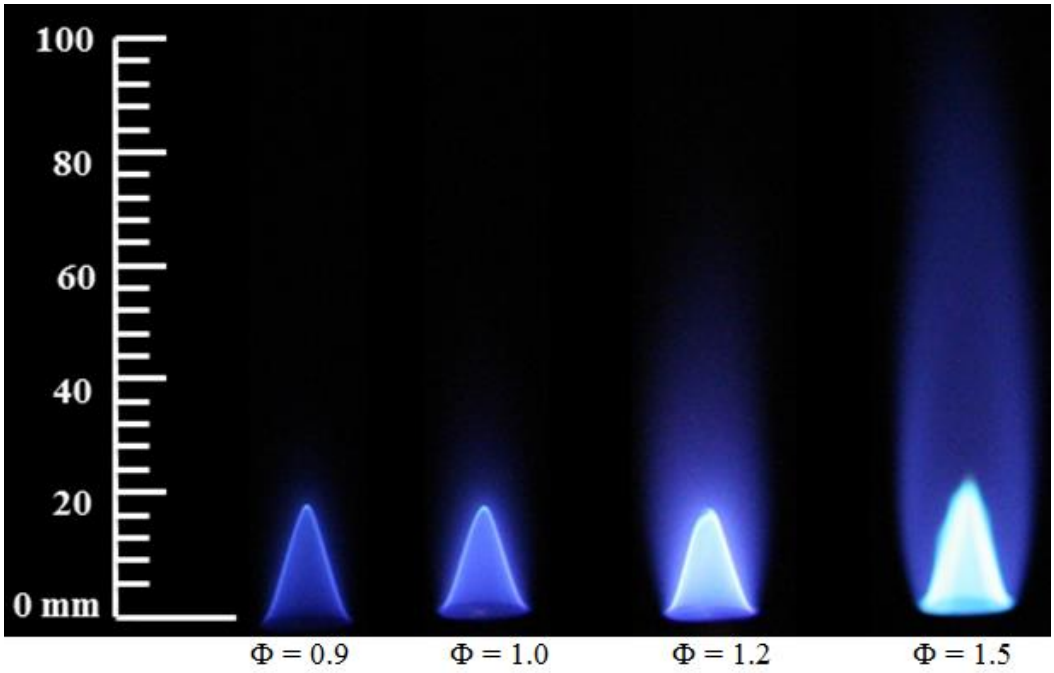

Figure E.19 Flame images of P27R73 at the tested equivalence ratios

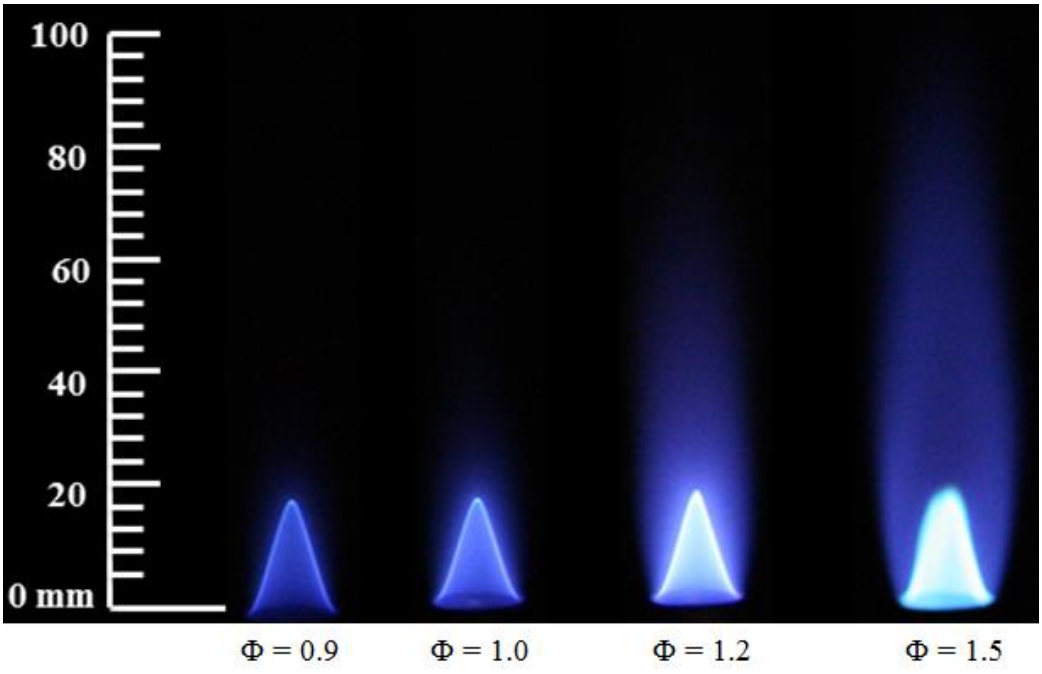

Figure E.20 Flame images of P14R86 at the tested equivalence ratios

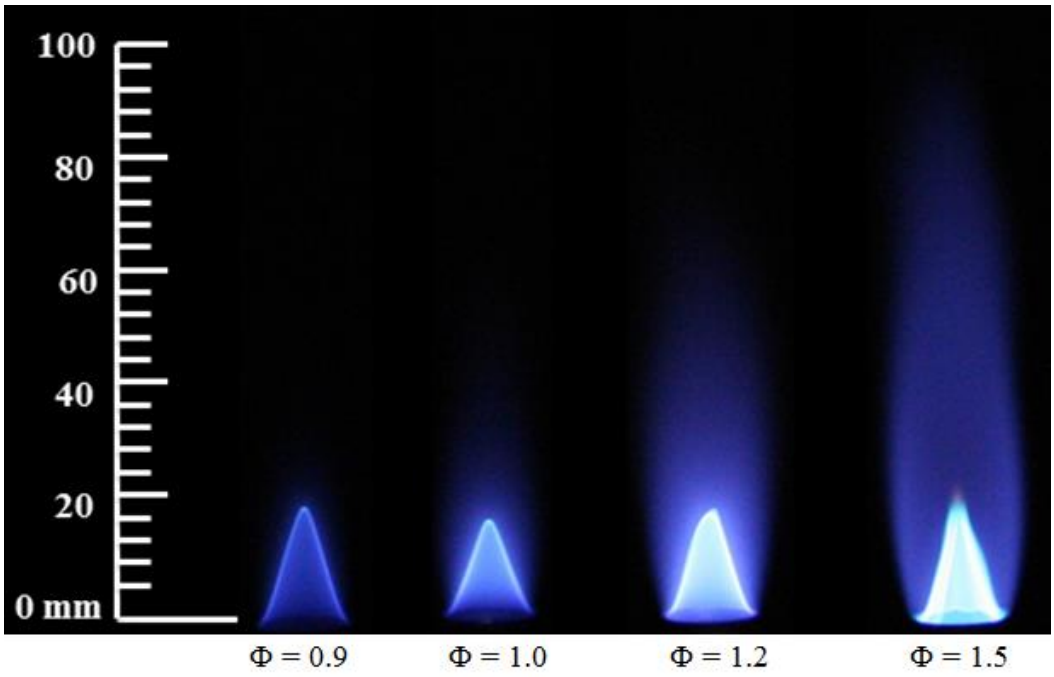

Figure E.21 Flame images of P82S18 at the tested equivalence ratios

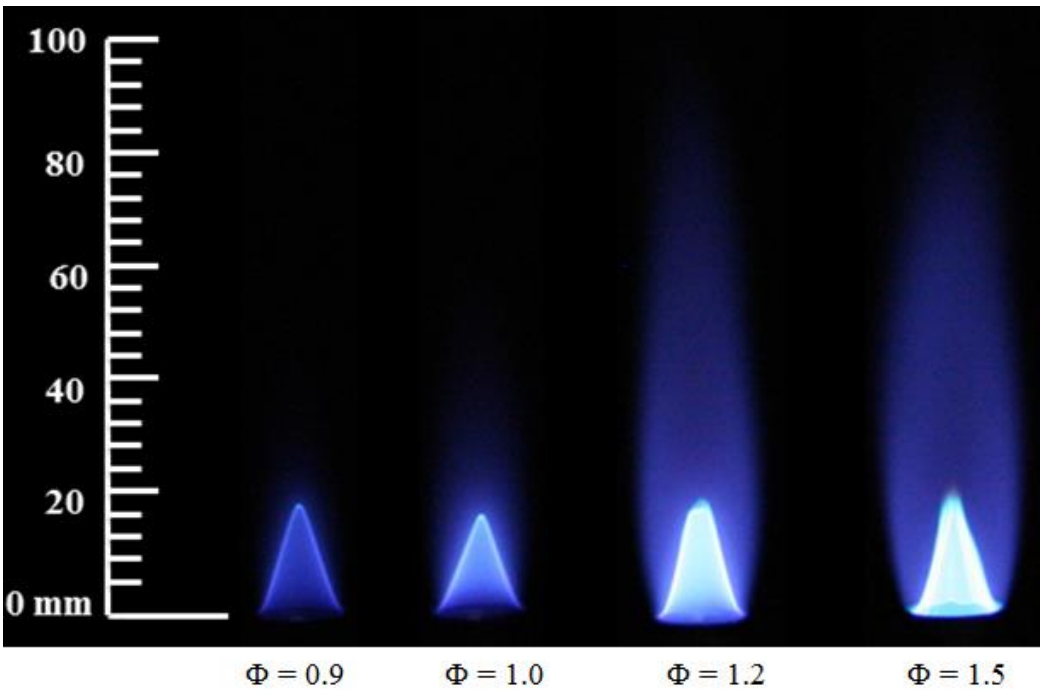

Figure E.22 Flame images of P71S29 at the tested equivalence ratios

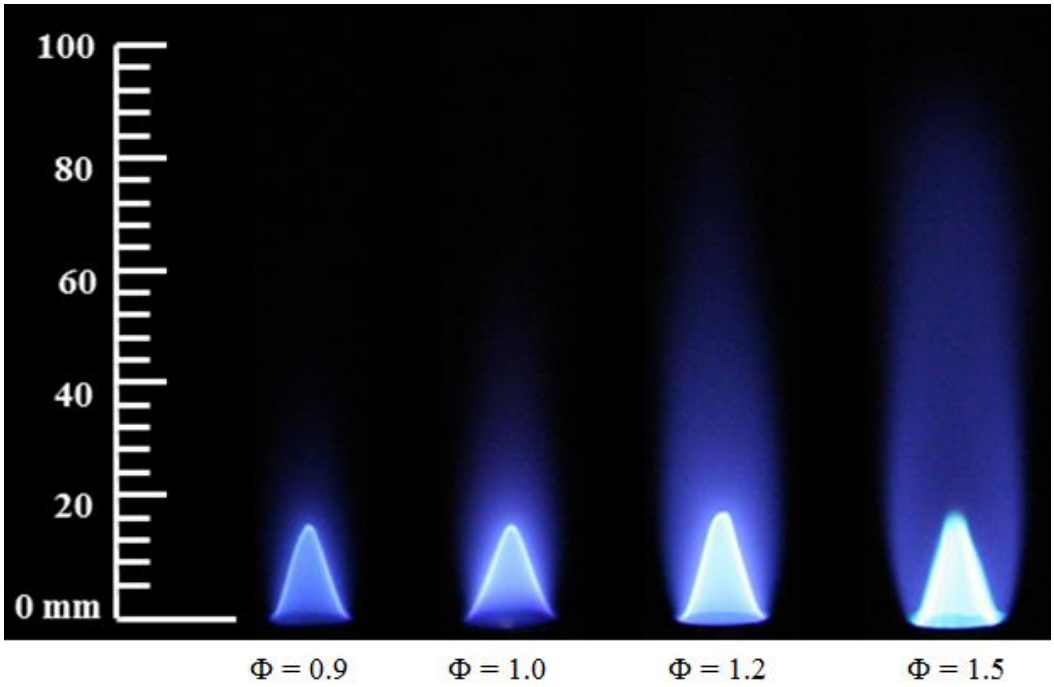

Figure E.23 Flame images of P59S41 at the tested equivalence ratios

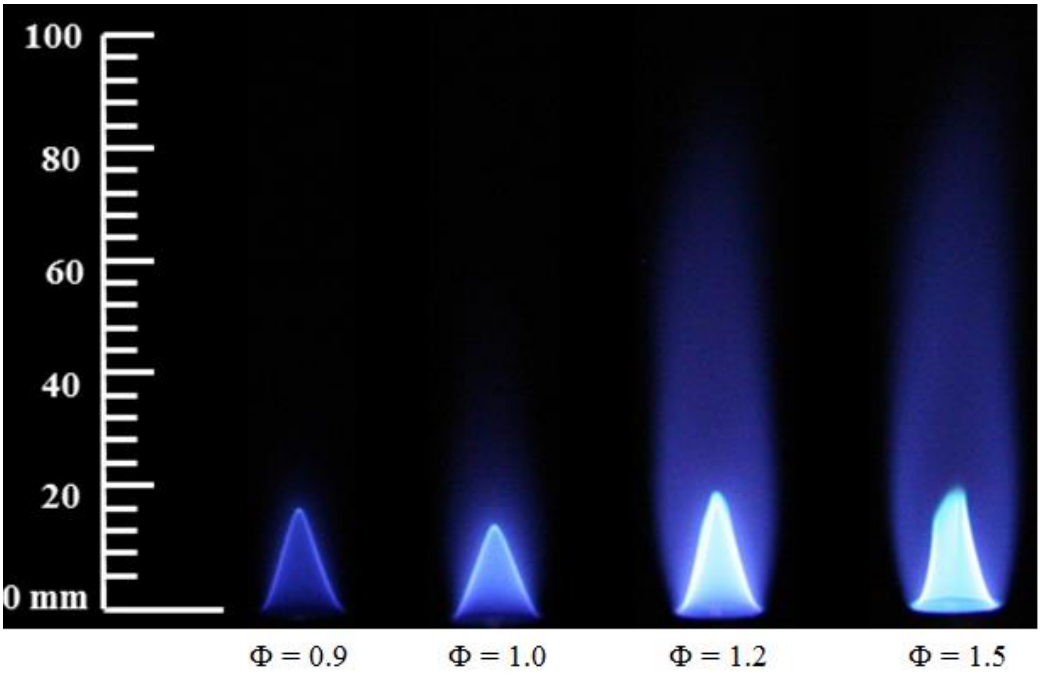

Figure E.24 Flame images of P47S53 at the tested equivalence ratios

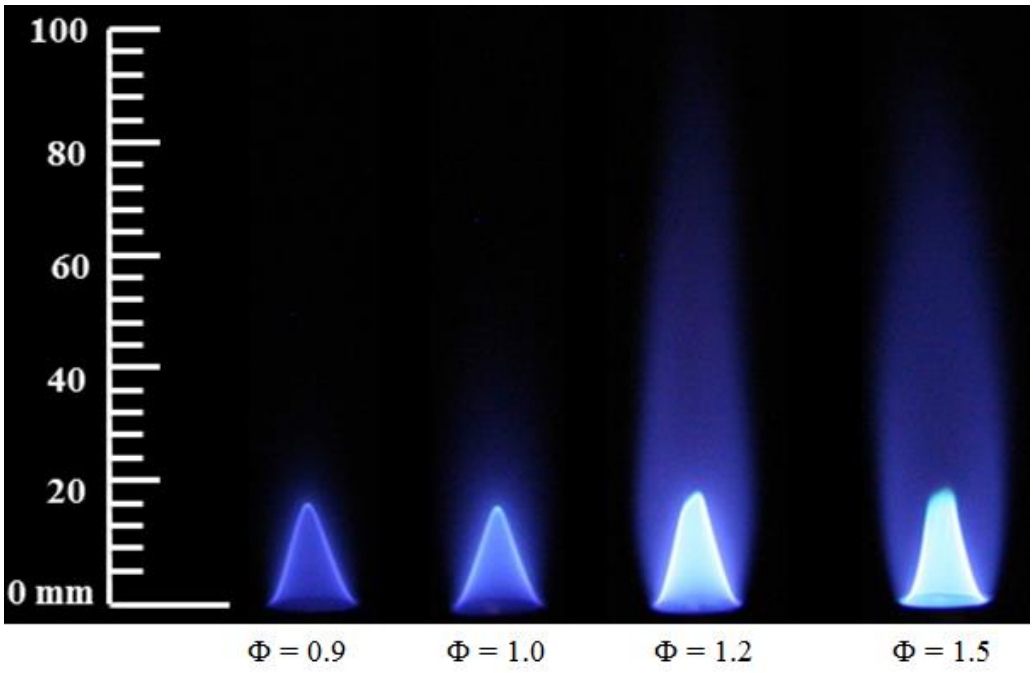

Figure E.25 Flame images of P35S65 at the tested equivalence ratios

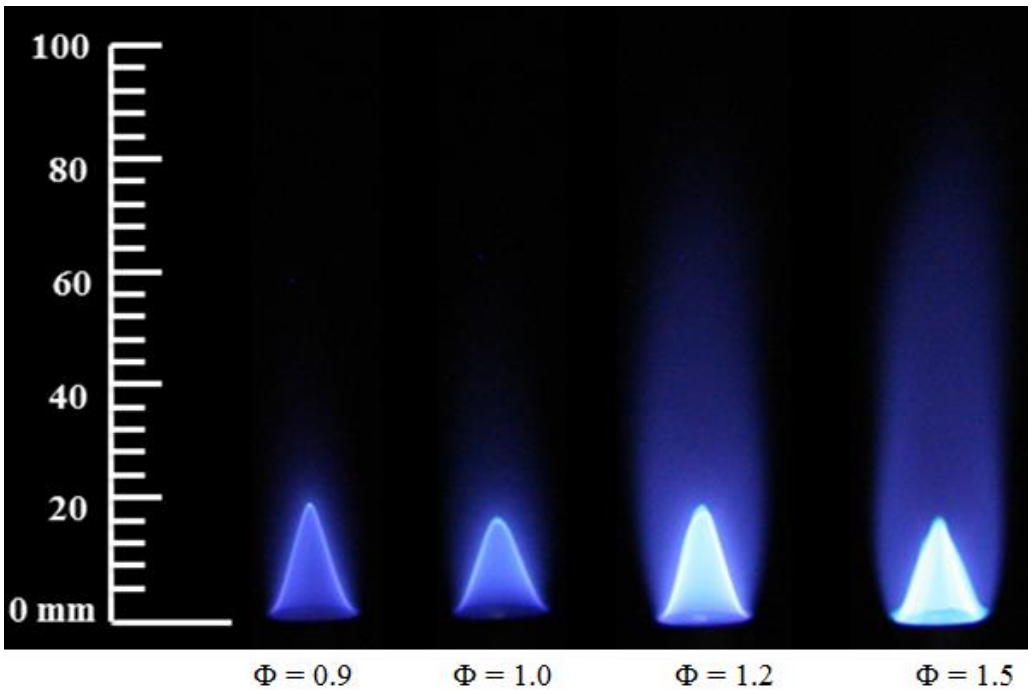

Figure E.26 Flame images of P27S76 at the tested equivalence ratios

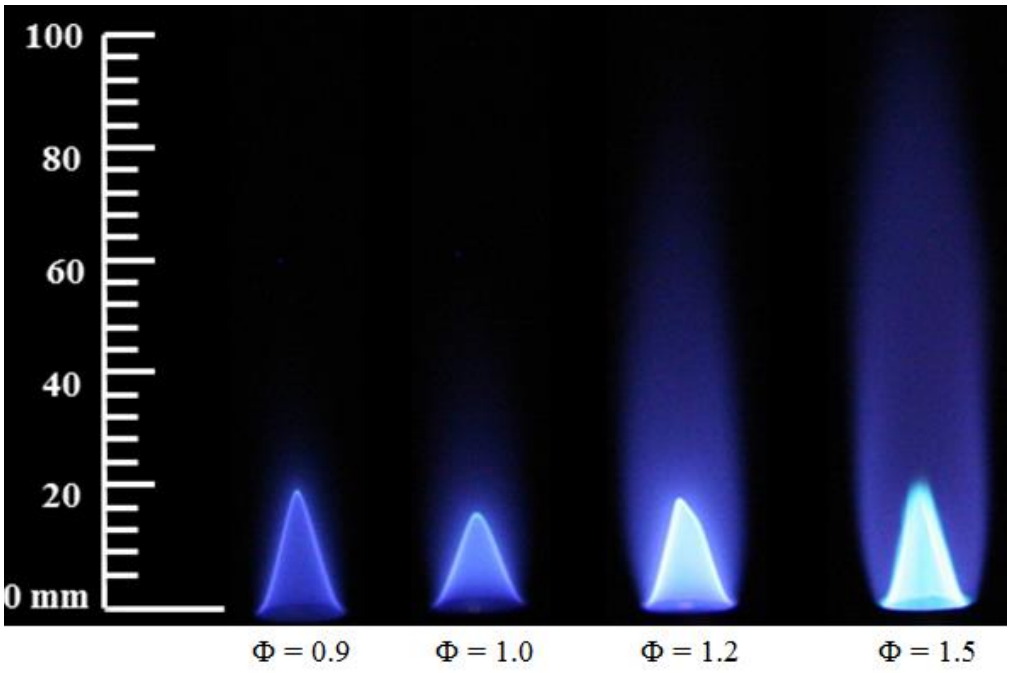

Figure E.27 Flame images of P12S88 at the tested equivalence ratios

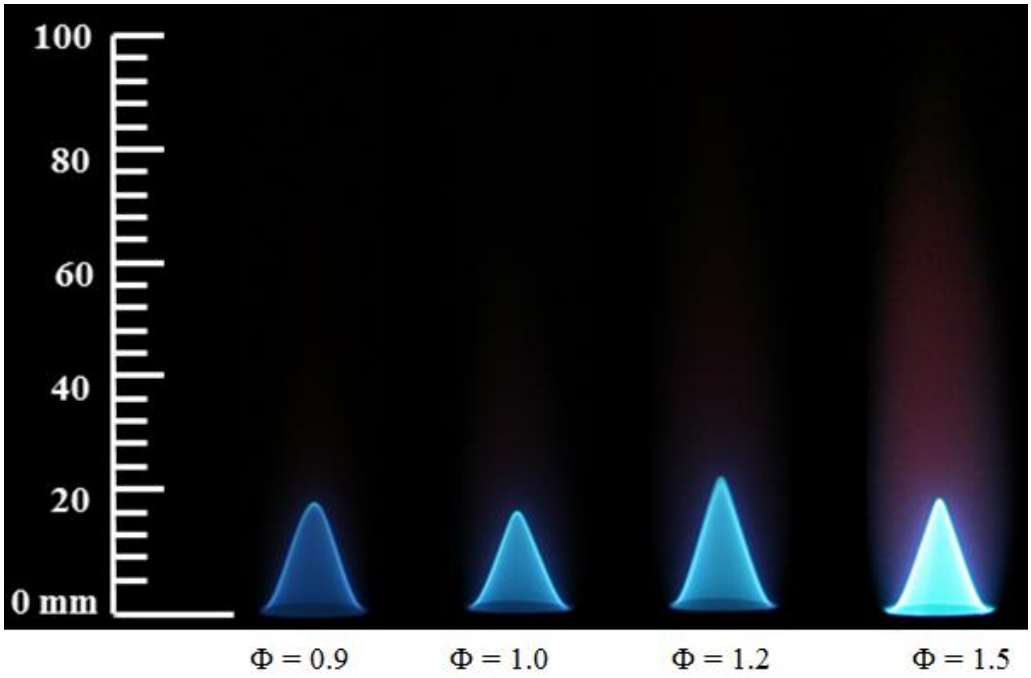

Figure E.28 Flame images of heptane at the tested equivalence ratios

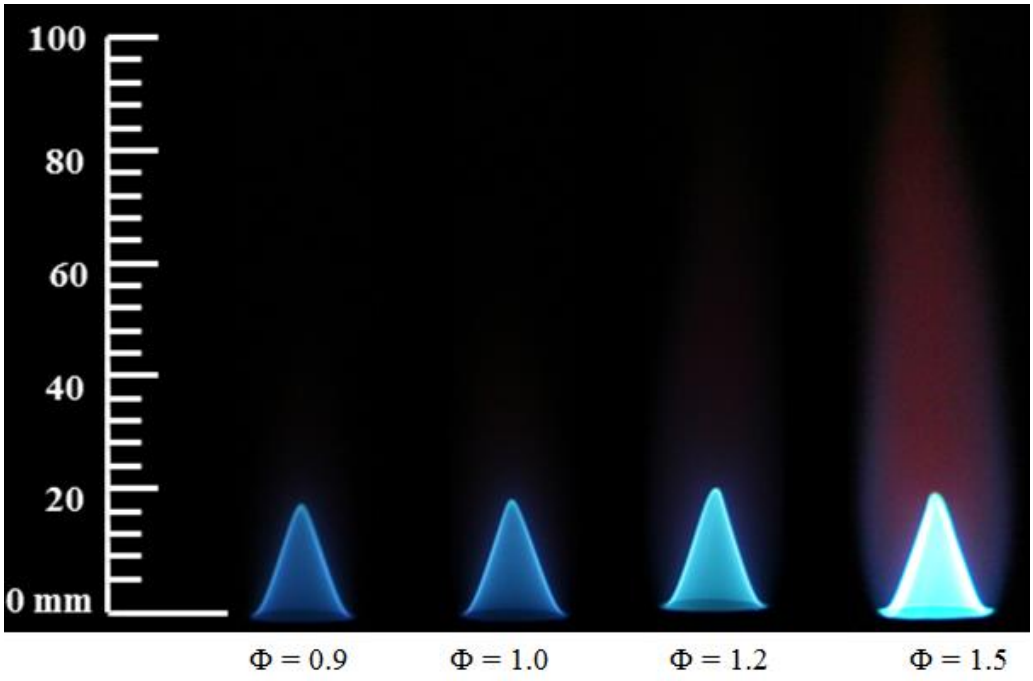

Figure E.29 Flame images of toluene at the tested equivalence ratios

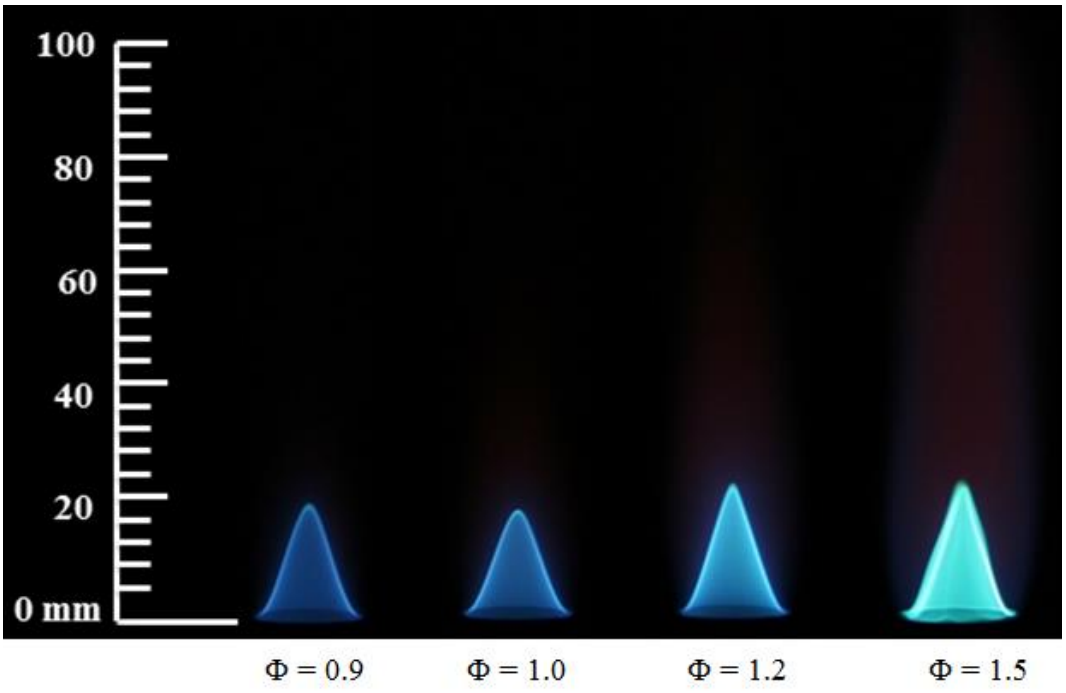

Figure E.30 Flame images of H92T08 at the tested equivalence ratios

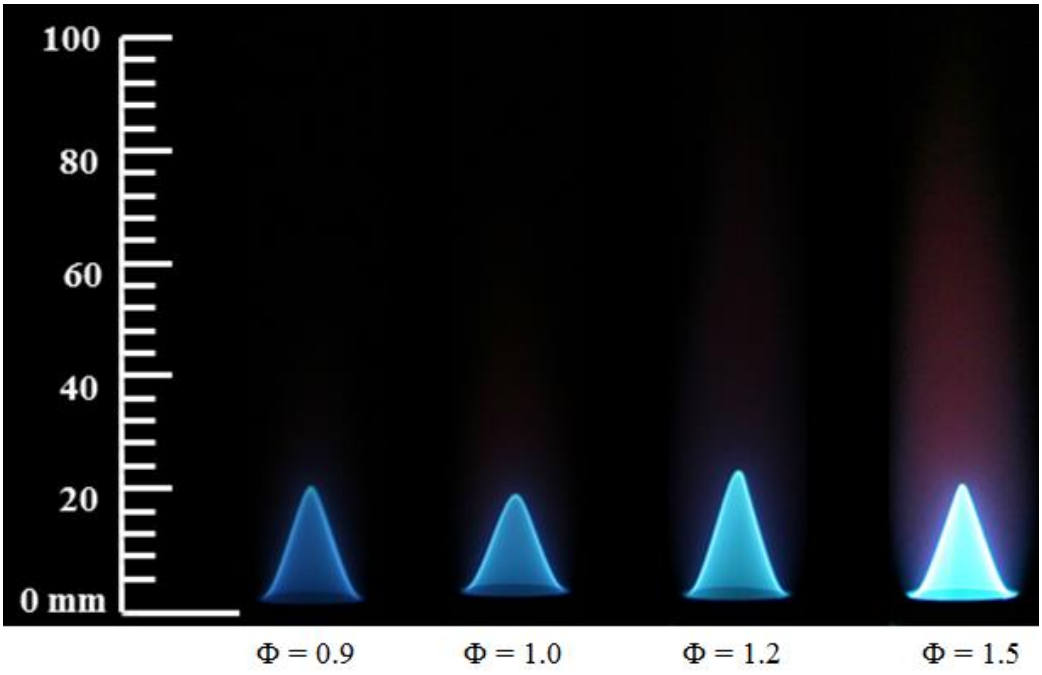

Figure E.31 Flame images of H80T20 at the tested equivalence ratios

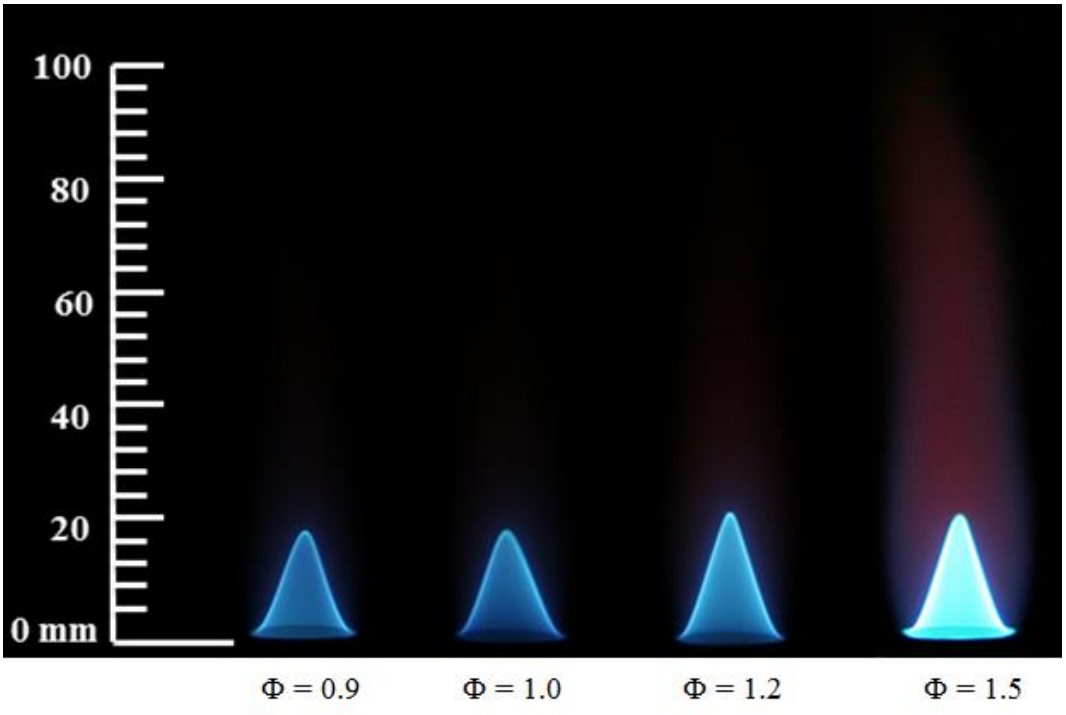

Figure E.32 Flame images of H65T35 at the tested equivalence ratios

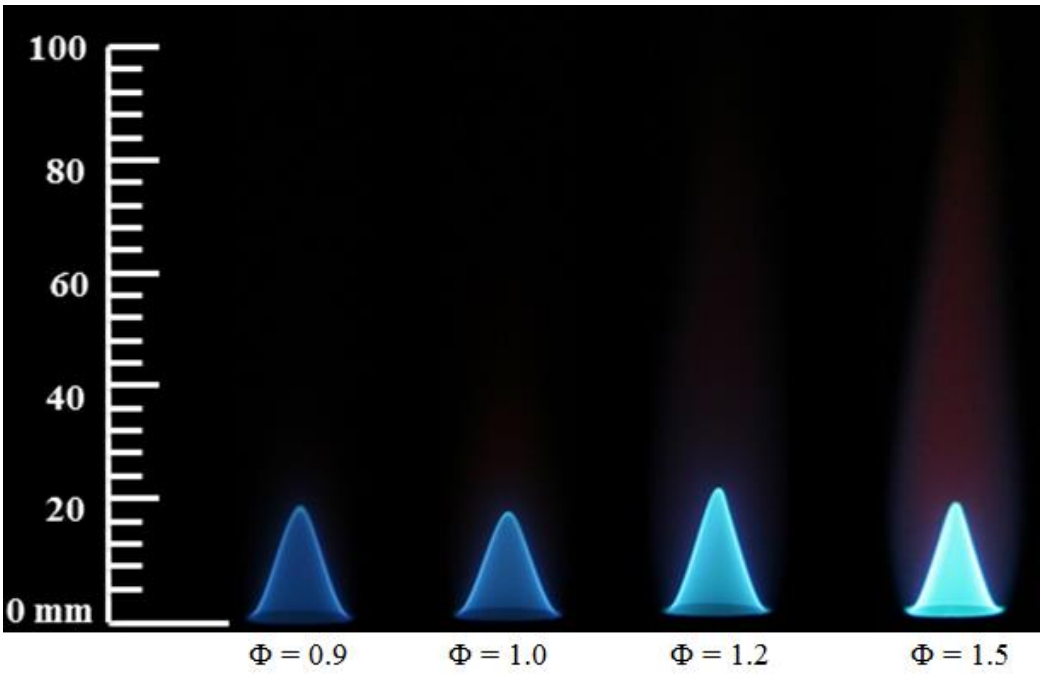

Figure E.33 Flame images of H58T42 at the tested equivalence ratios

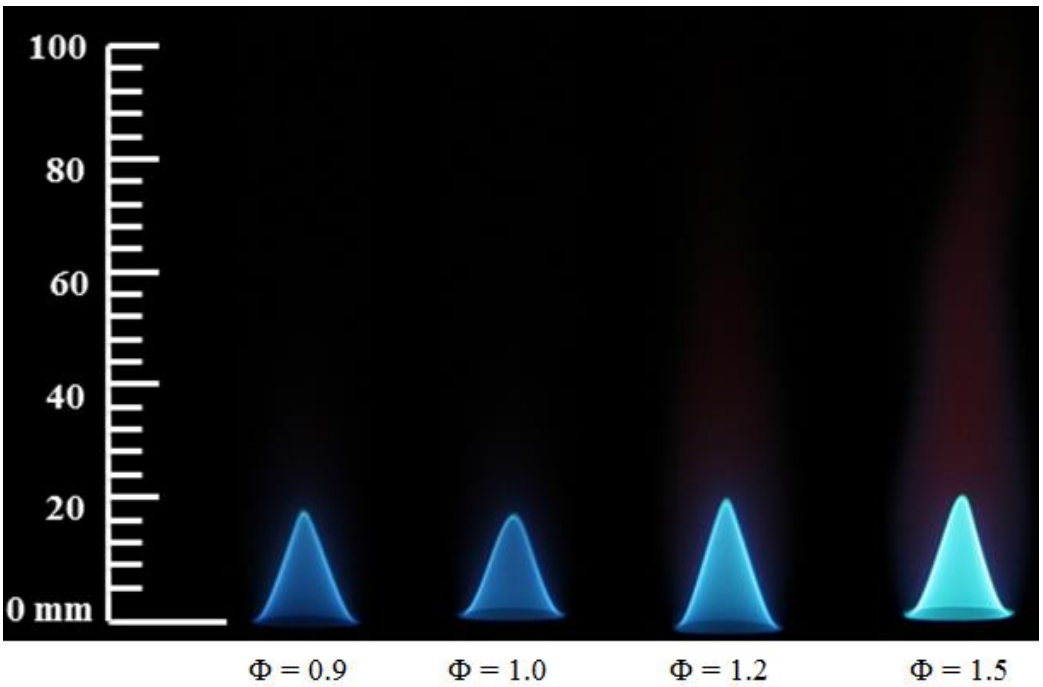

Figure E.34 Flame images of H45T55 at the tested equivalence ratios

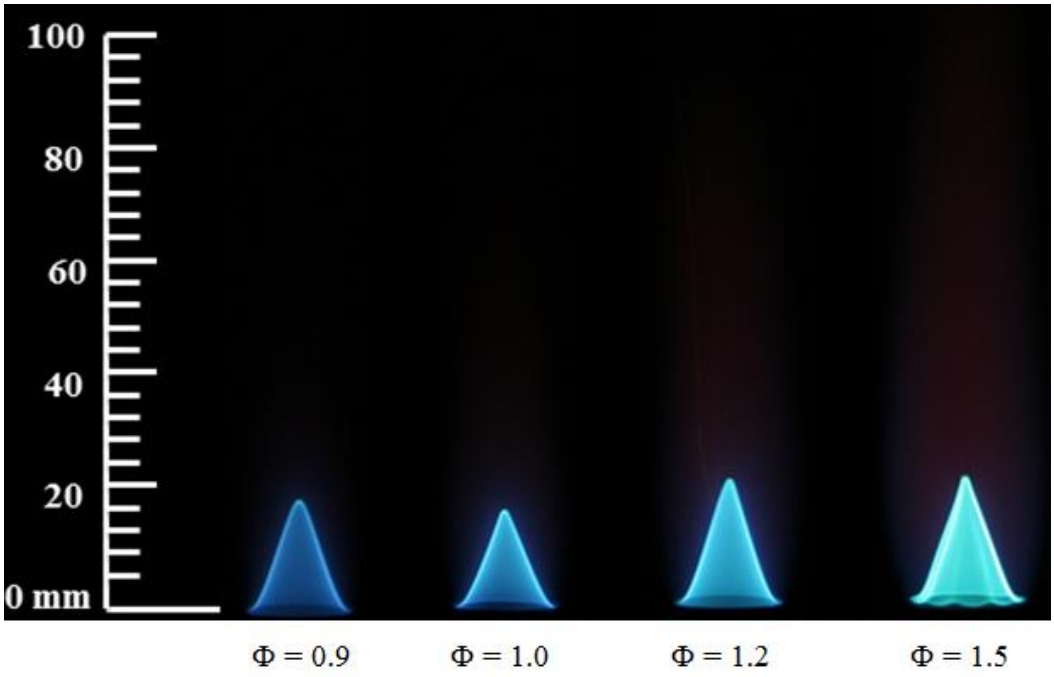

Figure E.35 Flame images of H32T68 at the tested equivalence ratios

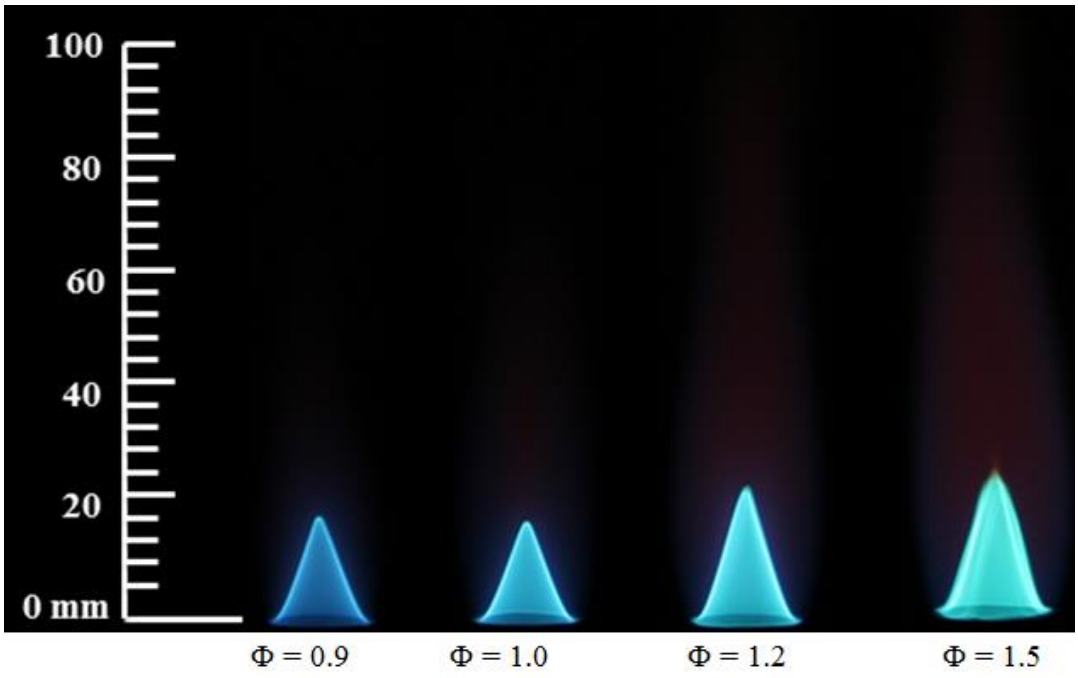

Figure E.36 Flame images of H12T88 at the tested equivalence ratios

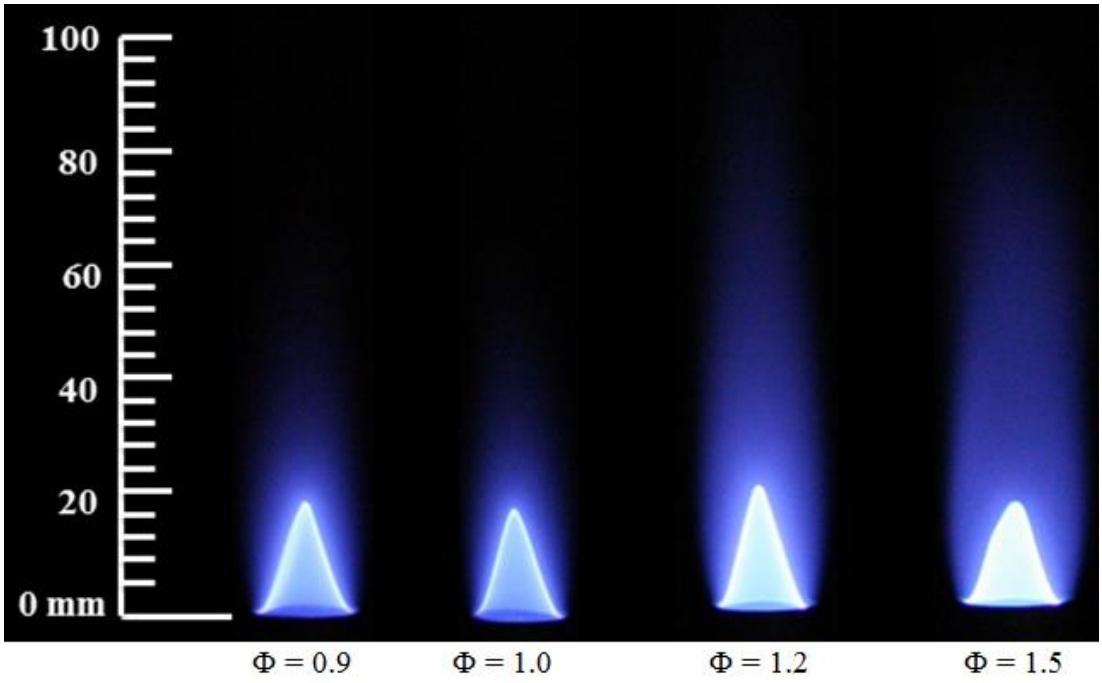

Figure E.37 Flame images of Jet A at the tested equivalence ratios

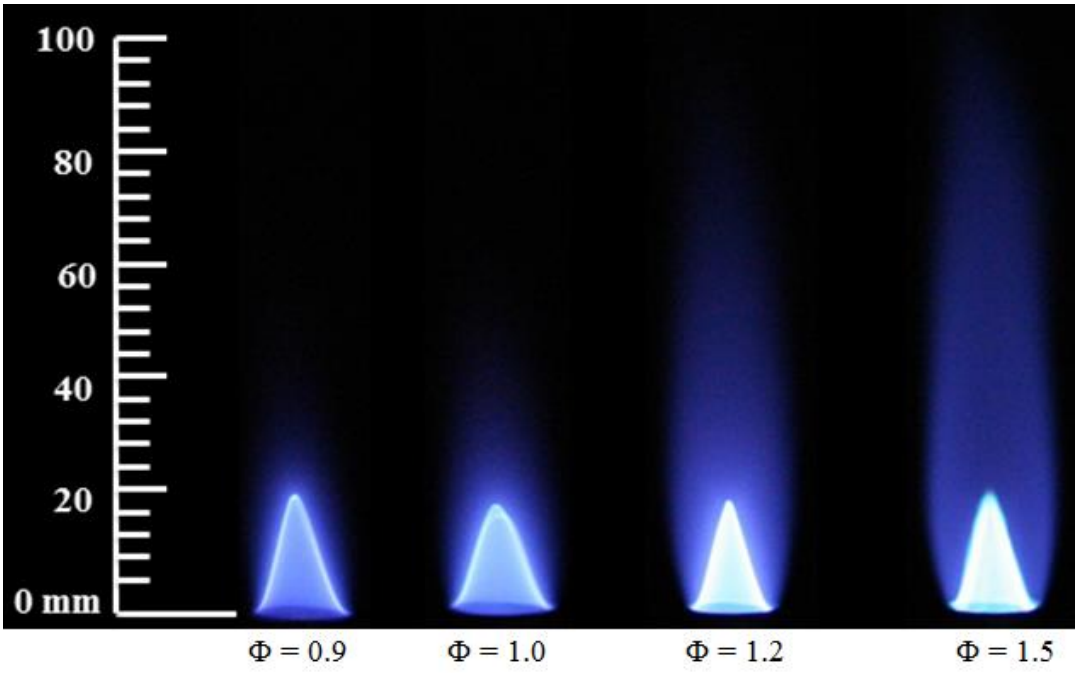

Figure E.38 Flame images of diesel at the tested equivalence ratios

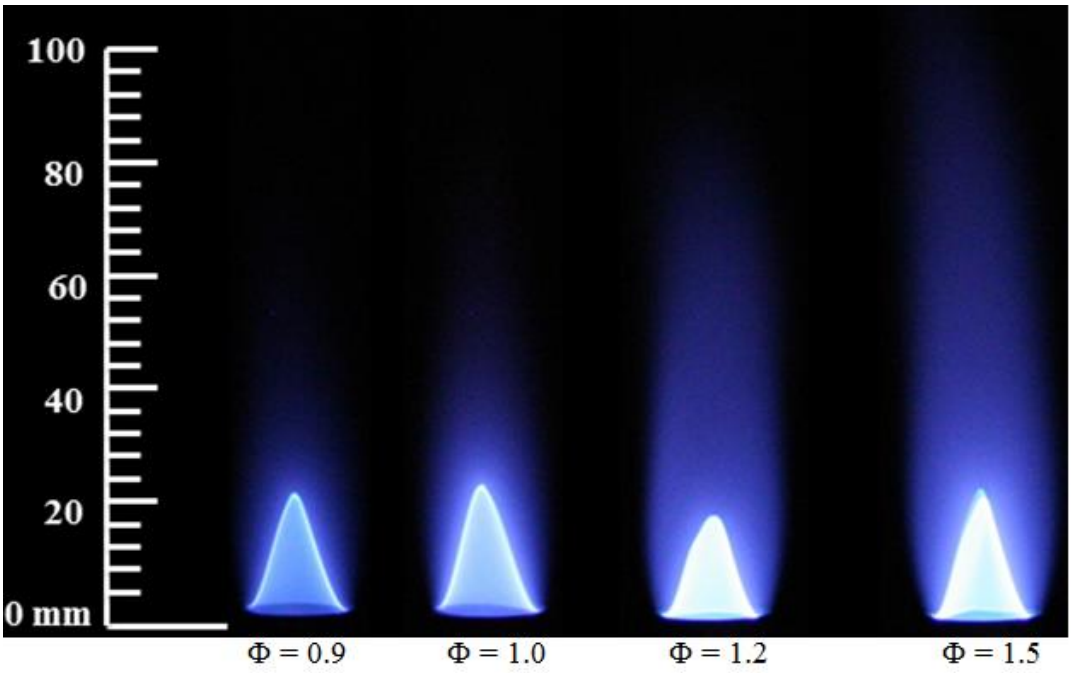

Figure E.39 Flame images of J80D20 at the tested equivalence ratios

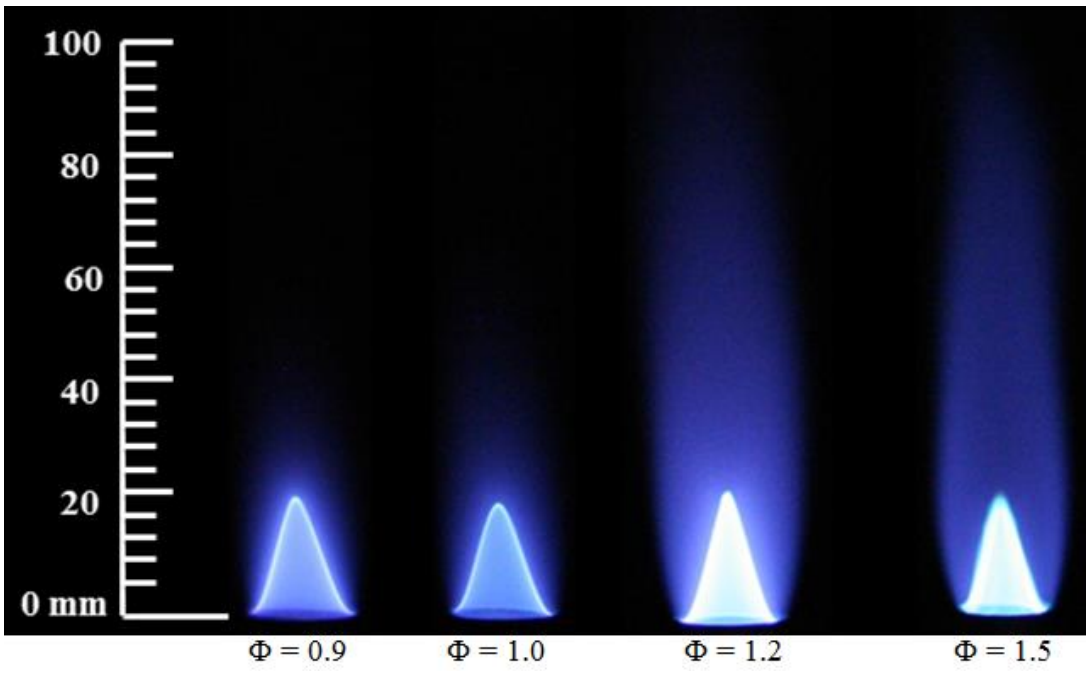

Figure E.40 Flame images of J60D40 at the tested equivalence ratios

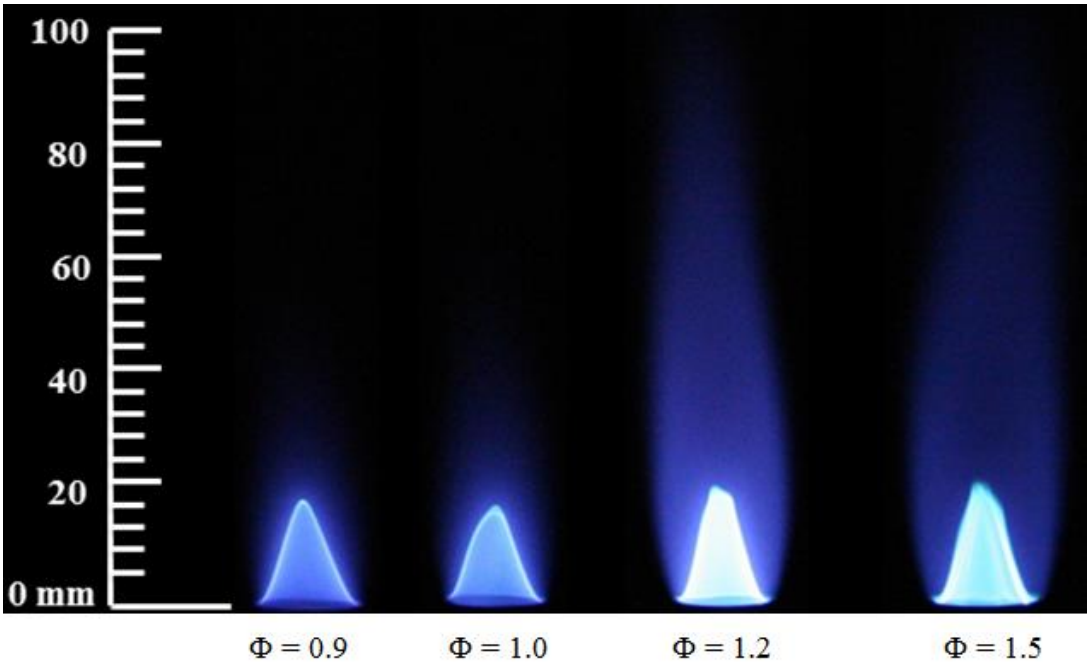

Figure E.41 Flame images of J34D66 at the tested equivalence ratios

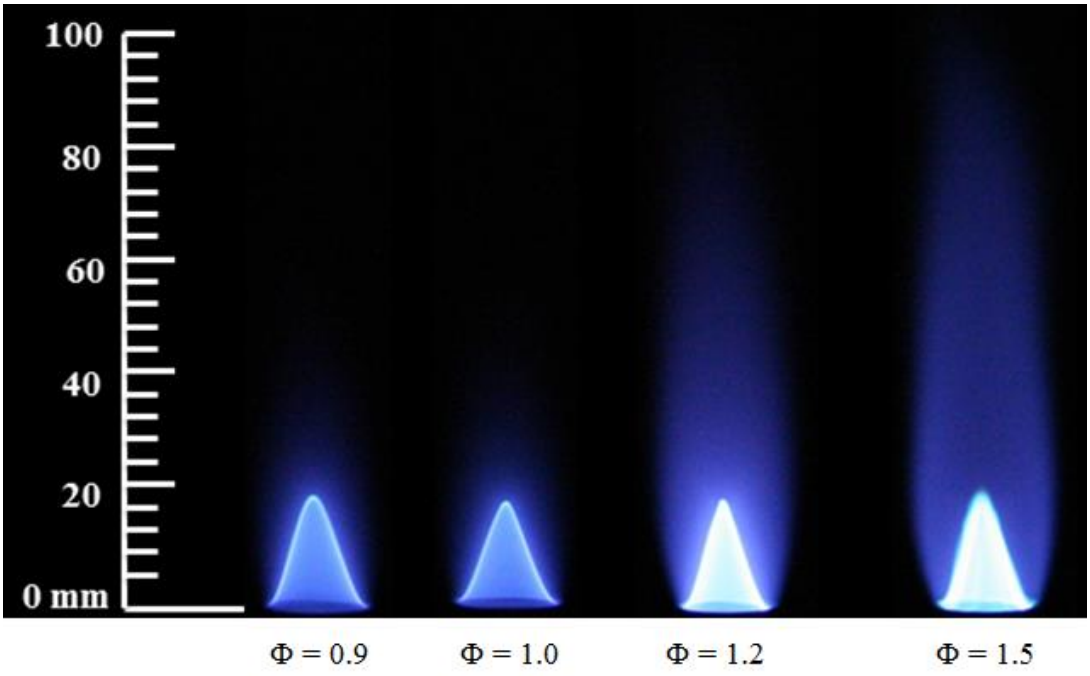

Figure E.42 Flame images of J20D80 at the tested equivalence ratios

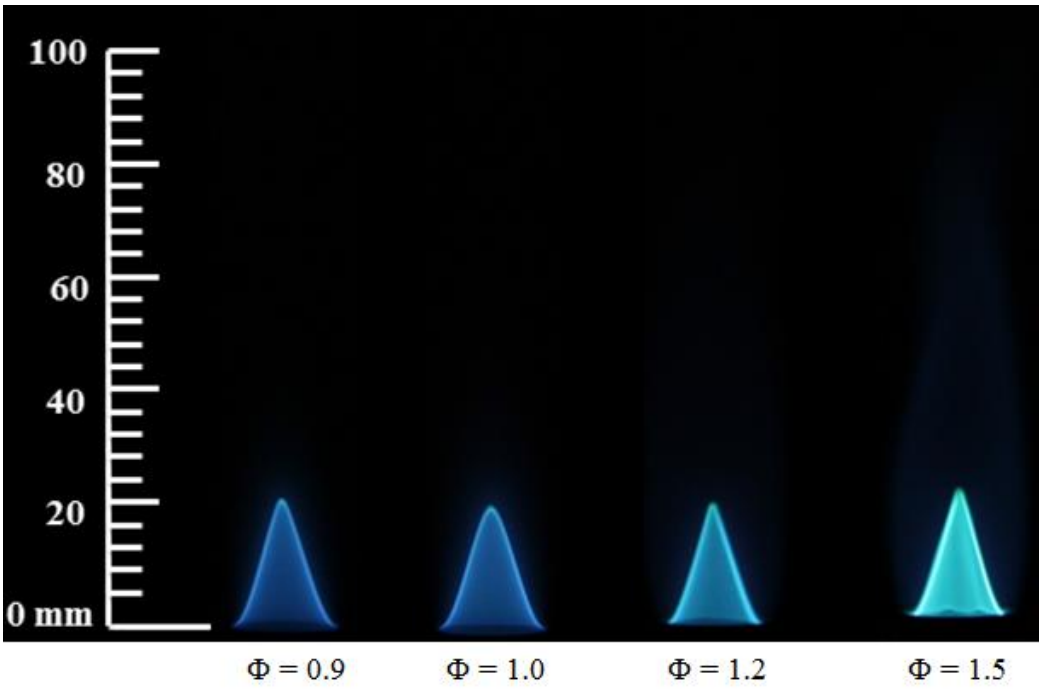

Figure E.43 Flame images of H65MO35 at the tested equivalence ratios

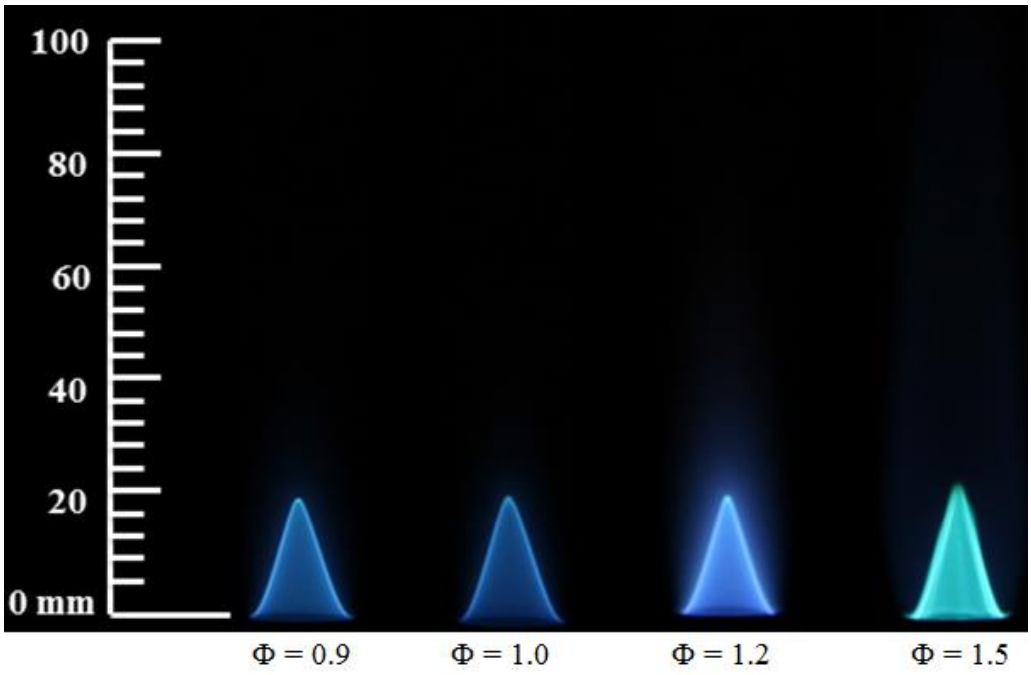

Figure E.44 Flame images of H30MO70 at the tested equivalence ratios

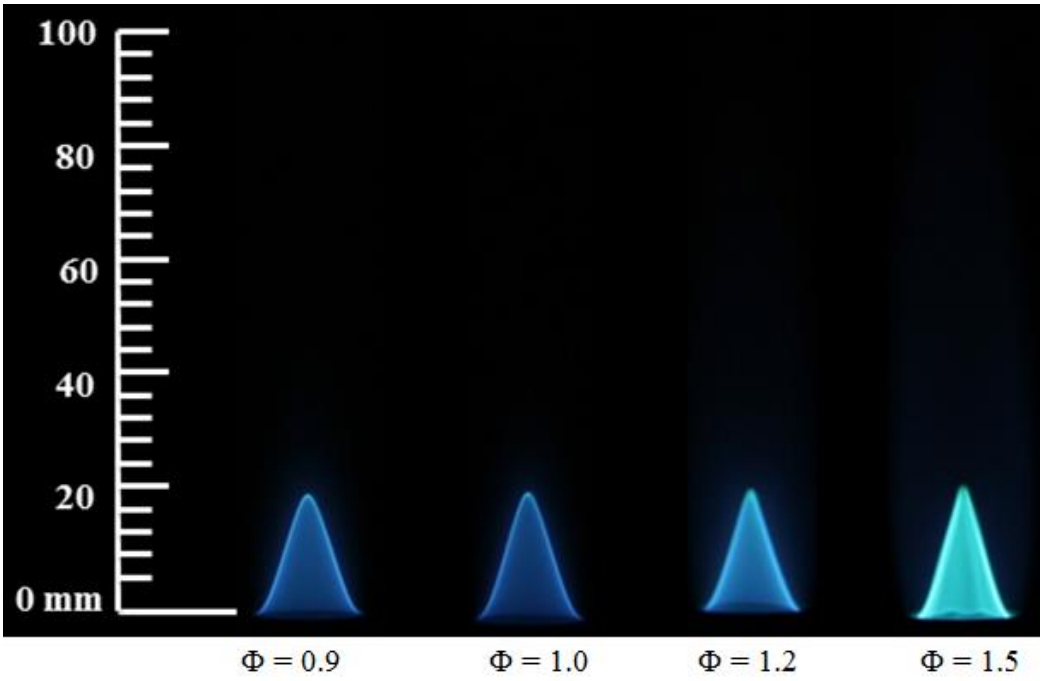

Figure E.45 Flame images of H08MO92 at the tested equivalence ratios

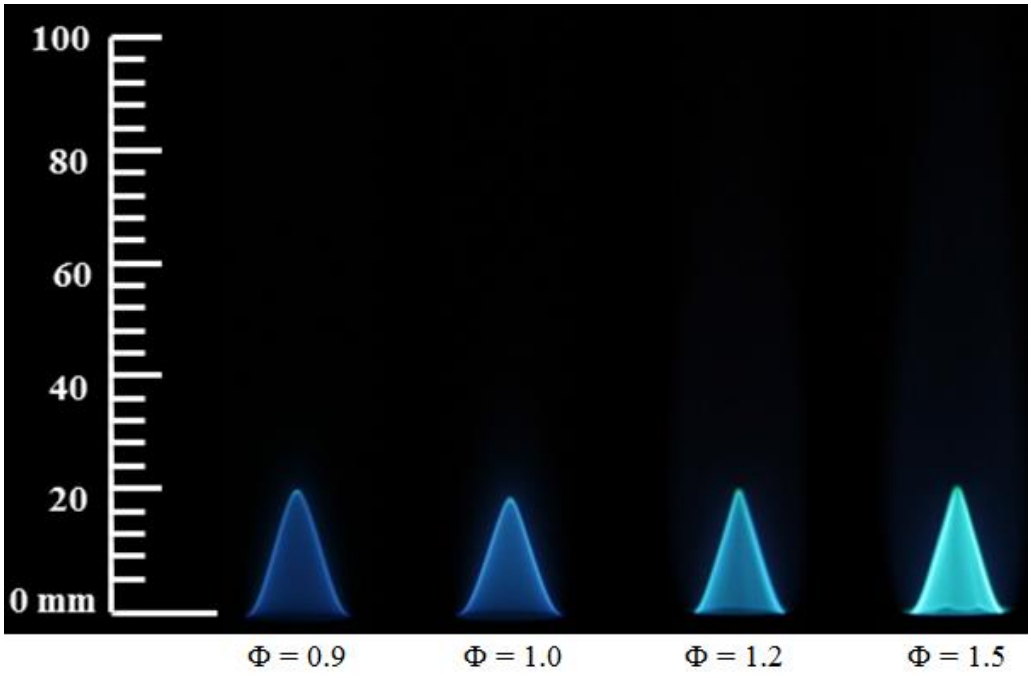

Figure E.46 Flame images of T10MO90 at the tested equivalence ratios

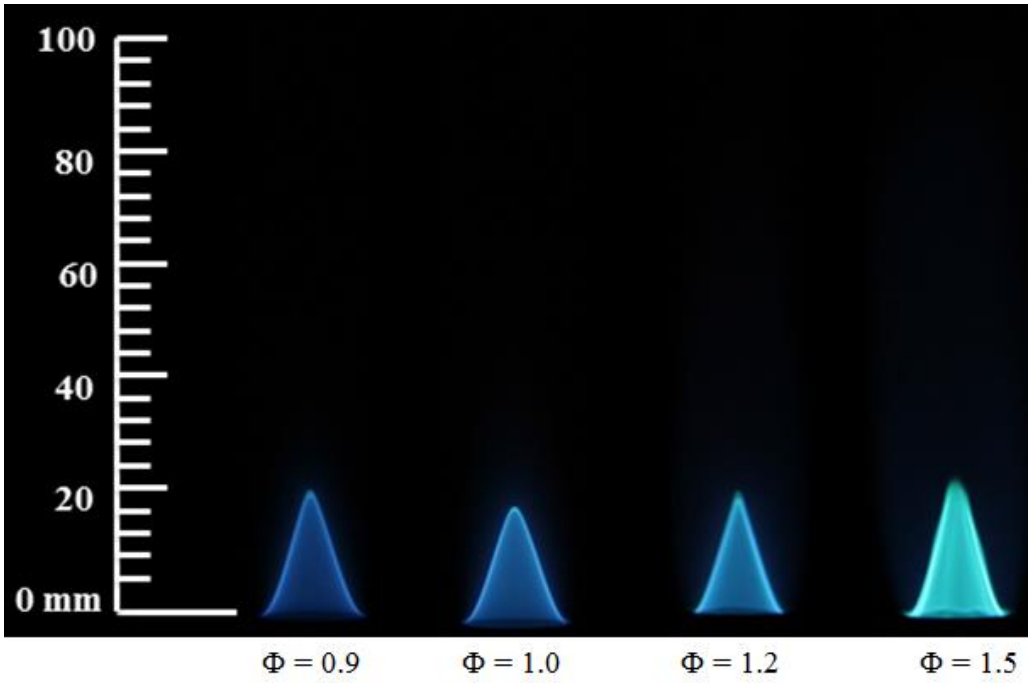

Figure E.47 Flame images of T23MO77 at the tested equivalence ratios

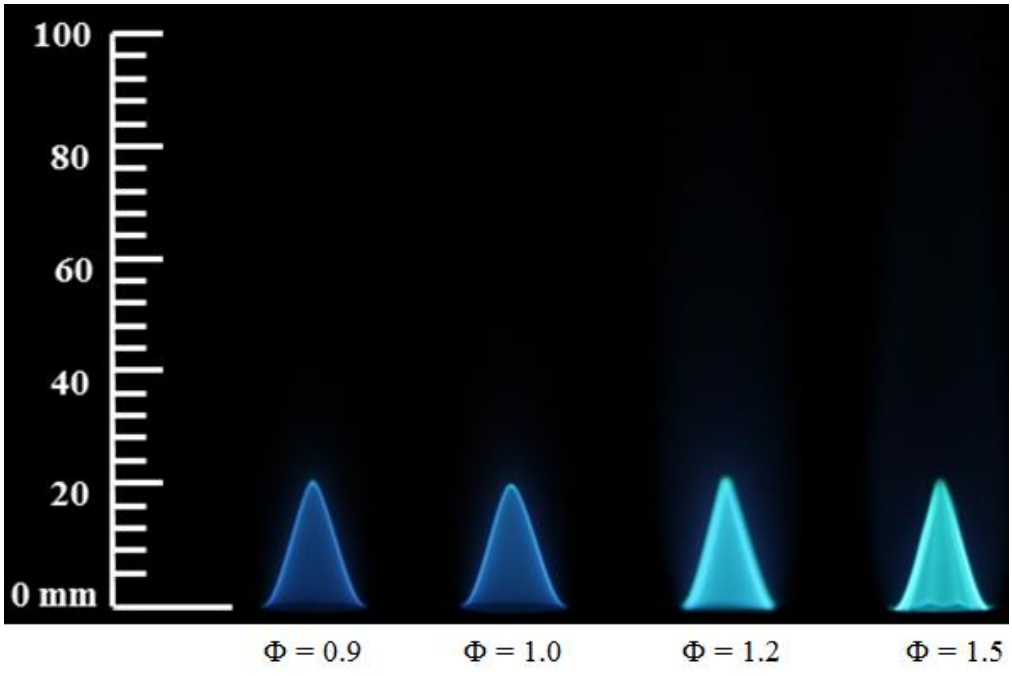

Figure E.48 Flame images of T55MO45 at the tested equivalence ratios

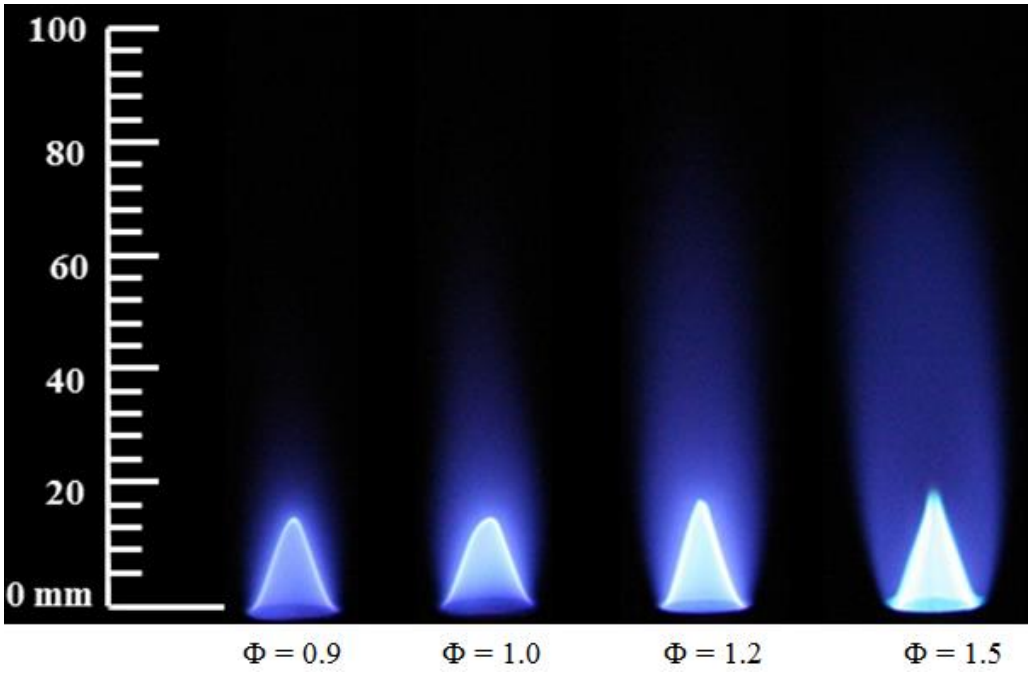

Figure E.49 Flame images of S75D25 at the tested equivalence ratios

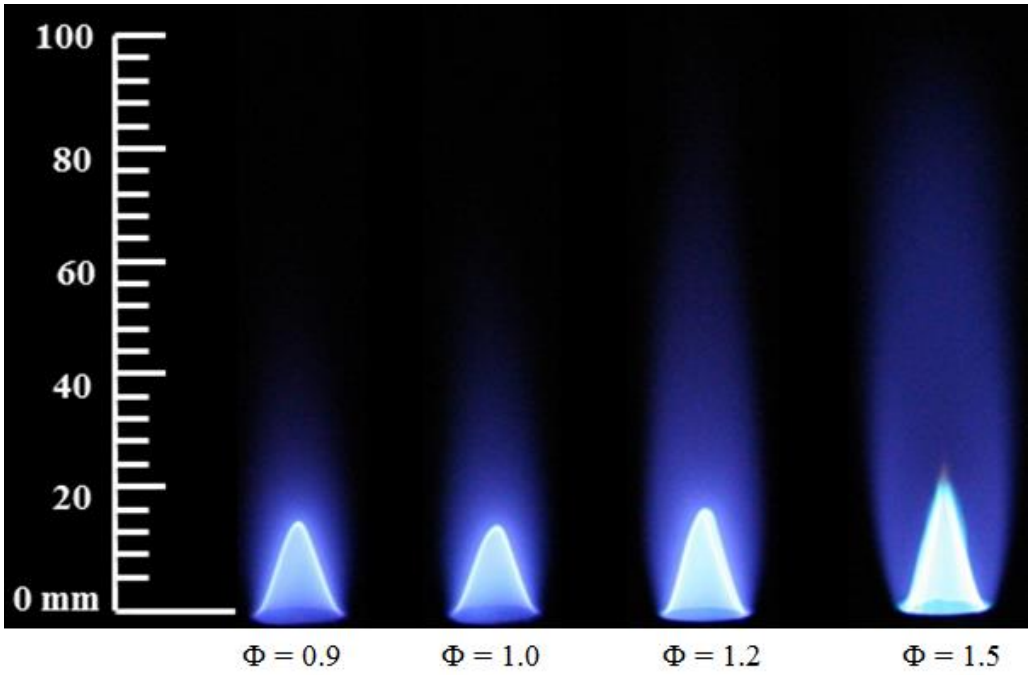

Figure E.50 Flame images of S50D50 at the tested equivalence ratios

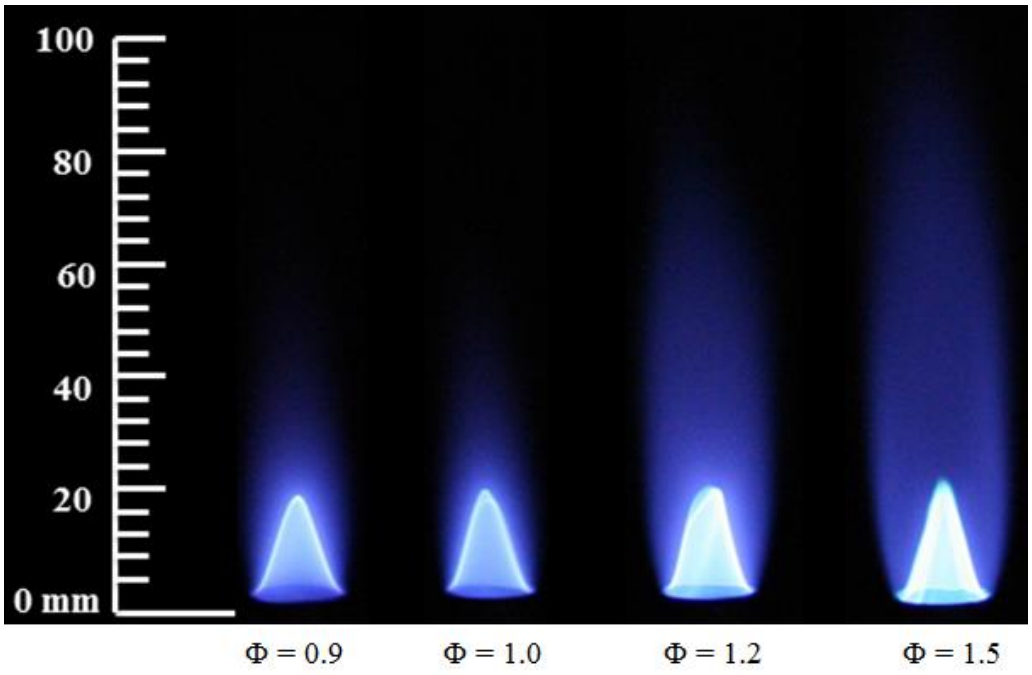

Figure E.51 Flame images of S25D75 at the tested equivalence ratios

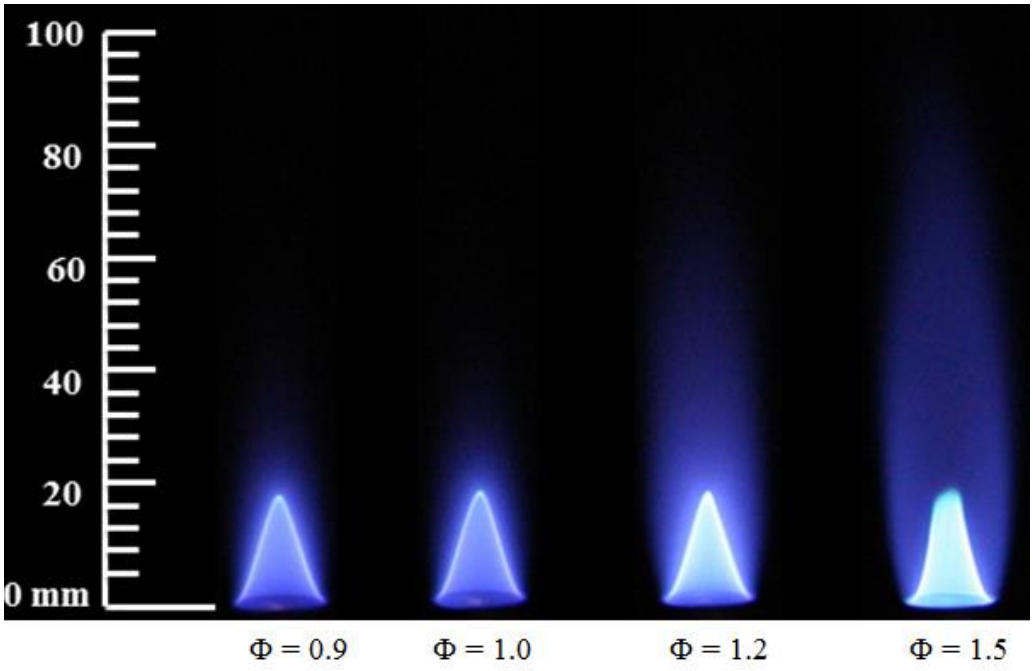

Figure E.52 Flame images of C75D25 at the tested equivalence ratios

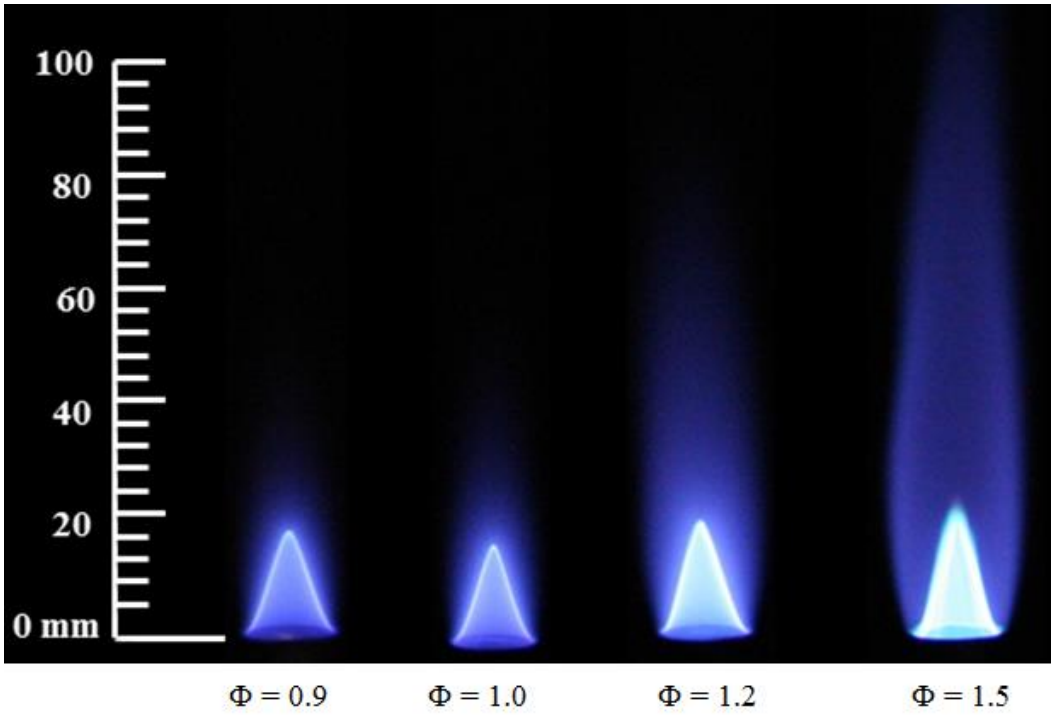

Figure E.53 Flame images of C50D50 at the tested equivalence ratios

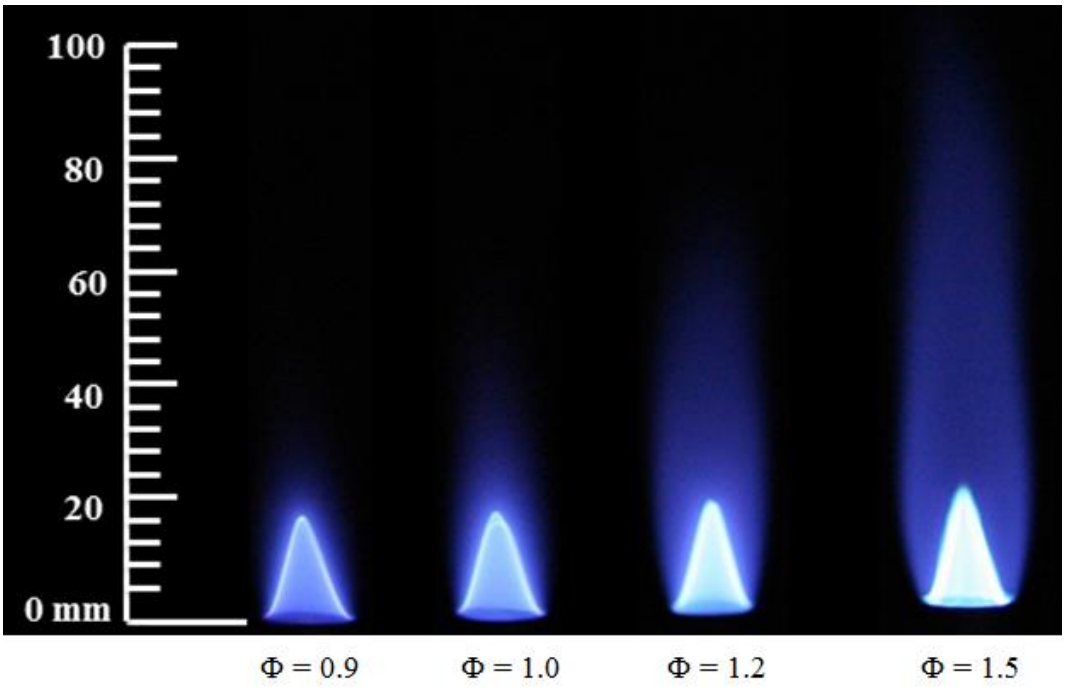

Figure E.54 Flame images of C25D75 at the tested equivalence ratios

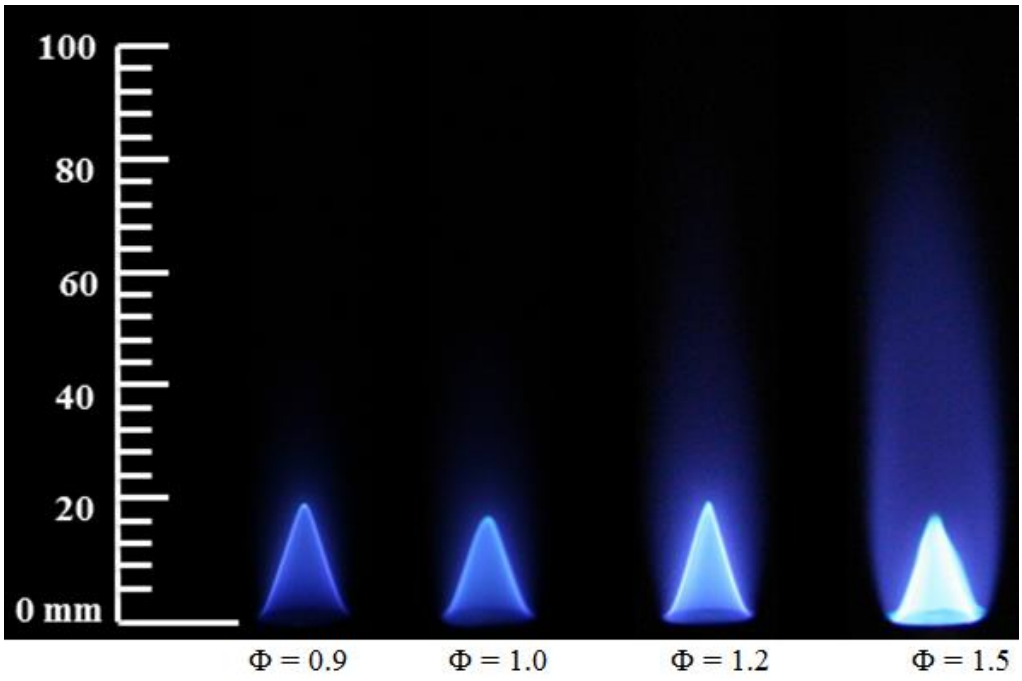

Figure E.55 Flame images of R75D25 at the tested equivalence ratios

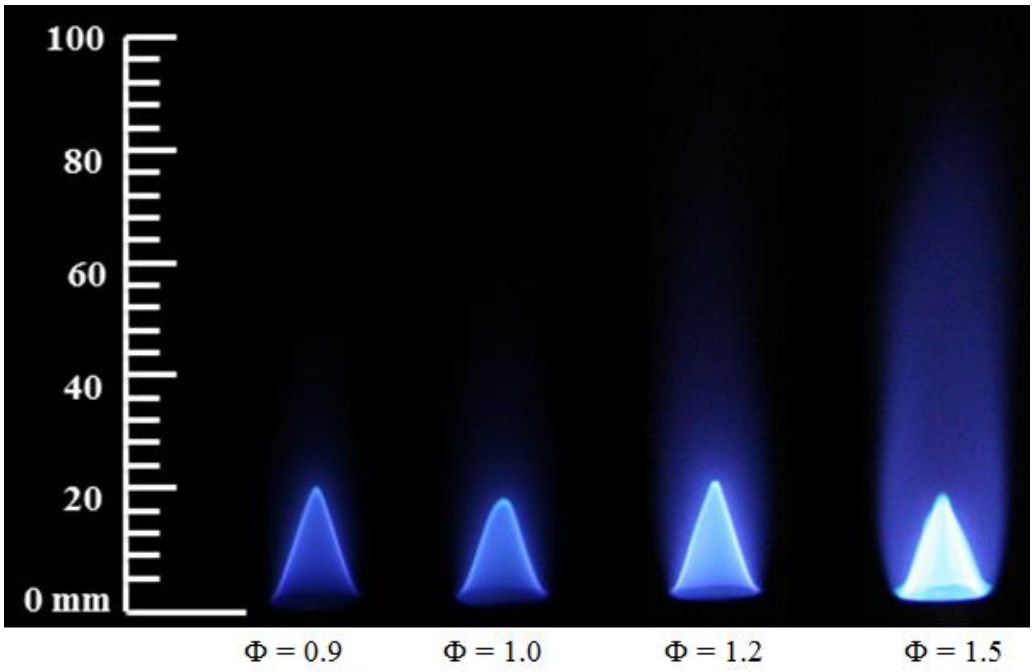

Figure E.56 Flame images of R50D50 at the tested equivalence ratios

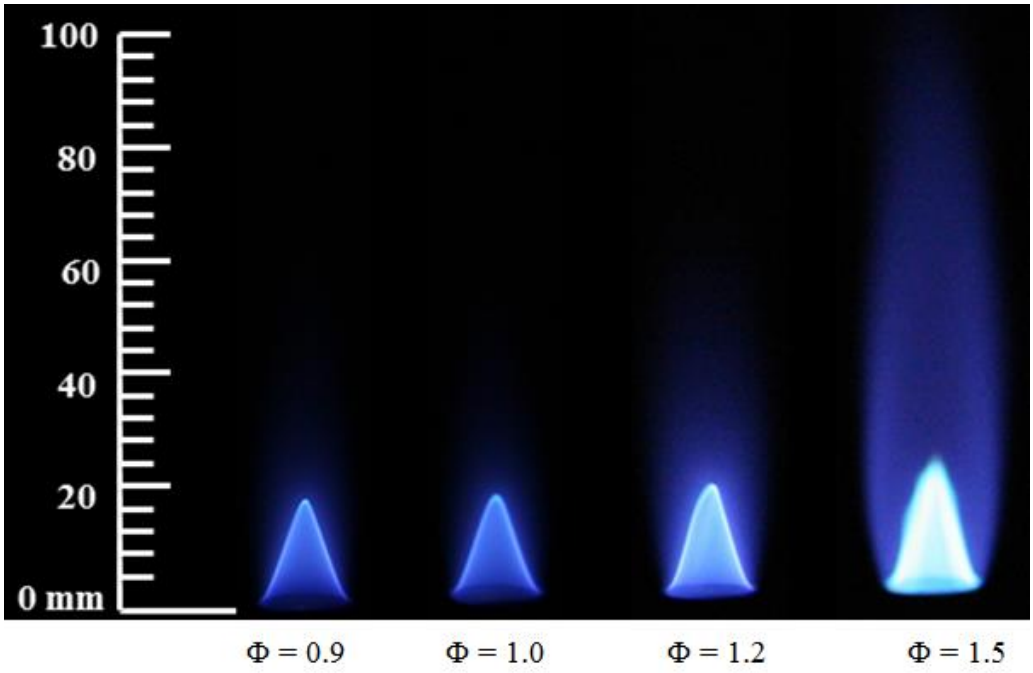

Figure E.57 Flame images of R25D75 at the tested equivalence ratios

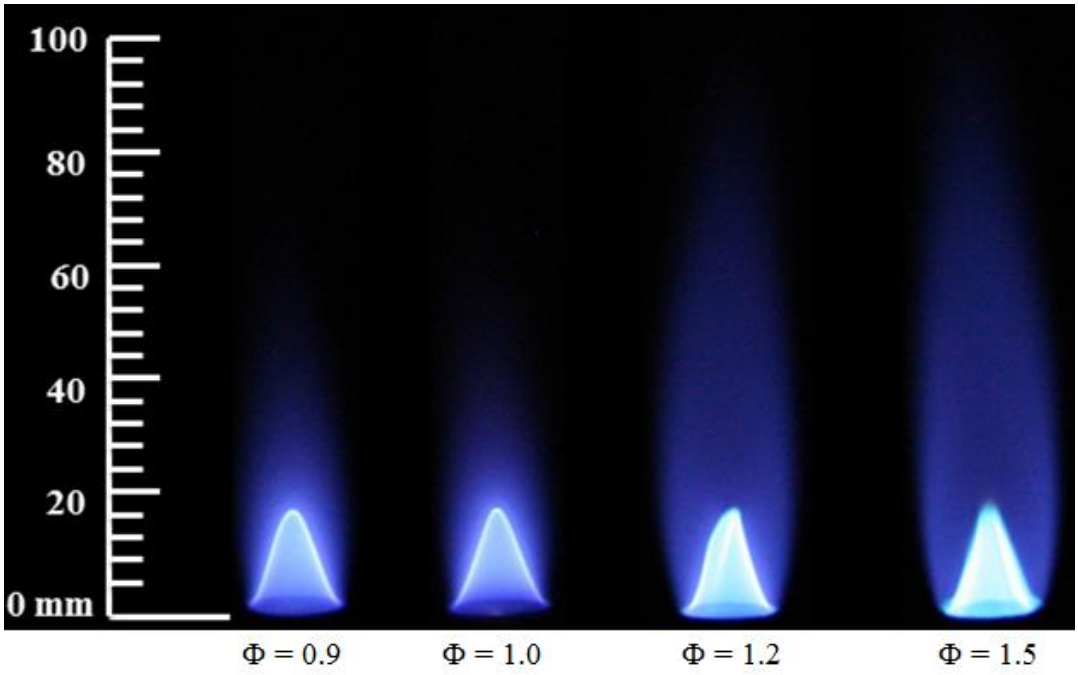

Figure E.58 Flame images of P75D25 at the tested equivalence ratios

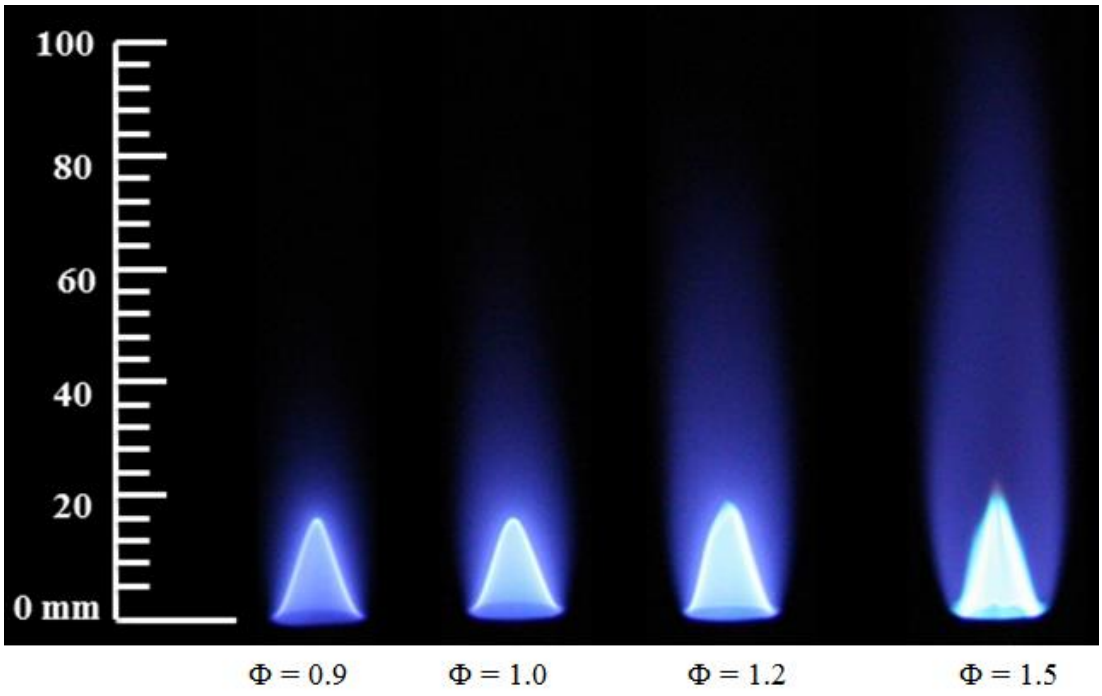

Figure E.59 Flame images of P50D50 at the tested equivalence ratios

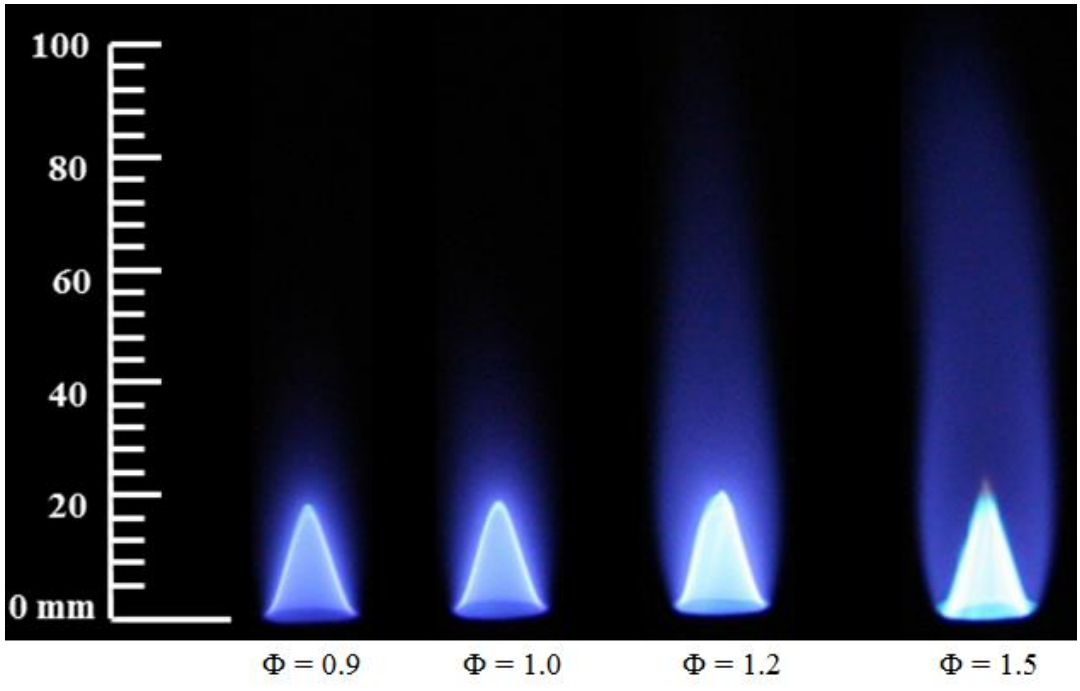

Figure E.60 Flame images of P25D75 at the tested equivalence ratios

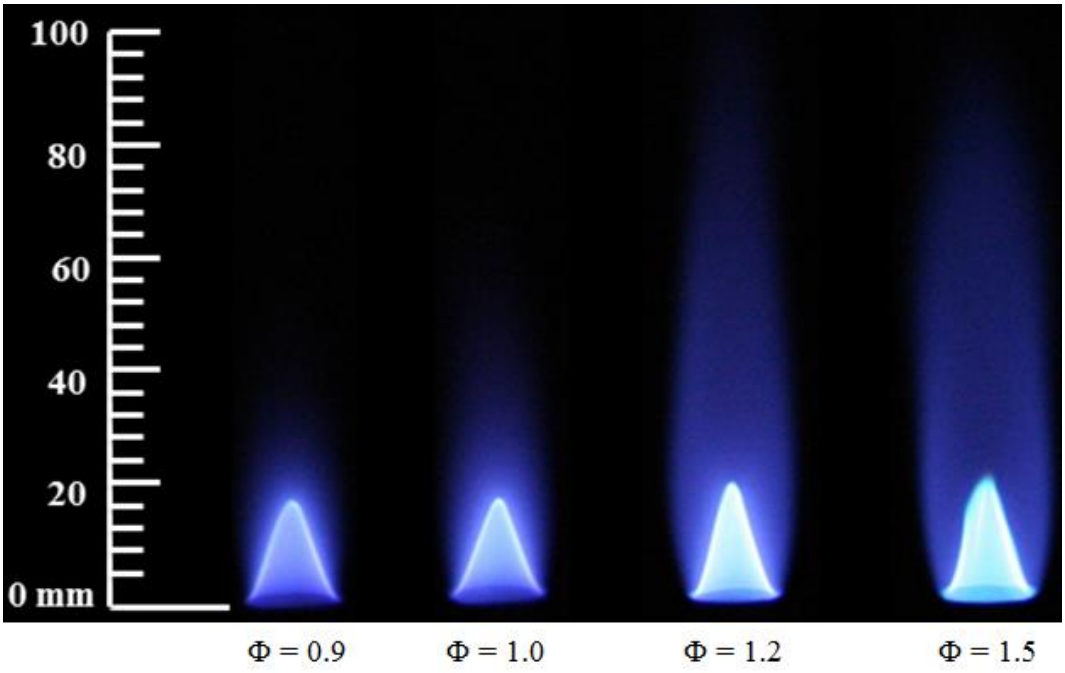

Figure E.61 Flame images of P75J25 at the tested equivalence ratios

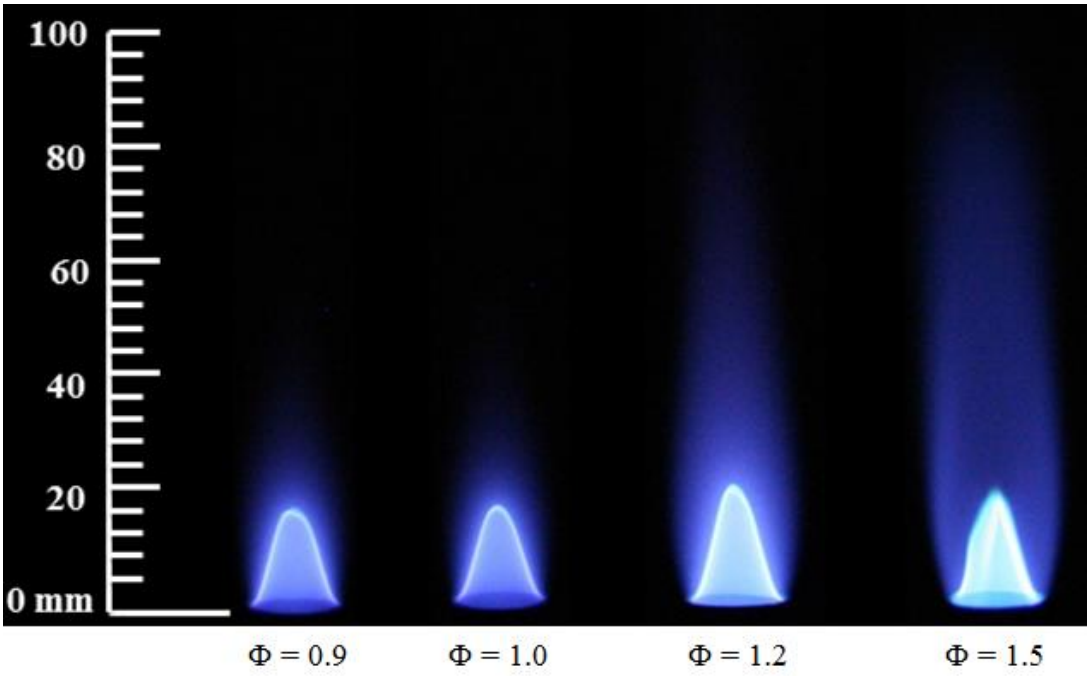

Figure E.62 Flame images of P50J50 at the tested equivalence ratios

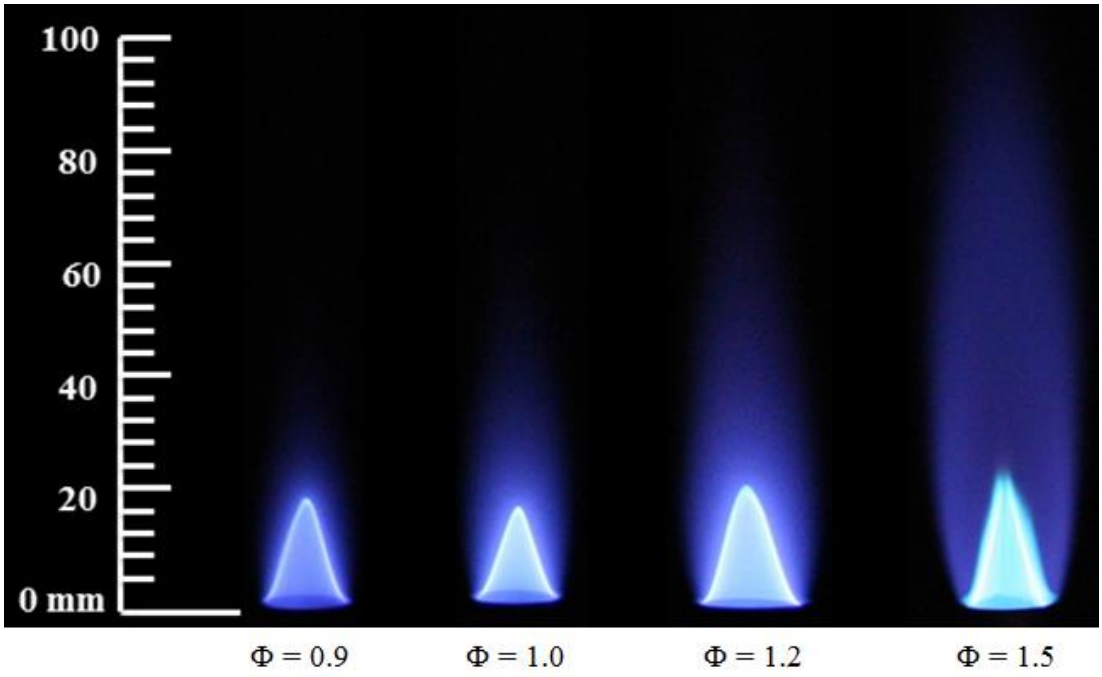

Figure E.63 Flame images of P25J75 at the tested equivalence ratios

APPENDIX F REACTIONS AND PARAMETERS OF NITRIC OXIDE FORMATION MECHANISMS

The Nitrogen chemistry kinetic mechanism (UCSD, 2004) developed by the combustion research group at the University of California, San Diego and their chemical kinetic parameters (refer section 8.3.5) are presented in this section.

S.No	Reaction	A cm^3/(gmol-s)	n	E
1	$O + N_2 \leftrightarrow NO + N$	1.470E+13	0.30	315
2	$N + O_2 \leftrightarrow NO + O$	6.400E+09	1.00	26.3
3	$N + OH \leftrightarrow NO + H$	3.800E+13	0.00	0
4	$N_2 + CH \leftrightarrow HCN + N$	4.400E+12	0.00	92
5	$HCN + O \leftrightarrow NCO + H$	1.400E+06	2.10	25.6
6	$NCO + M \leftrightarrow N+ CO + M$	3.100E+16	-0.50	201
7	$NCO + H \leftrightarrow CO + NH$	5.000E+13	0.00	0
8	$NCO + O \leftrightarrow NO + CO$	4.700E+13	0.00	0
9	$NCO + H_2 \leftrightarrow HNCO + H$	7.600E+02	3.00	16.7
10	$HCCO + NO \leftrightarrow HNCO + CO$	2.350E+13	0.00	0
11	$HNCO + M \leftrightarrow N + CO + M$	1.100E+16	0.00	360
12	$HNCO + H \leftrightarrow NH_2 + CO$	2.200E+07	1.70	15.9
13	$HNCO + O \leftrightarrow NCO + OH$	2.200E+06	2.11	47.9
14	$HNCO + O \leftrightarrow NH + CO_2$	9.600E+07	1.41	35.7
15	$HNCO + OH \leftrightarrow NCO + H_2O$	6.400E+05	2.00	10.7
16	$CH + H_2 \leftrightarrow HCN + H$	3.600E+08	1.55	12.6
17	$CN + H_2O \leftrightarrow HCN + OH$	7.800E+12	0.00	31.2
18	$CN + OH \leftrightarrow NCO + H$	4.200E+13	0.00	0
19	$CN + O_2 \leftrightarrow NCO + O$	7.200E+12	0.00	-1.75
20	$NH + H \leftrightarrow N + H_2$	1.000E+13	0.00	0
21	$NH + O \leftrightarrow NO + H$	9.200E+13	0.00	0
22	$NH + OH \leftrightarrow HNO + H$	4.000E+13	0.00	0

S.No	Reaction	A cm^3/(gmol-s)	n	E
23	$NH + OH \leftrightarrow N + H_2O$	5.000E+11	0.50	8.37
24	$NH + O_2 \leftrightarrow HNO + O$	4.600E+05	2.00	27.2
25	$NH + NO \leftrightarrow N_2O + H$	3.200E+14	-0.45	0
26	$NH + NO \leftrightarrow N_2 + OH$	2.200E+13	-0.23	0
27	$NH_2 + H \leftrightarrow NH + H_2$	4.000E+13	0.00	15.3
28	$NH_2 + O \leftrightarrow HNO + H$	9.900E+14	-0.50	0
29	$NH_2 + OH \leftrightarrow NH + H_2O$	4.000E+06	2.00	4.19
30	$NH_2 + NO \leftrightarrow N_2 + H_2O$	2.000E+20	-2.60	3.87
31	$NH_2 + NO \leftrightarrow N_2H + OH$	9.300E+11	0.00	0
32	$NH_3 + M \leftrightarrow NH_2 + H + M$	2.200E+16	0.00	391
33	$NH_3 + H \leftrightarrow NH_2 + H_2$	6.400E+05	2.39	42.6
34	$NH_3 + O \leftrightarrow NH_2 + OH$	9.400E+06	1.94	27.1
35	$NH_3 + OH \leftrightarrow NH_2 + H_2O$	2.040E+06	2.04	2.37
36	$N_2H \leftrightarrow N_2 + H$	1.000E+08	0.00	0
37	$N_2H + H \leftrightarrow N_2 + H_2$	1.000E+14	0.00	0
38	$N_2H + O \leftrightarrow N_2O + H$	1.000E+14	0.00	0
39	$N_2H + OH \leftrightarrow N_2 + H_2O$	5.000E+13	0.00	0
40	$HNO + M \leftrightarrow H + NO + M$	1.500E+16	0.00	204
41	$HNO + H \leftrightarrow NO + H_2$	4.400E+11	0.72	2.72
42	$HNO + OH \leftrightarrow NO + H_2O$	3.600E+13	0.00	0
43	$NO + CH_3 \leftrightarrow HCN + H_2O$	8.300E+11	0.00	67.3
44	$NO + CH_2 \leftrightarrow HNCO + H$	2.900E+12	0.00	-2.5
45	$NO + CH \leftrightarrow HCN + O$	1.100E+14	0.00	0
46	$N_2O \leftrightarrow N_2 + O$	2.000E+14	0.00	237
47	$N_2O + H \leftrightarrow N_2 + OH$	2.230E+14	0.00	70.1
48	$N_2O + O \leftrightarrow 2NO$	2.900E+13	0.00	96.9
49	$N_2O + OH \leftrightarrow N_2 + HO_2$	2.000E+12	0.00	41.8
50	$NO2 + M \leftrightarrow NO + O + M$	1.000E+16	0.00	276
51	$NO + HO_2 \leftrightarrow NO_2 + OH$	2.100E+12	0.00	-2.01
52	$NO_2 + H \leftrightarrow NO + OH$	3.500E+14	0.00	6.28
53	$NO_2 + O \leftrightarrow NO + O_2$	1.000E+13	0.00	2.51

Rate constants are given by, $k = AT^n \exp(-E_a/R_uT)$

The thermochemical data file and the chemical kinetic reaction mechanism can be found at: http://web.eng.ucsd.edu/mae/groups/combustion/mechanism.html

APPENDIX G AIR ENTRAINMENT CALCULATION FOR JET FLAME REACTOR MODEL

As discussed in section 8.5, the jet flame reactor model was incorporated with the effect of ambient air entrainment in to the flame. This section presents the employed procedure for calculating the air entrainment in to the flame.

The mass flow rate across any given axial plane can be calculated using the equation:

$$\dot{m}_{\text{axial plane}} = \int_0^R (\rho * u * 2\pi r)\, dr$$

$$\dot{m}_{\text{axial plane}} = 2\pi * \int_0^R (\rho * u * r)\, dr$$

$$\dot{m}_{\text{axial plane}} = 2\pi \left[\left(\frac{\rho_1 u_1 r_1 + \rho_2 u_2 r_2}{2} \right) \Delta r_1 + \left(\frac{\rho_1 u_1 r_1 + \rho_2 u_2 r_2}{2} \right) \Delta r_2 \right]$$

Hence the amount of air entrained into the flame between two axial heights can be approximated by subtracting the mass flow across the axial plane at those corresponding heights assuming infinitesimal steps in the axial direction.

The entrained air flow rate at each radial location at a particular flame height was calculated using the equation,

$$\Delta\dot{m}_i = \Delta\dot{m}_{total}\left(\frac{\rho_i u_i}{\sum_{i=1}^{R}\rho u}\right)$$

where $\Delta\dot{m}_i$ is the entrained mass flow at the radial location, i; $\Delta\dot{m}_{total}$ is the total entrained mass flow at the particular axial flame height; ρ_i and u_i are the local density and velocity calculated from the CFD simulations.

APPENDIX H FLAME TEMPERATURE CORRECTION FOR JET FLAME REACTOR MODEL

The jet flame reactor model over predicted the flame temperatures by about 9% - 18% among the tested flames in the computational analysis part of this dissertation (refer to section 8.6). These over predictions of temperature were expected since the heat loss from the flames by gas radiation was not accounted for in the model. As discussed in chapter 7, the appearance of tested flames was completely blue without any yellow luminous region; hence the radiation heat loss due to continuum radiation from soot in these flames is negligible. However, the gas band radiation due to water vapor, CO and CO_2 has significant contribution towards the radiation heat loss at this condition.

In order to illustrate this phenomenon, the radiation heat loss from the flames was estimated (Appendix D.8) and the temperature profiles were corrected for gas band radiation losses with the emissivity factor of combustion products taken into consideration.

According to Stefan - Boltzmann Law,

$$Q = \varepsilon * \sigma * T^4$$

where Q is the amount of heat radiated (W/m^2); ε is the emissivity of the combustion products; σ is the Stefan Boltzmann constant ($5.67*10^{-8}$ W/m^2K^4) and T is the flame temperature (K).

Hence the radiation correction for temperature is given by,

$$\frac{Q_{\text{with loss}}}{Q_{\text{without loss}}} = \left(\frac{T_{\text{with loss}}}{T_{\text{without loss}}}\right)^4$$

$$T_{\text{with loss}} = T_{\text{without loss}} \left(\frac{Q_{\text{with loss}}}{Q_{\text{without loss}}}\right)^{1/4}$$

The emissivity correction is estimated to be ε = 0.935 based on the partial pressures of CO_2 and water vapor from the gas emissivity chart (Hottel, 1927) and this value is found to be fairly constant for all the tested flames in this work.

A sample calculation of this correction for methyl oleate flame is presented in this section. The radiative heat loss for the tested flame was estimated to be 4% (Appendix D.8).

Hence, $\frac{Q_{\text{with loss}}}{Q_{\text{without loss}}} = 0.96$

At 10 mm flame height of MO flame, the axial temperature was predicted as 2050K.

$T_{\text{with loss}} = 2050 * (0.96)^{1/4}$

Flame temperature corrected for radiation $\rightarrow$ $T_{\text{with loss}} = 2009$ K

$T_{\text{corrected}} = \varepsilon * T_{\text{with loss}}$

$T_{\text{corrected}} = 0.935 * 2009 = 1878$ K

Hence the flame temperature corrected for both radiation loss and emissivity is 1878 K.

APPENDIX I NOMENCLATURE

English

A_i	Pre-exponential factor
B_i	Temperature exponent
AF	Air to fuel ratio
EI	Emission index
F	Radiative fraction of heat released
k	Thermal conductivity
L	Distance from flame centerline to pyrheliometer
LHV	Lower heating value
$\dot{m}$	Mass flow rate
MW	Molecular weight
N	Number of carbon atoms
$Q_{background}$	Background radiation
$Q_{corrected}$	Corrected total radiation
Q_{total}	Total flame radiation
R	Universal gas constant
Re	Reynolds number
u	Bulk velocity
t	Time
T	Temperature
Y	Mass fraction

Greek

χ	Mole fraction
Φ	Equivalence ratio
λ	Wavelength
μ	Dynamic viscosity
ρ	Density
τ	Stress tensor

Acronyms

BBO	Beta Barium Borate
CME	Canola methyl ester
CN	Cetane number
CxxDyy	Canola methyl ester/diesel blends (by volume)
CxxPyy	Canola/palm methyl ester blends (by volume)
CxxRyy	Canola/rapeseed methyl ester blends (by volume)
CxxSyy	Canola/soy methyl ester blends (by volume)
DOU	Degree of unsaturation
FDO	Frequency doubler option
HAB	Height above the burner
HxxMOyy	Heptane/ methyl oleate blends (by volume)
HxxTyy	Heptane/toluene blends (by volume)
ICCD	Intensified charged coupled device
IN	Iodine number
JxxDyy	JetA/diesel blends (by volume)
MO	Methyl oleate
OPO	Optical Parametric Oscillator
PLIF	Planar Laser Induced Fluorescence
PME	Palm methyl ester
PxxDyy	Palm methyl ester/diesel blends (by volume)
PxxJyy	Palm methyl ester/Jet A blends (by volume)
PxxRyy	Palm/rapeseed methyl ester blends (by volume)
PxxSyy	Palm/soy methyl ester blends (by volume)
RME	Rapeseed methyl ester
RxxDyy	Rapeseed methyl ester/diesel blends (by volume)
SME	Soy methyl ester
SxxDyy	Soy methyl ester/diesel blends (by volume)
TxxMOyy	Toluene/methyl oleate blends (by volume)